Transactions of the ASME, Journal of Heat Transfer (ISSN 0022-1481) is published monthly by The American Society of Mechanical Engineers, Three Park Avenue, New York, NY 10016. Periodicals postage paid at New York, NY and additional mailing offices. POSTMASTER: Send address changes to Transactions of the ASME, Journal of Heat Transfer, c/o THE AMERICAN SOCIETY OF MECHANICAL ENGINEERS, 22 Law Drive, Box 2300, Fairfield, NJ 07007-2300. **CHANGES OF ADDRESS** must be received at Society headquarters seven weeks before they are to be effective. Please send old label and new address. **STATEMENT from By-Laws.** The Society shall not be responsible for statements or opinions advanced in papers or ... printed in its publications (B7.1, Para. 3).

Journal of Heat Transfer

Published Monthly by ASME

VOLUME 132 • NUMBER 8 • AUGUST 2010

COMMENTARY

PHOTOGALLERY

RESEARCH PAPERS

Conduction

Electronic Cooling

(Contents continued on inside back cover)

This journal is printed on acid-free paper, which exceeds the ANSI Z39.48-1992 specification for permanence of paper and library materials. ♾™
♻ 85% recycled content, including 10% post-consumer fibers.

Journal of Heat Transfer Volume 132, Number 8 AUGUST 2010

The ASME Journal of Heat Transfer is abstracted and indexed in the following:

Applied Science and Technology Index, Chemical Abstracts, Chemical Engineering and Biotechnology Abstracts (Electronic equivalent of Process and Chemical Engineering), Civil Engineering Abstracts, Compendex (The electronic equivalent of Engineering Index), Corrosion Abstracts, Current Contents, E & P Health, Safety, and Environment, Ei EncompassLit, Engineered Materials Abstracts, Engineering Index, Enviroline (The electronic equivalent of Environment Abstracts), Environment Abstracts, Environmental Engineering Abstracts, Environmental Science and Pollution Management, Fluidex, Fuel and Energy Abstracts, Index to Scientific Reviews, INSPEC, International Building Services Abstracts, Mechanical & Transportation Engineering Abstracts, Mechanical Engineering Abstracts, METADEX (The electronic equivalent of Metals Abstracts and Alloys Index), Petroleum Abstracts, Process and Chemical Engineering, Referativnyi Zhurnal, Science Citation Index, SciSearch (The electronic equivalent of Science Citation Index), Theoretical Chemical Engineering

Commentary

Jacopo Buongiorno
Associate Professor of Nuclear Science and Engineering
Massachusetts Institute of Technology

David C. Venerus
Professor of Chemical Engineering
Illinois Institute of Technology

Dear Editor of *ASME Journal of Heat Transfer*,

Since late 2007 we have been leading the International Nanofluid Property Benchmark Exercise, or INPBE, an initiative aimed at eliminating the many inconsistencies in the thermal conductivity database of colloidal suspensions of nanoparticles, also known as "nanofluids." INPBE was supported by a grant from the National Science Foundation, and involved 34 organizations from the US, Belgium, China, France, Germany, India, Italy, Japan, Poland, Puerto Rico, Singapore, South Korea, Switzerland and the UK that participated in the exercise. A complete description of the exercise and its results has been published in an article that recently appeared in the *Journal of Applied Physics* (**106**, 094312, 2009). Viscosity data on the same series of samples collected by 10 INPBE participants will be published in *Applied Rheology*. However, given the general interest in nanofluids and the controversy surrounding their thermal conductivity, we believe the following brief summary may be of interest to the readership of *ASME Journal of Heat Transfer*, and aid the preparation of future research studies.

The thermal conductivity of four sets of identical samples of colloidally stable nanofluids was measured by the participating organizations, using a variety of experimental approaches, including the transient hot wire method, steady-state methods and optical methods, following identical protocols. The nanofluids tested in the exercise were comprised of aqueous and non-aqueous basefluids, metal and metal oxide particles, near-spherical and elongated particles, at low and high particle concentrations, as reported in Table 1.

The data analysis revealed that the data from most organizations lied within a relatively narrow band about the ensemble average, with only few outliers. Specifically, for all water-based samples tested, the data from most organizations deviated from the sample average by $\pm 5\%$ or less. For all PAO-based samples tested, the data from most organizations deviated from the sample average by $\pm 10\%$ or less.

The thermal conductivity enhancement afforded by the tested nanofluids increased with increasing particle loading, particle aspect ratio and decreasing basefluid thermal conductivity, as expected from Maxwells effective medium theory (*A Treatise on Electricity and Magnetism*, Clarendon, Oxford, 1881) and its generalization by Nan et al. (*J. Appl. Phys.* **81**(10), 15 May 1997). Also, Nan et al.'s theory was found to accurately reproduce the INPBE experimental data (see Fig. 1), thus suggesting that no anomalous enhancement of thermal conductivity was observed in the nanofluids tested in INPBE. As such, resorting to the other theories proposed in the literature (e.g., Brownian motion, liquid layering, aggregation) was not necessary for the interpretation of the INPBE database. It should be noted, however, that the ranges of parameters explored in INPBE, while broad, are not exhaustive. For example, only one nanofluid with metallic nanoparticles was tested, and only at very low concentration.

Some systematic differences in thermal conductivity measurements were seen for different measurement techniques. However, as long as the same measurement technique at the same temperature conditions was used to measure the thermal conductivity of the basefluid, the thermal conductivity enhancement was consistent between measurement techniques.

Table 1 INPBE nanofluid samples and summary of thermal conductivity data

Sample No.		Sample desription[a,b]	Measured thermal conductivity[c] (W/m K)	Measured thermal conductivity ratio[c] k/k_f
Set 1	Sample 1	Alumina nanorods (80×10 nm), 1% vol. in water	0.627±0.013	1.036±0.004
	Sample 2	De-ionized water	0.609±0.003	n/a[d]
	Sample 3	Alumina nanoparticles (10 nm), 1% vol. in PAO + surfactant	0.162±0.004	1.039±0.003
	Sample 4	Alumina nanoparticles (10 nm), 3% vol. in PAO + surfactant	0.174±0.005	1.121±0.004
	Sample 5	Alumina nanorods (80×10 nm), 1% vol. in PAO + surfactant	0.164±0.005	1.051±0.003
	Sample 6	Alumina nanorods (80×10 nm), 3% vol. in PAO + surfactant	0.182±0.006	1.176±0.005
	Sample 7	PAO + surfactant	0.156±0.005	n/a
Set 2	Sample 1	Gold nanoparticles (10 nm), 0.001% vol. in water + stabilizer	0.613±0.005	1.007±0.003
	Sample 2	Water + stabilizer	0.604±0.003	n/a
Set 3	Sample 1	Silica nanoparticles (22 nm), 31% vol. in water + stabilizer	0.729±0.007	1.204±0.010
	Sample 2	De-ionized water	0.604±0.002	n/a
Set 4	Sample 1	Mn-Zn ferrite nanoparticles (7 nm), 0.17% vol. in water + stabilizer	0.459±0.005	1.003±0.008
	Sample 2	Water + stabilizer	0.455±0.005	n/a

[a]Nominal values for nanoparticle concentration and size.
[b]PAO=polyalphaolefins lubricant.
[c]Sample average and standard error of the mean.
[d]Not applicable.

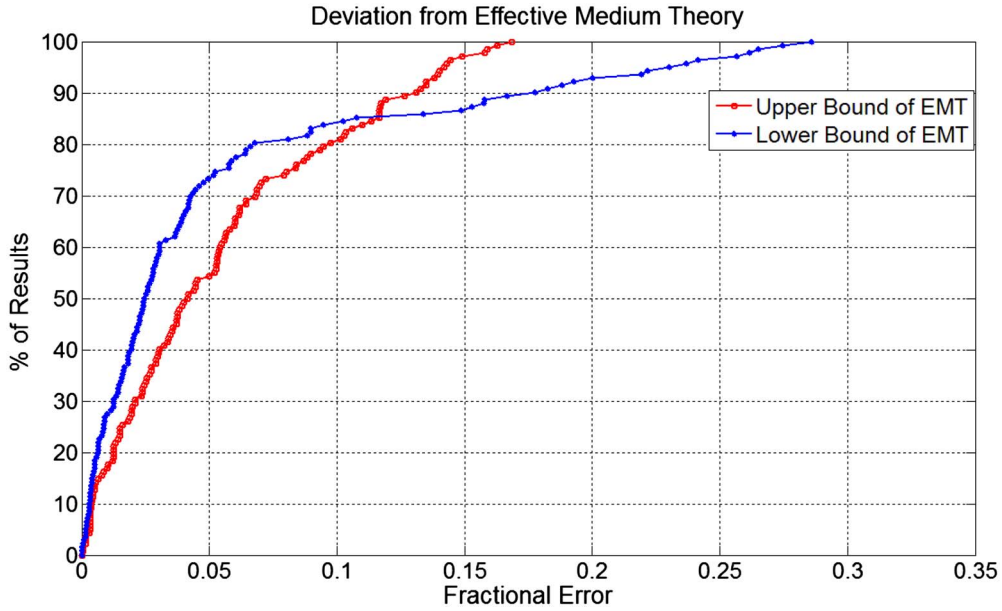

Fig. 1 Percentage of all INPBE experimental data that are predicted by Nan et al.'s theory within the error indicated on the *x* axis. EMT: Effective Medium Theory. Upper bound: zero interfacial thermal resistance. Lower bound: interfacial resistance equal to 10^{-8} m^2K/W.

Journal of Heat Transfer

Heat Transfer Photogallery

The Fourteenth Heat Transfer Photogallery was sponsored by the K-22 Heat Transfer Visualization Committee for the 2009 International Mechanical Engineering Congress and Exhibition (IMECE) held in Lake Buena Vista, Florida, on November 13–19, 2009. The peer-reviewed evaluation for the seven presented entries identified the four entries for publication in the ASME *Journal of Heat Transfer* August issue of 2010.

The purpose of publishing these entries is to draw attention to the innovative features of optical diagnostic techniques and aesthetic qualities of thermal processes. To focus on visualization images and schematics, the text is kept to a minimum and further details should be found directly from the authors. My wish is that the journal readers enjoy viewing these collections, acquire knowledge of the state-of-the-art features, and also promote their participation in the 2010-IMECE Photogallery to be held in Vancouver, Canada on November 12–18 [http://www.asmeconferences.org/Congress10].

The **Call for Photogallery for 2010-IMECE** is also announced in this issue of *Journal of Heat Transfer*.

Kenneth D. Kihm
Department of Mechanical, Aerospace,
and Biomedical Engineering,
University of Tennessee,
Knoxville, TN 37996-2210

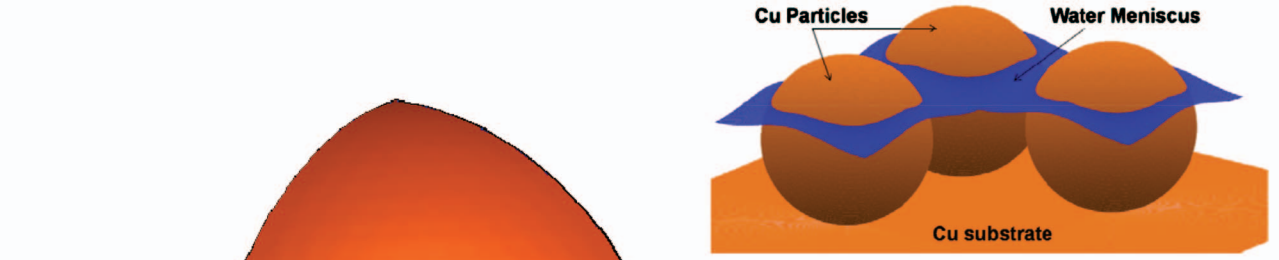

Liquid meniscus formed in the pore of *sintered copper particles* represented by *square-packed spheres* with assumptions *solid-liquid contact angle of 15°*, meniscus level at 1.4×radius and *wick porosity at 0.56*.

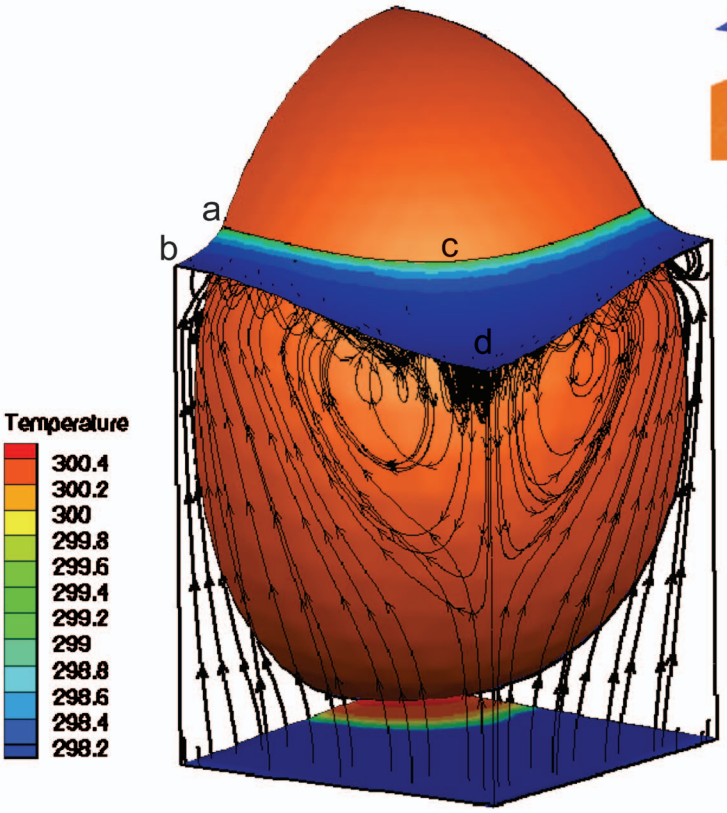

Complex-shaped toroidal vortex due to Marangoni convection observed in the wick pore during evaporation of water from sintered copper particles; temperature contours shown on the interface, liquid inlet and particle surface for solid wall temperature = 300.5 K and vapor temperature = 298 K.

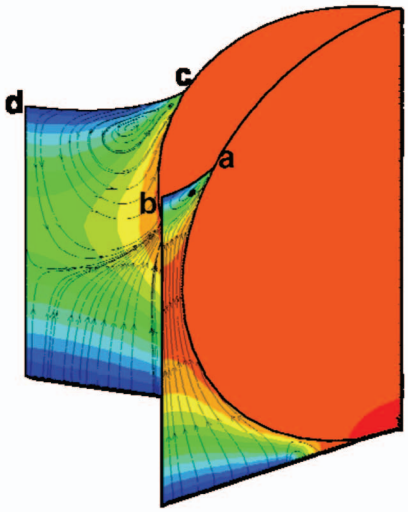

Marangoni vortices shown in the central (c-d) and narrow (a-b) planes in liquid region; vortex diameter is a maximum in the central plane and a minimum in the narrow plane.

Marangoni Convection and Thin-film Evaporation in Microstructured Wicks for Heat Pipes

Ram Ranjan, Jayathi Y. Murthy and Suresh V. Garimella
NSF Cooling Technologies Research Center
School of Mechanical Engineering, Purdue University, West Lafayette, Indiana 47907-2088 USA

An evaporating liquid meniscus is modeled under saturated vapor conditions in wick microstructures. The liquid-vapor interface shape is assumed to be static during evaporation. Liquid-vapor interface shapes in different wick geometries are obtained by solving the Young-Laplace equation using Surface Evolver. Mass, momentum and energy equations are solved numerically in the liquid domain. Evaporation at the interface is modeled using kinetic theory. Owing to non-isothermal evaporation from liquid-vapor interface, complex Marangoni convection vortices are observed below liquid-vapor interface in the pores of sintered particle wicks. More than 80% of total evaporation heat transfer from the meniscus occurs from 20% of the total meniscus area, identified as the thin-film area. Marangoni convection has less than a 5% effect in enhancing evaporation from the liquid-vapor interface for superheats < 5K (pertinent to heat pipes).

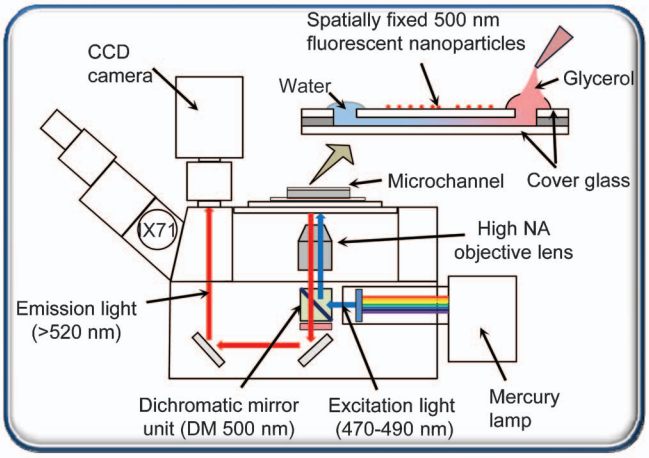

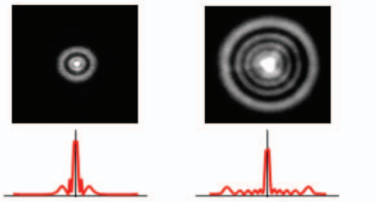

Glycerol (n = 1.477) **Water (n = 1.337)**

Diffraction patterns (Point Spread Function) of 500 nm fluorescent particles seen through different fluids

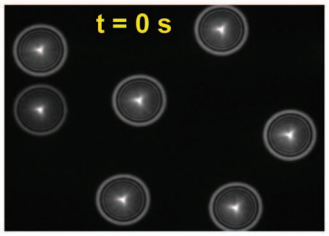

n = 1.337; 100% Water

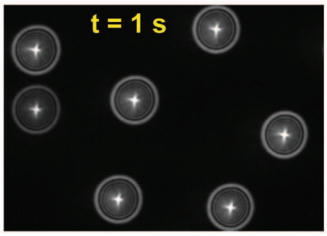

n = 1.355; 19% Glycerol

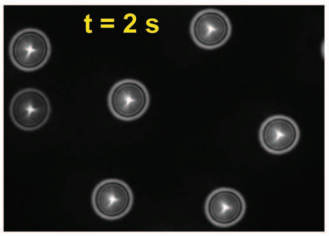

n = 1.385; 39% Glycerol

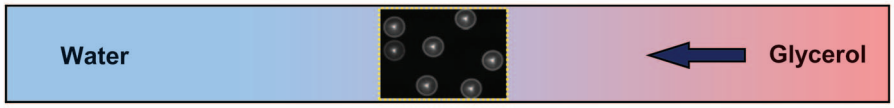

Fixed Imaging Area [107 μm x 80 μm]

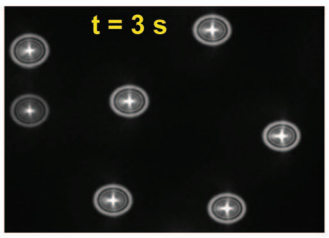

n = 1.422; 65% Glycerol

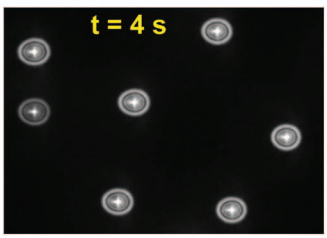

n = 1.458; 87% Glycerol

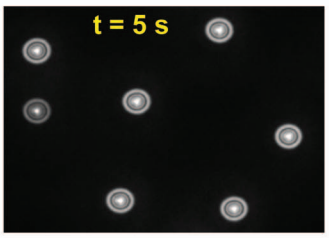

n = 1.477; 100% Glycerol

Nonintrusive Measurements of Mixture Concentration Fields (Water + Glycerol) by Analyzing Diffraction Image Patterns of Spatially Fixed Fluorescent Nanoparticles

Jae-Sung Park
School of Mechanical and Aerospace Engineering
Seoul National University, Seoul, South Korea

Kenneth D. Kihm
Mechanical, Aerospace and Biomedical Engineering
University of Tennessee, Knoxville, Tennessee

The 3-D diffraction image patterns of nanoparticles vary distinctively with the refractive index (RI) of a test medium when the nanoparticles are imaged through the medium, such as water (n = 1.337) or glycerol (n = 1.477). The out-most fringe ring diameter correlates directly with the RI and corresponding mixture concentration, and thus, proper analysis of diffraction patterns provides full-field information on the mixture concentration field. When glycerol flows into water in an open microchannel (100 μm wide), the time-dependent diffraction patterns of spatially fixed fluorescent nanoparticles (500 nm diameter) provide quantitative information on the evolving glycerol concentrations for the mixing region of the two miscible fluids.

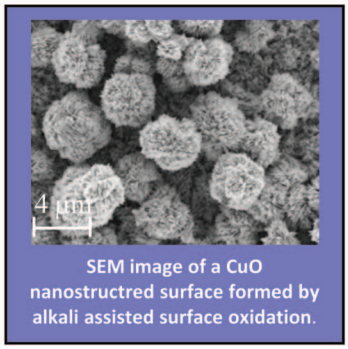

SEM image of a CuO nanostructred surface formed by alkali assisted surface oxidation.

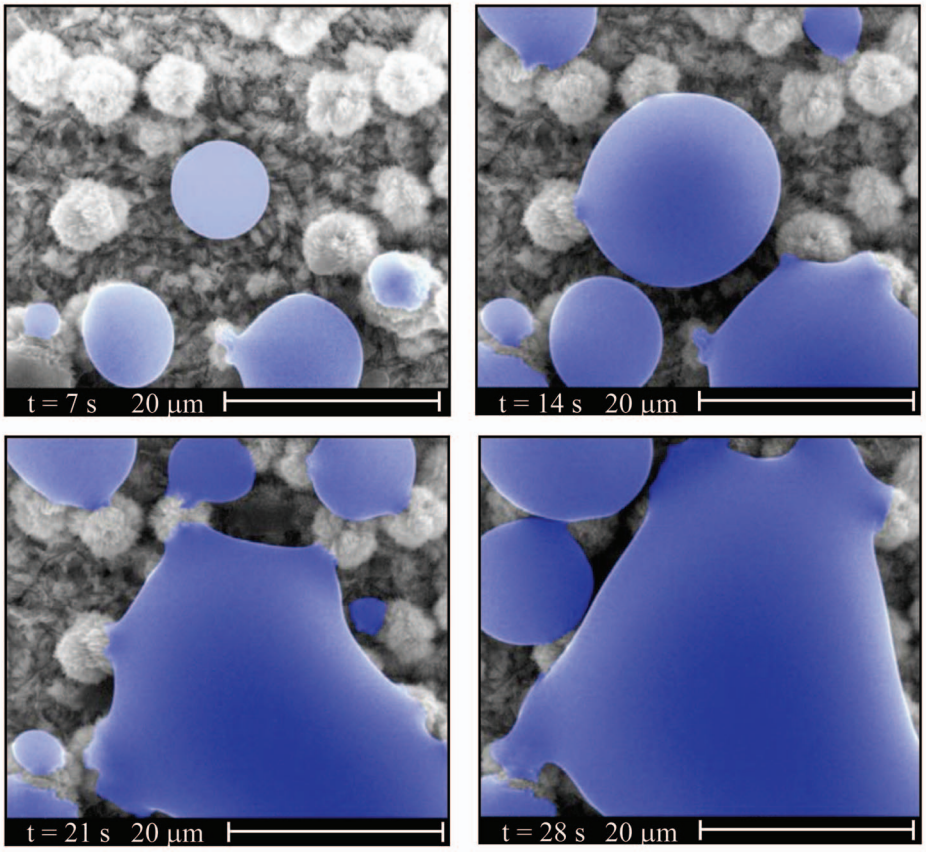

ESEM Imaging of Condensation on a Nanostructured Superhydrophobic Surface

C. Dietz, K. Rykaczewski, A. Fedorov, and Y. Joshi

Woodruff School of Mechanical Engineering, Georgia Institute of Technology, Atlanta, GA 30332

Environmental SEM images of water vapor at 5 Torr condensing on a CuO superhydrophobic surface held at 0°C. The drop growth, pinning on the surface, and coalescence is depicted in this series of images. The flower-like, CuO nanostructures, consisting of a ~3 μm diameter bud and ~200 nm thick petals, are formed by immersing copper into a solution of 2.5 M NaOH and 0.1 M $(NH_4)_2S_2O_8$. The self assembled nanostructures are then functionalized with a fluorinated polymer. The result is a superhydrophobic surface (a surface in which the contact angle is greater than 150°).

Condensation on a superhydrophobic surface may lead to a permanent increase in the heat transfer coefficient. By using an environmental SEM and a Peltier stage, high resolution images of water vapor condensing on these surfaces is visualized. Due to drop pinning on the structures, the drops are not spherical after coalescence. As a result, the surface tends to be wetted by the condensate, bringing in to question whether superhydrophobic surfaces are still superhydrophobic under ESEM operating conditions.

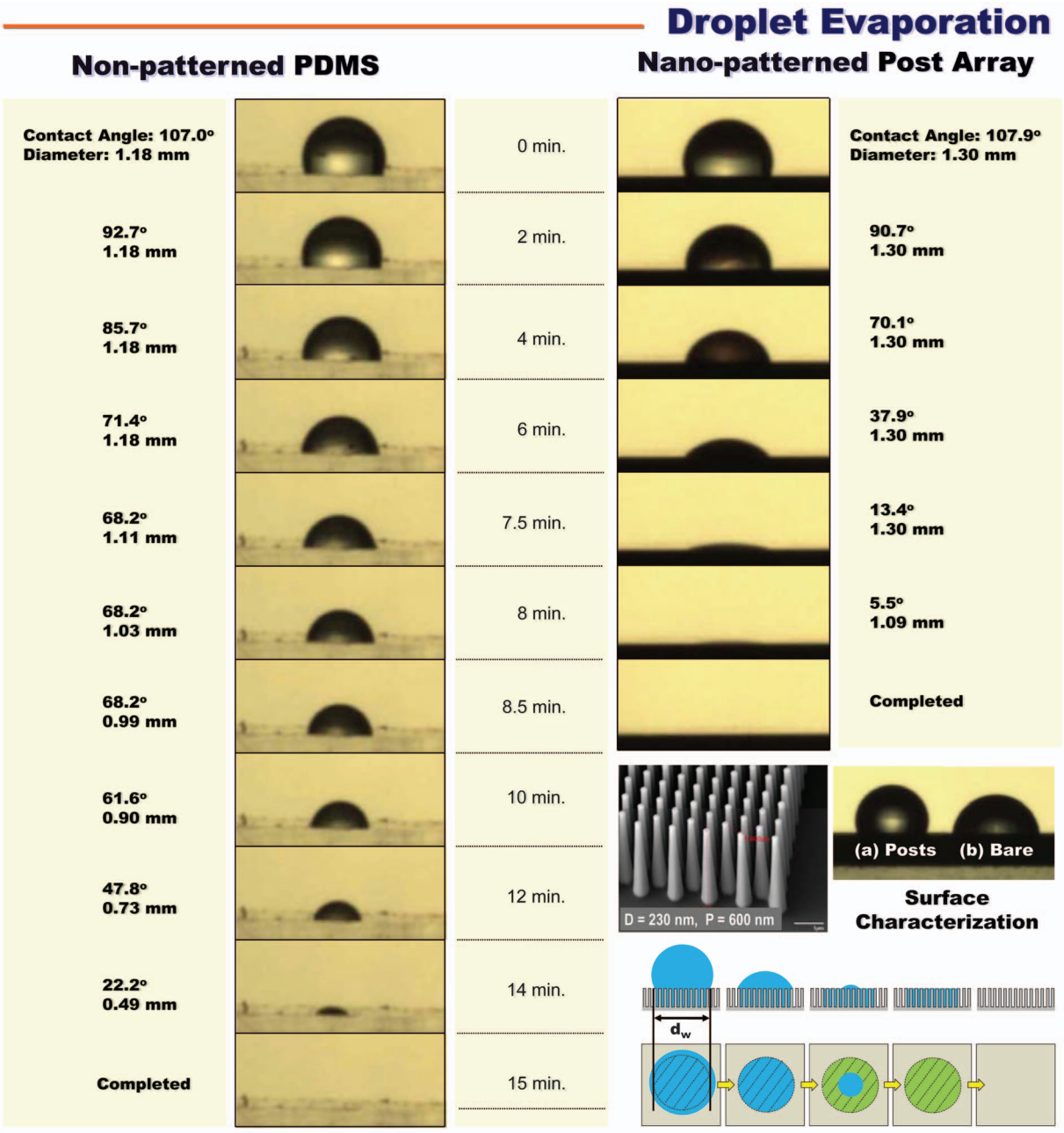

Evaporation Characteristics of Sessile Droplets on Nano-patterned Hydrophobic Surfaces

Dong Hwan Shin*, Seong Hyuk Lee*, Scott Retterer, and Chang Kyoung Choi*****
* Chung-Ang University, Seoul, Korea
** Oak Ridge National Laboratory, Oak Ridge, TN USA
*** Corresponding Author, Michigan Technological University, Houghton, MI USA

This study investigates the evaporating characteristics of 1μl water droplets on the hydrophobic surfaces of nano-diameter posts. The digital image analysis algorithm allowed us to obtain time-dependent contact angles, contact diameters, and center-heights for non-patterned PDMS surfaces and patterned silicon post array surfaces, which have the same hydrophobic contact angles. In the non-patterned surface case, the contact angles have three distinct stages during evaporation. However, in the patterned post array surface case, the contact angles decrease linearly. In the case of post array surfaces the initial wetting diameter remains unchanged until the portion of the droplet above the posts completely dries out. The edge shrinking velocity of the droplet shows nonlinear characteristics, and its magnitude becomes extremely large at the end of evaporation. Additionally it is observed that the droplet contact angle, predicted by Wenzel or Cassie & Baxter relations, are not agreeable for nano-post geometry.

Acknowledgement: *A portion of this research was conducted at the Center for Nanophase Materials Sciences, sponsored at Oak Ridge National Laboratory by the Division of Scientific User Facilities, U.S. Department of Energy. This work was also partially sponsored by the Manpower Development Program for Energy and Resources, supported by the Ministry of Knowledge and Economy (MKE) of the Korean government (SH Lee).*

Hosein Molavi
Researcher
Department of Mechanical Engineering,
Tarbiat Modares University,
Tehran 14115-143, Iran
e-mail: hn.molavi@gmail.com

Ramin K. Rahmani
Affiliate Research Scholar
Department of Mechanical,
Industrial and Manufacturing Engineering,
University of Toledo,
Toledo, OH 43606
e-mail: rkhrahmani@yahoo.com

Alireza Pourshaghaghy
Assistant Professor
Department of Industrial and Mechanical Engineering,
Islamic Azad University of Qazvin,
Qazvin 34197, Iran

Ebrahim Sharifi Tashnizi
Assistant Professor
Department of Industrial and Mechanical Engineering,
Tafresh University,
Tafresh 39518-79611, Iran

Ali Hakkaki-Fard
Graduate Student
Department of Mechanical Engineering,
McGill University,
Montreal, QC, H3A2T5, Canada

Heat Flux Estimation in a Nonlinear Inverse Heat Conduction Problem With Moving Boundary

The estimation of heat flux in the nonlinear heat conduction problem becomes more challenging when the material at the boundary loses its mass due to phase change, chemical erosion, oxidation, or mechanical removal. In this paper, a new gradient-type method with an adjoint problem is employed to predict the unknown time-varying heat flux at the receding surface in the nonlinear heat conduction problem. Particular features of this novel approach are discussed and examined. Results obtained by the new method for several test cases are benchmarked and analyzed using numerical experiments with simulated exact and noisy measurements. Exceedingly reliable estimation on the heat flux can be obtained from the knowledge of the transient temperature recordings, even in the case with measurement errors. In order to evaluate the performance characteristics of the present inverse scheme, simulations are conducted to analyze the effects of this technique with regard to the conjugate gradient method with an adjoint problem and variable metric method with an adjoint problem. The results obtained show that the present inverse scheme distinguishably accelerates the convergence rate, which approve the well capability of the method for this type of heat conduction problems.
[DOI: 10.1115/1.4001305]

Keywords: adjoint problem, estimation of heat flux, gradient-type methods, inverse problem, moving boundary

1 Introduction

The estimation of boundary conditions at the surface of a heat-conducting body from measured temperature profiles is typically called the inverse heat conduction problem (IHCP). Boundary estimation problems have many applications in various branches of science and engineering when surface temperatures and/or heat fluxes need to be established in the inaccessible areas of the surface from corresponding measurements at accessible areas. Specific examples are the determination of extremely high thermal loads during atmospheric reentry of a space vehicle, measurement of the heat flux or temperature inside of a combustion chamber, and determination of the net heat flux at the receding surface of an ablative material under supersonic plasma air stream using an arc jet facility. The solution to these inverse problems is not straightforward, as the unavoidable noise in the data can produce large or even unbounded deviations in the results. This is due to the "ill posed" nature of the IHCP [1].

The IHCP can be efficiently employed when some governing parameters of the heat transfer equations, such as thermal conductivity or heat flux, are not known precisely. Reliability of the inversion relies on the accuracy of the identified model. Prediction of the solution for the IHCP can be achieved via minimization of a sum of the squared error function, which is focused on the difference between the values of the measured temperatures and those obtained by an efficient computational method. The unknown thermal coefficients on the mathematical model (i.e., thermal properties, boundary or initial conditions) that lead to an acceptable value for the aforementioned error function (e.g., based on the iterative regularization method) are the solution of the IHCP. In addition to textbooks [1,2] available in the literature, numerous recent researches discussed the estimation of boundary conditions in the IHCP [3–18]. Most of the previous work was restricted to problems with constant thermophysical properties. However, the material properties are temperature-dependent for most realistic engineering problems. As a result, the heat conduction problem will become nonlinear. The estimation of the unknown boundary conditions for the nonlinear IHCP is more complicated than those for the linear IHCP [13–18]. Among the well-known methods for boundary estimation problems, the gradient methods have received the most attention. Gradient methods are typically applied on the entire time domain and use all of the temperature data simultaneously in estimation of any components of unknowns. Two important categories of gradient methods are the conjugate gradient method (CGM) and variable metric method (VMM). The first is used widely in the field and has been among the highly successful IHCP algorithms. A comprehensive discussion on CGM is found in the textbook of Özisik and Orlande [2]. The second category was recently employed by Kowsary et al. [10] for the estimation of space and time-varying heat flux. The solution of the IHCP by gradient-type methods requires the computation of the sensitivity matrix. This can be achieved with or without the presence of an adjoint problem. In the absence of an adjoint problem, the computation of sensitivity coefficients becomes a very time-consuming process for nonlinear problems [2].

Contributed by the Heat Transfer Division of ASME for publication in the JOURNAL OF HEAT TRANSFER. Manuscript received March 4, 2009; final manuscript received January 15, 2010; published online May 20, 2010. Assoc. Editor: Cholik Chan.

Hence, considerable attention is devoted to use an adjoint equation approach coupled with these methods in order to reduce the computational time. Although the conjugate gradient method with adjoint problem (CGMAP) has been investigated by many researchers, the variable metric method with adjoint problem (VMMAP) has never been examined in the IHCP archival literature, to the best knowledge of the authors. The primary focus of the present research, therefore, is the development and verification of such a technique. Due to the importance of the efficiency in IHCP algorithms, the search for the powerful and robust techniques is an ongoing process. The aim of this work is to introduce a novel approach in gradient-type methods, different from the ones in CGM and VMM, and evaluate its accuracy and efficiency with respect to CGMAP and VMMAP.

Heat flux estimation is particularly more of a challenge when the material at the boundary reaches its phase change temperature. It is worth mentioning that a few publications available in the literature considered the effect of moving boundary on the inverse problems [19–23]. de Oliveira and Orlande [21] applied the CGMAP to estimate the sum of convection and radiation heat flux at the surface of the charring ablator using simultaneously temperature measurement and the measurement of the position of the receding surface. They used an approximate technique (i.e., heat of ablation) for thermal response calculations. In practice, this technique is very simple in concept and straightforward to implement; however, it has several limitations. The heat conduction approximation does not account for material decomposition, where the density, thermal conductivity, and specific heat are functions of temperature, and also vary as the material is pyrolyzed going from a virgin to a charred composite. It also does not account for the pyrolysis gas percolating through the material and the energy absorbed via this process. These methods provide the systems designer with a "ball-park" answer, more as a starting point, but are lacking in that the steady state ablation assumption is usually not valid during the ablation process and will generally overpredict recession [24]. To overcome this problem, Hakkaki-Fard and Kowsary [22] employed CGMAP in order to predict the sum of convection and radiation heat flux at the ablating surface; however, the effect of gas enthalpy adjacent to the wall on the boundary conditions was ignored in their work. Ignoring the gas enthalpy at the wall can cause considerable deviation in predicting the correct temperature in the computational domain. Both studies were assumed that the temperature of the ablating surface is fixed. The selection of an ablation temperature is arbitrary and does not represent the actual surface temperature or pyrolysis/virgin material interface temperature in application. This can result in overly conservative predictions of thermal protection thicknesses to maintain structure temperatures at acceptable limits. Accordingly, if desired accuracy can be obtained for the required input parameters, attempting to characterize the actual chemical and mechanical processes occurring in the material and modeling the boundary layer interactions may enhance the accuracy of in-depth temperature predictions and provide a means of reducing the thermal protection system weight contribution [25]. In addition, there are two main shortcomings in the model developed in aforementioned studies. First, the thermophysical properties of ablators are assumed to be constant. However, their thermophysical properties are greatly affected because of the nature of the ablative materials and their applications (in which they are exposed to a wide temperature range). Typically, temperature-dependent properties augment the nonlinearity problem. Hence, for this kind of problems, estimation of the time-dependent heat flux is essential. Second, both studies used the fixed and constant grid spacing scheme for the solution of the governing equations. It is evident that the difference between the calculated and the measured temperatures appears as a time-dependent source term at fixed distances, depending on the sensor locations, in the adjoint problem. To account for this source term in the numerical solution, the fixed and constant grid spacing scheme is necessary. Employing this scheme in problems with moving boundary creates a large discontinuity in adjacent cell sizes at the receding surface, which could have negative numerical implications on the spatial discretization accuracy [26]. Thus, the lack of a highly efficient and accurate direct calculation schemes can be best recognized. To avoid the shortcomings noted above, Petrushevsky and Cohen [23] considered nonlinear inverse heat conduction with a moving boundary and used an entire domain parameter estimation approach with the heat flux estimation. They recognized the challenging task associated with the adjoint problem and preferred to sacrifice much time for receiving better results. However, in order to reduce the computational time, they provided the prescribed functional form of heat flux by the Fourier series. They assumed that an adequate analytical or numerical direct heat transfer model is available. Nevertheless, their results suffered from the accuracy associated with the Fourier series.

In the view of these shortcomings, the objective of the present study is to fill this gap, carrying out inverse numerical simulations without considering any prior information for the functional form of the unknown heat flux. A contracting grid scheme is employed in the present work, in which the overall number of nodes remains constant during the numerical simulation, and each node moves at a fraction of the surface recession rate to preserve the moving boundary of the studied body. With this method, however, challenges with the adjoint problem are still remained when internal sensors are present within the body. To address this difficulty, the present work focuses on simulated experiments performed in arc-jet wind tunnels, where temperature measurements are taken on the surface of a model, and the heat flux is extracted from these measurements. Thus, the ability to accurately estimate heat fluxes under these extreme conditions is limited by the type of temperature measurement techniques and position measurement schemes implemented. It might be worth mentioning that measurements of the position of the ablating surface can be performed with different experimental techniques, as described in Ref. [27]. Meanwhile, the surface temperature can be measured by using an optical pyrometer. In addition, a novel method is introduced as an optimization technique for minimizing the function of the sum of square errors. To the best knowledge of the authors, this is among the first technical papers (if not the very first one) that deals with the estimation of applied heat flux on moving boundary. Issues related to the computational requirements for a new gradient-type method are important and investigated in this paper.

2 Direct Problem

The physical problem considered here consists of a one-dimensional slab of thickness L, initially at the temperature $T_0(x)$. The surface of the slab at $x=L$ is exposed to a transient heat flux of $q(t)$, while the other surface at $x=0$ is kept insulated. As the slab is heated, it can chemically erode, oxidize, or change phase at the exposed surface, depending on the incident heat flux variation and the material characteristics. Hence, a moving boundary will appear in the considered domain. The mathematical formulation for the physical problem considered here can be written as

$$\rho c_p(T)\frac{\partial T}{\partial t} = \frac{\partial}{\partial x}\left(k(T)\frac{\partial T}{\partial x}\right) + \rho c_p(T)v(t)\cdot\frac{\partial T}{\partial x} \quad 0 \le x \le L(t) \tag{1}$$

$$-k(T)\frac{\partial T}{\partial x} = q(t) \quad x = L(t) \tag{2}$$

$$\frac{\partial T}{\partial x} = 0 \quad x = 0 \tag{3}$$

$$T(x,0) = T_0 \quad 0 \le x \le L(t) \tag{4}$$

where $L(t)$ is presumed known a priori in this problem.

Fig. 1 Initial-to-final grid comparison

3 Numerical Approach

The computational grid consists of equally spaced grid nodes along the x axis. The grid movement scheme employs the Landau [28] coordinate system as presented by Amar et al. [26]. It rearranges the spatial coordinate, in which the nondimensional thickness of the remaining domain at the particular location is always at unity for all times. The Landau coordinate at any location is given as

$$\eta(t) = \frac{x(t)}{L(t)} \tag{5}$$

Therefore, the translation of any node in a given time step can be expressed as follows:

$$\Delta x_i^{n+1} = x_i^{n+1} - x_i^n = \eta_i^n \dot{L}^n \Delta t \tag{6}$$

Consequently, the velocity of any node can be related to the surface recession rate by

$$v_i^n = \eta_i^n \dot{L}_i^n \tag{7}$$

Figure 1 conceptually shows an initial to final grid comparison for a one-dimensional uniform spaced grid.

The internal energy balance equation is discretized using the finite difference method. These equations are implicit in temperature. Since the internal energy balance equation is nonlinear in both the surface recession rate and temperature, a linearization method is used to find a solution. This is done by lagging the thermophysical properties and surface recession rate at one time step for the interior node equations. Then Eq. (1) can be written in finite difference form as

$$\frac{\rho C p_i^n (T_i^{n+1} - T_i^n)}{\Delta t} = \rho v_i^n C p_i^n \left(\frac{T_{i+1}^{n+1} - T_{i-1}^{n+1}}{\Delta x_{i-1}^{n+1}/2 + \Delta x_i^{n+1} + \Delta x_{i+1}^{n+1}/2} \right) + \frac{1}{\Delta x_i^{n+1}} \left(\frac{T_{i+1}^{n+1} - T_i^{n+1}}{\Delta x_{i+1}^{n+1}/2k_{i+1}^n + \Delta x_i^{n+1}/2k_i^n} - \frac{T_i^{n+1} - T_{i-1}^{n+1}}{\Delta x_i^{n+1}/2k_i^n + \Delta x_{i-1}^{n+1}/2k_{i-1}^n} \right) \tag{8}$$

Rearrangement and applying boundary conditions allow the above discretization equations to be as follows:

$$a_i T_{i-1} + b_i T_i + c_i T_{i+1} = d_i \quad \text{for} \quad i = 1, 2, \ldots K \tag{9}$$

where K denotes the number of nodes. Equation (9) can be extended into a tridiagonal matrix system and solved by the tridiagonal matrix algorithm [29].

4 Inverse Problem

In the inverse problem considered in this study, the time-dependent heat flux is regarded as being unknown and to be estimated from measured temperatures by sensors. The solution of the present inverse problem is to be obtained in such a way that the following function is minimized:

$$f(\boldsymbol{q}_i) = \sum_{j=1}^{N} \sum_{m=1}^{M} (T_{j,m}(\boldsymbol{q}_i) - Y_{j,m}) \tag{10}$$

where $Y_{j,m}$ are the measured temperatures and $T_{j,m}$ are the estimated temperatures at the measurement locations obtained by the developed direct code. M is the number of total time steps and N is the number of the used sensors.

Because of the temperature-dependence of thermal properties and the moving nature in the present study, the inverse problem can be considered nonlinear. Among the well-known methods for nonlinear inverse estimation problems, the gradient methods have received the most attention. The minimization procedure of the function (10) by utilizing the gradient-type methods is built as follows:

$$q_{i+1}(t) = q_i(t) - \beta_i d_i(t) \tag{11}$$

where the subscript i is the iteration number, β_i is the optimal step length, and $d_i(t)$ is the search direction vector. The success of these methods depends on effective choices of both the direction $d_i(t)$ and the step length β_i. Depending on the selection of the search direction, various types of gradient methods are existed. The search direction often has the form

$$d_i(t) = -B_i^{-1} \nabla f_i \tag{12}$$

In the steepest descent method, B_i is simply the identity matrix, while in Newton's method, B_i is the exact Hessian $\nabla^2 f_i$ [30]. In the Hestenes–Stiefel form of the conjugate gradient method $(B_i)^{-1}$ has the following form [30]:

$$(B_{i+1})^{-1} = \left(I - \frac{s_i [\nabla f_{i+1} - \nabla f_i]^T}{[\nabla f_{i+1} - \nabla f_i]^T s_i} \right) \tag{13}$$

where $s_i = \beta_i d_i(t)$. In the Fletcher–Reeves version of CGM, $(B_i)^{-1}$ is replaced by [30]

$$(B_{i+1})^{-1} = \left(I - \frac{d_i \nabla f_{i+1}^T}{\nabla f_i^T \nabla f_i} \right) \tag{14}$$

In quasi-Newton methods, B_i is an approximation to the Hessian that is updated at every iteration by means of a low-rank formula. For instance, the BFGS version of VMM uses the following equation for $(B_i)^{-1}$ [30]:

$$(B_{i+1})^{-1} = \left(I - \frac{s_i [\nabla f_{i+1} - \nabla f_i]^T}{[\nabla f_{i+1} - \nabla f_i]^T s_i} \right) (B_i)^{-1} \left(I - \frac{[\nabla f_{i+1} - \nabla f_i] s_i^T}{[\nabla f_{i+1} - \nabla f_i]^T s_i} \right) + \frac{s_i s_i^T}{[\nabla f_{i+1} - \nabla f_i]^T s_i} \tag{15}$$

Due to the existence of common terms in Eqs. (13) and (15), the Hestenes–Stiefel form of the conjugate gradient method is similar to a quasi-Newton method, but the matrix $(B_{i+1})^{-1}$ is not symmetric. To exploit the features of Eq. (13) and a symmetric matrix, one can symmetrize this matrix as $(B_{i+1})^{-1}[(B_{i+1})^{-1}]^T$

$$(B_{i+1})^{-1} = \left(I - \frac{s_i [\nabla f_{i+1} - \nabla f_i]^T}{[\nabla f_{i+1} - \nabla f_i]^T s_i} \right) \left(I - \frac{[\nabla f_{i+1} - \nabla f_i] s_i^T}{[\nabla f_{i+1} - \nabla f_i]^T s_i} \right) \tag{16}$$

This equation compromises between Eqs. (13) and (15), and is suggested to compute the search direction in this paper. The optimal step length β_i is chosen as the one that minimizes the function $f[q(t)]$ at each iteration i. By using a first-order Taylor series approximation of temperature $T(q_{i+1})$ in Eq. (10) and performing the minimization with respect to β_i, the following expression results for the search step size:

$$\beta_i = \frac{\sum_{j=1}^{N} \sum_{m=1}^{M} ((T_{j,m} - Y_{j,m}) \Delta T_{j,m}(d_i))}{\sum_{j=1}^{N} \sum_{m=1}^{M} (\Delta T_{j,m}(d_i))^2} \tag{17}$$

For the implementation of the iterative procedure described here, the sensitivity term $\Delta T_{j,m}(d_i)$ and gradient $\nabla f[q_i(t)]$ are required.

The former is determined with the sensitivity problem, and the latter with the adjoint problem. Both problems are briefly described next.

4.1 The Sensitivity Problem. The sensitivity problem is used to determine the variation in the dependent variables due to changes in the unknown quantity. Therefore, the sensitivity problem can be obtained by assuming that the temperature $T(x,t)$ is perturbed by an amount of $\Delta T(x,t)$, when the unknown heat flux $q(t)$ is perturbed by $\Delta q(t)$ in the specific direction. This perturbation on the temperature causes variations in the temperature-dependent physical properties [2]. The resulting perturbed properties are linearized using a first-order Taylor series approximation. Thus, the following problem for the sensitivity function $\Delta T(x,t)$ can be obtained:

$$\rho\frac{\partial(c_p(T)\Delta T)}{\partial t}=\frac{\partial^2}{\partial x^2}(k(T)\Delta T)+\rho v(t)\frac{\partial(c_p(T)\Delta T)}{\partial x};\quad 0\le x\le L(t) \tag{18}$$

$$-\frac{\partial(k(T)\Delta T)}{\partial x}=\Delta q(t);\quad x=L(t) \tag{19}$$

$$\frac{\partial\Delta T}{\partial x}=0;\quad x=0 \tag{20}$$

$$\Delta T(x,0)=0;\quad 0\le x\le L(t) \tag{21}$$

4.2 The Adjoint Problem. In order to derive the adjoint problem for heat flux, Eq. (1) is multiplied by the Lagrange multiplier function $\lambda(x,t)$, and the resulting expressions are integrated over the time and the space domain. Then the final results are added to the right hand side of Eq. (10) to yield the following expression for the functional $f[q(t)]$:

$$f[q(t)]=\int_{t=0}^{t_f}\sum_{j=1}^{N}[T(x_j,t)-Y_j(t)]^2dt+\int_{t=0}^{t_f}\int_{x=0}^{L(t)}\lambda(x,t)\times\left(\frac{\partial}{\partial x}\left[k(T)\frac{\partial T}{\partial x}\right]+\rho C_p(T)v(t)\cdot\frac{\partial T}{\partial x}-\rho Cp(T)\frac{\partial T}{\partial t}\right)dxdt \tag{22}$$

The variation Δf is obtained by perturbing q by Δq and T by ΔT in Eq. (22), subtracting from the resulting expression the original Eq. (22) and neglecting the second-order terms. We thus find

$$\Delta f[q(t)]=2\int_{t=0}^{t_f}\sum_{j=1}^{N}[Y_j(t)-T(x_j,t)]\Delta T dt+\int_{t=0}^{t_f}\int_{x=0}^{L(t)}\lambda(x,t)\times\left(\frac{\partial^2[k(T)\Delta T]}{\partial x^2}+\rho v(t)\frac{\partial[C_p(T)\Delta T]}{\partial x}-\rho\frac{\partial[Cp(T)\Delta T]}{\partial t}\right)dxdt \tag{23}$$

Using integration by parts, as well as the boundary and initial conditions, the derivatives are transferred to the Lagrange multiplier function. After some algebraic manipulation, the following adjoint differential equation is obtained for the Lagrange multiplier function $\lambda(x,t)$

$$\rho c_p(T)\frac{\partial\lambda}{\partial t}+k(T)\frac{\partial^2\lambda}{\partial x^2}-\rho c_p(T)v(t)\cdot\frac{\partial\lambda}{\partial x}+2\sum_{j=1}^{N}[T(x_j,t)-Y_j(t)]\delta(x-x_j)=0;\quad 0\le x\le L(t) \tag{24}$$

$$-k(T)\frac{\partial\lambda}{\partial x}+\rho c_P v(t)\lambda=2\sum_{j=1}^{N}[T(x_j,t)-Y_j(t)]\delta(x-x_j);\quad x=L(t) \tag{25}$$

$$\frac{\partial\lambda}{\partial x}=2\sum_{j=1}^{N}[T(x_j,t)-Y_j(t)]\delta(x-x_j);\quad x=0 \tag{26}$$

$$\lambda(x,t_f)=0;\quad 0\le x\le L(t) \tag{27}$$

When $\lambda(x,t)$ satisfies the above differential equation, the functional given by Eq. (23) reduces to

$$\Delta f[q(t)]=-\int_{t=0}^{t_f}\Delta q(t)\lambda(L(t),t)dt \tag{28}$$

By definition, the functional increment can be presented as

$$\Delta f[q(t)]=\int_{t=0}^{t_f}\Delta q(t)\,\nabla f[q(t)]dt \tag{29}$$

A comparison of Eqs. (28) and (29) leads to the following expression for the gradient of functional $\nabla f[q(t)]$:

$$\nabla f[q(t)]=-\lambda(L(t),t) \tag{30}$$

5 Stopping Criterion

When the measurements contain no additive noise, the following equation can be used as stopping criterion to terminate the iterative process Eq. (11):

$$\left|\frac{q_i^{k+1}-q_i^k}{q_i^{k+1}}\right|<\varepsilon,\quad i=1,\ldots M \tag{31}$$

where ε is a small number ($O(10^{-4}\sim10^{-6})$). However, in the presence of unavoidable noise embedded in the data, the iterative process is stopped in accordance with the discrepancy principle criterion [31], i.e., upon satisfaction of the following condition:

$$f(\boldsymbol{q})=\sum_{j=1}^{N}\sum_{m=1}^{M}[T_{j,m}(\boldsymbol{q})-Y_{j,m}]^2\approx\sum_{j=1}^{N}\sum_{m=1}^{M}\sigma_{j,m}^2\approx\delta \tag{32}$$

where δ is the integrated error of the measured data and having $\sigma_j(t)$ as standard deviation. If the standard deviation is adopted to be the identical for all data measurements, then the integrated error will have the following statement:

$$\delta=N\times M\times\sigma^2 \tag{33}$$

where σ is the standard deviation of the errors in the temperature. The criterion given by Eq. (32) is called the discrepancy principle, and is based on terminating the procedure as soon as the observation function is in the order of magnitude of the integrated error, which represents the best evaluation expected in the order of the data error.

6 Computational Algorithm for Inverse Method

The computational procedure for the proposed method can be summarized as follows.

Suppose $q_i(t)$ are available at iteration i (as initial estimated values for each iteration).

(1) Solve the direct problem with available estimated $q_i(t)$ to obtain the temperature field in the slab.
(2) Examine the stopping criterion given by Eqs. (31) and (32), depending upon the absence or presence of noise. If not satisfied, proceed to step 3.
(3) Solve the adjoint problem given by Eqs. (24)–(27) to obtain $\lambda(x,t)$.
(4) Calculate the gradient of functional given by Eq. (30).

Table 1 Effect of sensors position on the results

		Initial guess	Proposed method		VMMAP		CGMAP	
Data	Sensor Location	Q (W/m^2)	Number of iterations	q_{err} (%)	Number of iterations	q_{err} (%)	Number of iterations	q_{err} (%)
Noise-free	I	1	26	10^{-10}	38	10^{-10}	52	10^{-10}
Noise-free	II	1	141	3×10^{-7}	133	3×10^{-7}	842	3×10^{-7}
Noise-free	III	1	707	10^{-4}	407	10^{-4}	5000	0.13
Noisy	I	1	7	0.45	9	0.45	9	0.45
Noisy	II	1	10	1.8	17	1.8	16	1.28
Noisy	III	1	11	2.18	19	2.18	20	2.13

(5) Compute descent direction d first by applying Eq. (14) and (15), or (16), and then by Eq. (12).
(6) Set $\Delta q(t)=d_i(t)$ and then solve the sensitivity problem given by Eqs. (18)–(21).
(7) Compute the descent parameter β from Eq. (17).
(8) The updating rule for the gradient-type method, Eq. (11), is then applied to determine the new value for heat flux. Then, return to step 1.

7 Results and Discussion

In order to assess the accuracy and efficiency of the three discussed methods (i.e., the Fletcher–Reeves version of CGMAP, the BFGS form of VMMAP, and the proposed novel method specified by Eq. (16)), the performance of these methods are compared in prediction of the time-varying heat flux via conducting several test cases. All numerical simulations are performed for one-dimensional heat conduction problem in a slab of initial thickness L and over a time interval t_f, using the same computational grid. The measured temperatures $Y(t)$ applied in the function estimation procedure, are obtained from numerical simulations by the developed numerical code. These data, as well as surface position measurements, are perturbed by adding random errors to their exact values, $D_{exact}(t)$.

$$D(t) = D_{exact}(t) + \omega\sigma \tag{34}$$

where ω is a random variable being within -2.576 to 2.576 for a 99% confidence bound. In order to specify the deviation of the estimated heat flux ($\hat{q}(t)$) from the exact one ($q(t)$), relative error is defined as follows:

$$q_{\text{err}} = \frac{\int_{t=0}^{t_f}[q(t)-\hat{q}(t)]^2 dt}{\int_{t=0}^{t_f}[q(t)]^2 dt} \times 100\% \tag{35}$$

7.1 Linear Inverse Heat Conduction Problem Without Surface Ablation. This example considers a one-dimensional planar slab subjected to an unknown heat flux with a step time variation on the front face and an adiabatic rear face, extended from 0 cm to 5 cm. The constant thermal physical properties for this test are

$$L = 0.05 \text{ m}, \quad t_f = 100 \text{ s}, \quad q_m = 1000 \text{ kW/m}^2,$$

$$k = 75 \text{ W/m K}, \quad \rho Cp = 3{,}729{,}000 \quad \text{J/m}^3\text{ K}$$

A computational grid with 51 spatial nodes is used to solve the problem. The number of time steps taken is 101. In order to examine the impact of the sensor position on the results, three situations for sensor position are considered: (I) Sensor records transient temperature on the active surface; (II) sensor is embedded in the body at $x=1$ cm; and (III) sensor is placed at $x=2$ cm. Table 1 summarizes the results obtained for three studied methods with different sensor locations. At the first stage, the potential accuracy of the proposed method using exact data is investigated. The convergence criterion for noise-free data is given by Eq. (31), and the precision is taken to be $\varepsilon=10^{-6}$. As can be seen in Table 1, the closer sensor to the exposed surface produces more accurate results and higher convergence rate for three methods. When the temperature history is taken at an active surface, the results by the proposed method are obtained by only 26 iterations. When applying VMMAP and CGMAP methods, the number of iterations is increased to 38 and 52, respectively. The ratio of the iteration number between the proposed method, CGMAP, and VMMAP for noise-free data is about 2 and 1.5, respectively. It is found that the convergence rate of the developed algorithm based on Eq. (16) is quite faster than one for CGMAP and VMMAP. As the distance of the sensor position from an active surface increases, the superiority of VMMAP to the other two algorithms can be realized. Meanwhile, the convergence rate of CGMAP becomes quite poor. In the case of the sensor location at $x=2$ cm, CGMAP did not meet the ending criterion after 5000 iterations and VMMAP converges to the theoretical profile of heat flux within 407 iteration steps, which is quite smaller than the one for the proposed method. Using the proposed method, the theoretical profile of heat flux is recovered for all sensor locations. The great agreement between the exact solution and the estimated heat flux underlines the capability of the algorithm to find the accurate values in IHCP. It was observed that the difference between the values of the predicted heat flux and the exact solution is indistinguishable, even at the jump point of the heat flux; at the elapsed times of 20 s and 80 s, the difference between the exact value of heat flux and the estimated one is less than 3 W/m^2, which is less than 0.3%.

At the next stage, the verification of the proposed strategy for solving the IHCP with noisy data is considered. The measured temperatures with error $\sigma=3$ are obtained according to Eq. (34). The stopping criterion in this case is based on the discrepancy principle, Eq. (32). A comparison of the estimation error for three methods in Table 1 shows the same order of magnitude for the accuracy. However, the closer sensor to the active surface produces better results in the sense of the relative error. It is observed that the error in the estimated function is also small, in comparison to the added noise, and reliable results can still be obtained when measurement errors are included. Regarding the number of iterations to reach an acceptable result, the current method shows a higher convergence rate than other methods considered here, which shows its advantages over other methods in the presence of real (noisy) data. It should be pointed out that VMMAP and CGMAP converge in the same iteration steps. Figure 2 demonstrates the retrieved heat flux by the proposed strategy (i.e., Eq. (16)) when the temperature measurements at the active surface are applied. The estimated values are in good agreement with the exact values of heat flux; oscillation of the estimated values can be observed. The estimated values for heat flux follow the discontinuities with some dissipation. It may be worth mentioning that using a finer spatial grid did not show any impact on the inverse solution; however, it was observed that smaller value for time step could lead to larger value for the discrepancy principle criterion, as defined by Eq. (32). However, the number of heat flux components is increased. This results in an increase in the error value, which is distributed in the obtained data. As a result, the heat flux profile appears to be highly fluctuating.

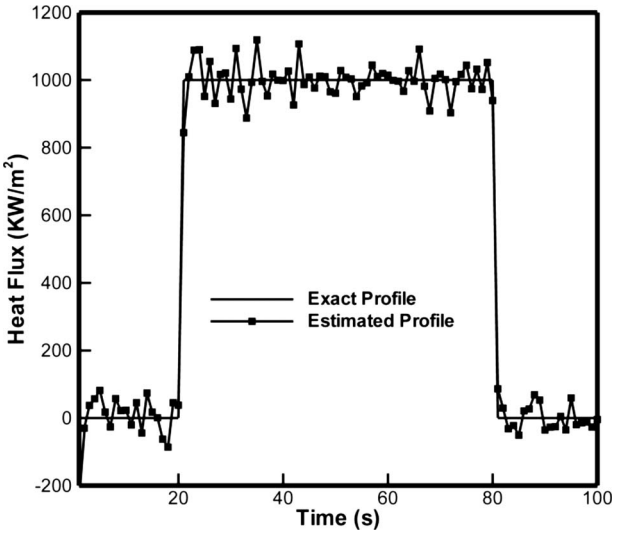

Fig. 2 The exact and estimated values of heat flux (noisy data)

In order to compare the accuracy and convergence rate of the three methods more explicitly, the reduction in their objective functional for two sets of data is plotted in Figs. 3(*a*) and 3(*b*). These figures are related to the first sensor location (i.e., active surface) since it revealed better behavior for meeting stopping criterion. As can be seen, using noise-free data, the proposed method leads to significantly smaller values for the objective function than CGMAP and VMMAP in the same iteration numbers. It might be worth pointing out that having more number of iterations for the noisy data may lead to a small value (e.g., in the order of machine zero) for the objective function; however, this small value does not guarantee better results, and discrepancy principle, Eq. (32), is used to avoid unstable results.

7.2 Inverse Conduction Problem With Variable Properties and No Receding Surface. For the second example, the estimation of heat flux at the surface of the heat-conducting body with temperature-dependent thermophysical properties is investigated. Regardless of the recession rate, the special test case for this illustration is given in Ref. [32]. The considered domain in this example is extended from 0 cm to 5 cm. The considered material is carbon-carbon with properties, as given in Table 2. The thermal conductivity and specific heat are considered as piecewise linear functions of temperature. The simulated data are taken every 0.1 s over an elapsed time of 30 s.

The results obtained using exact and inexact data and two stopping criteria for three methods are presented in Table 3. Using noise-free data, the excellent agreement between the exact solution and the estimated values can be seen. In this situation, with the knowledge of measured temperatures at active surface, the theoretical heat flux profile is recovered and the corresponding relative error is 0.00%. Furthermore, the present method is converged nearly twice as fast as other methods. In this situation, the CGMAP converges faster than VMMAP. This is maybe due to the nature of VMMAP in dealing with nonlinearity of the problem. Under this circumstance, as depicted in Figs. 4(*a*) and 4(*b*), the VMMAP has a slower convergence rate in comparison with two other methods. Figure 3 showed a considerable rate of convergence for VMMAP for every two iteration cycles in linear problems. It might be worth mentioning that the same behavior of the reduction function for the linear problem using VMM without the adjoint problem was also observed in Ref. [33]. As the sensor distance from the exposed surface increases, the proposed method needs considerable smaller iteration steps than other methods for meeting the convergence criterion. In addition, the VMMAP shows better behavior than the CGMAP for satisfying the stop-

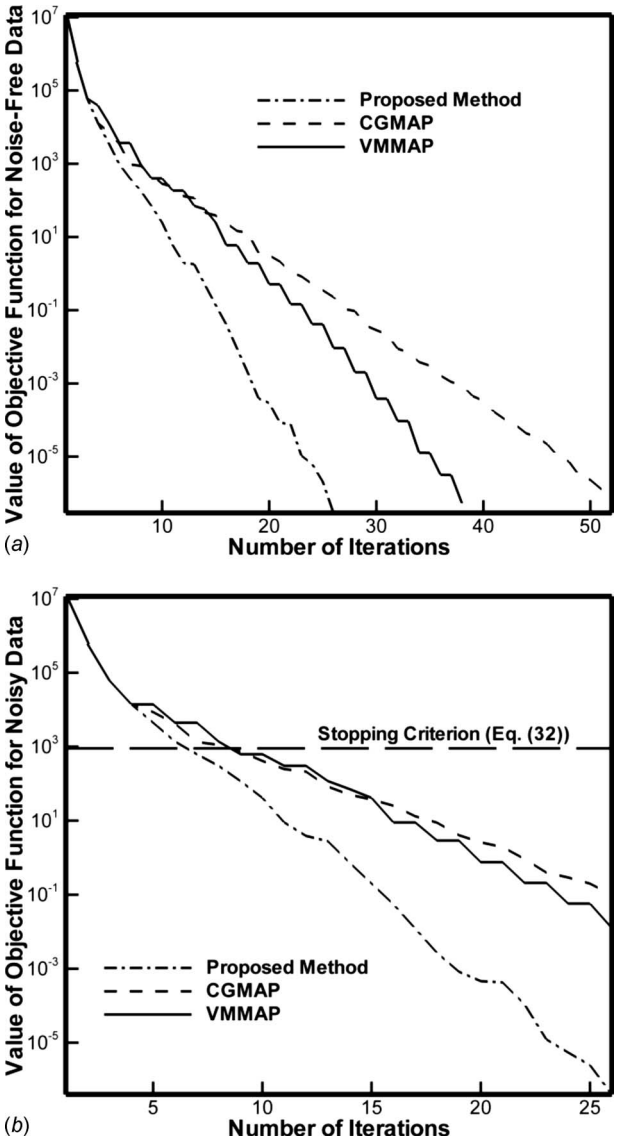

Fig. 3 (*a*) Reduction histories of the objective function for noise-free data (linear problem). (*b*) Reduction histories of the objective function for noisy data (linear problem).

Table 2 Carbon-carbon thermal properties

Temperature (K)	Thermal conductivity (W/m K)	Specific heat (J/kg K)	Density (kg/m^3)
300	123.6	720	1900
400	116.5	990	1900
600	102.8	1410	1900
800	90.6	1650	1900
1000	80.3	1790	1900
1200	71.6	1890	1900
1400	64.9	1950	1900
1600	59.8	2040	1900
1800	57	2070	1900
2000	55.1	2100	1900
2200	53.8	2130	1900
2400	53.1	2160	1900
5000	50	2230	1900

Table 3 Results of estimating heat flux

Data	Sensor distance from active surface (cm)	Initial guess q (W/m^2)	Proposed method: Number of iterations	Proposed method: q_{err} (%)	VMMAP: Number of iterations	VMMAP: q_{err} (%)	CGMAP: Number of iterations	CGMAP: q_{err} (%)
Noise-free	0	1	76	10^{-11}	158	10^{-11}	123	10^{-11}
Noise-free	1	1	93	3×10^{-2}	629	3×10^{-2}	775	3×10^{-2}
Noise-free	2	1	660	0.6	260	0.82	2000	0.57
Noisy (σ=5)	0	1	12	0.012	33	0.012	17	0.012
Noisy (σ=5)	1	1	37	0.083	70	0.08	37	0.067
Noisy (σ=5)	2	1	92	2.34	107	2	98	2.27

ping criterion. However, it is interesting to note that when the sensor is installed at $x=2$ cm, the value of the objective function in the VMMAP cannot be decreased below 2.74, and continuing more iterations results in nonconvergence. Regarding the inexact noisy data, the proposed strategy demonstrates a better behavior since it converges in less iterations, and low convergence rate can be seen for VMMAP. Since the rate of convergence is higher when sensor reports the surface temperatures, results for this sensor location will be discussed here. Figures 4(*a*) and 4(*b*) compare the rate of reduction in the objective function with regard to the number of iterations for each of the three studied methods. Figure 5 shows the recovered heat flux by the proposed method when noisy data are utilized. Each simulated temperature is disturbed by error with standard deviation of 5. The largest difference is monitored at the end of the simulated test. Nonetheless, the relative error in the reconstructed heat flux is small with regard to additive noise to the input data. The comparison between the theoretical and recovered heat flux profiles shows an acceptable agreement. Indeed, the reconstructed heat flux values are well spread out around the exact profile. The results prove the efficiency of the present algorithm.

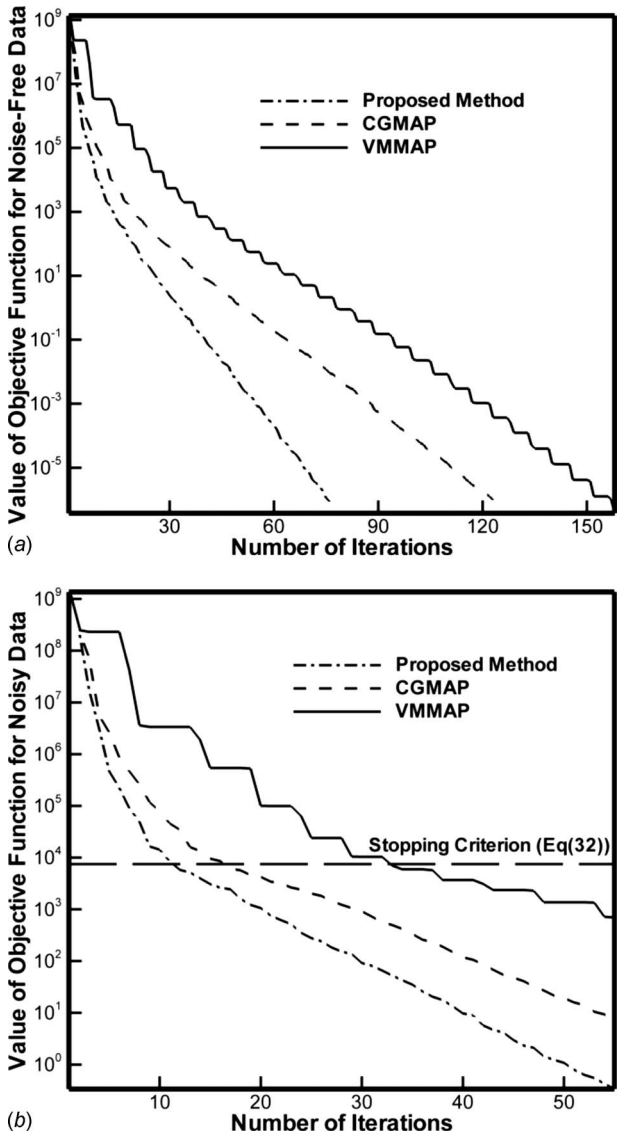

Fig. 4 (*a*) Reduction histories of the objective function for noise-free data (nonlinear problem without moving boundary). (*b*) Reduction histories of the objective function for noisy data (nonlinear problem without moving boundary).

7.3 Nonlinear Inverse Heat Conduction Problem With Moving Boundary. In this section, the developed algorithm will be applied to an inverse problem in ablative composites with moving boundary. Temperature measurements as well as surface recessions will be considered to be collected on the active surface where the unknown heat flux is acting. A test case is taken from Ref. [32] in order to examine the application of the proposed procedure for the inverse estimation of imposed heat flux on the moving boundary. This example solves the same problem presented in Sec. 7.2; however, the ablative material experiences surface thermochemical processes, which are significant enough to cause feasible surface recession. The prescribed values for surface measurements are considered in this example and plotted in Fig. 6. Four simulated sets of data are used in this test case: (1) nonnoisy data by which the inverse algorithm is tested; (2) temperature measurements containing errors with standard deviation equal to 5, according to Eq. (34); (3) available error in the measured

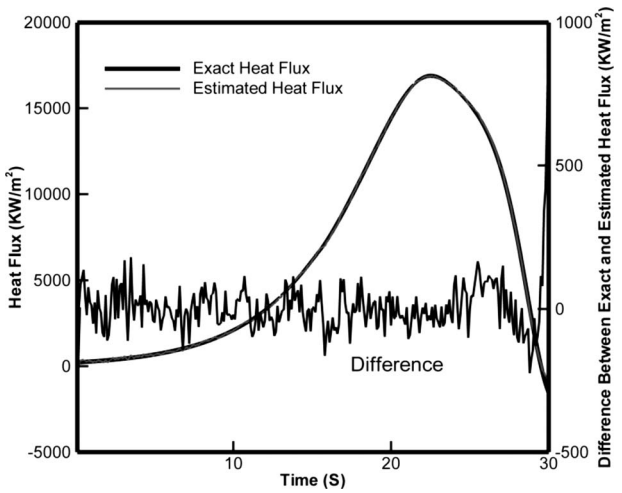

Fig. 5 The exact and estimated values of heat flux (noisy data)

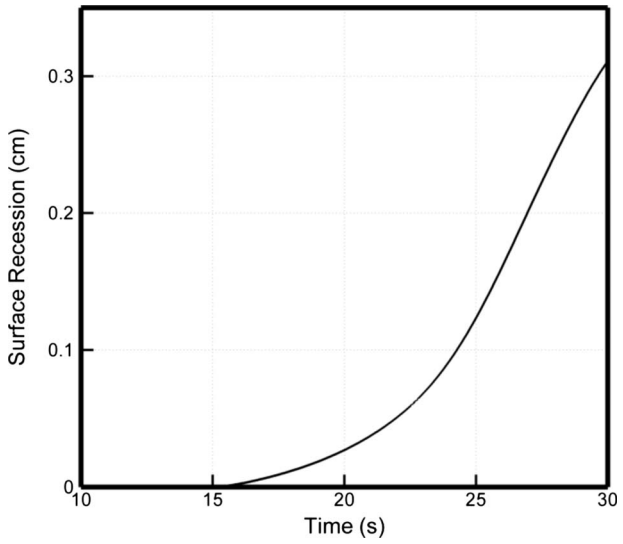

Fig. 6 The surface recession as a function of time

position of the exposed surface with deviations in the range of 0 mm to 1 mm. This situation can be achieved with $\sigma=3.88\times10^{-5}$ and positive values for ω in Eq. (34); and (4) additive noise with $\sigma=5$ and $\sigma=0.0388$ in Eq. (34) for temperature and position measurements, respectively. Before proceeding to the solution, it is appropriate to note that the surface recession rate $\dot{L}(t)$ is computed from the measured position of the active surface by the following equation:

$$\dot{L}(t)=\frac{L^{n+1}-L^{n}}{\Delta t} \tag{36}$$

where superscript n denotes the time level. Since the discrepancy principle is used in the case of errors for temperatures, this method is not capable of stopping the procedure for the inverse problem, when the errors in surface positions are considered. Under this circumstance, the Tikhonov regularization is employed in this study, in order to avoid the difficulties on the inverse problem solutions. The first-order Tikhonov term is added to the objective function (Eq. (10)) to regularize the solution

$$f(q_i)=\sum_{j=1}^{N}\sum_{m=1}^{M}(T_{j,m}(q_i)-Y_{j,m})^2+\alpha\sum_{j=1}^{M-1}(q_{i,j+1}-q_{i,j})^2 \tag{37}$$

where subscript j in the second term of right hand side of Eq. (37) denotes the jth component of the heat flux vector in iteration i. Choosing the optimal value for the regularization parameter α is a challenging task. A very small value for α reduces the temperature sum-of-squares, while it could also create oscillations in the estimated solution; whereas, larger values of α will produce the smooth solution, while it could also increase the value of the objective function. The optimal value for α can be achieved via trial and error procedure.

Combining the Tikhonov regularization method with the gradient-type methods modifies the gradient vector and the search step size in comparison to the traditional method, Eqs. (30) and (17), to stabilize the solution. The gradient of the objective function can be obtained by some manipulation in the procedure of deriving the adjoint problem as follows:

$$\nabla f[q_i(t)]=\begin{cases}2\alpha(q_{i,j+1}-q_{i,j})-\lambda(L(t),t) & \text{for } j=1\\ 2\alpha(q_{i,j+1}-q_{i,j})-2\alpha(q_{i,j}-q_{i,j-1})-\lambda(L(t),t) & \text{for } 2\le j\le M-1\\ -2\alpha(q_{i,j}-q_{i,j-1})-\lambda(L(t),t) & \text{for } j=M\end{cases} \tag{38}$$

The search step size β_i is computed from the following equation:

$$\beta_i=\frac{\sum_{j=1}^{M}\{T_j-Y_j\}\Delta T_j(d_i)+\alpha\sum_{j=1}^{M-1}(q_{i,j+1}-q_{i,j})(d_{i,j+1}-d_{i,j})}{\sum_{j=1}^{M}\{\Delta T_j(d_i)\}^2+\alpha\sum_{j=1}^{M-1}(d_{i,j+1}-d_{i,j})^2} \tag{39}$$

The results of the proposed method are compared with those calculated by the CGMAP and with the VMAPP, and are presented in Table 4. As it is seen, no convergence is yielded with or without errors in the simulated data when the VMMAP is employed. This makes the aforementioned method inefficient for applying on this class of IHCP. The estimation error, as defined in Eq. (35), is quite acceptable and is approximately the same for all cases. When the measured data contain no noise, the evaluated heat flux is retrieved of its theoretical profile and the error is to the machine zero. The convergence rate of the proposed method is 1.5 times of the one for the CGMAP approach. Considering noise in the simulated data can produce fluctuations with various magnitudes, depending on the types of errors in heat flux assessment. In this study, using a trial and error procedure, values of 3.7

Table 4 Results of estimating heat flux

	Initial guess	Proposed method		VMMAP		CGMAP	
Data	q (W/m^2)	Number of iterations	q_{err} (%)	Number of iterations	q_{err} (%)	Number of iterations	q_{err} (%)
Noise-free	1	102	10^{-11}	No convergence	-	149	10^{-11}
Noisy temperature measurement	1	-	1.18×10^{-2}	No convergence	-	-	1.18×10^{-2}
Noisy position measurement	1	-	1.8×10^{-2}	No convergence	-	-	1.8×10^{-2}
Full noisy data	1	-	2.8×10^{-2}	No convergence	-	-	2.8×10^{-2}

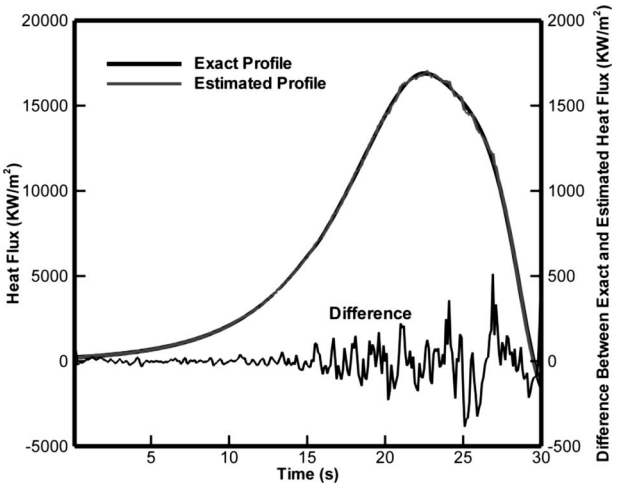

Fig. 7 The exact and estimated values of heat flux (noisy position measurements)

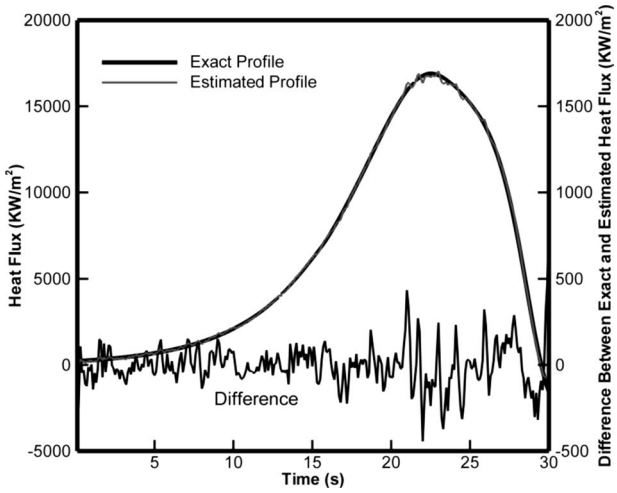

Fig. 9 The exact and estimated values of heat flux (noisy measured temperatures and locations)

$\times 10^{-10}$, 3.5×10^{-10}, and 4×10^{-10} are chosen as the Tikhonov parameter for inexact measured temperatures, noisy measured positions, and fully noisy data, respectively. Figures 7–9 illustrate the heat flux evolution for three sets of noisy data. The results are fairly acceptable and are not greatly affected by the errors. Because the exact heat flux is smooth, the wall heat flux is well reconstructed from temperature measurements taken at the exposed moving surface by the infrared scanner. In the case of additive noise in position measurements, the surface recession rate $\dot{L}(t)$ is depicted in Fig. 10 and is compared with its theoretical profile. Since this profile is not good enough, one should not expect that the results be as accurate as with the one obtained by considering noise in measured temperatures. As observed in Fig. 7, when the time reaches toward the end of the simulated experiment, the error in the measured recession rate augments, Fig. 10, and larger error is produced in the estimated heat flux. This can be best realized after the elapsed time of 27 s, where the surface position rate has maximum error. The results underline clearly the advantage of the proposed method when estimating time-dependent heat flux is demanded in the presence of moving boundary.

8 Conclusions

A novel method for accurate and efficient estimation of heat flux in the linear and nonlinear heat conduction problems under different conditions was presented. A systematic study was employed to explore the performance characteristics of three different versions of gradient-type methods associated with an adjoint problem in dealing with three different types of IHCP, in which the special attention was given to the importance of the moving boundary and its effects on the estimation procedure. Furthermore, exact and inexact surface position and surface temperature measurements were utilized for estimating the heat flux at the receding surface. The Tikhonov regularization technique was utilized to stop the iterative procedure before minimizing the objective function to protect the results from the noise in the data. Among further developments, introducing the adjoint feature of VMM and also a new search direction on the gradient-type methods can be mentioned. Performance comparison of the three methods revealed that all studied algorithms could produce results with the same order of accuracy, while the proposed method needs less number of iterations to converge. For the linear problem, the proposed method converges faster than CGMAP. Moreover, the ac-

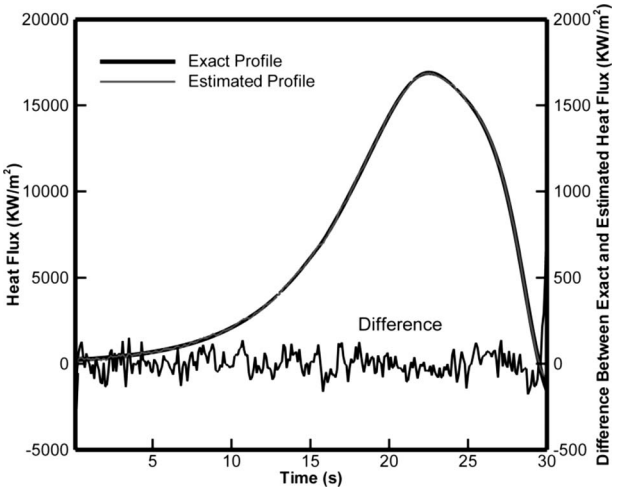

Fig. 8 The exact and estimated values of heat flux (noisy measured temperatures)

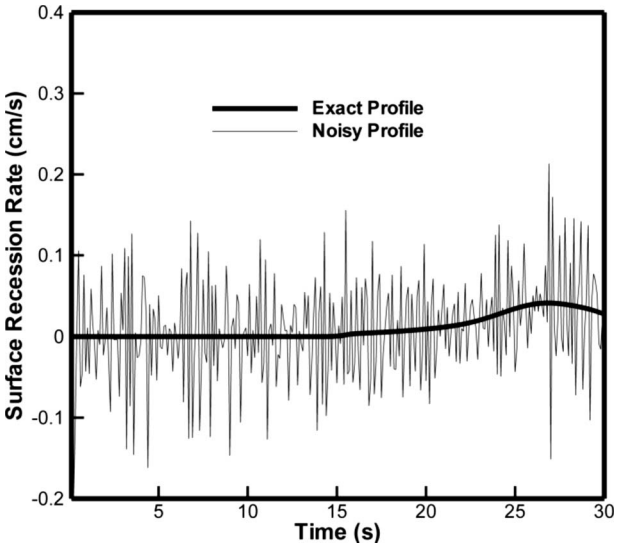

Fig. 10 The exact and used values of surface recession rate in this paper

curacy and convergence features of VMMAP depend upon the specific application. In the case of nonlinear problems, it was demonstrated that VMMAP presented poor convergence rate and even nonconverging behavior was observed with regard to the case of the moving boundary. A marked improvement of convergence rate makes the proposed procedure a viable method for analyzing nonlinear IHCP having surface ablation under the inherent advantage of good computational efficiency. Even in the case that the random measurement error is not small, the proposed method is able to provide a considerably acceptable estimation. The proposed solution technique can be implemented widely to other inverse problems and can accelerate the convergence rate. Certainly, it extends the capabilities of the inverse design from one-dimensional IHCPs to two- and three-dimensional problems, which are more realistic engineering problems in many cases.

Nomenclature

c_p = specific heat (J/kg K)
d = descent direction vector
Δt = time step (s)
f = the objective functional
I = identity matrix
k = thermal conductivity (W/m K)
L = slab thickness (m)
$\dot{L}$ = surface recession rate (m/s)
M = number of total time steps
N = number of sensors
$q(t)$ = unknown surface heat flux (W/m^2)
s = vector of descent direction
T = temperature (K)
T_0 = initial temperature (K)
t = time (s)
t_f = final time (s)
v = velocity of node (m/s)
x = space variable (m)
Y = temperature measured by sensors (K)
α = regularization parameter
β = descent parameter
γ = parameter in decent direction
Δ = small variation
ΔT = sensitivity function
δ = integrated error
ε = very small value
η = Landau coordinate
λ = adjoint variable
ρ = density (kg/m^3)
σ = standard deviation of the errors in the measured temperatures
ω = random variable
∇f = gradient of the objective functional

Subscripts

i = iteration number

Superscripts

T = transpose of a matrix

References

[1] Beck, J. V., Blackwell, B., and St. Clair, C. R., 1985, *Inverse Heat Conduction*, Wiley, New York.
[2] Özisik, M. N., and Orlande, H. R. B., 2000, *Inverse Heat Transfer Fundamentals and Applications*, Taylor & Francis, New York.
[3] Osman, A. M., and Beck, J. V., 1990, "Investigation of Transient Heat Transfer Coefficients in Quenching Experiments," ASME J. Heat Transfer, **112**, pp. 843–848.
[4] Beck, J. V., Blackwell, B., and Haji-Sheikh, A., 1996, "Comparison of Some Inverse Heat Conduction Methods Using Experimental Data," Int. J. Heat Mass Transfer, **39**(17), pp. 3649–3657.
[5] Osman, A. M., Dowding, K. J., and Beck, J. V., 1997, "Numerical Solution of the General Two-Dimensional Inverse Heat Conduction Problem (IHCP)," ASME J. Heat Transfer, **119**, pp. 38–45.
[6] Dowding, K. J., and Beck, J. V., 1999, "A Sequential Gradient Method for the Inverse Heat Conduction Problem (IHCP)," ASME J. Heat Transfer, **121**, pp. 300–306.
[7] Louahlia-Gualous, H., Panday, P. K., and Artioukhine, E. A., 2003, "Inverse Determination of the Local Heat Transfer Coefficients for Nucleate Boiling on a Horizontal Cylinder," ASME J. Heat Transfer, **125**, pp. 1087–1095.
[8] Lagier, G. L., Lemonnier, H., and Coutris, N., 2004, "A Numerical Solution of the Linear Multidimensional Unsteady Inverse Heat Conduction Problem With the Boundary Element," Int. J. Therm. Sci., **43**, pp. 145–155.
[9] Behbahani-nia, A., and Kowsary, F., 2004, "A Dual Reciprocity BE-Based Sequential Function Specification Solution Method for Inverse Heat Conduction Problems," Int. J. Heat Mass Transfer, **47**, pp. 1247–1255.
[10] Kowsary, F., Behbahani-nia, A., and Pourshaghaghy, A., 2006, "Transient Heat Flux Function Estimation Utilizing the Variable Metric Method," Int. Commun. Heat Mass Transfer, **33**, pp. 800–810.
[11] Huang, C. H., and Lin, C. Y., 2008, "Inverse Hyperbolic Conduction Problem in Estimating Two Unknown Surface Heat Fluxes Simultaneously," J. Thermophys. Heat Transfer, **22**(4), pp. 766–774.
[12] Hakkaki-Fard, A., Molavi, H., and Rahmani, R. K., 2009, "A Novel Method for Combined Parameter and Function Estimation Problems," *Proceedings of the 2009 ASME Summer Heat Transfer Conference*, San Francisco, CA, July 19–23.
[13] Beck, J. V., and Osman, A. M., 1989, "Nonlinear Inverse Problem for the Estimation of Time-and-Space Dependent Heat Transfer Coefficients," J. Thermophys. Heat Transfer, **3**(2), pp. 146–152.
[14] Yang, C. Y., 2003, "Estimation of Boundary Conditions in Nonlinear Inverse Heat Conduction Problems," J. Thermophys. Heat Transfer, **17**(3), pp. 389–395.
[15] Loulou, T., and Scott, E. P., 2003, "Estimation of 3-Dimensional Heat Flux From Surface Temperature Measurements Using an Iterative Regularization Method," Heat Mass Transfer, **39**, pp. 435–443.
[16] Daouas, N., and Radhouani, M. S., 2004, "A New Approach of the Kalman Filter Using Future Temperature Measurements for Nonlinear Inverse Heat Conduction Problems," Numer. Heat Transfer, Part B, **45**, pp. 565–585.
[17] Girault, M., and Petit, D., 2005, "Identification Methods in Nonlinear Heat Conduction. Part II: Inverse Problem Using a Reduced Model," Int. J. Heat Mass Transfer, **48**, pp. 119–133.
[18] Chen, H. T., and Wu, X. Y., 2007, "Estimation of Surface Conditions for Nonlinear Inverse Heat Conduction Problems Using the Hybrid Inverse Scheme," Numer. Heat Transfer, Part B, **51**, pp. 159–178.
[19] Molavi, H., Hakkaki-Fard, A., Pourshaban, I., Mahbubi Fard, M., and Rahmani, R. K., 2009, "Estimation of Temperature-Dependent Thermophysical Properties of Noncharring Ablator," J. Thermophys. Heat Transfer, **23**(1), pp. 50–58.
[20] Molavi, H., Pourshaban, I., Hakkaki-Fard, A., Molavi, M., Ayasoufi, A., and Rahmani, R. K., 2009, "Inverse Identification of Thermal Properties of Charring Ablators," Numer. Heat Transfer, Part B, **56**, pp. 478–501.
[21] de Oliveira, A. P., and Orlande, H. R. B., 2004, "Estimation of the Heat Flux at the Surface of Ablating Materials by Using Temperature and Surface Position Measurements," Inverse Probl. Sci. Eng., **12**(5), pp. 563–577.
[22] Hakkaki-Fard, A., and Kowsary, F., 2008, "Heat Flux Estimation in a Charring Ablator," Numer. Heat Transfer, Part A, **53**(5), pp. 543–560.
[23] Petrushevsky, V., and Cohen, S., 1999, "Nonlinear Inverse Heat Conduction With a Moving Boundary: Heat Flux and Surface Recession Estimation," ASME J. Heat Transfer, **121**, pp. 708–711.
[24] Dec, J., and Braun, R., 2006, "An Approximate Ablative Thermal Protection System Sizing Tool for Entry System Design," *Proceedings of the 44th AIAA Aerospace Sciences Meeting and Exhibit*, Reno, NV, Jan. 9–12.
[25] Russell, G. W., 2002, "Analytic Modeling and Experimental Validation of Intumescent Behavior of Charring Heatshield Materials," Ph.D. thesis, Mechanical Engineering Department, University of Alabama in Huntsville, AL.
[26] Amar, A. J., Blackwell, B. F., and Edwards, J. R., 2008, "One-Dimensional Ablation Using a Full Newton's Method and Finite Control Volume Procedure," J. Thermophys. Heat Transfer, **22**(1), pp. 71–82.
[27] Noffz, G. K., and Bowman, M. P., 1996, "Design and Laboratory Validation of a Capacitive Sensor for Measuring the Recession of a Thin-Layered Ablator," NASA Technical Memorandum No. 4777.
[28] Landau, H. G., 1950, "Heat Conduction in a Melting Solid," Q. Appl. Math., **8**, pp. 81–94.
[29] Patankar, S. V., 1986, *Numerical Heat Transfer and Fluid Flows*, Hemisphere, London.
[30] Glynn, P., and Robinson, S. M., 1999, *Numerical Optimization*, Springer-Verlag, New York.
[31] Alifanov, O. M., 1994, *Inverse Heat Transfer Problems*, Springer-Verlag, New York.
[32] Potts, R. L., 1995, "Application of Integral Methods to Ablation Charring Erosion, A Review," J. Spacecr. Rockets, **32**(2), pp. 200–209.
[33] Pourshaghaghy, A., Kowsary, F., and Behbahaninia, A., 2007, "Comparison of Four Different Versions of the Variable Metric Method for Solving Inverse Heat Conduction Problems," Heat Mass Transfer, **43**, pp. 285–294.

Criteria for Cross-Plane Dominated Thermal Transport in Multilayer Thin Film Systems During Modulated Laser Heating[1]

Patrick E. Hopkins[2]
e-mail: pehopki@sandia.gov

Justin R. Serrano

Leslie M. Phinney
ASME Fellow

Sean P. Kearney

Thomas W. Grasser

C. Thomas Harris[3]

Engineering Sciences Center,
Sandia National Laboratories,
P.O. Box 5800,
Albuquerque, NM 87185-0346

Pump-probe transient thermoreflectance (TTR) techniques are powerful tools for measuring the thermophysical properties of thin films, such as thermal conductivity, Λ, or thermal boundary conductance, G. This paper examines the assumption of one-dimensional heating on, Λ and G, determination in nanostructures using a pump-probe transient thermoreflectance technique. The traditionally used one-dimensional and axially symmetric cylindrical conduction models for thermal transport are reviewed. To test the assumptions of the thermal models, experimental data from Al films on bulk substrates (Si and glass) are taken with the TTR technique. This analysis is extended to thin film multilayer structures. The results show that at 11 MHz modulation frequency, thermal transport is indeed one dimensional. Error among the various models arises due to pulse accumulation and not accounting for residual heating. [DOI: 10.1115/1.4000993]

Keywords: pump-probe thermoreflectance, thin film thermal conductivity, thermal boundary conductance, radial heating, cross-plane transport

1 Introduction

Pump-probe transient thermoreflectance (TTR) techniques utilizing short pulsed lasers have been extensively used to measure thermal conductivity, Λ, and thermal boundary conductance, G, of nanomaterials and interfaces of nanomaterials, such as Λ in metal films [1], dielectric films [2], phase change materials [3], thermally anisotropic materials [4], superlattice structures [5], and layered nanolaminates [6,7], and G across metal-metal [8], metal-dielectric [9–13], and metal-liquid [14] interfaces. These transient thermoreflectance techniques measure the change in reflectance on the surface of a material as a function of time after a short pulsed heating event. The change in reflectance is related to the temperature change in the electrons in the material, and the measured change in temperature as a function of time is then related to Λ and G through a conduction heat equation.

Although the aforementioned Λ and G measurements use similar pump-probe time delayed TTR setups, there have been different assumptions regarding the heat transfer analyses in several of the studies; for example, for measurements of G at metal film/dielectric substrate interfaces, two different thermal analyses have been used for the same basic experimental conditions [12,13]. This paper examines the effects of different thermal analyses on determination of cross-plane Λ and G from TTR measurements on thin film samples by comparing one-dimensional and axisymmetric cylindrical models for thermal transport in TTR measurements. The models are fitted to TTR experimental data on Al/Si and Al/glass systems and extended to TTR data with thin Pt, SiO_2, and SiN_x films; the thermal properties of which are extremely important in both microfabricated structures and microelectromechanical systems (MEMS).

The experiments and analyses in this work are focused on pulsed laser heating from a Ti:sapphire oscillator with a fundamental output of 90 fs pulses at 80 MHz (12.5 ns between laser pulses); the laser pulses are then further modulated at 11 MHz to create a modulated heating event at the sample surface, and the temperature decay on the surface of the samples from this modulated heating events is monitored over ~ 4 ns. The laser pulses are treated as delta functions in time due to the ultrashort pulse width compared with the time delay of the experiments. The thermal penetration depth of the modulated heat source is estimated by $\sqrt{D/(\pi f)}$, where D is the diffusivity and f is the modulation frequency. For most solids subjected to megahertz thermal modulation rates, the thermal penetration depth is anywhere from 100 nm to 10 μm. To ensure mostly cross-plane (one-dimensional) transport, the laser spot size of the modulated heating source should be greater than the thermal penetration depth. Typical TTR experiments utilize pump spot sizes on the order of 10 μm. Therefore, for low diffusivity systems, the thermal transport measured in TTR experiments is nearly entirely cross plane due to the small thermal penetration depth. However, in high thermal diffusivity systems, in-plane thermal transport can become significant. The goal of this work is to determine when cross-plane transport is dominant in TTR experiments in various thin film systems. The regimes in which cross-plane transport dominate TTR measurements are discussed in more quantitative detail in the remainder of this work through the use of various thermal models and the development of a nondimensional number describing relative contributions of in-plane and cross-plane thermal transports.

2 Thermal Analysis

2.1 One-Dimensional Time-Domain Model. A one-dimensional heat transfer model for heat transfer between two conductive solids was used by several groups to determine G at several film/substrate interfaces [9–11,13]. This model is given by

[1]This manuscript has been authored by Sandia Corporation under Contract No. DE-AC04-94AL85000 with the U.S. Department of Energy. The United States Government retains, and by accepting the article for publication, the publisher acknowledges that the United States Government retains, a non-exclusive, paid-up, irrevocable, worldwide license to publish or reproduce the published form of this work, or allow others to do so, for United States Government purposes.

[2]Corresponding author.

[3]Joint appointment with the Department of Mechanical Engineering, Massachusetts Institute of Technology, Cambridge, MA 02139-4307.

Contributed by the Heat Transfer Division of ASME for publication in the JOURNAL OF HEAT TRANSFER. Manuscript received August 24, 2009; final manuscript received December 2, 2009; published online May 20, 2010. Assoc. Editor: Pamela M. Norris.

$$C_{1,2}\frac{\partial\theta_{1,2}(z,t)}{\partial t}=\Lambda_{1,2}\frac{\partial^2\theta_{1,2}(z,t)}{\theta z^2} \tag{1}$$

which describes heat conduction in the film (subscript 1) or substrate (subscript 2), where C is the volumetric heat capacity, θ is the temperature change due to the laser pulse, t is the time after the laser pulse, and z is the direction of heat flow. Since typical laser pulse widths in TTR experiments are on the order of hundreds of femtoseconds yet the measurements of G at the film/substrate interface and Λ in the underlying substrate are resolved on the order of nanoseconds, the heating event is assumed to be instantaneous and the initial conditions governing Eq. (1) are

$$\theta_1(z,0)=\frac{Q}{C_1\xi\pi w_0^2}\exp[-z/\xi] \tag{2}$$

and

$$\theta_2(z,0)=0 \tag{3}$$

where Q is the absorbed energy from the incident heating event (pump pulse), ξ is the energy deposition depth in the film, w_0 is the pump $1/e^2$ radius, and Eq. (3) imposes the semi-infinite substrate assumption. The energy deposition depth is given by $\xi=\lambda/(4\pi n_2)$ where λ is the laser pulse wavelength and n_2 is the extinction coefficient (imaginary component of the complex index of refraction) of the solid in which the laser pulse is interacting. In TTR experiments, placing a metal film on top of the material to be characterized ensures that the majority of the laser pulse energy is absorbed near the surface of the film. Since TTR experiments give a spatial resolution no less than ξ, this ensures resolution on the order of 10 nm. For example, the extinction coefficient for Al at 785 nm is 8.55 [15], yielding an energy penetration depth (and subsequent TTR resolution) of 7.3 nm. The boundary conditions at the film/substrate interface (that is, when z is equal to the film thickness d) governing Eq. (1) are given by

$$-\Lambda_{1,2}\frac{\partial\theta_{1,2}(d,t)}{\partial z}=G_{12}(\theta_1(d,t)-\theta_2(d,t)) \tag{4}$$

For purposes in this work, Eqs. (1)–(4) are called the one-dimensional time-domain model (1Dt). The 1Dt is solved using a Crank–Nicolson scheme to determine $\theta(t)$ at the surface of the film. Any analysis based on the 1Dt model assumes only one-dimensional transport and no effect from lateral heat spreading.

2.2 Axially Symmetric Frequency-Domain Model. In typical TTR experiments, the pump and probe beams have spatially Gaussian intensity distributions when incident on the film surface. Therefore, depending on the relative sizes and overlap of the beams, the radial distributions of the pump beam could affect the temperature measured by the probe beam. In this case, the 1Dt may not be applicable since it assumes that the probe reflectance, or the measured change in temperature, is measuring a uniformly heated plane at the surface of the film. To correct for this, Cahill [16] derived an expression for $\theta(r)$ at the surface of the film assuming radial spreading in a half-sphere from the pump pulse. Here we rederive Cahill's expression in a more general fashion.

The axially symmetric heat equation in cylindrical coordinates is given by

$$C_1\frac{\partial\theta_1(r,z,t)}{\partial t}=\Lambda_{1,z}\frac{\partial^2\theta_1(r,z,t)}{\partial z^2}+\frac{\Lambda_{1,r}}{r}\frac{\partial}{\partial r}\left(r\frac{\partial\theta_1(r,z,t)}{\partial r}\right) \tag{5}$$

where r is the radial coordinate, and the subscripts r and z denote the radial and cross-plane conductivities. Taking the Hankel transform along the radial, planar dimension, then applying a Fourier transform, Eq. (5) leads to

$$\frac{\partial^2\theta_1(r,z,\omega)}{\partial z^2}=q_1^2\theta_1(r,z,\omega) \tag{6}$$

where ω is the angular frequency and

$$q^2=\frac{\Lambda_r k^2+iC\omega}{\Lambda_z} \tag{7}$$

where k is the transform variable. This anisotropic q was used by Schmidt et al. [4] to determine the directionally dependent thermal conductivities of graphite in anisotropic structures. In this work, however, we consider isotropic materials and we are only interested in cross-plane properties, so $q^2=k^2+(iC\omega/\Lambda_z)$.

The temperature change in the surface of the film due to heat flow through underlying materials is easily taken into account through Carslaw and Jaeger's solution for steady periodic temperature change in composite slabs [17]. A convenient implementation of this is presented by Feldman [18] and discussed here. The change in surface temperature of material 1 is given by

$$F(k)=\frac{1}{\gamma_1}\left(\frac{F_{T1}^+ + F_{T1}^-}{F_{T1}^- - F_{T1}^+}\right) \tag{8}$$

where F_{T1}^+ and F_{T1}^- are temperature change coefficients related to the forward and backward propagating waves on the surface (top side) of material 1 and where $\gamma=\Lambda_z q$. The forward and backward propagating waves at the top side of material 1 are related to the waves on the bottom side through

$$\begin{bmatrix}F_{T1}^+\\F_{T1}^-\end{bmatrix}=\begin{bmatrix}\exp[-q_1d_1] & 0\\0 & \exp[q_1d_1]\end{bmatrix}\begin{bmatrix}F_{B1}^+\\F_{B1}^-\end{bmatrix} \tag{9}$$

where d is the material thickness. For material 1, the top side is assumed at the slab/air interface and the bottom side is assumed as the interface between material 1 and material 2 (i.e., film/substrate). Given a thermal boundary conductance G between material 1 and material 2, the temperature at the top of slab 2 is related to the temperature at the bottom side of slab 1 by

$$\begin{bmatrix}F_{B1}^+\\F_{B1}^-\end{bmatrix}=\frac{1}{2}\begin{bmatrix}1+\frac{\gamma_2}{\gamma_1}-\frac{\gamma_2}{G_{12}} & 1-\frac{\gamma_2}{\gamma_1}+\frac{\gamma_2}{G_{12}}\\1-\frac{\gamma_2}{\gamma_1}-\frac{\gamma_2}{G_{12}} & 1+\frac{\gamma_2}{\gamma_1}+\frac{\gamma_2}{G_{12}}\end{bmatrix}\begin{bmatrix}F_{T2}^+\\F_{T2}^-\end{bmatrix} \tag{10}$$

Assuming a bulk substrate, heat cannot reach the bottom side of slab 2 at rates comparable to the modulation frequency (semi-infinite), so there is no thermal buildup of waves and

$$\begin{bmatrix}F_{T2}^+\\F_{T2}^-\end{bmatrix}=\begin{bmatrix}0\\\exp[-q_2d_2]\end{bmatrix} \tag{11}$$

With Eqs. (9)–(11), this approach gives a straightforward method to solve for heat conduction through several materials and interfaces via successive implementation of Eqs. (9) and (10) for each layer and then Eq. (11) for the final, semi-infinite layer. This is much less computationally expensive than solving the 1Dt for each interface and material.

To determine the temperature oscillations on the surface of material 1 with the frequency-domain model in Eq. (6) due to cooling from underlying layers described by Eqs. (9)–(11), a top surface boundary condition must be imposed. In TTR, this is described by first convoluting Eq. (8) with the pump-beam distribution [4], given by

$$\theta(k)=F(k)\frac{A}{2\pi}\exp\left[\frac{-k^2w_0^2}{8}\right] \tag{12}$$

and then taking the weighted average of the surface temperature oscillations by the probe beam of $1/e^2$ radius w_1 [16] to yield

$$\theta(r,0,\omega)=\frac{A}{2\pi}\int_0^\infty F(k)\exp\left[\frac{-k^2(w_0^2+w_1^2)}{8}\right]kdk \tag{13}$$

Equation (13) gives the change in temperature as a function of heating event modulation frequency at the surface of the film. In this paper, Eq. (13) is called the axially symmetric frequency-domain model (Axf). The Axf has been used by several groups to

determine G [12,19] and, due to its simple extension to multilayer structures, the thermal conductivity of thin layers and multilayered structures [2,6,7,20–22]. Note that, in this development, the pump source is assumed to be applied only at the surface, so substrate effects on the pump distribution are nonexistent. Although Eq. (13) accounts for radial effects in TTR, it does not give the response as a function of time, which is measured in TTR. To examine the temporal evolution of Eq. (13), the response of the material systems to the laser and modulation repetition rates must be considered. This is described in detail in Sec. 2.3.

2.3 Laser Modulation and Thermal Accumulation Effects. Due to the relatively small change in voltage due to the probe thermoreflectance response as compared with the dc voltage from the reflected probe, a lock-in amplifier is used in the TTR data collection to monitor the temporal decay in the thermoreflectance response occurring at the modulation frequency of the heating event. The output of the lock-in amplifier serves to relate frequency-domain models to the time-domain. The lock-in output will be the magnitude R and phase ϕ of the probe signal at the heating event modulation frequency. Mathematically, the lock-in output takes the form of [4]

$$R\exp[i(\omega_0 t+\phi)] = Z(\omega_0)\exp[i\omega_0 t] \tag{14}$$

where ω_0 is the modulation frequency of the pump pulses and $Z(\omega_0)$ is the transfer function of the lock-in. In the frequency-domain, the transfer function can be represented as [16]

$$Z(\omega_0) = \frac{(2\pi)^2\chi}{\omega_s^2}\sum_{M=-\infty}^{\infty}\theta(\omega_0+M\omega_s)\exp[iM\omega_s\tau] \tag{15}$$

where θ is calculated with a frequency-domain model, such as the model discussed in Sec. 2.2, ω_s is the modulation frequency of the laser system (not the modulation frequency of the heating event; so for a $Ti:Al_2O_3$ oscillator, $\omega_s/2\pi$ is approximately 80 MHz), τ is the delay time between the pump and probe pulses, and χ is a constant that is related to the gain of the electronics, the power of the pump and probe pulses, and the thermoreflectance coefficient of the material. The thermoreflectance coefficient, which relates the change in temperature from the model to the change in reflectance measured in the experiment, is a material property that is related to the band structure, electronic transitions, and dielectric function [23]. In the low perturbation regime (i.e., small temperature rise of the film compared with ambient) in which this work is focused, the change in reflectance is linearly related to the change in temperature, and the thermoreflectance coefficient is a constant. We account for the thermoreflectance coefficient by normalizing the data to the model, as discussed in Sec. 3. From Eq. (15), the lock-in outputs are given by

$$X = \mathrm{Re}[Z(\omega_0)], \quad Y = \mathrm{Im}[Z(\omega_0)] \tag{16}$$

where X and Y are the real and imaginary components of the measured frequency response, and

$$R = \sqrt{X^2+Y^2}, \quad \phi = \tan^{-1}\left[\frac{Y}{X}\right] \tag{17}$$

By nature of Eq. (15), pulse-to-pulse heating and thermal accumulation due to pump modulation are taken into account with a frequency-domain model (note that, in this work, when calculating temporal response with the frequency-domain models, such as the Axf, it is implied that the frequency-domain models are used in conjunction with Eq. (15) to determine the time-domain response). Although a similar model can be derived for pulse accumulation in the time-domain [4], it has not been used in works using a 1Dt analysis, most likely due to the numerical cost, which negates the benefit of using the simplified model in the time-domain. Even with exact analytical forms of the conduction thermal diffusion equation obtained by Laplace transforms [24], accounting for pulse accumulation can be computationally expensive compared with that in the frequency-domain since, in the time-domain, the solution must take into account the multiple pulses in the pump modulation envelope occurring every 12.5 ns while providing picosecond resolution in the analysis.

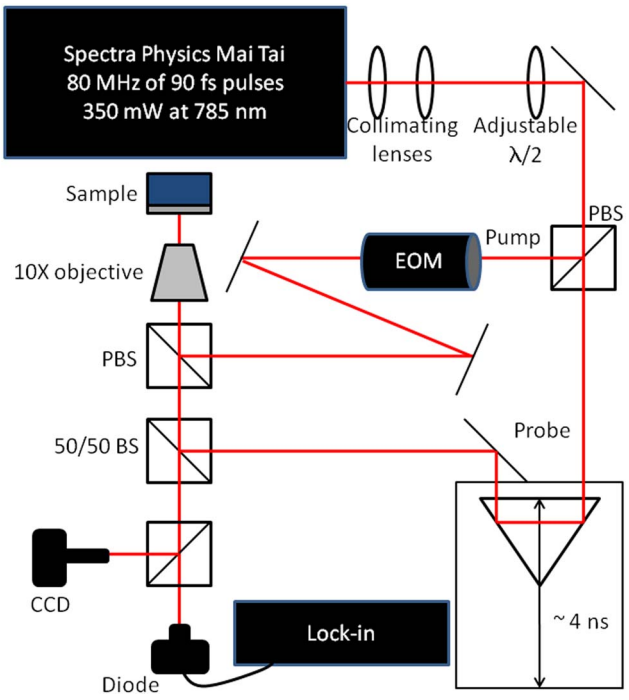

Fig. 1 Transient thermoreflectance setup at Sandia National Laboratories

3 Experimental Details

The various thermal models discussed in Sec. 2 are applied to data for determining G and Λ from pump-probe measurements using the transient thermoreflectance experimental setup at Sandia National Laboratories. The experimental setup, shown in Fig. 1, is nearly identical to similar setups that exploit coaxial pump-probe geometries discussed in previous works [4,25,26]. The laser pulses in this specific experimental setup emanate from a Spectra Physics Mai Tai oscillator outputting 350 mW of power at a repetition rate of 80 MHz and pulse widths of 90 fs at a wavelength of 785 nm. The setup shown in Fig. 1 differs from previous collinear setups by two slight modifications. First, the pulses are first passed through a pair of collimating lenses to minimize probe divergence at the sample surface due to the variable delay stage; upon characterization with a sweeping knife edge [27], the probe (and pump) radius at minimum pump-probe delay is ~ 15 μm and exhibits less than 1 μm divergence at maximum delay. Then, the pulse train passes through an adjustable half-waveplate before being split into the pump and probe paths by a polarizing beam splitter (PBS) cube; this fixes the pump and probe path as orthogonally polarized and the waveplate therefore allows for easy adjustment of the pump and probe powers; the relative pump and probe powers are adjusted to achieve a maximum thermoreflectance signal.

The data must be postprocessed to remove any electronic noise that would lead to unwanted signals. These signals would appear as a change in the imaginary component of the signal Y, as τ crosses zero, since Y should not change as the pump-probe delay time goes from negative to positive. Schmidt et al. [4] determined the change in the real and imaginary components of the signals and calculated a phase noise to subtract from the data. Cahill [16] corrected for this by multiplying the signal by a small phase factor. Here, we employ the following correction: The change in the

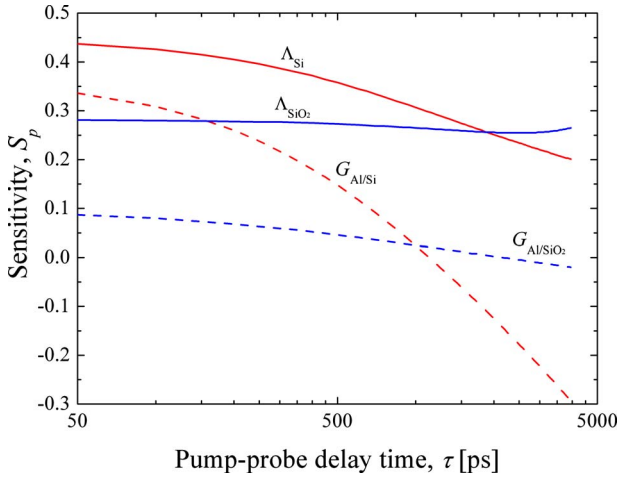

Fig. 2 Sensitivities of the Axf to G and Λ of the substrate in 100 nm Al/Si and Al/SiO_2 systems

lock-in signals as the delay time crosses $\tau=0$, ΔX, and ΔY are computed from the collected data. The measured signals are corrected by rotating the signal in the complex plane, so that the corrected values for X and Y are given by [28]

$$X_c = X\cos\left[\tan^{-1}\left[\frac{\Delta Y}{\Delta X}\right]\right] - Y\sin\left[\tan^{-1}\left[\frac{\Delta Y}{\Delta X}\right]\right] \tag{18}$$

and

$$Y_c = Y\cos\left[\tan^{-1}\left[\frac{\Delta Y}{\Delta X}\right]\right] + X\sin\left[\tan^{-1}\left[\frac{\Delta Y}{\Delta X}\right]\right] \tag{19}$$

A similar method of data correction was employed by Costescu et al. [19] to correct the data for radial diffusion in the substrate. In practice, the phase of the lock-in is adjusted before each measurements so that Y is constant as the stage moves across $\tau=0$ [16] so that Eqs. (18) and (19) can be used simply as a check to ensure that the phase adjustment has removed the majority of the instrument noise. This also allows for the instrument noise to be quantified in terms of the lock-in phase so that this adjustment can be used in future measurements and analysis [29].

To evaluate the various thermophysical properties of interest, we must determine an appropriate range in which to fit the various models to the experimental data. For example, a given material system may be extremely sensitive to changes in G over a certain range but not Λ. This aspect of the models is used to determine ranges in which to fit the various models to the data. Costescu et al. [19] defined a sensitivity factor as

$$S_p = \partial\ln\left[-\frac{X}{Y}\right]/\partial\ln[p] \tag{20}$$

where p is some thermophysical property of interest. To determine the sensitivity of G or Λ over the pump-probe delay time in the TTR data, we perturb the value of G or Λ by 1% in calculations of Eq. (20) so effectively our sensitivity becomes

$$S_p = 100\frac{Y}{X}\partial\left[\frac{X}{Y}\right] \tag{21}$$

where the derivative of the ratio is estimated by subtracting the model calculations from the perturbed model calculations. Figure 2 shows the sensitivities of the Axf as a function of pump-probe delay time for a 100 nm Al film on Si and SiO_2 substrates using the thermal parameters in Table 1 and assuming a 15 μm pump and probe spot size with an absorbed laser power of 1 mW. In the sensitivity calculations, the thermal boundary conductances are taken as 100 MW m^{-2} K^{-1} for Al/Si [13] and 50 MW m^{-2} K^{-1} for Al/SiO_2 [30]. There are two aspects of the sensitivity curve

Table 1 Thermophysical properties of Al, Si, and SiO_2 at 300 K [31]

	Λ (W m^{-1} K^{-1})	C (MJ m^{-3} K^{-1})
Al	237	2.44
Si	148	1.66
SiO_2	1.4	1.97

that are important when fitting the model to the TTR data: the magnitude and the curvature. An optimal sensitivity curve will exhibit a large magnitude and variance over the pump-probe delay time. For example, the sensitivity to the thermal conductivity of the Si substrate is ideal since it is relatively large and very dynamic compared with that of SiO_2. The sensitivity to G across the Al/Si interface is also appealing but loses sensitivity around 500–1000 ps. Note that the sensitivity of the model in the Al/SiO_2 system is primarily due to the thermal conductivity of the substrate. For low thermal conductivity structures, this is powerful if only the thermal conductivity needs to be determined and not G since it reduces the number of free parameters in the fit. We do not include the sensitivity to the Al film thermal conductivity since the TTR measurements are nearly insensitive to this parameter over the majority of the pump-probe time delay. Assuming a diffusivity of Al as $D=97.1\times10^{-6}$ m^2 s^{-1}, the time it takes for the heat to diffuse through the film is given by $\tau\approx d^2/D$ where d is the film thickness [31]. For a 100 nm Al film, the thermal energy has fully diffused through the film thickness after only 100 ps.

TTR data on a 100 nm Al film evaporated onto a single crystalline, lightly doped Si substrate and a glass microscope cover slide (primarily SiO_2) are shown in Fig. 3 along with Axf and 1Dt model calculations. The thermal conductivity of the 100 nm Al film is 200 W m^{-1} K^{-1} as determined from electrical resistivity measurements and the Wiedemann–Franz law. Although this procedure for determining the Al thermal conductivity is really a

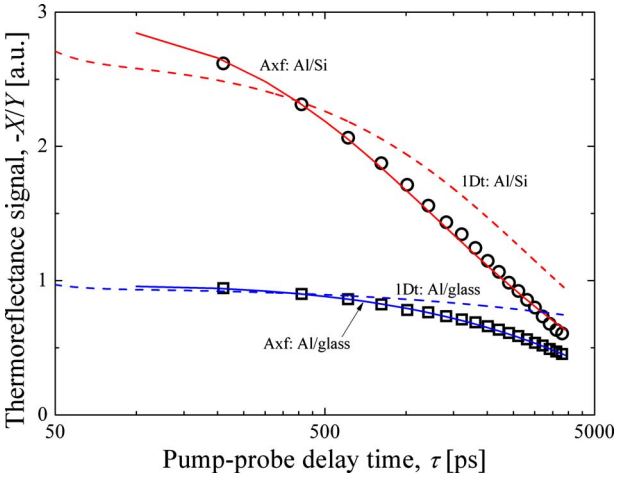

Fig. 3 TTR data from scans on 100 nm Al films evaporated on Si (circles) and glass (squares) substrates along with the best fit from the Axf model scaled at 400 ps. Using the best fit values of G and Λ_2 from the Axf, the 1Dt is calculated and scaled to the data showing that the 1Dt fails to capture some aspects of the data. The thermophysical properties determined from Axf model best fits are $G=90$ MW m^{-2} K^{-1} for the Al/Si interface, $\Lambda=142$ W m^{-1} K^{-1} for Si, and $G=40$ MW m^{-2} K^{-1} and $\Lambda=1.0$ W m^{-1} K^{-1} for the glass substrate. The measured thermal conductivity of the glass substrate is lower than that of pure SiO_2 since the substrate in this case is a glass microscope slide, so the various impurities will reduce the thermal conductivity below that of pure SiO_2.

measure of in-plane conductivity where the model requires cross plane, since the Al film is amorphous, it is valid to assume that the in-plane and cross-plane conductivities are equivalent for a 100 nm Al film. The Axf model, which is assumed here as the more precise model since it takes into account pulse accumulation and radial spreading, is scaled at 400 ps and G_{12} and Λ_2 are adjusted to determine the best fit. Using the best fit values from the Axf, the 1Dt is calculated and scaled to the data in Fig. 3. The data shown here are the real component of the lock-in signal divided by the imaginary component, i.e., $-X/Y$. This approach of normalizing the signal by the imaginary component of the voltage cancels out detection noise and makes the signal insensitive to various experimental parameters that can be difficult to account for during data analysis [16]. This approach is the same as using the phase of the signal [4,14]. Note that we also scale the models to the data at some time t. We choose 400 ps as the scale time since any nonequilibrium phenomena in the Al film have equilibrated and thermal diffusion in the Al film is negligible compared with the diffusion across the Al/substrate interface and in the substrate. The advantage of scaling the model to the data is that precise values for spot sizes or absorbed laser power are no longer needed. However, these inputs are critical if the transport is not purely 1D, and if radial transport plays a role in the TTR measurements, then precise values for spot sizes must be known. However, as will be shown in later sections, 1D transport can be assumed in many cases, which significantly simplifies data analysis.

In Fig. 3, the 1Dt model and the data do not exhibit great agreement in trends. Since we assume that the Axf is the more precise model, the 1Dt fails to predict the thermophysical properties of interest in TTR at 11 MHz modulation frequency. Therefore, the question is as follows: Why does the 1Dt fail? There are two major differences between the 1Dt and Axf. One is the effect of pulse accumulation from the repetition rate of the pump pulses. This aspect on thermal analyses of TTR data has been extensively studied previously and will not be repeated here. However, in short, it must be taken into account analytically in the thermal models (i.e., Sec. 2.3) [4], or the data must be corrected by accounting for the pump-phase [27]. In the remainder of this work, we will focus on the dimensionality assumption in TTR experiments; that is, we will answer the following question: When does radial transport need to be considered in TTR analyses?

4 One-Dimensional Versus Axially Symmetric Transport

The most straightforward way to compare the effects of radial transport on G and Λ is to replace the Axf model presented in Sec. 2.2 with a one-dimensional model. The heat equation in one-dimensional Cartesian coordinates is given by Eq. (6) only

$$q^2 = \frac{iC\omega}{\Lambda_z} \tag{22}$$

The temperature is given by

$$F(\omega) = \frac{1}{\gamma_1}\left(\frac{F_{T1}^{+} + F_{T1}^{-}}{F_{T1}^{-} - F_{T1}^{+}}\right) \tag{23}$$

where the various coefficients are evaluated based on the algorithm outlined in Sec. 2.2. Note that Eq. (22) is in the frequency-domain and not in the time-domain. Since no radial heating is assumed, no convolution of the frequency response and the pump pulse is necessary. Therefore, the temperature change due to pump heating is given by

$$\theta(\omega) = F(\omega)\frac{A}{\pi w_0^2} \tag{24}$$

However, we are interested in only the fraction of the temperature change measured by the probe beam, so the measured temperature change is

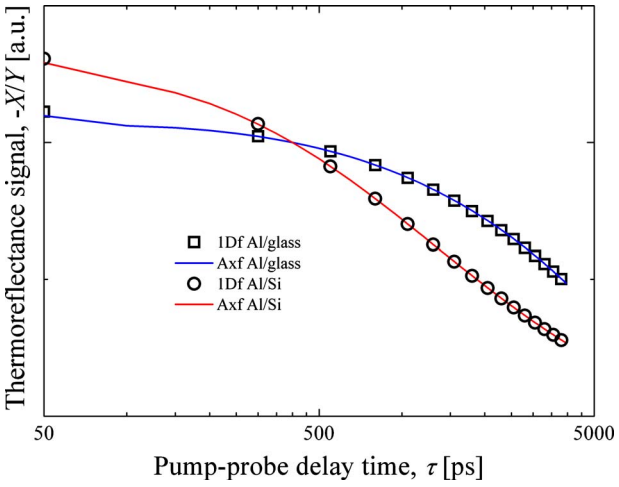

Fig. 4 Comparison of 1Df and Axf for a 100 nm Al film on a Si and glass substrate using the material properties determined from the fit in Fig. 3. The 1Dt and Axf are identical for these two material systems.

$$\theta(\omega) = F(\omega)\frac{Aw_1^2}{\pi w_0^4} \tag{25}$$

Note if $w_0 = w_1$, Eq. (25) reduces to Eq. (24).

Using Eq. (25) with the analyses in Sec. 2.2 (multilayer analysis, Eqs. (9)–(11)) and Sec. 2.3 (modulation analysis, Eqs. (15) and (16)), a one-dimensional frequency-domain model (1Df) is obtained. The 1Df and Axf for the Al/Si and Al/SiO_2 systems in Fig. 3 are compared in Fig. 4. The calculations of the Axf and 1Df are identical for the Al/Si and Al/SiO_2 systems over the delay times of interest. In addition, the 1Df fit to the data and best fits that are determined are identical to those found using the Axf (see Fig. 3 caption). This means that the discrepancy between the models shown in Fig. 3 is due to pulse accumulation and not dimensionality. This is intuitive, since the only difference between the development of the 1Dt and the 1Df is the analysis that accounts for the modulated heating event and pulse accumulation, and therefore, given purely cross-plane thermal transport, the 1Dt and 1Df will only differ if pulse-to-pulse residual heating cannot be ignored; this aspect of pulse accumulation is treated in detail by Schmidt et al. [4]. Therefore, a 1D assumption is appropriate for thermal analyses of TTR data on film/substrate systems at modulation frequencies of 11 MHz. This ensures that at 11 MHz the cross-plane properties of material systems are measured.

5 Condition for One-Dimensional Transport

To examine the regimes where one-dimensional, cross-plane transport dominates the thermal processes, we calculate the ratio of the 1Df signal to the Axf signal as a function of heating event modulation frequency. We define the signals as the ratio of the real to imaginary temperature rises predicted from the models, $-T_{\mathrm{Re}}/T_{\mathrm{Im}}$. This parallels the ratio of lock-in signals previously discussed—i.e., $-X/Y$. Figure 5 shows the predictions of the ratio of the 1Df to Axf signals assuming a 15 μm probe spot radius. Figure 5(a) shows the calculations assuming a 1:1 pump/probe radius ratio (i.e., 15 μm pump radius) and Fig. 5(b) shows results assuming a 5:1 ratio (i.e., 75 μm pump radius). We consider modulation frequencies that are typical in TTR experiments—10 kHz–20 MHz. For these simulations, we assume an 100 nm Al film on a semi-infinite substrate with various thermal diffusivities, $D = \Lambda/C$ as indicated in the figure, and a constant thermal boundary conductance of 50 MW m^{-2} K^{-1}. The Al thermal properties are assumed as bulk and listed in Table 1.

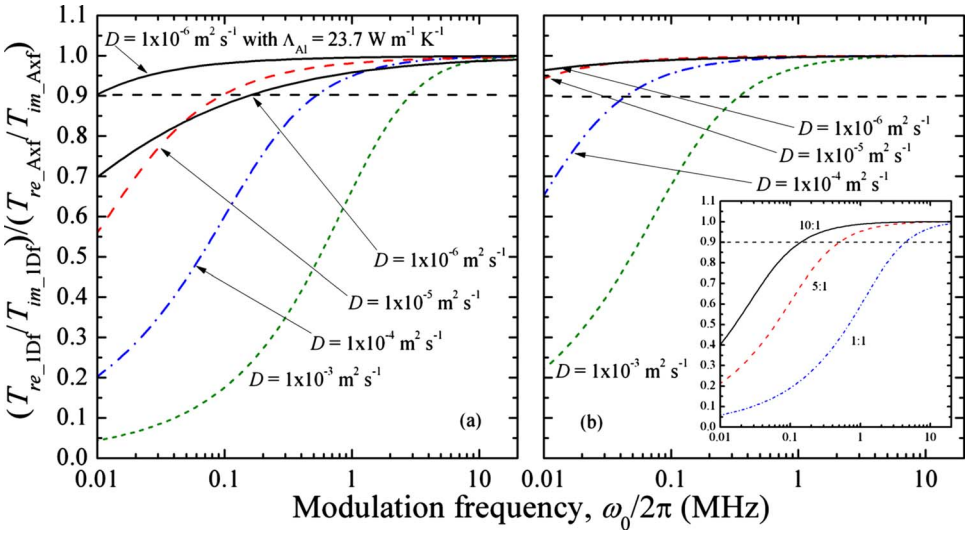

Fig. 5 Ratio of the 1Df signal to the Axf signal as a function of heating event modulation frequency where the signals are defined as the ratio of the real to imaginary temperature rises predicted from the models, $-T_{Re}/T_{Im}$. An acceptable range to assume one-dimensional cross-plane transport is defined as when the 1Df signal ratio is within 90% of the Axf signal ratio as indicated by the horizontal dashed line. (*a*) Calculations assuming a 1:1 pump/probe radius ratio (i.e., 15 μm pump radius) shows that one-dimensional transport is achieved at modulation frequencies above 500 kHz except when the substrate material has diffusivities comparable to that of diamond ($D \sim 1 \times 10^{-3}$ m^2 s^{-1}), in which case radial transport must be taken into account at modulation frequencies as high as 2 MHz. (*b*) Calculations assuming a 5:1 ratio (i.e., 75 μm pump radius). Radial heating is less apparent as the pump spot size increases. The inset of (*b*) shows the 1Df/Axf ratio for an 100 nm Al film on graphite for three pump-probe spot size ratios—10:1, 5:1, and 1:1.

We define an "acceptable" range to assume one-dimensional cross-plane transport when the 1Df signal ratio is within 90% of the Axf signal ratio; this factor is indicated in Fig. 5 by the horizontal dashed line. When considering the same pump and probe spot sizes (Fig. 5(*a*)), one-dimensional transport is achieved at modulation frequencies above 500 kHz except when the substrate material has diffusivities comparable to that of diamond ($D \sim 1 \times 10^{-3}$ m^2 s^{-1}), in which case radial transport must be taken into account at modulation frequencies as high as 2 MHz. An interesting aspect of dimensionality in transport is observed in the lowest diffusivity calculations (diffusivities comparable to SiO_2, ($D \sim 1 \times 10^{-6}$ m^2 s^{-1})). As the diffusivity of the substrate decreases from that comparable to diamond, the trends in the comparative ratio follow similar patterns; lower diffusivities mean one-dimensional transport can be assumed, and the curvature as a function of frequency follows similar trends. However, in low diffusivity substrates, the curvature as a function of frequency does not resemble that of the other diffusivity curves. This is due to the fact that as frequency decreases the thermal penetration depth becomes smaller, such that the density of heat deposited in the Al film is larger. In a nonconducting substrate, radial diffusion in the conducting Al film spreads heat much more quickly than in the substrate, so that the effect of radial spreading in the Al film affects the dimensionality of the heat flow in the film substrate system as more heat is deposited in the Al film (i.e., as the thermal penetration depth decreases). To test this analysis, we repeat these same calculations assuming that the Al film has a thermal conductivity that is 10% of bulk, and, as shown in Fig. 5(*a*), the trends follow those of the higher diffusivity substrates. This could lend insight into a unique experimental study in which to determine the in-plane thermal conductivity of thin-metal films. Figure 5(*b*) shows the same calculations in Fig. 5(*a*) only assuming a 5:1 pump-to-probe spot size ratio. As expected, the effect of radial heating is less severe as the pump spot size increases. This leads to a general conceptual conclusion that to ensure purely one-dimensional thermal transport, the heating event should be modulated at high frequencies and deposited over a large area (heat deposited in system should resemble a short, fat cylinder). The inset of Fig. 5(*b*) shows the 1Df/Axf ratio for an 100 nm Al film on graphite, a highly anisotropic system in which radial measurements were recently performed with TTR by Schmidt et al. [4]. For the graphite calculations, we assume $\Lambda_z = 5.7$ W m^{-1} K^{-1}, $\Lambda_r = 1950$ W m^{-1} K^{-1}, $C = 1.56$ MW m^{-2} K^{-1}, and $G_{Al/graphite} = 50$ MW m^{-2} K^{-1} [4,31]. The calculations are performed for three pump-probe spot size ratios—10:1, 5:1, and 1:1. In graphite, the effects of radial heating become apparent at higher modulation frequencies than in isotropic structures, which is intuitive since the in-plane (radial) direction is much more conductive than the cross-plane direction.

Using this conceptual conclusion, we define a nondimensional number H to determine when one-dimensional heating can be assumed, given by

$$H = \frac{w_0 + \ell_r}{\ell_z} \tag{26}$$

where w_0 is the radius of the heating event, ℓ_r is the distance the heat travels in the radial direction (i.e., an effective thermal spreading distance), and ℓ_z is the thermal penetration depth in the cross-plane direction. Where the cross-plane thermal penetration depth is defined as $\ell_z = \sqrt{2D_z/\omega_0}$, the thermal spreading distance can be derived to take a similar form as $\ell_r = \sqrt{2D_r/\omega_0}$ where D_r is the diffusivity in the radial direction. To ensure one-dimensional thermal transport, $H \gg 1$. For an isotropic material, the condition for one-dimensional transport is

$$H = \frac{w_0}{\ell} \gg 1 \tag{27}$$

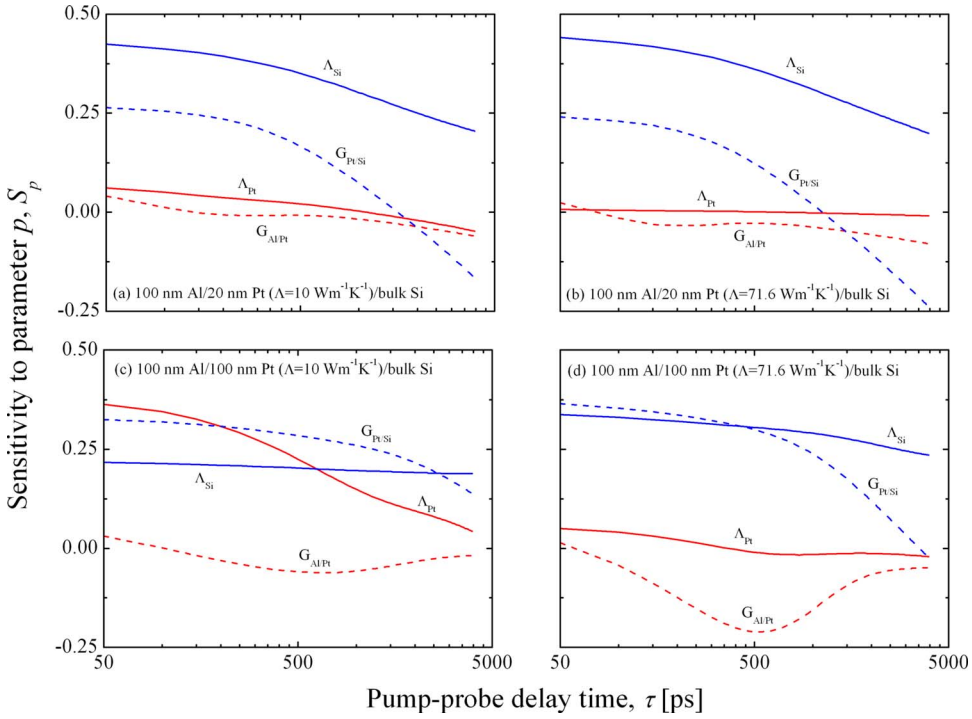

Fig. 6 Sensitivities of the Axf as a function of pump-probe delay time for four different Pt films of varying thickness and thermal conductivity. The various conductivities assumed for the Pt films are listed in the figures. Other parameters used for these calculations are $G_{Al/Pt}$ =500 MW m^{-2} K^{-1}, C_{Pt}=2.85 MJ m^{-3} K^{-1}, and $G_{Pt/Si}$=140 MW m^{-2} K^{-1}. The properties used for the Al film and bulk Si substrate are listed in Table 1.

As previously discussed and following from Eq. (27), to ensure one-dimensional transport, a large heating spot size and a small thermal penetration depth (high frequency) are desired.

6 Multilayer Films

To test the effects of radial conduction on thermal conductivity measurements in thin films, we grew and deposited a series of thin-metal and dielectric films (75 nm Pt, 51 nm SiO_2, 46 nm SiN_x, and 232 nm SiN_x films) on polished Si [100] substrates with 1 Ω cm resistivity, capped with an 80 nm film of Al for our TTR transducer layer. All metal films were deposited using electron beam evaporation, with the Pt metal film requiring a 3 nm chromium adhesion layer. Before the Pt deposition, the Si substrate was subjected to a dilute hydrofluoric acid (HF) dip. The SiO_2 film consisted of a dry thermal oxide, and the low pressure chemical vapor deposition (LPCVD) SiN_x films were deposited in a low-stress (100 MPa) state. A standard RCA clean was performed on the Si substrates before the growth and deposition of the SiO_2 and SiN_x films.

Before measuring the thermal properties of these film systems, we analyze the sensitivity of the models to the various thermal boundary conductances and thermal conductivities that will be driving the TTR signal using Eq. (21). Figure 6 shows the measurement sensitivities of the Axf to the various thermal conductances in the Al/Pt/Si sample. Although the Pt sample is 75 nm, since the conductivity is unknown, we model four different scenarios to show the range of sensitivities: (a) 20 nm Pt film with Λ=10 W m^{-1} K^{-1}, (b) 20 nm Pt film with Λ=71.6 W m^{-1} K^{-1}, (c) 100 nm Pt film with Λ=10 W m^{-1} K^{-1}, and (d) 100 nm Pt film with Λ=71.6 W m^{-1} K^{-1}. In the thinner Pt film cases ((a) and (b)), the sensitivity to the thermal conductivity is small, with a nearly zero sensitivity to the Pt thermal conductivity in the high conductivity case. In this case, the thermal signal will be dominated by G at the Pt/Si interface and Λ_{Si}. As the thickness of the Pt film is increased, the sensitivity to the thermal conductivity of the film increases. In addition, as the film conductivity decreases, the sensitivity increases. This is intuitive since a thicker, less conductive film will offer more thermal resistance.

Where the Pt thin film is relatively thermally conductive, the SiN_x and SiO_2 films are expected to be substantially less conductive. Therefore, the sensitivity of the TTR signal to a nonconductive film is shown in Fig. 7. The thermal response is still relatively sensitive to the underlying Si substrate thermal conductivity for a 50 nm SiO_2 film and also sensitive to the SiO_2/Si thermal boundary conductance, as seen in Fig. 7(*a*). However, increasing the thickness of the SiO_2 film to 250 nm causes the thermal response to be completely insensitive to the properties of the substrate (Fig. 7(*b*)). For comparison, Fig. 7(*c*) shows the thermal response when the 250 nm SiO_2 film is replaced with a conductive Pt film of the same thickness. Note that the thermal signal becomes very sensitive to the Si interfacial conductance and conductivity since the Pt film offers very little resistance to the thermal circuit.

TTR data on these samples were taken at 11 MHz pump modulation frequency; a summary of the TTR fitting results is summarized in Table 2. For the Pt system, since the thermal measurement is relatively insensitive to the Pt conductivity, we estimate Λ_{Pt} from electrical resistivity measurements as 40.5 W m^{-1} K^{-1}. Note that any errors in the Pt thermal conductivity do not propagate into the other reported results on this system since the measurement is relatively insensitive to Λ_{Pt} with conductivity of this order of magnitude (see Fig. 6). We take $G_{Pt/Si}$ as 140 MW m^{-2} K^{-1} [13] leaving $G_{Al/Pt}$ as the only free parameter that we determine as 290 MW m^{-2} K^{-1}. This result is quite surprising as the measured G at the Al/Pt interface is approximately the same as those measured at Al/semiconductor interfaces [13] and over an order of magnitude less than the conductance measured at Al–Cu metal-metal interfaces. The reduction in the measured $G_{Pt/Si}$ from the previously measured $G_{Al/Cu}$ [8] could be due to the band structures of the two metals comprising each interface. Both Al and Cu are free electron metals, and the electrons in the

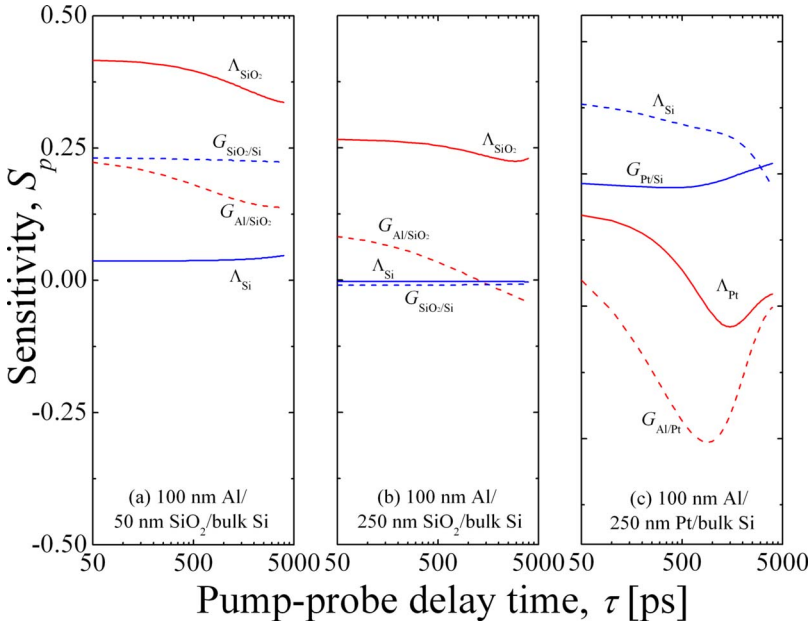

Fig. 7 Sensitivities of the Axf as a function of pump-probe delay time for two SiO_2 films with thicknesses of (*a*) 50 nm and (*b*) 250 nm. The thermal response with these insulative films is relatively insensitive to the thermal conductivity of the substrate over the pump-probe delay time. For comparison, the sensitivity of using a conductive Pt film of 250 nm is shown in (*c*). The thermal properties for the 250 nm Pt film are assumed bulk (see Fig. 5), and the other parameters assumed for these calculations were $G_{Al/Pt}$=500 MW m^{-2} K^{-1}, C_{Pt} =2.85 MJ m^{-3} K^{-1} , and $G_{Pt/Si}$=140 MW m^{-2} K^{-1}.

parabolic conduction bands contribute to thermal conduction. These relatively low effective masses of the electrons lead to low electrical resistivities, and so the thermal boundary conductance between the low electrically resistive free electron metal will be large. However, Pt is much more electrically resistive than copper, and it has a complicated band structure with relatively flat *d*-bands overlapping the Fermi surface. Although the low electrical resistivity of the Pt will reduce $G_{Al/Pt}$ to below that of $G_{Al/Cu}$, the presence of *s*-band electrons in Al interacting with *d*-band electrons in Pt can cause phonon emission for momentum conservation leading to an additional electron-phonon resistance that would decrease $G_{Al/Pt}$ to values similar to $G_{Pt/Si}$.

The TTR signals of the three other thin film samples (51 nm SiO_2, 46 nm SiN_x, and 232 nm SiN_x) are primarily dominated by the thermal conductivity of the film. The heat capacity for SiN_x used in the fit is C_{SiN_x}=1.65 MJ m^{-3} K^{-1} [31]. The thermal conductivity of the 232 nm SiN_x film was measured as 3.5 W m^{-1} K^{-1}, with G_{Al/SiN_x} as 110 MW m^{-2} K^{-1}. Using this value for G_{Al/SiN_x} in the fit of the 46 nm SiN_x film, we determine the thermal conductivity of the 46 nm SiN_x film as 3.1 W m^{-1} K^{-1} with $G_{SiN_x/Si}$ as 50 MW m^{-1} K^{-1}. Finally, we determine the thermal conductivity of the SiO_2 film as 1.2 W m^{-1} K^{-1}, with G_{Al/SiO_2} as 100 MW m^{-1} K^{-1} and $G_{SiO_2/Si}$ as 20 MW m^{-1} K^{-1}. The values for thermal conductivity of the thin dielectric films are slightly higher than previously reported measurements [30], which is expected due to the higher quality of the films in this study. In addition, the values for thermal boundary conductance agree well with previously reported values for metal/dielectric interfaces, but are lower for the dielectric/dielectric interface conductances [30,32].

Table 2 TTR measurements on multilayer thin film samples

	G_{12} (MW m^{-2} K^{-1})	Λ_2 (W m^{-1} K^{-1})	G_{23} (MW m^{-2} K^{-1})
Al/75 nm Pt/Si	290 ± 150	40.5	140
Al/232 nm SiN_x/Si	110	3.5 ± 0.2	-
Al/46 nm SiN_x/Si	110	3.1 ± 0.1	50 ± 2.8
Al/51 nm SiO_2/Si	100	1.2 ± .1	20 ± 4.0

All properties determined from TTR fits with the Axf were also fitted with the 1Df to determine the effect of dimensionality. In all scenarios in this work, the Axf and 1Df yielded the exact same result, indicating that the thermal transport was completely 1D (cross plane). This is expected for these samples since the pump modulation frequency is 11 MHz and the thermal response is almost entirely cross plane, as apparent from the analysis in Sec. 5 (see Fig. 5). At the high pump modulation frequency used in this work (11 MHz), the thermal penetration depth is relatively small; the multilayer samples measured in this section yield $H \sim 10-100 \gg 1$, which ensures that the TTR measurements are probing the cross-plane transport. A lower modulation frequency would lead to a larger penetration depth, which could lead to significant radial heating depending on the spot size [4].

7 Conclusions

This paper examines the assumption of one-dimensional heating and pulse accumulation on G and Λ determination in nanostructures using a pump-probe transient thermoreflectance technique. The traditionally used one-dimensional and axially symmetric cylindrical conduction models are reviewed in Sec. 2, along with the lock-in response that takes into account pulse accumulation and residual heating. To test the assumptions of the models, experimental data of Al films on bulk substrates (Si and glass) are taken with the TTR technique described in Sec. 3. The sensitivity of the Axf to the various thermophysical parameters is discussed in Sec. 4, along with the fitting algorithm and assumptions. To determine the error associated with assuming one-dimensional thermal transport, the Axf is compared with a one-

dimensional frequency-domain model. This analysis is extended to thin film multilayer structures. Results show that at 11 MHz modulation frequency, thermal transport is indeed one dimensional. Error among the various models arises due to pulse accumulation and not accounting for residual heating.

Acknowledgment

P.E.H. is greatly appreciative for funding from the LDRD program office through the Sandia National Laboratories Harry S. Truman Fellowship. This work was performed, in part, at the Center for Integrated Nanotechnologies, a U.S. Department of Energy, Office of Basic Energy Sciences user facility; the authors would like to thank John Sullivan for assistance regarding work at the Center for Integrated Nanotechnologies. C.T.H. would also like to thank Gang Chen at M.I.T. for collaborative advising. Sandia is a multiprogram laboratory operated by Sandia Corporation, a Lockheed-Martin Co., for the U.S. Department of Energy's National Nuclear Security Administration under Contract No. DE-AC04-94AL85000.

Nomenclature

- A = power absorbed at the sample surface, W
- C = heat capacity, J m^{-3} K^{-1}
- D = thermal diffusivity, m^2 s^{-1}
- d = film thickness, m
- F = change in temperature in Hankel space, K
- G = thermal boundary conductance, W m^{-2} K^{-1}
- H = nondimensional number to determine when thermal transport is primarily one dimensional
- J_0 = zeroth order Bessel function
- k = transform variable, m^{-1}
- ℓ = thermal penetration depth, m
- M = index in frequency-domain representation of lock-in transfer function
- m = index in time-domain representation of lock-in transfer function
- n_2 = extinction coefficient
- p = thermophysical property of interest
- Q = energy per pulse, J
- R = magnitude of lock-in signal
- r = direction radial to sample surface, m
- S = sensitivity
- t = time, s
- t_m = heating event time, s
- w = $1/e^2$ laser spot radius, m
- X = real component of lock-in frequency response
- Y = imaginary component of lock-in frequency response
- z = direction normal to the sample surface, m

Greek Symbols

- δ = change in
- χ = proportionality constant in lock-in transfer function
- θ = measured change in temperature, K
- Λ = thermal conductivity, W m^{-1} K^{-1}
- λ = laser wavelength, m
- ϕ = phase of lock-in signal
- ω = angular frequency, rad s^{-1}
- ξ = optical penetration depth, m
- τ = pump-probe delay time, s

Subscripts

- 0 = pump
- 1 = layer 1 (top layer/metal film)
- 2 = layer 2
- 12 = from layer 1 to layer 2
- B = bottom
- c = corrected for electronic noise
- Im = imaginary
- p = probe
- r = radial
- Re = real
- s = laser system
- T = top
- z = cross plane

References

[1] Paddock, C. A., and Eesley, G. L., 1986, "Transient Thermoreflectance From Thin Metal Films," J. Appl. Phys., **60**, pp. 285–290.

[2] Koh, Y. K., and Cahill, D. G., 2007, "Frequency Dependence of the Thermal Conductivity of Semiconductor Alloys," Phys. Rev. B, **76**, p. 075207.

[3] Lyeo, H.-K., Cahill, D. G., Lee, B.-S., and Abelson, J. R., 2006, "Thermal Conductivity of Phase-Change Material $Ge_2Sb_2Te_5$," Appl. Phys. Lett., **89**, p. 151904.

[4] Schmidt, A. J., Chen, X., and Chen, G., 2008, "Pulse Accumulation, Radial Heat Conduction, and Anisotropic Thermal Conductivity in Pump-Probe Transient Thermoreflectance," Rev. Sci. Instrum., **79**, p. 114902.

[5] Capinski, W. S., Maris, H. J., Ruf, T., Cardona, M., Ploog, K., and Katzer, D. S., 1999, "Thermal-Conductivity Measurements of GaAs/AlAs Superlattices Using a Picosecond Optical Pump-and-Probe Technique," Phys. Rev. B, **59**, pp. 8105–8113.

[6] Chiritescu, C., Cahill, D. G., Nguyen, N., Johnson, D., Bodapati, A., Keblinski, P., and Zschack, P., 2007, "Ultralow Thermal Conductivity in Disordered, Layered WSe_2 Crystals," Science, **315**, pp. 351–353.

[7] Costescu, R. M., Cahill, D. G., Fabreguette, F. H., Sechrist, Z. A., and George, S. M., 2004, "Ultra-Low Thermal Conductivity in W/Al_2O_3 Nanolaminates," Science, **303**, pp. 989–990.

[8] Gundrum, B. C., Cahill, D. G., and Averback, R. S., 2005, "Thermal Conductance of Metal-Metal Interfaces," Phys. Rev. B, **72**, p. 245426.

[9] Hopkins, P. E., Norris, P. M., Stevens, R. J., Beechem, T., and Graham, S., 2008, "Influence of Interfacial Mixing on Thermal Boundary Conductance Across a Chromium/Silicon Interface," ASME J. Heat Transfer, **130**, p. 062402.

[10] Hopkins, P. E., Stevens, R. J., and Norris, P. M., 2008, "Influence of Inelastic Scattering at Metal-Dielectric Interfaces," ASME J. Heat Transfer, **130**, p. 022401.

[11] Stoner, R. J., and Maris, H. J., 1993, "Kapitza Conductance and Heat Flow Between Solids at Temperatures From 50 to 300 K," Phys. Rev. B, **48**, pp. 16373–16387.

[12] Lyeo, H.-K., and Cahill, D. G., 2006, "Thermal Conductance of Interfaces Between Highly Dissimilar Materials," Phys. Rev. B, **73**, p. 144301.

[13] Stevens, R. J., Smith, A. N., and Norris, P. M., 2005, "Measurement of Thermal Boundary Conductance of a Series of Metal-Dielectric Interfaces by the Transient Thermoreflectance Technique," ASME J. Heat Transfer, **127**, pp. 315–322.

[14] Schmidt, A., Chiesa, M., Chen, X., and Chen, G., 2008, "An Optical Pump-Probe Technique for Measuring the Thermal Conductivity of Liquids," Rev. Sci. Instrum., **79**, p. 064902.

[15] Palik, E. D., 1985, *Handbook of Optical Constants of Solids*, Academic, Orlando, FL.

[16] Cahill, D. G., 2004, "Analysis of Heat Flow in Layered Structures for Time-Domain Thermoreflectance," Rev. Sci. Instrum., **75**, pp. 5119–5122.

[17] Carslaw, H. S., and Jaeger, J. C., 1959, "Steady Periodic Temperature in Composite Slabs," *Conduction of Heat in Solids*, 2nd ed., Oxford University Press, New York, pp. 109–112.

[18] Feldman, A., 1999, "Algorithm for Solutions of the Thermal Diffusion Equation in a Stratified Medium With a Modulated Heating Source," High Temp. - High Press., **31**, pp. 293–298.

[19] Costescu, R. M., Wall, M. A., and Cahill, D. G., 2003, "Thermal Conductance of Epitaxial Interfaces," Phys. Rev. B, **67**, p. 054302.

[20] Chiritescu, C., Cahill, D. G., Heibeman, C., Lin, Q., Mortensen, C., Nguyen, N. T., Johnson, D., Rostek, R., and Bottner, H., 2008, "Low Thermal Conductivity in Nanoscale Layered Materials Synthesized by the Method of Modulated Elemental Reactants," J. Appl. Phys., **104**, p. 033533.

[21] Costescu, R. M., Bullen, A. J., Matamis, G., O'hara, K. E., and Cahill, D. G., 2002, "Thermal Conductivity and Sound Velocities of Hydrogen-Silsequioxane Low-*k* Dielectrics," Phys. Rev. B, **65**, p. 094205.

[22] Koh, Y. K., Cao, Y., Cahill, D. G., and Jena, D., 2009, "Heat-Transport Mechanisms in Superlattices," Adv. Funct. Mater., **19**, pp. 610–615.

[23] Hopkins, P. E., 2009, "Effects of Electron-Boundary Scattering on Changes in Thermoreflectance in Thin Metal Films Undergoing Intraband Transitions," J. Appl. Phys., **105**, p. 093517.

[24] Ezzahri, Y., Grauby, S., Dilhaire, S., Rampnoux, J. M., and Claeys, W., 2007, "Cross-Plan Si/SiGe Superlattice Acoustic and Thermal Properties Measurement by Picosecond Ultrasonics," J. Appl. Phys., **101**, p. 013705.

[25] Cahill, D. G., Ford, W. K., Goodson, K. E., Mahan, G. D., Majumdar, A., Maris, H. J., Merlin, R., and Phillpot, S. R., 2003, "Nanoscale Thermal Transport," J. Appl. Phys., **93**, pp. 793–818.

[26] Cahill, D. G., Goodson, K. E., and Majumdar, A., 2002, "Thermometry and

Thermal Transport in Micro/Nanoscale Solid-State Devices and Structures," ASME J. Heat Transfer, **124**, pp. 223–241.
[27] Stevens, R. J., Smith, A. N., and Norris, P. M., 2006, "Signal Analysis and Characterization of Experimental Setup for the Transient Thermoreflectance Technique," Rev. Sci. Instrum., **77**, p. 084901.
[28] Schmidt, A. J., 2008, "Optical Characterization of Thermal Transport From the Nanoscale to the Macroscale," Ph.D. thesis, Massachusetts Institute of Technology, Cambridge, MA.
[29] Schmidt, A. J., Cheaito, R., and Chiesa, M., 2009, "A Frequency-Domain Thermoreflectance Method for the Characterization of Thermal Properties," Rev. Sci. Instrum., **80**, p. 094901.
[30] Lee, S.-M., and Cahill, D. G., 1997, "Heat Transport in Thin Dielectric Films," J. Appl. Phys., **81**, pp. 2590–2595.
[31] Incropera, F., and Dewitt, D. P., 1996, *Fundamentals of Heat and Mass Transfer*, Wiley, New York.
[32] Norris, P. M., and Hopkins, P. E., 2009, "Examining Interfacial Diffuse Phonon Scattering Through Transient Thermoreflectance Measurements of Thermal Boundary Conductance," ASME J. Heat Transfer, **131**, p. 043207.

A Meshless Finite Difference Method for Conjugate Heat Conduction Problems

Chandrashekhar Varanasi[1]
e-mail: vvc@purdue.edu

Jayathi Y. Murthy
e-mail: jmurthy@ecn.purdue.edu

Sanjay Mathur
e-mail: smathur@purdue.edu

School of Mechanical Engineering,
Purdue University,
West Lafayette, IN 47906

A meshless finite difference method is developed for solving conjugate heat transfer problems. Starting with an arbitrary distribution of mesh points, derivatives are evaluated using a weighted least-squares procedure. The resulting system of algebraic equations is sparse and is solved using an algebraic multigrid method. The implementation of the Neumann, Dirichlet, and mixed boundary conditions within this framework is described. For conjugate heat transfer problems, continuity of the heat flux and temperature are imposed on mesh points at multimaterial interfaces. The method is verified through application to classical heat conduction problems with known analytical solutions. It is then applied to the solution of conjugate heat transfer problems in complex geometries, and the solutions so obtained are compared with more conventional unstructured finite volume methods. The method improves on existing meshless methods for conjugate heat conduction by eliminating spurious oscillations previously observed. Metrics for accuracy are provided and future extensions are discussed. [DOI: 10.1115/1.4001363]

Keywords: finite point method, weighted least-squares, conjugate heat conduction

1 Introduction

During the last three decades, computational fluid dynamics (CFD) has become an integral part of industrial practice. The development of sophisticated computer aided design (CAD) tools for geometry creation, unstructured solution-adaptive meshing, as well as versatile unstructured solution techniques, have significantly expanded the use of CFD. Despite these successes, it is widely acknowledged that mesh generation remains the single biggest bottleneck to the future expansion of CFD for complex industrial problems. Mesh generation may account for as much as 80% of user time, and the inability to generate good meshes compromises solution stability and accuracy. As a result, there has been a great deal of interest in developing meshless methods for computational fluid dynamics in order to eliminate the mesh generation step altogether.

Though meshless methods have been an active area of research for the last decade, their applications have been primarily in the area of solid mechanics. Belytschko et al. [1] presented an extensive review of this field. Li and Liu [2], and Babuška et al. [3] presented a more recent review of the subject. Meshless methods can be broadly categorized as particle (Lagrangian) methods and element-free Galerkin methods. The smoothed particle hydrodynamics (SPH) method, introduced by Lucy and Monaghan [4,5], is one of the oldest particle methods. Originally used for astrophysics simulations, it has been used also in fluid flow simulation. However, the method lacks consistency for an unstructured distribution of points [1]. Duarte and Oden presented the hp-cloud method [6], which has been used in solid mechanics, along with various other mesh-free Galerkin methods [1]. These methods have the drawback of requiring a background mesh to carry out quadrature, diminishing some of the advantages of meshless techniques. Another class of meshless methods is based on the finite difference technique. Finite difference methods (FDMs) compute for the partial derivatives appearing in a governing equation directly. Traditionally, finite difference methods have been limited to structured or body-fitted meshes. However, the discretization obtained using the FDM is based on a Taylor series expansion, which is valid in the neighborhood of a given point. This idea can now be used to construct a discretization of the governing equation using a random distribution of points. Oñate et al. [7,8] presented such an idea using a weighted least-squares method to obtain approximations to the derivatives and presented a stabilized finite point method (FPM) to solve the convection-diffusion equation. They provided a description of how to compute for the stabilization parameter in Ref. [9]. In Ref. [10], Idelsohn et al. generalized the least-squares idea to finite element methods (FEMs), and explored its application to incompressible flow using a time-splitting technique in Refs. [11–13]. In Ref. [14], they extended the time-splitting technique to a particle method to simulate free surface flows. Compressible flows were dealt with in Ref. [15]. Aluru and Li [16] introduced the finite cloud method, which combines collocation with a fixed kernel technique for the construction of interpolation functions.

Conjugate heat conduction has been studied within a weighted least-squares framework in Refs. [17,18]. Here, published methods differ in the way in which interface heat transfer is handled. Sadat et al. [17] proposed a two-stage weighted least-squares (WLS) method in which the flux $k_m \nabla T$ is computed at each point first, and the divergence of this quantity is computed numerically at each point to obtain the discretization. This technique is prone to checkerboarding, as is known from established CFD methods, since both the first and second derivatives are evaluated at the same mesh point. At the interface, the heat flux is computed using one of the thermal conductivites of the two domains, and its derivative then computed for inclusion in the diffusion equation. The answer computed would differ depending on which the thermal conductivity value was used at the interface [18]. The method was found to produce oscillatory temperature profiles for high conductivity ratios, of the order of 100. Fang et al. [18] built it based on Ref. [17]. They also used the two-stage idea, but restricted the stencil of points for temperature gradient evaluation to the side of the interface under consideration. The heat fluxes from the two sides of the interface were averaged to obtain the average interface heat flux, which was then used in the second stage of the weighted least-squares scheme to compute for the second deriva-

[1]Corresponding author.

Contributed by the Heat Transfer Division of ASME for publication in the JOURNAL OF HEAT TRANSFER. Manuscript received April 15, 2009; final manuscript received February 25, 2010; published online June 9, 2010. Assoc. Editor: Walter W. Yuen.

tives. The discretization still computes for the first and second derivatives at the same mesh point, making the method still prone to checkerboarding.

In the current work, WLS discretization is applied to solution of conjugate heat conduction problems. A second-order discretization scheme is developed for steady conduction problems in domains with spatially varying thermal conductivity, both continuous and discontinuous. The resulting discrete algebraic equations are solved using an algebraic multigrid (AMG) method. The method is shown to work well by comparisons to analytical solutions and to solutions obtained using conventional unstructured finite volume techniques. In the remainder of the paper, the governing equations and boundary conditions for the problem under consideration are first presented. Details of the discretization procedure, the order of accuracy of the method, and the solution technique used to solve the resulting linear system are described in Secs. 3 and 4. Implementational issues are addressed in Sec. 5. Results obtained using this method are then presented and include comparisons with benchmark solutions and the application of the method to a heat conduction problem in a domain consisting of materials of different thermal conductivity. Finally, conclusions are drawn, and directions for future work are discussed.

2 Governing Equations and Boundary Conditions

We consider the steady heat diffusion equation in a two-dimensional domain. The domain consists of different materials with distinct thermal conductivities, and the thermal conductivity in each subdomain is allowed to vary as a function of the position or temperature. The domain is divided on the basis of the material into regions Ω_m $(m=1,2\ldots)$. We denote the interface between regions l and m by $\partial\Omega_{lm}$. The governing equations for region m may then be written as

$$k_m\nabla^2 T_m + \boldsymbol{\nabla k_m}\cdot\boldsymbol{\nabla T_m} + s = 0 \quad \text{in } \Omega_m \tag{1}$$

In a two-dimensional domain, the above equation can be written as

$$k_m\left(\frac{\partial^2 T_m}{\partial x^2}+\frac{\partial^2 T_m}{\partial y^2}\right)+\frac{\partial k_m}{\partial x}\frac{\partial T_m}{\partial x}+\frac{\partial k_m}{\partial y}\frac{\partial T_m}{\partial y}+s=0 \quad \text{in } \Omega_m \tag{2}$$

At the interface between two materials l and m, continuity of temperature implies

$$T_l = T_m \tag{3}$$

Furthermore, the balance of heat fluxes requires

$$-k_l\boldsymbol{n}\cdot\boldsymbol{\nabla}T_l = -k_m\boldsymbol{n}\cdot\boldsymbol{\nabla}T_m \tag{4}$$

The above equations are subject to the boundary conditions imposed on the external boundary of the domain $\partial\Omega$. The boundary conditions may be of Dirichlet, Neumann, or mixed type. In general, they may be represented as

$$ak_m\boldsymbol{n}\cdot\boldsymbol{\nabla}T_m + bT_m = g(\boldsymbol{x}_{\partial\Omega}) \tag{5}$$

where m is the index of the material bordering the boundary. The coefficients a and b may be varied to obtain the various boundary conditions mentioned above. $g(\boldsymbol{x})$ is a space-dependant function.

3 Numerical Method

The numerical method is based on a WLS interpolation. The idea is to fit, in the least-squares sense, a polynomial of required degree to a stencil of neighbors [19]. The resulting polynomial coefficients can then be used to compute for the approximations to the derivatives that appear in the governing equations. Consider a point (x_p,y_p) at which the WLS interpolation is to be computed. Let (x_i',y_i') $(i=1,2,\ldots,N)$ be the set of points used for constructing the WLS approximation. Let $u^h(x,y)$ be the approximation to the function $u(x,y)=f(x,y)-f(x_p,y_p)$ in the neighborhood of the point (x_p,y_p) containing the points (x_i',y_i'). The objective of a WLS interpolation is to project the function $u(x,y)$ onto the space spanned by the basis functions $p_i(x,y)$ $(i=1,2,\ldots,P)$ and minimize the weighted residual. The WLS method for two dimensions is presented here. The basis functions chosen for this work admit for an interpolation of second-order accuracy and are given by

$$p_1(x,y) = x - x_p$$

$$p_2(x,y) = y - y_p$$

$$p_3(x,y) = (x - x_p)^2$$

$$p_4(x,y) = (y - y_p)^2$$

$$p_5(x,y) = (x - x_p)(y - y_p) \tag{6}$$

Note that $p_0=1$ has been omitted since we are interpolating for $u(x,y)=f(x,y)-f(x_p,y_p)$. The number of polynomials in the basis will depend on the order of the interpolation and the dimension of space involved. For example, a similar basis for second-order interpolation in three dimensions will include the additional polynomials $p(x,y,z)=z-z_p$, $p(x,y,z)=(z-z_p)(x-x_p)$, $p(x,y,z)=(y-y_p)(z-z_p)$, and $p(x,y,z)=(z-z_p)^2$. Let the cardinality of the set of polynomials that form the basis be P. In order to obtain a WLS fit, it is required that $N\geq P$. The WLS approximation to a function $u(x,y)$ is given by

$$u^h(x,y) = \hat{a}\cdot\hat{p}(x,y) \tag{7}$$

where $\hat{a}$ is the coefficient vector of size $(P\times 1)$ and $\hat{p}(x,y)$ denotes the $(P\times 1)$ vector obtained by computing the polynomials in the basis at any point. From now on, we adopt the notation of representing vectors by hatted variables. For example, function u^h evaluated at the N neighbors is denoted by $\hat{u}^h$. Representing $x-x_p$ by Δx, etc.

$$\hat{p}(x,y) = \begin{bmatrix}\Delta x & \Delta y & \Delta x^2 & \Delta y^2 & \Delta x\Delta y\end{bmatrix}^T \tag{8}$$

The aim of the WLS procedure is therefore to compute for $\hat{a}$ in order to minimize the error between $\hat{u}(x,y)$ and $\hat{u}^h(x,y)$ in a weighted residual sense. Define the discrete weighted error between $\hat{u}(x,y)$ and $\hat{u}^h(x,y)$ as

$$J \equiv \sum_i^N w(r_i)[u^h(x_i,y_i) - u(x,y)]^2 \tag{9}$$

The coefficient vector $\hat{a}$ can now be computed using the N points (x_i',y_i') so as to minimize the error defined above. Let W represent the weight matrix, which is a $(N\times N)$ diagonal matrix

$$W = \begin{pmatrix} w_1 & 0 & 0 & \cdots & 0 \\ 0 & w_2 & 0 & \cdots & 0 \\ 0 & 0 & w_3 & & \vdots \\ \vdots & 0 & 0 & \ddots & 0 \\ 0 & \cdots & 0 & 0 & w_N \end{pmatrix}$$

where

$$w_i = w(r_i) \quad i = 1,\ldots,N$$

$$r_i = \sqrt{(x_p - x_i)^2 + (y_p - y_i)^2}$$

The weight function used in this work is an exponential function and $w(r_i)$ is defined as

$$w(r_i) = e^{-(3r_i/h)^2}$$

where h is the radius, which contains all the neighbors (x_i',y_i') about point (x_p,y_p), which is called the smoothing radius. The weight function serves to minimize the contribution of points far off from (x_p,y_p). Let $\hat{u}^h$ be the $(N\times 1)$ vector obtained by evaluating the approximation function at the N neighbor points. The weighted error vector is now made orthogonal in the discrete

sense to the function space spanned by the basis functions. We define F to be the $(N\times P)$ array with respect to which the weighted error vector is orthogonalized. In two dimensions and for second-order accuracy, F is given by

$$F=\begin{pmatrix} x_1 & y_1 & x_1^2 & y_1^2 & x_1y_1 \\ x_2 & y_2 & x_2^2 & y_2^2 & x_2y_2 \\ \vdots & \vdots & \vdots & \vdots & \vdots \\ x_N & y_N & x_N^2 & y_N^2 & x_Ny_N \end{pmatrix}$$

The error minimization equation then reads

$$(F\hat{a})^T[W(F\hat{a}-\hat{u})]=0 \Rightarrow (F\hat{a})^TWF\hat{a}=(F\hat{a})^TW\hat{u}$$

Premultiplying by $(F\hat{a})$ and canceling the scalar coefficient results to

$$WF\hat{a}=W\hat{u}$$

Premultiplying now by F^T, we obtain an equation in which $\hat{a}$ is multiplied by an invertible matrix F^TWF, which gives an equation for determining the coefficient vector $\hat{a}$

$$\hat{a}=(F^TWF)^{-1}(F^TW)\hat{u} \tag{10}$$

Comparing the WLS approximation hence obtained and the Taylor series about the point (x_p,y_p)

$$f(x,y)=f(x_p,y_p)+\frac{\partial f}{\partial x}\Delta x+\frac{\partial f}{\partial y}\Delta y+\frac{\partial^2 f}{\partial x^2}\Delta x^2+\frac{\partial^2 f}{\partial y^2}\Delta y^2 + 2\frac{\partial^2 f}{\partial x\,\partial y}\Delta x\Delta y+\ldots$$

$$u^h(x,y)=f(x,y)-f(x_p,y_p)=a_1\Delta x+a_2\Delta y+a_3\Delta x^2+a_4\Delta y^2 + a_5\Delta x\Delta x \tag{11}$$

the required derivatives are thus obtained. For sake of elucidation, let us study how a_1 is obtained. Let $(F^TWF)^{-1}(F^TW)$ in Eq. (10) be represented by C (where C is a $P\times N$ matrix.) Denote the first row of C by C_1. Hence, C_1 is a $1\times N$ vector. a_1 is then given by the product of

$$a_1=C_1\hat{u}$$

Similarly other a_i may be found. Comparing now to the Taylor series

$$a_1=\frac{\partial f}{\partial x}=C_1\hat{u}$$

The right hand side above is a product between a $(1\times N)$ row vector and a $(N\times 1)$ column vector. Denoting each element of C_1 as a_1^{pi}, the above vector product can be expressed as the sum

$$a_1=\sum_{i=1}^{N}a_1^{pi}u_i$$

Therefore, for the steady diffusion equation, the discretization process leads to a system of equations of the type

$$\sum_{i=1}^{N}a_3^{pi}(T_m^i-T_m^p)+\sum_{i=1}^{N}a_4^{pi}(T_m^i-T_m^p)=b_p \tag{12}$$

where summation over all neighbors of point p is implied. a_3^{pi} here denotes a_3 (which is the $\partial^2 f/\partial x^2$ operator) computed at point p and so on. From now on, the coefficients stemming from operators for different derivatives will not be distinguished, and will all be represented by a^{pi}. A drawback of the method is that the discretization procedure does not assure positivity of all a^{pi}.

4 Boundary and Interface Conditions

We now turn our attention to implementation of boundary and interface conditions. The domain is divided into three types of mesh points: interior, boundary, and interface. Dirichlet boundaries are simple to handle. The value of the function at Dirichlet boundary points is known, and hence, no discretization equation is written for these points. For Neumann boundary points, where the slope of the function is specified, an equation similar to Eq. (12) arises. For example, consider the implementation of

$$\boldsymbol{n}\cdot\nabla f=0$$

on a boundary point. Expanding the equation above, we obtain in two dimensions

$$n_x\frac{\partial f}{\partial x}+n_y\frac{\partial f}{\partial y}=0$$

Thus, substituting the discrete form for each of the derivatives appearing in the boundary condition, we obtain an equation similar to Eq. (12). Mixed boundary conditions are handled similarly.

We now turn to the interface between two different materials. Our method differs from existing methods primarily in the manner in which the interface points are treated. Sadat et al. [17] evaluated an approach in which the gradient ∇k in Eq. (1) was evaluated using weighted least-squares, even across interfaces, resulting in large errors as the degree of heterogeneity increased. Subsequently, Sadat et al. [17] and Fang et al. [18] developed a two-stage WLS procedure, whereby the first stage computed $k\nabla T$ at the interface and the second stage evaluated its derivates for direct substitution into the heat diffusion equation. In our procedure, Eq. (1) is solved only in the bulk of each material, using mesh points only within the relevant subdomain. At the interface, we explicitly impose temperature and flux continuity. This is done by placing mesh points on the interface, ensuring the continuity of the temperature. A finite difference implementation of Eq. (4) at the interface points determines the interface temperature. Care is taken to ensure that each side of Eq. (4) employs mesh points only in the corresponding subdomain. This approach does not require the use of sharply varying functions to capture the thermal conductivity variation across the interface. Also, since a two-stage procedure colocating first and second derivatives is not used, the current method avoids the checkerboarding problem.

In our implementation, the heat flux from material l is set equal to that from material m by computing for the discrete one-sided heat fluxes and equating them to each other. This results in a discrete equation of the form

$$-k_l\sum_{i}^{N_l}a_{pi}(T_l^i-T^p)=-k_m\sum_{i}^{N_m}a_{pi}(T_m^i-T^p) \tag{13}$$

where T^p is the interface temperature, T_l^i is the temperature of the ith neighbor of material type l, and T_m^i is the temperature of the ith neighbor of material type m. a_{pi} denotes the discrete first derivative operator dotted with the normal at the interface.

4.1 Accuracy of the Method. The method can capture all polynomials/functions included in the basis of the method. Hence, for the basis used, we obtain second-order accuracy. Further, by including suitable functions in the basis, functions with discontinuities can be captured by using this method. The interface condition, however, uses a first order interpolation. Hence, the order of accuracy of the method is less than the second order for problems involving multiple materials.

5 Implementation

The method has been implemented using a C++ code that uses a tree representation of mesh point data structures, enabling an efficient search for neighbors [20]. The utility of the WLS method lies in the fact that it allows easy addition or removal of points,

since only the tree structure needs to be updated. This possibility has been kept in mind when implementing the method in the code. A central element of the solution algorithm involves first searching for all neighbors of a point (x_p, y_p) in a circle of radius h. For conjugate heat conduction problems, only like-material neighbors are searched for. Once a stencil of neighbors has been found, the coefficient vector $\hat{a}$ must be found. The coefficient vector $\hat{a}$ is stored as a vector of operators in each mesh point data structure. It is found using Eq. (10). The inversion is carried out using a Gaussian elimination method. N is typically around 8 in a two-dimensional geometry, making the operation computationally inexpensive. Having obtained the coefficients $\hat{a}$, the system of equations for the heat conduction problem is set up. Since neighbor indices can be arbitrary, an efficient storage strategy for the resulting sparse matrix is needed. The compressed row storage format has been used in this work. The system of equations thus obtained is now solved using the AMG method described in Refs. [21,22]. The WLS procedure does not guarantee that the coefficients in Eq. (12) are positive. Iterative methods require diagonal dominance to guarantee convergence. To guarantee diagonal dominance, terms appearing with negative coefficients are shifted to the source term. Thus Eq. (12) is rewritten as

$$\sum_{i=1}^{N_<} a^{pi}(T_m^i - T_m^p) + \sum_{i=1}^{N_>} a^{pi}(T_m^i - T_m^p) = b_p \tag{14}$$

where $N_<$ is the number of negative coefficients and $N_>$ is the number of positive coefficients, with $N_< + N_> = N$. The terms on the left hand side with $a^{pi} < 0$ are shifted to the right hand side and evaluated at the prevailing values of the temperature

$$\sum_{i=1}^{N_>} a^{pi}(T_m^i - T_m^p) = b_p - \sum_{i=1}^{N_<} a^{pi}(T_m^i - T_m^p)^* \tag{15}$$

The right hand side is updated in an outer loop once per outer iteration, while the AMG solves the equation set with a fixed right hand side within the outer iteration. This procedure restores positivity of all coefficients in the nominally linear equation system and guarantees diagonal dominance of the modified coefficient matrix; however, multiple outer iterations are necessary, even for linear problems. This treatment was found to be necessary to obtain convergence for problems with high conductivity ratios.

6 Results

First, the dependence of interpolation accuracy on the smoothing radius and the sharpness of the Gaussian weight function is tested. Then, a number of conduction problems are computed here to establish the numerical characteristics of the method. The method is first tested against benchmark solutions for conduction in a domain of constant conductivity, with both uniform and nonuniform distributions of points. Thereafter, a simple one-dimensional conjugate conduction problem is studied. Finally, the method is applied to a domain with distributed regions of materials with different conductivities, and the computed solutions are compared with results obtained using the commercial software FLUENT [23].

6.1 Problem 1: Influence of the Interpolation Parameters. The interpolation technique developed in this work depends on two parameters: the smoothing radius of a point and the sharpness of the Gaussian weight function. The smoothing radius h of a point is governed by the minimum number of points to be included in the stencil, which is a user input. In general, the smoothing radius varies from point to point. For robustness, it is desired that the method be relatively insensitive to variation in the smoothing radius. Simultaneously, the sharpness of the Gaussian weight function influences the condition number of the matrix that is inverted in order to obtain the coefficients for various derivatives (Eq. (10)). A weight function that falls to zero too quickly would discard all information provided by points that are at a greater radial distance. The sharpness of the Gaussian depends on σ, since this parameter governs the rate of decay of the weight function

$$w(r) = e^{-(\sigma r/h)^2}$$

In this section, we explore the influence of both h and σ on the accuracy of the interpolation. In order to do so, the second derivative with respect to x and y are computed for a known function, namely

$$f(x,y) = x^2(1+x) + y^2(1+y)$$

$$\frac{\partial^2 f}{\partial x^2}_{\text{exact}} = 2(1+3x)$$

$$\frac{\partial^2 f}{\partial y^2}_{\text{exact}} = 2(1+3y)$$

and the competed values are compared with the analytical ones. The average root mean squared (rms) percent error of the interpolation is defined as

$$\varepsilon = 100 \times \left(\frac{1}{\nu} \sum_{\nu} \left[\left(\frac{\partial^2 f}{\partial x^2}_{\text{computed}} - \frac{\partial^2 f}{\partial x^2}_{\text{exact}} \right) \Big/ \frac{\partial^2 f}{\partial x^2}_{\text{exact}} \right]^2 \right)^{1/2} \tag{16}$$

and similarly for the y-derivatives. First, the minimum number of points in a stencil is varied to change the smoothing radius, keeping the parameter σ fixed at 3. The variation in ε with the minimum number of neighbors in the stencil is shown in Fig. 1. The value of h marked at the symbols is the average smoothing radius for all the points in the domain. The computational domain is a nonuniform distribution of 906 interior points. It is seen that the error does not vary significantly over the range of smoothing radii. This is a favorable property of the interpolation technique, implying that small differences in the smoothing radius do not affect the accuracy greatly.

We now study the variation in the accuracy with the sharpness of the Gaussian weight function. The same computational domain is chosen as the one above, and the minimum number of neighbors in a stencil is held fixed at 7. We choose $\sigma = 2$, 3, and 4. The resulting variation in the error of the interpolation is shown in Fig. 2. The error increases for $\sigma = 4$ as expected. However, this change

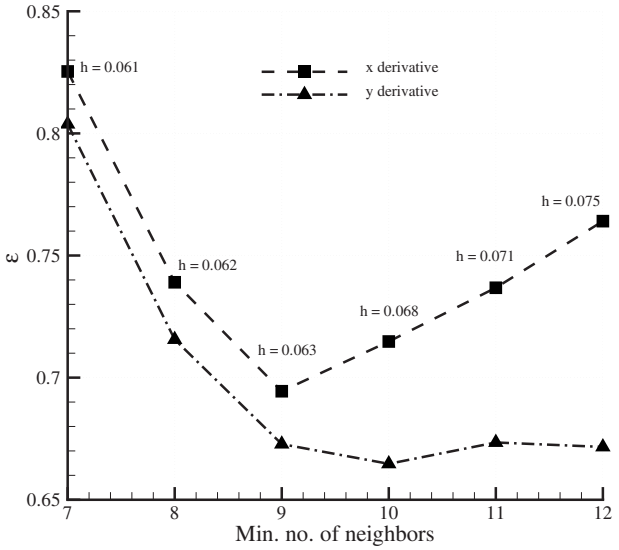

Fig. 1 Problem 1—variation in the rms percent error with the number of neighbors (σ=3)

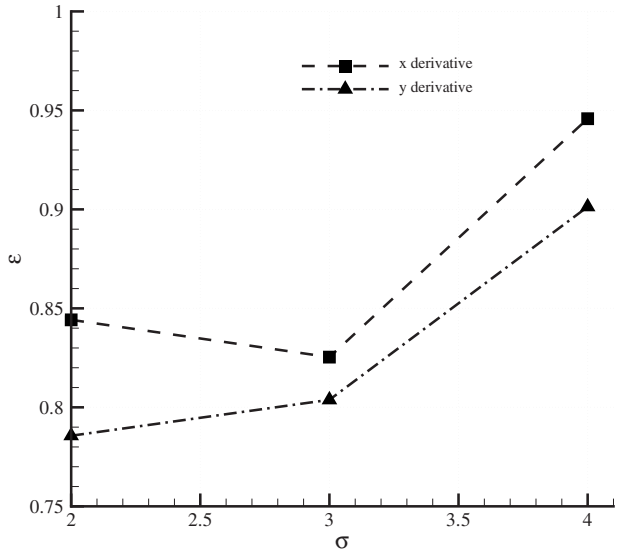

Fig. 2 Problem 1—variation in the rms percent error with sharpness of the Gaussian weight function (N_{min}=7)

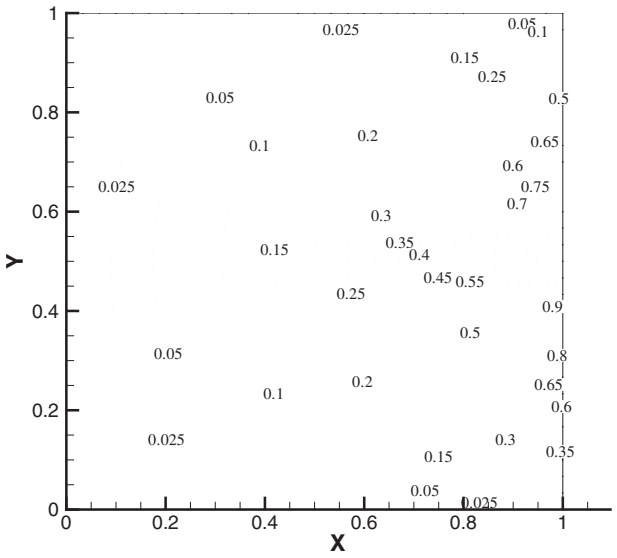

Fig. 3 Problem 2—solution for the heat conduction problem obtained on a nonuniform distribution of 906 points

again is not very significant. This implies that the performance of the interpolation is fairly robust and not very sensitive to variations in the input parameters.

6.2 Problem 2: Conduction in a Domain With a Single Material

6.2.1 Constant Conductivity Material. The method is first applied to a problem for which the analytical solution is known. The problem chosen is heat conduction in a constant conductivity square domain with all Dirichlet boundary conditions. The domain is a unit square with corner coordinates (0,0), (0,1), (1,0), and (1,1) The temperature boundary condition at all but the $x=1$ boundary is $T=0$. On $x=1$, the temperature profile is given by

$$T(x=1,y)=\sin\ \pi y$$

The steady state solution for this problem is given by

$$T_{ex}(x,y)=\frac{\sin\ \pi y\ \sinh\ \pi x}{\sinh\ \pi}$$

This solution was chosen to benchmark the results since the solution is not a polynomial, and the boundary conditions do not impose a discontinuity, defining the residual for each iteration as

$$\rho=\left|b_p-\sum_{i=1}^{N}a^{pi}(T_m^i-T_m^p)\right| \tag{17}$$

Computations are carried out until $\rho<1.0\times10^{-7}$. A contour plot of the temperature obtained by the numerical method is shown in Fig. 3 and shows the expected behavior. The order of accuracy of the method is considered next. Figure 4 plots the average absolute error (compared with the analytical solution) versus the number of points in one direction on a log-log scale for a uniform distribution of points. Here, ν is the number of points in the x-direction used for the computation. The slope of the curve represents the order of accuracy of the method and shows second-order convergence. Convergence for a random distribution of points (Fig. 5) is shown in Fig. 6, and also exhibits approximately second-order convergence. The WLS method is not conservative, as is expected from a scheme akin to finite difference discretization of the governing equations. The percent error in the heat balance ε_q is defined as

$$\varepsilon_q=100\times\frac{|q_{in}-q_{out}|}{q_{in}} \tag{18}$$

where q_{in} represents the heat transfer rate into the domain at $x=1$ and q_{out} is the sum of the heat transfer rates out of the domain at the other boundaries. These quantities are evaluated numerically from the computed solution using

$$q_{in}=\int_{y=0}^{y=1}-k\frac{\partial T}{\partial x}dy$$

and similar formulae for the other boundaries to compute for q_{out}. Numerical integration is carried out with a trapezoid rule. The variation in the percent error in the heat flux with the number of computational points is shown in Tables 1 and 2.

6.2.2 Material With Nonconstant Thermal Conductivity. The one-dimensional heat diffusion equation with space-dependant conductivity and no source term is

$$k\frac{d^2T}{dx^2}+\frac{dk}{dx}\frac{dT}{dx}=0 \tag{19}$$

The above equation is subject to the boundary conditions

$$T(x=0)=0$$

$$T(x=1)=1$$

We consider the case for which $k=1+x$. The results are compared with the analytical solution given by

$$T(x)=\frac{1}{\ln(2)}\ln(1+x)\quad\text{for}\ \ k=1+x$$

The variation in the error with increasing resolution of points is presented in Fig. 7. The results correspond to regular and irregular point distributions. The regular point distributions consist of 225, 900, and 3600 interior points, while the irregular distribution consists of 226, 906, and 3598 interior points. Approximately second-order convergence is obtained for both cases.

A case of temperature-dependant thermal conductivities is also tested. The k versus T characteristics of air are chosen for this case, with

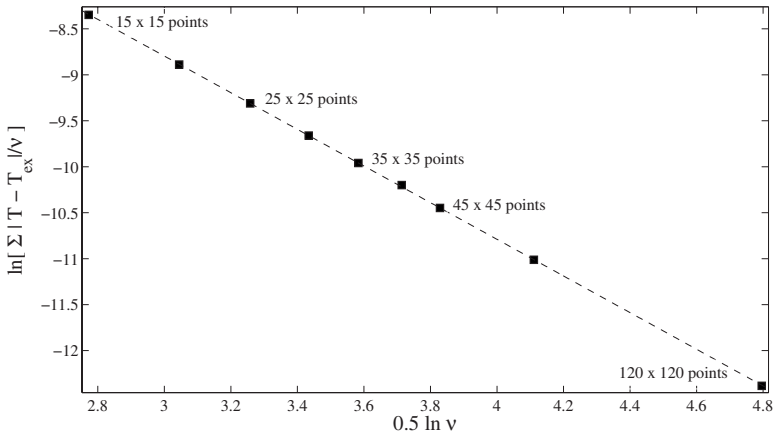

Fig. 4 Problem 2—convergence rate for a uniform distribution of points

$$k(T) = 1.5207^{-11}T^3 - 4.857^{-8}T^2 + 1.0184 \times 10^{-4}T - 3.933 \times 10^{-4}$$

where temperature is in Kelvin and thermal conductivity is in W/m K [24]. The domain chosen for computation is again a unit square with boundary conditions

$$x = 0, \quad T = T_1 = 300 \ K$$

$$x = 1, \quad T = T_2 = 800 \ K$$

$$y = 0, \quad \frac{\partial T}{\partial y} = 0$$

$$y = 1, \quad \frac{\partial T}{\partial y} = 0$$

This temperature difference leads to a doubling of the thermal conductivity in the domain, with $k=0.0262$ W/m K at $x=0$ and $k=0.0578$ W/m K at $x=1$. The expected variation in the temperature is one-dimensional along the x-axis, which is indeed observed in the computation. The dimensionless horizontal center line temperature profile $T^*=(T-T_1)/(T_2-T_1)$ is shown in Fig. 8. The computation corresponds to a regular distribution of points with 14,400 interior points. The analytical solution is obtained by integrating the heat diffusion equation and results in a quartic equation for $T(x)$, which was solved numerically. The agreement with our numerical solution is excellent, with an average temperature error of less than 0.1%.

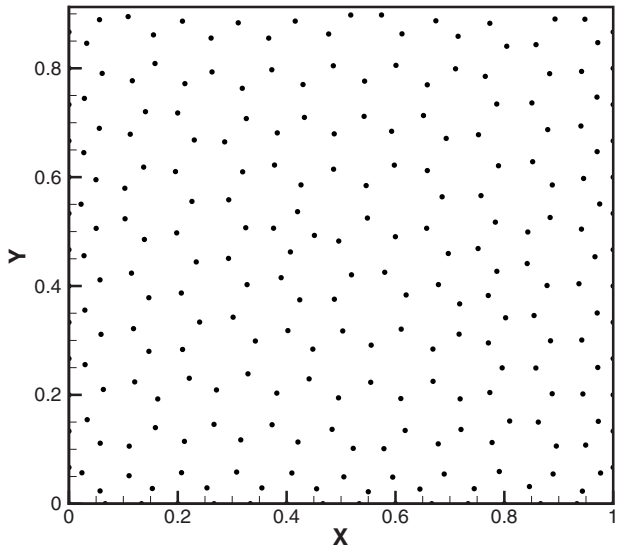

Fig. 5 Problem 2—nonuniform distribution of 226 points used for the computation

6.3 Problem 3: One-Dimensional Conduction in a Domain With Materials of Different Conductivities. The next set of results pertains to a domain, as shown in Fig. 9. The boundaries at $y=0,1$ are adiabatic, i.e., $T(0,y)=0$ and $T(1,y)=1$. The exact solution to this problem is one-dimensional, with straight lines of

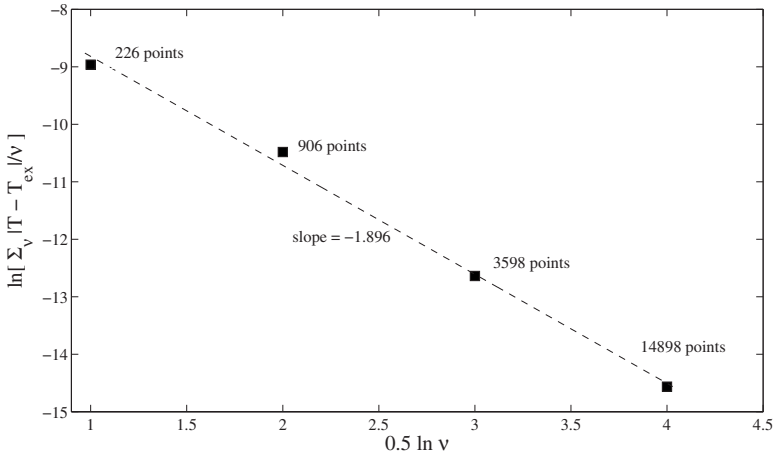

Fig. 6 Problem 2–convergence rate for a nonuniform distribution of points

Table 1 Variation in percent error in the heat flux with the number of computational points (uniform distribution)

No. of points	Percent error
285	5.50
1020	3.88
2205	2.87
3840	2.26
14,880	1.22
40,800	0.752
252,000	0.00

Table 2 Variation in percent error in the heat flux with the number of computational points (nonuniform distribution)

No. of points	Percent error
286	1.13
1026	0.237
3838	0.086
14898	0.022

different slopes in subdomains Ω_1 and Ω_2. The accuracy of the current method is second order, and hence, a straight line profile is expected to be exactly captured. This is indeed observed, as seen in Fig. 9. This figure shows the solution obtained for a conductivity ratio $k_2/k_1=1000$. The accuracy of the solution is independent of the density of points, the conductivity ratio, and the nature of their arrangement, i.e., uniform or random. The computed solution coincides exactly with the exact solution, with errors $O(1\times10^{-15})$. Since the computed solution coincides with the exact solution to machine zero, flux balance is also exactly obtained. This is in contrast to the method presented in Ref. [18], where finite errors in the flux balance have been reported. The conductivity ratio poses no limitation on the stability or accuracy of the method.

6.4 Problem 4: Conjugate Heat Conduction in 2D Domain. Consider a domain with material distribution, as shown in Fig. 10. The dashed boxes represent a material of conductivity k_2 embedded in a background material of conductivity k_1. The boundary conditions on the external boundaries of the domain are given by

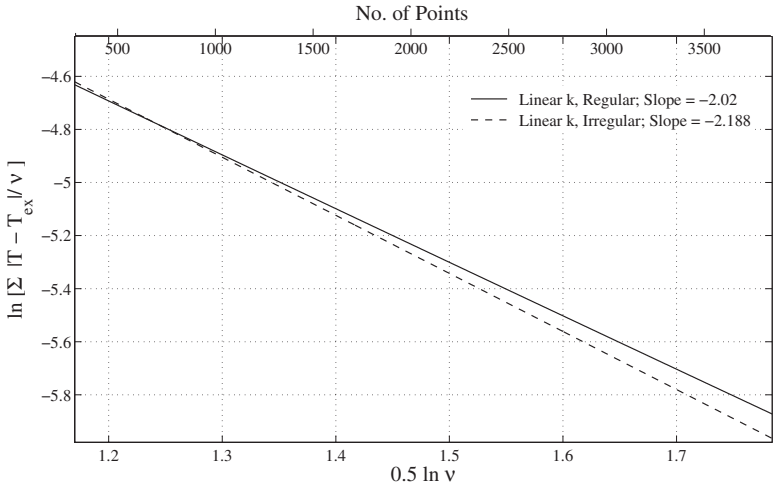

Fig. 7 Problem 2–convergence rate for linear variation in conductivity

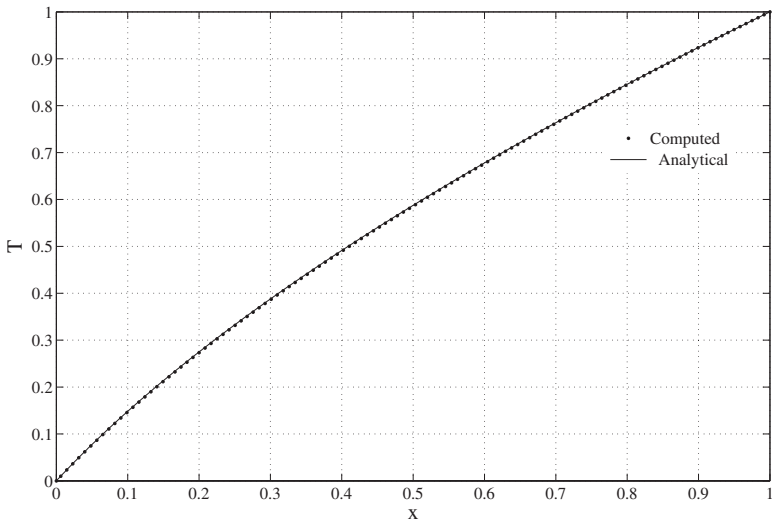

Fig. 8 Problem 2–horizontal center line temperature profile for *k* versus *T* characteristic of air (nondimensionalized)

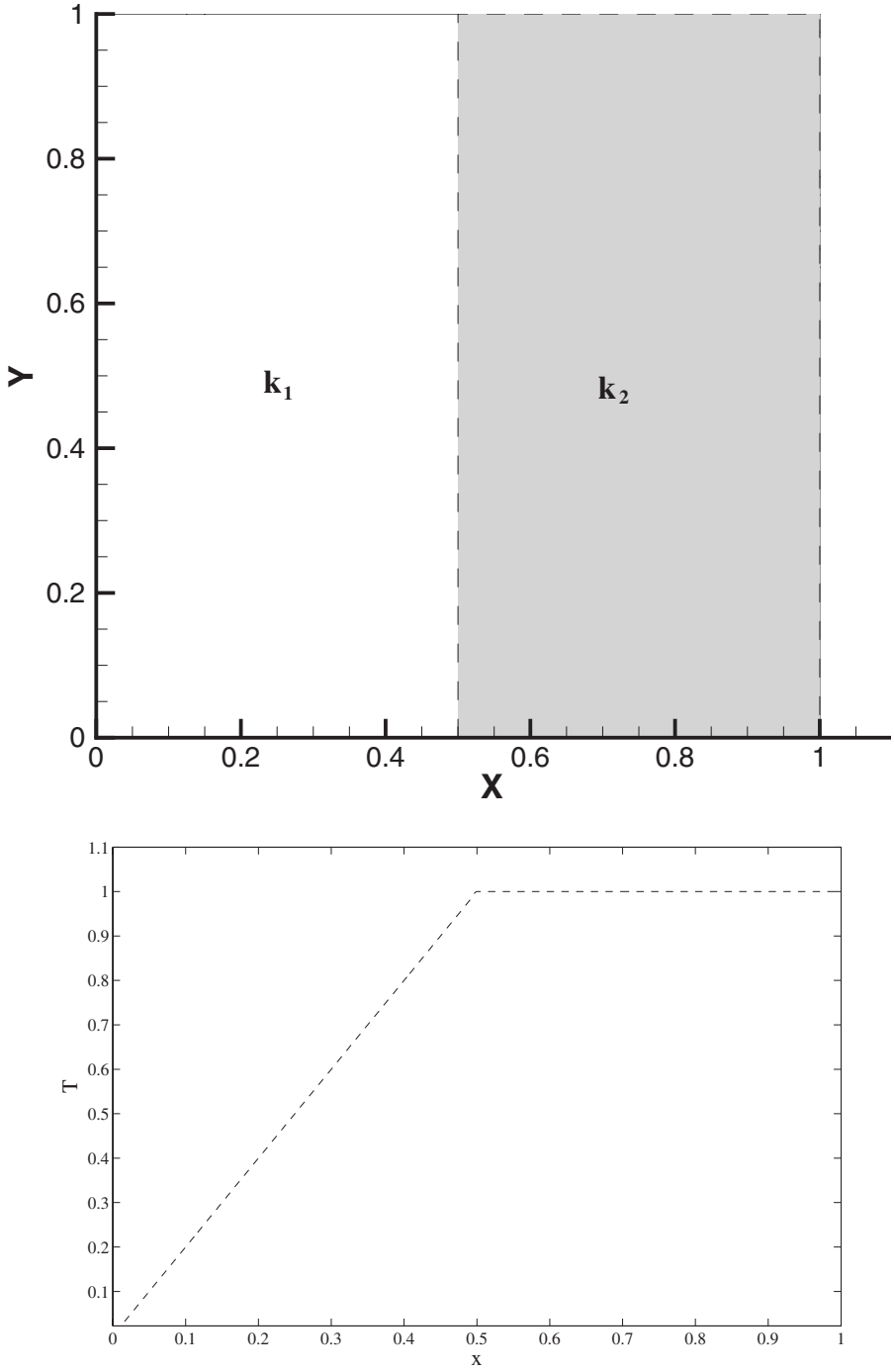

Fig. 9 Problem 3–domain for two-dimensional conjugate conduction and one-dimensional temperature profile in a domain with $k_2/k_1=1000$

$$T(0,y) = 0, \quad T(1,y) = 1$$

$$\left(\frac{\partial T}{\partial y}\right)_{y=0} = \quad 0\left(\frac{\partial T}{\partial y}\right)_{y=1} = 0$$

Continuity of the temperature and heat flux is applied at the interface between the two materials, as shown in Eqs. (3) and (4). The results are computed on point distributions of varying density, with both uniform and random distributions of points. The resulting temperature profile for a 1600 point uniform distribution and different conductivity ratios is shown in Fig. 10. The same for a scattered distribution of points with comparable point density is shown in Figs. 11.

Next, the temperature profiles computed using the WLS scheme are compared with those obtained using FLUENT. Conductivity ratios of 2, 100, and 1000 are considered, using both uniform and nonuniform distributions of points for the WLS scheme. The nonuniform distribution of points used for the WLS method was obtained by perturbing positions of regular point distributions. The perturbation at any point was allowed to be at most 15% of the spacing for a regular distribution in any direction. A nonuniform distribution of 40×40 points refers to 40 edge nodes of the nonuniform mesh. The FLUENT solution is obtained using an unstruc-

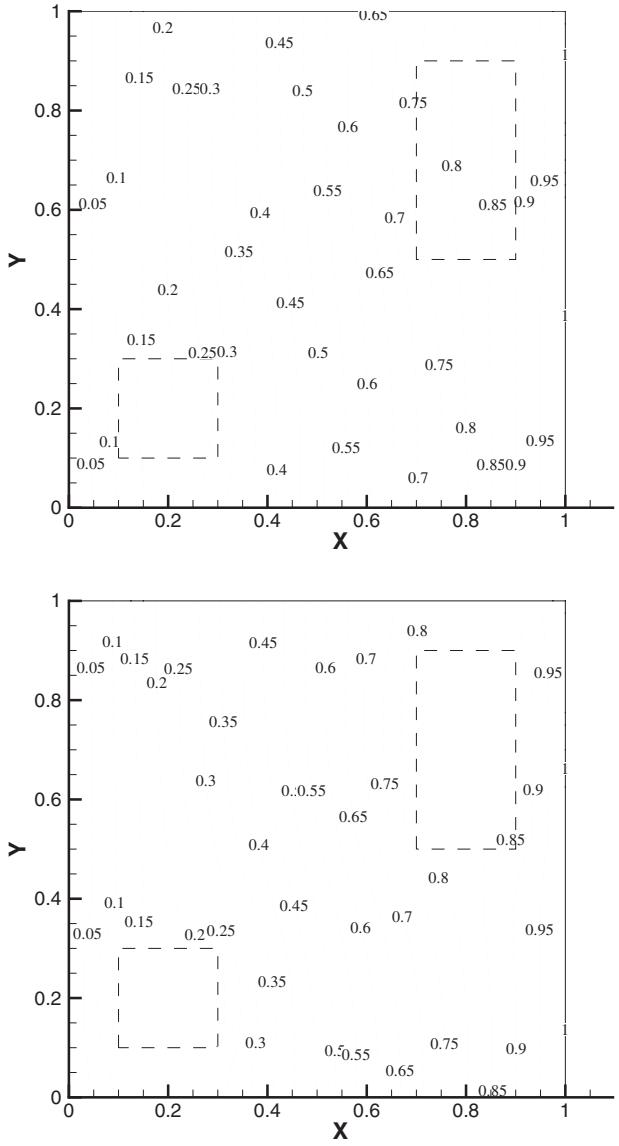

Fig. 10 Problem 4–temperature distribution computed on a uniform arrangement of 1680 points $k_2/k_1=2$ and 1000

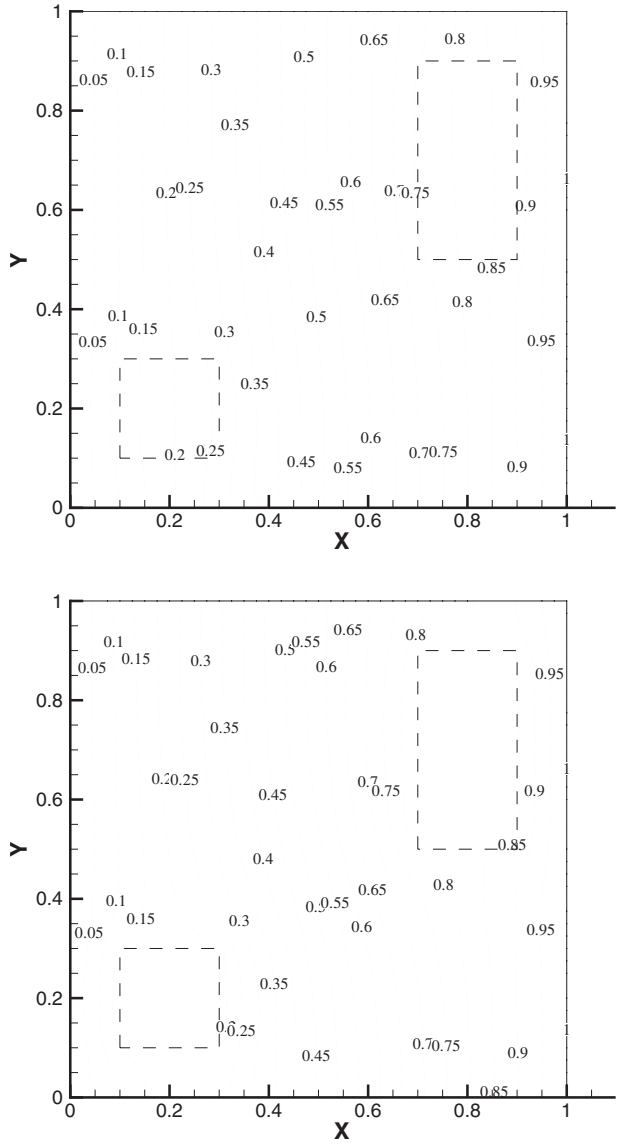

Fig. 11 Problem 4–temperature distribution computed on a nonuniform arrangement of 1680 points $k_2/k_1=2$ and 1000

tured mesh with 90,602 cells. Table 3 lists the total number of points for various point distributions. The solution obtained using FLUENT on a mesh with 90,602 cells is found to be mesh-independent and is used as a reference. Figure 12 shows the temperature profile at $y=0.7$ for a uniform distribution of points with varying density and different conductivity ratios. Figure 13 shows the same for an nonuniform distribution of points. It is noted that the location of the interface is sharply captured by the WLS method, since computational points have been explicitly placed at the interface. The profiles are found to match the FLUENT solution very well for all point densities. The error in heat balance again goes to zero with increasing point density, as seen in Fig. 14.

7 Conclusions

A meshless method for the simulation of conjugate heat conduction problems has been developed in this work. The weighted least-squares method is used to compute for partial derivatives, and interface conditions are imposed by applying the continuity of the temperature and heat flux at the interface and using one-sided representations of the temperature derivatives on either side of the interface. The methodology is shown to match the analytical solutions for single-material domains, and to yield exact solutions to simple one-dimensional conjugate conduction problems. The temperature error decreases at a rate that is approximately second-order for single-material heat conduction problems. Though the method is not conservative, heat balance error decreases quadratically with increasing density of points. Furthermore, spurious temperature oscillations observed in published meshless formulations for conjugate heat transfer are not observed, even for conductivity ratios as high as 1000. The current method may be extended to include second-order accurate interface conditions, and is especially amenable to solution adaptivity. Future extensions also include the generalization to convection-diffusion and fluid flow problems, and to fluid-structure interaction computations.

Table 3 Number of points for various point distributions

Label	No. of points
40×40	1680
50×50	2600
60×60	3720
120×120	14,640

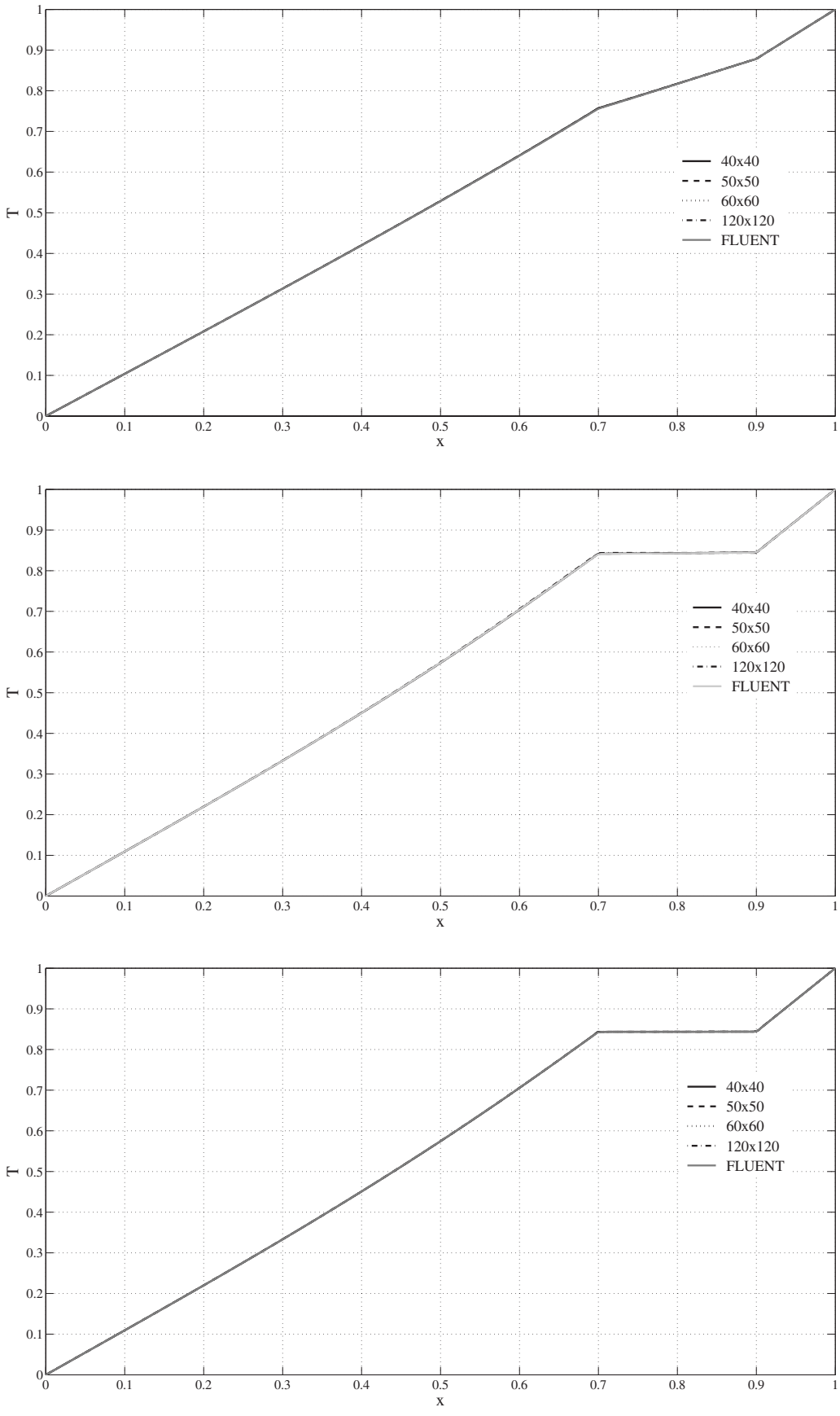

Fig. 12 Problem 4–temperature profile at $y=0.7$ for $k_2/k_1=2$, 100, and 1000 (uniform point distribution)

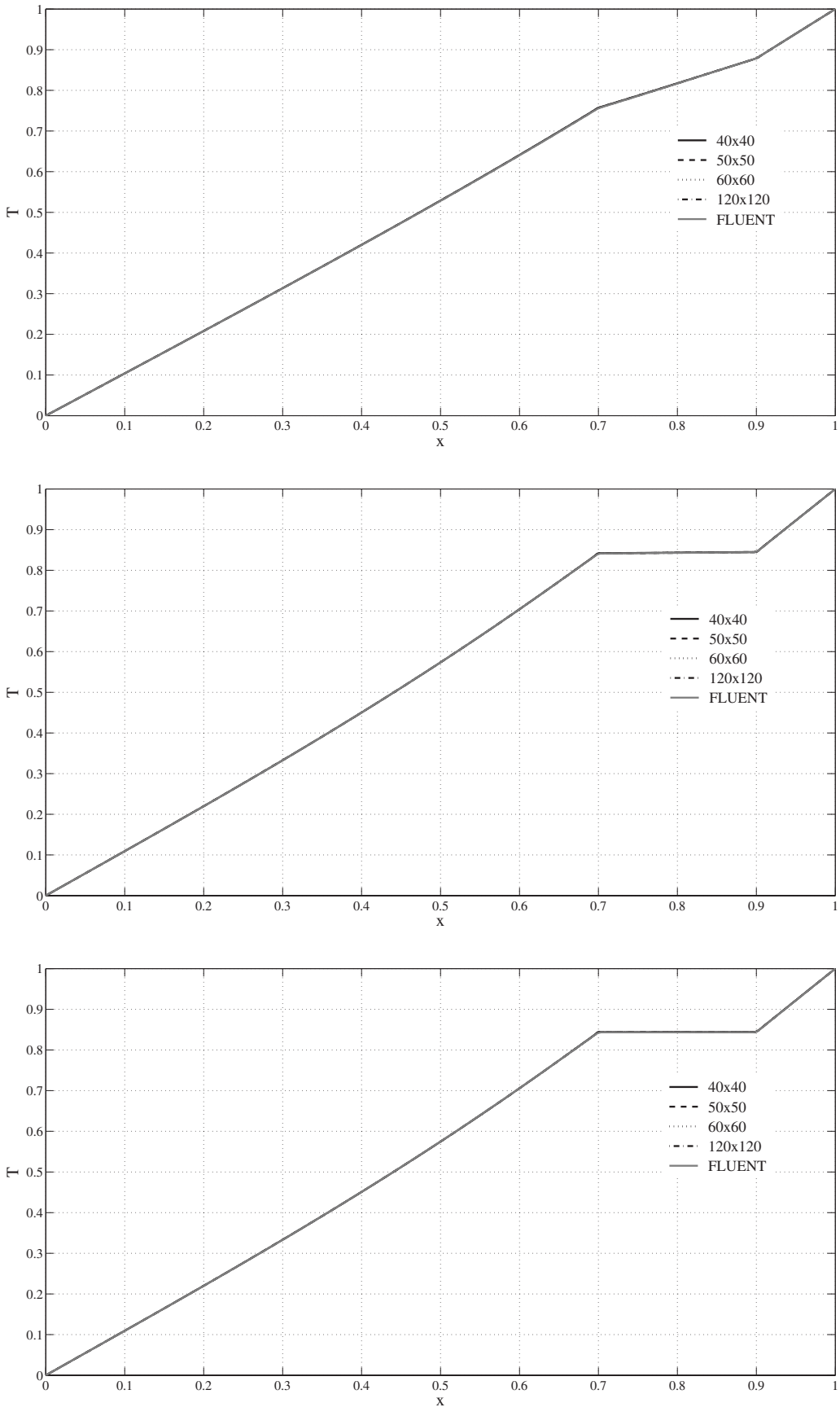

Fig. 13 Problem 4–temperature profile at $y=0.7$ for $k_2/k_1=2$, 100, and 1000 (nonuniform point distribution)

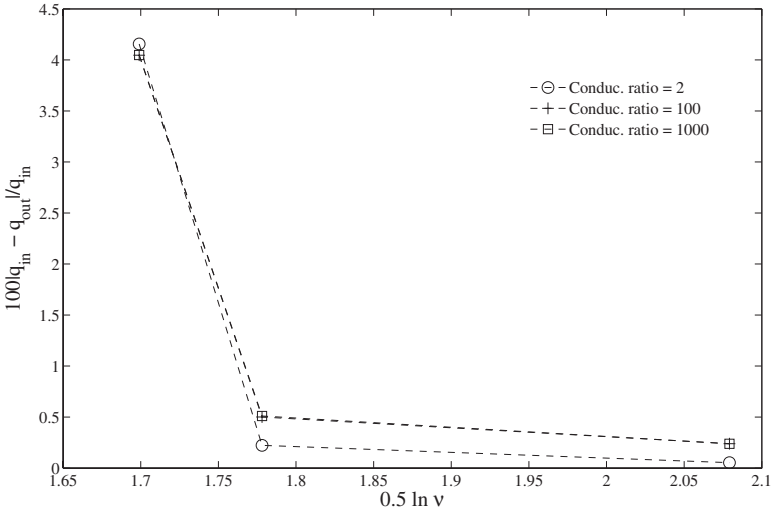

Fig. 14 Problem 4–variation in percent error in the heat balance with increasing density of points for different conductivity ratios (uniform point distribution)

Nomenclature

a = scalar
$\hat{a}$ = coefficient vector
a^{pi} = ith coefficient in the discretization about point p
b = scalar
b_p = source term in the equation for point p
F = $(N \times P)$ matrix
g = space-dependant function
h = smoothing radius
i = neighbor index
J = discrete weighted residual
k_m = thermal conductivity of material m
m = material index
N = total number of neighbors of point (x_p, y_p)
$N_<$ = number of negative coefficients
$N_>$ = number of positive coefficients
$\boldsymbol{n}$ = surface normal
$p_i(x,y)$ = basis functions
P = total number of basis functions
q_{in} = heat transfer rate entering the domain
q_{out} = heat transfer rate exiting the domain
s = source term in the heat diffusion equation
T_{ex} = exact solution
T_m = temperature in domain with material index m
T_m^i = temperature at point i in material with conductivity k_m
T^* = temperature
$u(x,y)$ = local function equal to $f(x,y) - f(x_p, y_p)$
$\hat{u}^h$ = vector of the approximate function
$u^h(x,y)$ = approximation to function $u(x,y)$
w = weight function
W = weight matrix
(x,y) = point in a two-dimensional domain
(x_p, y_p) = point in a two-dimensional domain
(x_i', y_i') = neighbors of (x_p, y_p)
(x,y,z) = point in a three-dimensional domain

Greek Symbols

$\partial\Omega$ = domain boundary
$\partial\Omega_{lm}$ = interface between materials l and m
Δx = difference in the x-coordinates of two points
Δy = difference in the y-coordinates of two points
ε_q = percent error in the heat balance
Ω_m = subdomain m

Subscripts and Superscripts

i = index
l = material number
m = material number
p = point p

References

[1] Belytschko, T., Krongauz, Y., Organ, D., Fleming, M., and Krysl, P., 1996, "Meshless Methods: An Overview and Recent Developments," Comput. Methods Appl. Mech. Eng., **139**, pp. 3–47.
[2] Li, S., and Liu, W. K., 2002, "Meshfree and Particle Methods and Their Applications," Appl. Mech. Rev., **55**(1), pp. 1–34.
[3] Babuška, I., Banerjee, U., and Osborn, J., 2003, "Survey of Meshless and Generalized Finite Element Methods: A Unified Approach," Acta Numerica, **12**, pp. 1–125.
[4] Lucy, L. B., 1977, "A Numerical Approach to the Testing of the Fission Hypothesis," Astron. J., **82**, pp. 1013–24.
[5] Gingold, R. A., and Monaghan, J. J., 1977, "Smoothed Particle Hydrodynamics: Theory and Application to Non-Spherical Stars," Mon. Not. R. Astron. Soc., **181**, pp. 375–389.
[6] Duarte, C. A., and Oden, J. T., 1998, "H-p Clouds—An h-p Meshless Method," Numer. Methods Partial Differ. Equ., **12**, pp. 673–705.
[7] Oñate, E., Idelsohn, S., Zienkiewicz, O., Taylor, R., and Sacco, C., 1996, "A Stabilized Finite Point Method for Analysis of Fluid Mechanics Problems," Comput. Methods Appl. Mech. Eng., **139**, pp. 315–346.
[8] Oñate, E., 1998, "Derivation of Stabilized Equations for Numerical Solution of Advective-Diffusive Transport and Fluid Flow Problems," Comput. Methods Appl. Mech. Eng., **151**, pp. 233–265.
[9] Oñate, E., García, J., and Idelsohn, S., 1997, "Computation of the Stabilization Parameter for the Finite Element Solution of Advective-Diffusive Problems," Int. J. Numer. Methods Fluids, **25**, pp. 1385–1407.
[10] Idelsohn, S. R., Oñate, E., Calvo, N., and Pin, F. D., 2003, "The Meshless Finite Element Method," Int. J. Numer. Methods Eng., **58**, pp. 893–912.
[11] Oñate, E., 2000, "A Stabilized Finite Element Method for Incompressible Viscous Flows Using a Finite Increment Calculus Formulation," Comput. Methods Appl. Mech. Eng., **182**, pp. 355–370.
[12] Oñate, E., and Idelsohn, S., 1998, "A Mesh-Free Finite Point Method for Advective-Diffusive Transport and Fluid Flow Problems," Comput. Mech., **21**, pp. 283–292.
[13] Oñate, E., Sacco, C., and Idelsohn, S., 2000, "A Finite Point Method for Incompressible Flow Problems," Comput. Visualization Sci., **3**, pp. 65–75.
[14] Idelsohn, S. R., Oñate, E., and Pin, F. D., 2004, "The Particle Finite Element Method: A Powerful Tool to Solve Incompressible Flows With Free-Surfaces and Breaking Waves," Int. J. Numer. Methods Eng., **61**, pp. 964–989.
[15] Löhner, R., Sacco, C., Oñate, E., and Idelsohn, S., "A Finite Point Method for Compressible Flow," Technical Report No. MS 4C7, School of Computational Science and Informatics, George Mason University.

[16] Aluru, N. R., and Li, G., 2001, "Finite Cloud Method: A True Meshless Technique Based on a Fixed Reproducing Kernel Approximation," Int. J. Numer. Methods Eng., **50**(10), pp. 2373–2410.
[17] Sadat, H., D., N., Gbahoue, L., and Sophy, T., 2006. "On the Solution of Heterogeneous Heat Conduction Problems by a Diffuse Approximation Meshless Method," Numer. Heat Transfer, Part B, **50**, pp. 491–498.
[18] Fang, J., Zhao, G., Zhao, J., and Parriaux, A., 2009, "On the Truly Meshless Solution of Heat Conduction Problems in Heterogeneous Media," Numer. Heat Transfer, Part B, **55**(1), pp. 1–13.
[19] Lancaster, P., and Salkauskas, K., 1981, "Surfaces Generated by Moving Least Squares Methods," Math. Comput., **155**(37), pp. 141–148.
[20] Finkel, R. A., and Bentley, J. L., 1974, "Quad Trees a Data Structure for Retrieval on Composite Keys," Acta Informatica, **4**, pp. 1–9.
[21] Hutchinson, B. R., and Raithby, G. D., 1986, "A Multigrid Method Based on the Additive Correction Strategy," Numer. Heat Transfer, Part A, **9**(5), pp. 511–537.
[22] Mathur, S., and Murthy, J. Y., 1997, "A Pressure-Based Method for Unstructured Meshes," Numer. Heat Transfer, **31**(2), pp. 195–215.
[23] 2006. *FLUENT 6.3 Users' Guide*, Fluent Inc., Lebanon, NH.
[24] Incropera, F. P., de Witt, D. P., Bergman, T. L., and Levine, A. S., 2007, *Introduction to Heat Transfer*, Wiley, Hoboken, NJ.

Numerical Simulation of Convective Heat Transfer Modes in a Rectangular Area With a Heat Source and Conducting Walls

G. V. Kuznetsov
Faculty of Thermal Power Engineering,
Tomsk Polytechnic University,
30 Lenin Avenue,
634050 Tomsk, Russia

M. A. Sheremet[1]
Faculty of Mechanics and Mathematics,
Tomsk State University,
36 Lenin Avenue,
634050 Tomsk, Russia
e-mail: michael-sher@yandex.ru

Laminar conjugate heat transfer in a rectangular area having finite thickness heat-conducting walls at local heating has been analyzed numerically. The heat source located on the left wall is kept at constant temperature during the whole process. Conjugate heat transfer is complicated by the forced flow. The governing unsteady, two-dimensional flow and energy equations for the gas cavity and unsteady heat conduction equation for solid walls, written in dimensionless form, have been solved using implicit finite-difference method. The solution has been obtained in terms of the stream function and the vorticity vector. The effects of the Grashof number Gr, the Reynolds number Re, and the dimensionless time on the flow structure and heat transfer characteristics have been investigated in detail. Results have been obtained for the following parameters: $10^3 \le Gr \le 10^7$, $100 \le Re \le 1000$, *and* $Pr = 0.7$. *Typical distributions of thermohydrodynamic parameters describing features of investigated process have been received. Interference of convective flows (forced, natural, and mixed modes) in the presence of conducting solid walls has been analyzed. The increase in Gr is determined to lead to both the intensification of the convective flow caused by the presence of the heat source and the blocking of the forced flow nearby the upper wall. The nonmonotomic variations in the average Nusselt number with Gr for solid-fluid interfaces have been obtained. The increase in Re is shown to lead to cooling of the gas cavity caused by the forced flow. Evolution of analyzed process at time variation has been displayed. The diagram of the heat convection modes depending on the Grashof and Reynolds numbers has been obtained. The analysis of heat convection modes in a typical subsystem of the electronic equipment is oriented not only toward applied development in microelectronics, but also it can be considered as test database at creation of numerical codes of convective heat transfer simulation in complicated energy systems. Comparison of the obtained results can be made by means of both streamlines and temperature fields at different values of the Grashof number and Reynolds number, and the average Nusselt numbers at solid-fluid interfaces.* [DOI: 10.1115/1.4001303]

Keywords: convection modes, conjugate heat transfer, laminar flow, heat source

1 Introduction

Thermal modes of the electronic components substantially define reliability of their work [1,2]. Miniaturization of electronic devices and hence the increase in the amount of heat dissipated per unit volume has led to necessity of attention concentration on a thermal state of an object. Thus one of the crucial issues is the selection of a cooling method [3–10]. Now a lot of researches concerning cooling of electronic components [3–10] were led, but at the same time the small attention was given to the analysis of influence of the time as the analyzed problem is essentially nonstationary, of solid walls having finite thickness and of nonlinear heat exchange with an environment on velocity and temperature fields in a fluid cavity. At the same time, the effect of heat-conducting walls having finite thickness leads to the significant changes in thermal modes of the system [11,12].

Hong et al. [6] presented results of a numerical study on the hydrodynamic and thermal characteristics of a right-angled fractal-shaped microchannel network heat sink with application to integrated microelectronic cooling. The conjugate heat transfer model predicted the thermal characteristics accurately. Due to the structural limitation of right-angled fractal-shaped microchannel network, hotsports were found to appear on the bottom wall of the heat sink where the microchannels are sparsely distributed. Polat and Bilgen [7] carried out a numerical investigation of conjugate heat transfer in inclined open shallow cavities. Only one thick wall facing the opening was heated by a constant heat flux, sides perpendicular to the heated wall were insulated and the opening was in contact with a fluid at constant temperature and pressure. The effect of Rayleigh number and the inclination angle on the fluid flow and heat transfer was analyzed. It is found that the volume flow rate and the heat transfer are both increasing function of Rayleigh number and the aspect ratio and decreasing function of the dimensionless conductivity ratio. Madhusudhana Rao and Narasimham [8] numerically studied conjugate mixed convection from protruding heat-generating ribs attached to substrates forming vertical channel walls. The heat sources and substrates simulate integrated circuit packages attached to printed circuit boards.

[1]Corresponding author.

Contributed by the Heat Transfer Division of ASME for publication in the JOURNAL OF HEAT TRANSFER. Manuscript received November 5, 2008; final manuscript received February 14, 2010; published online May 20, 2010. Assoc. Editor: Roger Schmidt

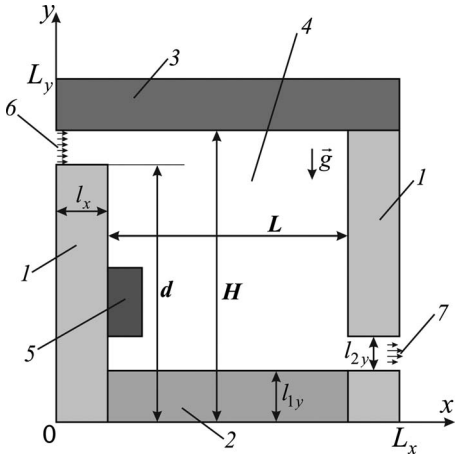

Fig. 1 A scheme of the system: (1–3) solid walls; (4) fluid; (5) heat source; (6) inlet; (7) outlet

It is shown that simple adiabatic boundary condition for the substrate and isothermal or isoflux condition for the heat source portions are not appropriate and that the conjugate nature of the problem should be duly considered taking into account the heat conduction in both the components and the substrate. Even a lower thermal conductivity substrate can be very effective in terms of heat removal and redistribution of the heat from the components. Muftuoglu and Bilgen [9] determined optimum positions of a discrete heater placed on the vertical wall facing the opening of cavities. Best thermal performance was obtained by positioning the discrete heater at off center and slightly closer to the bottom. The Nusselt number and the volume flow rate in and out the open cavity were an increasing function of the Rayleigh number and the wall thickness, and a decreasing function of the conductivity ratio. Premachandran and Balaji [10] presented the results of a numerical study of conjugate convection with surface radiation from horizontal channel with protruding heat sources. The dimensionless temperature and the effect of radiation interaction decrease as the Reynolds number increase. As the emissivity of the protruding heat source and substrate increases, the dimensionless maximum temperature decreases. The radiation contribution increases from 12% to 20%, as the emissivity of protruding heat source increases from 0.1 to 0.85.

But all of the above studies have neglected either the effect of transient factor or the effect of convective-radiative heat exchange with an environment.

The objective of this work is the mathematical simulation of convective heat transfer in a rectangular area with a heat source in view of conductive heat transfer through the solid walls having finite thickness, and also at presence of the external forced flow caused by a moderate ventilation mode.

2 Analysis

2.1 Physical Model and Assumptions. The physical model of transient conjugate heat transfer and the coordinate system under consideration are schematically shown in Fig. 1.

The system considered consists of rectangles with different sizes and thermophysical characteristics. A heat source located on internal border of the left wall is characterized by a constant temperature during the whole process. The heat source is a heat-generating element of electronic equipment having constant temperature at his surface. Horizontal ($y=0$, $y=L_y$) and vertical ($x=L_x$) walls of the finite thickness forming the gas cavity are assumed to be adiabatic or line of symmetry from outside. These conditions reflect the possible presence of similar objects beyond external borders. Convective-radiative heat exchange with an environment is modeled on the outer boundary $x=0$. These conditions allow to evaluate the effect of an environment by means of convection and radiation on heat transfer modes of the typical element of the electronic equipment. A constant horizontal flow velocity has been set at inlet (zone 6 in Fig. 1). The symmetry conditions in a longitudinal direction like mild boundary conditions for the gas flow have been set at outlet (zone 7).

It is assumed in the analysis that the thermophysical properties of the solid walls and of the gas are independent of temperature, and the flow is laminar. The fluid is Newtonian and incompressible, and the Boussinesq approximation is valid. The fluid motion and heat transfer in the cavity are supposed to be two dimensional. Radiation heat exchange between the walls is neglected in comparison with convection, and the fluid is presumed to be radiatively nonparticipating. Viscous heat dissipation in the fluid is assumed to be negligible in comparison with conduction and convection.

2.2 Governing Equations. The heat transfer process in considered area (Fig. 1) is described by transient two-dimensional equations under Boussinesq approach in the gas cavity [13–15] and by the unsteady two-dimensional heat conduction equation for the solid walls [16] with nonlinear boundary conditions.

The mathematical model is formulated in terms of the dimensionless variables such as stream function, vorticity, and temperature. The length of the decision region along axis x is chosen as a scale distance. The following correlations are used for reduction to dimensionless form of the equations:

$$X = x/L_x, \quad Y = y/L_x, \quad \tau = t/t_0, \quad U = u/V_{\text{in}}, \quad V = v/V_{\text{in}},$$

$$\Theta = (T - T_0)/(T_{\text{hs}} - T_0), \quad \Psi = \psi/\psi_0, \quad \Omega = \omega/\omega_0$$

where $\psi_0 = V_{\text{in}} L_x$, $\omega_0 = V_{\text{in}}/L_x$.

The governing equations of conjugate heat transfer in dimensionless form become the following.

- In the fluid cavity (4 in Fig. 1),

$$\frac{\partial \Omega}{\partial \tau} + \frac{\partial \Psi}{\partial Y}\frac{\partial \Omega}{\partial X} - \frac{\partial \Psi}{\partial X}\frac{\partial \Omega}{\partial Y} = \frac{1}{\text{Re}}\left(\frac{\partial^2 \Omega}{\partial X^2} + \frac{\partial^2 \Omega}{\partial Y^2}\right) + \frac{\text{Gr}}{\text{Re}^2}\frac{\partial \Theta}{\partial X} \tag{1}$$

$$\frac{\partial^2 \Psi}{\partial X^2} + \frac{\partial^2 \Psi}{\partial Y^2} = -\Omega \tag{2}$$

$$\frac{\partial \Theta}{\partial \tau} + \frac{\partial \Psi}{\partial Y}\frac{\partial \Theta}{\partial X} - \frac{\partial \Psi}{\partial X}\frac{\partial \Theta}{\partial Y} = \frac{1}{\text{Re Pr}}\left(\frac{\partial^2 \Theta}{\partial X^2} + \frac{\partial^2 \Theta}{\partial Y^2}\right) \tag{3}$$

- For the solid walls (1–3 in Fig. 1),

$$\frac{1}{\text{Fo}_i}\frac{\partial \Theta_i}{\partial \tau} = \frac{\partial^2 \Theta_i}{\partial X^2} + \frac{\partial^2 \Theta_i}{\partial Y^2}, \quad i = \overline{1,3} \tag{4}$$

2.3 Initial and Boundary Conditions. Initial and boundary conditions for the formulated problems (1)–(4) look like the following.

Initial conditions.

$$\Psi(X,Y,0) = 0, \quad \Omega(X,Y,0) = 0$$

$\Theta(X,Y,0) = 0$ with the exception of heat source, on which during the whole process $\Theta = 1$.

Boundary conditions.

- At $X=0$, the conditions considering heat exchange with an environment due to convection and radiation are realized:

$$\frac{\partial \Theta_i(X,Y,\tau)}{\partial X} = \text{Bi}_i \cdot \Theta_i(X,Y,\tau) + \text{Bi}_i \cdot \frac{T_0 - T_e}{T_{\text{hs}} - T_0} + Q_i \tag{5}$$

where

$$Q_i = N_i \cdot \left[\left(\Theta_i(X,Y,\tau) + \frac{T_0}{T_{\text{hs}} - T_0} \right)^4 - \left(\frac{T_e}{T_{\text{hs}} - T_0} \right)^4 \right]$$

$i=1,3,4$ according to Fig. 1.

- Adiabatic conditions or symmetry conditions are set on other external borders:

$$\frac{\partial \Theta_i(X,Y,\tau)}{\partial X^{\text{nr}}} = 0 \quad \text{where} \quad X^1 \equiv X, X^2 \equiv Y, \quad i = \overline{1,4}$$

These conditions reflect the possible presence of similar objects beyond external borders.

- Conditions of fourth kind are accomplished at all parts of the decision region where there is an interface of materials with different thermophysical characteristics:

$$\Theta_i = \Theta_j, \quad \frac{\partial \Theta_i}{\partial X^{\text{nr}}} = k_{j,i} \frac{\partial \Theta_j}{\partial X^{\text{nr}}}, \quad i,j = \overline{1,4}, \ i \neq j, \quad \text{nr} = 1,2$$

These physically based boundary conditions determine the temperature continuity and the heat flux continuity at the interfaces of materials with different thermophysical properties.

- At inlet (zone 6), boundary conditions of the third kind (5) for the energy equation are considered. For the stream function and the vorticity,

$$\Psi = Y - \frac{d}{L_x}, \quad \Omega = 0$$

Boundary conditions for the stream function at inlet (zone 6, Fig. 1) are determined by means of the known horizontal flow velocity. As $U=1$ and $V=0$ at $X=0$, then taking into account $U=\partial\Psi/\partial Y$, we obtain the following condition:

$$\Psi = \int_{d/L_x}^{Y} U dY = Y - \frac{d}{L_x}$$

- At outlet (zone 7),

$$\frac{\partial \Psi}{\partial X} = \frac{\partial \Omega}{\partial X} = \frac{\partial \Theta}{\partial X} = 0$$

- At internal solid-fluid interfaces ($Y=d/L_x, \quad Y=l_{1y}/L_x$) parallel to an axis $0X$,

$$\Psi = 0, \quad \frac{\partial \Psi}{\partial Y} = 0, \quad \Theta_i = \Theta_4, \quad \frac{\partial \Theta_i}{\partial Y} = k_{4,i} \frac{\partial \Theta_4}{\partial Y}, \quad i = 1,2$$

- At internal solid-fluid interface ($X=l_x/L_x$) parallel to an axis $0Y$,

$$\Psi = 0, \quad \frac{\partial \Psi}{\partial X} = 0, \quad \Theta_1 = \Theta_4, \quad \frac{\partial \Theta_1}{\partial X} = k_{4,1} \frac{\partial \Theta_4}{\partial X}$$

- At internal solid-fluid interfaces ($Y=H/L_x, Y=l_{1y}+l_{2y}/L_x$) parallel to an axis $0X$,

$$\Psi = \frac{H-d}{L_x}, \quad \frac{\partial \Psi}{\partial Y} = 0, \quad \Theta_i = \Theta_4, \quad \frac{\partial \Theta_i}{\partial Y} = k_{4,i} \frac{\partial \Theta_4}{\partial Y},$$

$$i = 1,3$$

- At internal solid-fluid interface ($X=l_x+L/L_x$) parallel to an axis $0Y$,

$$\Psi = \frac{H-d}{L_x}, \quad \frac{\partial \Psi}{\partial X} = 0, \quad \Theta_1 = \Theta_4, \quad \frac{\partial \Theta_1}{\partial X} = k_{4,1} \frac{\partial \Theta_4}{\partial X}$$

2.4 Solution Methodology. The problems (1)–(4) with corresponding boundary and initial conditions have been solved by means of finite-difference method [15,17–19] on a uniform grid of 200×200. The grid size in the wall was 30 for each direction.

Equations (1)–(4) were solved sequentially; each time step was started from the temperature field computation both in the gas cavity and in the solid walls (Eqs. (3) and (4)), and then the Poisson equation (2) was solved for the stream function. The boundary conditions for the vorticity vector were determined thereafter and Eq. (1) was solved.

The monotone scheme of Samarsky [18] was used for convective terms in the evolutionary equations. Approximation of diffusion terms was entered with usage of the central finite differences. Vorticity values at solid walls were defined by Woods formula [17,19]. The locally one-dimensional scheme of Samarsky was used to solve Eqs. (1)–(4). In this scheme, the solution to a two-dimensional scheme reduces to sequential solution to one-dimensional systems. In this case, the solution to one-dimensional system reduces to a sequential solution to systems of difference equations with tridiagonal matrices by tridiagonal matrix algorithm (TDMA) [18]. It is to be noted here that the approximation of convective terms considered to be averaged with respect to U and $|U|$ (V and $|V|$) in order for the scheme be independent of the velocity sign [17]. An implicit difference scheme was used. The evolutionary term represented a one-sided difference in time and had the first order of accuracy in time step. All the derivatives with respect to spatial coordinates were approximated with the second order of accuracy in the step along the coordinate. The simple iteration technique was applied to resolve the nonlinear boundary condition of the third kind (5). Exploitable locally one-dimensional scheme is absolutely stable [18]. The difference approximation order of the original differential problem is $O(\tau_t + h_x^2 + h_y^2)$, where τ_t is the dimensionless time step, and h_x and h_y are the dimensionless grid steps along horizontal and vertical Cartesian coordinates.

The Poisson equation (2) for the stream function has been solved on each time step by the pseudo-unsteady method [17]; that is, the solution of unsteady problem was considered by analogy with the solution of Eqs. (1), (3), and (4). The convergence condition to the stationary solution had the following form:

$$\max_{l,m} |\Psi_{l,m}^{p+1} - \Psi_{l,m}^{p}| < \tilde{\varepsilon} \tag{6}$$

where p is the iteration number, l and m are the grid node coordinates, and $\tilde{\varepsilon}$ is the accuracy of computations.

Table 1 Variations in the average Nusselt number on vertical walls with the Rayleigh number

Ra	[20]	[21]	Present study with a uniform grid 100×100
10^3	1.118	1.121	1.117
10^4	2.243	2.286	2.241
10^5	4.519	4.546	4.509
10^6	8.800	8.652	8.841

3 Grid Independence Study and Validation

The independence of the solution with respect to the grid size is studied for the Rayleigh number of 10^7. Two different grid sizes of 200×200 and 300×300 are used for the grid independence study. The maximum difference in terms of the average Nusselt number at solid-fluid interfaces for various grids is less than 1%, indicating that a 200×200 grid is sufficient to model accurately the heat transfer and fluid flow inside the area.

Accuracy of the program developed by the authors was checked by preparing the benchmark solutions both for nonconjugate and conjugate problems. In the case of nonconjugate analysis, well-known benchmark of 2D natural convection in a square enclosure with differentially heated vertical walls and adiabatic horizontal walls, for $\text{Ra}=10^3, 10^4, 10^5, 10^6$, in terms of the average Nusselt number [20,21]. These benchmark results are shown in Table 1. It

Table 2 Variations in the average Nusselt number with Grashof number and the thermal conductivity ratio

Gr	k_{solid}/k_{fluid}	[12]	[22]	Present study
10^3	1	0.877	0.87	0.872
	5		1.02	1.023
	10		1.04	1.046
10^5	1	2.082	2.08	2.116
	5		3.42	3.421
	10		3.72	3.781
10^6	1	2.843	2.87	3.002
	5		5.89	6.306
	10		6.81	6.935

can be seen that the agreement is very good.

To validate the numerical code for conjugate natural convection in an enclosure having finite thickness wall has been considered for Grashof number in the range from 10^3 to 10^6 and the results obtained are compared with [12,22]. Table 2 gives a comparison of these results in the form of the average Nusselt number.

It is clear that the results obtained from present code compare well with the published results.

4 Results and Discussion

Numerical simulation of the boundary problems (1)–(4) with corresponding initial and boundary conditions has been realized with following values of dimensionless groups: $10^3 \le Gr \le 10^7$, $100 \le Re \le 1000$, and $Pr=0.7$. Dimensionless defining temperatures accepted the following values: $\Theta_e=-1$, $\Theta_{hs}=1$, and $\Theta_0=0$. The main attention was paid to the effects of the dimensionless time, and also the Grashof number (Gr) and the Reynolds number (Re), characterizing the strength of heat source and external forced flow (or ventilation), respectively, on distributions of the basic characteristics of the investigated process.

4.1 Effect of the Dimensionless Time. The unknown quantities time dependence introduces essential features at formation of the thermohydrodynamic flow modes. The transient factor is caused not only by the gas cavity hydrodynamic and thermal field development dynamics but also by the thermal lag of the solid walls. The latter leads to the origin and the development of the new vortical structures. It is also linked to distribution of disturbances from the solid phase elements.

Figure 2 demonstrates the dynamics of thermohydrodynamic field formation at $Re=700$, $Gr=10^6$. The arrows on streamlines indicate the direction of the fluid motion.

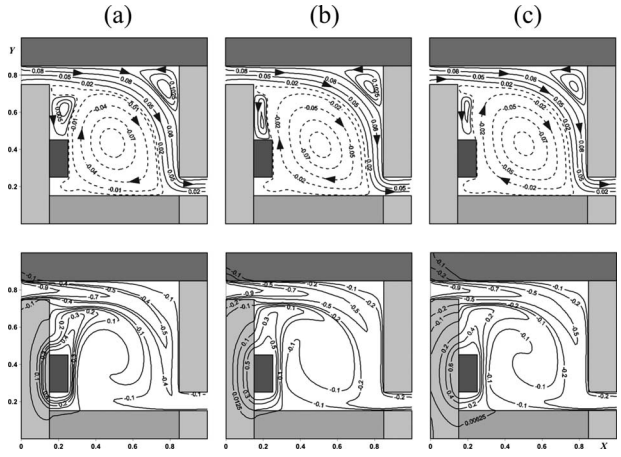

Fig. 2 Streamlines Ψ and temperature fields Θ at Re=700, Gr=10⁶: (*a*) τ=20, (*b*) τ=40, and (*c*) τ=100

The central natural-convective cell, forced fluid tube, and two secondary vortexes are shaped at $\tau=20$ (Fig. 2(*a*)) in the gas cavity. The appearance of the latter is linked both with the geometry features of the considered decision region and with the formation of the nonuniform temperature field. The thermal plume develops above the heat source. Its structure reflects the gas masses motion in the convective cell.

The vortex over the heat source is distorted under the central circulating motion influence at increase in τ up to $\tau=40$ (Fig. 2(*b*)). The sizes of the latter increase. The heat source thermal plume begins to lean to the solid wall owing to the influence of the external flow low temperature front.

The formation of the some quasisteady hydrodynamic mode occurs at $\tau=100$ (Fig. 2(*c*)). There is the average temperature decrease in the gas cavity, which caused by the presence of the forced flow. The gas masses having negative dimensionless temperature circulate in the convective cell. The advance of the low temperature front in the left wall from an environment is visible.

The results of the conducted analysis can be integrally presented in the form of the average Nusselt number at the solid-fluid interfaces that depend on the Grashof number:

$$Nu_{\text{right wall}} = \frac{1}{0.6}\int_{0.25}^{0.85} \left|\frac{\partial\Theta}{\partial X}\right|_{X=0.85} dY,$$

$$Nu_{\text{top}} = \frac{1}{0.85}\int_{0}^{0.85} \left|\frac{\partial\Theta}{\partial Y}\right|_{Y=0.85} dX,$$

$$Nu_{\text{bottom}} = \frac{1}{0.85}\int_{0.15}^{1.0} \left|\frac{\partial\Theta}{\partial Y}\right|_{Y=0.15} dX$$

The dependence of the average Nusselt numbers at three fluid-solid interfaces on the Grashof number is presented in Fig. 3.

4.2 Effect of the Grashof Number. Figure 4 shows the streamlines and temperature fields corresponding conjugate heat transfer mode at $Re=500$, $\tau=100$.

The most intensive convective cell is shaped in the center of the gas cavity at $Gr=10^4$ (Fig. 4(*a*)). The recirculation flows are located in the angle zones of decision region. These flows are formed owing to geometrical specificity of the research object. The direction of the gas motion in the convective cell is defined by both the external forced flow and the natural-convective flow caused by the heat source. This interaction is clearly reflected by the temperature field. The convective-radiative heat exchange with the environment is modeled at $X=0$. The environmental temperature is lower than the initial temperature of the decision region. Therefore, the flow initiated by external sources cools the cavity intensively enough. This figure demonstrates that the low temperature front borrows the greater part of the gas cavity. It is evidence of the forced convection dominance as natural-convective flow due to an insignificant role of the buoyancy force ($Gr=10^4$) does not promote two-dimensional heat plume diffusion from the heat source deep into the cavity. Also Fig. 4(*a*) reflects the influence of the environment on the left solid wall.

There is cooling of the solid wall both at inlet and at the bottom of the cavity. The central part of the left wall is cooled not so intensively, the reason for that is the influence of the heat source, expressed by the diffusion of the highest temperature thermal wave within the wall.

The increase in the Grashof number up to $Gr=10^5$ (Fig. 4(*b*)) leads to the increase in the circulation velocity of the gas particles in the central convective cell. The recirculation zone under the heat source diffuses into the central vortex and at the same time secondary flow scales above the heat source increase. The thermal plume from the heat source, by repeating the streamlines change character, moves to the cavity center. The latter leads to the tem-

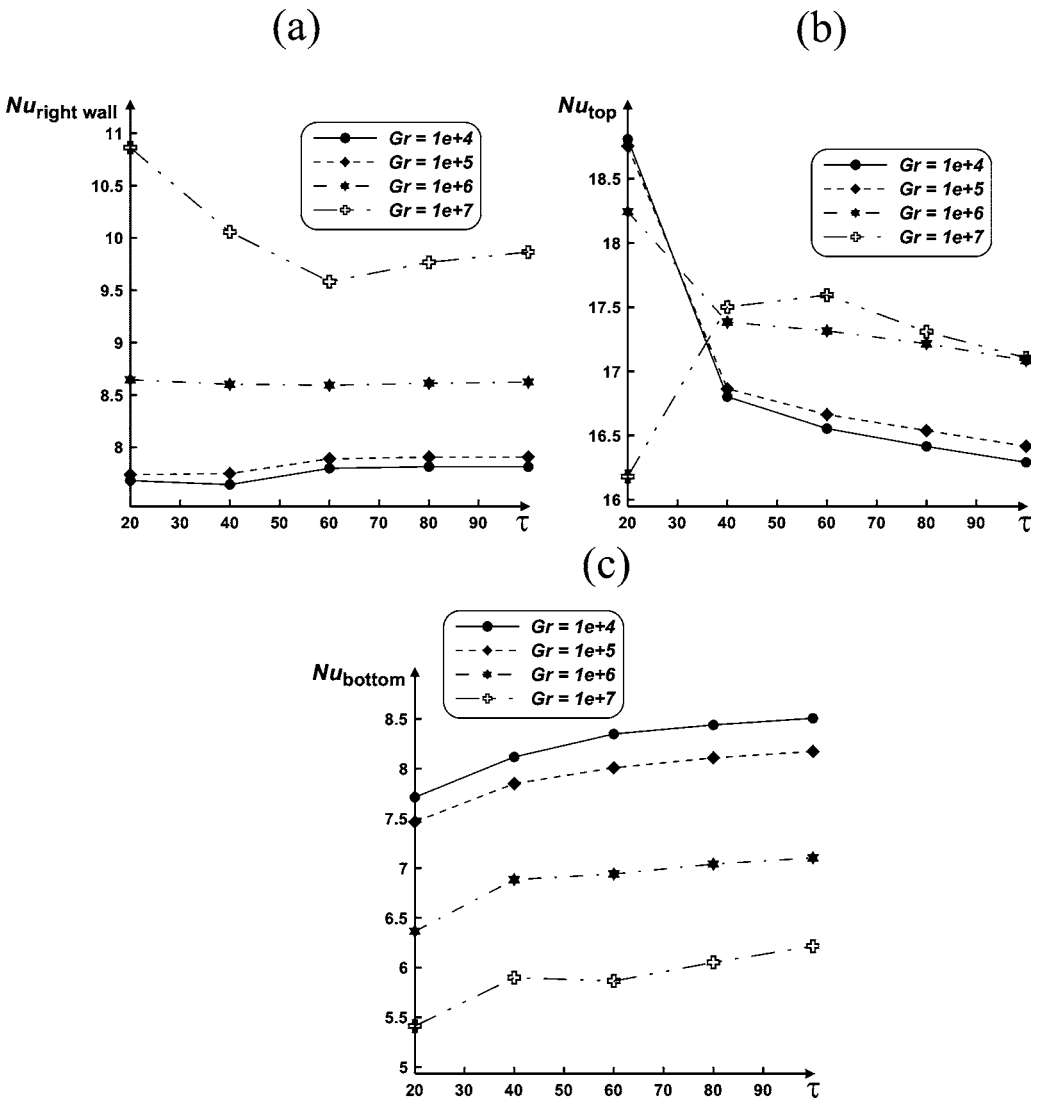

Fig. 3 Variations in the average Nusselt number with the dimensionless time and the Grashof number at Re=700: (*a*) $Nu_{right\ wall}$, (*b*) Nu_{top}, and (*c*) Nu_{bottom}

perature field redistribution of the convective cell (for example, the isotherm corresponding dimensionless temperature equals −0.2 at the bottom of the gas cavity covers the smaller area in comparison with similar isotherm in Fig. 4(*a*).

There is an increase in the maximal flow velocity in the central convective cell at $Gr=10^6$ (Fig. 4(*c*)). The secondary flow scale above the heat source increases also. The amplification of the main convective cell scales and the recirculation zone, located in the upper right corner, is observed. This fact affects to the external forced flow blocking. The described hydrodynamic changes in turn influence the temperature field. The forced flow blocking leads to the increase in the average temperature in the center of the gas cavity. At the same time, the forced convective flow leads to the intensification of the conductive heat transfer in the right solid phase element (Fig. 1, zone 7).

The further increase in the Grashof number up to $Gr=10^7$ (Fig. 4(*d*)) leads to the essential intensification of the central vortex circulation. The scales of this motion are increased that leads to the secondary flow deformation above the heat source. At the same time, the central vortex undergoes the structural alteration linked to the possible partition of the core cell. The increase in the recirculation zone sizes located in the upper right corner combined with the main convective cell leads to the decrease in both the forced flow velocity and the fluid tube diameter of this flow. These things affect the nature of the thermal plume diffusion above the heat source (the thermal plume is pressed to the left wall, owing to the intensive convective cell motion). The thermal wave of the high temperature has already come up to the right wall. Nonmonotonic behavior of the isotherms in the upper right corner caused by the increased area of the recirculation zone influence is noticeable.

The graphic dependences (Fig. 5) of the average Nusselt number describing the generalized heat transfer coefficient at $X=0.85$, $Y=0.15$, and $Y=0.85$ on the Grashof number evidently show nonmonotonic nature of the heat transfer progress between the gas cavity and solid walls for Gr varying from 10^3 to 10^7.

The average Nusselt number $Nu_{right\ wall}$ increases in all range of Gr changes. It corresponds to the gradual increase in the temperature gradient at this border. The Grashof number increase at constant Re corresponds to the reduction in the natural convection boundary layer thickness $\delta \approx O(1/\sqrt[4]{Gr})$ (at $Gr=10^7 \Rightarrow \delta \approx O(0.02)$, and at calculation in the present work $h_x=0.005$, where h_x is the dimensionless grid step along horizontal Cartesian coordinate). The reduction in the boundary layer thickness leads to the increase in the temperature gradient.

The average Nusselt number Nu_{top} curve is a nonmonotone. There is the increase in Nusselt number at $10^3 \leq Gr \leq 10^6$. It is

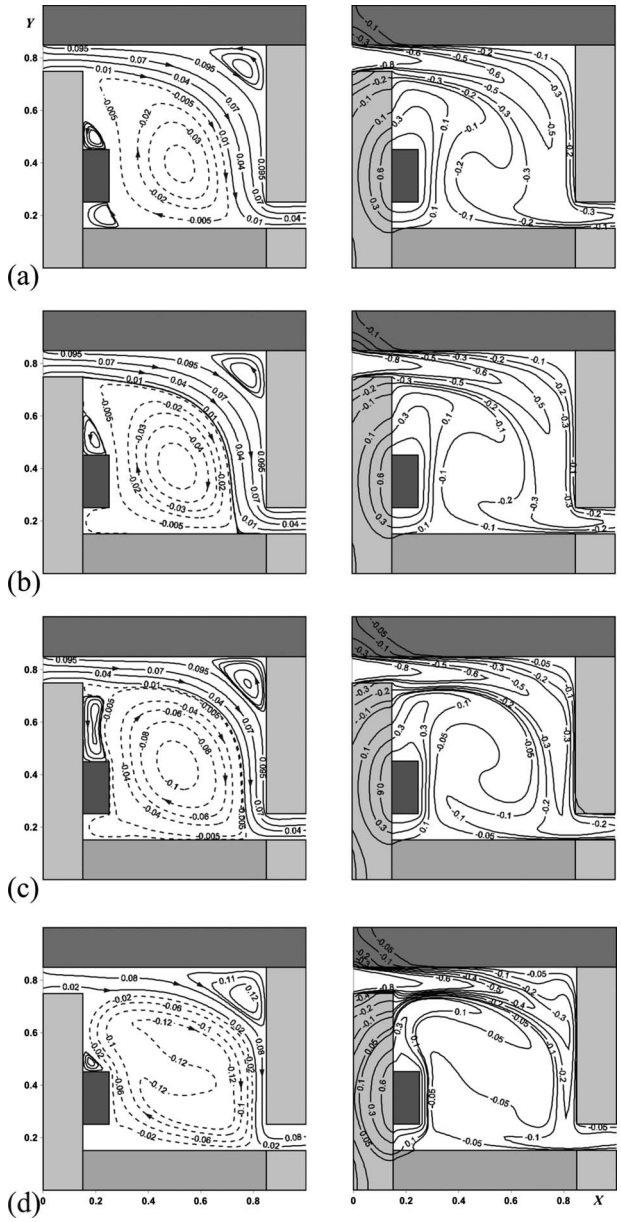

Fig. 4 Streamlines Ψ and temperature fields Θ at Re=500, τ =100: (*a*) Gr=10^4, (*b*) Gr=10^5, (*c*) Gr=10^6, and (*d*) Gr=10^7

possible to explain by the decrease in the thermal boundary layer thickness at the upper wall and also by the closing of the forced fluid tube. The Nusselt number decreases at $10^6 < \mathrm{Gr} \leq 10^7$. It is linked to the increase in the stagnant zone sizes at the right upper corner area and, accordingly, with the temperature gradient reduction.

The average Nusselt number $\mathrm{Nu}_{\mathrm{bottom}}$ decreases while Gr increases, which is caused by gradual dislodgment of the low temperature front due to the intensification of natural convection.

4.3 Effect of the Reynolds Number. Figures 6 and 7 demonstrate the streamlines and isotherms corresponding to the conjugate heat transfer mode for τ=100, Re=100,300,900, and Gr $=10^5, 10^6, 10^7$.

The effect of forced flow intensity on the thermal and hydrodynamic field formation has been analyzed.

The convective cell and two stagnant zones are formed in the center of the gas cavity at Gr=10^5 and Re=100. It is caused by the gas cavity geometry. Owing to low velocity of the external

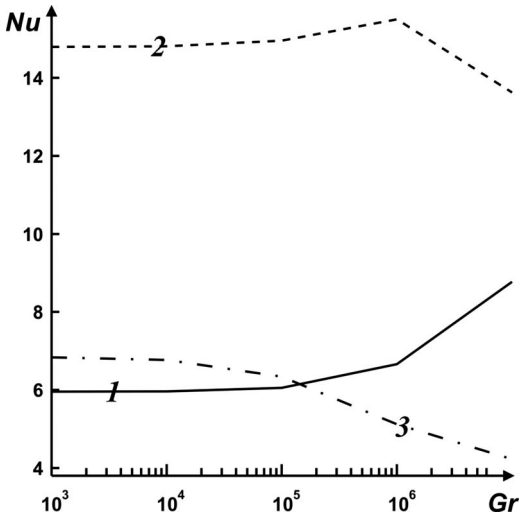

Fig. 5 Variations in the average Nusselt numbers with Grashof number for Re=500, τ=100: (1) $\mathrm{Nu}_{\mathrm{right\ wall}}$, (2) $\mathrm{Nu}_{\mathrm{top}}$, and (3) $\mathrm{Nu}_{\mathrm{bottom}}$

forced flow, the external fluid tube expansion is observed. The latter leads to some central vortex deformation. The velocity field influences on the temperature distribution (Fig. 6). The low temperature front penetrates into the cavity lightly.

The isotherm distribution (Fig. 7) from the heat source reflects the presence of the ascending warm flows and descending cold flows. The external forced fluid tube at Re=300 is constricted, which leads to the increase in the central vortex-type flow sizes and, accordingly, to the reduction in the secondary vortex scales located above the heat source.

The maximal velocity of the gas motion in the convective cell core decreases 1.5 times. Thus the low temperature front reaches the outlet. There is an intermixing of the gas masses having positive and negative temperatures in the convective cell. The average temperature in the gas cavity decreases. The further increase in Re number up to Re=900 leads to the decrease in velocity in the central whirl core and to negligible contraction of the forced fluid

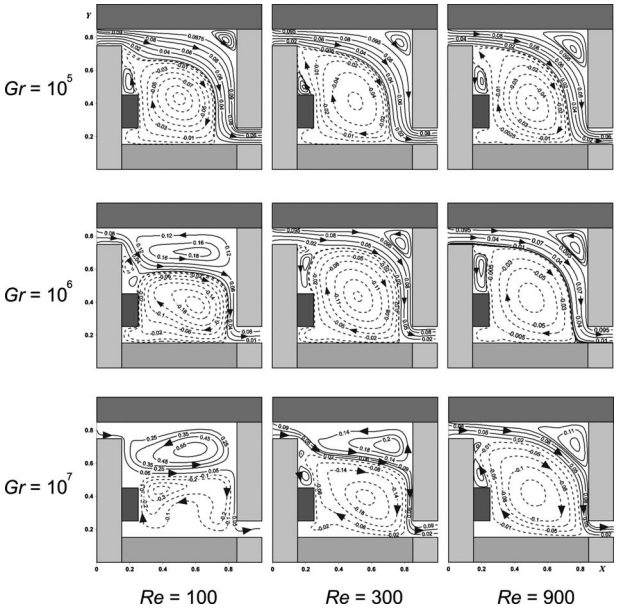

Fig. 6 Streamlines Ψ at τ=100 depending on Re and Gr numbers

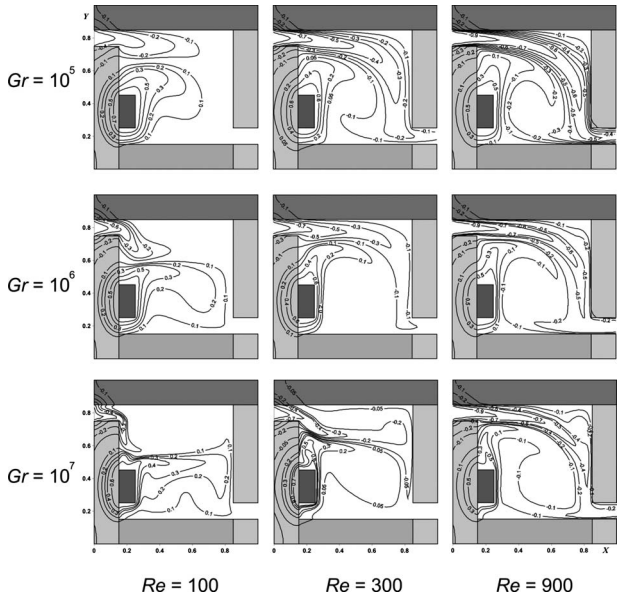

Fig. 7 Temperature fields Θ at τ=100 depending on Re and Gr numbers

tube.

Thus the sizes of the recirculation zone located in the right upper corner of the gas cavity increase. The average gas temperature continues to decrease. The thermal plume from the heat source is slightly deformed owing to influence of the convective cell low temperature front. Caused by the external forced flow, conductive heat transfer intensification in the solid walls is visible in the outlet zone. The integral heat transfer coefficient Nu (Fig. 8) at three solid-fluid interfaces monotonously increases with the increase in Re. It is linked to an intensification of heat sink from the internal solid walls borders.

The increase in Gr by ten times leads to changes in the thermohydrodynamics fields. The circulating motion at the top of the cavity is formed at Re=100 in the gas cavity besides the convective cell caused by influence of the heat source. This whirl together with the central circulating motion constricts the fluid tube of the external forced flow. It leads to the decrease in this flow velocity in comparison with the mode for $Gr=10^5$, Re=100. The temperature field undergoes essential changes—the low temperature front of the inlet spreads in a vertical direction toward heat source. The thermal plume covers a large area but spreads in a horizontal direction. Some deformation of the thermal two-dimensional plume from the heat source owing to the influence of the inlet low temperature is observed. The increase in Re up to Re=300 leads to the increase in the central convective cell sizes, to essential decrease in scales of the recirculating flow located earlier at the top of the gas cavity, and to the diffusion of this

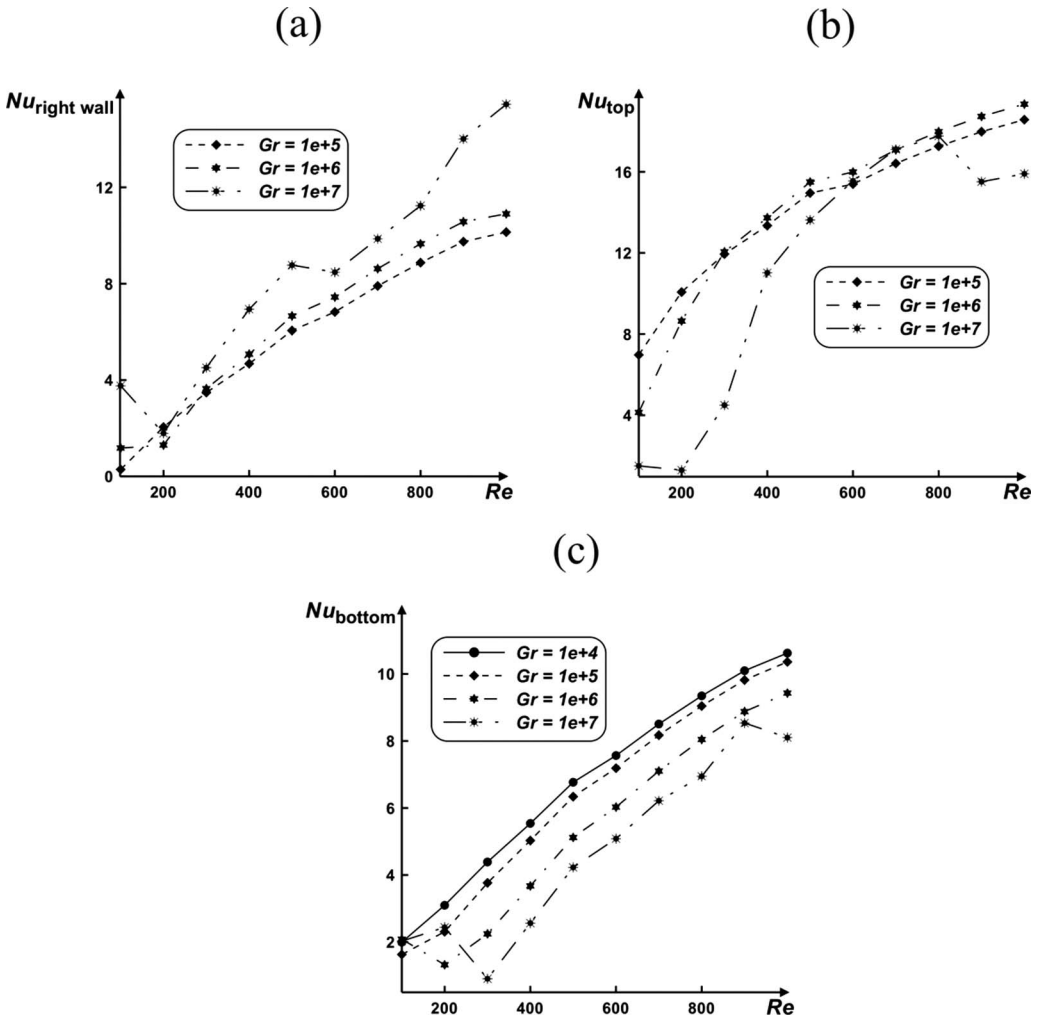

Fig. 8 Variations of the average Nusselt number with Re and Gr at τ=100: (*a*) $Nu_{right\ wall}$, (*b*) Nu_{top}, and (*c*) Nu_{bottom}

vortex into the right upper corner zone.

The decrease in velocity of the central cell core and formation of reset flow above the heat source are visible. There is also an expansion of the forced flow fluid tube. The heat source thermal plume is extended along the vertical coordinate and the inlet low temperature front is deformed. Isotherms of the negative temperature reach the outlet.

The decrease in velocity of the central convective cell core and the increase in the secondary vortex flow sizes in the right upper corner zone are observed at $\mathrm{Re}=900$. It is reflected in nonmonotonic isotherm structure in this part of the gas cavity. Figure 7 shows the essential intensification of the forced convection. It leads to the significant temperature pulldown in the gas cavity. There is a circulation of the cooled gas masses in the convective cell. Also the intensification of the conductive heat transfer in the rigid wall near the outlet caused by the external forced flow is visible. The penetration depth of the isotherm corresponding the dimensionless temperature -0.1 is less than similar isotherm at $\mathrm{Gr}=10^5$, $\mathrm{Re}=900$. All this leads to more intensive increase in the average Nusselt numbers (Fig. 8) $\mathrm{Nu}_{\mathrm{right\ wall}}$ and $\mathrm{Nu}_{\mathrm{top}}$. The average Nusselt number $\mathrm{Nu}_{\mathrm{bottom}}$ also monotonously increases, but its values are below in comparison with similar indications for $\mathrm{Gr}=10^5$.

The circulating flow formation at the top of the gas cavity is observed at $\mathrm{Gr}=10^7$ and $\mathrm{Re}=100$. The sizes of this flow increase. The gas velocity in the core of flow is essentially larger than the one at $\mathrm{Gr}=10^6$. The flow caused by the presence of temperature nonuniformity undergoes essential structural alterations. The forced fluid tube is constricted up to the minimal sizes. It is linked to interaction of vortical cells. The low temperature front (Fig. 7) verges toward the heat source more and more and distorts the radiant thermal plume. The increase in buoyancy force at $\mathrm{Re}=100$ leads to formation of the descending plume from the inlet and to increase in the area scales subject to influence of the high temperature front. There is an increase in the sizes of the natural-convective cell at $\mathrm{Re}=300$ and the distortion of the secondary recirculating flow located at the top of the gas cavity. The forced fluid tube expands, but it is narrow enough in comparison with the mode of $\mathrm{Gr}=10^6$. The thermal plume from the heat source (Fig. 7) interacts with the low temperature front. The convective cell core consists of the warm enough gas masses. At $\mathrm{Re}=900$ the recirculating zone sizes at the top of the gas cavity decrease and it displaces to the right upper corner that is reflected on the forced fluid tube expansion and on increase in the influence scales of the natural-convective cell. The heat source thermal plume reaches border of the inlet, but thus it tends to the solid wall. It is linked to circulation of cold gas masses in central convective cell. The heat conduction intensification in a considered mode is already less visible than in the previous cases. The average Nusselt numbers (Fig. 8) at the typical solid-fluid interfaces have nonmonotone shape. This fact is explained by possible formation of the transient heat transfer mode and as result by the heat transfer steady development loss.

4.4 The Heat Convection Modes. The Grashof number defined a role of the buoyancy force is the similarity criterion describing natural convection. The Reynolds number defines the role of inertial forces at forced convection. The process representing interaction between the external forced flow and the natural convection on the assumption of conjugate statement was considered in the analyzed problem. As a result of the conducted analysis, the diagram of the heat convection modes (Fig. 9) has been obtained. The forced flow leads to the distribution of the low temperature front, while the natural convection reflects the influence of the heat source. The condition based on which a selection of the heat convection mode passed was the following. The negative dimensionless average temperature in the core of the convective cell corresponded to the forced convection mode, the positive dimensionless average temperature—to the natural convection mode, and if $\Theta \in (-0.05, 0.05)$—the mixed convection mode.

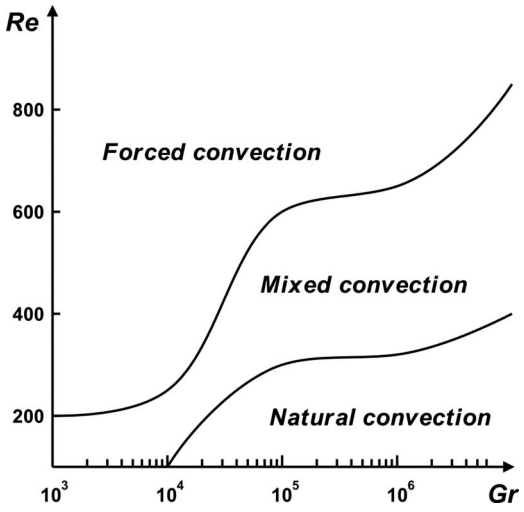

Fig. 9 The heat convection modes

The analysis of heat convection modes in a typical subsystem of the electronic equipment is oriented not only toward applied development in microelectronics but also it can be considered as test database at creation of numerical codes of convective heat transfer simulation in complicated energy systems. Comparison of the obtained results can be made by means of both streamlines and temperature fields at different values of the Grashof number and Reynolds number, and the average Nusselt numbers at solid-fluid interfaces.

5 Conclusions

The conjugate convective-conductive heat transfer problem in rectangular area has been numerically solved at the presence of the local heat source and forced flow in conditions of convective-radiative heat exchange with an environment. The research area represented the typical electronic component. The hydrodynamics and heat transfer features corresponding various flow patterns $10^3 \le \mathrm{Gr} \le 10^7$, $100 \le \mathrm{Re} \le 1000$, and $\mathrm{Pr}=0.7$ have been emphasized. The effects of the Grashof and Reynolds numbers and the dimensionless time on both the local characteristics (streamlines and temperature fields) and the integral characteristics (the average Nusselt number at three solid-fluid interfaces) have been analyzed. The diagram of the heat convection modes depending on the Grashof and Reynolds numbers has been received.

The obtained results allow to evolve heat convection modes for electronic systems that are similar to the rectangular area depicted in Fig. 1. Such opportunity is necessary for engineers at designing and optimization of the complete units of the electronic equipment.

Acknowledgment

This study has been supported by the Russian Foundation for Basic Research through Grant No. 08-08-00402-a.

Nomenclature

$\mathrm{Bi}=hL_x/k$ = Biot number
d = height of the left wall
$\mathrm{Fo}=\alpha t_0/L_x^2$ = Fourier number
g_x = acceleration of gravity (horizontal projection)
g_y = acceleration of gravity (vertical projection)
$\mathrm{Gr}=g_y\beta(T_{\mathrm{hs}}-T_0)L_x^3/\nu^2$ = Grashof number
h = heat transfer factor

h_x = dimensionless grid step along horizontal Cartesian coordinate
h_y = dimensionless grid step along vertical Cartesian coordinate
H = distance from $y=0$ to upper wall
k = thermal conductivity
$k_{i,j}=k_i/k_j$ = thermal conductivity ratio
l_{1y} = thickness of the foundation
l_{2y} = height of outlet
L = length of the gas cavity
L_x = length of the enclosure
L_y = height of the enclosure
$N=\varepsilon\sigma L_x(T_{\mathrm{hs}}-T_0)^3/k$ = Stark number
$\mathrm{Pr}=\nu/\alpha$ = Prandtl number
$\mathrm{Re}=V_{\mathrm{in}}L_x/\nu$ = Reynolds number
t = time
t_0 = time scale
T_0 = initial temperature
T_e = environmental temperature
T_{hs} = temperature on heat source
u = velocity in the horizontal direction
U = dimensionless velocity in the horizontal direction
v = velocity in the vertical direction
V = dimensionless velocity in the vertical direction
V_{in} = velocity scale
x = horizontal Cartesian coordinate
X = dimensionless horizontal Cartesian coordinate
y = vertical Cartesian coordinate
Y = dimensionless vertical Cartesian coordinate

Greek Symbols

α = thermal diffusivity
β = coefficient of volumetric thermal expansion
ε = specific emissivity factor
$\tilde{\varepsilon}$ = calculation accuracy
Θ = dimensionless temperature
ν = kinematic viscosity
σ = Stephen–Boltzmann constant
τ = dimensionless time
τ_t = dimensionless time step
ψ = stream function
ψ_0 = stream function scale
Ψ = dimensionless stream function
ω = vorticity
ω_0 = vorticity scale
Ω = dimensionless vorticity

Subscripts

i = number of the decision region element (Fig. 1)
e = environment
hs = heat source
in = inlet
l,m = grid points indices
n = number of reference vector
p = iteration number

References

[1] Dul'nev, G. N., and Tarnovsky, N. N., 1971, *Heat Modes of Electronic Devices*, Energy, Leningrad, Russia.
[2] Jaluria, Y., 1998, *Design and Optimization of Thermal Systems*, McGraw-Hill, New York.
[3] Sathe, S., and Sammakia, B., 1998, "A Review of Recent Developments in Some Practical Aspects of Air-Cooled Electronic Packages," ASME J. Heat Transfer, **120**, pp. 830–839.
[4] Icoz, T., and Jaluria, Y., 2004, "Design of Cooling Systems for Electronic Equipment Using Both Experimental and Numerical Inputs," ASME J. Electron. Packag., **126**, pp. 465–471.
[5] Icoz, T., Verma, N., and Jaluria, Y., 2006, "Design of Air and Liquid Cooling Systems for Electronic Components Using Concurrent Simulation and Experiment," ASME J. Electron. Packag., **128**, pp. 466–478.
[6] Hong, F. J., Cheng, P., Ge, H., and Joo, G. T., 2007, "Conjugate Heat Transfer in Fractal-Shaped Microchannel Network Heat Sink for Integrated Microelectronic Cooling Application," Int. J. Heat Mass Transfer, **50**, pp. 4986–4998.
[7] Polat, O., and Bilgen, E., 2003, "Conjugate Heat Transfer in Inclined Open Shallow Cavities," Int. J. Heat Mass Transfer, **46**, pp. 1563–1573.
[8] Madhusudhana Rao, G., and Narasimham, G. S. V. L., 2007, "Laminar Conjugate Mixed Convection in a Vertical Channel With Heat Generating Components," Int. J. Heat Mass Transfer, **50**, pp. 3561–3574.
[9] Muftuoglu, A., and Bilgen, E., 2008, "Conjugate Heat Transfer in Open Cavities With a Discrete Heater at Its Optimized Position," Int. J. Heat Mass Transfer, **51**, pp. 779–788.
[10] Premachandran, B., and Balaji, C., 2006, "Conjugate Mixed Convection With Surface Radiation From a Horizontal Channel With Protruding Heat Sources," Int. J. Heat Mass Transfer, **49**, pp. 3568–3582.
[11] Liaqat, A., and Baytas, A. C., 2001, "Numerical Comparison of Conjugate and Non-Conjugate Natural Convection for Internally Heated Semi-Circular Pools," Int. J. Heat Fluid Flow, **22**, pp. 650–656.
[12] Liaqat, A., and Baytas, A. C., 2001, "Conjugate Natural Convection in a Square Enclosure Containing Volumetric Sources," Int. J. Heat Mass Transfer, **44**, pp. 3273–3280.
[13] Jaluria, Y., 1980, *Natural Convection Heat and Mass Transfer*, Pergamon, New York.
[14] Bejan, A., 2004, *Convection Heat Transfer*, Wiley, New York.
[15] Kuznetsov, G. V., and Sheremet, M. A., 2006, "Two-Dimensional Problem of Natural Convection in a Rectangular Domain With Local Heating and Heat-Conducting Boundaries of Finite Thickness," Fluid Dyn., **41**, pp. 881–890.
[16] Luikov, A. V., 1967, *Theory of Thermal Conductivity*, Vysshaya shkola, Moscow, Russia.
[17] Paskonov, V. M., Polezhaev, V. I., and Chudov, L. A., 1984, *Numerical Simulation of Heat and Mass Transfer Processes*, Nauka, Moscow, Russia.
[18] Samarsky, A. A., 1977, *The Theory of Difference Schemes*, Nauka, Moscow, Russia.
[19] Roache, P., 1976, *Computational Fluid Dynamics*, Hermosa, Albuquerque, NM.
[20] De Vahl Davis, G., 1983, "Natural Convection of Air in a Square Cavity: A Bench Numerical Solution," Int. J. Numer. Methods Fluids, **3**, pp. 249–264.
[21] Dixit, H. N., and Babu, V., 2006, "Simulation of High Rayleigh Number Natural Convection in a Square Cavity Using the Lattice Boltzmann Method," Int. J. Heat Mass Transfer, **49**, pp. 727–739.
[22] Kaminski, D. A., and Prakash, C., 1986, "Conjugate Natural Convection in a Square Enclosure Effect of Conduction on One of the Vertical Walls," Int. J. Heat Mass Transfer, **29**, pp. 1979–1988.

W. Escher
Zurich Research Laboratory,
IBM Research GmbH,
Rüschlikon 8803, Switzerland;
Department of Mechanical and Process Engineering,
Laboratory of Thermodynamics in Emerging Technologies,
ETH Zurich,
Zurich 8092, Switzerland

T. Brunschwiler

B. Michel

Zurich Research Laboratory,
IBM Research GmbH,
Rüschlikon 8803, Switzerland

D. Poulikakos[1]
Department of Mechanical and Process Engineering,
Laboratory of Thermodynamics in Emerging Technologies,
ETH Zurich,
Zurich 8092, Switzerland
e-mail: dimos.poulikakos@ethz.ch

Experimental Investigation of an Ultrathin Manifold Microchannel Heat Sink for Liquid-Cooled Chips

We report an experimental investigation of a novel, high performance ultrathin manifold microchannel heat sink. The heat sink consists of impinging liquid slot-jets on a structured surface fed with liquid coolant by an overlying two-dimensional manifold. We developed a fabrication and packaging procedure to manufacture prototypes by means of standard microprocessing. A closed fluid loop for precise hydrodynamic and thermal characterization of six different test vehicles was built. We studied the influence of the number of manifold systems, the width of the heat transfer microchannels, the volumetric flow rate, and the pumping power on the hydrodynamic and thermal performance of the heat sink. A design with 12.5 manifold systems and 25 μm wide microchannels as the heat transfer structure provided the optimum choice of design parameters. For a volumetric flow rate of 1.3 l/min we demonstrated a total thermal resistance between the maximum heater temperature and fluid inlet temperature of 0.09 $cm^2 K/W$ with a pressure drop of 0.22 bar on a 2×2 cm^2 chip. This allows for cooling power densities of more than 700 W/cm^2 for a maximum temperature difference between the chip and the fluid inlet of 65 K. The total height of the heat sink did not exceed 2 mm, and includes a 500 μm thick thermal test chip structured by 300 μm deep microchannels for heat transfer. Furthermore, we discuss the influence of elevated fluid inlet temperatures, allowing possible reuse of the thermal energy, and demonstrate an enhancement of the heat sink cooling efficiency of more than 40% for a temperature rise of 50 K.
[DOI: 10.1115/1.4001306]

Keywords: manifold, microchannels, impinging jet, heat transfer, electronics cooling

1 Introduction

Recent trends of miniaturization of transistors and of increased integration levels on computer chips enabled a substantial enhancement of the performance of microelectronic devices. However, the increased circuit density and clock frequency lead to an extensive growth of heat dissipation rates of microprocessors, which cannot be removed by traditional air cooling solutions [1]. The current method to address this problem is to reduce the air inlet temperature in datacenters, which causes a significant growth of energy consumption, and thus, a large increase in the operating costs. Brunschwiler et al. [2] showed that a significant reduction in the total heat sink thermal resistance allows for datacenter operation at higher input temperatures above the free cooling limit. This enables the elimination of chillers and, along with this, a reduction of more than 90% of the energy required for cooling. The increased output temperatures of the coolant offer the possibility of energy reuse, which would further increase the efficiency of a datacenter. Furthermore air cooled heat sinks impede the progress of increased integration density as they typically feature large form factors due to a required large surface area and volume for heat transfer. Thinner heat sink structures would provide the opportunity for a denser package of circuit boards, and thus, a reduction in the communication pathlength and of required space for data centers. Hence, there is a strong need for more efficient and compact cooling solutions.

Tuckerman and Pease [3] first introduced the idea of using liquid cooled microchannel heat sinks for cooling electronics. They demonstrated total thermal resistances down to 0.1 $cm^2 K/W$ by implementing 50 μm wide and 300 μm deep microchannels on a 1 cm^2 chip. However, the low thermal resistance was achieved at the expense of large pressure drops across the heat sink. Since then, there have been several studies on different designs for microchannel heat sinks, and a number of reviews are available [4–6]. Improvement to the conventional design can be achieved by introducing hierarchical structured two-dimensional arrays with either bifurcating [7–10] or heterogeneous branching channel networks [11,12] for fluid supply and drain. However, the hydrodynamic resistance of two-dimensional networks results in nonacceptable pressure losses across the heat sink for the required high volumetric flow rates [13]. Harpole and Eninger [14] suggested dividing the heat transfer structure into several zones fed from the third dimension in order to reduce the overall pressure drop of the system. Their idea was studied theoretically, numerically, and experimentally in several investigations [15–20]. Colgan et al. [21] introduced staggered short fins instead of continuous fins for the heat transfer structure. The staggered arrangement provides higher heat transfer coefficients but at the cost of an increased pressure drop. They divided the heat exchange structure of 3 cm^2 into six different zones fed with water or a fluorinated fluid from the top. For a water flow rate of 1.25 l/min they demonstrated an average unit thermal resistance of 0.12 $cm^2 K/W$ at pressure drops of about 0.4 bar.

None of the previous studies considered the influence of the manifold on the hydrodynamic and thermal performance of the system. This is an appropriate simplification as long as there are no size constrictions in the third dimension. Brunschwiler et al. [22] considered the influence of the manifold on the performance of the heat sink. They proposed direct single-phase liquid jet impingement on the backside of the chip in combination with a hierarchical tree-like branching manifold system being stacked into the third dimension. The manifold system feeds and drains an array of 40,000 unit cells uniformly distributed on an area of

[1]Corresponding author.

Contributed by the Heat Transfer Division of ASME for publication in the JOURNAL OF HEAT TRANSFER. Manuscript received May 27, 2009; final manuscript received January 28, 2010; published online June 2, 2010. Assoc. Editor: Roger Schmidt.

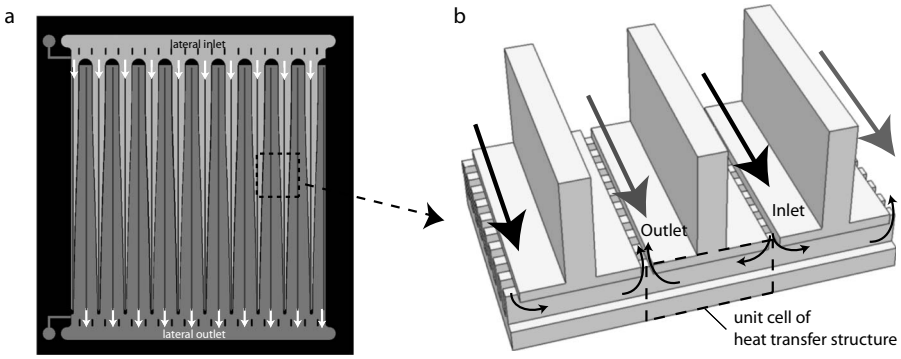

Fig. 1 Schematic of a manifold microchannel heat sink: (*a*) top view of the manifold with $K=9.5$; (*b*) isometric section view

4 cm^2. They demonstrated a minimum unit thermal resistance of 0.17 K cm^2/W (720 μm chip) at a flow rate of 2.5 l/min and a pressure drop of 0.35 bar. However, with denser packages, there is a demand for thin and efficient heat sinks with only lateral access for fluid supply and drain. In a previous publication [23] we proposed a design for an ultra thin manifold microchannel heat sink. The heat sink consists of impinging liquid slot-jets on a structured surface fed by an overlying two-dimensional manifold system, which requires no access from the third dimension. The proposed design was studied numerically by means of three-dimensional numerical computations and a semi-empirical one-dimensional model. We investigated the basic physical phenomena in the heat transfer structure and the manifold system. We demonstrated for an optimized design a total thermal resistance of 0.087 cm^2 K/W for a volumetric flow rate of 1l/min and a pressure drop <0.1 bar.

In this paper we present a thorough experimental characterization of the previously proposed heat sink design concept. We fabricated six different prototypes by means of standard microprocessing. We varied the channel width of the heat transfer microchannel array and the number of manifold systems. A test setup was established, which allows for detailed characterization of the test vehicles. We measured the differential pressure drop across the heat sink and the spatial temperature distribution at the heater surface, and derived the total thermal resistance of the heat sink as a function of the volumetric flow rate. We studied the influence of the microchannel width and the number of manifold systems on the hydrodynamic and thermal performances of the heat sink. The experimental results were compared with the previously proposed semi-empirical one-dimensional model and validated the numerical results qualitatively and quantitatively within an error of 25%. Furthermore, in relation to possible reuse of the generated thermal energy in electronic chips, we discuss the impact of higher fluid inlet temperatures on the performance of the system and demonstrate a cooling efficiency enhancement of the more than 40% for a inlet temperature rise of 50 K.

2 Experimental Methods

2.1 Design and Fabrication. The proposed microchannel heat sink consists of a manifold layer feeding an underlying heat transfer structure of hundreds of parallel microchannel integrated into the backside of the heat dissipating microelectronic device. The microchannel array is divided into thousands of heat transfer unit cells by the overlaying manifold (see Fig. 1). The fluid enters the manifold system by a lateral fluid supply and branches into parallel manifold inlet channels. As the fluid flows along the tapered inlet channels it uniformly branches into the underlying microchannels through the slit nozzles located at the bottom surface of the manifold channel. After impinging directly at the backside of the chip, the fluid undergoes a 90 deg turn and travels along the microchannels orthogonally orientated with respect to the manifold (Fig. 1). While flowing through the heat transfer channel structure the fluid removes the heat from the electronic components attached below. Subsequently, the fluid leaves the heat transfer microchannel structure upwards through the slit nozzle and merges into the outlet manifold channel, which guides the fluid to a lateral return (Fig. 1). To achieve a uniform cooling capability, the same amount of fluid passes through each unit cell of the microchannel. By introducing tapered inlet and expanding outlet channels a constant pressure gradient across the microchannel array is provided, resulting in a uniform fluid distribution [23].

A test vehicle of the proposed design consists of two silicon dies and a glass chip being all 28×28 mm^2 in size. The microchannel heat sink was fabricated using photolithography and deep reactive ion etching (DRIE) of silicon on 150 mm wafers. One chip contains the heat transfer structure (HT-chip), namely, a 20×20 mm^2 array of parallel microchannels being etched into the center of a 525 μm thick silicon chip. At the back side of the HT-chip, which is covered by about 70 nm thick silicon oxide layer, we deposited a 300 nm thick NiCr 80/20 metal layer with a low temperature coefficient of resistance (TCR) of 80 ppm/K being structured by a lift-off resist. The metal layer functions as a resistive heater with a total electrical resistance of 3.1 Ω and is of the same size as the microchannel array.

To measure the temperature at the heater plane we embedded two resistive temperature detectors (RTDs), which divided the heater layer into three sections. The RTDs consisted of a 300 nm thick gold layer shaped as a 10 μm wide and 1.5 mm long serpentine with a total length of 10.3 mm and a mean TCR of 2320 ppm/K. The leads for the four point measurement of the RTD resistance were 100 μm wide and were directed in pairs to the oppositely arranged contact pads (see Fig. 2(*b*)). Consequently the heater sections were separated by a 250 μm gap, providing space for the RTDs. The manifold system and the nozzle array, which connected the manifold and the microchannels, were etched in a double sided DRIE sequence into a 1 mm thick silicon chip (M-chip). The manifold channels were formed first to a depth of 650 μm. In the second step the array of 100 μm wide slit nozzles were etched 350 μm deep on the opposite side of the chip. Wider nozzles would be preferable in order to minimize pressure drop [23]. However, the width of 100 μm was chosen for mechanical and practical reasons, as wider nozzles would collide with the channel width at the end of the tapered manifold inlet channel. The manifold channels were covered by a 500 μm thick glass chip. The 150 mm glass wafer was coated with a $4-5$ μm thick polyimide. A leak-proof bond between the silicon wafer containing the M-chips and the glass wafer was achieved in vacuum, by applying a uniform pressure of 7 bar through a membrane to the package backside at 350 °C in a membrane oven. The package was cut by a dicing saw into individual chips and bonded to the HT-chips, covered by a $4-5$ μm thick polyimide, which was deposited on the HT-chip and structured by an O_2 plasma prior to the etching process. We used a flip chip bonder to align the two

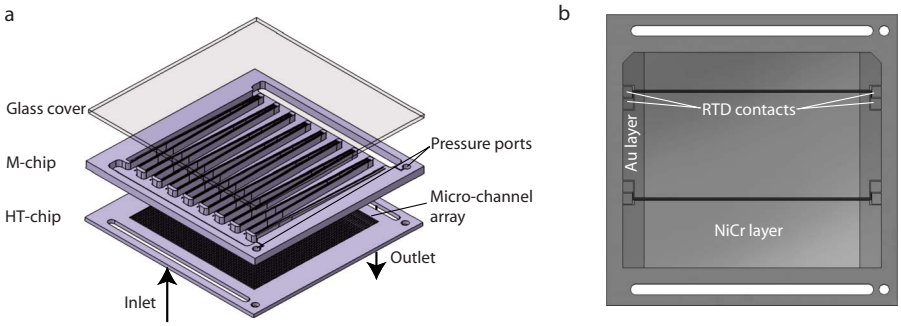

Fig. 2 (*a*) **3D CAD drawing—isometric view on a test vehicle;** (*b*) **backside of the HT-chip showing the thin film metal heater with embedded RTDs**

chips with an accuracy of ± 1 μm and prebonded the package at 350°C in a force controlled mode. For the final bond the package was exposed to a pressure of 2 bar at 350°C in a membrane oven. The total height of the heat sink, including a 500 μm thick thermal test chip (HT-chip) structured by 300 μm deep microchannels, did not exceed 2 mm.

As we pointed out in Ref. [23] the channel width and the number of manifold systems in parallel are the crucial parameters for the performance of the heat sink. Therefore, we fabricated the microchannel array with three different channel widths. The channel depth of the different designs varied slightly as well due to DRIE etch-rate lag, which is a gas diffusion dominated feature size dependent effect. Manifolds with 9.5 and 12.5 systems in parallel were produced. It should be noted that one manifold system was considered as one inlet and one outlet channel, whereas at the edges just half of a manifold system was created (cf. Fig. 1(*a*)). In total six different test vehicles were available for thermal and hydrodynamic characterizations (see Table 1).

2.2 Test Setup and Fluid Loop. We designed a test section to interface the individual test vehicles (see Fig. 3(*a*)). The main body of the test section was fabricated in a machine able glass ceramic due to its low thermal conductivity and mechanical strength. The test vehicles were interfaced by clamping them against a fluorinated rubber gasket bonded to the glass ceramic support by polydimethylsiloxane (PDMS). Thus, the fluid and pressure ports of the test vehicles and the support were tightly connected. At the same time, the electrical contact pads of the test vehicle were contacted by 62 spring-loaded probes. We used eight probes for connecting the RTDs, six probes were employed to

Table 1 Dimensions of the test vehicles

	Chip 1	Chip 2	Chip 3	Chip 4	Chip 5	Chip 6
Channel width, $w_{\mathrm{HT,ch}}$ (μm)	108	107	59	56	26	27
Number of manifold systems, K	9.5	12.5	9.5	12.5	9.5	12.5
Fin thickness, $w_{\mathrm{HT},w}$ (μm)	92	93	41	44	13	12
Channel height, $h_{\mathrm{HT,ch}}$ (μm)	298	298	264	264	226	226
Nozzle width, $w_{\mathrm{HT},N}$ (μm)	132	136	136	135	133	133
Manifold wall thickness, $w_{M,w}$ (μm)	85	85	84	87	85	87
$K=9.5$	$w^{\mathrm{in}}_{M,\mathrm{ch}}(\xi)=w^{\mathrm{in}}_{M,\mathrm{ch},0}(-4\times10^{8}\xi^{5}m^{-5}+1.22\times10^{7}\xi^{4}m^{-4}+1.72\times10^{5}\xi^{3}m^{-3}-8.2\times10^{3}\xi^{2}m^{-2}+16\xi m^{-1}+1)$					
$K=12.5$	$w^{\mathrm{in}}_{M,\mathrm{ch}}(\xi)=w^{\mathrm{in}}_{M,\mathrm{ch},0}(7.2\times10^{8}\xi^{5}m^{-5}-3.25\times10^{7}\xi^{4}m^{-4}+6.6\times10^{5}\xi^{3}m^{-3}-8.14\times10^{3}\xi^{2}m^{-2}+1.45\xi m^{-1}+1)$					

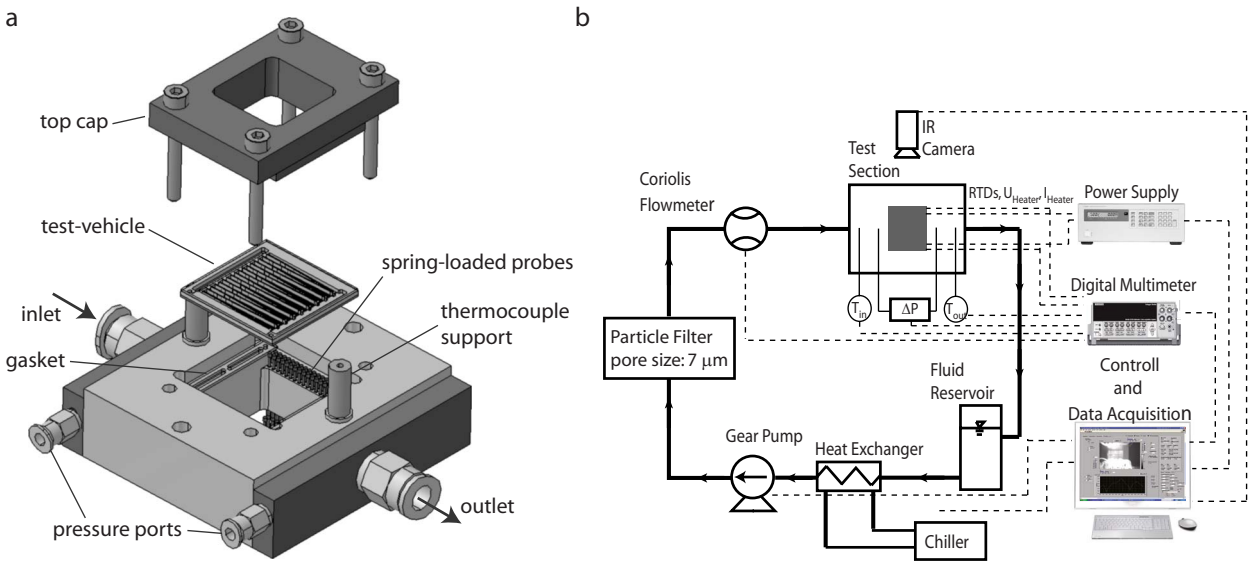

Fig. 3 (*a*) **3D CAD drawing of the test section;** (*b*) **Schematic of the flow loop**

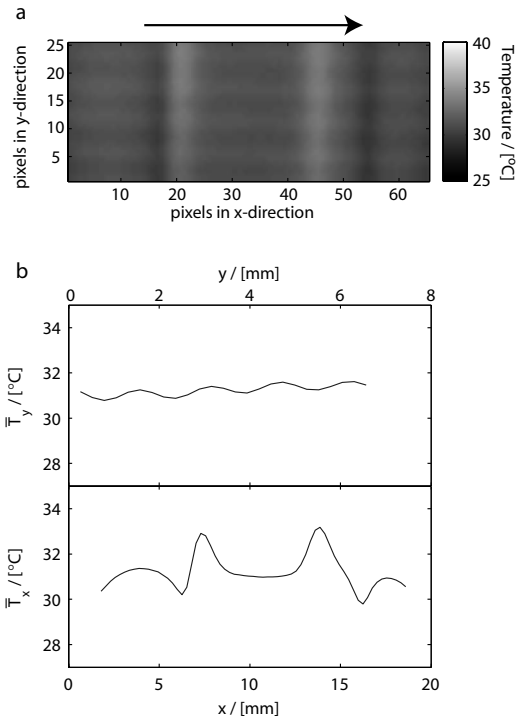

Fig. 4 (*a*) Spatial temperature distribution of a section of the heater being measured by an IR camera: the arrow indicates the flow direction in the manifold system; (*b*) top part: temperature distribution in the *y*-direction being averaged along the *x*-direction, bottom part: Temperature distribution in the *x*-direction being averaged along the *y*-direction

measure the on-chip potential difference across each section of the heater, and the remaining 48 probes provided the electrical connection to the heater, delivering a maximum current of 17 A. Hence, the power dissipation was limited to 850 W. The heat loss from the fluid to ambient was less than 1.5% at typical operation conditions, and the parasitic thermal resistance of the test set up was 20 cm^2 K/W.

The test section was integrated into a closed fluid loop. The flow was driven by a magnetic gear pump. We used a Coriolis flow meter to determine the volumetric flow rate with an error of <3 ml/min. Two T-type thermocouples were integrated into the test section to measure the fluid inlet and outlet temperatures (error ± 0.1 K). The pressure drop across the heat sink was quantified by a differential pressure transducer (error ± 5 mbar). We measured the on-chip power dissipation by detecting the input current and the on-chip potential difference of each section of the heater. Two RTDs were used to determine the heater plane temperatures at two different locations. We obtained the spatial temperature profile of the heater surface by an infrared camera. A secondary heat exchanger connected to a chiller was used to remove the heat and to control the fluid inlet temperature of 20 ± 1°C. The data reading of the sensors was performed by a digital multimeter and relay switching card, while we recorded the data and operated the system via LABVIEW™.

3 Results and Discussion

In order to characterize the cooling uniformity and to determine the heat sink maximum total thermal resistance, we measured the spatial temperature distribution of the resistive heater by means of an infrared camera. Figure 4(*a*) shows the temperature distribution of a segment of the heater surface of chip 4 ($w_{\text{HT,ch}}=50$ μm and $K=12.5$), operated at a total volumetric flow rate of $\dot{V}=1$ l/min and a heat input of $q''_{\text{chip}}=100$ W/cm^2. From the infrared image we computed average temperatures in *x*- and *y*-directions presented in Fig. 4(*b*) and defined as

$$\overline{T_i} = \frac{1}{N_j}\sum_{j=1}^{N_j} T_j \quad \text{and} \quad \overline{T_j} = \frac{1}{N_i}\sum_{i=1}^{N_i} T_i \tag{1}$$

where i and j are the pixel counts, and N_i and N_j are the total numbers of pixels in *x*- and *y*-directions, respectively. The corresponding flow orientation in the manifold system is indicated by the arrow. The fluid entered the heat sink on the left and branched into parallel manifold inlet channels. From the inlet channel the fluid was distributed to the underlying heat transfer structure through the slit nozzles. When the flow entered the heat transfer structure, fluid impinged directly on the bottom surface of the microchannel, suppressing a development of a hydrodynamic and a thermal boundary layer. Consequently, in this region, high heat transfer coefficients were obtained, resulting in colder heater sections directly underneath the inlet nozzles. This can be seen in the infrared image (cf. Fig. 4(*a*)) as darker horizontal lines and more quantitative by the local minima in $\overline{T_y}$ (Fig. 4(*b*)). After impinging on the microchannel bottom surface, the flow underwent a 90 deg turn and traveled along the microchannels, orientated orthogonally to the manifold channels. The fluid heated up along the channel and additionally a hydrodynamic and thermal boundary layer developed, causing a reduction in the local heat transfer coefficient. Toward the end of a unit cell of the microchannel array, the fluid exited through the outlet nozzle, connecting the microchannel to the outlet manifold channel. Thus, a stagnation zone formed opposite to the outlet nozzle, resulting in a decrease in the heat transfer rate and in an increase in the heater temperature toward the outlet (cf. Figs. 4(*a*) and 4(*b*)). From the averaged temperature profile in the *y*-direction we can see that the temperature difference form inlet to outlet was about 0.5 K.

Assuming a uniform fluid distribution along the manifold system we would expect a constant temperature in the *x*-direction of the heat sink. Except for the spreading effects at the edges of the heat sink, we observed two major deviations from a constant chip temperature along the *x*-direction. There are two considerable temperature minima at $x=6.25$ mm and $x=16.25$ mm, and two maxima at $x=6.66$ mm and $x=13.33$ mm. The positions of the temperature minima correspond to the location of the RTDs. As described earlier, the heater was divided into three sections by the RTDs, causing a strip of 250 μm in width without any heat input. The lack of heat input caused the temperature drop at the position of the RTDs, which can be clearly seen in the temperature profile.

To understand the temperature maxima, a closer look at the design of the manifold chip is needed. The base plate of the manifold chip was just about 350 μm in thickness and was perforated with 20 mm long slits representing the inlet and outlet nozzles. To ensure a structural stability and reliability of the manifold chip during the fabrication and packaging process, we decided not to have continuous slits, but to leave uncut 25 μm wide solid regions at one third and two third of the nozzle length. These regions are functioning as bracings and stiffened the chip. The fact that the locations of the bracings matched well with the positions of the maxima corroborates the assumption that the bracings had an influence on the fluid distribution and consequently on the heat transfer. Thus, we studied numerically their influence on the fluid distribution by a three-dimensional model of a unit cell of the heat sink, as illustrated in Fig. 5(*b*). The heat sink was represented by an inlet manifold channel, the heat transfer structure, and an outlet manifold channel. Due to the symmetry of the problem we considered half of an inlet and outlet manifold channel. To save computational time the heat transfer structure was considered as a porous media with an anisotropic permeability to account for the impermeable channel walls. The flow field in the manifold domain and the heat transfer structure were determined by solving the three–dimensional continuity and Navier–Stokes equations,

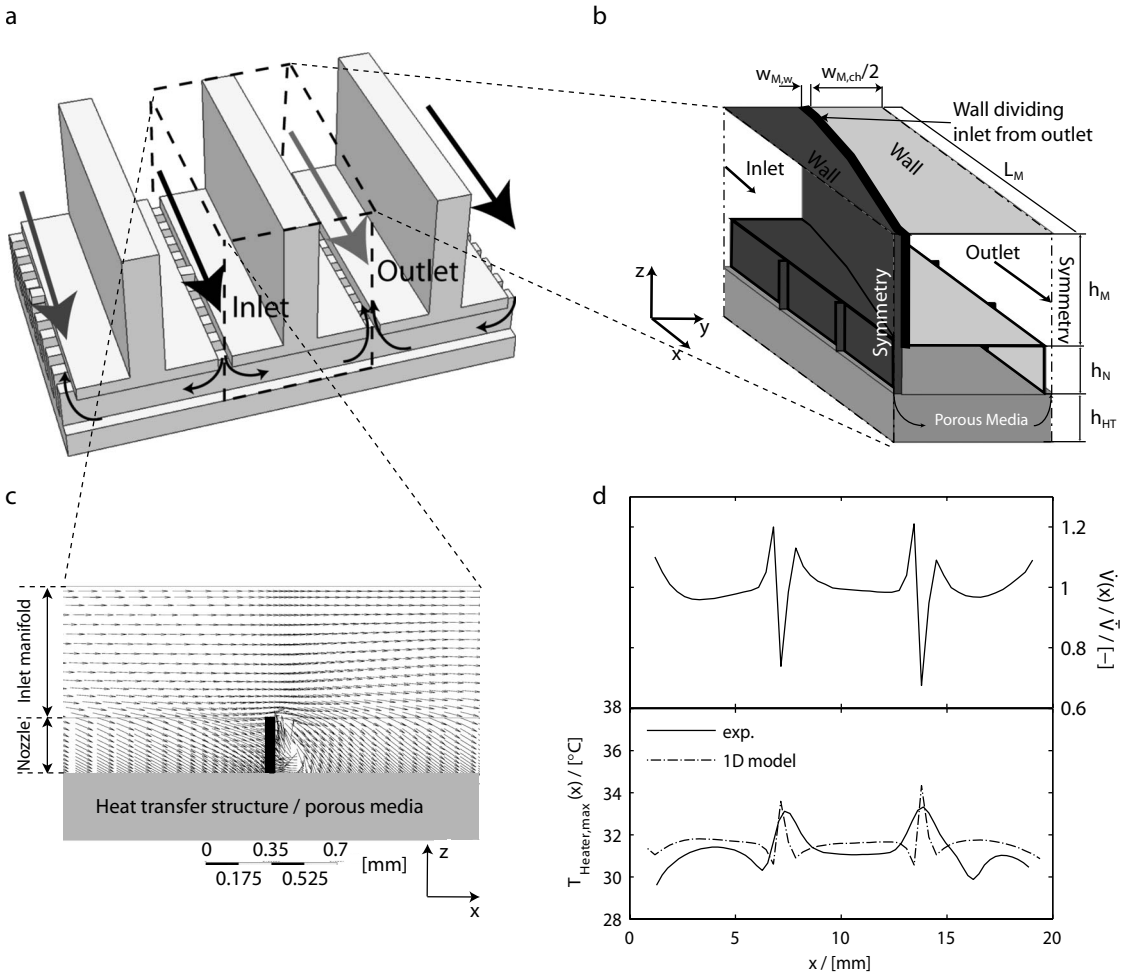

Fig. 5 (***a***) **Isometric section view indicating a unit cell of the heat sink;** (***b***) **computational domain of a unit cell of the manifold microchannel heat sink;** (***c***) **normalized velocity vectors at the *XZ*-center plane of the inlet manifold channel around a bracing; and** (***d***) **top part: relative volume flux distribution along the manifold system in the porous media, bottom part: comparison of the experimentally and theoretically determined maximum heater temperatures along the manifold system**

whereas for the heat transfer domain an additional source term, which was based on the Forchheimer modification of Darcy's law, was introduced to account for the porosity and permeability of the heat transfer structure. At the inlet we applied a constant mass flux boundary condition, and at the outlet an average static pressure of zero was set. All other faces were considered as walls with a no slip boundary condition. The set of partial differential equations with the boundary conditions described above was solved numerically with a finite volume second order high resolution discretization scheme on a structured grid using the solver CFX 11 (ANSYS™). A coupled algebraic multigrid solver is used in conjunction with a convergence criterion for the root mean square mass and momentum residuals of 10^{-5}. The domain was approximated by an anisotropic grid of 611,600 hexagonal cells, whereas the mesh size was verified by a mesh independence study. A more detailed description of the modeling methodology can be found in Ref. [23].

Figure 5(*c*) shows the normalized velocity vectors at the *XZ*-center plane of the inlet manifold channel at the position around a bracing for a total volumetric flow rate of 1 l/min. As can be seen from the vector field there is a typical laminar layer flow field in the main channel. At the bottom of the channel the fluid was sucked toward the nozzle into the heat transfer structure and underwent a change in momentum. We observed a substantial distortion of the fluid distribution by the bracing. Upstream of the bracing the flow inside the nozzle was blocked, whereas downstream, we observed stalling at the edge of the bracing, causing a recirculation zone behind the bracing inside the nozzle. This recirculation zone blocked a substantial part of the heat transfer structure for fluid supply, resulting in an increased local bulk thermal resistance. To study this phenomenon quantitatively we computed for the local relative volumetric flow rate through 56 planes equally distributed along the center *XZ*-plane of the heat transfer structure with a width $\Delta\zeta$ of 0.5 mm and the height of the heat transfer structure

$$\dot{V}_i^* = \frac{\int_{s_i-\Delta\zeta/2}^{s_i+\Delta\zeta/2}\int_{\eta=0}^{\eta=h_{\mathrm{HT}}}\dot{V}_i d\eta d\zeta}{\frac{1}{N}\sum_{i=1}^{N}\int_{s_i-\Delta\zeta/2}^{s_i+\Delta\zeta/2}\int_{\eta=0}^{\eta=h_{\mathrm{HT}}}\dot{V}_i d\eta d\zeta} \tag{2}$$

As seen from Fig. 5(*d*), there was a small increase in the volumetric flow rate upstream of a bracing and a sharp drop behind. We used the local fluid distribution to determine the theoretical maximum local heater temperature $T_{x,\mathrm{heater}}$ of each of the 56 sections as we considered the change in the bulk thermal resistance due to the fluctuations in fluid distribution

$$T_{\mathrm{heater,max}}(x) = R''_{\mathrm{tot}}(x)\dot{q}''_{\mathrm{heater}} + T_{\mathrm{in}} \tag{3}$$

The model to determine the total thermal resistance of the heat sink accounts for a conductive thermal resistance R''_{cnd} of the silicon base, a convection resistance R''_{cnv}, assuming a parallel heat

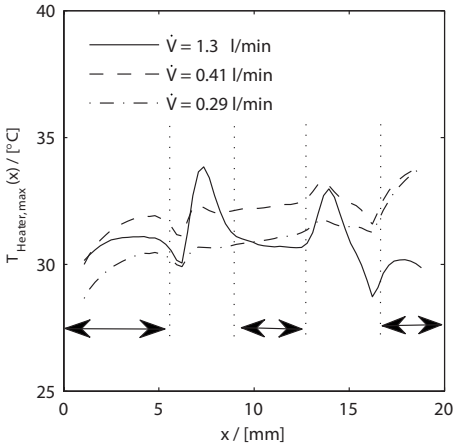

Fig. 6 Local maximum heater temperature for three different flow rates: arrows indicate the range for determination of the absolute maximum heater temperature

flux from the channel base and from the channel wall into the fluid considering a fin efficiency, and a bulk thermal resistance R''_{bulk} due to the finite heat capacity of the fluid

$$R''_{\text{tot}}(x) = R''_{\text{cnv}} + R''_{\text{cnd}} + R''_{\text{bulk}}(\dot{V}(x)) \tag{4}$$

The individual resistances are read as

$$R''_{\text{cnd}} = \frac{h_{\text{HT,ch}}}{\lambda_s}, \quad R''_{\text{cnv}} = \frac{w_{\text{HT,ch}} + w_{\text{HT},w}}{w_{\text{HT,ch}}\alpha_{\text{cnv}} + 2h_{\text{HT,ch}}\alpha_{\text{cnv}}\gamma_w}, \quad R''_{\text{bulk}} = \frac{L_{\text{ch}}(w_{\text{HT,ch}} + w_{\text{HT},w})}{c_{p,f}\rho_f \dot{V}_{\text{HT,ch}}} \tag{5}$$

A detailed discussion of the individual components can be found in Ref. [23].

In Fig. 5(*d*) we compare the experimentally determined local maximum heater temperature in the *x*-direction to the theoretically expected heater temperature according to Eq. (3) for a heat flux density of 100 W/cm^2 and a volumetric flow rate of 1 l/min. To determine the local maximum heater temperatures, as plotted in Fig. 5(*d*), we took the averaged heater temperatures in the *x*-direction and added the maximum deviation of $\overline{T_y}$ from the average temperature. This way we account for the elevated heater temperature at the end of a unit cell of the heat transfer structure due to the heating of the fluid along the channel. Accordingly, the local maximum heater temperature was defined as

$$T_{\text{heater,max}}(x) = \overline{T_x} + |\overline{T} - \overline{T_{y,\text{max}}}| \tag{6}$$

Both temperature profiles were in close agreement with the position and the actual temperatures of the maxima. Thus we could demonstrate that the maxima were caused by an induced flow disturbance due to the bracings. In addition this phenomenon points out the strong impact of fluid maldistribution on the thermal performance of the system and emphasizes the need of a thorough design of the manifold and precise fabrication technologies for establishing high performance heat sinks.

Since these bracings would not be needed in a fully automated process, it is acceptable to ignore these maxima. In addition, we did not consider the minima caused by the RTDs. Consequently, we considered the temperature distribution in the ranges being illustrated in Fig. 6 to determine the absolute maximum heater temperature $T_{\text{heater,max2}}$, which was applied to compute for the total thermal resistance of the system defined as

$$R''_{\text{tot}} = \frac{T_{\text{heater,max2}} - T_{\text{in}}}{\dot{q}''_{\text{heater}}} \tag{7}$$

We characterized the total thermal resistance of the test vehicles at a constant temperature difference between the maximum heater temperature and fluid inlet temperature of $\Delta T_{\text{max}} = 15$ K and controlled the heater input power. The temperature difference of $\Delta T_{\text{max}} = 15$ K was chosen after a sensitivity study of the total thermal resistance of the system as a function of ΔT_{max}. The total thermal resistance reached an asymptotic value for $\Delta T_{\text{max}} > 11$ K, and its error was determined to be less than ± 0.005 cm^2 K/W. Figure 6 shows the local maximum heater temperature for three different volumetric flow rates. For a flow rate of 1.3 l/min the temperature nonuniformity in the considered range is less than 1 K. If the flow rate is reduced by one third it can be seen that the heater temperature increases at the end of the manifold system. This can be either caused by a change in the fluid distribution due to lower flow rates or by heating up of the fluid along the manifold inlet channel. This phenomenon was more pronounced for a flow rate of 0.29 l/min, resulting in a nonuniformity of about 5 K. As we will demonstrate in the following, at these low flow rates the thermal performance of the heat sink was strongly dominated by its bulk thermal resistance and was thus strongly sensitive to small nonuniformities in the flow rate.

We characterized six test vehicles summarized in Table 1 according to their hydrodynamic and thermal performance. Figure 7(*a*) shows the pressure drop of all six test vehicles as a function of the volumetric flow rate. The examined range of the volumetric

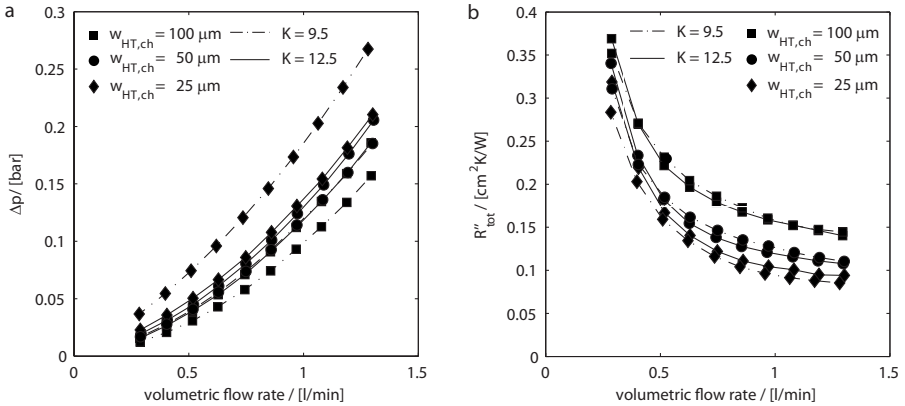

Fig. 7 (*a*) Total pressure drop across the heat sink and (*b*) maximum total thermal resistance as a function of the volumetric flow rate for all six test vehicles

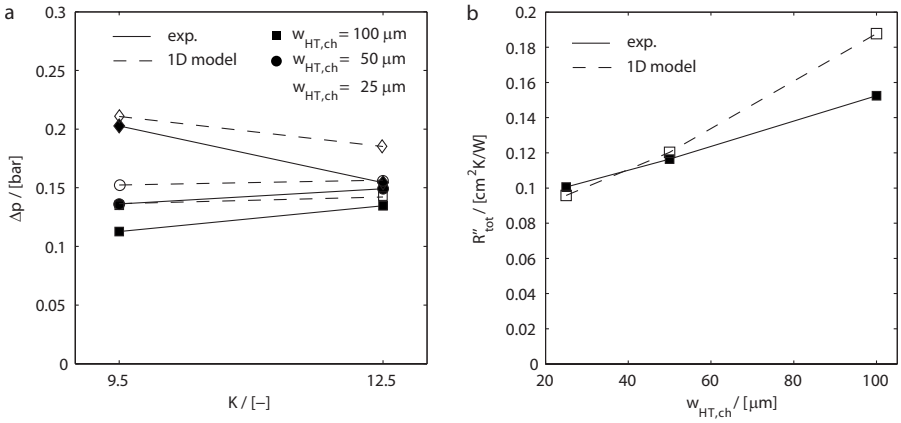

Fig. 8 Comparison of the experimentally and theoretically determined (*a*) total pressure drop across the heat sink as a function of the number of manifold systems for varying channel width $w_{HT,ch}$ and (*b*) maximum total thermal resistance as a function of the channel width $w_{HT,ch}$ for $K=9.5$ and a volumetric flow rate of 1.08 l/min

flow rate corresponds to a Reynolds number range at the manifold inlet of $450 < \mathrm{Re}_{M,\mathrm{in}} < 2800$, where we define the Reynolds number at the inlet as

$$\mathrm{Re}_{M,\mathrm{in}} = \frac{u_{M,\mathrm{in}}(w_{M,\mathrm{in}}h_M)^{0.5}}{\nu} \tag{8}$$

Hence we studied the performance of the heat sink from the laminar regime to the border zone of the transition regime between the laminar and turbulent flows in the manifold channel. The Reynolds number for the flow through the heat transfer structure was in the order of unity. Qualitatively for all test vehicles we observed a similar power-law dependence with an exponent being slightly larger than unity between the pressure drop across the heat sink and the volumetric flow rate. We did not observe a rapid change in the pressure drop at a certain volumetric flow rate in any of the test vehicles, indicating that there is no transition from laminar to turbulent flow. The highest hydrodynamic resistance was measured for chip 5 ($w_{HT,ch}=25$ μm and $K=9.5$), whereas chip 2 ($w_{HT,ch}=100$ μm and $K=12.5$) provided the smallest hydrodynamic resistance. The total hydrodynamic resistance depends on both the number of manifold systems K and the width of the heat transferring microchannels $w_{HT,ch}$.

To discuss this dependency more in-depth we present in Fig. 8(*a*) the pressure drop of all six test vehicles for a constant volumetric flow rate of 1.08 l/min. The test vehicles with $w_{HT,ch}=100$ μm exhibit a smaller pressure drop for $K=9.5$ manifold systems than for $K=12.5$. The total pressure drop across the heat sink is composed of the pressure losses across the manifold system and across the heat transfer structure

$$\Delta p_{\mathrm{tot}} = \Delta p_M + \Delta p_{\mathrm{HT}} \tag{9}$$

where the individual terms are read as

$$\Delta p_{\mathrm{HT}} = 4f_{\mathrm{app},N}\frac{\rho_f u_N^2 L_N}{d_N} + \frac{2f_{\mathrm{app,ch}}\rho_f u_{\mathrm{ch}}^2 L_{\mathrm{ch}}}{d_{\mathrm{ch}}} + 0.4\frac{\rho_f u_{\mathrm{N}}^2}{2} + \frac{\rho_f u_{\mathrm{ch}}^2}{2} \tag{10}$$

and

$$\Delta p_M = \int_0^{L_{\mathrm{M}}} -\frac{2f_{\mathrm{app}}(\xi_M,\overline{u_M})\rho_f \overline{u_M^2}(\xi_M)}{d_M(\xi_M)} d\xi_M \tag{11}$$

A detailed discussion of the equations can be found in Ref. [23].

If we increase the number of manifold systems, the initial cross section of a manifold channel narrows as the width of the manifold channel is reduced according to

$$w_{\mathrm{M,ch}} = \frac{L_{\mathrm{heater}}}{2K} - w_{\mathrm{M,w}} \tag{12}$$

where $w_{M,w}$ is the minimum wall thickness required for sufficient structural stability. The pressure drop across a rectangular straight channel is proportional to the volumetric flow rate and drops with the fourth power of the hydraulic diameter. Following Muzychka and Yovanovich [24] we defined the hydraulic diameter d_h as the square root of the channel cross section. Assuming that the flow branched uniformly into the parallel manifold systems, the volumetric flow rate through each manifold system is read as

$$\dot{V}_M = \frac{\dot{V}_{\mathrm{tot}}}{K} \tag{13}$$

Hence along with Eqs. (12) and (13) the pressure drop across the manifold was directly proportional to the number of manifold systems K and can be written as

$$\Delta p \sim \frac{C_1 \dot{V} L_{\mathrm{ch}}}{d_h^4} \quad \text{with} \quad d_h = (hw)^{0.5} \Rightarrow \Delta p_M \sim C_2 \dot{V}_{\mathrm{tot}} K \tag{14}$$

On the other hand increasing the number of manifold systems reduces the fluid path through the heat transfer structure, and thus, its hydrodynamic resistance. Thus an increasing total pressure drop across the heat sink with increasing number of manifold systems demonstrates that the rise of the hydrodynamic resistance of the manifold systems outweighed the reduction in the pressure loss across the heat transfer structure. If the channel width of the heat transfer structure $w_{HT,ch}$ is reduced, we increase its hydrodynamic resistance, while keeping the pressure loss across the manifold system unaffected. Thus, below a certain channel width $w_{HT,ch}$, the pressure loss across the heat transfer structure will dominate the overall pressure drop of the heat sink. Consequently, in this range, a reduction in the hydrodynamic resistance of the heat transfer structure due to an increased number of manifold systems from $K=9.5$ to 12.5 would overweigh the accompanied rise of pressure loss across the manifold. As seen from Fig. 8(*a*) for a channel width of $w_{HT,ch}=50$ μm less manifold systems ($K=9.5$) were beneficial, whereas for a channel width of $w_{HT,ch}=25$ μm it was favorable to increase the number of manifold systems to $K=12.5$. Hence, for the present parameter set, the transition formed a manifold dominated to a heat transfer structure dominated hydrodynamic resistance, which occurred between $w_{HT,ch}=50$ μm and 25 μm.

In a previous paper [23] we presented a semi-empirical one-dimensional model developed based on the results of a three-dimensional numerical model. It considers the pressure drop across the manifold, nozzles, and microchannels. To demonstrate its accuracy, we applied this model to the present test vehicles and used the geometric parameters, as summarized in Table 1 as input parameters. In Fig. 8(*a*) we compare the pressure losses of all six test vehicles estimated by the semi-empirical one-dimensional model to the experimental results. The model represents the hydrodynamic performance qualitatively and quantitatively with a maximum deviation of less than 25%.

The total thermal resistance of the six test vehicles as a function of the volumetric flow rate is presented in Fig. 7(*b*). We observed a power-law decay of the total thermal resistance for an increased volumetric flow rate. As shown in Ref. [23] this power-law decay was caused by a reduction in the bulk thermal resistance of the heat sink. The test vehicle chips 5 and 6 with a channel width of the heat transfer structure of $w_{HT,ch}=25$ μm provided the smallest total thermal resistance for a given volumetric low rate. Increasing the channel width $w_{HT,ch}$ results in higher total thermal resistances, as shown in Fig. 7(*b*).

The number of manifold systems K had no significant influence on the thermal performance of the heat sinks. For a constant total volumetric flow rate a reduction in the number of manifold systems causes an increase in the local volumetric flow rate through one unit cell of the heat transfer structure. We demonstrated numerically in Ref. [23] that the convective thermal resistance is almost unaffected by an increase in the local volumetric flow rate, hence, by an increase in velocity. In addition, the bulk thermal resistance of the system remains the same as the fluid path length through the heat transfer structure decays proportional to the number of manifold systems and compensates the increased local volumetric flow rate. Hence, we would not expect a dependency of the total thermal resistance on the number of manifold systems, which is consistent with the experiment (cf. Fig. 7(*b*)).

Figure 8(*b*) illustrates the total thermal resistance of the heat sink as a function of the channel width of the heat transfer structure for a constant volumetric flow rate of 1.08 l/min and a number of manifold systems $K=9.5$. The total thermal resistance increases linearly with increasing channel width. In addition, we plotted the total thermal resistance being computed by means of the semi-empirical one-dimensional model (cf. Eq. (4)). The model shows qualitatively the same dependency between the total thermal resistance and the width of the channels of the heat transfer structure. However, there is a discrepancy in the slope of the functional relationship, which becomes obvious especially for the larger channel width of $w_{HT,ch}=100$ μm. The semi-empirical one-dimensional model does not explicitly account for any heat transfer from the nozzle walls into the fluid. The test vehicles with a channel width of $w_{HT,ch}=100$ μm had aspect ratios of about three, providing a good thermal connection through the channel walls to the nozzle section (fin efficiency of 86%). This might be the reason for underestimating the thermal performance of the system especially for larger channel widths. Nevertheless, the maximum quantitative deviation is less than 25%.

In the following, we compare the efficiency of the different heat sink designs. The efficiency of a heat sink is defined by the ratio of the removed heat flux per invested pumping power, also known as its coefficient of performance (COP) [25]. This scales reversely with the total thermal resistance of the system. Hence, a lower total thermal resistance at a constant pumping power demonstrates a higher heat sink performance. In Fig. 9 we compare the total thermal resistance of the different designs with a number of manifold channels of $K=9.5$ as a function of an idealized pumping power P, which is defined as

$$P = \Delta p \dot{V}_{tot} \tag{15}$$

In the case of high pumping powers and high volumetric flow rates the design of the heat transfer structure with the smallest channel width, namely, $w_{HT,ch}=25$ μm, performed most efficiently, although it showed the highest hydrodynamic resistance (cf. Fig. 7(*a*)). At a constant pumping power the volumetric flow rate was lower for the test vehicle with $w_{HT,ch}=25$ μm than for the other two designs with larger channels, and consequently, it resulted in a higher bulk thermal resistance. However, due to the lower convective thermal resistance of this test vehicle, the available thermal mass flux was used more efficiently resulting in higher outlet temperatures for a constant heat flux.

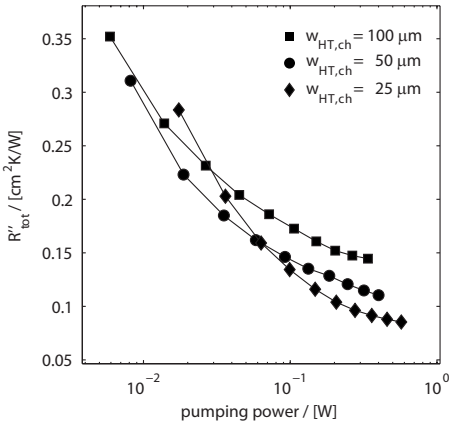

Fig. 9 Maximum total thermal resistance as a function of the pumping power for varying channel width $w_{HT,ch}$ and $K=9.5$

If the pumping power is reduced, the increase in the total thermal resistance of the test vehicle with $w_{HT,ch}=25$ μm was more pronounced than for the other two devices. Since the convective thermal resistance was lower than the one of the other devices, the transition at which the bulk thermal resistance became the dominant part in the resistance chain occurred at higher volumetric flow rates, and consequently, at higher pumping powers. Thus the total thermal resistance of the test vehicle with $w_{HT,ch}=25$ μm showed a stronger dependence on the pumping power. For pumping powers below 0.06 W it would be beneficial to increase the channel width of the heat transfer structure from $w_{HT,ch}=25$ μm to 50 μm in order to reduce the hydrodynamic resistance, and therefore, the bulk thermal resistance. At this point the increase in the convective thermal resistance due to an enlargement of the channel width would be compensated by the reduction in the bulk thermal resistance.

Next, we demonstrate the potential of the heat sink design to be used in combination with elevated inlet temperatures to reduce the datacenter energy costs and to make energy reuse possible. We studied the influence of increased fluid inlet temperatures on the performance of the best performing test vehicle with a channel width of $w_{HT,ch}=25$ μm and a number of manifold systems of $K=12.5$. Figure 10(*a*) depicts the pressure drop and the total thermal resistance of this device as a function of the fluid inlet temperature at a constant volumetric flow rate of 1 l/min and a constant heat flux density of 100 W/cm^2. An increase in the fluid inlet temperature from 20°C to 70°C lowered the pressure drop across the heat sink by about 40% due to a 60% reduction in the dynamic viscosity of water. The pressure drop reduction was not linear as the dynamic viscosity of water decays exponentially with temperature.

On the other hand, the total thermal resistance of the heat sink was increased by about 12%, mainly attributed to a 20% reduction in the silicon thermal conductivity. A reduction in the thermal conductivity of silicon contributed to an increase in the conduction thermal resistance of the silicon base, causing a 6% increase in the total thermal resistance. In addition, the fin efficiency was decreased, causing a reduction in the convective thermal resistance. Simultaneously, the fluid thermal conductivity was increased by about 10%, resulting in an increased convective heat

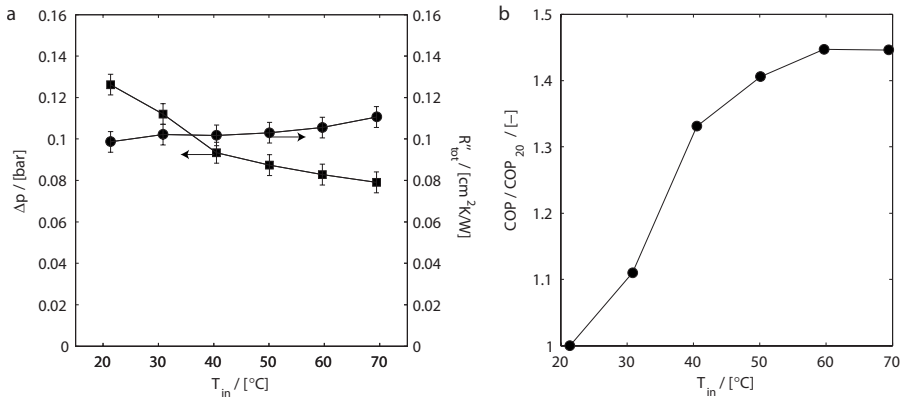

Fig. 10 (*a*) Total pressure drop (squares) and maximum total thermal resistance (circles) and (*b*) relative COP as a function of the fluid inlet temperature for $w_{HT,ch}=25$ μm, $K=12.5$, $\dot{q}''_{heater}=100$ W/cm^2, and $\dot{V}=1$ l/min

transfer. However, the total thermal resistance of the heat sink was only slightly affected by the convective thermal resistance as it accounts for only a share of 20% of the chain of thermal resistances. The volumetric heat capacity of the fluid decreased by about 2%, which directly affected the bulk thermal resistance of the system. To evaluate the increase in efficiency of the heat sink due to elevated inlet temperatures, we determined the relative COP, normalized to the COP at 20°C. Hence, we write the relative coefficient of performance for a constant maximum temperature difference between heater and fluid inlet as

$$\frac{COP}{COP_{20}} = \frac{\dot{q}_{\text{heater}}}{P}\frac{P_{20}}{\dot{q}_{\text{heater},20}} = \frac{P_{20}}{P}\frac{R''_{\text{tot},20}\Delta T_{\max}}{R''_{\text{tot}}\Delta T_{\max,20}} = \frac{P_{20}}{P}\frac{R''_{\text{tot},20}}{R''_{\text{tot}}} \quad (16)$$

Figure 10(*b*) depicts the relative enhancement in the COP as a function of the fluid inlet temperature. Due to the nonlinear behavior of the pressure drop as a function of the inlet temperature (cf. Fig. 10(*a*)) we observed a saturation curve for the COP. At inlet temperatures above 60°C, the pumping power reduction and the increase in the total thermal resistance were balanced. Hence, a further rise of the inlet temperature did not influence the efficiency of the heat sink. Concluding, the performance of the heat sink could be enhanced by more than 40% for a 50 K rise of the fluid inlet temperature (compared with an inlet temperature of 20°C), resulting in a maximum heater temperature of 81°C for a fluid inlet temperature of 70°C.

4 Conclusion

A novel, ultrathin manifold microchannel heat sink was fabricated and investigated experimentally. We processed six different prototypes with varying channel widths of the heat transfer structure and different numbers of manifold systems. A test loop for accurate hydrodynamic and thermal characterizations of the test vehicles was established. We studied experimentally the sensitivity of the heat sink hydrodynamic and thermal performance on the width of the microchannels, the number of manifold systems, the volumetric flow rate, and the pumping power. The present experimental results validated our previous semi-empirical one-dimensional model [23] qualitatively and quantitatively within a maximum deviation of 25%.

It was demonstrated that the optimum design of the heat sink was determined by the interaction between the number of manifolds and the channel width of the heat transfer structure. The optimum was shifted to wider heat transfer channels for lower pumping powers. The best performing prototype ($w_{HT,ch}=25$ and $K=12.5$) closest to the optimum choice of design parameters provides a total thermal resistance of 0.09 cm^2 K/W at a volumetric flow rate of 1.3 l/min and a pressure drop of 0.22 bar for a four square centimeter chip area and an inlet temperature of 20°C. This allows for cooling power densities of more than 700 W/cm^2 for a maximum temperature difference between th fluid inlet and maximum chip temperature of 65 K.

Typical power densities of high performance microprocessors are currently in the range of 100 W/cm^2. Our current optimum design ($w_{HT,ch}=25$ μm and $K=12.5$) allows for elevated inlet temperatures of up to 70°C, resulting in a maximum chip temperature of 81°C for a flow rate of 1 l/min. The low thermal resistance and the tolerable high inlet temperatures provide the possibility of free cooling in all climate zones, eliminating the need for chillers. In addition, the rise of the inlet temperature to 70°C enhances the overall efficiency of the heat sink by more than 40%. Hence, not only the possibility of energy reuse is provided by increasing the inlet temperatures, but the overall performance of the cooling solution is enhanced by a reduction in the total pressure drop across the heat sink.

The current performance of the heat sink could be further improved by reducing the nozzle length and by increasing the manifold channel height. This would drastically lower the hydrodynamic resistance of the heat sink [23]. A reduction in the hydrodynamic resistance of the manifold would shift the design optimum toward higher numbers of manifold systems. Hence, the flow path through the heat transfer structure would be reduced, which allows for narrower channel widths of the heat transfer structure and accordingly entails a reduced total thermal resistance of the heat sink.

If there is a demand for other liquid coolants than water, the optimum design of the heat sink will change. For example, the operation with fluids having lower heat capacity than water would shift the optimum to larger heat transfer channels and less manifold systems in parallel in order to reduce the hydrodynamic resistance of the system and therewith increase the volumetric flow rate to compensate the increased bulk thermal resistance. Hence the decoupling of the fluid distribution from the intrinsic heat transfer provides the advantage of damping effects from, e.g., changed fluid properties.

The proposed design implies that the heat transfer structure, namely, the microchannel array, is incorporated directly in the back side of the microelectronic device. If a patterning of the microelectronic device was not desired, the heat transfer structure could be fabricated in a separate silicon chip, which could be bonded to the microelectronic device by a eutectic AuSn 80/20 thin film solder, as proposed by Brunschwiler et al. [26]. The AuSn provides a bulk thermal conductivity of 57 W/m K at a bondline thickness of about 5 μm, resulting in an additional conductive thermal resistance of less than 0.001 cm^2 K/W. Therefore, the thermal resistance of the bond is almost negligible, and

the total thermal resistance of the cooling solution can be determined by accounting for the additional conduction resistance of the microelectronic device.

Acknowledgment

This work was supported by KTI/CTI under Project No. P. 8074.1 NMPP-N. We acknowledge Reto Waelchli, Wulf Glatz, Stephan Paredes, Javier Goicochea, Ingmar Meijer, Ute Drechsler, and Martin Witzig for their technical contributions and discussions, and Walter Riess for the financial support.

Notation

c = constant
c_p = heat capacity (J/kg K)
COP = coefficient of performance
d = characteristic diameter (m)
f = friction factor
h = height (m)
K = number of parallel manifold systems
L = length (m)
N = quantity indicator
p = pressure (Pa)
P = pumping power (W)
$\dot{q}$ = heat flux (W)
R = thermal resistance (K/W^{-1})
T = temperature (K)
$\dot{V}$ = volumetric flow rate ($m^3\ s^{-1}$)
w = width (m)
x,y,z = global coordinates (m)

Greek Letters

α = heat transfer coefficient ($W/m^2\ K$)
γ = fin efficiency
λ = thermal conductivity (W/m K)
ρ = density (kg/m^3)
ξ = local coordinate in the streamwise direction (m)
ζ, η = local coordinate in the transverse direction (m)

Subscript/Superscript

$''$ = area normalized (m^{-2})
i,j = indices
ch = channel
cnd = conduction
cnv = convection
f = fluid
h = hydraulic
HT = heat transfer structure
in = inlet
M = manifold
max = maximum
N = nozzle
s = solid
tot = total
w = wall

References

[1] Sauciuc, I., Chrysler, G., Mahajan, R., and Szleper, M., 2003, "Air-Cooling Extension—Performance Limits for Processor Cooling Applications," *Proceedings of the 19th IEEE SEMI-THERM Symposium*, pp. 74–81.
[2] Brunschwiler, T., Smith, B., Ruetsche, E., and Michel, B., 2009, "Toward Zero-Emission Data Centers Through Direct Reuse of Thermal Energy," IBM J. Res. Dev., **53**(3), pp. 11:1–11:13.
[3] Tuckerman, D. B., and Pease, R. F. W., 1981, "Implications of High-Performance Heat Sinking for Electron Devices," IEEE Trans. Electron Devices, **28**(10), pp. 1230–1231.
[4] Agostini, B., Fabbri, M., Park, J. E., Wojtan, L., Thome, J. R., and Michel, B., 2007, "State of the Art of High Heat Flux Cooling Technologies," Heat Transfer Eng., **28**(4), pp. 258–281.
[5] Kandlikar, S. G., 2005, "High Flux Heat Removal With Microchannels—A Roadmap of Challenges and Opportunities," Heat Transfer Eng., **26**(8), pp. 5–14.
[6] Hassan, I., Phutthavong, P., and Abdelgawad, M., 2004, "Microchannel Heat Sinks: An Overview of the State-of-the-Art," Nanoscale Microscale Thermophys. Eng., **8**(3), pp. 183–205.
[7] Chen, Y. P., and Cheng, P., 2002, "Heat Transfer and Pressure Drop in Fractal Tree-Like Microchannel Nets," Int. J. Heat Mass Transfer, **45**(13), pp. 2643–2648.
[8] Chen, Y. P., and Cheng, P., 2005, "An Experimental Investigation on the Thermal Efficiency of Fractal Tree-Like Microchannel Nets," Int. Commun. Heat Mass Transfer, **32**(7), pp. 931–938.
[9] Perret, C., Boussey, J., Schaeffer, C., and Coyaud, M., 2000, "Analytic Modeling, Optimization, and Realization of Cooling Devices in Silicon Technology," IEEE Trans. Compon. Packag. Technol., **23**(4), pp. 665–672.
[10] Senn, S. M., and Poulikakos, D., 2004, "Laminar Mixing, Heat Transfer and Pressure Drop in Tree-Like Microchannel Nets and Their Application for Thermal Management in Polymer Electrolyte Fuel Cells," J. Power Sources, **130**(1–2), pp. 178–191.
[11] Bejan, A., and Errera, M. R., 2000, "Convective Trees of Fluid Channels for Volumetric Cooling," Int. J. Heat Mass Transfer, **43**(17), pp. 3105–3118.
[12] Calame, J. P., Park, D., Bass, R., Myers, R. E., and Safier, P. N., 2009, "Investigation of Hierarchically Branched-Microchannel Coolers Fabricated by Deep Reactive Ion Etching for Electronics Cooling Applications," ASME J. Heat Transfer, **131**(5), pp. 051401–051409.
[13] Escher, W., Michel, B., and Poulikakos, D., 2009, "Efficiency of Optimized Bifurcating Tree-Like and Parallel Microchannel Networks in the Cooling of Electronics," Int. J. Heat Mass Transfer, **52**(5–6), pp. 1421–1430.
[14] Harpole, G. M., and Eninger, J. E., 1991, "Micro-Channel Heat Exchanger Optimization," *Proceedings of the Seventh Annual IEEE Semiconductor Thermal Measurement and Management Symposium*, Phoenix, AZ, pp. 59–63.
[15] Copeland, D., 1995, "Manifold Microchannel Heat Sinks: Analysis and Optimization," Therm. Sci. Eng., **3**(1), pp. 7–12.
[16] Copeland, D., Takahira, H., Nakayama, W., and Pak, B. C., 1995, "Manifold Microchannel Heat Sinks: Theory and Experiment," *Proceedings of the. International Electronic Packaging Conference (INTERPACK '95)*, Lahaina, HI, T. R. Hsu, A. Bar-Cohen, and W. Nakayama, eds., Vol. 2, pp. 829–835.
[17] Copeland, D., Behnia, M., and Nakayama, W., 1996, "Manifold Microchannel Heat Sinks: Isothermal Analysis," *Proceedungs of the Fifth InterSociety Conference on Thermal Phenomena in Electronic Systems (I-THERM V)*, Orlando, FL, pp. 96–102.
[18] Copeland, D., Behnia, M., and Nakayama, W., 1998, "Manifold Microchannel Heat Sinks: Conjugate and Extended Models," International Journal of Microelectronic Packaging, Materials and Technologies, **1**(2), pp. 139–152.
[19] Ryu, J. H., Choi, D. H., and Kim, S. J., 2003, "Three-Dimensional Numerical Optimization of a Manifold Microchannel Heat Sink," Int. J. Heat Mass Transfer, **46**(9), pp. 1553–1562.
[20] Kermani, E., Dessiatoun, S., Shooshtari, A., and Ohadi, M. M., 2009, "Experimental Investigation of Heat Transfer Performance of a Manifold Microchannel Heat Sink for Cooling of Concentrated Solar Cells," 2009 IEEE 59th Electronic Components and Technology Conference, San Diego, CA.
[21] Colgan, E. G., Furman, B., Gaynes, M., Labianca, N., Magerlein, J. H., Polastre, R., Bezama, R., Marston, K., and Schmidt, R., 2006, "High Performance and Subambient Silicon Microchannel Cooling," *Proceedings of the Fourth International Conference on Nanochannels, Microchannels, and Minichannels*, Limerick, Ireland, pp. 1046–1051.
[22] Brunschwiler, T., Rothuizen, H., Fabbri, M., Kloter, U., and Michel, B., 2006, "Direct Liquid Jet Impingement Cooling With Micronsized Nozzle Array and Distributed Return Architecture," *2006 Proceedings 10th Intersociety Conference on Thermal and Thermomechanical Phenomena in Electronics Systems*, San Diego, CA.
[23] Escher, W., Michel, B., and Poulikakos, D., 2010, "A Novel High Performance, Ultra Thin Heat Sink for Electronics," Int. J. Heat Fluid Flow to be published.10.1016/j.ijheatfluidflow.2010.03.001
[24] Muzychka, Y. S., and Yovanovich, M. M., 2004, "Laminar Forced Convection Heat Transfer in the Combined Entry Region of Non-Circular Ducts," ASME J. Heat Transfer, **126**(1), pp. 54–61.
[25] Steinke, M. E., and Kandlikar, S. G., 2006, "Single-Phase Liquid Heat Transfer in Plain and Enhanced Microchannels," *Proceedings of the Fourth ASME International Conference on Nanochannels, Microchannels, and Minichannels*, Limerick, Ireland, pp. 943–951.
[26] Brunschwiler, T., Michel, B., Rothuizen, H., Kloter, U., Wunderle, B., Oppermann, H., and Reichl, H., 2008, "Forced Convective Interlayer Cooling in Vertically Integrated Packages," *Proceedings of the 11th IEEE Intersociety Conference on Thermal and Thermomechanical Phenomena in Electronic Systems*, Orlando, FL, pp. 1114–1125.

Fluid Flow and Heat Transfer in a Horizontal Channel With Divergent Top Wall and Heated From Below

C. S. Yang
Department of Computer Science and Information Engineering,
Far East University,
Hsin-Shih,
Tainan County 744, Taiwan

D. Z. Jeng
Aeronautics Systems Research Division,
Chung-Shan Institute of Science and Technology,
Taichung 407, Taiwan

C. W. Liu

C. G. Liu

C. Gau[1]

Institute of Aeronautics and Astronautics and
Center for Micro/Nano Science and Technology,
National Cheng Kung University,
Tainan 70101, Taiwan
e-mail: gauc@mail.ncku.edu.tw

Secondary flow structure and its enhancement on the heat transfer in a horizontal divergent channel have been studied. The bottom wall is horizontal and is heated uniformly while the opposite top wall is insulated and inclined with respect to the horizontal plane so as to create a divergent angle of 3 deg. At the entrance of the channel, the aspect ratios for the width to the height and the channel length to the height are 6.67 and 15, respectively. The Reynolds number ranges from 100 to 2000 and the buoyancy parameter Gr/Re^2 from 0 to 405. Both flow visualization and temperature fluctuation measurements at different locations are made to indicate the flow structure and oscillation of the secondary flow. The adverse pressure gradient in the divergent channel causes a thicker heated layer in the bottom and earlier initiation of secondary flow. Interaction between neighboring vortices and plumes becomes more severe and highly unstable. This precludes the formation of steady two-dimensional longitudinal vortex rolls in the downstream and leads to an earlier and larger enhancement of the heat transfer than the case of the parallel-plate channel. The effects of the buoyancy parameter and the divergence of the channel on the secondary flow structure and the Nusselt number are presented and discussed. [DOI: 10.1115/1.4001606]

Keywords: mixed convection in horizontal divergent channel, divergent channel flow heated from below, secondary flow structure, mixing convection heat transfer

1 Introduction

Mixed convection in channels has received great interest in the past 3 decades for its practical application in the solar energy collectors, heat exchangers, geothermal energy systems, chemical deposition of solid layer in the semiconductor industry, and the cooling of the nuclear reactors and modern electronic equipments. For a horizontal channel heated from below, the buoyancy force can induce secondary flow, which shortens the thermal developing length, may induce transition to turbulent flow, and enhance the heat transfer [1–5]. The secondary flow is observed to be in the form of longitudinal vortex rolls, which, as a result of the shear force imposed by the mainstream, begin to bifurcate and curl back to the heated surface such that a mushroom configuration is seen when viewed in the spanwise direction. It is found that the flow structure and heat transfer depend very much on the Rayleigh number, the Reynolds number, the Prandtl number, and the aspect ratio (width to height ratio) of the channel. In addition, the formation of the plume and the resulting mushroom-shaped vortices in the upstream can gradually transform into the two-dimensional convection rolls in the downstream. The transformation process involves a three-dimensional flow variation and has not been explored in detail before. Due to the difference in the Pr number, the complete transformation process for the experiments with water may not be used to infer the experiments with air.

The earlier work on the mixed convection, especially the secondary flow structure and its effect on the heat transfer, in the parallel-plate channel was analyzed by Yasuo and Yutaka [5] who can predict both the first and second type vortex rolls of the fully developed buoyancy induced secondary flow in an asymmetric isothermal channel. Longitudinal convection rolls are observed in the experiments with air, which are used to check the validity of the analysis. In the developing region, Hwang and Liu [3] observed the mushroom-shaped plume associated with vortices and found that the wavelength of the plume decreases and approaches the prediction based on the linear stability analysis as the aspect ratio increases. For the experiments with water, the complete transformation process of the secondary flow from the mushroom-shaped plume to the vortices, the breakdown of vortices, and the transition to the turbulent flow is visualized [6,7]. For $Gr < 1.5 \times 10^7$, the number of plume produced is $A/2$, but with increasing Gr to 8.0×10^8, the number increases to approximately $4A$. This behavior is consistent with the results for the experiments with water [1,8]. However, in the experiments with air [4,9], the periodic spanwise temperature distributions with wavelength of the channel height have been measured and obtained when $Ra > 8000$, which suggests the appearance of the second type vortex rolls as predicted by Yasuo and Yutaka. The critical Rayleigh numbers for the onset of secondary flow were also studied in the fully developed region [10–12] and both the thermal entry and the combined entry region [2,4,13,14]. Correlations for the onset of thermal instability are obtained for both the experiments with water and air. It is found that as the critical Rayleigh number increases, the onset of instability moves upstream and the corresponding wave numbers increase. Theoretical analyses [15–17] were also performed to predict the onset of the thermal instability. The predictions are close to the experimental data. For the heat transfer, significant enhancement in the heat transfer due to the secondary flow is found. However, longitudinal periodicity in the Nusselt number upstream of the fully developed region is found only in the experiments with water [6,7], but is not reported in the experiments with air [2,14]. From the review of literature, it appears that the results obtained for the critical Rayleigh number for

[1]Corresponding author.

Contributed by the Heat Transfer Division of ASME for publication in the JOURNAL OF HEAT TRANSFER. Manuscript received February 12, 2009; final manuscript received February 10, 2010; published online June 10, 2010. Assoc. Editor: Roger Schmidt.

the initiation of the plume, the number of plume produced, and the heat transfer characteristic between the experiments with water and the ones with air are different.

Numerical studies are also performed to study the occurrence and the structure of the secondary flow and the enhancement of heat transfer in both the developing and fully developed regions [18–23]. The trends obtained in general are consistent with the experimental observations. However, most of the numerical calculations assume steady laminar flow. This may not be true for the initiation, growth of the plumes and vortices, and the transformation into two-dimensional convection rolls. Further improvement in the numerical calculation is still needed.

However, in practical application, the channel wall may not be in perfect parallel such as in cooling passage of electronics where slight channel convergence or divergence may occur. Large convergence or divergence in channel may occur in nozzle or diffuser. The sight convergence in the top wall has a practical application in chemical vapor deposition process where the convergence of the channel has the effect to make the species transport more uniform. In fact, the convergence of channel can accelerate the mainstream, which results in suppressing the turbulence and reducing the buoyancy effect. It can completely change the transformation process and greatly alter the secondary flow structure and the heat transfer [24,25]. In addition, the onset of secondary flow can be significantly affected by the convergence or divergence of the channel [24,26], which leads to earlier initiation or retardation of heat transfer enhancement. In a heated vertical divergent channel, however, it is found [26] that the divergence of channel decelerates the flow, thereby destabilizing the flow and increasing the buoyancy effect, which leads to a deeper penetration of the reversed flow into the channel. The destabilization effect of the divergent channel can lead to breakdown of vortices and to transition to turbulent flow, which can significantly enhance the heat transfer. In addition, even a slight divergence of the channel can greatly alter the secondary flow structures and, hence, the heat transfer performance. However, in a horizontal divergent channel heated from a side, the mixed convection flow can be significantly affected, which leads to earlier initiation of the secondary circulation flow [27]. However, this flow variation does not have a significant effect on the heat transfer. It appears that the effect of channel divergence on both the mixed convection flow and heat transfer is an interesting phenomenon. However, a complete study on this topic is still very few. Deeper understanding of the flow and heat transfer is still needed.

The present paper describes an experimental study of mixed convection in a heated horizontal divergent channel. A uniform air flow is provided at the channel entrance, and exits to the ambient after passing through the test section. The bottom wall is maintained in the horizontal position and is heated uniformly, while the opposite, top wall has a divergent angle of 3 deg to the horizontal plane. That is, the downstream end of the top wall is tilted away from the bottom wall, and is well-insulated. The objective of this investigation is to study the mixed convection flow, especially the secondary flow structure and the heat transfer, in a heated horizontal divergent channel. Results of both the flow visualization by introducing smoke at the inlet and the heat transfer measurements along the heated wall are presented. The effects of the buoyancy parameter and the Reynolds number on the flow structure and the Nusselt number are reported.

2 Experimental Apparatus and Procedures

Experiments are performed in a Plexiglas channel, as shown in Fig. 1. The channel is 45 cm in length, 20 cm in width inside, and 3cm in height at the entrance. The heated wall is kept horizontal and the opposite wall is titled with a divergence angle of 3 deg. Therefore, the exit of the channel has a height of 7.72 cm. The heated wall is made of a 2 cm thick balsa wood and electrically heated. This is achieved by gluing seven of 0.015 cm thick stainless steel foil strips on the entire bottom wall and passing an

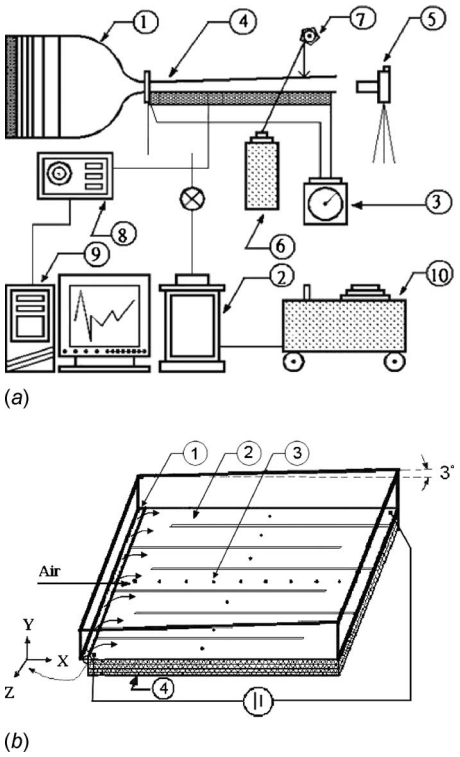

Fig. 1 Schematic for (*a*) the experimental setup, which includes (1) wind tunnel, (2) smoke generator, (3) dc power supply, (4) Plexiglas channel, (5) camera, (6) laser, (7) rotating mirror, (8) data acquisition system, (9) personal computer, and (10) compressor to blow smoke from smoke generator into the channel; and (*b*) the horizontal divergent channel, which includes (1) slot for smoke injection, (2) stainless steel foil, and (3) seven rows of thermocouples in the transverse direction

electric current through the foil heater. dc power is used to provide the electric energy for generating the desired heat flux. For better insulation, a 12 cm thick foamed rubber is glued on the back of the heated wall. All the other side walls are wrapped with a 3 cm thick foam rubber.

Since the temperature variation of the heated wall may be large in the transverse direction, the heated wall is instrumented with seven rows of Chromel-Alumel thermocouples. One row of the thermocouples is along the centerline of the wall. The distance between two neighboring rows is 2.5 cm, and the spacing between two neighboring thermocouples in each row is 2 cm. Therefore, there are a total of 22 thermocouples in each row. All thermocouples are calibrated in a constant temperature bath and the measurement error is found to be within $\pm 0.1°C$. All the temperature signals are acquired with a FLUKE-2287A data logger connected to a computer for direct processing. The temperature data are taken when the entire system reaches steady state, usually in 3–4 h.

For the flow visualization experiments, a smoke generator is used to supply smoke of fine particles. Smoke enters the channel from a slot of 1 mm width located on the bottom surface in the immediate upstream of the channel entrance. A transverse sheet of light perpendicular to the bottom heated wall is used to visualize the spanwise structure of secondary flow, while the sheet of light from the end parallel to the flow passage is used to visualize the flow structure from the top view when it is necessary. The flow patterns at the upstream, the central, and the downstream regions can be observed and recorded.

The wind tunnel, as shown in Fig. 1(*a*), is the same as the one used in the studies of mixed convection in a heated horizontal parallel-plate and convergent channel [24] or vertical channels

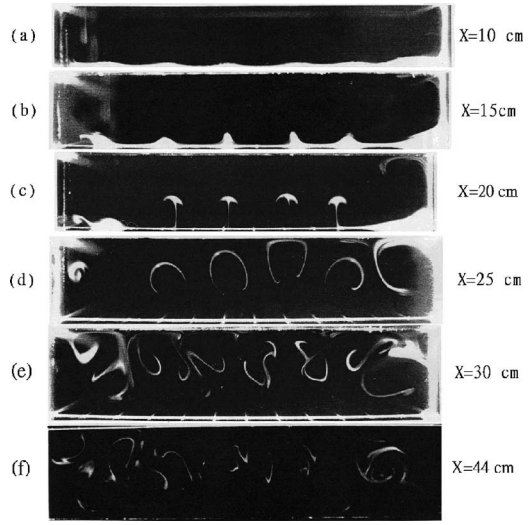

Fig. 2 Flow structure in a divergent channel with $Gr/Re^2=20$ and $Re=500$ at different locations (end view)

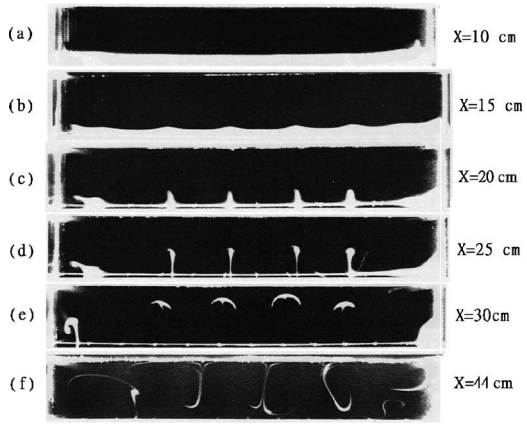

Fig. 3 Flow structure in a parallel-plate channel with $Gr/Re^2=20$ and $Re=500$ at different locations (end view)

[26,28]; hence a detailed description is omitted here. The calibration needed for velocity measurement is also described by Huang et al. [24]. The total heat input in a single heating strip can be determined by the electric voltage and current passing through the strip. By subtracting conduction and radiation losses from the total energy supplied, the local heat transfer coefficient is evaluated by the following equation:

$$h_r = (q_r - q_{\text{rad}} - q_{\text{cond}})/(T_w - T_r) \tag{1}$$

where T_w is the average temperature of a single strip, and r refers to the bulk mean condition. The conduction heat loss from the heated wall is estimated by a one-dimensional conduction equation in a composite wall. The procedure to calculate the radiation loss from the heated wall is very similar to the one described in Ref. [29] and will not be repeated here. The thermal physical properties used in the local Nusselt number are evaluated at the bulk mean temperature of the flow, while those in the Reynolds and Grashof numbers are evaluated at the inlet temperature.

The uncertainty of the experimental data is determined according to the procedure proposed by Kline and McClintock [30]. The maximum uncertainty of local Nusselt number is 5.6%, while that for the Reynolds and Grashof numbers are 6.2% and 7.8%, respectively.

3 Results and Discussions

3.1 Flow Visualizations. Since the smoke layer is very thin in the bottom, an almost equally spaced, stationary wave can be clearly observed at an earlier stage, as shown in Fig. 2(*a*) for the divergent channel and Fig. 3(*b*) for the parallel-plate channel. The parallel-plate channel has the same length and width as the divergent channel, and has a channel height of 3 cm. Due to the destabilization effect in the divergent channel, the stationary wave occurs at a much earlier stage than in the parallel-plate channel. The amplitude of this stationary wave grows as flow moves downstream until the wave head protrudes into the core as a small finger with a small bud on the top, as shown in Figs. 2(*b*) and 3(*c*). The small bud grows in size until a mushroom-shaped cap is formed, as shown in Figs. 2(*c*) and 3(*e*). The mushroom-shaped plumes grow and extend laterally until they reach the neighboring plumes and roll downward becoming convection rolls. It is noted that the divergence of channel can decelerate the flow, at the same time the adverse pressure gradient tends to make the flow unstable. Therefore, the secondary flow occurred, as shown in Fig. 2, is somewhat different from the results for parallel-plate channel, as shown in Fig. 3. It appears that the plume can be initiated at a much earlier stage. This is attributed to the deceleration of flow, which makes the heated layer thicker and protrusion of heated layer into the core at an earlier stage. Due to the destabilization effect of the adverse pressure gradient, the plumes produced are not stable. They oscillate in spanwise direction. In addition, the deceleration of flow can effectively lead to the local increase in Gr/Re^2. Therefore, the mushroom-shaped vortices extend laterally in a more rapid speed than in the parallel-plate channel, which causes interaction with the neighboring vortices and form a complicated flow structure, as shown in Figs. 2(*e*) and 2(*f*).

The interaction of vortices is not observed in the parallel-plate channel for $Re=500$ and $Gr/Re^2=20$, as shown in Figs. 3(*e*) and 3(*f*). Since the channel cross section in the downstream of the divergent channel is relatively large, which gives the plumes more space to grow, the plumes and vortices produced in the divergent channel are greater. The greater plume produced requires to suck up more fluid of the heated layer on the bottom wall. This can significantly reduce the thermal boundary layer thickness along the bottom wall, and lead to a significant enhancement in the heat transfer.

When the buoyancy parameter is greater, the formation of plume and interaction of neighboring vortices in the divergent channel can occur at an earlier stage than in the parallel-plate channel. The earlier interaction of plumes leads to a reduction in the thickness of the bottom heated layer, which can increase the heat transfer. The interaction between vortices is so severe that the mushroom-shaped vortex structure cannot be visualized in the downstream region. However, the flow is still very steady and laminar, and no transition to turbulent flow has occurred. Since the channel height is relatively large in the downstream, this makes the heated fluid smoke to stay in the upper region of the channel.

When the buoyancy parameter is higher, the occurrence of stationary wave and protrusion of wave head into the core as a small finger with a small bud is initiated at a much earlier stage, as shown in Fig. 4(*b*) for $Gr/Re^2=60$ and $Re=500$. The mushroom-shaped plumes also grow at a much earlier stage and extend laterally until they interact each other, as shown in Figs. 4(*c*) and 4(*d*). One can find that as the plumes grow in size, they suck up the heated flow on the bottom wall. This action can significantly reduce the thickness of the thermal boundary layer and enhance the heat transfer. Due to divergence of channel, formation of plume and interaction between neighboring vortices can occur at a much earlier stage than in the parallel-plate channel [24]. It is expected that this leads to an earlier enhancement of heat transfer.

Up to $x=15$ cm, the plume activity is very steady. For ≥ 18 cm, however, both the effects of deceleration flow and adverse pressure gradient make the interaction between vortices so intense that they cause the plumes unstable. The plumes may os-

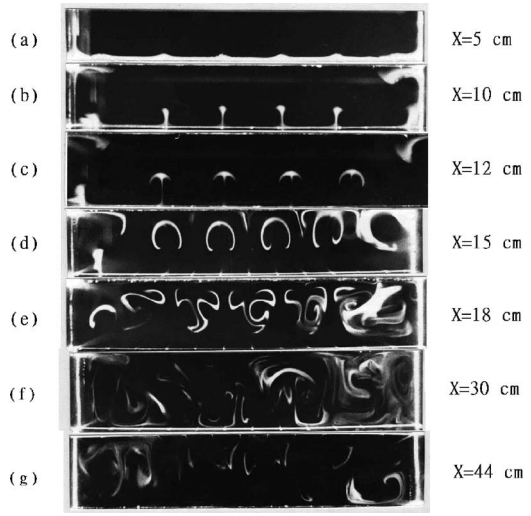

Fig. 4 Flow structure in a divergent channel with $Gr/Re^2=60$ and $Re=500$ at different locations

cillate, shift, and combine with neighboring plumes, which make the entire flow highly unstable, as shown in Fig. 4(*e*). In the parallel-plate channel, however, the plumes and the entire flow are more stable [24]. Eventually, the combination process leads to possible formation of longitudinal convection rolls. However, due to the unstable nature of the decelerated flow, development of longitudinal convection rolls cannot be established, as shown in Fig. 4(*f*), even in a longer channel. The relatively large space near the exit makes the heated fluid stay in the upper region of the channel, as shown in Fig. 4(*g*). Since the rising heated flow can reduce pressure in the bottom, which leads to suck in the cold flow from the outside and forms flow reversal along the bottom wall near the exit, the cold reversed flow moving upstream from the outside can be concluded from the upstream motion of the bottom smoke near the exit.

For parallel-plate channel heated at a higher buoyancy parameter, the mushroom-shaped plume or vortices can be transformed into two-dimensional convection rolls in the downstream, as shown in Fig. 5 for $Gr/Re^2=450$ and $Re=105$. Each of the plumes can roll back and form a two-dimensional circulation cell, as shown in Figs. 5(*a*)–5(*c*). However, some of the small convection cells are not stable due to the narrow width in size, which can readily combine with the neighboring small cell to form a larger one. Finally, all the small narrow size cells combine with the neighboring smaller cells and form a total of four stable, longitudinal convection rolls in the entire cross section of the channel, as

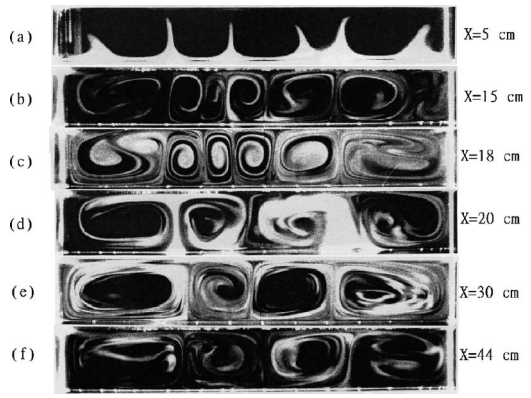

Fig. 5 Flow structure in a parallel-plate channel with $Gr/Re^2=450$ and $Re=105$ at different locations

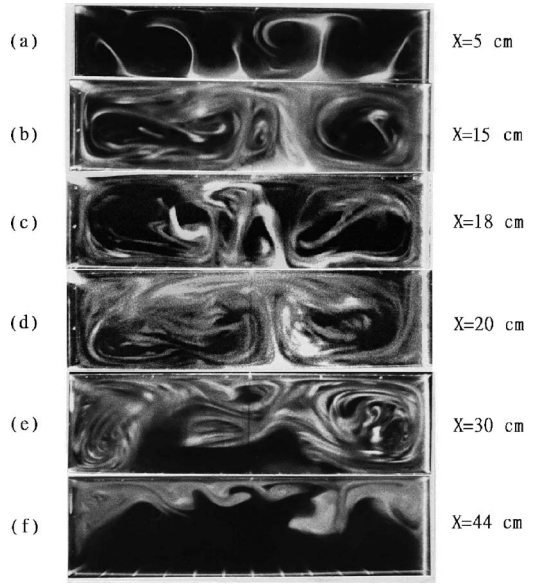

Fig. 6 Flow structure in a divergent channel with $Gr/Re^2=450$ and $Re=105$ at different locations

shown in different sections of the channel in Figs. 5(*d*)–5(*f*). In a divergent channel, however, due to destabilization effect, the plume produced in the upstream is highly unstable as shown in Fig. 6(*a*) for $Gr/Re^2=450$ and $Re=105$. Therefore, formation of a stable circulation cell is not possible. The unstable plumes extend laterally and combine directly with the neighboring ones and form a much greater circulation cell. However, these large cells are highly unstable, as shown in Figs. 6(*b*)–6(*d*), that the number of cells could not be counted. In addition, deeper penetration of the cold reversed flow from the exit of channel is found, which pushes the heated flow to stay in the upper part of the channel, as shown in Figs. 6(*e*) and 6(*f*). This leads to a result that the two-dimensional, longitudinal convection rolls cannot be established in the divergent channel, as shown in Figs. 6(*e*) and 6(*f*). The reversed flow can be confirmed with the measurement of relatively low temperature near the exit. Although the flow structure is very complex and unsteady and the divergence of channel tends to destabilize the flow, the clear structure of the smoke suggests that transition to turbulent flow has not occurred near the exit.

For $Re=1000$ and $Gr/Re^2=10$, the plume produced is highly unstable, as shown in Fig. 7. In addition to the causes contributed to the instability of plume described in the parallel-plate channel [24], the bottom heated layer in the divergent channel is thicker and more unstable than in the parallel-plate channel. This makes additional contribution to the instability of plumes and vortices. The shape, size, and position of each plume vary from time to time, as shown in Figs. 7(*b*)–7(*e*). In addition, the relatively thick heated layer in the bottom can make the earlier initiation of plume. At $x=25$ cm, well established mushroom-shaped plumes can be formed in the divergent channel; while in the parallel-plate channel, the protrusion of the bottom layer has just appeared as small fingers. Due to the destabilization effect of the adverse pressure gradient, interaction between plumes occurs at an earlier stage than the case of parallel-plate channel [24], and forms a complex flow structure near the exit, as shown more clearly in Figs. 7(*a*) and 7(*f*).

4 Temperature Fluctuations

The temperature fluctuation is measured, at the central location along the duct at different axial distances. The temperature fluctuation in the divergent channel is initiated at an earlier stage than in the parallel-plate channel, as shown in Fig. 8(*b*) for Gr/Re^2

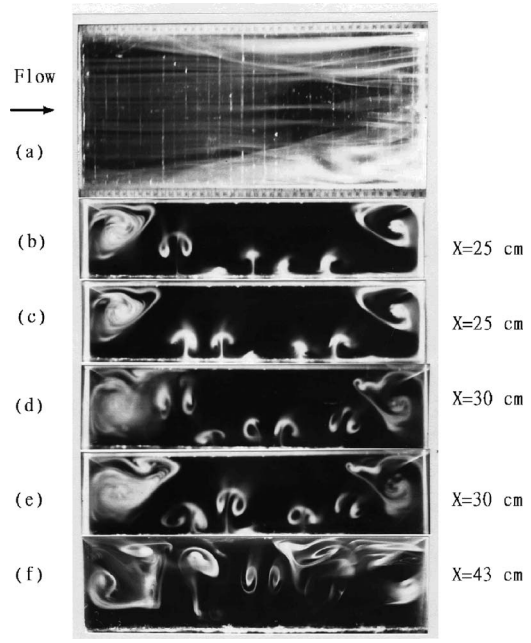

Fig. 7 Flow structure in a divergent channel with $Gr/Re^2=10$ and $Re=1000$; (*a*) top view, photograph is taken in a plane close to the bottom wall; ((*b*)–(*f*)) end view

=20 and Re=500, where plume activity and interaction between vortices have already occurred in the divergent channel. This is attributed to the deceleration of flow, which makes the heated layer thicker and protrusion of the heated layer to the core at an earlier stage. The occurrence of small amplitude and high frequency of temperature fluctuation, as shown in Figs. 8(*c*) and 8(*d*), suggests the occurrence of interaction between vortices, as shown in Figs. 2(*d*) and 2(*e*). Due to adverse pressure gradient effect, flow tends to separate from wall and flow reversal may occur near the exit. Since the bottom heated fluid tends to move upward, a lower pressure can be created on the bottom wall, which can suck in the cold air from the outside. Therefore, the

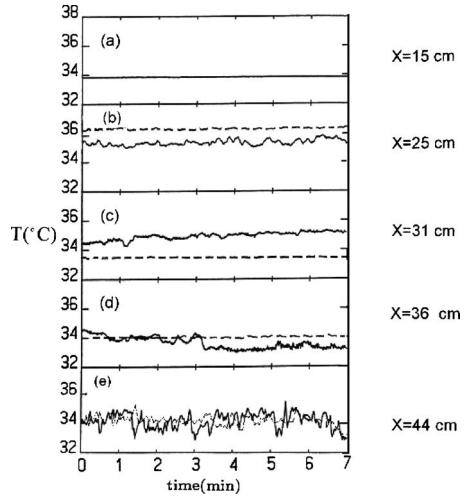

Fig. 8 Comparison of temperature fluctuations between the case of divergent channel and the case of a parallel-plate channel with $Gr/Re^2=20$ and $Re=500$ at (*a*) $x=15$ cm, (*b*) $x=25$ cm, (*c*) $x=31$ cm, (*d*) $x=36$ cm, and (*e*) $x=44$ cm (the dotted lines are the mean temperature fluctuations in the parallel-plate channel, and the inlet temperature for both parallel-plate channel and the divergent channel is 27°C)

occurrence of cold reversed flow can reduce the mean temperature, as shown in Fig. 8(*e*), and enhance fluctuations of temperature. The cold, reversed flow was clearly observed in flow visualization experiments when the buoyancy parameter is high; i.e., $Gr/Re^2=60$ and $Re=500$. Slight reduction in mean temperature occurs from $x=25$ cm to $x=44$ cm. This is attributed to the divergence of channel, which makes the plume and vortex activity very intense in this region and lead to suck up more fluid in the bottom heated layer and reduce the layer thickness. Therefore, enhancement in the heat transfer by the secondary flow in this region is expected to be very significant. The more intense activity of plumes and vortices in the divergent channel makes severer fluctuations of temperature, as shown in Fig. 8(*e*).

As the bottom wall heat flux increases, the fluctuation of temperature can be initiated at an earlier stage, as shown in Fig. 9(*b*) for $Gr/Re^2=60$ and $Re=500$. The amplitude and frequency of the temperature fluctuation for divergent channel are significantly higher than the case of parallel-plate channel [24]. This is due to the more intense activity of plume in the divergent channel. The deceleration of flow makes the buoyancy force become more effective to drive the plume activity. In addition, the adverse pressure gradient can make the bottom heated layer thicker and protrusion of the heated layer into the core at an earlier stage. This has also been concluded in the flow visualization experiments. Interaction between vortices starts to occur close to $x=18$ cm, which makes additional contribution to the temperature fluctuation, as shown in Fig. 8(*c*). It appears that interaction between vortices for divergent channel occurs at an earlier stage than the parallel-plate channel [24].

The large temperature rise, as shown in Fig. 9(*d*), is due to the plume, which moves across the thermocouple probe. Intense plume activities such as shifting of plume and interaction with neighboring plumes are observed in the flow visualization experiments. It appears that the fluctuation of temperature inside the plume is more intense than outside of it. At $x=36$ cm, the large amplitude of temperature fluctuation is attributed to the combination between plumes leading to the possible development of longitudinal convection rolls. It appears that the large amplitude of temperature fluctuation does not suggest transition and occurrence of turbulent flow. However, the divergence of channel tends to preclude formation of longitudinal convection rolls but leads to formation of flow reversal near the exit. The significant reduction in mean temperature near the exit suggests the occurrence of reversed flow, which moves upstream along the bottom wall from the outside. Excluding the time period when the plumes pass through the probe and raise the temperature significantly, instead of the increase, the decrease in mean temperature occurs from $x=12$ cm to $x=25$ cm. Therefore, significant enhancement of heat transfer by the secondary flow in this region can be expected.

For $Gr/Re^2=450$ and $Re=105$, the mainstream velocity is low while the buoyancy force is relatively large, and the divergence of channel can make the bottom heated layer thicker and lead to more intense activities of plume and vortex. This causes the temperature fluctuation more irregular and has a larger amplitude than the case of parallel-plate channel, especially in the downstream region. However, the large amplitude of temperature fluctuation in the downstream near the exit is attributed mostly to the occurrence of the flow reversal along the bottom wall. The decrease in mean temperature also occurs from $x=5$ cm to $x=15$ cm. Heat transfer enhancement by the secondary flow in this region is also expected as the case for parallel-plate channel.

For $Gr/Re^2=10$ and $Re=1000$, the Reynolds number is double, and at the same time the Grashof number increases quadruply. This is the case when the mainstream velocity is relatively high and the buoyancy force is not small. Since the large heat flux along the bottom wall makes the bottom heated layer relatively thick, the relatively high flow velocity in the core makes the heated layer in the bottom highly unstable. Fluctuations of temperature can be seen clearly for $x\leq 15$ cm, which is in the region

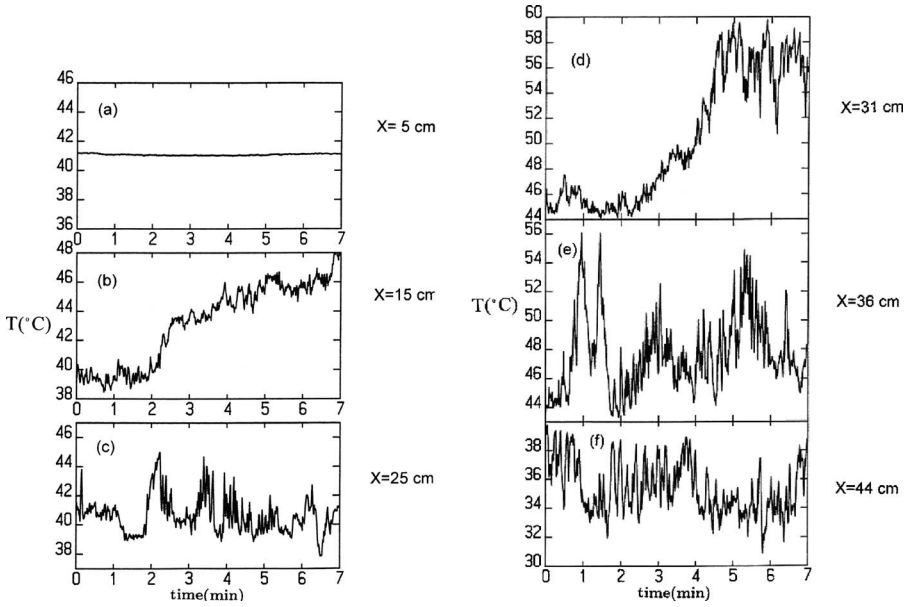

Fig. 9 Temperature fluctuations in a horizontal divergent channel with $Gr/Re^2=60$ and $Re=500$ at (*a*) $x=5$ cm, (*b*) $x=15$ cm, (*c*) $x=25$ cm, (*d*) $x=31$ cm, (*e*) $x=36$ cm, and (*f*) $x=44$ cm

where fingers or plumes have not yet initiated. However, the divergence of channel can make the heated layer thicker and more unstable that the fluctuation in temperature becomes more intense and irregular than the case in parallel-plate channel, as shown in Fig. 10(*b*) for $Gr/Re^2=10$ and $Re=1000$. Due to earlier initiation of the plume and vortex activity in the divergent channel, significantly larger amplitude and variation in frequency of temperature fluctuations than the case of the parallel-plate channel are found, as shown in Fig. 10(*c*) for $x=25$ cm. The more intense activities of plume and vortex interaction due to the destabilization effect of the decelerated flow in the divergent channel make additional contribution to the fluctuation in temperature. This makes a larger amplitude of fluctuation in the divergent channel, as shown in Fig. 10(*d*). In the downstream, however, the plumes and vortices have already mixed with the core that the fluctuations of temperature are significantly reduced. Therefore, the temperature fluctuation in the downstream of the divergent channel is not as intense as in the parallel-plate channel.

In general, the mean temperature of the fluctuations in the upstream of the divergent channel is higher than the case of parallel-plate channel due to the relative thickness of the heated bottom layer in the divergent channel. Despite the cold reverse flow, which reduces the mean temperature near the exit, however, the mean temperature of the fluctuations in the downstream of the

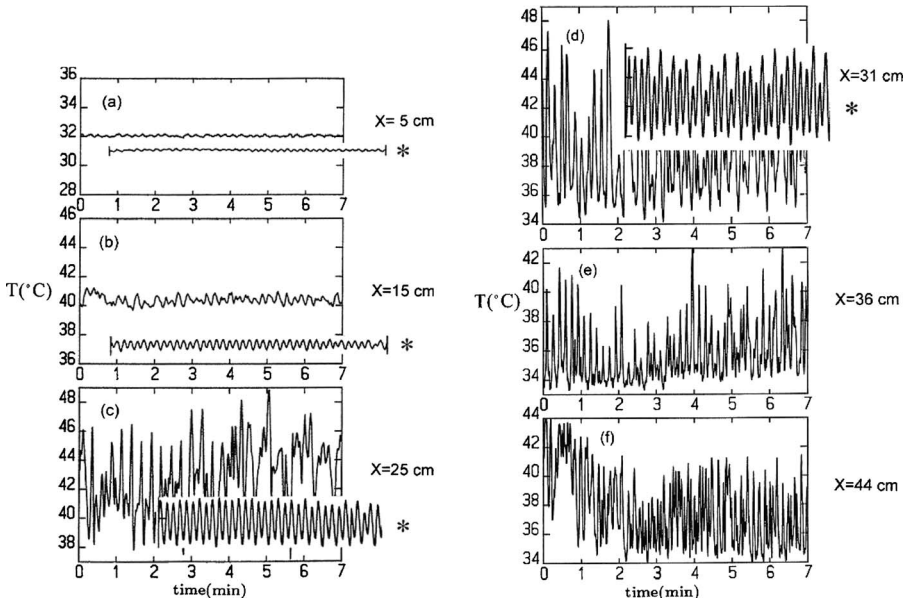

Fig. 10 Comparison of temperature fluctuations between the case of divergent channel and the case of the parallel-plate channel with $Gr/Re^2=10$ and $Re=1000$ at (*a*) $x=5$ cm, (*b*) $x=15$ cm, (*c*) $x=25$ cm, (*d*) $x=31$ cm, (*e*) $x=36$ cm, and (*f*) $x=44$ cm (* means temperature fluctuations in the parallel-plate channel)

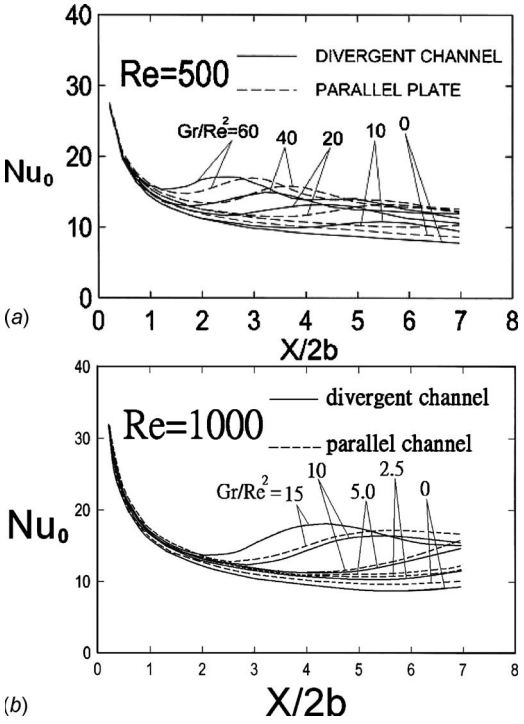

Fig. 11 Comparison of the Nusselt number distributions at different Gr/Re^2 between the case of divergent channel and the case of parallel-plate channel at (*a*) Re=500 and (*b*) Re=1000

divergent channel is lower due to the relative intense activity of the plumes and vortices, which reduces the thickness of the heated bottom layer. One can expect that the former case leads to a lower while the latter leads to a higher heat transfer in the divergent channel than in the parallel-plate channel.

5 Mixed Convection Heat Transfer

The current heat transfer data were validated by comparing our data for the case of pure forced convection in the parallel-plate channel with the results published previously. The agreement was found to be very good [24,26,28].

For the divergent channel, the pure forced convection heat transfer is less than the case of the parallel-plate channel, especially in the downstream region where deceleration of mainstream becomes significant, which can reduce the heat transfer, as shown in Fig. 11. However, when the buoyancy force sets in, it can enhance the heat transfer and make the heat transfer results even higher than the case of parallel-plate channel. This is apparently attributed to the destabilization effect of the decelerated flow in the divergent channel. However, in the upstream where the buoyancy parameter is very small, deceleration of mainstream in the divergent channel can still make the heat transfer less than the results of the parallel-plate channel. By comparing the flow visualization results with the Nusselt number distribution, one can find that the onset of heat transfer enhancement occurs at the location where stationary wave is clearly formed along the heated layer in the bottom. The minimum in the heat transfer occurs in the location where the bottom heated layer is going to protrude into the core. The maximum in the heat transfer corresponds to the location where the size of the plume has reached the maximum. At this stage, the plume has grown in such a size that it has exhausted the complete fluid of the heated layer in the bottom. The mushroom cap has reached the top wall and the neighboring plumes have contacted with each other. When the buoyancy parameter increases, the increase in the Nusselt number in the downstream region propagates upstream, as shown in Fig. 10, due to the earlier initiation of the secondary flow.

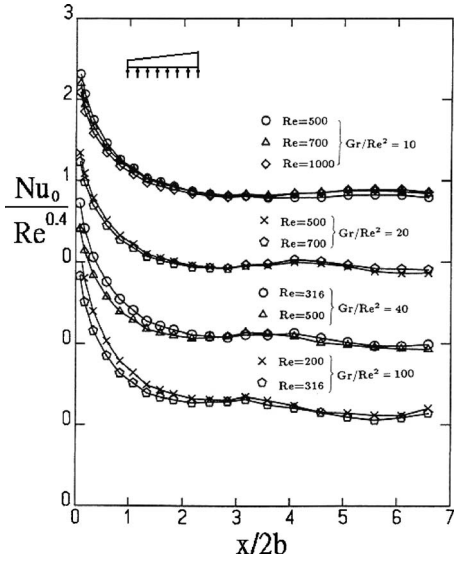

Fig. 12 Normalization of the Nusselt numbers for the case of the divergent channel

In order to eliminate the Reynolds number effect, the Nusselt number is divided by $Re^{0.4}$. The normalized Nusselt number can be shown to be independent of the Reynolds number in the experimental ranges covered since all the normalized Nusselt numbers at different Reynolds numbers collapse into a single curve, as shown in Fig. 12. Therefore, the normalized Nusselt numbers at different buoyancy parameters are chosen to present the heat transfer data, as shown in Fig. 13. The same normalized Nusselt numbers, which collapse into a single curve at different Reynolds numbers, are also found in the heated vertical channels [26,28]. The increase in the buoyancy parameter Gr/Re^2 can be achieved by decreasing the Reynolds number. The oscillation of the Nusselt number still exists, as shown in Fig. 13, due to protrusion and rise up of the bottom heated layer, and the downwash of the upper cold flow. The oscillation of the normalized Nusselt number also moves upstream as the buoyancy parameter increases. In addition, the rise up of the normalized Nusselt number occurs at an earlier stage in the divergent channel than in the parallel-plate channel. When Gr/Re^2 is large, the Nusselt number in the downstream region of the divergent channel is much greater than the results in the parallel-plate channel. This is due to the occurrence of flow reversal in the exit region of the divergent channel, which can significantly enhance the heat transfer.

6 Conclusions

Secondary flow structure and its enhancement on the heat transfer in a horizontal divergent channel with bottom wall heated have

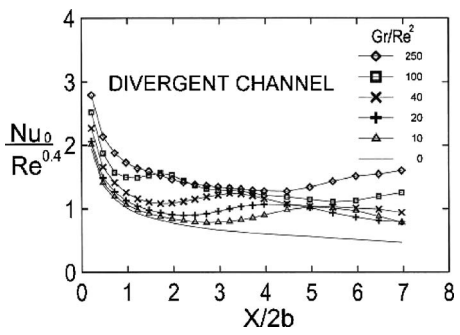

Fig. 13 The normalized Nusselt number $Nu/Re^{0.4}$ distributions at different Gr/Re^2 for the divergent channel

been investigated experimentally. A similar type of a secondary flow appearing as mushroom-shaped plumes associated with vortices is also formed in the divergent channel. However, deceleration of the mainstream causes a thicker heated layer in the bottom, an earlier protrusion of the plumes, and more intense interaction between neighboring plumes or vortices, which leads to an earlier and larger enhancement of the heat transfer than the case of the parallel-plate channel. The destabilization effect of the adverse pressure gradient makes the interaction between neighboring plumes highly unsteady in the downstream, which makes the formation of two-dimensional convection rolls difficult. When the buoyancy parameter is large enough, flow reversal can occur along the heated wall in the bottom, which can significantly enhance the heat transfer.

Temperature fluctuation measurements at different locations are used to infer the detailed flow structure and the initiation and oscillation of the bottom heated layer and the secondary flow. The flow structure inferred confirms with the flow visualization results. The divergence of the channel causes an earlier initiation of the fluctuations. In addition, the fluctuations of temperature can be amplified by the destabilization effect of the adverse pressure gradient. The heat transfer enhancement in the divergent channel is more pronounced than in the parallel-plate channel due to this destabilization effect. Finally, in addition to the parameter of $x/2b$, the normalized Nusselt numbers can be represented as only a function of $\mathrm{Gr}/\mathrm{Re}^2$ in the divergent channel.

Nomenclature

b = channel height at the entrance
g = gravitational acceleration
Gr = Grashof number, $g\beta q(2b)^4/k\nu^2$
h = convective heat transfer coefficient
k = thermal conductivity of air
Nu = local Nusselt number, $h(2b)/k$
Pr = Prandtl number, ν/α
q = heat flux
Re = Reynolds number defined at the inlet of the channel, $u_s(2b)/\nu$
T = temperature
u = inlet velocity
x,y = coordinate parallel, and normal to the heated wall

Greek Symbols

β = coefficient of expansion
ν = kinematic viscosity

Subscripts

r = refers to bulk mean
w = refers to heated wall
0 = refers to inlet

References

[1] Gilpin, R. R., Imura, H., and Cheng, K. C., 1978, "Experiments on the Onset of Longitudinal Vortices in Horizontal Blasius Flow Heated From Below," ASME J. Heat Transfer, **100**, pp. 71–77.
[2] Maughan, J. R., and Incropera, F. P., 1987, "Experiments on Mixed Convection Heat Transfer for Airflow in a Horizontal Rectangular and Inclined Channel," Int. J. Heat Mass Transfer, **30**, pp. 1307–1318.
[3] Hwang, G. J., and Liu, C. L., 1976, "An Experimental Study of Convective Instability in the Thermal Entrance Region of a Horizontal Parallel-Plate Channel Heated From Below," Can. J. Chem. Eng., **54**, pp. 521–525.
[4] Kamotani, Y., Ostrach, S., and Miao, H., 1979, "Convective Heat Transfer Augmentation by Means of Thermal Instability," ASME J. Heat Transfer, **101**, pp. 222–226.
[5] Yasuo, M., and Yutaka, U., 1966, "Forced Convection Heat Transfer Between Horizontal Flat Plate," Int. J. Heat Mass Transfer, **9**, pp. 803–817.
[6] Osborne, D. G., and Incropera, F. P., 1985, "Laminar Mixed Convection Heat Transfer for Flow Between Horizontal Parallel Plates With Asymmetric Heating," Int. J. Heat Mass Transfer, **28**, pp. 207–217.
[7] Incropera, F. P., Knox, A. L., and Maughan, J. R., 1987, "Mixed Convection Flow and Heat Transfer in the Entry Region of a Horizontal Rectangular Duct," ASME J. Heat Transfer, **109**, pp. 434–439.
[8] Davis, E. J., and Choi, C. K., 1977, "Cellular Convection With Liquid-Film Flow," J. Fluid Mech., **81**(3), pp. 565–592.
[9] Kamotani, Y., and Ostrach, S., 1976, "Effect of Thermal Instability on Thermally Developing Laminar Channel Flow," ASME J. Heat Transfer, **98**, pp. 62–66.
[10] Akiyama, M., Hwang, G. H., and Cheng, K. C., 1971, "Experiments in the Onset of Longitudinal Vortices in Laminar Forced Convection Between Horizontal Plates," ASME J. Heat Transfer, **93**, pp. 335–341.
[11] Ostrach, S., and Kamotani, Y., 1975, "Heat Transfer Augmentation in Laminar Fully Developed Channel Flow by Means of Heating From Below," ASME J. Heat Transfer, **97**, pp. 220–225.
[12] Kuan-Cheng, C., Ouazzani, J., and Rosenberger, F., 1987, "Mixed Convection Between Horizontal Plates—II. Fully Developed Flow," Int. J. Heat Mass Transfer, **30**, pp. 1655–1662.
[13] Kuan-Cheng, C., and Rosenberger, F., 1987, "Mixed Convection Between Horizontal Plates—I. Entrance Effects," Int. J. Heat Mass Transfer, **30**, pp. 1645–1654.
[14] Maughan, J. R., and Incropera, F. P., 1990, "Regions of Heat Transfer Enhancement for Laminar Mixed Convection in a Parallel Plate Channel," Int. J. Heat Mass Transfer, **33**, pp. 555–570.
[15] Lee, F. S., and Hwang, G. J., 1991, "Transient Analysis on the Onset of Thermal Instability in the Thermal Entrance Region of a Horizontal Parallel Plate Channel," ASME J. Heat Transfer, **113**, pp. 363–370.
[16] Lee, F. S., and Hwang, G. J., 1991, "The Effect of Asymmetric Heating on the Onset of Thermal Instability in the Thermal Entrance Region of a Parallel Plate Channel," Int. J. Heat Mass Transfer, **34**, pp. 2207–2218.
[17] Lin, J. N., Chou, F. C., and Tzeng, P. Y., 1991, "Theoretical Prediction of the Onset of Thermal Instability in the Thermal Entrance Region of Horizontal Rectangular Channels," Int. J. Heat Fluid Flow, **12**, pp. 218–224.
[18] Abou-Ellail, M. M. M., and Morcos, S. M., 1983, "Buoyancy Effects in the Entrance Region of Horizontal Rectangular Channels," ASME J. Heat Transfer, **105**, p. 924.
[19] Mahaney, H. V., Incropera, F. P., and Ramadhyani, S., 1987, "Development of Laminar Mixed Convection in the Thermal Entrance Region of Horizontal Rectangular Ducts," Numer. Heat Transfer, **12**, pp. 137–155.
[20] Maughan, J. R., and Incropera, F. P., 1990, "Fully Developed Mixed Convection in a Horizontal Channel Heated Uniformly From Above and Below," Numer. Heat Transfer, **17**, pp. 417–430.
[21] Chou, F. C., and Hwang, G. J., 1987, "Vorticity-Method for Graetz Problem With the Effect of Natural Convection in a Horizontal Rectangular Channel With Uniform Wall Heat Flux," ASME J. Heat Transfer, **109**, pp. 704–710.
[22] Lin, J. N., and Chou, F. C., 1989, "Laminar Mixed Convention in the Thermal Entrance Region of Horizontal Isothermal Rectangular Channels," Can. J. Chem. Eng., **67**, pp. 361–367.
[23] Nyce, T. A., Ouazzani, J., Durand-Daubin, A., and Rosenberger, F., 1992, "Mixed Convection in a Horizontal Rectangular Channel—Experimental and Numerical Velocity Distributions," Int. J. Heat Mass Transfer, **35**, pp. 1481–1494.
[24] Gau, C., Liu, C. W., Huang, T. M., and Aung, W., 1999, "Secondary Flow and Enhancement of Heat Transfer in Horizontal Parallel-Plate and Convergent Channels Heating From Below," Int. J. Heat Mass Transfer, **42**, pp. 2629–2647.
[25] Wilson, K. S. Chiu, Richards, C. J., and Jaluria, Y., 2000, "Flow Structure and Heat Transfer in a Horizontal Converging Channel Heated From Below," Phys. Fluids, **12**(8), pp. 2128–2136.
[26] Gau, C., Huang, T. M., and Aung, W., 1996, "Flow and Mixed Convection Heat Transfer in a Divergent Heated Vertical Channel," ASME J. Heat Transfer, **118**(3), pp. 606–615.
[27] Yang, C. S., Liu, C. G., and Gau, C., 2009, "Study of Channel Divergence on the Flow and Heat Transfer in Horizontal Ducts Heated From a Side," Int. J. Therm. Sci., **48**(1), pp. 105–113.
[28] Huang, T. M., Gau, C., and Aung, W., 1995, "Mixed Convection Flow and Heat Transfer in a Vertical Convergent Channel," Int. J. Heat Mass Transfer, **38**(13), pp. 2445–2456.
[29] Webb, B. W., and Hill, D. P., 1989, "High Rayleigh Number Laminar Natural Convection in an Asymmetrically Heated Vertical Channel," ASME J. Heat Transfer, **111**, pp. 649–656.
[30] Kline, S. J., and McClintock, F. A., 1953, "Describing Uncertainties in Single-Sample Experiments," Mech. Eng. (Am. Soc. Mech. Eng.), **75**, pp. 3–12.

A Scale Analysis Based Theoretical Force Balance Model for Critical Heat Flux (CHF) During Saturated Flow Boiling in Microchannels and Minichannels

Satish G. Kandlikar
Fellow ASME
Department of Mechanical Engineering,
Rochester Institute of Technology,
Rochester, NY 14623
e-mail: sgkeme@rit.edu

*Accurate prediction of critical heat flux (CHF) in microchannels and minichannels is of great interest in estimating the safe operational limits of cooling systems employing flow boiling. Scale analysis is applied to identify the relevant forces leading to the CHF condition. Using these forces, a local parameter model is developed to predict the flow boiling CHF. The theoretical model is an extension of an earlier pool boiling CHF model and incorporates force balance among the evaporation momentum, surface tension, inertia, and viscous forces. Weber number, capillary number, and a new nondimensional group introduced earlier by Kandlikar (2004, "Heat Transfer Mechanisms During Flow Boiling in Microchannels," ASME J. Heat Transfer, **126**, pp. 8–16), K_2, representing the ratio of evaporation momentum to surface tension forces, emerged as main groups in quantifying the narrow channel effects on CHF. The constants in the model were calculated from the available experimental data. The mean error with ten data sets is 19.7% with 76% data falling within ±30% error band and 93% within ±50% error band. The length to diameter ratio emerged as a parameter indicating a stepwise regime change. The success of the model indicates that flow boiling CHF can be modeled as a local phenomenon and the scale analysis is able to reveal important information regarding fundamental mechanisms leading to the CHF condition.*
[DOI: 10.1115/1.4001124]

Keywords: microchannels, minichannels, CHF, critical heat flux, flow boiling, evaporation momentum, boiling

1 Introduction

High heat flux removal with flow boiling is an important process in many applications. It continues to receive great attention from the nuclear, steam power generation, and chemical process industries. Safety and efficiency considerations have provided major impetus for experimental, numerical, and analytical research in this area.

Researchers have focused on the flow boiling phenomena in minichannels and microchannels to address the recent demands for high heat flux removal from electronic equipment and computer chips. As the cooling requirements are raised, understanding the fundamental mechanisms and estimating the limits due to the critical heat flux (CHF) condition in these geometries becomes important.

In the design of flow boiling equipment, reliable methods to predict CHF are needed. Although exhaustive numerical codes to this end have been developed, particularly in the nuclear industry, predictive correlations developed from large data sets covering a wide range of conditions are often sought. In the absence of a clear understanding of the basic mechanism, it is common practice to employ a large number of system variables, often in nondimensional form, and perform advanced regression analysis to arrive at correlations that serve as predictive tools over the range of parameters covered in the parent data sets.

A model-based approach, however, is desirable for predicting CHF. As new fluids are introduced in different applications, such as new refrigerants and dielectric fluids for chip cooling, a model-based technique is expected to provide better guidance at predicting the CHF limits. It is also expected to provide a better predictive capability for different channel sizes.

The present work is aimed at developing a theoretical model based on scale analysis for predicting CHF condition. The model development, determination of the constants (scaling factors), validation of the predictive technique, and discussion on parametric trends are presented in this paper.

2 Literature Review

Critical heat flux has been extensively studied in literature using experimental, analytical, and numerical techniques. Early developments related to nuclear and power industries are well summarized in a number of publications, e.g., Refs. [1–3]. The focus here is on small diameter channels, covering the ranges of minichannels (200 μm–3 mm) and microchannels (10–200 μm).

A few excellent reviews on this topic have been published in literature [4–6]. Tong and Tang [4] and Celata and Mariani [5] provided a detailed description of the mechanisms, parametric relationships, and correlations applicable to tubes that may be considered as minichannels and conventional sized channels.

Small diameter tubes face boiling instability that may lead to premature CHF condition. Bergles and Kandlikar [6] discuss the relative importance of upstream compressible volume instability and excursive instability. Using the pump characteristics map, they were able to identify the conditions responsible for these

Contributed by the Heat Transfer Division of ASME for publication in the JOURNAL OF HEAT TRANSFER. Manuscript received September 19, 2009; final manuscript received December 26, 2009; published online June 9, 2010. Assoc. Editor: Louis C. Chow.

types of instabilities. These instabilities were also reported by Wang et al. [7]. Using inlet flow restrictors, employing artificial nucleation cavities, and incorporating localized heaters for initiating boiling are among several techniques recommended for reducing or eliminating instabilities [8–10].

3 CHF Models and Correlations in Literature

Earlier efforts on modeling in pool boiling heat transfer were focused on correlation development, resulting in some of the well known correlations by Rohsenow [11], Stephan and Abdelsalam [12], and Cooper [13]. At the same time, models for arriving at the CHF condition based on physical phenomenon were also developed. The models employed were based on flooding [14], destruction of stability between liquid-vapor interface [15,16], coaxial two-phase flow instability [17], liquid flow inhibition to the heater surface [18], instability in vapor jets above nucleating bubbles [19], critical Weber number based on a force balance [20], small jet instability in the microlayer [21,22], effect of size and geometry on vapor column instability [23], contact angle effect [24], temperature of the heater surface under dry patches [25], and incorporation of evaporation momentum force in a force balance at the base of a nucleating bubble [26].

A number of investigators developed CHF models based on the liquid film dryout using the balance of liquid in the form of film and entrained droplets in the vapor. This approach was employed for macroscale application by Whalley et al. [27]. It is relevant for CHF at higher qualities.

Revellin and Thome [28] proposed a model for dryout in round tubes resulting from evaporation of liquid film by considering gravity, surface tension, and vapor shear forces on the film. CHF was considered to be caused by the Kelvin–Helmholtz instability in the liquid film. The constant in the film thickness expression was back-calculated using experimental CHF data of Wojtan et al. [29]. Kosar [30] used an approach incorporating liquid mass balance and film dryout to correlate saturated flow boiling data for water and refrigerants.

A number of researchers used regression analysis on a large number of data sets to obtain a CHF correlation. The nondimensional groups used included Weber number, boiling number, Reynolds number, density ratio of the two phases, heated length to diameter ratio, and Bond number. One of the most successful correlations for macroscale channels was by Katto and Ohno [31]. They used the Weber number, length to diameter ratio, and density ratio with different groupings of these nondimensional numbers. Using experimental data from literature, they evaluated thirteen constants (six coefficients and seven exponents) in their correlation scheme. Qu and Mudawar [32] developed a correlation for boiling number as a product of three parameters—Weber number, density ratio, and length to diameter ratio—with individual exponents and a leading constant, and obtained the constants using only their own data [32,33] for water and R-113. The experimental data from other investigators' data could not be correlated well, indicating the need to use a broader data set in the correlation development.

Sarma et al. [34] conducted a dimensional analysis and developed five groups in their correlations for subcooled and low quality CHF. In particular, the heat flux was correlated using a new term $(qD/\mu_L h_{fg})$ with good agreement for small diameter channels. The results for circular tubes of diameters between 0.8 mm and 3 mm were correlated with an average deviation of 20%.

Roday and Jensen [35] used the same dimensionless groups used by Katto and Ohno [31] and obtained the seven constants in a correlation somewhat simpler than Katto and Ohno. Their own experimental data with water and R123 in 0.427 mm and 0.7 mm hydraulic diameter rectangular channels at critical qualities of less than 0.2 were used in a regression analysis resulting in an RMS error of 35%. They also found that the correlations by Katto and Ohno [31] and Qu and Mudawar [32] were unable to predict their data for smaller diameter channels employing low mass fluxes.

Recently, Kosar et al. [36] conducted CHF experiments at very high mass fluxes ranging from 1500 to 53,000 kg/m^2 s in 127–254 μm inner diameter stainless steel tubes, 2–12 cm in lengths at qualities below 0.15. They correlated their results directly using the system parameters: tube length to diameter ratio, mass flux, pressure, liquid subcooling, and wall superheat and obtained the values of 27 constants. The experimental data could be correlated within 27%. Some of the earlier data from Bergles [37] and Vandervort et al. [38] could also be correlated by another equation for subcooled flow boiling within 10%. Their correlation indicated a strong dependence on mass flux.

Zhang et al. [39] reviewed the available CHF correlations for the saturated region by Bowring [40], Katto [41], Katto and Ohno [31], and Shah [42] and for the subcooled region by Tong [43], Inasaka and Nariai [44], Celata et al. [45], and Hall and Mudawar [46]. They presented a detailed comparison of correlations with minichannel data from literature. Although the Qu and Mudawar [32] correlation was found to predict well for their data own sets, later investigators, including Wojtan et al. [29], Revellin and Thome [28], Roday and Jensen [35], and Kosar [30], found significant deviations for small diameter channels. Zhang et al. [39] further showed that the Shah and Katto–Ohno correlations predicted the larger diameter data well but were unsatisfactory for some of the recent minichannel data. Zhang et al. [39] developed a somewhat simpler correlation using Weber number, density ratio, and length to diameter ratio. Using 1300 data points from literature, they evaluated the three coefficients and five exponents in their correlation. The average mean deviation was 16.8% with the entire data set.

It is seen from literature review that the available correlations are generally based on identifying relevant parameters, then combining them into nondimensional groups and developing a correlation based on a regression analysis with the available experimental data. In some of the more exhaustive studies, the functional form of the correlation was determined from the parametric trends in the data sets. The case of dryout as a termination of the liquid film is seen to be more amenable to analytical treatment for CHF determination.

In the present work, a force balance model developed earlier for pool boiling [26] is extended to cover flow boiling in small diameter channels. The resulting equation is presented in terms of the nondimensional groups that have been identified from a scale analysis. The model development, comparison with available experimental data and parametric trends are presented in the remainder of the paper.

4 Scale Analysis and Model Development

Critical heat flux is postulated here as a local parameter dependent phenomenon. Furthermore, this limiting heat transfer condition is assumed to occur not at the moment when wall dryout occurs, since dryout and rewetting are common occurrences during the boiling process. Such dryout is present at the base of a nucleating bubble or at high heat fluxes in pool boiling. Similar phenomenon occurs in flow boiling during nucleation and bubble growth as well as during the dryout of film in the slug flow regime. CHF is postulated to occur when the liquid is unable to rewet the walls, except for the natural exhaustion of liquid supply at higher qualities.

The motion of the three-phase contact line during evaporation has been studied by a number of investigators. Kandlikar and Steinke [47] used high-speed video to see the motion of the contact line and the liquid-vapor interface of droplets contacting a heated glass surface maintained above the temperature corresponding to the CHF condition. They identified the motion of the liquid front underneath the bulk of the advancing liquid on a dry surface, leaving a thin vapor film between the liquid and the heater, as the cutback phenomenon. Sefiane et al. [48] proposed that the vapor recoil, a result of momentum force caused by evaporation at the interface, induced instabilities at the interface

near the contact line. The rewetting process is mainly focused around the contact line. The dominant forces during pool boiling are surface tension and gravity. Using these forces, Kandlikar [26] developed a CHF model for pool boiling incorporating the effects of receding contact angle and heater surface orientation. This model is extended in the present work to flow boiling by including the effects of additional relevant forces apparent at the contact line arising from the flow.

The CHF model being considered here is focused on minichannels and microchannels, defined as channels with hydraulic diameters in the ranges of 3 mm–200 μm and 200–10 μm, respectively. Following the scale analysis presented by Kandlikar [49], the evaporation momentum, surface tension, shear, inertia, and gravity forces normalized on the basis of the diameter are given by the following expressions:

$$F'_M \sim \left(\frac{q}{h_{fg}}\right)^2 \frac{D}{\rho_V} \tag{1}$$

$$F'_S \sim \sigma \cos(\theta) D/D \sim \sigma \tag{2}$$

$$F'_\tau \sim \frac{\mu V}{D} D^2/D = \mu V = \frac{\mu G}{\rho} \tag{3}$$

$$F'_I \sim \rho V^2 \frac{D^2}{D} = \frac{G^2 D}{\rho} \tag{4}$$

$$F'_G \sim (\rho_L - \rho_v) g D^3/D = (\rho_L - \rho_v) g D^2 \tag{5}$$

The density ρ in Eqs. (3) and (4) refers to the appropriate fluid density. The variation in the evaporation momentum, surface tension, shear, inertia, and gravity forces with tube diameter are shown in Figs. 1(*a*) and 1(*b*) for water and refrigerant FC-72, respectively, for a mass flux of 50 kg/m^2 s and a heat flux of 1 MW/m^2. It is seen that the relative importance of surface tension and shear forces rises at smaller diameters; whereas the inertia effects are still important, but their relative contribution is reduced.

It is also seen from Figs. 1(*a*) and 1(*b*) that the gravity term decreases rapidly as the channel diameter becomes smaller. As expected, it does not appear in any of the CHF correlations for microchannels and is not included in the present work. The use of surface tension force is quite common in CHF correlations as the interface behavior at the contact line near the wall plays an important role. It is interesting to note that the shear term becomes more important at microscale. The success of the Sarma correlation utilizing the viscosity term confirms this observation. The evaporation momentum force, shown at $q=1$ MW/m^2, becomes relatively more important at smaller diameters. It may also be noted that this force is more dominant for FC72 as compared with water. The evaporation momentum force is responsible for CHF, and a higher value (while other forces are of the same order of magnitude) indicates that CHF for FC-72 would be considerably lower than water under the same flow conditions. Since the latent heat governs this force, the scale analysis indicates that a low latent heat value for all fluorinated refrigerants would result in low CHF values for a given value of evaporation momentum force.

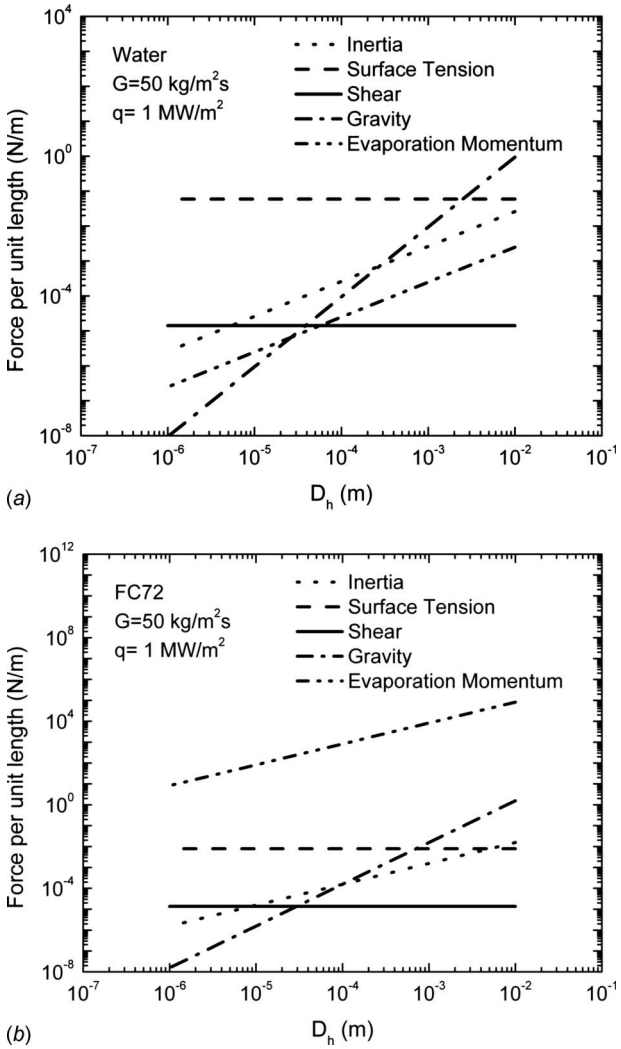

Fig. 1 Results of a scaling analysis showing effect of channel diameter on forces experienced at the evaporating interface during flow boiling: (*a*) water and (*b*) FC-72

5 Model Development

CHF is postulated to occur when the advancing liquid front (upstream) is unable to wet the heater surface again after it becomes dry during the flow boiling process. The high evaporation rate at the interface creates an evaporation momentum force due to the higher velocity vapor leaving the interface. The changes in the interface shape at the contact line have been confirmed by high-speed photographic observations of falling droplets on a heater surface maintained well above the saturation temperature [47]. Although the dynamic contact angle of the rapidly receding interface is difficult to measure, Phan et al. [50] suggested that a microcontact angle may exist that would represent the interface shape near the interface. Since the interface may not be considered as being under a quasi-equilibrium condition, the "microcontact angle" may not necessarily be an intrinsic property representing the surface energy but simply an indication that the interface is deformed in response to the large forces resulting from the high local evaporation rate at its surface.

A local force balance at the contact line was successfully employed earlier in modeling pool boiling CHF [26]. It is extended to flow boiling by assuming all the forces to be apparent at the contact line. This approach reveals the underlying interactions among various parameters and provides an equation relating CHF to the local flow conditions. Using the experimental data, the constants in such model-based equation are then calculated. Other assumptions made in the model are steady-state and steady flow conditions, and constant and uniform properties at saturation conditions. Although local transient conduction in the wall is expected to play at least a secondary role, it is neglected in the present analysis.

Consider a 2D element of the interface close to the heater surface, as shown in Fig. 2. The flow is from left to right. The heated surface ahead of the interface is dry.

The forces acting on the interface in the vicinity of the heater surface are: (i) surface tension forces $F_{S,1}$ and $F_{S,2}$, (ii) inertia

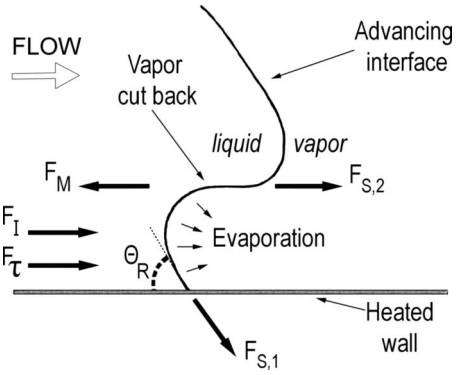

Fig. 2 Forces acting on the liquid-vapor interface near the heater surface at the initiation of CHF condition

force F_I due to the bulk flow, (iii) shear force F_τ due to viscous effects, and (iv) evaporation momentum force F_M resulting from the velocity difference between the approaching liquid and evaporating vapor at the interface. The forces, shown in Fig. 2, are expressed per unit length of the contact line as follows.

Surface tension forces per unit length, using the receding contact angle θ_R are given by

$$F'_{S,1} = \sigma \cos\ \theta_R \tag{6a}$$

$$F'_{S,2} = \sigma \tag{6b}$$

The inertia force is calculated as the product of the liquid mass flow rate and the average flow velocity calculated by using average density.

$$F'_I = \frac{\left[G(1-x)\left(\frac{\pi}{4}D^2\right)\right]\left(\frac{G}{\rho_m}\right)}{\pi D} = \frac{G^2(1-x)D}{4\rho_m} \sim \frac{G^2(1-x)D_h}{\rho_m} \tag{7}$$

where ρ_m is the specific volume averaged density given by

$$\frac{1}{\rho_m} = \frac{x}{\rho_V} + \frac{1-x}{\rho_L} \tag{8}$$

The viscous (shear) force is calculated using liquid flow from Eq. (3) based on the scale analysis presented earlier.

$$F'_\tau = \frac{\mu_L G(1-x)}{\rho_L} \tag{9}$$

Liquid properties are used in the above equation as the liquid phase is in contact with the wall prior to CHF.

The evaporation momentum force is calculated as the product of the evaporation mass flux times the vapor velocity (the velocity of the liquid approaching the interface is neglected since its specific volume is quite small compared with vapor at pressures far below the critical pressure). Following Eq. (1) presented in the scale analysis, the evaporation momentum force per unit length is expressed as:

$$F'_M = \left(\frac{q}{h_{fg}}\right)^2 \frac{D_h}{\rho_V} \tag{10}$$

CHF is postulated to occur when the evaporation momentum force overcomes the sum of the inertia, surface tension, and viscous (shear) forces. Setting the equality condition, and replacing various constants with individual coefficients a_1, a_2, and a_3 for each of the three terms respectively, the following expression for CHF is obtained:

$$F'_M = a_1(F'_{S,1} + F'_{S,2}) + a_2 F'_I + a_3 F'_\tau \tag{11}$$

Substituting the expressions for each force from Eqs. (6*a*), (6*b*), and (7)–(10) and replacing D with D_h, to accommodate different cross-sections, the following equation is obtained:

$$\left(\frac{q_{\mathrm{CHF}}}{h_{fg}}\right)^2\left(\frac{D_h}{\rho_V}\right) = a_1\sigma(1+\cos\ \theta_R) + a_2\frac{G^2 D_h(1-x)}{\rho_m} + a_3\frac{\mu_L G(1-x)}{\rho_L} \tag{12a}$$

Dividing by σ throughout results in the following equation:

$$\left(\frac{q_{\mathrm{CHF}}}{h_{fg}}\right)^2\left(\frac{D_h}{\rho_V\sigma}\right) = a_1(1+\cos\ \theta_R) + a_2\frac{G^2 D_h(1-x)}{\rho_m\sigma} + a_3\frac{\mu_L G(1-x)}{\rho_L\sigma} \tag{12b}$$

Introducing the respective nondimensional groups, Eq. (12*b*) is expressed as

$$\mathrm{K}_{2,\mathrm{CHF}} = a_1(1+\cos\ \theta_R) + a_2\ \mathrm{We}(1-x) + a_3\ \mathrm{Ca}(1-x) \tag{13}$$

The nondimensional group K_2 was first introduced by Kandlikar [51] to represent the ratio of the evaporation momentum force to the surface tension force. The capillary number Ca represents the ratio of the viscous to surface tension forces and Weber number We represents the ratio of inertia to surface tension forces. The equations for each nondimensional group in Eq. (13) are as follows:

$$\mathrm{K}_{2,\mathrm{CHF}} = \left(\frac{q_{\mathrm{CHF}}}{h_{fg}}\right)^2\left(\frac{D_h}{\rho_V\sigma}\right) \tag{14}$$

$$\mathrm{We} = \frac{G^2 D_h}{\rho_m\sigma} \tag{15}$$

$$\mathrm{Ca} = \frac{\mu_L G}{\rho_L\sigma} \tag{16}$$

The specific volume averaged density ρ_m in Eq. (15) for We is given by Eq. (8). All properties are evaluated at the saturation conditions.

Equation (13) represents the resulting model for predicting flow boiling CHF in narrow channels under saturated conditions. Since this equation is derived using the scale analysis, the values of the constants a_1, a_2, and a_3 need to be determined. The experimental data from literature are employed for this purpose.

6 Experimental CHF Data and Evaluation of the Model Constants

Experimental data from literature are compiled in the hydraulic diameter range covering microchannels ($10\ \mu\mathrm{m} < D \leq 200\ \mu\mathrm{m}$) and slightly beyond the minichannel range ($200\ \mu\mathrm{m} < D \leq 3$ mm) [52,53]. To determine the constants, the values of quality and saturation temperature or pressure are needed along with mass flux, heat flux, and channel dimensions. Since the L/D ratio is used extensively in the existing CHF correlations, many published data sets report L/D values and not quality. It was also not possible to recreate this data from the published information with certainty for some of these data sets. Therefore, in the present work only the data sets which explicitly report simultaneous values of quality, heat flux, mass flux, and saturation temperature are included.

Table 1 shows the details of the data sets used [32,36,54–63] in the present work. Although some of the data sets deal primarily with subcooled CHF, a few data points presented therein under saturated conditions are utilized in this work. The hydraulic diameter range is from 127 μm to 3.36 mm, although the focus is on the lower range of diameters. The table is arranged in the ascending order of diameters. The ranges of relevant parameters, including We and Ca are included in the table. Some of the data points from the data sources were not included because the data points

Table 1 Details of the experimental data sets used in the model development

Author/year	Fluid	Material	L/D	G (kg/m^2 s)	CHF (MW/m^2)	Exit x	Test section	P (MPa)	We	$Ca \times 10^3$
Kosar et al., 2009 [36]	Water	SS single tube	88–352	10,000–53,000	5.50–41.00	0.015–0.15	D=0.127–0.254 mm	0.42–1.55	6339–86,196	41–123
Kosar et al., 2005 [54]	Water	Rect. five parallel Si microch.	44	41–303	0.48–2.50	0.47–0.89	0.200×0.264 mm^2	0.047–0.101	9–583	0.2–17.6
Kosar and Peles, 2007 [55]	R123	Rect., five parallel Si microch.	44	292–1117	0.28–1.06	0.003–0.046	0.200×0.264 mm^2	0.227–0.520	1.7–81.7	5.4–22.8
Kuan and Kandlikar, 2009 [56]	Water	Rect. six parallel Cu microch.	232	50.4–231.7	0.21–0.54	0.387–776	D_h= 0.273 mm	0.1	15–162	0.2–1.1
Kuan and Kandlikar, 2009 [56]	R123	Rect. six parallel Cu microch.	232	410–534	0.14–0.20	0.857–0.927	D_h= 0.273 mm	0.23–0.27	354–592	7.6–98.7
Roday and Jensen, 2009 [57]	Water	Single SS tubes	139	320	0.80–1.26	0.45–0.85	ID: 0.286 mm	Water 0.102	372–703	1.6
Qu and Mudawar, 2004 [32]	Water, R113	Copper, 21 parallel channels	132	86–368	1.05–2.16	0.172–0.562	0.821×0.215 mm^2	0.112–0.114	3–253	0.4–1.8
Martin-Callizo et al., 2008 [58]	R22, R134a, R245fa	SS single circular tube	481	180–535	0.025–0.069	0.78–0.98	D_h= 0.64 mm	0.21–1.19	52–551	3.2–11.7
Inasaka and Nariai, 1992, [59]	Water	SS Single circular tube	10–50	7000–20,000	22.5–30.0	0.0025–0.039	D_h= 1–2 mm	0.101	35,578–128,133	34.6–98.9
Roach et al., 1999 [60]	Water	SS circular tubes	137	256–1037	0.86–2.96	0.362–0.928	ID: 1.17 mm	0.346–1.037	301–6585	1.0–4.1
Sumith et al., 2003 [61]	Water	Lexan milled-single ch.	69	23–152	0.146–0.724	0.56–0.86	ID: 1.45 mm	Pin: 0.10075	17–537	0.1–0.7
Cheng et al., 1997 [62]	R12	SS single tube	100	1000–3000	0.14–0.48	0.003–0.59	0.2 mm	1–2.3	500–46,000	19.4–117
Agostini et al., 2009 [63]	R236fa	67 parallel Si microch.	60	277–992	221–522	0.53–1.0	D_h= 3.36 mm	0.21–0.36	134–941	5.1–19.0

immediately following them at nearly the same conditions had not yet attained the CHF. Also, the data points beyond $x>0.8$ showed erratic behavior. The data sets cover water, R12, R113, R123, R22, R236fa, and R245fa.

Since the forces shown in Fig. 2 are dependent on the channel diameter as well as flow conditions, and as large ranges of diameters and flow rates are covered in the data sets, first an attempt was made to find out if the data can be classified according to some nondimensional group. A particular trend was observed with the Weber number that distinguished the data in two ranges. These ranges were identified as follows:

- Low inertia region (LIR): We$<$900.
- High inertia region (HIR): We$\geq$900.

Furthermore, the LIR region was found to be split into two CHF subregions. They are classified as follows:

- low inertia region-lower CHF subregion (LIR-LC)
- low inertia region-higher CHF subregion (LIR-HC)

Transition criterion between LIR-LC and LIR-HC could not be identified based on the nondimensional numbers. It was found to be dependent on some of the parameters in the experimental system employed, specifically the L/D ratio. Such transitions were also found in the high inertia region (We$\geq$900) and HIR-LC and HIR-HC subregions are introduced.

The constants a_1, a_2, and a_3 in Eq. (13) were evaluated using all data sets and the deviations were plotted against Weber number. As noted earlier, a transition range was observed at We around 900.

The final equations from the model based on the employed data sets are as follows.

LIR: We$<$900

High CHF subregion: LIR-HC—$L/D\leq 140$.

$$K_{2,CHF} = a_1(1+\cos\theta) + a_2\ We(1-x) + a_3\ Ca(1-x) \quad (17)$$

Low CHF subregion: LIR-LC—$L/D\geq 230$

$$K_{2,CHF} = a_4[a_1(1 + \cos\theta) + a_2\ We(1-x) + a_3\ Ca(1-x)] \quad (18)$$

HIR: We ≥ 900

High CHF subregion: HIR-HC—$L/D \leq 60$

$$K_{2,CHF} = a_1(1 + \cos\theta) + a_2\ We(1-x) + a_3\ Ca(1-x) \quad (19)$$

Low CHF subregion: HIR-LC—$L/D \geq 100$

$$K_{2,CHF} = a_4[a_1(1 + \cos\theta) + a_2\ We(1-x) + a_3\ Ca(1-x)] \quad (20)$$

Since the changes between HC and LC subregions in both LIR and HIR regions are stepwise, as seen by the addition of the multiplier a_4 in Eqs. (18) and (20) as compared with Eqs. (17) and (19), CHF in the transition region cannot be interpolated. Additional experimental data are needed to further accurately define the transition criteria. It is noted that Eqs. (17) and (19), and Eqs. (18) and (20), respectively, are identical, except that the transition criteria based on L/D values are different.

Improved Constant a_4 in the HIR-LC Region,

HIR: We ≥ 900

Based on purely empirical considerations, Eq. (20) in the HIR-LC region is slightly modified to improve the agreement with the experimental data.

$$K_{2,CHF} = a_5\left(\frac{1}{We\ Ca}\right)^n [a_1(1 + \cos\theta) + a_2\ We(1-x) + a_3\ Ca(1-x)] \quad (21)$$

The use of the product of We·Ca in the coefficient in Eq. (21) is not based on any theoretical considerations. It reflects some secondary effects that are correlated with this product in the available data sets. Since the improvement is small, caution is warranted until further testing is done with additional data.

The coefficients a_1–a_5 and n in Eqs. (17)–(21) are scaling parameters. Although they may be dependent on some of the system and operating parameters, they are assumed to be constants and are evaluated using available experimental data.

$$a_1 = 1.03 \times 10^{-4}$$

$$a_2 = 5.78 \times 10^{-5}$$

$$a_3 = 0.783$$

$$a_4 = 0.125$$

$$a_5 = 0.14$$

$$n = 0.07 \quad (22)$$

The specific functional form of the coefficients may be evaluated in the future with the availability of larger experimental data sets. Definitions of various parameters used in Eqs. (17)–(21) are given in Eqs. (8) and (14)–(16). The values of the constants are derived from the experimental data listed in Table 1. It must be noted that the data sets consist of different channel shapes and sizes, uncertainty bounds in the experiments, wall materials and material surface conditions, as well as different ranges of nondimensional parameters covering up to five orders of magnitudes variation. As additional reliable data are reported in the future, further refinements in the values of the constants and the classification ranges are expected to emerge.

The abrupt change indicated by a factor of 0.125 with constant a_4 in Eqs. (18) and (20) for the Weber number range beyond 900 was derived from the data sets as described above. It is believed that this Weber number classification distinguishes the microscale CHF behavior from the miniscale/microscale CHF behavior. It will be later shown to be strongly related to the L/D ratio and possible unstable condition.

7 Results and Discussion

Table 2 shows the mean errors, and percent data points falling in 30% and 50% error bands. In general, the experimental uncertainty in the parent data is between 7% and 13% as reported by the respective investigators.

For water and seven refrigerants, the overall mean error for all data sets is −1.7% indicating that the model prediction is well balanced for the data sets being considered. The absolute mean error is 19.7%. A total of 76% of data points fall within an error band of ±30% while 93% of data points fall within an error band of ±50%. About 7% of data points in the data sets were considered as outliers since their CHF values were significantly different from their neighboring points, often resulting in errors of 80% or higher. Since their number is small, and their behavior was found to be oddly different from their neighboring points, this deletion is considered to be reasonable.

Figure 3 shows a cumulative plot comparing the experimental and predicted values of CHF. It is seen that the predictions are quite good. A 30% error band is shown to contain a large number of data points. The log-log plot is used to depict the large range of CHF values covered by the model.

Some specific comments are made concerning the HC and LC subregions. It is seen that in the low inertia region, below We < 900, Kosar et al. [54], Kosar and Peles [55], Qu and Mudawar [32], and Kuan and Kandlikar [56] R123 data follow the predicted HC/LC classification and fall in the LIR-HC. However, a few data sets, Kuan and Kandlikar [56] water data, Roday and Jensen [57] water data, and Martin-Callizo et al. [58], data fall in the LIR-LC region. It is seen that the transition occurs at L/D between 140 and 230 based on the present data set. Tube material and fluid may also be playing deciding roles in this subregion. However, no definitive pattern could be proposed at this time based on the limited data available in this range. Broadly, higher L/D ratios with copper channels seem to lead to LIR-LC region, although as stated earlier, it could not be firmly presented as a classification criterion at this time.

The ability of the force balance model, in conjunction with the CHF mechanism depicted in Fig. 2, and the use of nondimensional groups to represent the complex CHF phenomenon are highlighted by relatively simple equations, Eqs. (17)–(21). The results showing parametric trends are presented below.

Figure 4 shows the variation in $K_{2,CHF}$ with We at $x=0.1$ plotted using Eqs. (17)–(20) for two different Ca of 1×10^{-3} and 100×10^{-3}. Although the plots are shown over the entire We range, HC and LC regions present two states in both LIR and HIR regions based on the respective L/D criteria.

Figures 5 and 6 show the slight difference between Eqs. (20) and (21) in the region We > 900 for $Ca=1\times10^{-3}$ and $Ca=100\times10^{-3}$, respectively, at $x=0.1$. The difference becomes smaller at higher values of $Ca=100\times10^{-3}$ as shown in Fig. 6. At higher We values, reduction in the $K_{2,CHF}$ is thus represented by the multiplier $0.14/(We\times Ca)^{0.07}$.

Another aspect of interest is the contribution from different forces to the $K_{2,CHF}$ value. Figure 7 shows the contributions from surface tension, inertia, and capillary forces. The sum of these contributions makes up $K_{2,CHF}$ at any given Weber number shown in the plot.

At a lower value of $Ca=1\times10^{-3}$, shown in Fig. 7, the contributions from inertia and viscous forces are about the same at We = 12. At higher We, the contribution from the inertia force rises dramatically and becomes the dominant term beyond We > 200. On the other hand, for $Ca=100\times10^{-3}$ shown in Fig. 8, the contribution from viscous force is overwhelmingly large as compared with the inertia force, at lower values of We. At around We = 1

Table 2 Comparison of the present CHF model with experimental data from literature

Author/year	x_{exit}	No. of points	Abs. mean error (%)	Mean error (%)	Data in 30% error band (%)	Data in 50% error band (%)	CHF region
Kosar et al., 2009 [36]	0.003–0.046	15	23.5	7.5	40	70	HIR-LC
Kosar et al., 2005, [54]	0.47–0.89	8	15.6	−10.7	100	100	LIR-HC
Kosar and Peles, 2007 [55]	0.003–0.046	30	16.7	−11.9	80	100	LIR-HC
Kuan and Kandlikar 2008, water [56]	0.387–0.776	6	12.8	9.4	83	100	LIR-LC
Kuan and Kandlikar 2008, [56] (R123)	0.857–0.927	6	17.5	17.5	67	100	LIR-HC
Roday and Jensen, 2009 [57]	0.45–0.85	5	24.8	−14.5	100	100	LIR-LC
Qu and Mudawar, 2004 [32]	0.172–0.562	18	12.2	4.6	94	100	LIR-HC
Martin-Callizo et al., 2008 [58]	0.78–0.98	11	31.1	28.3	55	91	LIR-LC
Inasaka and Nariai, 1992 [59]	0.0025–0.039	4	16.6	−9.3	75	100	HIR-HC
Roach et al., 1999 [60]	0.362–0.928	29	12.8	−4.6	91	100	HIR-LC[a]
Sumith et al., 2003 [61]	0.56–0.86	6	30.0	~0	33	60	LIR-HC
Cheng et al., 1997 [62]	0.003–0.59	38	18.	−14.4	95	100	HIR-LC
Agostini et al., 2008 [63]	0.53– ~1.00	23	25.0	−22.0	72	86	LIR-HC[b]
Overall	0.003– ~1.00	199	19.7	−1.7	76	93	

Notes: LIR is low inertia region, HIR is high inertia region, HC is region with higher values of CHF, LC is region with lower values of CHF. Transition criteria between LIR and HIR is based on Weber number. LIR is We < 900 and HIR is We ≥ 900. Transition criteria between HC and LC are based on the L/D ratio.
[a]Two points lie in the LIR-LC region.
[b]Two points fall in the HIR-HC region.

$\times 10^3$, the two contributions are equal in magnitude. The value of $K_{2,CHF}$ is largely governed by the viscous forces in this range.

Effect of channel hydraulic diameter on the individual contributions from different forces is shown in Figs. 9 and 10 for water and R123, respectively. These figures are plotted for a saturation pressure of 1 atm, $x=0.1$, and $G=200$ kg/m^2 s. It may be noted at the outset that for smaller diameter tubes, a lower value of G may be appropriate from practical considerations and the relative distribution of the three contributions will be altered accordingly. Nevertheless, this comparison provides an insight into parametric trends for these two fluids.

The plot shown in Fig. 9 for water indicates the dominance of the inertia term above $D=150$ μm. Below this diameter, the viscous term becomes dominant. However, for R123, shown in Fig. 10, the viscous term is dominant for D lower than 2.2 mm, covering almost the entire minichannel and microchannel ranges. The difference between water and refrigerants is clearly exemplified through these plots.

As stated earlier, at smaller diameters, lower values of G are appropriate due to pressure drop considerations. Figures 11 and 12 show the variation in $K_{2,CHF}$ with D_h for water and R123, respec-

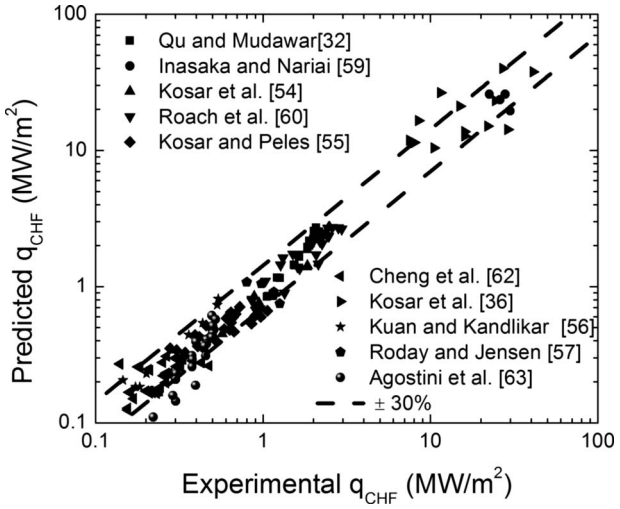

Fig. 3 Comparison of the experimental and CHF from model predictions for ten data sets with eight fluids in D_h range from 127 μm to 3.36 mm

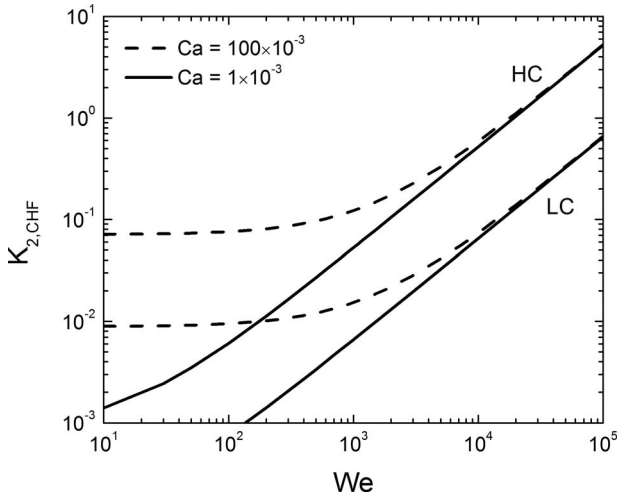

Fig. 4 Variation in $K_{2,CHF}$ with We in high CHF (HC) and low CHF (LC) regions at $x=0.1$ plotted using Eqs. (17)–(20) without employing the LIR-HIR and L/D criteria

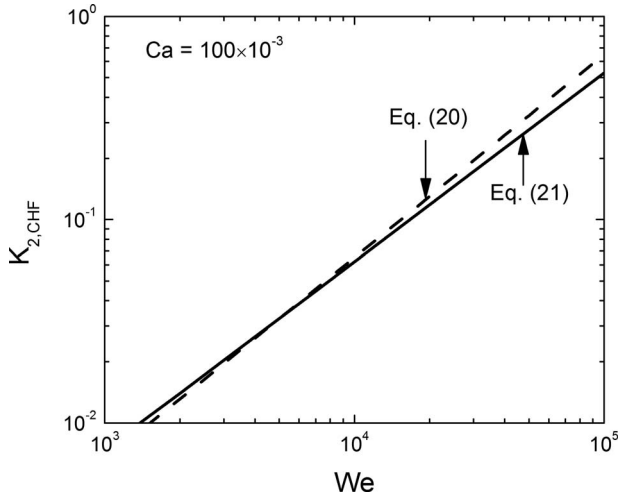

Fig. 6 Variation in $K_{2,CHF}$ with We in the HIR-LC (We>900) using Eqs. (20) and (21) for $x=0.1$ and Ca=100×10^{-3}

tively, at $G=20$ kg/m^2 s. At these conditions, the contribution from the surface tension term rises above the other two terms and the CHF would be dominated by the surface tension effects. Experimental data are needed in this range to validate these trends.

It is clear from Figs. 7–10 that at lower values of We, generally encountered in boiling at microscale, the viscous forces play a very important role. At higher values of We, the inertia forces are dominant. This also explains why the correlation of Sarma et al. [34], which incorporates the liquid viscosity, was particularly successful in representing the minichannel CHF data. The effect of viscous forces is seen to be more pronounced for refrigerants. The correlations, such as by Katto and Ohno [31], employed Weber number as the main parameter and were successful in representing the macroscale CHF data. However, since they relied on empirical data fit, it resulted in complex correlation form with large number of constants.

The condition at which the contributions from the inertia term and viscous term are equal represents the transition from the inertia controlled region to viscous controlled region. Equating the two terms, we get

$$a_2\ \mathrm{We} = a_3\ \mathrm{Ca} \tag{23}$$

Thus, the transition occurs at

$$\frac{\mathrm{We}}{\mathrm{Ca}} = \frac{a_3}{a_2} = \frac{0.783}{5.78\times10^{-5}} = 13{,}547 \tag{24}$$

Alternatively, substituting the definitions of We and Ca, the diameter at which the transition from inertia controlled to viscous controlled CHF occurs for given flow conditions is given by

$$D_{h,\mathrm{transition}} = 13{,}547\frac{\mu_L}{G}\frac{\rho_m}{\rho_L} \tag{25}$$

Since this equation is in dimensional form, SI units should be used. Alternatively, the liquid Reynolds number at this transition may be expressed as

$$\mathrm{Re}_{\mathrm{transition}} = \frac{GD_{h,\mathrm{transition}}}{\mu_L} = 13{,}547\frac{\rho_m}{\rho_L} \tag{26}$$

This diameter or Reynolds number represents the transition point below which the microscale effects represented by the capillary number term begin to dominate the CHF phenomenon.

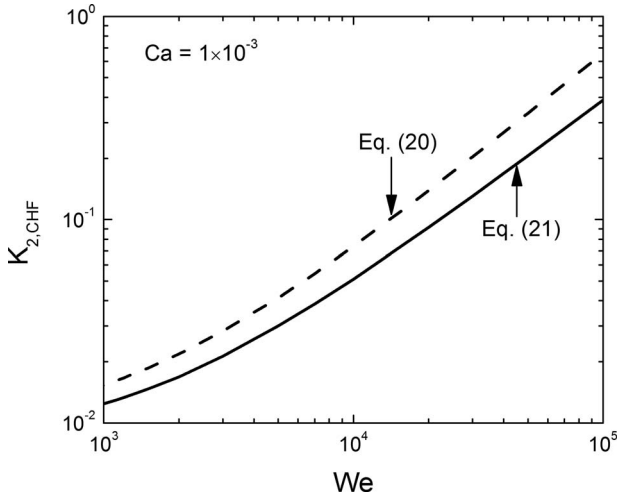

Fig. 5 Variation in $K_{2,CHF}$ with We in the HIR-LC (We>900) using Eqs. (20) and (21) for $x=0.1$ and Ca=1×10^{-3}

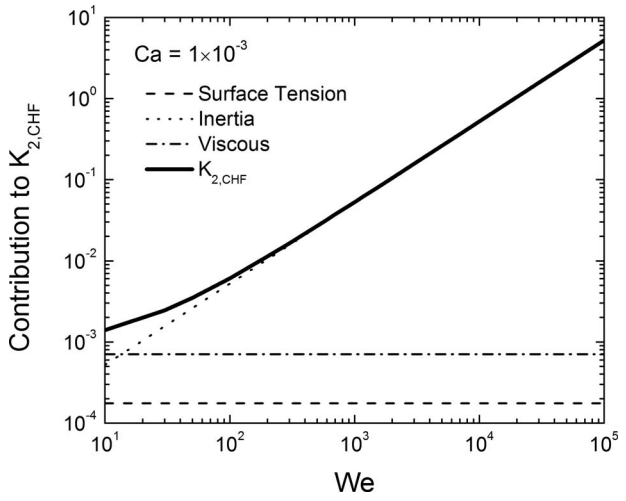

Fig. 7 Contributions from surface tension, inertia, and viscous forces to the CHF at $x=0.1$ and Ca=1×10^{-3}

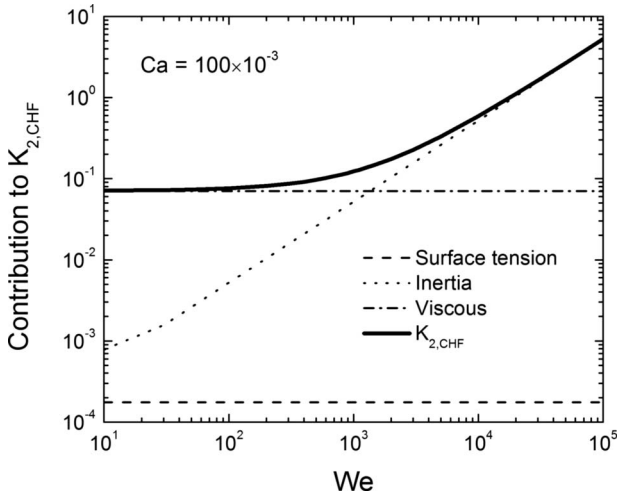

Fig. 8 Contributions from surface tension, inertia, and viscous forces to the CHF at $x=0.1$ and $Ca=100\times10^{-3}$

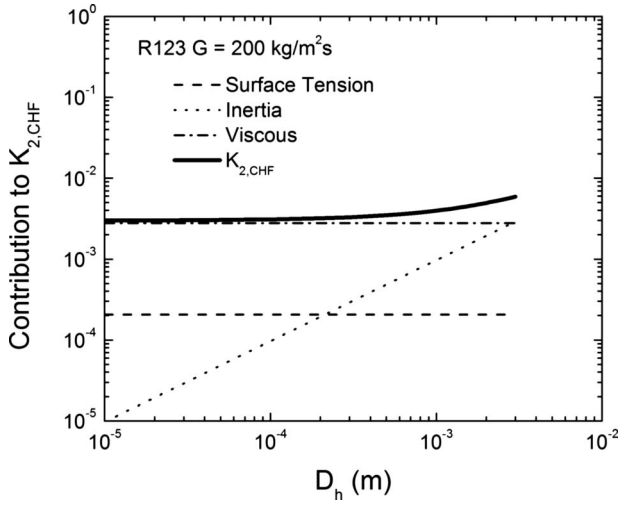

Fig. 10 Variation in $K_{2,CHF}$ and different terms in Eq. (13) with hydraulic diameter for R123 at 1 atm saturation pressure in the HC region for $x=0.1$ and $G=20$ kg/m^2 s

8 Effect of L/D Ratio

The flow boiling CHF has been modeled in literature using the L/D ratio as a parameter. This parameter enables the estimation of the local condition (quality) at the CHF location. Conducting an energy balance for a circular tube from the inlet section to the CHF location, the following equation can be derived. Note that the inlet quality will be negative for subcooled inlet.

$$G \times \frac{\pi}{4} D^2 \times (x_{\text{CHF}} - x_{\text{inlet}}) h_{fg} = \pi D L \times q_{\text{CHF}} \tag{27}$$

Rearranging, the L/D ratio at the CHF location is given by

$$\left(\frac{L}{D}\right) = \frac{(x_{\text{CHF}} - x_{\text{inlet}})}{4} \left(\frac{q_{\text{CHF}}}{G h_{fg}}\right)^{-1} \tag{28}$$

In other words, the L/D ratio may be expressed in terms of the heat flux, mass flux, latent heat, inlet quality, and the local quality at CHF. Since the CHF is considered as a local phenomenon in the present model, the inlet quality itself is not considered to have any effect unless the test section is quite short, or the CHF occurs close to the inlet section.

Therefore, it may not be essential to incorporate the L/D ratio separately in the model. It is seen that although the model developed in this paper utilizes x and not L/D directly, it is able to predict the CHF quite well. In fact, using the L/D ratio introduces the inlet quality in the CHF modeling and may be another source of nonlinearity (along with the multiplicative form used among the nondimensional variables) in the earlier correlations.

Celata and Mariani [5] explained that the L/D ratio affects the CHF by introducing entrance region type effects, which depend on the operating parameters. The effect of L/D on CHF was studied by Inasaka and Nariai [59]. Figure 13 shows their results of L/D effect on CHF with tube diameter as a parameter. It is seen that for subcooled CHF close to the saturation condition, this L/D effect is insignificant for channel diameters below 1 mm.

Another purpose served by the L/D ratio is to distinguish between the departure from nucleate boiling and dryout type CHF. In the present model, the HC and LC regions help to distinguish these regions. The flow boiling in microchannels has been observed to have similarities with pool boiling [64] with some of the flow boiling heat transfer data at low mass fluxes being well cor-

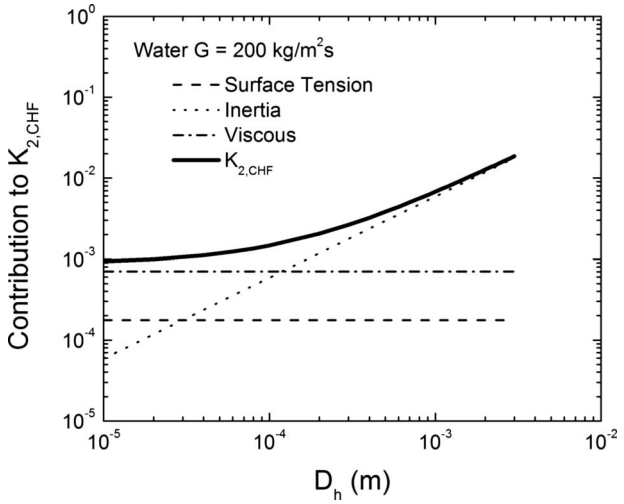

Fig. 9 Variation in $K_{2,CHF}$ and different terms in Eq. (13) with hydraulic diameter for water at 1 atm saturation pressure in the HC Region for $x=0.1$ and $G=20$ kg/m^2 s

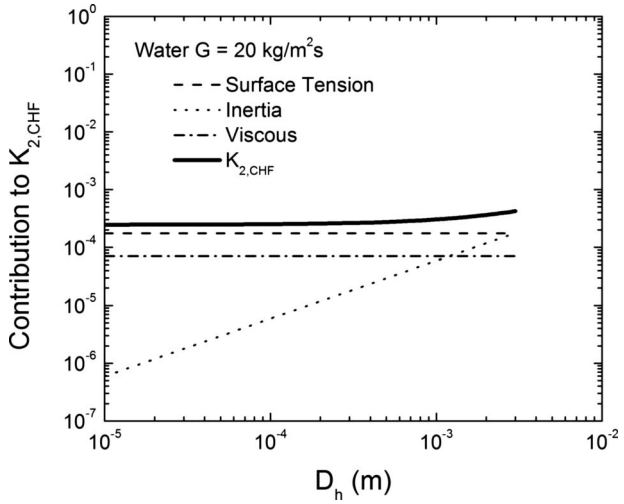

Fig. 11 Variation in $K_{2,CHF}$ with hydraulic diameter for water at 1 atm saturation pressure in the HC region for $x=0.1$ and $G=20$ kg/m^2 s

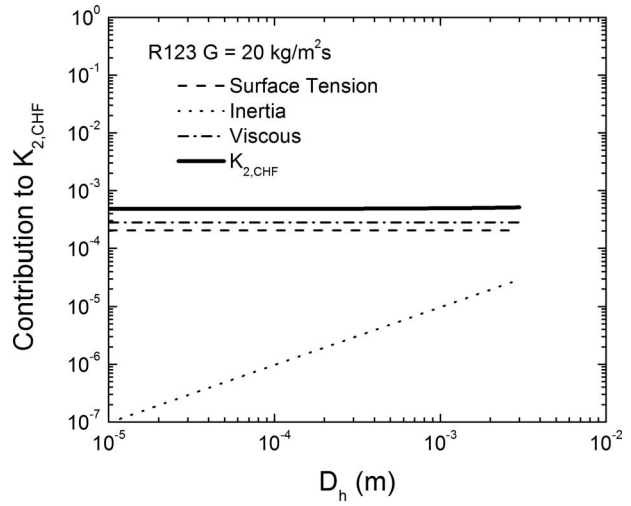

Fig. 12 Variation in $K_{2,CHF}$ and different terms in Eq. (13) with hydraulic diameter for R123 at 1 atm saturation pressure in the HC region for $x=0.1$ and $G=20$ kg/m^2 s

related by pool boiling correlations [49,51]. The implication of this finding as it relates to CHF is not explored in literature since the nature of CHF attained in the experimental data is not described by the investigators while reporting their results.

9 Criteria for Transition Between HC-LC Regions

Figure 14 shows a plot of experimental data sets in the HC or LC region plotted against their respective L/D ratios. The plot indicates a transition between $L/D=140-230$. Secondary effects of fluids are seen to influence the Kuan and Kandlikar's [56] R123 data that falls in LIR-HC region.

Figure 15 similarly shows the data sets for the HIR-HC and HIR-LC subregions. Here a transition around 60–100 is indicated. With the limited available data at this time, determination of the specific transition boundaries and transition criterion must wait until more data become available in these ranges of conditions. These plots are used in arriving at the HC-LC transition criteria in Eqs. (17)–(20). The stepwise change in q_{CHF} from HC to LC subregions by a factor of $(a_4)^{0.5}=0.35$ is related to channels with higher L/D ratios. The cause for this behavior is not clear but it is

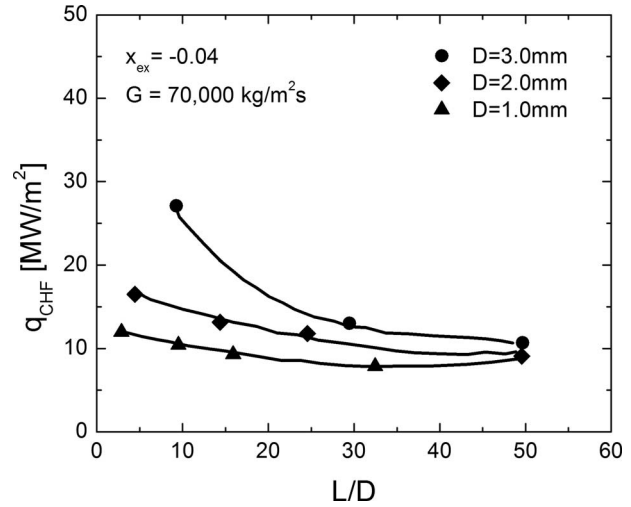

Fig. 13 Effect of L/D ratio on CHF for a fixed exit quality of 0.04 and a mass flux of 70,000 kg/m^2 s for $D=1$ mm, 2 mm, and 3 mm. Replotted from Inasaka and Nariai [59].

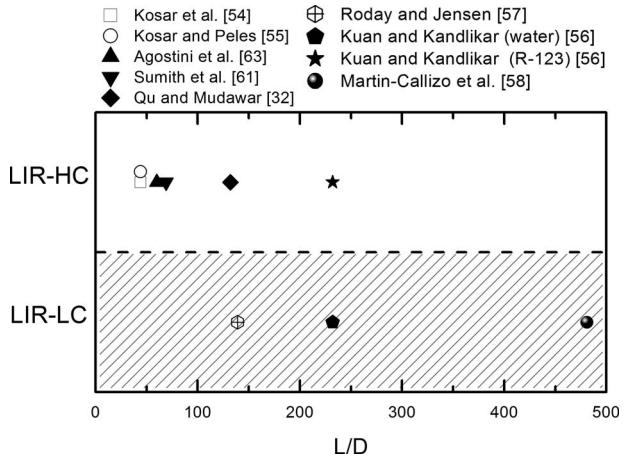

Fig. 14 Effect of L/D ratio on CHF in LIR-HC and LIR-LC regions indicating a transition region $140<L/D<230$

believed that the flow instability as suggested by Kandlikar [65] and regime changes are possible reasons. Additional experimental work is needed to further define these regions, their transition boundaries and reasons for the associated severe degradation in CHF.

10 Effect of Channel Material on CHF

The channel materials employed in the present data sets include stainless steel, silicon, and copper. The conjugate heat conduction effect introduces temperature fluctuations in response to the variation in heat transfer coefficient with the passage of bubbles and liquid-vapor interface. However, the present data set is too limited to evaluate this effect. Specific experiments directed to quantify these effects are recommended. It should be noted that higher thermal conductivity materials are used in high heat flux cooling applications, and investigation with low thermal conductivity walls may not provide practical information in the design of microchannel cooling systems. Similarly, the effect of surface roughness on CHF also needs further investigation.

11 Comparison of the Model With Previous CHF Correlations

The present model is a departure from earlier empirical correlations. Table 3 lists some important differences between the two approaches. It is derived based on the hypothesis that the CHF is a local phenomenon and is a result of the inability of the liquid front to rewet the heater surface upstream of a triple-phase contact

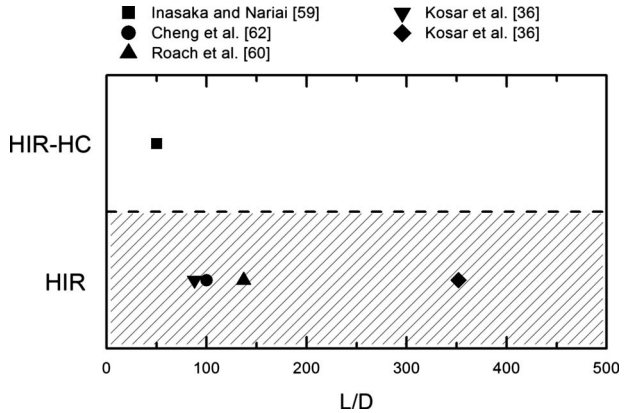

Fig. 15 Effect of L/D ratio on CHF in HIR-HC and HIR regions indicating a transition around $L/D=60-80$

Table 3 Comparison of the present model with available CHF correlations

Previous correlations	Present model
Employ empirically derived nondimensional groups	Nondimensional groups derived from force balance analysis
Use L/D ratio, introducing unintended additional parameters	Uses x_{CHF} directly as a parameter
Complex equation form because of empiricism	Simple form resulting from model-based force balance approach
Unable to account for inertia, viscous, and surface tension effects in a seamless fashion from macroscale to microscale	Additive form provides broad-range coverage over We and Ca numbers (over three orders of magnitude variation)
Unable to provide mechanistic understanding of CHF	Two-regions, HC and LC are identified based on L/D ratio as a switching parameter resulting in 35% degradation in CHF from HC to LC region
	Role of inertia at macroscale, inertia and shear at miniscale and microscale, and surface tension at the lower end of microscale identified

line at the wall. Scaling analysis indicated that the gravitational forces are not important. Evaporation momentum force is seen as the main cause leading to CHF though vapor cutback under the liquid front. The nondimensional number K_2 by Kandlikar is able to capture the effect of this force in CHF modeling.

12 Scale Effect on CHF Mechanism

The relative importance of different forces is seen to shift as a function of the scale. Based on the discussion above, the dominant forces relevant in CHF mechanism at different scales are identified below:

1. macroscale—inertia
2. miniscale and microscale—inertia and viscous
3. lower end of microscale—viscous and surface tension
4. nanoscale—surface tension

13 Conclusions

Critical heat flux during flow boiling in microchannels and minichannels is modeled using the local parameters quality, heat flux, mass flux, and fluid properties. The force balance model for pool boiling is extended to flow boiling and includes the evaporation momentum, surface tension, inertia, and viscous forces at the contact line of the liquid-vapor interface. The vapor cutback phenomenon causes the vapor to push the interface under the liquid, thus preventing the rewetting of the heater surface. The scale analysis indicates that the gravitational forces are negligible, and the viscous forces become increasingly important for smaller channels. For channels below 200 μm, the surface tension forces begin to play a more important role at lower mass fluxes.

The CHF model is presented in terms of the three nondimensional groups representing the respective ratios of the forces: evaporation momentum to surface tension—K_2 proposed by Kandlikar [51] and inertia to surface tension—Weber number, We, and viscous to surface tension—capillary number Ca. A comparison of the model with the experimental data indicates that there are two distinct regions distinguished by $We < 900$ and $We \geq 900$. Additional subregions that yielded a high or low stepwise change in CHF, termed as HC and LC, respectively, were identified based on the L/D ratio.

The experimental data from literature covering a hydraulic diameter range from 127 μm to 3.36 mm were used to obtain the constants that define the contributions from each of the three nondimensional groups. The experimental data from literature could be predicted with a mean error of 19.5%; 76% of the data could be predicted within $\pm 30\%$ error band and 93% data could be predicted within $\pm 50\%$ error band.

The use of local quality in place of L/D ratio, in conjunction with a force balance model derived from scale analysis, yielded an accurate description of the flow boiling CHF. The ratio L/D is seen to influence the transition between HC and LC regions, indicating a stepwise regime change. The coefficients representing the scale constants were evaluated from the experimental data.

The model provides an insight into CHF transition mechanisms. The relative magnitudes of inertia and viscous forces determine the transition among macroscale, miniscale, and microscale phenomena. Further reduction in scale influences the transition from viscous to surface tension dominated CHF.

Although the model predicts the tested experimental data well, current lack of large amount of experimental data for minichannels and microchannels reveals an urgent need for experimental flow boiling CHF data for different fluids over a wide range of parameters. Until such data become available and are employed in evaluating the transition boundaries, the present model should be used with caution for predictive purposes. The ranges of parameters covered by the current model are hydraulic diameter from 0.127 mm to 3.36 mm, quality from 0.003 to 0.98, We from 1.7 to 86,196, Ca from 0.1×10^{-3} to 117×10^{-3}, and L/D from 10 to 352.

Acknowledgment

The work was conducted in the Thermal Analysis, Microfluidics and Fuel Cell Laboratory at Rochester Institute of Technology. The computational support provided by RIT co-op students David Hein and Frank Forkl is gratefully acknowledged.

Nomenclature

a_1–a_5 = constants in Eqs. (12*a*), (12*b*), (13), and (17)–(21), values given in Eq. (22)
Ca = Capillary number, defined by Eq. (16)
D = diameter, m
D_h = hydraulic diameter, m
h_{fg} = enthalpy of vaporization, J/kg
F = force, N
F' = force per unit length, N/m
G = mass flux, kg/m^2 s
g = gravitational acceleration, m/s^2
K_2 = nondimensional group introduced by Kandlikar [51], Eq. (14)
n = exponent in Eq. (21), value given in Eq. (22)
q = heat flux, W/m^2
V = velocity, m/s
We = Weber number, defined by Eq. (15)
x = quality

Greek Letters

θ_R = receding contact angle, deg
μ = viscosity, N/m

ρ = density, kg/m^3
ρ_m = average density, given by Eq. (8)
σ = surface tension, N/m

Subscripts

exit = at the exit section
CHF = at critical heat flux condition
G = gravity
I = inertia
inlet = at the inlet section
L = liquid
M = evaporation momentum
S = surface tension
v = vapor
τ = shear (viscous)

References

[1] Katto, Y., 1985, "Critical Heat Flux," *Advances in Heat Transfer*, J. P. Hartnett and T. F. Irvine, eds., Academic Press, New York, Vol. 17.
[2] Hewitt, G. F., 1982, "Burnout," *Handbook of Multiphase Systems*, G. Hetsroni, ed., Hemisphere, New York.
[3] Bergles, A. E., 1976, "Burnout in Boiling Heat Transfer, Part II: Subcooled and Low Quality Forced-Convection Systems," *Two-Phase Flows and Heat Transfer*, S. Kakac and T. N. Veziroglu, eds., Hemisphere, Washington, DC, Vol. II.
[4] Tong, L. S., and Tang, Y. S., 1997, "Flow Boiling Crisis," *Boiling Heat Transfer and Two-Phase Flow*, Taylor & Francis, Washington, DC, Chap. 5.
[5] Celata, G. P., and Mariani, A., 1999, "CHF and Post-CHF Heat Transfer," *Handbook of Phase Change: Boiling and Condensation*, S. G. Kandlikar, M. Shoji, and V. K. Dhir, eds., Taylor & Francis, Philadelphia, PA, Chap. 17.
[6] Bergles, A. E., and Kandlikar, S. G., 2005, "On the Nature of Critical Heat Flux in Microchannels," ASME J. Heat Transfer, **127**(1), pp. 101–107.
[7] Wang, G. D., Cheng, P., and Wu, H. Y., 2007, "Unstable and Stable Flow Boiling in Parallel Microchannels and in a Single Microchannel," Int. J. Heat Mass Transfer, **50**, pp. 4297–4310.
[8] Kandlikar, S. G., Kuan, W. K., Willistein, D. A., and Borrelli, J., 2006, "Stabilization of Flow Boiling in Microchannels Using Pressure Drop Elements and Fabricated Nucleation Sites," ASME J. Heat Transfer, **128**(4), pp. 389–396.
[9] Kuo, C. J., and Peles, Y., 2008, "Flow Boiling Instabilities in Microchannels and Means for Mitigation by Reentrant Cavities," ASME J. Heat Transfer, **130**, p. 072402.
[10] Kandlikar, S. G., 2009, "Methods for Stabilizing Flow in Channels and Systems Thereof," U.S. Patent No. 7,575,046.
[11] Rohsenow, W. M., 1952, "A Method of Correlating Heat Transfer Data for Surface Boiling of Liquids," Trans. ASME, **74**, pp. 969–976.
[12] Stephan, K., and Abdelsalam, M., 1980, "A New Correlation for Natural Convection Boiling," Int. J. Heat Mass Transfer, **23**, pp. 73–87.
[13] Cooper, M. G., 1984, "Saturation Nucleate Pool Boiling—A Simple Correlation," IChemE Symposium Series, Vol. 86, pp. 786–793.
[14] Bonilla, C. F., and Perry, C. W., 1941, "Heat Transmission to Boiling Binary Liquid Mixtures," Transactions of American Society of Chemical Engineers, **37**, pp. 685–705.
[15] Kutateladze, S. S., 1948, "On the Transition to Film Boiling Under Natural Convection," Kotloturbostroenie, No. 3, pp. 10–12.
[16] Kutateladze, S. S., 1951, "A Hydrodynamic Theory of Changes in a Boiling Process Under Free Convection," Izvestia Akademia Nauk, S.S.S.R., Otdelenie Tekhnicheski Nauk, No. 4, p. 529.
[17] Borishanskii, V. M., 1955, "On the Problem of Generalizing Experimental Data on the Cessation of Bubble Boiling in Large Volume of Liquids," Ts. K.I.T., 28, Moscow.
[18] Rohsenow, W. M., and Griffith, P., 1956, "Correlation of Maximum Heat Transfer Data for Boiling of Saturated Liquids," Chem. Eng. Prog., Symp. Ser., **52**, pp. 47–49.
[19] Zuber, N., 1959, "Hydrodynamic Aspects of Boiling Heat Transfer," Ph.D. thesis, Research Laboratory, Los Angeles and Ramo-Wooldridge Corporation, University of California, Los Angeles, CA.
[20] Chang, Y. P., 1961, "An Analysis of the Critical Conditions and Burnout in Boiling Heat Transfer," USAEC Report No. TID-14004, Washington, DC.
[21] Katto, Y., and Yokoya, S., 1968, "Principal Mechanism of Boiling Crisis in Pool Boiling," Int. J. Heat Mass Transfer, **11**, pp. 993–1002.
[22] Haramura, Y., and Katto, Y., 1983, "New Hydrodynamic Model of Critical Heat Flux Applicable Widely to Both Pool and Forced Convection Boiling on Submerged Bodies in Saturated Liquids," Int. J. Heat Mass Transfer, **26**, pp. 389–399.
[23] Lienhard, J. H., and Dhir, V. K., 1973, "Extended Hydrodynamic Theory of the Peak and Minimum Pool Boiling Heat Fluxes," NASA Report No. CR-2270, Contract No. NGL 18-001-035.
[24] Kirichenko, Y. A., and Cherniakov, P. S., 1973, "Determination of the First Critical Thermal Heat Flux on Flat Heaters," J. Eng. Phys., **20**, pp. 699–702.
[25] Unal, C., Daw, V., and Nelson, R. A., 1992, "Unifying the Controlling Mechanisms for the Critical Heat Flux and Quenching: The Ability of Liquid to Contact the Hot Surface," ASME J. Heat Transfer, **114**, pp. 972–982.
[26] Kandlikar, S. G., 2001, "A Theoretical Model to Predict Pool Boiling CHF Incorporating Effects of Contact Angle and Orientation," ASME J. Heat Transfer, **123**, pp. 1071–1079.
[27] Whalley, P. B., Hutchinson, P., and Hewitt, G. F., 1974, "The Calculation of Critical Heat Flux in Forced Convective Boiling," International Heat Transfer Conference, Tokyo, Vol. IV, pp. 290–294.
[28] Revellin, R., and Thome, J. R., 2008, "A Theoretical Model for the Prediction of the Critical heat Flux in Heated Microchannels," Int. J. Heat Mass Transfer, **51**, pp. 1216–1225.
[29] Wojtan, L., Revellin, R., and Thome, J. R., 2006, "Investigation of Saturated Heat Flux in a Single, Uniformly Heated Microchannel," Exp. Therm. Fluid Sci., **30**, pp. 765–774.
[30] Kosar, A., 2009, "A Model to Predict Saturated Critical Heat Flux in Minichannels and Microchannels," Int. J. Therm. Sci., **48**, pp. 261–270.
[31] Katto, Y., and Ohno, H., 1984, "An Improved Version of the Generalized Correlation of Critical Heat Flux for the Forced Convective Boiling in Uniformly Heated Vertical Tubes," Int. J. Heat Mass Transfer, **27**(9), pp. 1641–1648.
[32] Qu, W., and Mudawar, I., 2004, "Measurement and Correlation of Critical Heat Flux in Two-Phase Micro-Channel Heat Sinks," Int. J. Heat Mass Transfer, **47**, pp. 2045–2059.
[33] Bowers, M. B., and Mudawar, I., 1994, "High Flux Boiling in Low Flow Rate, Low Pressure Drop Mini-Channel and Micro-Channel Heat Sinks," Int. J. Heat Mass Transfer, **37**, pp. 321–332.
[34] Sarma, P. K., Srinivas, V., Sharma, K. V., Dharma, R., and Celata, G. P., 2006, "A Correlation to Evaluate Critical Heat Flux in Small Diameter Tubes Under Subcooled Conditions of the Coolant," Int. J. Heat Mass Transfer, **49**, pp. 42–51.
[35] Roday, A. P., and Jensen, M. K., 2009, "Study of the Critical Heat Flux Condition With Water and R-123 During Flow Boiling in Microtubes. Part II—Comparison of Data With Correlations and Establishment of a New Subcooled CHF Correlation," Int. J. Heat Mass Transfer, **52**, pp. 3250–3256.
[36] Kosar, A., Peles, Y., Bergles, A. E., and Cole, G. S., 2009, "Experimental Investigation of Critical Heat Flux in Microchannels for Flow-Field Probes," ASME Paper No. ICNMM2009-82214.
[37] Bergles, A. E., 1963, "Subcooled Burnout in Tubes of Small Diameter," ASME Paper No. 63-WA-182.
[38] Vandervort, C. L., Bergles, A. E., and Jensen, M. K., 1994, "An Experimental-Study of Critical Heat-Flux in Very High Heat Flux Subcooling Boiling," Int. J. Heat Mass Transfer, **37**, pp. 161–173.
[39] Zhang, W., Hibiki, T., Mishima, K., and Mi, Y., 2006, "Correlation of Critical Heat Flux for Flow Boiling of Water in Mini-Channels," Int. J. Heat Mass Transfer, **49**, pp. 1058–1072.
[40] Bowring, R. W., 1972, "A Simple but Accurate Round Tube Uniform Heat Flux, Dryout Correlation Over the Pressure Range 0.7–17 MN/m2 (100–2500 psia)," United Kingdom Atomic Energy Authority, Paper No. AEEW-R 789.
[41] Katto, Y., 1978, "A Generalized Correlation of Critical Heat Flux for the Forced Convection Boiling in Vertical Uniformly Heated Round Tubes," Int. J. Heat Mass Transfer, **21**, pp. 1527–1542.
[42] Shah, M. M., 1987, "Improved General Correlation for Critical Heat Flux During Upflow in Uniformly Heated Vertical Tubes," Int. J. Heat Fluid Flow, **8**, pp. 326–335.
[43] Tong, L. S., 1968, "Boundary-Layer Analysis of the Flow Boiling Crisis," Int. J. Heat Mass Transfer, **11**, pp. 1208–1211.
[44] Inasaka, F., and Nariai, H., 1987, "Critical Heat Flux and Flow Characteristics of Subcooled Flow Boiling in Narrow Tubes," JSME Int. J., **30**, pp. 1595–1600.
[45] Celata, G. P., Cumo, M., and Mariani, A., 1994, "Assessment of Correlations and Models for the Prediction of CHF in Water Subcooled Flow Boiling," Int. J. Heat Mass Transfer, **37**, pp. 237–255.
[46] Hall, D. D., and Mudawar, I., 2000, "Critical Heat Flux (CHF) for Water Flow in Tubes—II. Subcooled CHF Correlations," Int. J. Heat Mass Transfer, **43**, pp. 2605–2640.
[47] Kandlikar, S. G., and Steinke, M. E., 2002, "Contact Angles and Interface Behavior During Rapid Evaporation of Liquid on a Heated Surface," Int. J. Heat Mass Transfer, **45**, pp. 3771–3780.
[48] Sefiane, K., Benielli, D., and Steinchen, A., 1998, "A New Mechanism for Pool Boiling Crisis, Recoil Instability and Contact Angle Influence," Colloids Surf., A, **142**, pp. 361–373.
[49] Kandlikar, S. G., "Scale Effects on Flow Boiling in Microchannels: A Fundamental Perspective," Int. J. Therm. Sci., in press.
[50] Phan, H. T., Caney, N., Marty, P., Colasson, S., and Gavillet, J., 2009, "How Does Wettability Influence Nucleate Boiling," C. R. Mec., **337**, 251–259.
[51] Kandlikar, S. G., 2004, "Heat Transfer Mechanisms During Flow Boiling in Microchannels," ASME J. Heat Transfer, **126**, pp. 8–16.
[52] Kandlikar, S. G., and Grande, W. J., 2003, "Evolution of Microchannel Flow Passages—Thermohydraulic Performance and Fabrication Technology," Heat Transfer Eng., **24**(1), pp. 3–17.
[53] Kandlikar, S. G., 2006, *Heat Transfer and Fluid Flow in Minichannels and Microchannels*, Elsevier, Kidlington, Oxford, UK.
[54] Kosar, A., Kuo, C.-J., and Peles, Y., 2005, "Boiling Heat Transfer in Rectangular Microchannels With Reentrant Cavities," Int. J. Heat Mass Transfer, **48**, pp. 4867–4886.
[55] Kosar, A., and Peles, Y., 2007, "Critical Heat Flux of R-123 in Silicon-Based Microchannels," ASME J. Heat Transfer, **129**, pp. 844–851.
[56] Kuan, W. K., and Kandlikar, S. G., 2008, "Critical Heat Flux Measurement

and Model for Refrigerant-123 Under Stabilized Flow Conditions in Microchannels," ASME J. Heat Transfer, **130**(3), p. 034503.
[57] Roday, A. P., and Jensen, M. K., 2009, "Study of the Critical Heat Flux Condition With Water and R-123 during Flow Boiling in Microtubes. Part I—Experimental Results and Discussion of Parametric Trends," Int. J. Heat Mass Transfer, **52**, pp. 3235–3249.
[58] Martin-Callizo, C., Ali, R., and Palm, B., 2008, "Dryout Incipience and Critical Heat Flux in Saturated Flow Boiling of Refrigerants in a Vertical Uniformly Heated Microchannel," *Proceedings of the ASME Sixth International Conference on Nanochannels, Microchannels and Minichannels*, pp. 708–712.
[59] Inasaka, F., and Nariai, H., 1992, "Critical Heat Flux of Subcooled Flow Boiling in Uniformly Heated Straight Tubes," Fusion Eng. Des., **19**, pp. 329–337.
[60] Roach, G. M., Abdel-Khalik, S. I., Ghiaasiaan, S. M., Dowling, M. F., and Jeter, S. M., 1999, "Low-Flow Critical Heat Flux in Heated Microchannels," Nucl. Sci. Eng., **131**, pp. 411–425.
[61] Sumith, B., Kaminaga, F., and Matsumura, K., 2003, "Saturated Boiling of Water in a Vertical Small Diameter Tube," Exp. Therm. Fluid Sci., **27**, pp. 789–801.
[62] Cheng, X., Erbacher, F. J., Muller, U., and Pang, F. G., 1997, "Critical Heat Flux in Uniformly Heated Vertical Tubes," Int. J. Heat Mass Transfer, **40**, pp. 2929–2939.
[63] Agostini, B., Revellin, R., Thome, J. R., Fabbri, M., Michel, B., Calmi, D., and Kloter, U., 2008, "High Heat Flux Flow Boiling in Silicon Multi-Microchannels—Part III: Saturated Critical Heat Flux of R236fa and Two-Phase Pressure Drops," Int. J. Heat Mass Transfer, **51**, pp. 5426–5442.
[64] Kandlikar, S. G., 2010, "Similarities and Difference Between Pool Boiling and Flow Boiling Heat Transfer in Microchannels," Heat Transfer Eng., **31**(3), pp. 159–167.
[65] Kandlikar, S. G., 2002, "Fundamental Issues Related to Flow Boiling in Minichannels and Microchannels," Exp. Therm. Fluid Sci., **26**(2–4), pp. 389–407.

Bubble Dynamics for Nucleate Pool Boiling of Electrolyte Solutions

Seyed Ali Alavi Fazel[1]

Seyed Baher Shafaee
e-mail: bahershafaee@yahoo.com

Department of Chemical Engineering,
Islamic Azad University,
Mahshahr, Khuzestan Province 63519, Iran
e-mail: alavifazel@gmail.com

Bubble dynamics is the most important subphenomenon, which basically affects the nucleate pool boiling heat transfer coefficient. Previous investigations state that the effect of physical properties of liquid and vapor phases on bubble departure diameter are often conflicting. In this article, extensive new experimental data are presented for the bubble departure diameter for various electrolyte aqueous solutions over a wide range of heat fluxes and concentrations. Experimental results show that the bubble detachment diameter increase with increasing either boiling heat flux or electrolyte concentration. Experimental results also present a close relation between the dimensionless capillary and bond numbers. A new model for the prediction of vapor bubble departure diameter in nucleate boiling for the electrolyte solutions is proposed, which predicts the experimental data with a satisfactory accuracy. [DOI: 10.1115/1.4001315]

Keywords: pool boiling, bubble diameter, electrolyte solutions

1 Introduction

Nucleate pool boiling heat transfer is widely used in desalination, chemical, petrochemical, refrigeration and power plants, either to generate vapor or because of its very high heat transfer coefficient relative to other heat transfer mechanisms. The very high heat transfer coefficient is related to three different heat transfer mechanisms, including: (1) convection; (2) the intense microconvection from the liquid adjacent to the heat transfer area, which is induced by liquid motions during bubble growth and departure; and (3) heat transfer through the evaporation of the microlayer between bubbles and heat transfer area. Generally, bubbles may be induced in a liquid in two ways. First, by impulsive depressurization of the liquid, and the second way is by addition of heat to a liquid at constant pressure. Nucleation refers to the initiation of the embryonic bubble, which is classified to homogeneous and heterogeneous nucleation modes. In heterogeneous nucleation, which is the focal point of this article, the appearances of boiling bubbles are a result of liquid vaporization at the interface through a heated surface [1–7].

Many attempts were made to model these phenomena and combine them through bubble dynamics to make them possible to predict the boiling heat transfer coefficients [2,3,8–11]. In these models, the heat transfer surface is divided into two different areas: (1) area beneath the bubbles, which includes liquid evaporation and convection from the liquid sublayer to the bubbles; and (2) area affected by liquid motion induced by bubble movements. In the second divided area, the superheated liquid is transported into the bulk of liquid in the wake of departing bubbles and is replaced by the cooler liquid. It is proved that the quantity of the replaced cooler liquid by vapor bubbles are proportional to the bubble diameter to power two [10]. The bubble diameter is also a key parameter for prediction of nucleate pool boiling heat transfer coefficients by a variety of empirical correlations [12–14]. Because of the inadequacy of this critical information, a theoretical model for prediction of the nucleate boiling heat transfer coefficient is still at the early stage of development [15–19].

2 Literature Review

Many correlations are developed for the prediction of the bubble diameter for the nucleate pool boiling condition for different applications, which most are summarized in Table 1. All of the proposed correlations are either simple with a limited range of validity or complicated and requires an iterative procedure. The Fritz [20] model is one of the most reliable existing models for prediction of the bubble diameter for boiling of pure liquids and also liquid mixtures. However, this correlation has shown a significant deviation from experimental data from electrolyte solutions. Stephan [21] has modified the Fritz [20] model by involving three dimensionless Jacob, Prandtl, and Archimedes numbers. This correction has some improvements relative to the predictions of the Fritz [20] model for some systems, excluding the electrolyte solutions. However, the calculations are an iterative procedure. Van Stralen and Zijl [22] proposed an empirical model for nucleate boiling by considering bubble growth mechanisms. This model includes the Jacob number and thermal diffusivity of the solution. Cole [23] modified the contact angle and proposed that the effect of system pressure is involved through a modified Jacob number. Zeng et al. [24] assumed that the dominant forces leading to bubble detachment would be the unsteady growth and the bouncy forces. They developed their model based on an empirical expression for bubble growth mechanisms. This model can be used only if specific information on the vapor bubble growth parameters is available [25]. Yang et al. [26] developed a correlation for the prediction of the vapor bubble diameter by considering the analogy between nucleate boiling and forced convection heat transfer. The key parameter of this model is given graphically as a function of the Jacob number, and there are not any explicit mathematical correlation proposed. Jamialahmadi et al. [27] developed an empirical correlation for electrolyte solutions. This correlation predicts the bubble diameter specifically for electrolyte solutions. In this correlation, the bubble diameter is correlated with heat flux only, and the impact of electrolyte concentration and also pressure are not included. Again, in some of the existing models [21–23,28], the dimensionless Jacob number is involved, which is a function of the surface temperature and is fundamentally unknown for any given system. However, the surface temperature could be predicted through an iterative procedure by the existing correlations developed for predicting the boiling heat transfer co-

[1]Corresponding author.

Contributed by the Heat Transfer Division of ASME for publication in the JOURNAL OF HEAT TRANSFER. Manuscript received September 6, 2009; final manuscript received February 15, 2010; published online June 10, 2010. Assoc. Editor: Louis C. Chow.

Table 1 Correlations suggested for the prediction of bubble size

Reference	Correlation	Application
Fritz [20]	$D = 0.0146\theta\sqrt{\frac{2\sigma}{g(\rho_l - \rho_v)}}$ θ=35 deg for mixtures and 45 deg for water	Pure liquids and mixtures
Ruckenstein [28]	$D = \left[\frac{3\pi^2\rho_l\hat{\alpha}_l g^{0.5}(\rho_l - \rho_v)^{0.5}}{\sigma^{3/2}}\right]\mathrm{Ja}^{4/3}\sqrt{\frac{2\sigma}{g(\rho_l - \rho_v)}}$	Not specified
Cole–Rohsenow [29]	$D = C\ \mathrm{Ja}^{5/4}\sqrt{\frac{\sigma g_0}{g(\rho_l - \rho_v)}}$ $C=1.5\times10^{-4}$ for water and 4.65×10^{-4} for others	Not specified
Cole [23]	$D = 0.04\ \mathrm{Ja}\sqrt{\frac{2\sigma}{g(\rho_l - \rho_v)}}$	Pure liquids and mixtures
Van Stralen et al. [22]	$D = 2.63\left(\frac{\mathrm{Ja}^2\hat{\alpha}_l^2}{g}\right)^{1/3}\left[1 + \left(\frac{2\pi}{3\ \mathrm{Ja}}\right)^{1/2}\right]^{1/4}$	Pure liquids and mixtures
Stephan [21]	$D = 0.25\left[1 + \left(\frac{\mathrm{Ja}}{\mathrm{Pr}}\right)^2\frac{100{,}000}{\mathrm{Ar}}\right]^{0.5}\sqrt{\frac{2\sigma}{g(\rho_l - \rho_v)}}$	Pure liquids and mixtures
Yang et al. [26]	$D = 3.0557\times10^{+3}\frac{\rho_l}{\rho_v}\frac{\sqrt{C_{pl}T^{\mathrm{sat}}}}{H_{fg}}\frac{\hat{\alpha}\ \mathrm{Pr}_l^{3/5}}{\eta}$	Not specified
Jamialahmadi et al. [27]	$D = \left(96.75 + \frac{0.01425(q/A)}{\ln(q/A)}\right)^{-1}$	Electrolyte solutions

efficient conjugated with the Newton's cooling law. A significant error, especially in subcooled boiling systems, should be expected through this iterative procedure.

3 Experimental Apparatus

Figure 1 presents the experimental equipment used in the present measurements. This boiling vessel is a vertical hollow cylinder of stainless steel, containing 38 l of test liquid connected to a vertical condenser to condense and recycle the evaporated water. The whole system is heavily isolated to prevent heat loss. The temperature of the liquid inside the tank is continuously monitored and controlled to any predetermined set point by a thermoregulator and a band heater. Before any experiment, the liquid is preheated to any predetermined temperature. The test section is a horizontal rod heater with a diameter of 10.67 mm and a heating length of 99.1 mm, which can be observed and photographed through observation glasses. This heater consists of an internally heated stainless steel sheathed rod, and four stainless steel sheathed thermocouples with an exterior diameter of 0.25 mm entrenched along the circumference of the heater close to the heating surface. This heating section provided a very uniform heat flux. The boiling heat flux is calculated by the products of the electrical current, electrical potential, and the cosine of the phase lag divided to the heating area, i.e., $I.V.\cos\varphi$. The voltage-current phase lag is measured by an oscilloscope equal to about φ=8 deg. According to the geometrical characteristics of the rod heater (Fig. 1), the heating area is equal to 0.005199 m^2 and the heat flux could be calculated by $q/A=190.41.I.V$ [W m^{-2}].

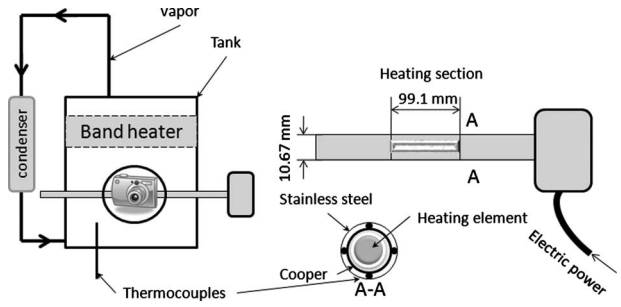

Fig. 1 The experimental apparatus design

For each experiment, the picture of the boiling phenomena was taken using a high speed camera. These recordings are used to determine the static bubble diameter. A Hewlett-Packard HP Photo

Smart R507 has been used as the image acquisition system. Typical photo information are: F-stop = $f/5.5$, exposure time = 1/90 s, ISO speed = 100, resolution = 300×300 dpi^2, focal length = 10 mm, maximum aperture = 2.6, and flash energy = 26 bcps.

4 Experimental Procedure

Initially, the entire system, including the rod heater and the inside of the tank, were cleaned and the test solution was introduced. The vacuum pump is then turned on and the pressure of the system is kept low at about 10 kPa (abs) for 5 hrs to allow the entire dissolved gases to strip away from the test solution. Following this, the temperature of the system is set to a predetermined temperature. This procedure provides a homogeneous condition right through. Then the electric power was slowly supplied to the rod heater and increased gradually to a constant predetermined value to generate any specific heat flux. The data acquisition system and digital camera were simultaneously switched on to record the required parameters, including the rod heater surface temperature, bulk temperature, heat flux, and also all visual information. Some runs were repeated twice and even thrice to ensure the reproducibility of the experiments. Each experiment can take about 2 min to reach to steady state at any specific condition. The experiments have been performed in subcooled and also saturated conditions. For a correct measurement, it is necessary to ignore the extreme oversized and undersized bubbles and make an average from the rest of the data. The formation of very large bubbles is due to the bubbles coalescence, and the development of very small bubbles is because of bubbles brakeage, which is the result of shearing of vapor through the liquid phase. The development location of both of these bubble types are relatively far away from the heating element, not directly induced by the boiling phenomenon, and are consequently ignored. In this investigation, the diameters of all bubbles within any of the taken photos have been measured and the arithmetic average has been assigned to the bubble departure diameter for any specific condition. Typically, any photo includes about 30–50 bubbles depending on the bubble size. To determine the diameters of the nonspherical bubbles, the bubble project area has been measured using picture scanning software and the diameter of a hypothetical circle with same area is calculated. Potentially, there are different sources of errors through measurements, including (a) concentration: max. $\pm 2\%$ (weight) and max. $\pm 2\%$ (volume); (b) heat flux: max. $\pm 2\%$ (current) and max. $\pm 3\%$ (voltage); and (c) temperature: max. $\pm 2\%$.

5 Test Solutions

Heat transfer experiments were performed with aqueous NaCl, Na_2SO_4, and KNO_3 solutions. The decisive factors for selecting these solutes were based on the solubility of the salts in water, the valence, and the size of the respective ions. The solubility curves of the selected salts in water shows that the solubility of Na_2SO_4 and NaCl are nearly independent of the temperature, and the experimental concentrations are far away from the saturation point. In addition, the solubility of KNO_3 in water increases with increasing temperature. Therefore, it is guaranteed that no deposits form on the surface of the heating element in the range of experiments. The boiling temperatures of aqueous solutions of these salts can be fitted with excellent accuracy to the following general equation, over a wide range of salt concentrations [27]:

$$T_b = a_0 + a_1 c^{a_2} \tag{1}$$

The fitted coefficients for the examined electrolytes are summarized in Table 2. The measurements are based on clear observation of salt sediments into a known volume of water at any specific temperature.

Table 2 Coefficients for Eq. (1) [27]

Solute	a_0 (K)	a_1 (m^3/kg)	a_2
NaCl	373.15	0.00589	1.223
Na_2SO_4	373.15	0.01293	0.906
KNO_3	373.15	0.0154	0.886

6 Results and Discussion

The experimental values of measured bubble diameters are presented in Table 3. The data show that the bubble diameter increase, either by increasing heat flux at any constant concentration or by increasing concentration at any constant heat flux.

Figure 2 typically correlates the experimental data with major existing models for the NaCl solution. Most predictions have a similar trend for increasing bubble diameter versus increasing heat flux, however roughly, the maximum of 40% relative difference is clear among different existing models.

The electrolyte solutes including NaCl, KNO_3, and Na_2SO_4 completely dissociate in water and form ions. Each ion is surrounded by cluster of water and the ions are heavily repulsed from the interface and keeps in the bulk of solution. It is well known that the surface tension at the interface between the vapor and liquid solution is higher than that of pure water, due to the existence of nonevaporating ions. Figure 3 presents the measured static equilibrium of surface tension of the test solution as a function of the concentration and bulk temperature. However, higher attractive forces between water and ions will quickly force the ions to the bulk of solution from the interface. As the result, it is anticipated that the dynamic interfacial tension between the vapor and solution due to the swift evaporation of water during bubble generation to be less than the static equilibrium surface tension. Therefore, increasing the electrolyte concentration could increase the bubble departure diameter and decrease the active nucleate site density. Surface tension can also be predicted by the following correlation [30]:

$$\sigma = \sigma_w + RT\Gamma_{MX}^{wo} \ln \frac{1}{1 + K_{MX} a_{MX}} \tag{2}$$

where R, T, and a_{MX} are the universal gas constant, absolute temperatures, and activity of the electrolyte MX, respectively. In addition, σ_w is the pure water surface tension at the system temperature, Γ_{MX}^{wo} is the excess of MX in the unit cross-sectional area of the surface region over the moles, and K_{MX} is the adsorption equilibrium constant.

7 Modeling

It is generally understood that the application of the equations of motion to simple geometries is not applicable for determining the bubble volume on its own. Consequently, a pure mathematical dynamic modeling of bubble formation, especially at high heat fluxes, is very complicated. To highlight this complication, a deviation of a pure mathematical model is presented here, based on the equilibrium condition, and the results are correlated with the experimental data [31]. Bubble equilibrium is a consequence of three types of equilibrium. Consider a spherical isolated bubble with radius r_e in the bulk of a liquid. For this bubble to remain intact, three conditions must be convened. These are mechanical equilibrium, thermal equilibrium, and equal chemical potentials. For the mechanical equilibrium, the algebraic summation of all the forces applied to the bubble should be zero:

$$\sum F = \text{internal pressure force} + \text{external pressure force} + \text{surface tension force} = 0$$

After substitution of these forces to the above equation, respectively:

Table 3 The experimental values of measured bubble diameters

	NaCl			KNO_3			Na_2SO_4		
q/A [a]	x [b]	T_b [c]	D [d]	x [b]	T_b [c]	D [d]	x [b]	T_b [c]	D [d]
47770	0.10	65	0.0018	0.10	65	0.0013	0.10	63	0.0015
10,9470	0.10	67	0.0020	0.10	69	0.0015	0.10	65	0.0018
148,080	0.10	69	0.0023	0.10	69.5	0.0020	0.10	67	0.0023
203,020	0.10	72	0.0025	0.10	70	0.0023	0.10	70	0.0024
261,540	0.10	75	0.0030	0.10	71	0.0028	0.10	72	0.0028
300,000	0.10	77	0.0033	0.10	73	0.0030	0.10	75	0.0030
47,770	0.20	70	0.0020	0.20	67	0.0015	0.19	68	0.0018
109,470	0.20	72	0.0023	0.20	69	0.0018	0.19	70	0.0020
148,080	0.20	75	0.0025	0.20	70	0.0023	0.19	72	0.0025
203,020	0.20	77	0.0028	0.20	71	0.0025	0.19	75	0.0028
261,540	0.20	80	0.0033	0.20	73	0.0030	0.19	77	0.0033
300,000	0.20	82.5	0.0035	0.20	75	0.0033	0.19	80	0.0035
47,770	0.47	72	0.0025	0.41	69	0.0020	0.44	70	0.0023
109,470	0.48	75	0.0026	0.41	70	0.0023	0.44	73	0.0025
148,080	0.48	77	0.0030	0.41	73	0.0025	0.44	75	0.0028
203,020	0.48	80	0.0033	0.41	75	0.0028	0.44	76	0.0030
261,540	0.48	83	0.0038	0.41	78	0.0033	0.45	78	0.0035
300,000	0.48	85	0.0040	0.41	80	0.0035	0.45	81	0.0038

[a]Heat flux (W m^{-2}).
[b]Mass fraction.
[c]Bulk temperature (°C).
[d]Measured bubble diameter (m).

$$\pi r_e^2 P_v + \pi r_e^2 P_l + 2\pi r_e \sigma = 0 \rightarrow P_v - P_l = 2\sigma r_e \quad (3)$$

Clearly, for equal temperatures in the liquid side and the vapor side, we know that $P_v > P_l$. This means that liquid surrounding the bubble must be superheated. In the aforementioned modeling, it is assumed that there are no gases dissolved in the liquid. For the thermal equilibrium, the temperature of the vapor and liquid are equal. Otherwise, a combination of heat and mass transfer processes would occur to establish thermal equilibrium at a larger bubble size, or cause the bubble to collapse.

The contact angle is a measure of the wet-ability of a liquid. Wetting itself is defined as the ability of liquids to form a boundary surface with solids. Due to the action of surface tension, a wetting liquid in a capillary tube has a surface with a contact angle smaller than 90 deg. Nonwetting liquids have convex surfaces and an angle of contact greater than 90 deg. Surface treatment strongly affects the liquid wet-ability. Wetting liquids fill surface cavities, prevent nucleation, and affect the nucleation site density. Because of a very high complexity of the contact angle measurement, the average value of 35 deg is considered in this research for all mixtures, as reported by Fritz [20].

Bubble grows from cavities in a surface. Figure 4 presents a surface cavity, which is also called the nucleation site. The transferred energy from the heated surface to the trapped vapor in this cavity (stage I) causes it to grow. Stage II shows the moment that the bubble has reached at the mouth of the cavity. At this point, the bubble volume keeps increasing while the radius keeps decreasing. The minimum radius is reached when the bubble radius becomes equal to the radius of the cavity $r_b = r_c$ (stage III). The growth of the bubble beyond this point depends on the degree of superheating of the liquid. If sufficient superheating exists, bubbles eventually leave the nucleation sites toward the bulk.

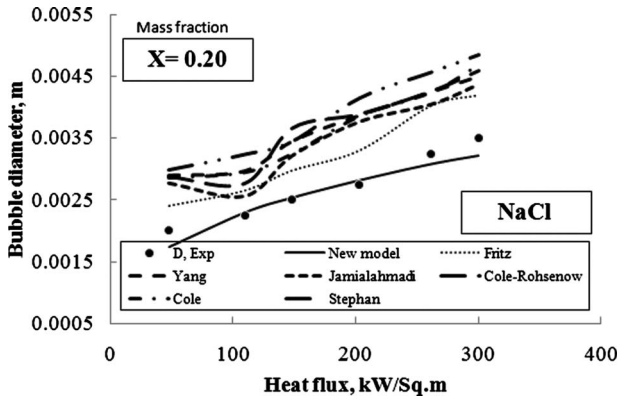

Fig. 2 Typical comparison between existing models and experimental data of bubble diameter

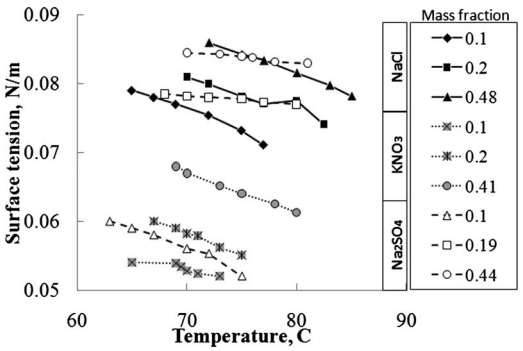

Fig. 3 Measured static equilibrium of surface tension of tested solutions

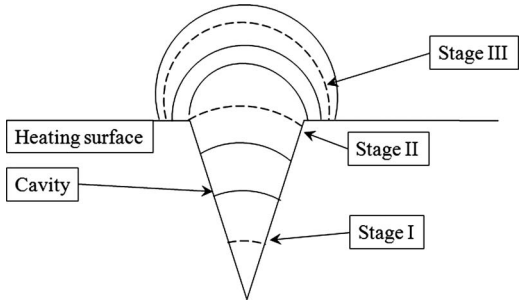

Fig. 4 Different stages of bubble generation on the surface

Table 4 The parameter ψ in various correlations

Correlation	Parameter ψ
Equation (5)	$\psi=\sqrt{3}$
Fritz [20]	$\psi=0.0146\sqrt{2}\theta$
Ruckenstein [28]	$\psi=\left[\frac{3\pi^2\rho_l\hat{\alpha}_l g^{0.5}(\rho_l-\rho_v)^{0.5}}{\sigma^{3/2}}\right]\ \mathrm{Ja}^{4/3}\sqrt{2}$
Cole and Rohsenow [29]	$\psi=C\ \mathrm{Ja}^{5/4}\sqrt{g_0}$ $C=1.5\times10^{-4}$ for water and 4.65×10^{-4} for others
Cole [23]	$\psi=0.04\ \mathrm{Ja}\sqrt{2}$
Stephan [21]	$\psi=0.25\left[1+\left(\frac{\mathrm{Ja}}{\mathrm{Pr}}\right)^2\frac{100{,}000}{\mathrm{Ar}}\right]^{0.5}$

These stages are known as the waiting period, growth period, agitation or displacement of liquid in the thermal sublayer period, and departure (or collapse) period. It is shown that $1/r_b$ is proportional to the liquid superheat T_l-T_{sat}. Figure 4 also shows that the radius of the cavity (r_c) determines the amount of superheat required for the vapor bubble to nucleate at that site.

The departure diameter refers to the diameter of a bubble at the moment that the bubble leaves the heated surface. For a single bubble where the interactions of the adjacent bubbles are ignored, the bubble diameter could be generally estimated by considering the force balance between buoyancy and surface tension

$$\pi D\sigma=\frac{\pi D^3}{3}(\rho_l-\rho_v)g \tag{4}$$

Therefore

$$D=\sqrt{3}\sqrt{\frac{\sigma}{(\rho_l-\rho_v)g}} \tag{5}$$

However, by increasing the heat flux, adjacent bubbles will induce a lateral motion of liquid, which significantly affects the bubble departure diameter. In addition, at higher heat fluxes, the density of nucleation sites will increase. Consequently, any attached bubble on the heating surface may be supplied through two interconnected bubble stems from two adjacent bubble formation points. Therefore, a high error is expected by Eq. (5). Note that this theoretical model is achieved from the force balances at the ending of the expansion stage of bubble growth on top of a cavity.

In this research, in accordance to Fig. 4, the growth of a vapor bubble through a cavity is divided into two different phases. In the first phase, the growth happens inside the cavity, and the second stage is the later period of growth of the vapor bubble on the tip of the cavity. This stage develops until the buoyancy forces surpass the surface tension forces, which are holding the vapor bubble on the cavity. Equating these two forces states that the bubble diameter is proportional to the term of $\sqrt{\sigma/(\rho_l-\rho_v)g}$. Alternatively, symbolizing this proportional constant by ψ, this relation can be simplified to

$$\mathrm{Bo}=\psi^2 \tag{6}$$

where Bo, the Bond number, is defined by the ratio of gravitational force to those of surface tension force. Many attempts have been made to develop a predictive model for the parameter of ψ in the past literature. For different existing models, this mentioned parameter is summarized in Table 4.

Table 5 The average relative error for predictions of the bubble diameter

Correlation	NaCl (%)	KNO_3 (%)	Na_2SO_4 (%)
Fritz [20]	19	22	19
Yang [26]	24	41	35
Jamialahmadi [27]	25	14	13
Cole–Rohsenow [29]	31	31	28
Cole [23]	30	27	34
Stephan [21]	38	34	45
New model	2	10	5

In the first stage, the trapped vapor shifts through the cavity when the pressure drop crosswise the cavity prevails over the trapping capillary forces. In this investigation, the flow of vapor within the cavity is approximated by Poisseulle's equation [32]. By the concepts of dimensional analysis and scaling rules, it can be proved that the first stage of bubble formation is a function of the dimensionless group, representing the ratio of viscous forces to capillary forces [33,34]. The ratio of viscous forces to the capillary forces is defined by $a=(\mu_v V)/(\sigma\cos\theta)$, the capillary number, where V, the vapor velocity passing through the capillary channel, could be calculated simply by $V=(q/A)/(H_{fg}\cdot\rho_v)$. The capillary dimensionless number relates the magnitude of viscous forces to capillary forces in the first stage of bubble formation within the cavity. The capillary number can be amplified by either (I) increasing the vapor velocity by increasing heat flux or decreasing the heat of vaporization or vapor density; (II) increasing the vapor phase viscosity; (III) increasing the contact angle connecting the vapor and cavity; or (IV) reducing interfacial tension between the vapor and liquid phase within the cavity.

The functionality of the parameter ψ may be expressed as

$$\psi=m\mathrm{Ca}^n \tag{7}$$

Parameters m and n are a function of cavity density, length, and size. Equation (7) has been proposed, based on experimental data and the impact of different parameters on bubble departure diameter. A new correlation for the bubble departure diameter is developed here by combining Eqs. (6) and (7) as

$$\mathrm{Bo}^{1/2}=m\mathrm{Ca}^n \tag{8}$$

The tuning parameters in Eq. (8) can be estimated from the experimental data. A high number of experimental data over a wide range of possible operating parameters have been collected from the present work. All the collected experimental data are used to tune the parameters, which are found equal to $m=40$ and $n=(1/3)$ for all tested electrolyte solutions at different boiling conditions with a satisfactory accuracy. The final predictive correlation for prediction of the bubble departure diameter in electrolyte solution can be alternatively expressed as the following form:

$$D=40\sqrt[3]{\frac{\mu_v\left(\frac{q/A}{H_{fg}\rho_v}\right)}{\sigma\cos\theta}}\sqrt{\frac{\sigma}{g(\rho_l-\rho_v)}} \tag{9}$$

Table 5 compares the performance of different correlations for the bubble diameter for different solutions. The values in Table 5 reflect the absolute average relative error (AARE), which is defined by $\mathrm{AARE}\%=\left|\left(D^{\mathrm{predicted}}/D^{\mathrm{measured}}\right)-1\right|\times100$. Figure 5 graphically presents the experimentally measured versus predicted dimensionless Bond number for all tested solutions and different correlations.

8 Conclusions

An experimental and theoretical investigation on vapor bubble formation under nucleate saturated and subcooled pool boiling conditions has been performed using a variety of electrolyte solu-

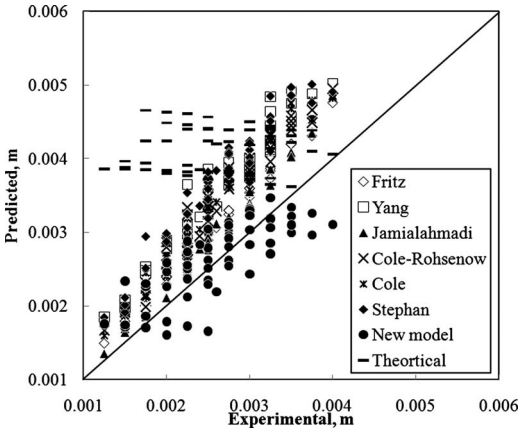

Fig. 5 Experimental versus predicted bubble departure diameter for all test solutions and different correlations

tions. It is observed that interfacial, viscous, and bouncy forces are the major contributing parameters to the vapor bubble departure diameter, and they should be taken into consideration at all ranges of heat fluxes and concentrations. Finally, the experimental results are used to develop a practical model for the prediction of the vapor bubble departure diameter for electrolyte solutions. Taking into consideration the complication of the bubble formation mechanism under nucleate boiling conditions, the quantitative agreement between measured and predicted values are satisfactory.

Nomenclature

A = area
a = activity
a_0, a_1, a_2 = constant in Eq. (1)
Ar = Archimedes number: $(g\rho_l(\rho_l-\rho_v)/\mu_l^2)[(\sigma/g(\rho_l-\rho_v))]^{3/2}$
Bo = Bond number: $g(\rho_l-\rho_v)D^2/\sigma$
c = concentration (kg m^{-3})
C = constant
Ca = Capillary number: $\mu_v V/\sigma\cos\theta$
D = bubble diameter (m)
F = force (N)
g = acceleration due to gravity (m s^{-2})
g_o = gravity acceleration correction factor
H_{fg} = heat of vaporization (J/kg)
I = electrical current (A)
Ja = Jacob number: $\rho_l C_{pl}(T_w-T_b)/\rho_v H_{fg}$
K = adsorption equilibrium constant
m = constant in Eq. (7)
n = constant in Eq. (7)
P = pressure (Pa)
Pr = Prandtl number: $C_{pl}\mu_l/k_l$
q = heat (W)
R = universal gas constant
r = radius (m)
T = temperature (°C or K)
V = velocity (m s^{-1}) or voltage (V)

Greek Symbols

$\hat{a}$ = heat diffusivity (m^2 s^{-1})
Γ = surface excess (m^2 mol^{-1})
η = constant
θ = contact angle (deg)
ρ = density (kg m^{-3})
σ = interfacial tension (N m^{-1})
φ = V/I phase lag
ψ = constant

Subscripts and Superscripts

0 = standard sate or saturated
b = bulk or bubble
c = cavity
e = equilibrium
l = liquid
v = vapor
w = water

References

[1] Westwater, J. W., 1956, "Boiling of liquids," Adv. Chem. Eng., **1**, pp. 1–76.
[2] Chi-Yeh, H., and Griffith, P., 1965, "The Mechanism of Heat Transfer in Nucleate Pool Boiling, Int.—Part I: Bubble Initiation, Growth and Departure," Int. J. Heat Mass Transfer, **8**, pp. 887–904.
[3] Chi-Yeh, H., and Griffith, P., 1965, "The Mechanism of Heat Transfer in Nucleate Pool Boiling—Part II: The Heat Flux-Temperature Difference Relation," Int. J. Heat Mass Transfer, **8**, pp. 905–914.
[4] Cooper, M. G., 1969, "The Microlayer and Bubble Growth in Nucleate Pool Boiling," Int. J. Heat Mass Transfer, **12**, pp. 915–933.
[5] Corty, C., and Foust, R. S., 1971, "Surface Variables in Nucleate Boiling," Chem. Eng. Prog., Symp. Ser., **51**(17), pp. 1–12.
[6] Collier, J. G., 1972, *Convective Boiling and Condensation*, McGraw-Hill, London.
[7] Zeitoun, O., and Shoukri, M., 1996, "Bubble Behavior and Mean Diameter in Subcooled Flow Boiling," Trans. ASME, Ser. B, **118**, pp. 110–116.
[8] Mikic, B. B., and Rohsenow, W. M., 1969, "A New Correlation of Pool Boiling Data Including the Effect of Heat Surface Characteristics," ASME J. Heat Transfer, **91**, pp. 245–250.
[9] Shoukri, M., and Judd, R. L., 1978, "On the Influence of Surface Conditions in Nucleate Boiling—The Concept of Bubble Flux Density," ASME J. Heat Transfer, **100**, pp. 618–623.
[10] Blöchl, R., 1986, "Zum Einfluß der Oberlächenstruktur unterschiedlich bearbeiteter Heizflächen auf die Wärmeübertragung beim Blasensieden," Ph.D. thesis, University of Karlsruhe, Germany.
[11] Jamialahmadi, M., Blöchl, R., and Müller-Steinhagen, H., 1991, "Pool Boiling Heat Transfer to Saturated Water and Refrigerant 113," Can. J. Chem. Eng., **69**, pp. 746–754.
[12] Rohsenow, W. M., 1952, "A Method of Correlating Heat Transfer Data for Surface Boiling Liquids," Trans. ASME, **74**, pp. 969–975.
[13] Stephan, K., 1979, "Preußer, Wärmeübergang und maximale Wärmestromdichte beim Behältersieden binärer und ternärer und ternärer Flüssigkeitsgemische," Chem.-Ing.-Tech., MS **649/79**, pp. 293–300.
[14] Stephan, K., and Abdelsalam, M., 1980, "Heat Transfer Correlations for Natural Convection Boiling," Int. J. Heat Mass Transfer, **23**, pp. 73–87.
[15] Bonjour, J., Clausse, M., and Lallemand, M., 2000, "Experimental Study of the Coalescence Phenomenon During Nucleate Pool Boiling," Exp. Therm. Fluid Sci., **20**, pp. 180–187.
[16] Lee, H. C., Oh, B. D., Bae, S. W., and Kim, M. H., 2003, "Single Bubble Growth in Saturated Pool Boiling on a Constant Wall Temperature Surface," Int. J. Multiphase Flow, **29**, pp. 1857–1874.
[17] Christopher, D. M., Wang, H., and Peng, X., 2006, "Numerical Analysis of the Dynamics of Moving Vapor Bubbles," Int. J. Heat Mass Transfer, **49**, pp. 3626–3633.
[18] Mukherejee, A., and Kandlikar, S. G., 2007, "Numerical Study of Single Bubbles With Dynamic Contact Angle During Nucleate Pool Boiling," Int. J. Heat Mass Transfer **50**, pp. 127–138.
[19] Genske, P., and Stephan, K., 2006, "Numerical Simulation of Heat Transfer During Growth of Single Vapor Bubbles in Nucleate Boiling," Int. J. Therm. Sci., **45**, pp. 299–309.
[20] Fritz, W., 1935, "Berechunung des maximal volumens von Dampfblasen," Phys. Z., **36**, pp. 379–384.
[21] Stephan, K., 1992, "Saturated Pool Boiling and Subcooled Flow Boiling of Mixtures," Ph.D. thesis, University of Auckland, New Zealand.
[22] Van Stralen, S. J. D., and Zijl, W., 1978, "Fundamental Developments in Bubble Dynamics," *Proceedings of the Sixth International Heat Transfer Conference*, Toronto, Vol. 6, pp. 429–450.
[23] Cole, R., 1967, "Bubble Frequencies and Departure Volumes at Subatmospheric Pressures," AIChE J., **13**, pp. 779–783.
[24] Zeng, L. Z., Klausner, J. F., and Mei, R., 1993, "A Unified Model for the Prediction of Bubble Detachment Diameters in Boiling Systems, Part 1: Pool Boiling," Int. J. Heat Mass Transfer, **36**, pp. 2261–2270.
[25] McFadden, P. W., and Grassmann, P., 1962, "The Relation Between Bubble Frequency and Diameter During Nucleate Pool Boiling," Int. J. Heat Mass Transfer, **5**, pp. 169–173.
[26] Yang, C., Wu, Y., Yuan, X., and Ma, C., 2000, "Study on Bubble Dynamics for Pool Nucleate Boiling," Int. J. Heat Mass Transfer, **43**, pp. 203–208.
[27] Jamialahmadi, M., Helalizadeh, A., and Müller-Steinhagen, H., 2004, "Pool boiling Heat Transfer to Electrolyte Solutions," Int. J. Heat Mass Transfer, **47**, pp. 729–742.
[28] Ruckenstein, R., 1964, "Recent Trends in Boiling Heat Transfer Research," Appl. Mech. Rev., **17**, pp. 663–672.

[29] Cole, R., and Rohsenow, W. M., 1966, "Correlation of Bubble Departure Diameters for Boiling of Saturated Liquids," Chem. Eng. Prog., Symp. Ser., **65**(92), pp. 211–213.
[30] Li, Z., and Lu, B. C.-Y., 2001, "Surface Tension of Aqueous Electrolyte Solutions at High Concentrations—Representation and Prediction," Chem. Eng. Sci., **56**, pp. 2879–2888.
[31] Massoud, M., 2005, Engineering Thermofluids.
[32] Sutera, S. P., and Skalak, R., 1993, "The History of Poiseuille's Law," Annu. Rev. Fluid Mech., **25**, pp. 1–20.
[33] Bejan, A., 1984, *Convection Heat Transfer*, 1st ed., Wiley, New York.
[34] Milanova, D., and Kumar, R., 2005, "Fluid Mechanics and Thermodynamics," Appl. Phys. Lett., **87**, p. 233107.

Rendering the Transient Hot Wire Experimental Method for Thermal Conductivity Estimation to Two-Phase Systems—Theoretical Leading Order Results

Peter Vadasz[1]
Professor
Fellow ASME
Department of Mechanical Engineering,
Northern Arizona University,
P.O. Box 15600,
Flagstaff, AZ 86001
e-mail: peter.vadasz@nau.edu

The transient hot wire experimental method for estimating the thermal conductivity of fluids and solids is well established as the most accurate, reliable, and robust technique. It essentially relies on a simple analytical formula derived from the solution of the heat conduction from a line heat source embedded in the target medium. This simple and elegant analytical formulation was derived for uniform and homogeneous fluids or solids. Its extension to two-phase or composite systems, while in practical application, does not have any theoretical basis, and it is by no means obvious that the latter may be applied without corrections to such heterogeneous systems. When it is actually applied as for single-phase systems, it is clearly incorrect. This paper presents preliminary results at the leading order (in the sense of an expansion of the solution in powers of time, applicable to short time scales, consistent with the validity of the transient hot wire method), which render the transient hot wire method to two-phase and composite systems. While these leading order approximations extend the applicability of the same analytical formula to two-phase systems, they also produce additional conditions that need to be fulfilled for such an application to provide reliable experimental results. [DOI: 10.1115/1.4001314]

Keywords: transient hot wire, porous media, nanofluids, effective thermal conductivity, two-phase heat conduction

1 Introduction

The transient hot wire (THW) method is well established as the most accurate, reliable, and robust technique [1]) for evaluating the thermal conductivity of fluids [2–4] and solids [5]. It replaced the steady state methods primarily because of the difficulty to determine if the steady state conditions have indeed been established and for fluids, the difficulty in preventing the occurrence of natural convection and consequently, the difficulty in eliminating the effects of natural convection on the heat flux. While the application of the method to gases is straightforward its corresponding application to electrically conducting liquids and solids needs further attention. Experiments conducted in nanofluid suspensions listed above [6] used a thin electrical insulation coating layer to cover the platinum wire instead of using the bare metallic wire, a technique developed by Nagasaka and Nagashima [7]. The latter is aimed at preventing problems such as electrical current flow through the liquid, causing ambiguity of the heat generation in the wire. Alternatively, Assael et al. [8] pioneered the use of tantalum wires, which were anodized in situ to form a coating layer of tantalum pentoxide (Ta_2O_5), which is an electrical insulator. The use of tantalum wires instead of coated platinum wires seems to be the preferred method in the present practice. In the case of solids, Assael et al. [6,9–11] demonstrated the importance of using an intermediate soft solid material between the hot wire and the solid of interest in order to eliminate or substantially reduce the contact thermal resistances. Therefore, the bare metallic wire can only be used for gases [12] or electrically insulating liquids such as oils.

Assael et al. [6,9–11] developed a new application of the transient hot wire method by using a commercial software to solve for the whole temperature-time curve by trial and error until it fits the experimental data, at which point the thermal conductivity (k) and the heat capacity (ρc_p) of the material are found. Assael et al. [6,9–11] showed the development of this method specifically for solids with only one example used for applying it to fluids, and without discussing the possible effects of convection on the latter. Preventing effects of convection in fluids is a particular emphasis that is substantially distinct from its application to solids. All these demonstrations still use experimental standards (e.g., diameter or cross sectional extent of the wire, length of the wire, and wire material) that are within the validity range of the classical transient hot wire method described above, although experimental results for time ranges of microseconds can be used when using the proposed method.

Unfortunately, the theoretical support for existing experimental methods is stretched to its limits, and their recent applications frequently extend beyond these limits. Examples of such extensions are the application of the transient hot wire method for evaluating the effective thermal conductivity of nanofluid suspensions [13,14] or porous insulating foams [15,16]. Possible limitations of the applicability of the THW method were discussed and identified by Vadasz [17], who concluded that it is incorrect to apply the method directly without the required corrections to the two-phase systems.

The present paper presents the preliminary results at the leading order (in the sense of an expansion of the solution in powers of time, applicable to short times, scales consistent with the validity

[1]Corresponding author. Also at the Faculty of Engineering, University of KZ Natal, Durban, South Africa.

Contributed by the Heat Transfer Division of ASME for publication in the JOURNAL OF HEAT TRANSFER. Manuscript received August 17, 2009; final manuscript received February 11, 2010 published online June 2, 2010. Editor: Yogesh Jaluria.

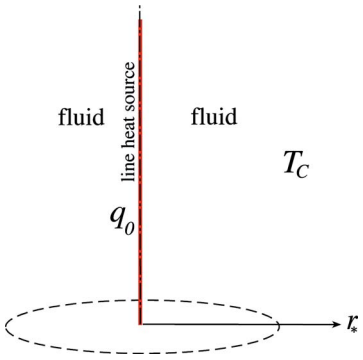

Fig. 1 The line heat source analytical problem underlying the transient hot wire method

of the Transient Hot Wire method), which render the transient hot wire method to two-phase and composite systems. While these leading order approximations extend the applicability of the method to two-phase systems, they also produce additional conditions that need to be fulfilled for such an application to provide reliable experimental results.

We introduce here a *contextual notation* to distinguish between dimensional and dimensionless variables and parameters. It implies that an asterisk subscript identifies the dimensional values only when ambiguity arises when the asterisk is omitted. For example r_* is the dimensional radial coordinate, while r is its corresponding dimensionless counterpart. However k_s is the effective solid phase thermal conductivity, a dimensional parameter that appears without an asterisk subscript without causing ambiguity. The only exception to this rule is the temperature, which is defined by $T=T_*-T_o$ as the dimensional temperature taken with respect to a reference value T_o.

2 Single-Phase Line Heat Source Solution

The line heat source solution for the problem of conduction in a single-phase fluid (or solid) is well known and classical [18,19]. It is presented here as a reference point to be used later in the two-phase problem.

Let us consider a wire of finite diameter and infinite vertical extent embedded into the target single-phase fluid (or solid), as presented in Fig. 1. The finite diameter is considered initially because it is more convenient to convert Ohm's heating parameters that are used in the transient hot wire method to a finite, although very thin, wire diameter. Eventually the heat flux resulting from such a finite diameter wire will be evaluated in the limit when the wire radius tends to zero, thus converting it into the line heat source. The radius of this thin wire is taken as r_w, and the amount of heat rate generated per unit length of the wire by an electric current i (A) passing through the wire is $\dot{q}_L$ (W/m). This amount of generated heat rate is related to the electric current i and the electrical resistivity ρ_e (Ω m) of the wire via the relationship $\dot{q}_L = i^2\rho_e/A$, where ρ_e is related to the electrical resistance R of any wire having a finite length L and cross sectional area A by $R = \rho_e L/A$. This heat rate per unit length generated within the wire by Ohm's heating can be converted into the corresponding amount of radial heat flux from the wire to the surrounding fluid (or solid) in the form

$$\dot{q}_L = (q_{r^*})_{r_*=r_w}\frac{2\pi r_w L}{L} = 2\pi r_w (q_{r^*})_{r_*=r_w} = -2\pi r_w k\left(\frac{\partial T}{\partial r_*}\right)_{r_*=r_w}$$

$$= -2\pi k\left(r_*\frac{\partial T}{\partial r_*}\right)_{r_*=r_w} \tag{1}$$

where q_{r^*} at $r_*=r_w$ is the radial heat flux from the wire and the dimensional temperature T is defined relative to a reference temperature value T_o such that $T=T_*-T_o$. Therefore, one obtains in the limit of $r_w\to 0$ the conditions equivalent to a line heat source in the form

$$\lim_{r_w\to 0}\left(r_*\frac{\partial T}{\partial r_*}\right)_{r=r_w} = -\frac{\dot{q}_L}{2\pi k} \tag{2}$$

providing a boundary condition for the problem under consideration. The equation for heat conduction through the target fluid (solid) is

$$\frac{\partial T}{\partial t_*} = \frac{\alpha}{r_*}\frac{\partial}{\partial r_*}\left(r_*\frac{\partial T}{\partial r_*}\right) \tag{3}$$

where $\alpha=k/\rho c_p$ is the fluid's thermal diffusivity subject to the following initial and boundary conditions:

$$t_* = 0: T = 0 \tag{4}$$

$$r_*\to\infty: T = 0 \tag{5}$$

in addition to the boundary condition (2).

The solution to the heat conduction problem formulated by Eq. (3), initial condition (4), and boundary conditions (2) and (5) is obtained by introducing a Boltzmann transformation via a dimensionless similarity variable η defined in the form

$$\eta = \frac{r_*^2}{4\alpha t_*} \tag{6}$$

Replacing the derivatives in Eq. (3) with the corresponding derivatives involving η yields an ordinary differential equation in the form

$$\frac{d}{d\eta}\left(\eta\frac{dT}{d\eta}\right) + \eta\frac{dT}{d\eta} = 0 \tag{7}$$

The initial and boundary conditions (4) and (5) are converted into the following boundary condition in terms of the similarity variable η in the form

$$\eta\to\infty: T = 0 \tag{8}$$

and the boundary condition (2) is converted into the following boundary condition in terms of η

$$\lim_{\eta\to 0}\left(2\eta\frac{dT}{d\eta}\right)_{\eta} = -\frac{\dot{q}_L}{2\pi k} \tag{9}$$

Equation (7) and the boundary conditions (8) and (9) constitute a two-point boundary value problem that may be solved via the introduction of the following notation:

$$\phi = \eta\frac{dT}{d\eta} \tag{10}$$

transforming the second order Eq. (7) into the following first order equation in terms of ϕ

$$\frac{d\phi}{d\eta} + \phi = 0 \tag{11}$$

providing the following solution:

$$\phi = \eta\frac{dT}{d\eta} = A_o e^{-\eta} \tag{12}$$

and a second integration yields

$$T = A_o\int\frac{e^{-\eta}}{\eta} + B_o \tag{13}$$

By introducing the boundary conditions (8) and (9) into Eq. (13) leads to the following complete analytical solution:

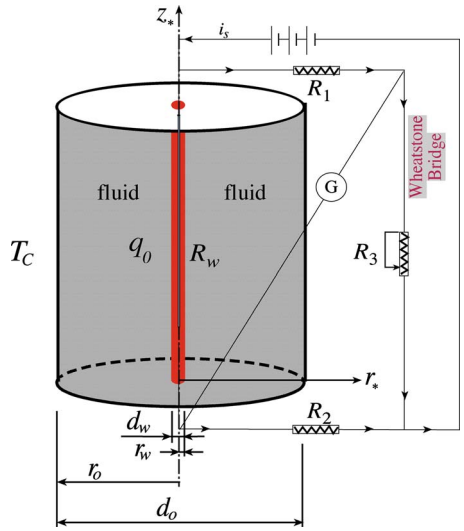

Fig. 2 Typical schematic setup for a transient hot wire experiment in a pure fluid

$$T = \frac{\dot{q}_L}{4\pi k}\int_{\eta}^{\infty}\frac{e^{-\eta}}{\eta}d\eta = \frac{\dot{q}_L}{4\pi k}\mathrm{Ei}(\eta) = \frac{\dot{q}_L}{4\pi k}\mathrm{Ei}\left(\frac{r_*^2}{4\alpha t_*}\right) \tag{14}$$

where $\mathrm{Ei}(\eta)=\int_{\eta}^{\infty}(e^{-\eta}/\eta)d\eta$ is the exponential integral function. Equation (14) is used in the evaluation of the fluid's (solid's) thermal conductivity when using the transient hot wire method.

3 Transient Hot Wire Method for Homogeneous Fluids

The THW method consists in principle of determining the thermal conductivity of a target material/fluid by observing the rate at which the temperature of a very thin platinum/tantalum wire (5–80 μm) increases with time after a step change in the voltage has been applied to it. The platinum/tantalum wire is embedded vertically in the target material/fluid (see Fig. 2) and serves as a heat source as well as a thermometer. The temperature of the platinum/tantalum wire is established by measuring its electrical resistance, the latter being related to the temperature via a relationship of the form [20]

$$R_w = R_o[1 + \beta_1(T - T_o) + \beta_2(T - T_o)^2] \tag{15}$$

The quadratic term in Eq. (15) adds only 0.4% to the resistance value over a wide temperature change of 100°C and 0.004% over a temperature change of 10°C [20], and therefore, the linear part is already very accurate. The requirement for a very thin (5–80 μm in diameter) platinum/tantalum wire is due to the need to obtain a uniform temperature across the cross section of the wire in a time scale that is substantially shorter than the time scale of thermal diffusion to the neighboring fluid (this effect is sometimes mentioned in the literature as the neglect of the heat capacity of the wire for which a correction is usually needed). For platinum having a thermal diffusivity of $\alpha_{\mathrm{Pt}}=2.6\times10^{-5}$ m^2/s [21] and a micrometer size wire radius (4.81×10^{-5} m) the transient within the wire will disappear within ~0.1 ms, and therefore, the readings that are being taken at times that are much longer than 0.1 ms ($t\gg0.1$ ms) correspond to a uniform temperature over the wire's cross section.

A Wheatstone bridge is used to measure the electrical resistance R_w of the platinum/tantalum wire. The electrical resistance of a potentiometer R_3 is adjusted until the reading of the galvanometer G shows zero current. When the bridge is balanced, as indicated by a zero current reading on the galvanometer G, the value of R_w can be established from the known electrical resistances R_1, R_2, and R_3 by using the balanced Wheatstone bridge relationship $R_w = R_1R_3/R_2$.

Because of the very small diameter (micrometer size) and high thermal conductivity of the platinum/tantalum wire, the latter can be regarded as a line heat source in an otherwise infinite cylindrical medium qualifying for application of the analytical solution presented in Sec. 2 in Eq. (14). The rate of heat generated per unit length (L) of the platinum wire is therefore $\dot{q}_L = iV/L = i^2R_w/L$ (W m^{-1}), where i is the electric current flowing through the wire, V is the voltage drop across the wire, and R_w is the wire's electrical resistance. The closed form temperature solution presented in Eq. (14) can be expanded in an infinite series as follows

$$T = \frac{\dot{q}_L}{4\pi k}\mathrm{Ei}\left(\frac{r_*^2}{4\alpha t_*}\right) = \frac{\dot{q}_L}{4\pi k}\left[-\gamma_{\mathrm{Eu}} + \ln\left(\frac{4\alpha t_*}{r_*^2}\right) + \frac{r_*^2}{4\alpha t_*} - \frac{r_*^4}{64\alpha^2 t_*^2} + \frac{r_*^6}{1152\alpha^3 t_*^3} - \cdots\right] \tag{16}$$

where $\mathrm{Ei}(\bullet)$ represents the exponential integral function and $\gamma_{\mathrm{Eu}} = \ln(\sigma_{\mathrm{Eu}}) = 0.5772156649$ is Euler's constant. For a line heat source embedded in a cylindrical cell of infinite radial extent and filled with the target fluid, one can use the approximation $r_*^2/4\alpha t_* \ll 1$ in Eq. (16) to truncate the infinite series and yield

$$T \approx \frac{i^2R_w}{4\pi kL}\left[-\gamma_{\mathrm{Eu}} + \ln\left(\frac{4\alpha t_*}{r_*^2}\right) + O\left(\frac{r_*^2}{4\alpha t_*}\right)\right] \tag{17}$$

where we replaced the heat source with its explicit dependence on i, R_w, and L, i.e., $\dot{q}_L = i^2R_w/L$. Equation (17) reveals a linear relationship, on a logarithmic time scale, between the temperature and time. Therefore, one way of evaluating the thermal conductivity is from the slope of this relationship evaluated at $r_* = r_w$, for example, in the form

$$T \approx \frac{i^2R_w}{4\pi kL}\left[\ln(t_*) - \gamma_{\mathrm{Eu}} - \ln\left(\frac{r_w^2}{4\alpha}\right) + O\left(\frac{r_*^2}{4\alpha t_*}\right)\right] \tag{18}$$

where it is evident that the thermal conductivity can be evaluated from the slope of this line on a logarithmic time scale, and the effect of the thermal diffusivity is isolated on the y-intersect only. For $r_* = r_w$ the condition for the series truncation $r_w^2/4\alpha t_* \ll 1$ can be expressed in the following equivalent form that provides the validity condition of the approximation in the form

$$t_* \gg t_{o^*} = \frac{r_w^2}{4\alpha} \tag{19}$$

The value of $t_{o^*} = r_w^2/4\alpha$ provides a validity condition of the experimental readings, i.e., $t_* \gg t_{o^*}$. For any two readings of temperature T_1 and T_2 recorded at times t_{1^*} and t_{2^*}, respectively, the temperature difference $(T_2 - T_1)$ can be approximated by using Eq. (17), as long as the latter validity condition is fulfilled, in the form

$$(T_2 - T_1) \approx \frac{i^2R_w}{4\pi kL}\left[\ln\left(\frac{t_{2^*}}{t_{1^*}}\right)\right] \tag{20}$$

From Eq. (20) one can express the thermal conductivity k explicitly in the form

$$k \approx \frac{i^2R_w}{4\pi(T_2 - T_1)L}\left[\ln\left(\frac{t_{2^*}}{t_{1^*}}\right)\right] \tag{21}$$

Equation (21) (which does not include the thermal diffusivity) is a very accurate way of estimating the thermal conductivity, as long as the validity conditions for applying the derivations used above are fulfilled. A finite length of the platinum wire, the finite size of the cylindrical container, the heat capacity of the platinum/tantalum wire, and possibly, the natural convection effects are examples of the possible deviations of any realistic system from the one used in deriving Eq. (21). De Groot et al. [2], Healy et al.

[3], and Kestin and Wakeham [4] introduced an assessment of these deviations and possible corrections to the THW readings to improve the accuracy of the results. In general all the deviations indicated above could be eliminated via the proposed corrections, provided that the validity condition listed in Eq. (19) is enforced as well as an additional condition that ensures that natural convection is absent or its effect on heat transfer is negligibly small. The validity condition (19) implies the application of Eq. (21) for long times only. However, when evaluating this condition (19) to the data used in the nanofluid suspension experiments one obtains explicitly the following values. For a diameter of 76.2 μm of platinum wire used by Eastman et al. [13], Lee et al. [22], Choi et al. [14], and an electrical insulation coating thickness of 10 μm, the wire radius is $r_w=4.81\times10^{-5}$ m, producing $t_{o^*}=r_w^2/4\alpha=13.7$ ms for ethylene glycol and $t_{o^*}=r_w^2/4\alpha=7.2$ ms for oil, leading to the validity condition $t_*\gg13.7$ ms for ethylene glycol and $t_*\gg7.2$ ms for oil. The long times beyond which the solution (21) can be used reliably are therefore of the order of hundreds of milliseconds, not so long in the actual practical sense. On the other hand the experimental time range is limited from the above as well in order to ensure the lack of natural convection that develops at longer time scales. Xuan and Li [23] estimated this upper limit for the time that an experiment may last before natural convection develops at about 5s. They indicate that "*An experiment lasts about 5s. If the time is longer, the temperature difference between the hot-wire and the sample fluid increases and free convection takes place, which may result in errors.*" Lee et al. [22], while using the THW method and providing experimental data in the time range of 1 s and 10 s, indicated in their Fig. 3 the "*valid range of data reduction*" to be between 3 s and 6 s. Our estimations evaluated above confirm these lower limits as a very safe constraint, and we assume that the upper limits listed by Xuan and Li [23] and Lee et al. [22] are also good estimates. Within this time range the experimental results should produce a linear relationship, on a logarithmic time scale, between the temperature and time.

4 Problem Formulation for Two-Phase Systems

Inherent assumptions for the existence of an effective thermal conductivity for two-phase systems such as porous insulating foams [15,16] having properties that are similar to homogeneous materials are being made even without mentioning them. The practice of using the terminology "effective thermal conductivity" over the years yielded a "tradition" of not even challenging its existence—a natural internalization but rather incorrect. A direct result of this practice is the obvious application of single-phase measurement methods to porous media. In addition to the important question raised above, and to compensate for the possibility that such an accurate representation of the effective thermal conductivity has its limitations, the averaging concept can be applied by defining a representative elementary volume (REV) and averaging the dependent variables over this REV. The resulting effect in addition to the heat transferred within each phase is the heat conduction over the interface separating the two phases (interphase heat transfer). Evaluating this heat transfer is possible for regular geometries, such as the spherical one used by Maxwell [24], Batchelor [25], Batchelor and Green [26], Jeffrey [27], Davis [28], Lu and Lin [29], and Bonnecaze and Brady [30,31], or their extensions [32]; however, it becomes increasingly more difficult as the geometry becomes more complicated. Heat conduction in porous media subject to the lack of local thermal equilibrium (LaLotheq) is governed at the macrolevel by the following equations that represent averages over each phase within a REV

$$\gamma_s\frac{\partial T_s}{\partial t_*}=k_s\nabla_*^2T_s-Q_{sf} \tag{22}$$

$$\gamma_f\frac{\partial T_f}{\partial t_*}=k_f\nabla_*^2T_f+Q_{sf} \tag{23}$$

where Q_{sf} represents the rate of heat generation in the fluid phase within the REV due to the heat transferred over the fluid-solid interface, T_s, T_f, γ_s, γ_f, k_s, and k_f are the average temperatures, effective heat capacities, and effective thermal conductivities of the solid and fluid phases, respectively. The traditional formulation of the rate of heat generation in the fluid phase within the REV due to the heat transferred over the fluid-solid interface uses a linear relationship between Q_{sf} and the average temperature difference between the phases in the form $Q_{sf}=h(T_s-T_f)$. In this discussion one can assume that h is an independent property, while in reality h depends on the thermal conductivities and heat capacities of both phases, on the interface heat transfer area A_{sf}, and on other factors. Then, a change in h will occur due to changes in A_{sf}, k_f, k_s, γ_f, and γ_s.

The lack of macroscopic level conduction mechanism in fluid suspensions (with the solid fraction ε being related to the porosity/fluid fraction φ, by $\varepsilon=(1-\varphi)$), i.e., the heat transfer within the solid phase, which is expressed by the fact that the solid particles represent the dispersed phase in the fluid suspension and therefore the solid particles can conduct heat between themselves only via the neighboring fluid, leads to setting $k_s=0$ in Eq. (22). The latter yields from Eqs. (22) and (23) the averaged equations applicable to fluid suspensions. When steady state is accomplished in fluid suspensions $\partial T_s/\partial t_*=\partial T_f/\partial t_*=0$, leading to local thermal equilibrium between the solid and fluid phases, i.e., $T_s(\mathbf{r})=T_f(\mathbf{r})$, a condition that does not necessarily apply in porous media. By using Eqs. (22) and (23) for a line heat source and by introducing the following dimensionless variables $t=t_*h/\gamma_f$, $r^2=r_*^2h/k_f$, $\theta_s=(T_{s^*}-T_o)/(\dot{q}_L/2\pi k_f)$, and $\theta_f=(T_{f^*}-T_o)/(\dot{q}_L/2\pi k_f)$, as needed for the application of the THW method, renders these equations into their corresponding dimensionless form

$$\frac{1}{\chi}\frac{\partial\theta_s}{\partial t}=\frac{1}{\sigma r}\frac{\partial}{\partial r}\left(r\frac{\partial\theta_s}{\partial r}\right)-(\theta_s-\theta_f) \tag{24}$$

$$\frac{\partial\theta_f}{\partial t}=\frac{1}{r}\frac{\partial}{\partial r}\left(r\frac{\partial\theta_f}{\partial r}\right)+(\theta_s-\theta_f) \tag{25}$$

where $\chi=\gamma_f/\gamma_s$, $\sigma=k_f/k_s$, and $\kappa=\alpha_f/\alpha_s=\sigma/\chi$ represent the heat capacity, thermal conductivity, and thermal diffusivity ratios, respectively. Introducing a Boltzmann transformation in the form

$$\eta=\frac{r^2}{4t}=\frac{r_*^2}{4\alpha_f t_*} \tag{26}$$

transforms Eqs. (24) and (25) into the following equivalent, but not self-similar, form

$$t\frac{\partial\theta_s}{\partial t}=\kappa^{-1}\frac{\partial}{\partial\eta}\left(\eta\frac{\partial\theta_s}{\partial\eta}\right)+\eta\frac{\partial\theta_s}{\partial\eta}-\chi t(\theta_s-\theta_f) \tag{27}$$

$$t\frac{\partial\theta_f}{\partial t}=\frac{\partial}{\partial\eta}\left(\eta\frac{\partial\theta_f}{\partial\eta}\right)+\eta\frac{\partial\theta_f}{\partial\eta}+t(\theta_s-\theta_f) \tag{28}$$

5 Leading Order Solution for Two-Phase Systems

The corresponding single-phase Eq. (7) presented in Sec. 2 was self-similar, a result of utmost importance because it is this self-similarity that produced the simple solution expressed by Eq. (14) and made the application of the THW method possible. Nevertheless, Eqs. (27) and (28) produce interesting self-similar solutions for short times $t\ll1$, (and we will see that these are precisely the times that the THW method is focused on), by using the following short time expansion:

$$\theta_i = \theta_i^{(0)} + t\theta_i^{(1)} + t^2\theta_i^{(2)} + O(t^3) \quad \forall\, i = s, f \tag{29}$$

Substituting expansion (29) into Eqs. (27) and (28), and grouping terms having like-powers of t produces a hierarchy of differential equations for each order. Then the equations at leading order (the equations for $\theta_i^{(0)}$) decouple and take the form

$$\kappa^{-1}\frac{d}{d\eta}\left(\eta\frac{d\theta_s^{(0)}}{d\eta}\right) + \eta\frac{d\theta_s^{(0)}}{d\eta} = 0 \tag{30}$$

$$\frac{d}{d\eta}\left(\eta\frac{d\theta_f^{(0)}}{d\eta}\right) + \eta\frac{d\theta_f^{(0)}}{d\eta} = 0 \tag{31}$$

hence, restoring at leading order the single-phase self-similarity at short times, despite the two-phase nature of the problem. The solution to Eqs. (30) and (31) subject to the hot wire boundary conditions $\lim_{r_w\to 0}[r_*(\partial T_i/\partial r_*)]_{r=r_w} = -\dot{q}_L/2\pi k_i$ and $r_*\to\infty: T_i = 0$ for $i = s, f$ converted to the boundary conditions in terms of η and $\theta_i^{(0)}$ in the form

$$\eta\to\infty: \theta_i^{(0)} = 0; \quad \lim_{\eta\to 0}\left(2\eta\frac{d\theta_i^{(0)}}{d\eta}\right)_\eta = -\sigma_i \quad \text{for } i = s, f \tag{32}$$

where $\sigma_i = \sigma = k_f/k_s$ for $i = s$, and $\sigma_i = 1$ for $i = f$, can be obtained by substituting

$$\phi_i = \eta\frac{d\theta_i^{(0)}}{d\eta} \quad \text{for } i = s, f \tag{33}$$

into Eqs. (30) and (31), leading to

$$\frac{d\phi_s}{d\eta} + \kappa\phi_s = 0 \tag{34}$$

$$\frac{d\phi_f}{d\eta} + \phi_f = 0 \tag{35}$$

Direct integration of Eq. (34) yields

$$\phi_s = \eta\frac{d\theta_s^{(0)}}{d\eta} = A_{so}e^{-\kappa\eta} \tag{36}$$

A second integration of Eq. (36) yields

$$\theta_s^{(0)} = A_{so}\int\frac{e^{-\kappa\eta}}{\eta}d\eta + B_{so} \tag{37}$$

After substituting the boundary conditions (32) the solution takes the final form

$$\theta_s^{(0)} = \frac{\sigma}{2}\int_{\kappa\eta}^{\infty}\frac{e^{-\kappa\tilde{\eta}}}{\tilde{\eta}}d\tilde{\eta} = \frac{\sigma}{2}\mathrm{Ei}(\kappa\eta) = \frac{\sigma}{2}\mathrm{Ei}\left(\frac{r_*^2}{4\alpha_s t_*}\right) \tag{38}$$

where $\tilde{\eta}$ is a dummy integration variable. The solution for $\theta_f^{(0)}$ is obtained in an identical way and can be presented in the form

$$\theta_f^{(0)} = \frac{1}{2}\int_{\eta}^{\infty}\frac{e^{-\tilde{\eta}}}{\tilde{\eta}}d\tilde{\eta} = \frac{1}{2}\mathrm{Ei}(\eta) = \frac{1}{2}\mathrm{Ei}\left(\frac{r_*^2}{4\alpha_f t_*}\right) \tag{39}$$

Converting $\theta_i^{(0)}$ back to dimensional form by using the definitions $\theta_s^{(0)} = (T_{s^*}^{(0)} - T_o)/(\dot{q}_L/2\pi k_f)$ and $\theta_f^{(0)} = (T_{f^*}^{(0)} - T_o)/(\dot{q}_L/2\pi k_f)$ leads to the following solutions:

$$(T_{s^*}^{(0)} - T_o) = \frac{\dot{q}_L}{4\pi k_s}\mathrm{Ei}\left(\frac{r_*^2}{4\alpha_s t_*}\right) = \frac{\dot{q}_L}{4\pi k_s}\left[-\gamma_{\mathrm{Eu}} + \ln\left(\frac{4\alpha_s t_*}{r_*^2}\right) + O\left(\frac{r_*^2}{4\alpha_s t_*}\right)\right] \tag{40}$$

$$(T_{f^*}^{(0)} - T_o) = \frac{\dot{q}_L}{4\pi k_f}\mathrm{Ei}\left(\frac{r_*^2}{4\alpha_f t_*}\right) = \frac{\dot{q}_L}{4\pi k_f}\left[-\gamma_{\mathrm{Eu}} + \ln\left(\frac{4\alpha_f t_*}{r_*^2}\right) + O\left(\frac{r_*^2}{4\alpha_f t_*}\right)\right] \tag{41}$$

These solutions can be used to approximate the effective thermal conductivity of the solid and fluid phases, respectively, for any pairs of two temperature readings $(T_{f1^*}^{(0)},\ T_{s1^*}^{(0)})$ and $(T_{f2^*}^{(0)},\ T_{s2^*}^{(0)})$ taken at subsequent times t_{1^*} and t_{2^*}, respectively, after neglecting the terms, which are $O(r_*^2/4\alpha_s t_*)$ and $O(r_*^2/4\alpha_f t_*)$, in the form

$$(T_{s2^*}^{(0)} - T_{s1^*}^{(0)}) = \frac{\dot{q}_L}{4\pi k_s}\left[\ln\left(\frac{4\alpha_s t_{2^*}}{r_*^2}\right) - \ln\left(\frac{4\alpha_s t_{1^*}}{r_*^2}\right)\right] = \frac{\dot{q}_L}{4\pi k_s}\ln\left(\frac{t_{2^*}}{t_{1^*}}\right) \tag{42}$$

$$(T_{f2^*}^{(0)} - T_{f1^*}^{(0)}) = \frac{\dot{q}_L}{4\pi k_f}\left[\ln\left(\frac{4\alpha_f t_{2^*}}{r_*^2}\right) - \ln\left(\frac{4\alpha_f t_{1^*}}{r_*^2}\right)\right] = \frac{\dot{q}_L}{4\pi k_f}\ln\left(\frac{t_{2^*}}{t_{1^*}}\right) \tag{43}$$

The effective thermal conductivities of the solid and fluid phases can be then extracted from Eqs. (42) and (43), and can presented in the form

$$k_s \approx \frac{\dot{q}_L}{4\pi(T_{s2^*}^{(0)} - T_{s1^*}^{(0)})}\left[\ln\left(\frac{t_{2^*}}{t_{1^*}}\right)\right] \tag{44}$$

$$k_f \approx \frac{\dot{q}_L}{4\pi(T_{f2^*}^{(0)} - T_{f1^*}^{(0)})}\left[\ln\left(\frac{t_{2^*}}{t_{1^*}}\right)\right] \tag{45}$$

Note that we obtained here the effective thermal conductivities for each phase, assuming that the wire temperature was affected by that particular phase only. In reality the wire is exposed to both phases in some unknown percentage combination that is a topic for further research based on the approach presented by Vadasz [33–35]. Once the results from such research become available it will provide a simple correction to Eqs. (44) and (45), which could be used directly to evaluate the effective thermal conductivities of each phase accurately. The evaluation of the effective thermal conductivity of the whole two-phase system (assuming it exists for transients too, its existence being proven for steady state by Maxwell [24], subject to certain conditions) forms also the basis for further investigation. Nevertheless, the results presented in Eqs. (44) and (45) demonstrate evidently that the effort in this direction is warranted, and the rendering of the transient hot wire experimental method to two-phase systems is possible.

6 Validity Conditions of the Transient Hot Wire Method for Two-Phase Systems

These results are quite promising because they indicate that the THW method may be applied with some higher order corrections in porous media or nanofluid suspensions as well; however, we need to check the conditions under which the latter applies. Clearly a condition similar to Eq. (19), which is applicable to single-phase, applies here as well as the truncation of Eqs. (40) and (41) requires $t_* \gg t_o$, where the value of the minimum time is $t_o = \max[(r_w^2/4\alpha_f), (r_w^2/4\alpha_s)]$. In addition, the leading order solutions (40) and (41) apply for dimensionless short times only, i.e., for $t = t_* h/\gamma_f \ll 1$. Note also that an inherent, but reasonable, assumption was included in the derivation of the leading order equations (Eqs. (30) and (31)), implying that $\chi = \gamma_f/\gamma_s = O(1)$, i.e., $\gamma_f \sim \gamma_s$ at least in their order of magnitude. Therefore the condition $t = t_* h/\gamma_f \ll 1$ implies $t_* \ll \gamma_f/h$, or similarly $t_* \ll \gamma_s/h$. These conditions specify the range of short times that are needed for the approximated solutions (40) and (41) leading to Eqs. (44) and (45) to be valid. Combining the two conditions above produces

$$t_o \ll t_* \ll t_m \tag{46}$$

where $t_o = \max[(r_w^2/4\alpha_f),(r_w^2/4\alpha_s)]$ and $t_m = \min[(\gamma_f/h),(\gamma_s/h)]$. The requirement that $t_m \gg t_o$, is necessary and sufficient for such a time interval to exist and makes the THW experimental method applicable to two-phase systems. This requirement implies $\gamma_f/h \gg r_w^2/4\alpha_f$ (assuming $\chi = \gamma_f/\gamma_s = O(1)$), leading to

$$h \ll \frac{4k_f}{r_w^2} \tag{47}$$

This condition is the requirement for the existence of a time interval (THW method validity window) over which the THW method may produce reliable results in two-phase applications. It reveals the significant impact that the interface heat transfer coefficient h has the applicability of the THW method to two-phase systems. For example, in the limit of very high values of the interface heat transfer coefficient, e.g., $h \to \infty$ condition (47) can never be satisfied, while for very low values of h, e.g., in the limit of $h \to 0$, it is always satisfied.

In fluid suspensions such as in porous media, the parameter h, carrying units of $\mathrm{W/m^{-3}\,K^{-1}}$, represents an integral heat transfer coefficient for the heat conduction at the solid-fluid interface within an REV. Its general relationship to the surface area-to-volume ratio (specific area) was derived by Vadasz [17] by using relationships that are available for the respective coefficient in fluid saturated porous media [36–41]. Most of the reported evaluations of h in porous media listed above were derived with a particular focus on convection rather than conduction heat transfer. Their applicability and accuracy for conduction are therefore questionable. The implication of the derived relationship presented by Vadasz [17] is that the heat transfer coefficient is related to the particle size by the inversely quadratic relationship $h = [k_f/d_p^2]s(\varepsilon, k_f/k_s)$. While the particular form of the function $s(\varepsilon, k_f/k_s)$ and its possible further dependence on the particle size d_p as well, especially if the particle size is reduced to nanoscale levels, is not established for the case of suspensions, the general dependence of the heat transfer coefficient on the particle size is evident. This dependence of the heat transfer coefficient on the particle size introduces the effect of the surface area-to-volume ratio (specific area), which was claimed by Eastman et al. [13] to be missing in the classical models of evaluating the effective thermal conductivity of the suspension. One should, however, bear in mind that further dependence on the particle size might be anticipated, as the particle size is reduced to the nanoscale level, implying a consequential reduction in the value of h to somewhat compensate for the otherwise substantial increase in h as the particle size is reduced.

7 Conclusions

Simple analytical expressions to be used with the application of the transient hot wire method in two-phase systems were derived as leading order approximations. The validity conditions impose restrictions on the value of the interface heat transfer coefficient in two-phase systems, a condition that was nonexistent in the corresponding single-phase application. More work is needed in three distinct directions in order to allow one to make a definite conclusion on the feasibility of rendering the THW method to two-phase systems. The first direction is to derive a method for independent evaluation of the interface heat transfer coefficient, hence transforming the validity condition into a practical method to assess and design the experimental procedure. Presently not knowing how to estimate the value of h becomes an impediment in enforcing such a condition in any experiment. The second direction is linked with the development of a method that indicates in what precise combination each phase present affects the wire's temperature by using an approach suggested by Vadasz [33–35]. The third one suggests producing the complete theoretical solution to the present two-phase problem at higher orders and deriving the validity conditions for such solutions too. It is anticipated that including higher order solutions in the analysis may relax some of the limitations obtained at the leading order in terms of the restricted validity conditions.

Nomenclature

Latin Symbols

- A = cross sectional area of the wire ($\mathrm{m^2}$)
- A_{sf} = solid-fluid interface heat transfer area ($\mathrm{m^2}$)
- c_p = fluid's specific heat for the single phase (J/kg K) (dimensional)
- $c_{p,f}, c_s$ = fluid and solid phases specific heat, respectively, (J/kg K) (dimensional)
- Ei = exponential integral function
- h = integral heat transfer coefficient for the heat conduction at the solid-fluid interface, ($\mathrm{W/m^3\,K}$) (dimensional)
- i = electric current passing through the wire (A)
- i_s = electric current supplied by the source (A)]
- k = thermal conductivity of the fluid for the single phase (W/m K) (dimensional)
- k_s = effective thermal conductivity of the solid phase, equals $(1-\varphi)\tilde{k}_s$ (W/m K) (dimensional)
- $\tilde{k}_s$ = thermal conductivity of the solid phase (W/m K) (dimensional)
- k_f = effective thermal conductivity of the fluid phase, equals $\varphi\tilde{k}_f$ (W/m K) (dimensional)
- $\tilde{k}_f$ = thermal conductivity of the fluid phase, (W/m K) (dimensional)
- L = the length of the wire (m)
- $\dot{q}_L$ = amount of heat generated per unit length of wire (W/m)
- q_{r^*} = radial component of the heat flux ($\mathrm{W/m^2}$)
- $\boldsymbol{q}$ = heat flux vector ($\mathrm{W/m^2}$) (dimensional)
- Q_{sf} = rate of heat generation in the fluid phase due to the heat transferred over the fluid-solid interface, ($\mathrm{W/m^3}$)
- r_* = radial coordinate (m) (dimensional)
- r = dimensionless radial coordinate, equals $r_*/\sqrt{k_f/h}$
- r_w = wire's radius (m) (dimensional)
- R = electrical resistance (Ω) (dimensional)
- R_w = electrical resistance of the wire (Ω)
- R_o = a reference value of the electrical resistance (Ω)
- R_1, R_2 = fixed electrical resistances in the Wheatstone bridge (Ω)
- R_3 = variable electrical resistance (Ω) (potentiometer) in the Wheatstone bridge
- t_* = time (s) (dimensional)
- t = dimensionless time, equals $t_* h/\gamma_f$
- T = temperature, equals $(T_* - T_o)$ (K) (dimensional)
- T_C = coldest boundary temperature (K) (dimensional)
- V = voltage drop across the wire (V)
- z_* = vertical coordinate (m) (dimensional)

Greek Symbols

- α = fluid's thermal diffusivity for the single phase, equals $k/\rho c_p$ ($\mathrm{m^2/s}$) (dimensional)
- α_f = fluid phase effective thermal diffusivity, equals k_f/γ_f ($\mathrm{m^2/s}$) (dimensional)
- α_s = solid phase effective thermal diffusivity, equals k_s/γ_s ($\mathrm{m^2/s}$) (dimensional)

χ = heat capacity ratio, equals γ_f/γ_s
γ_s = solid phase effective heat capacity, equals $(1-\varphi)\rho_s c_s$ (dimensional)
γ_f = fluid phase effective heat capacity, equals $\varphi\rho_f c_{p,f}$ (dimensional)
γ_{Eu} = Euler's constant, equals 0.5772156649
ε = solid fraction, equals $(1-\varphi)$
θ_s = dimensionless solid phase temperature, equals $(T_{s^*}-T_o)/(\dot{q}_L/2\pi k_f)$
θ_f = dimensionless fluid phase temperature, equals $(T_{f^*}-T_o)/(\dot{q}_L/2\pi k_f)$
φ = porosity/fluid fraction (dimensionless)
ϕ = dependent variable following the transformation $\phi=\eta(\partial T/\partial\eta)$
ρ_e = electrical resistivity of the wire (Ω m)
ρ = fluid's density for single phase (kg/m^3)
ρ_f = fluid phase density (kg/m^3)
ρ_s = solid phase density (kg/m^3)
σ = thermal conductivity ratio, equals k_f/k_s (dimensionless)
η = similarity variable, equals $r_*^2/4\alpha t_*$ (dimensionless)
κ = thermal diffusivity ratio, equals $\alpha_f/\alpha_s=\sigma/\chi$ (dimensionless)

Subscripts

* = corresponding to dimensional values, except for cases where there is no ambiguity, as listed in this nomenclature
s = related to the solid phase
f = related to the fluid phase

References

[1] Hammerschmidt, U., and Sabuga, W., 2000, "Transient Hot Wire (THW) Method: Uncertainty Assessment," Int. J. Thermophys., **21**, pp. 1255–1278.
[2] De Groot, J. J., Kestin, J., and Sookiazian, H., 1974, "Instrument to Measure the Thermal Conductivity of Gases," Physica (Amsterdam), **75**, pp. 454–482.
[3] Healy, J. J., de Groot, J. J., and Kestin, J., 1976, "The Theory of the Transient Hot-Wire Method for Measuring Thermal Conductivity," Physica C, **82**, pp. 392–408.
[4] Kestin, J., and Wakeham, W. A., 1978, "A Contribution to the Theory of the Transient Hot-Wire Technique for Thermal Conductivity Measurements," Physica A, **92**, pp. 102–116.
[5] Assael, M. J., Dix, M., Gialou, K., Vozar, L., and Wakeham, W. A., 2002, "Application of the Transient Hot-Wire Technique to the Measurement of the Thermal Conductivity of Solids," Int. J. Thermophys., **23**, pp. 615–633.
[6] Assael, M. J., and Gialou, K., 2003, "A Transient Hot Wire Instrument for the Measurement of the Thermal Conductivity of Solids up to 590 K," Int. J. Thermophys., **24**, pp. 667–674.
[7] Nagasaka, Y., and Nagashima, A., 1981, "Absolute Measurement of the Thermal Conductivity of Electrically Conducting Liquids by the Transient Hot-Wire Method," J. Phys. E, **14**, pp. 1435–1440.
[8] Assael, M. J., Chen, C.-F., Metaxa, I., and Wakeham, W. A., 2004, "Thermal Conductivity of Suspensions of Carbon Nanotubes in Water," Int. J. Thermophys., **25**, pp. 971–985.
[9] Assael, M. J., and Gialou, K., 2003, "Measurement of Thermal Conductivity of Stainless Steel AISI 304L up to 590 K," Int. J. Thermophys., **24**, pp. 1145–1153.
[10] Assael, M. J., Gialou, K., Kakosimos, K., and Metaxa, I., 2004, "Thermal Conductivity of Reference Solid Materials," Int. J. Thermophys., **25**, pp. 397–408.
[11] Assael, M. J., Antoniadis, K. D., Kakosimos, K., and Metaxa, I. N., 2008, "An Improved Application of the Transient Hot-Wire Technique for the Absolute Accurate Measurement of the Thermal Conductivity of Pyroceram 9606 Up to 420 K," Int. J. Thermophys., **29**, pp. 445–456.
[12] de Groot, J. J., Kestin, J., Sookiazian, H., and Wakeham, W. A., 1978, "The Thermal Conductivity of Four Monatomic Gases as a Function of Density Near Room Temperature," Physica A, **92**, pp. 117–144.
[13] Eastman, J. A., Choi, S. U. S., Li, S., Yu, W., and Thompson, L. J., 2001, "Anomalously Increased Effective Thermal Conductivities of Ethylene Glycol-Based Nanofluids Containing Copper Nanoparticles," Appl. Phys. Lett., **78**, pp. 718–720.
[14] Choi, S. U. S., Zhang, Z. G., Yu, W., Lockwood, F. E., and Grulke, E. A., 2001, "Anomalous Thermal Conductivity Enhancement in Nanotube Suspensions," Appl. Phys. Lett., **79**, pp. 2252–2254.
[15] Coquard, R., and Bailis, D., 2006, "Modeling of Heat Transfer in Low-Density EPS Foams," ASME J. Heat Transfer, **128**, pp. 538–549.
[16] Coquard, R., and Bailis, D., 2006, "Experimental and Theoretical Study of the Hot-Wire Method Applied to Low-Density Thermal Insulators," Int. J. Heat Mass Transfer, **49**, pp. 4511–4524.
[17] Vadasz, P., 2006, "Heat Conduction in Nanofluid Suspensions," ASME J. Heat Transfer, **128**, pp. 465–477.
[18] Carslaw, H. S., and Jaeger, J. C., 1946, *Conduction of Heat in Solids*, 2nd ed., Oxford University Press, New York.
[19] Özisik, M. N., 1993, *Heat Conduction*, 2nd ed., Wiley, New York.
[20] Bentley, J. P., 1984, "Temperature Sensor Characteristics and Measurement System Design," J. Phys. E, **17**, pp. 430–439.
[21] Martinsons, C., Levick, A., and Edwards, G., 2001, "Precise Measurements of Thermal Diffusivity by Photothermal Radiometry for Semi-Infinite Targets Using Accurately Determined Boundary Conditions," Anal. Sci., **17**, pp. 114–117.
[22] Lee, S., Choi, S. U.-S., Li, S., and Eastman, J. A., 1999, "Measuring Thermal Conductivity of Fluids Containing Oxide Nanoparticles," ASME J. Heat Transfer, **121**, pp. 280–289.
[23] Xuan, Y., and Li, Q., 2000, "Heat Transfer Enhancement of Nanofluids," Int. J. Heat Flow Fluid, **21**, pp. 58–64.
[24] Maxwell, J. C., 1891, *A Treatise on Electricity and Magnetism*, 3rd ed., Clarendon, Oxford, pp. 435–441.
[25] Batchelor, G. K., 1972, "Sedimentation in a Dilute Dispersion of Spheres," J. Fluid Mech., **52**, pp. 245–268.
[26] Batchelor, G. K., and Green, J. T., 1972, "The Hydrodynamic Interaction of Two Small Freely-Moving Spheres in a Linear Flow Field," J. Fluid Mech., **56**, pp. 375–400.
[27] Jeffrey, D. J., 1973, "Conduction Through a Random Suspension of Spheres," Proc. R. Soc. London, Ser. A, **335**, pp. 355–367.
[28] Davis, R. H., 1986, "The Effective Thermal Conductivity of a Composite Material With Spherical Inclusions," Int. J. Thermophys., **7**, pp. 609–620.
[29] Lu, S., and Lin, H., 1996, "Effective Conductivity of Composites Containing Aligned Spheroidal Inclusions of Finite Conductivity," J. Appl. Phys., **79**, pp. 6761–6769.
[30] Bonnecaze, R. T., and Brady, J. F., 1991, "The Effective Conductivity of Random Suspensions of Spherical Particles," Proc. R. Soc. London, Ser. A, **432**, pp. 445–465.
[31] Bonnecaze, R. T., and Brady, J. F., 1990, "A Method for Determining the Effective Conductivity of Dispersions of Particles," Proc. R. Soc. London, Ser. A, **430**, pp. 285–313.
[32] Hamilton, R. L., and Crosser, O. K., 1962, "Thermal Conductivity of Heterogeneous Two-Component Systems," I&EC Fundamentals, **1**, pp. 187–191.
[33] Vadasz, P., 2007, "Rendering the Transient Hot Wire Experimental Method to Dual-Phase Applications," *Proceedings of the Fifth International Conference on Heat Transfer, Fluid Mechanics and Thermodynamics (HEFAT), Sun City, South Africa*, Paper No. HEFAT2007-K2.
[34] Vadasz, P., 2007, "Rendering the Transient Hot Wire Experimental Method to Dual-Phase Applications," ASME Paper No. IMECE2007-41071.
[35] Vadasz, P., 2007, "Rendering the Transient Hot Wire Experimental Method to Porous Media Applications," *Proceedings of the Second International Conference on Porous Media and Its Applications in Science Engineering and Industry*, Kauai, HI.
[36] Quintard, M., and Whitaker, S., 1995, "Local Thermal Equilibrium for Transient Heat Conduction: Theory and Comparison With Numerical Experiments," Int. J. Heat Mass Transfer, **38**, pp. 2779–2796.
[37] Alazmi, B., and Vafai, K., 2002, "Constant Wall Heat Flux Boundary Conditions in Porous Media Under Local Thermal Non-Equilibrium Conditions," Int. J. Heat Mass Transfer, **45**, pp. 3071–3087.
[38] Amiri, A., and Vafai, K., 1994, "Analysis of Dispersion Effects and Non-Thermal Equilibrium, Non-Darcian, Variable Porosity Incompressible Flow Through Porous Media," Int. J. Heat Mass Transfer, **37**, pp. 939–954.
[39] Wakao, N., Kaguei, S., and Funazkri, T., 1979, "Effect of Fluid Dispersion Coefficients on Particle-to-Fluid Heat Transfer Coefficients in Packed Beds," Chem. Eng. Sci., **34**, pp. 325–336.
[40] Wakao, N., and Kaguei, S., 1982, "Effect of Fluid Dispersion Coefficients on Particle-to-Fluid Heat Transfer Coefficients in Packed Beds," *Heat and Mass Transfer in Packed Beds*, Gordon and Breach, New York.
[41] Kuwahara, F., Shirota, M., and Nakayama, A., 2001, "A Numerical Study of Interfacial Convective Heat Transfer Coefficient in Two-Energy Equation Model for Convection in Porous Media," Int. J. Heat Mass Transfer, **44**, pp. 1153–1159.

Manuel Daniel-Leal
e-mail: manuel.daniel@ciemat.es

Luciano Romero-Barajas
e-mail: luciano.romero@ciemat.es

CIEMAT,
Avenida Complutense 22,
28040 Madrid, Spain

Jose L. Perez-Diaz[1]
Mem. ASME
Departamento Ingenieria Mecanica,
Universidad Carlos III,
Avenida Universidad 30,
28911 Leganes, Spain

Thermal Conductance of a Multilayer Drift Chamber: An Experimental Approach

Drift chambers in the compact muon solenoid (CMS) detector are piled modular structures joined together by a structural adhesive. This structure is used for the detection and tracking of high energy particles—particularly muons. According to Fourier's law, the conductance of a multilayered drift chamber prototype can be measured using a simple device based on the thermal transience between two heat sinks. The heat gradients in the global CMS detector in operation at the European Council for Nuclear Research are estimated in this way. The resultant values are used to determine whether to include a forced cooling device in the CMS. [DOI: 10.1115/1.4001103]

Keywords: thermal conductance, thermal transient, multilayer, drift chamber

1 Introduction

The compact muon solenoid (CMS) is a hermetic muon spectrometer with a large geometric acceptance, recently installed at the large hadron collider (LHC) at the European Council for Nuclear Research (CERN). The excellent resolution of the energy and momentum measurements of CMS rely on a high precision mechanical design and good control over any kind of distortion. In particular, thermal gradients and any associated deformities must be kept under strict control. Drift chambers in the CMS detector (Fig. 1) are piled modular structures joined together by a structural adhesive. They comprise several multilayers and a rigidizer panel (Fig. 2). Every multilayer consists of four drift tubes layered over one another. The cells in a layer are rotated half their width, in relation to their closest neighbor.

A layer consists of a flat set of drift cells, with two aluminum plates on either side, and parallel aluminum beams at intervals. A drift cell is the volume between two consecutive beams of the same layer (Fig. 3).

The CMS detector is compact, and heat is generated by the detection electronics inside it. This heat has to be extracted in order for the detector to function correctly.

This paper details the design and manufacture of a prototype drift chamber that can measure its own thermal conductance and determine the need for a forced cooling device in the CMS detector. The measurements gathered from this prototype have also been used to assess the precision of the drift chambers in the CMS detector.

The electronics associated with drift chambers, in particular, the amplifiers, generate an intense flow of heat that must be extracted. It is estimated that the front-end electronics (Fig. 4) generate 50 mW per channel. The power of all associated electronics generate up to 100 mW. The largest chambers in CMS have a thousand channels, therefore, one such chamber dissipates 100 W [1,2].

Not only may thermal expansion disrupt the performance of the detector, but this heat may also affect the mechanical structure, as it is comprised of different modules joined together with adhesive (araldite 2012). This adhesive looses its mechanical properties at between 200°C and 300°C [3].

2 Description

The complexity of the thermal behavior of the honeycomb-like modules and the layered structure makes it difficult to either calculate or estimate theoretically the overall conductance of the drift chambers. Therefore, a method was devised, designed to enable the measurement of heat conductance with adequate precision. The experimental device, as shown in Fig. 5, consisted of the following.

- Two prismatic and sealed reservoirs made of aluminum. They measured $400\times400\times50$ mm^3 and had two holes for the inlet and outlet of water. Each one had six temperature sensors AD592AN [4] located on one side (Fig. 6), and were installed on an aluminum base (Fig. 7). The sensors were accurate to within 0.35°C.
- Two multilayers made of four layers, each with nine 40 $\times10$ mm^2 drift cells. One was made with 40 beams fixed with isolating strips all along both sides. The other had no isolating strips.
- A prismatic honeycomb aluminum rigidizer measuring 400 $\times400\times50$ mm^3. Four isolating polystyrene plates of 50 mm, two measuring 400×400 mm^2, and a further two of 400×500 mm^2. The fully assembled experimental model—excluding the isolating plates—is shown in Fig. 8. The two isolating plates not shown were placed on the front and

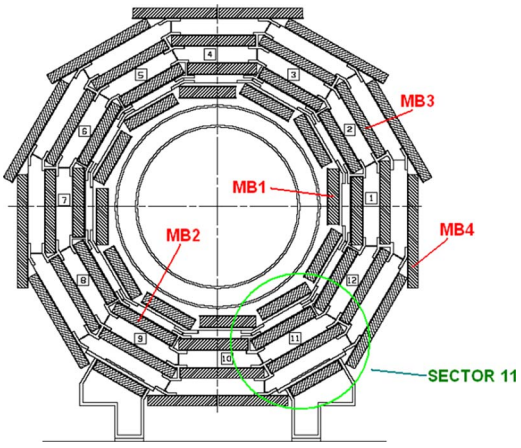

Fig. 1 Sector distribution in the drift chambers in CMS

[1]Corresponding author.

Contributed by the Heat Transfer Division of ASME for publication in the JOURNAL OF HEAT TRANSFER. Manuscript received September 14, 2009; final manuscript received December 27, 2009; published online June 4, 2010. Assoc. Editor: Pamela M. Norris.

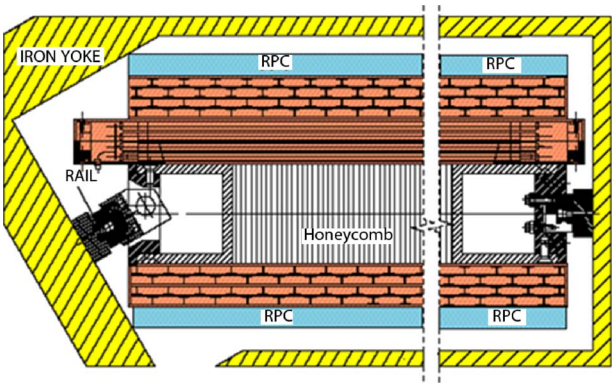

Fig. 2 MB2 type drift chamber mounted in CMS

back. These plates also covered the top and bottom of the device in order to make the system adiabatic.

3 Method

The experiment measured the temperature change over time when the reservoirs were filled with water at different temperatures—T_1 and T_2. Heat flowed from the hotter reservoir to the cooler one until the temperatures were the same.

Hot (A) and cool (B) reservoirs are shown schematically in Fig. 9. Using Fourier's law [5], the expression for thermal jump is

$$T_1 - T_2 = e^{-\alpha t} \tag{1}$$

where

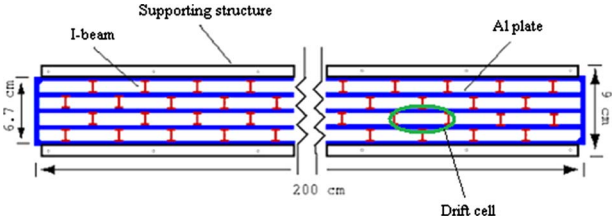

Fig. 3 Cross section of a multilayer. The plates and the beams are the boundaries of the drift cells, which are full of air.

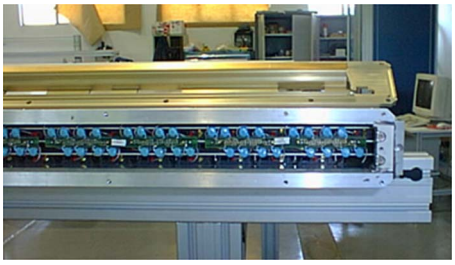

Fig. 4 Front end electronics instrumentation

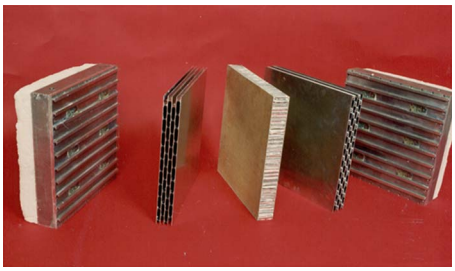

Fig. 5 Modules of the prototype

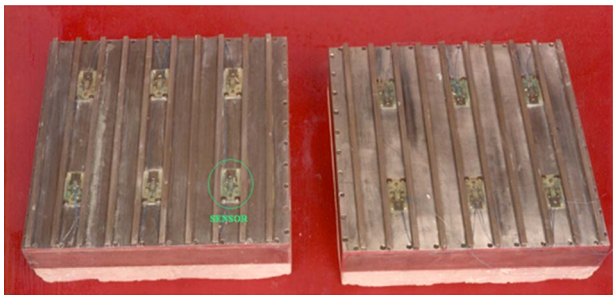

Fig. 6 Location of the sensors in the reservoirs

$$\alpha = \frac{2\lambda}{C} \tag{2}$$

and

$$\lambda = \frac{kA}{L} \tag{3}$$

where λ is the total thermal conductance, k is the thermal conductivity, A is the cross section, L is the length, C is the heat capacity, and t is the time. This thermal capacity C was estimated using the known masses of water and aluminum (7.647 ± 0.001 kg and 0.428 ± 0.001 kg, respectively), and their tabulated specific thermal capacities [6]: $c_{p\ \text{water}} = 4.18$ kJ/kg K and $c_{p\ \text{Al.}} = 0.897$ kJ/kg K.

The experiment was designed to establish the conductance of the different modules and their combinations by measuring the

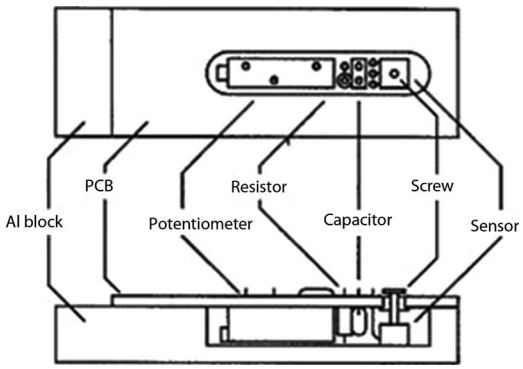

Fig. 7 Sensor module

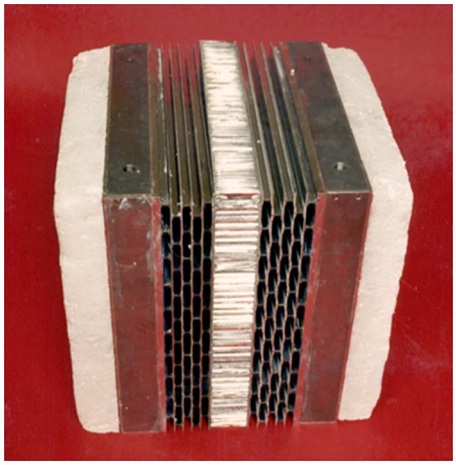

Fig. 8 Assembled experimental device

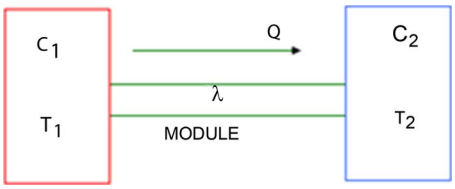

Fig. 9 Schematic diagram showing the heat flow

temperatures of the water reservoirs at different times (t). Initially, a reservoir was filled with hot water (50°C), and the other with fresh water.

Equation (1) shows a typical decreasing exponential evolution, and therefore, the jump in temperature is a sloping straight line $-\alpha$ (2) when shown using a logarithmic scale for the ordinates. Using the (standard and well-known) mean squares method to determine the slope, a precise calculation of the conductance can be achieved for the individual modules, and ultimately for the whole system (3), as shown in Fig. 10. This last combination is similar to that of a chamber in the CMS detector.

3.1 Calibration. In order to calibrate this device, the conductance of the reservoirs, including conduction and convection, was ascertained by joining them together (Fig. 11). Having completed this calibration, the units were separated, and the experiment was carried out, following standard procedures. The thermal resistance, calculated as the inverse of the conductance, can then be used to calculate the conductance of the modules and the chamber.

Figure 12 shows both the jump in temperature and the mean temperature in a logarithmic scale versus time. Ideally the mean temperature should remain constant. In fact, it slightly decreases because the system is not entirely adiabatic—there is a small heat flow through the isolation plates. Thus, a precision of less than 2% is assured.

The conductance may be calculated using Eq. (2), where α is the slope from Fig. 12, and can be written as

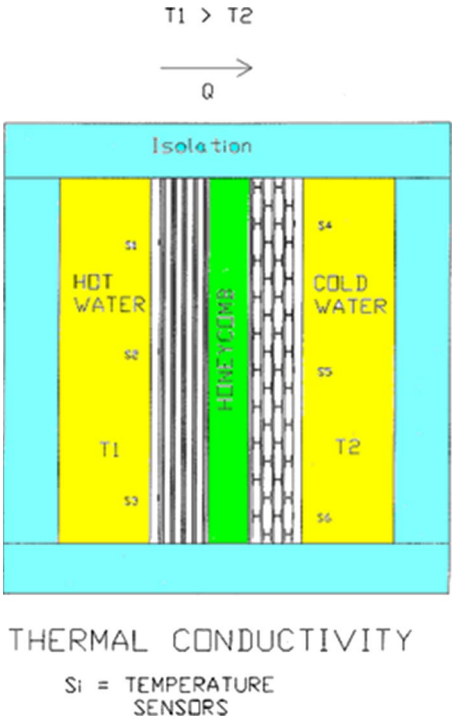

Fig. 10 Cross section of the prototype in the experimental device

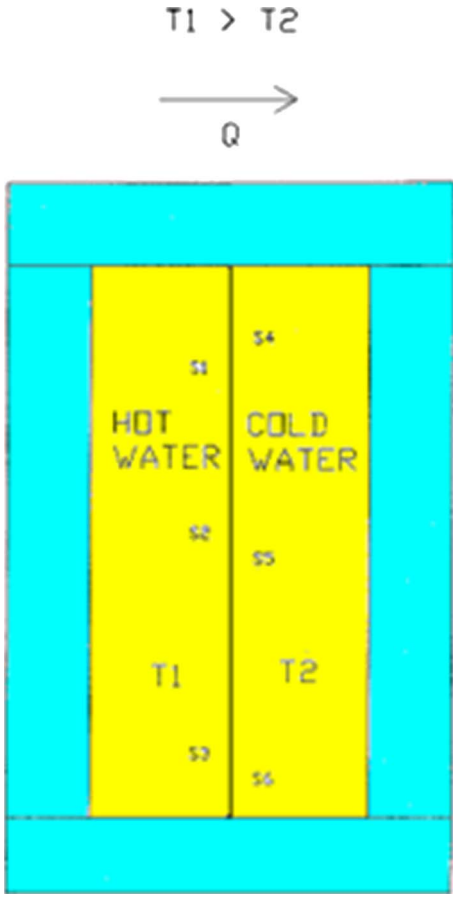

Fig. 11 Device for measuring the conductance of the thermal reservoirs

$$\frac{\ln(T_1 - T_2)}{t_2 - t_1} = \alpha \tag{4}$$

The results were

$$\propto = 4.20 \pm 0.07 \times 10^{-4}\ \mathrm{S}^{-1}$$

and the total conductance

$$\lambda = 6.79 \pm 0.12\ \mathrm{W/°C}$$

for the reservoirs.

3.2 Conductance of the Modules. Figure 13 shows the electrical circuit analog to the system when measuring the conductance of a modulus. R_0 is the thermal resistance of the reservoirs and R_M is the resistance of the modulus being tested.

Figure 14 shows the thermal jump versus time for a modulus (with and without isolating strips) and for the honeycomb rigidizer spacer. The resulting values of these three tests are shown in Table 1. The heat capacity of the modules has been calculated separately for each of the different components that they comprise.

The effect of the isolating strips clearly shows a fourfold decrease in the thermal conductance of the modulus. Partly, as a result of this, the isolating strips were entirely removed from the final design condition.

After the conductance of each module was established, the overall conductance of a chamber in CMS was calculated, which is composed of three modules without isolating strips and two honeycomb rigidizer spacers. This can be written as

$$\frac{1}{\lambda_c} = \frac{3}{\lambda_{SA}} + \frac{2}{\lambda_H} \tag{5}$$

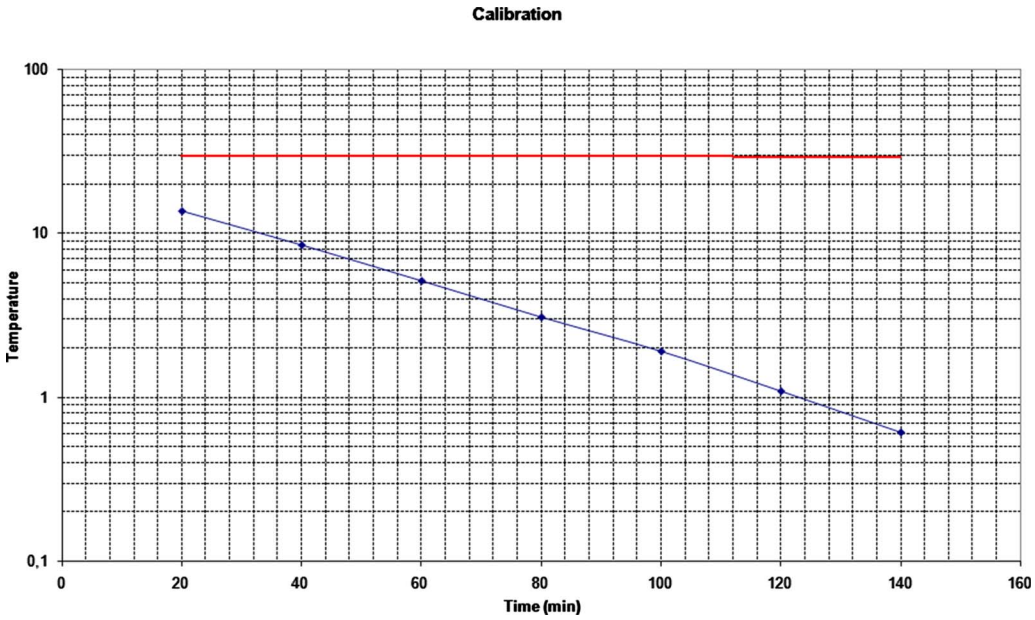

Fig. 12 $\ln(T_1 - T_2)$ and $\ln(T_1 + T_2)$ versus time in the calibration with the reservoirs

where λ_c is the total conductance of the chamber.

Using the values in Table 1, the total conductance of the chamber was found to be

$$\lambda_C = 0.59 \pm 0.02 \ \ \mathrm{W/^\circ C}$$

As the effective area for the heat flow was 400.0×400.0 mm^2, the specific conductance can be calculated as the ratio between the total conductance and area, giving

$$\zeta = 3.71 \pm 0.15 \ \ \mathrm{W/^\circ C\ m^2}$$

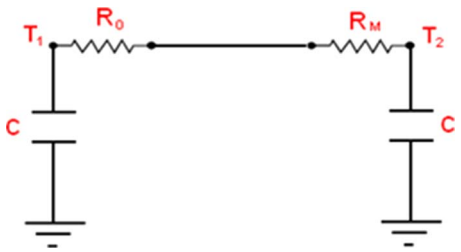

Fig. 13 Scheme of the system when measuring the conductance of a module

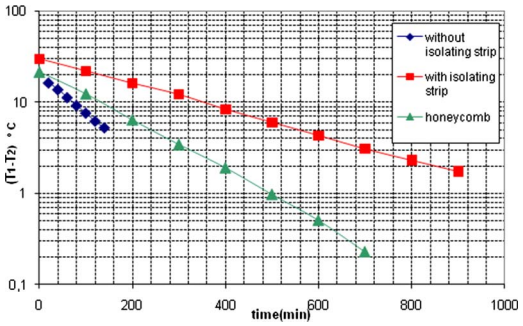

Fig. 14 Temperature jump versus time for a module with isolating strips between the aluminum beams and the plates, for a module without isolating strips and for a module with a honeycomb spacer

4 Application to the CMS Thermal Design

The whole thermal gradient in the CMS detector can be determined using the results of these experiments. The CMS diameter is 15 m. The muon chambers are placed in layers around the vacuum tube where the beams travel (Figs. 15–17).

By assuming that the layers of chambers are concentric around the point of interaction, Fig. 17 acts as an accurate representation of the drift chamber.

The dimensions of the chambers in the four layers are different, as shown in Table 2. They are called MB1, MB2, MB3, and MB4, respectively (Fig. 17).

The design of the analog circuit is shown in Fig. 18. The heat flow through S_1 at every MB1 chamber can be estimated as

Table 1 Total conductance of the different modules

Module	Total conductance (W/°C)
Multilayered module without isolating strips	$\lambda_{SA} = 3.9 \pm 0.1$
Multilayered module with isolating strips	$\lambda_{CA} = 1.01 \pm 0.03$
Honeycomb rigidizer spacer	$\lambda_H = 2.19 \pm 0.06$

Fig. 15 Front view of the CMS detector

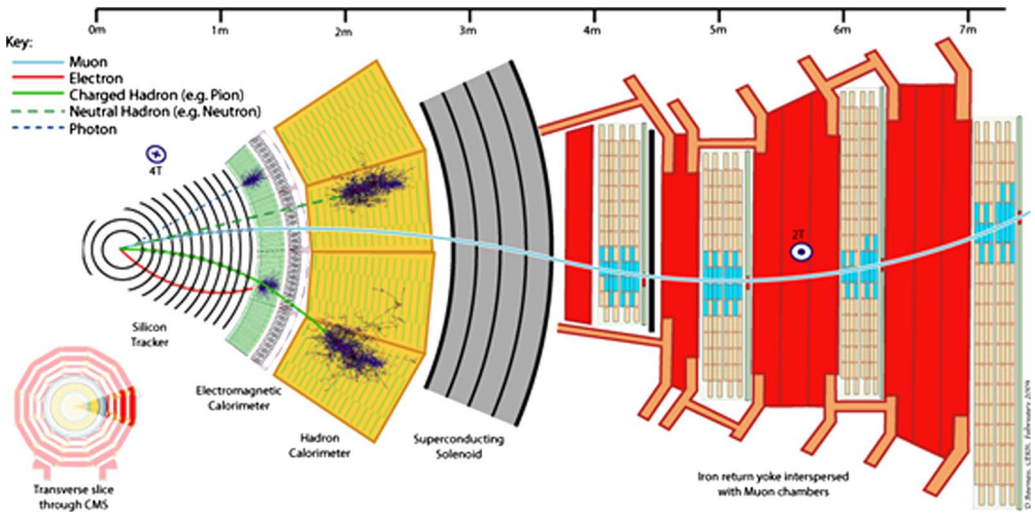

Fig. 16 Scheme of the drift chambers arranged in the CMS

$$Q_1 = P \cdot S_1 \tag{6}$$

where P is the thermal power per unit surface of the chamber and ΔT_1 is the temperature jump across the MB1 chamber. The heat flows for chambers MB2, MB3, and MB4 can be estimated in the same way as

$$Q_2 = P \cdot S_2 \tag{7}$$

$$Q_3 = P \cdot S_3 \tag{8}$$

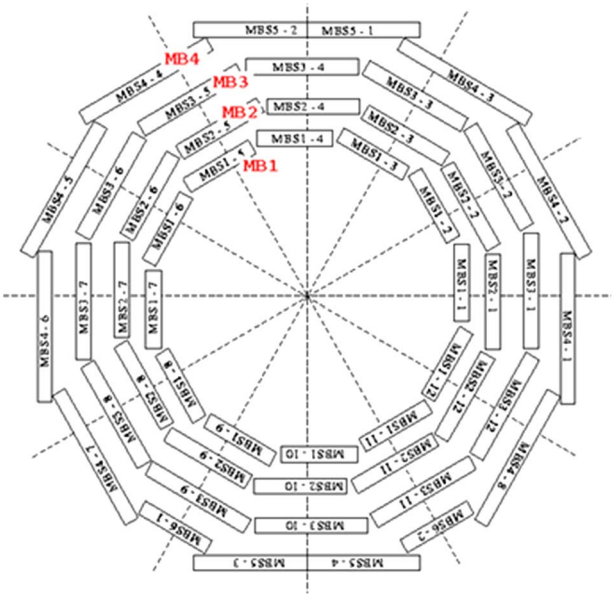

Fig. 17 Position of the drift chamber in a cross section of the CMS

Table 2 Dimensions of the drift chambers in CMS [7]

	Sector	X (mm)	Y (mm)	Z (mm)
MB1 station	All	1990	290	2536
MB2 station	All	2450	290	2536
MB3 station	All	3030	290	2536
MB4 station	Average		290	2536

$$Q_4 = P \cdot S_4 \tag{9}$$

The total temperature jump is given by

$$\Delta T = \Delta T_1 + \Delta T_2 + \Delta T_3 + \Delta T_4 \tag{10}$$

where

$$\Delta T_1 = P/2\lambda \tag{11}$$

$$\Delta T_2 = P/\lambda\left(S_1/S_2 + \tfrac{1}{2}\right) \tag{12}$$

$$\Delta T_3 = P/\lambda\left(S_1/S_3 + S_2/S_3 + \tfrac{1}{2}\right) \tag{13}$$

$$\Delta T_4 = P/\lambda\left(S_1/S_4 + S_2/S_4 + S_3/S_4 + \tfrac{1}{2}\right) \tag{14}$$

With a dissipated power of 100 W per chamber, and taking into account a transfer surface in a chamber of 2.5×2.5 m^2, the following value is obtained:

$$P = 16.0 \pm 0.2 \ \text{W/m}^2$$

As the transfer surface for a type of chamber can be estimated to be $Si = 2\pi RiZ$, where Z is the common length (2.5 m each), and Ri is the distance from the point of interaction (PI) to the chamber, as defined in Fig. 16. The resulting temperature jump will be $\Delta T = 25 \pm 1\,^\circ\text{C}$.

This temperature jump is too high for a detector and indicates the need for a forced cooling system. Finally, a system, based on water pipes, was selected as it has been successfully proven in previous detectors, e.g., L3 at LEP.

5 Conclusions

The isolating strips had a great effect on thermal conductance, reducing it fourfold, and were eventually discarded.

Dissipation of heat by natural convection in air is not possible due to the compactness of the detector. Furthermore, the excessive

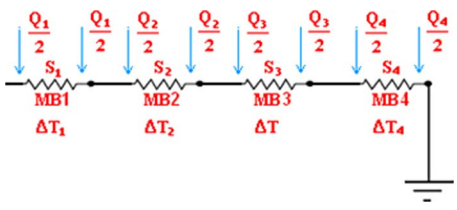

Fig. 18 Analog scheme for the heat flows in CMS

thermal gradient produced by the system has been demonstrated. These factors make clear the need for a forced cooling system.

Nomenclature

A = cross section
C = heat capacity
$c_{p\ \mathrm{water}}$ = specific thermal capacity of water
$c_{p\ \mathrm{Al}}$ = specific thermal capacity of aluminum
k = thermal conductivity
L = length
P = thermal power per unit surface of the chamber
Q_i = heat flow through Si at every MBi chamber
R_0 = thermal resistance of the reservoirs
R_M = thermal resistance of the modulus being tested
Si = surface of chamber MBi
T = temperature
ΔT_i = temperature jump across the MBi chamber
ΔT = total temperature jump across the MBi chamber
t = time
$\alpha = 2\lambda / C$ = rate of variation in the temperature with time
λ = total thermal conductance
λ_c = total conductance of the chamber
λ_{SA} = total conductance of the multilayered module without isolating strips
λ_{CA} = total conductance of the multilayered module with isolating strips
λ_H = total conductance of the honeycomb rigidizer spacer
ζ = specific conductance

References

[1] 1994, The CMS Collaboration, The Compact Muon Solenoid, Technical Proposal, CERN/LHCC/9438, LHCC/P1.
[2] 1997, The CMS Collaboration, The Muon Project, Technical Design Report, CERN/LHCC 9732, CMS TDR 3.
[3] http://www.intertronics.co.uk/data/ara2012.pdf
[4] http://www.datasheetcatalog.net/es/datasheets_pdf/A/D/5/9/AD592AN.shtml
[5] Holman, J. P., 2002, *Heat Transfer*, McGraw-Hill, New York.
[6] Lide, D. R., 2001, *Handbook of Chemistry and Physics*, CRC, Boca Raton, FL.
[7] http://wwwae.ciemat.es/cms/

Thermohydraulics of Laminar Flow Through Rectangular and Square Ducts With Axial Corrugation Roughness and Twisted Tapes With Oblique Teeth

Sujoy Kumar Saha[1]
Professor
ENEA Casaccia Research Centre,
Institute of Thermal Fluid Dynamics,
Office Building F-20,
Via Anguillarese 301,
00123 S. M. Galeria,
Rome, Italy
e-mail: sujoy_k_saha@hotmail.com

The heat transfer and the pressure drop characteristics of laminar flow of viscous oil ($175 < Pr < 538$) through rectangular and square ducts with combined internal axial corrugations on all the surfaces of the ducts and with twisted-tape inserts with and without oblique teeth have been studied experimentally. The axial corrugations in combination with both twisted tapes with and without oblique teeth have been found to perform better than either axial corrugations or twisted-tape inserts acting alone. The heat transfer and the pressure drop measurements have been taken in separate test sections. Heat transfer tests were carried out in electrically heated stainless steel ducts incorporating uniform wall heat flux boundary conditions. Pressure drop tests were carried out in acrylic ducts. The flow friction and thermal characteristics are governed by duct aspect ratio, corrugation angle, corrugation pitch, twist ratio, space ratio, length, tooth horizontal length and tooth angle of the twisted tapes, Reynolds number, and Prandtl number. Correlations developed for friction factor and Nusselt number have predicted the experimental data satisfactorily. The performance of the geometry under investigation has been evaluated. It has been found that based on constant pumping power, up to 45% heat duty increase occurs for the combined axial corrugation and twisted-tape insert case compared with the individual axial corrugation and twisted-tape insert cases in the measured experimental parameters space. On the constant heat duty basis, the pumping power has been reduced up to 30% for the combined enhancement geometry than the individual enhancement geometries. [DOI: 10.1115/1.4001313]

Keywords: Augmentation, enhancement, forced convection, laminar, axial corrugation, twisted-tape inserts, oblique teeth

1 Introduction

Three-dimensional corrugated channels are used in plate-type heat exchangers and rotary regenerators. The corrugated channel geometry is specified by corrugation angle and corrugation pitch. Typically sinusoidal channels are used. Figure 1 shows the corrugation in the four walls of the square crosssection duct. The effect of corrugation angle was investigated by a number of investigators [1,2]. The electrochemical technique was used in Ref. [1] to obtain the mass transfer coefficient. The corrugation angle ranged from 0 deg (corresponding to parallel straight duct of sinusoidal cross section) to 90 deg (corrugations normal to the main flow). Both friction factor and Nusselt number increase monotonically up to the corrugation angle 80 deg. Beyond 80 deg, they decrease slightly and approach the values of a two-dimensional corrugated channel. Focke and Knibbe [3] have shown that at corrugation angle 45 deg, the fluid flow is predominantly along the furrows. On reaching the plate edge, the fluid streams are reflected and return to the opposite plate edge along the furrows. Focke et al. [1] suggested similar flow patterns up to corrugation angle 60 deg. The reason for increase and decrease in the friction factor and Nusselt number is the positive and negative interaction of crisscrossing fluid streams inducing secondary swirl motion, change in flow pattern, and accelerating or decelerating effect on them. The complex interactions between the fluid streams lead to early transition to turbulence.

Stasiek et al. [2] investigated the effect of corrugation pitch to channel height ratio. Local heat transfer coefficients were obtained from liquid crystal thermography.

Abdel-Kariem and Fletcher [4] developed friction factor and Nusselt number correlations.

For laminar regime,

$$\mathrm{Nu} = 0.777\ \mathrm{Re}^{0.444}\ \mathrm{Pr}^{0.4}\left(\frac{\theta}{45}\right)^{0.67} \tag{1}$$

$$f = 15\ \mathrm{Re}^{-0.3}\left(\frac{\theta}{45}\right)^{2.5} \tag{2}$$

Twisted tapes, as shown in Fig. 2(*a*), cause the flow to spiral along the tube length. The tape inserts generally do not have good thermal contact with the tube wall, so the tape does not act as a fin.

Continuous twisted-tape shown in Fig. 2(*a*) has been extensively investigated. Variants of the twisted-tape that have been evaluated include short sections of twisted tapes at the tube inlet or periodically spaced along the tube length. Bergles and Joshi [5] presented a survey of the performance of the different types of swirl flow devices for laminar flow.

[1]Corresponding author. On leave from Mechanical Engineering Department, Bengal Engineering and Science University, Shibpur Howrah 711 103, West Bengal, India.

Contributed by the Heat Transfer Division of ASME for publication in the JOURNAL OF HEAT TRANSFER. Manuscript received July 16, 2009; final manuscript received January 28, 2010; published online June 2, 2010. Assoc. Editor: Yutaka Asako.

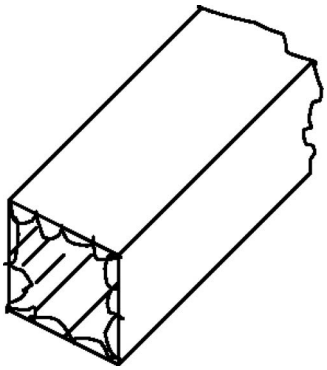

Fig. 1 Square duct with internal axial corrugation

To allow easy insertion of the tape, a clearance fit is maintained giving quite small heat transfer from the tape. The blockage caused by the finite tape thickness increases the average velocity. Marner and Bergles [6,7] showed that twisted tapes provide 300% heat transfer enhancement for laminar flow over smooth tube value.

Date [8] performed numerical predictions for the twisted-tape in fully developed laminar flow for uniform wall heat flux with constant fluid properties. Date's analysis also shows that the Nusselt number increases with increasing Pr and Re, contrary to laminar flow in plain tubes. Hong and Bergles [9] reported laminar flow ethylene glycol experimental data and they developed a correlation for predicting Nu. Date and Singham [10] developed empirical power-law correlations to fit their numerical predictions of the friction factor. Saha and Dutta [11] investigated the effect of shortening the twisted-tape length for oil in laminar flow by installing a short length tape at the inlet end in their electrically heated test section. As the tape length decreases, both friction factor and Nusselt number decrease. They have observed little improved thermohydraulic performance with short length twisted-tape. Saha and Dutta [11] also tested twisted tapes having gradually decreasing pitches and they observed reduction in both friction factor and Nusselt number compared with those of uniform pitch. Patil [12] investigated the effect of reducing the tape width in laminar flow of a pseudoplastic power-law fluid under constant wall temperature condition. The friction factor and the Nusselt number decreased as the tape width decreased. They observed worsening of thermohydraulic performance. Saha et al. [13]

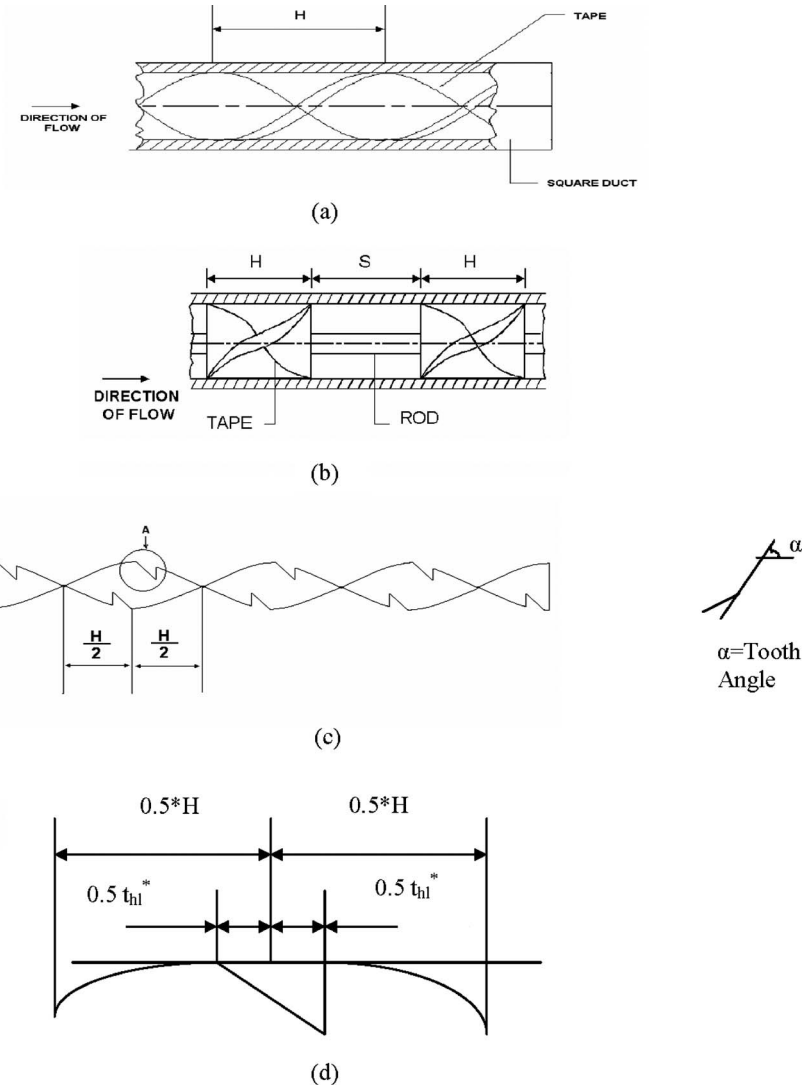

Fig. 2 Different types of twisted tapes: (*a*) full-length twisted-tape insert inside a duct, (*b*) regularly spaced twisted-tape elements, (*c*) full-length twisted-tape with oblique teeth, and (*d*) detail A of (*c*)

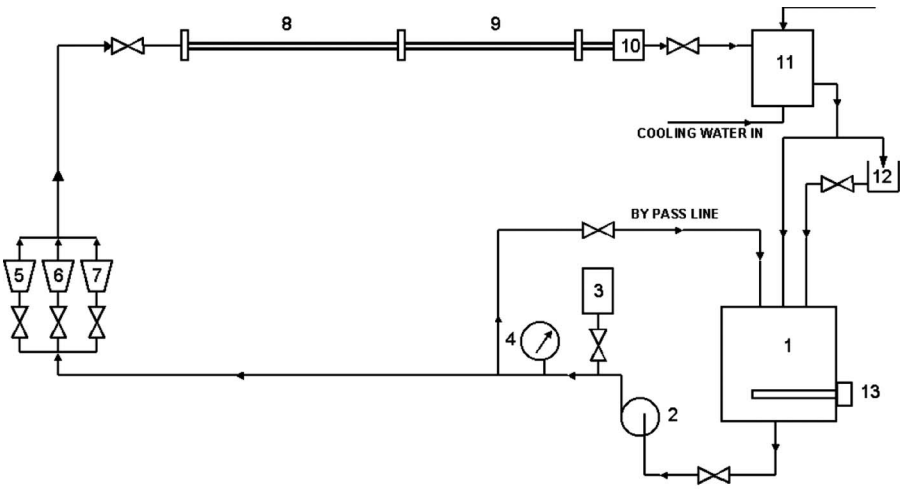

1. RESERVOIR
2. PUMP
3. ACCUMULATOR
4. PRESSURE GAUGE
5-7. ROTA METERS
8. CALMING SECTION
9. TEST SECTION
10. MIXING CHAMBER
11. HEAT EXCHANGER
12. WEIGHING PLATFORM
13. HEATER

Fig. 3 Schematic of the experimental setup

showed that under certain circumstances, the segmented twisted tapes perform better than the continuous twisted tapes.

Saha and Dutta [11] investigated the effect of number of tape module in twisted-tape section in the segment twisted-tape geometry for laminar flow of oil. They observed that significant reductions both in the friction factor and the Nusselt number occur as the number of twists increase from 1 to 2, but not further when the number of twists increases from 2 to 3. Date and Saha [14] numerically predicted the friction and heat transfer characteristics of laminar flow in a circular tube fitted with regularly spaced twisted-tape elements. The predictions reasonably agreed with the experimental data of water [13]. More information on twisted tapes may be obtained from Refs. [15–28].

From the above discussion, it is observed that axial corrugations and twisted tapes have been investigated, especially for the circular tube. However, the combined effect of axial corrugations and twisted-tape inserts has not been studied in the past; this is particularly true for square and rectangular ducts. The helical fluid flow due to axial corrugations coupled with twisted-tape-generated swirl flow is likely to give larger swirl intensity and vortex in the flow. Also there may be enhanced fluid mixing with increased heat and momentum diffusion. This may increase heat transfer even if it may also give increased pressure drop. In this paper, therefore, the combined effect of axial corrugations and twisted-tape inserts in circular ducts, square, and rectangular ducts has been comprehensively studied experimentally. The heat transfer and friction characteristics have been presented. Friction factor and Nusselt number correlations have been presented. Also the performance of this combined geometry has been evaluated.

2 Description of the Experimental Setup

A schematic diagram of the experimental setup is shown in Fig. 3. The setup consisted of (i) a storage tank in which the working fluid was stored, (ii) a working fluid circulating loop, (iii) test section, (iv) calming section, (v) an accumulator, (vi) a cooling water supply system (necessary for the heat transfer tests only), and (vii) a mixing chamber (necessary for the heat transfer tests only). The working fluid, viscous oil, was circulated through the loop by a gear pump (item 2 in Fig. 3) driven by a 1.5 kW electric motor. The working fluid was stored in a storage tank (item 1 in Fig. 3) of 0.07 m^3 capacity. The storage tank was a rectangular box made of mild steel. Its length, breadth, and height were 0.9 m, 0.395 m, and 0.5 m, respectively. The level of the fluid in the storage tank was indicated by a glass level indicator.

For the heat transfer tests, the working fluid was heated by two 2 kW heaters in the storage tank. The heaters were connected through autotransformers so that the heating rate could be adjusted and the fluid could be heated to the desired temperature level. The working fluid passed through one of the three rotameters (items 5–7 in Fig. 3), the calming section (item 8 in Fig. 3) to allow the velocity profile to develop fully at the entry to the test section (item 9 in Fig. 3) where the heat addition took place, a mixing chamber (item 10 in Fig. 3) for thorough mixing of the fluid, a heat exchanger coil (item 11 in Fig. 3) for the removal of heat, and a weighing platform (item 12 in Fig. 3) before the fluid returned to the reservoir. An accumulator (item 3 in Fig. 3) in the circulating loop limited the fluctuation of the pressure. A pressure gauge (item 4 in Fig. 3) indicated the delivery pressure of the pump.

Three heat transfer test sections were smooth 18/8 stainless steel ducts (made of sheets by soldering) having width $\times$ depth $=(1)13\times13$ mm^2 (square duct, AR=1, D_h=13 mm), (2) 13×26 mm^2 (rectangular duct, AR=0.5, D_h=17.33 mm), and (3) 13×39 mm^2 (rectangular duct, AR=0.333, D_h=19.50 mm). All the test sections had a length of 2 m. The test sections were heated electrically by wrapping uniformly two nichrome heater wires (20 gauge and 1.6 Ω/m) of identical length in parallel. The resistance of each wire was 30.275 Ω. The heater wires of each test section were connected through autotransformers. The power supplied to each of the test sections was measured by calibrated watt meters and this was cross-checked by measurements with digital voltmeter and ammeter. Porcelain beads on the heater wires ensured that the heater wires were electrically insulated from the test sections.

The inlet and outlet bulk fluid temperatures to the test sections were measured accurately by thermocouples placed in wells 5 cm upstream from the inlet and 20 cm downstream from the outlet of each test section. The fluid was assumed to have uniform temperature along the cross section at the inlet of the test channel. The mixing chamber at the exit of the test section was meant for thorough mixing of the circulating fluid. It consisted of a rectangular

box of mild steel with rectangular plates arranged inside in such a fashion that the working fluid moved in a tortuous path to give a uniform temperature across the cross section. In addition, five mixing baffles made out of brass sheet were mounted on a thin rod at fixed intervals and inserted into the duct just prior to the inlet of the mixing chamber. Each brass sector occupied about $\frac{3}{4}$ of the cross-sectional area of the duct. A copper duct of length 2.25 m was used as the calming section. The calming section ensured that a fully developed velocity profile was obtained at the entrance to the test section.

In order to reduce axial conduction of heat at the ends of the test sections, Teflon spacer disks of thickness 3 cm each were used on either side of the test sections. The spacers were bored and finished to match the test section dimensions. Teflon bushes fixed at pitch circle holes of the M.S. flanges eliminated metal to metal contact and minimized heat loss by conduction. Thus the test section was thermally insulated from rest of the ducting.

Each test section had 28 thermocouples brazed at seven axial positions on the outer surface of the duct wall to measure its temperature. The axial positions of the thermocouples from the onset of heating along the downstream direction were 0.05 m, 0.5 m. 1.00 m, 1.25 m, 1.50 m, 1.75 m, and 1.95 m, respectively. At each axial position, four thermocouples were placed at the middle of the edges. It may be noted that more thermocouples were located in the second half of the duct where the temperature profile was likely to be fully developed. Axial grooves 6 mm long, 1.5 mm wide, and 0.6 mm deep were cut at each thermocouple location on the outer surface of the duct to facilitate brazing of the thermocouples. The thermocouple wires were covered with plastic sleeve except for the first 12 cm near the duct wall where there were fine porcelain beads to withstand the high temperature of the wall. All the thermocouple wires at each axial position were bunched together and those were taken out radially and connected to a selector switch box. Each test section duct was first wrapped with glass fiber tape over which the heater wires with porcelain beads on them were wound. It was then covered with a layer of asbestos rope, which in turn was insulated with glass wool of thickness 120 mm to minimize heat loss in the radial direction.

The circulating fluid was cooled by water in a coil-in-shell heat exchanger. The shell was a cylindrical drum, 0.34 m in diameter and 0.40 m long, made of M.S. sheet. It had two openings—one at the bottom for coolant inlet and the other at the top for coolant outlet. The working fluid passed through a copper tube 10 mm i.d. 12 mm o.d. and 18 m long, made into two coaxial coils having 0.31 m and 0.25 m pitch circle diameters. To augment the heat transfer coefficient between the coolant and the outer surface of the duct, the velocity of the coolant past the tube coils was increased by putting a closed empty cylinder drum (30 cm long and 22 cm diameter) coaxially. Thus the copper tube coils were effectively placed in the annular space between the inner cylinder drum and the outer shell. The base of the inner drum was welded to three small pieces of rods, which were in turn welded to the bottom of the shell. The gaps between the shell and the inner drum at the top and bottom were equal and allowed coolant to flow without much pressure drop.

The cooling water supply system consisted of a reservoir, a centrifugal pump, an overhead tank, a rotameter, a bypass line, and a line from the overhead tank to the heat exchanger. Water from the reservoir was continuously pumped into the overhead tank at a rate slightly higher than the supply rate to the heat exchanger by regulating a bypass valve. The overflow line maintained the level of water in the overhead tank constant. The cooling water flow rate to the heat exchanger through a rotameter was regulated by a valve.

The working fluid circulating loop had three rotameters to cover a wide range of flow rates. These rotameters gave a measure of the flow rate and accordingly valves were adjusted to get approximately the desired flow rate. However, the actual flow rate was measured by collecting the working fluid in a container placed on the platform of a weighing machine, which had a resolution of 0.001 kg. The time of collection was recorded by a stop watch (resolution of 0.1 s). The whole pipeline through which the working fluid passed was covered with glass wool; special care was taken in insulating the calming section and the test section.

Fig. 4 Square corrugated duct connected with end flange

On the delivery side of the pump, an accumulator was fixed to the pipeline through a gate valve to minimize the pressure fluctuation. This ensured the uniform flow rate of the working fluid. The accumulator was cylindrical in shape and it was made from M.S. sheet. It was 0.35 m in length and 0.20 m in diameter. A pressure gauge fitted to the pipeline next to the accumulator showed the delivery pressure of the pump. The bypass valve in the working fluid loop was adjusted so that the delivery pressure of the pump did not exceed the designed working pressure of the pump.

The thermocouples used for measuring the temperatures were of 34 gauge copper-Constantan wire. They were fabricated from a single roll and the wire was calibrated at the ice point and the steam point. The thermocouples were connected to a 36 point selector switch box, which in turn was connected to a digital multimeter and a single cold junction at 0 °C. The rotameters were also calibrated.

The pressure drop test sections were smooth acrylic ducts (made of sheets using adhesive), 3.05 m long and cross sections identical to those of heat transfer test sections. In each pressure drop channel, 12 pressure taps along the top ribbed wall were made of 30 mm long, 4.5 mm o.d. pieces of acrylic tubes for static pressure drop measurement. Pressure taps were at distances of 1.19 m, 1.26 m, 1.33 m, 1.40 m, 1.47 m, 1.54 m, 2.60 m, 2.67 m, 2.74 m, 2.81 m, 2.88 m, and 2.95 m from the upstream end of the pressure drop test channels. Pressure drops in the test channel were measured by using vertical U-tube mercury manometer. Threads were cut on a lathe on one end of the taps and the drilled holes on the test sections were threaded internally by "0" BA taps. The threaded portion of each pressure tap was covered with Teflon tape before this was inserted into a tapped hole on the duct wall to prevent leakage. Additionally, rigidity on the taps was ensured by using Araldite. The pressure taps were connected by flexible PVC tubing to a U-tube Hg manometer. Brass corrugations were fixed (by adhesive in pressure drop test acrylic channels and by brazing in stainless steel heat transfer test channels) periodically in line on the top, bottom, and two side walls of whole length of each channel in a required distribution. Twisted-tape inserts were made of stainless steel sheet and rod. The twist ratio was 2.5, and the space ratio was 2.5. Corrugation angles were 30 deg and 60 deg. The nondimensional lengths of the twisted tapes were 0.5 and 1. The nondimensional corrugation pitches P/e were 2.0437 and 5.6481, and the twisted-tape nondimensional tooth horizontal lengths were 0.01538 and 0.03077. The twisted-tape tooth angles were 10 deg and 30 deg. Figures 4 and 5 show the corrugated channel and the twisted tapes.

Fig. 5 Full-length, short length, and regularly spaced twisted-tape elements with and without oblique teeth

3 Operating Procedure and Data Reduction

After the experimental setup was assembled, the storage tank was filled with the working fluid so that both the heaters (item 13 in Fig. 3) were immersed in oil. The loop was then checked for leaks. Preliminary experiments were carried out to check the reliability of the thermocouples. Heaters in the oil reservoir were switched on and oil was pumped through the test section without any heat input to it. The cooling water was circulated through the heat exchanger. When the steady state was reached after a few hours, all the thermocouple readings were taken and those were found to match with each other within a few microvolts.

In an experimental run, the gear pump was switched on and the heat input to the storage tank was set to the desired level to bring the oil to a predetermined temperature. The oil flow rate was controlled to the desired value by adjusting the valves; the approximate flow rate was obtained from the rotameter. The heaters to the test sections were then switched on and the required heat input was supplied by adjusting the autotransformers. During the experiments, only some predetermined heat inputs were supplied in order to get some particular values of heat flux. The cooling water pump was switched on and the valve controlling the flow of water to the heat exchanger was operated to give the desired flow rate. The bypass valve was also adjusted so that water trickled down the overflow line continuously and the water level in the overhead tank remained constant. The oil temperature at the inlet to the test section was controlled by adjusting the heat input to the reservoir and the cooling water flow rate to the heat exchanger.

A steady state was usually obtained after 5–6 h. In this state, all the thermocouple readings were noted. The mass flow rate was measured by collecting the fluid in a container placed on the platform of a weighing machine for 1 min. The power input to the test section was obtained from calibrated watt meters and this was cross-checked by the measurements with voltmeter and ammeter.

Before the measurements were taken, the test section was freed from air-bubbles.

The net heat input q_1 $(=V^2/R)$ to the fluid was determined from the electrical energy input to the system. The enthalpy rise q_2 of the fluid was calculated from the equation

$$q_2 = \dot{m} C_p (T_{bo} - T_{bi})$$

The set of data taken in a run was accepted only if the difference between the net heat input q_1 and the enthalpy rise q_2 was less than 3%. In such a case, the actual heat input to the test section was taken as the average of q_1 and q_2.

The bulk temperature of the fluid at any axial position at a distance z from the inlet was computed by assuming a linear temperature variation along the length. The duct inner wall temperatures were determined from the measured values of the outer wall temperature by applying the one dimensional heat conduction equation.

The circumferentially averaged inner wall temperature (T_{wi}) at any axial position was taken as the arithmetic mean of the inner wall temperatures at that axial position. The heat transfer coefficient (h_n) at any axial position was determined from the heat flux based on the inner surface area, the average inner wall temperature, and the calculated fluid bulk mean temperature at that axial position:

$$h_n = q''/(T_{wi} - T_b)$$

$$\mathrm{Nu}_{n,n=1,2,\ldots,7} = (h_{n,n=1,2,\ldots,7} D_h)/k_{n,n=1,2,\ldots,7}$$

The local Nusselt numbers were axially averaged by trapezoidal rule. The first two local values were averaged from the upstream end. Thereafter, this average value was used to average with the third local value. This marching procedure was followed until the extreme downstream end local value was reached.

Thermocouples were placed in the small gap length of about 2–3 mm between two successive turns of the heater wire. The properties of the fluid were evaluated at the mean bulk temperature.

An uncertainty analysis [29] carried out showed that, in the worst case, the uncertainties involved in the estimation of friction factors were within $\pm 6\%$ and those involved in the estimation of Nusselt number were within $\pm 5\%$. In majority of the data, the uncertainties were much less.

4 Results and Discussion

In this section, the results of the present investigation are presented and discussed. The experimental setup was validated by the present heat transfer and pressure drop data for the plain circular and square ducts with the standard data, Figs. 6 and 7.

4.1 Pressure Drop Results. Laminar flow is a relatively complex subject because the flow is influenced by the following conditions: (1) the thermal boundary condition, (2) entrance region effects, (3) natural convection at low Reynolds number, (4) fluid property variation across the boundary layer, and (5) the duct cross-sectional shape. Furthermore, the local Nusselt number will be different for simultaneously developing velocity and temperature profiles, as compared with a fully developed velocity profile.

In the present case of the corrugated and twisted-tape inserted noncircular ducts, the flow is very complicated and the flow dynamics is not easily amenable to numerical solution. Therefore, the present experimental data have been generated and are presented in this section. Early transition to turbulence and the turbulent flowlike behavior has been observed. It may be mentioned here that, in the present experiment, the differential pressure drop has been measured at points far removed from the tube entrance where entry-length problem does not exist.

4.2 Effect of Duct Aspect Ratio. Laminar velocity and temperature profile solutions have been obtained for the fully developed flow case for smooth square ducts and rectangular ducts of different aspect ratios. The applicable equation of motion for steady, constant-property, fully developed flow with no body forces can be readily deduced from the Navier–Stokes equation. By assuming axial pressure gradient, a constant over the flow cross section, the equation can be solved by various procedures, including numerically. In most cases the shear stress will vary around the periphery of the tube, but if a mean shear stress with respect to peripheral area is defined, and this is the stress needed to calculate pressure drop, a friction coefficient is defined. Fully developed friction coefficients for the family of rectangular ducts, extending from the square to flow between parallel plates, have been plotted. However, all these plots are for smooth tubes. The energy equation can also be solved for smooth tube. The duct geometry in the present investigation is, however, very complicated and the thermal-flow dynamics is very involved. The

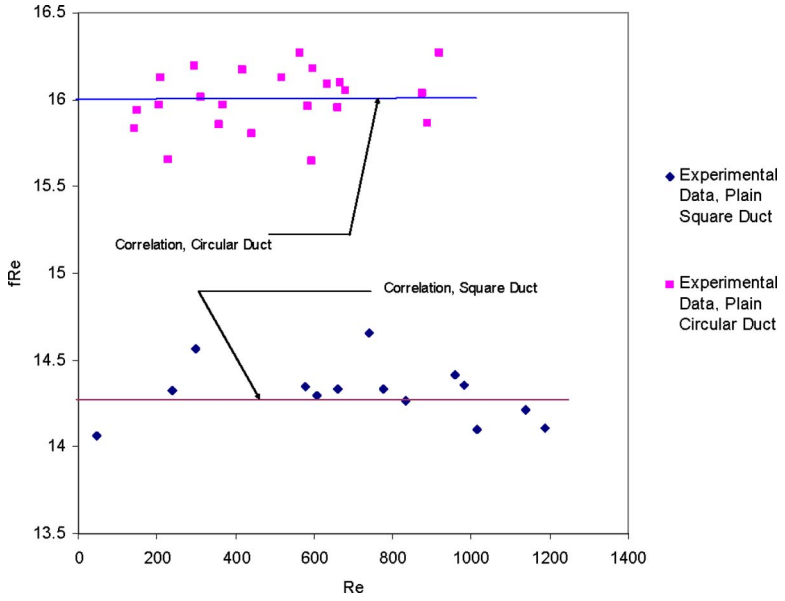

Fig. 6 Comparison of the present experimental friction factor data with the correlation (validation of the experimental setup)

theoretical analysis of the present thermal-flow situation is almost impossible. Therefore, the experimental data is generated.

Irrespective of the corrugation pitch and corrugation angle, the friction factor is the minimum for circular duct and it increases, although not very much, for noncircular duct as the duct aspect ratio decreases ($AR \leq 1$). This is true for all short length, full-length, and regularly spaced twisted-tape elements, as shown in Fig. 8.

4.3 Effect of Corrugation Angle and Corrugation Pitch. Three-dimensional corrugated channels are used in plate-type heat exchangers and rotary regenerators. Typically sinusoidal channels are used. Both heat transfer and pressure drop increase monotonically up to a certain corrugation angle. Beyond that value, they decrease slightly and approach the values of a two-dimensional corrugated channel. Up to a certain low value of corrugation angle, the fluid flow is predominantly along the furrows [3]. On reaching the corrugation edge, the fluid streams are reflected and return to the opposite edge along the furrows [1,3]. Two sets of criss-crossing induce secondary swirling motions due to the velocity component of the fluid moving along the opposite furrows in a direction perpendicular to the furrow. For lower corrugation angle, the interaction between fluid streams is positive, i.e., each of the crossing streams has a velocity component in the same direction as the stream it crosses. For higher corrugation angle, the interaction is negative, so that cross streams have a retarding effect on each other eventually leading to a change in flow pattern; the reflection occurs and the flow forms a zigzag pattern causing decrease in heat transfer and pressure drop. The complex interactions between fluid streams lead to early transition to turbulence.

Irrespective of whether the duct is circular or noncircular with $AR \leq 1$, the effect of corrugation angle on friction factor is similar; this is true for all types of twisted tapes. As the corrugation

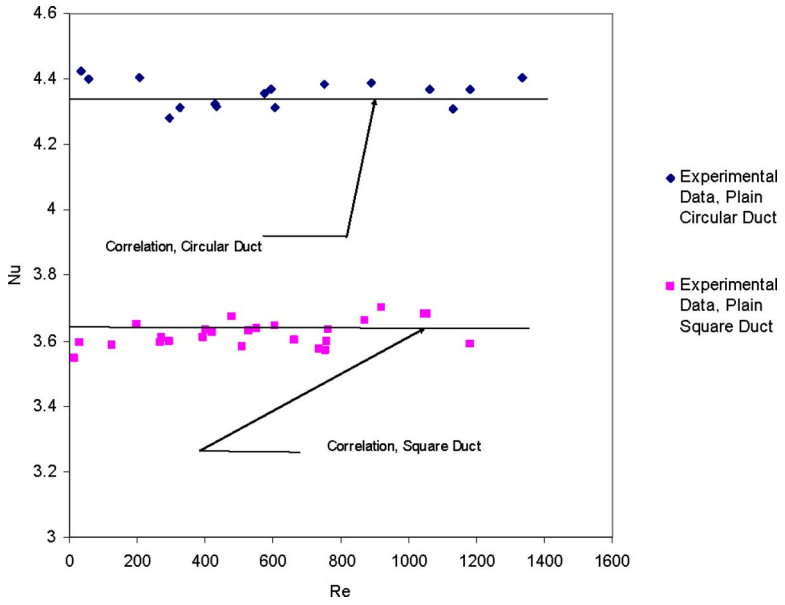

Fig. 7 Comparison of the present experimental Nusselt number data with the correlation (validation of the experimental setup)

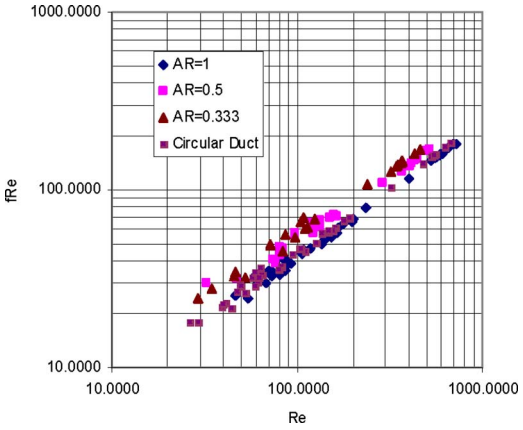

Fig. 8 Effect of Duct aspect ratio on friction factor short length twisted-tape: tooth angle=10 deg, t_{hl}=0.03077; corrugation angle=60 deg, P/e=2.0437

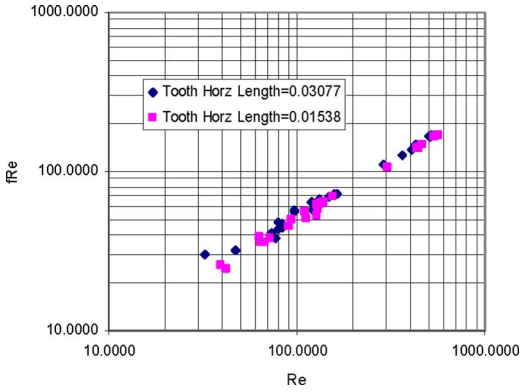

Fig. 11 Effect of tooth horizontal length on friction factor short length twisted-tape: tooth angle=10 deg; corrugation angle =60 deg, P/e=2.0437, AR=0.5

angle increases, the friction factor increases. As the corrugation pitch increases, the friction factor decreases, Figs. 9 and 10.

4.4 Effect of Twisted-Tape Tooth Angle and Tooth Horizontal Length. Irrespective of whether the duct is circular or noncircular with AR$\leq$1, the effect of twisted-tape tooth angle and tooth horizontal length on friction factor is similar; this is true for all types of twisted tapes. As the twisted-tape tooth horizontal length and angle increase, the friction factor increases, Figs. 11–15. This is due to the increased fluid mixing of asymmetric velocity profiles and associated momentum loss of the fluid. However, the friction factor is a strong and a weak function of tooth angle and tooth horizontal length, respectively.

The present experimental data compared well within $\pm$10% with the experimental friction factor data, Eq. (2) of Abdel-Kariem and Fletcher [4], Fig. 16.

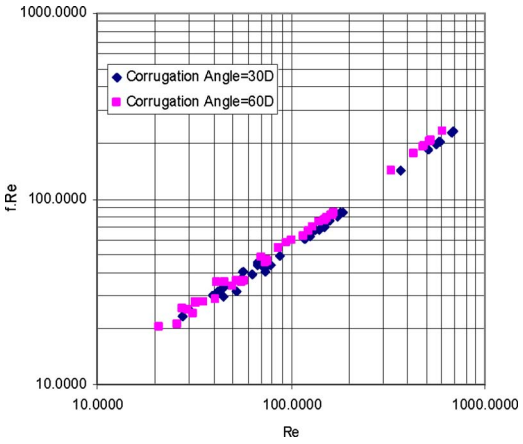

Fig. 9 Effect of corrugation angle on friction factor short length twisted-tape: tooth angle=10 deg, t_{hl}=0.01538, P/e =2.0437, AR=0.5

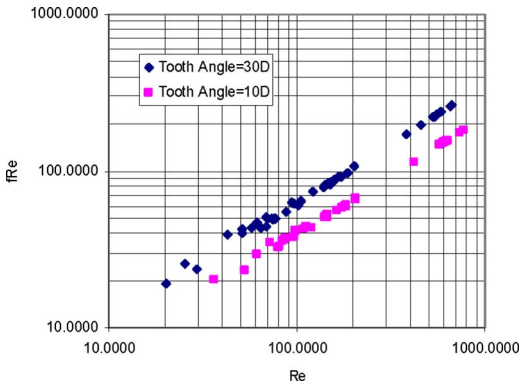

Fig. 12 Effect of tooth angle on friction factor short length twisted-tape: t_{hl}=0.01538; corrugation angle=30 deg, P/e =5.6481, AR=0.5

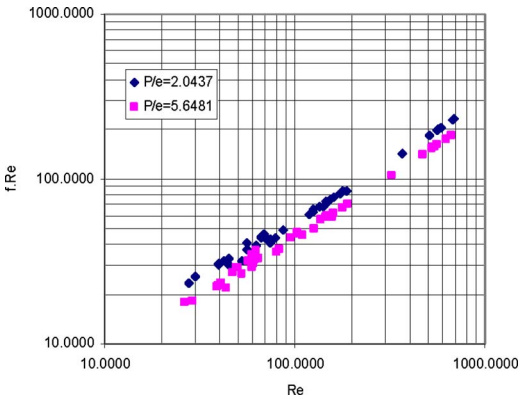

Fig. 10 Effect of corrugation pitch on friction factor short length twisted-tape: tooth angle=10 deg, t_{hl}=0.01538; corrugation angle=30 deg, AR=0.5

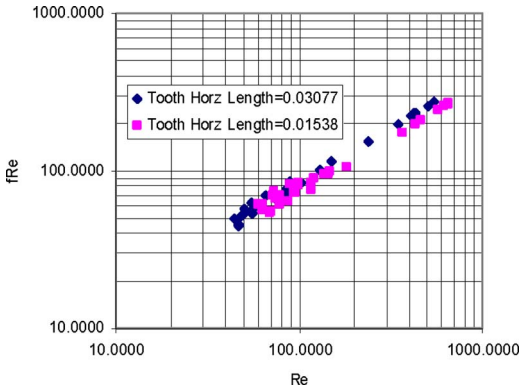

Fig. 13 Effect of tooth horizontal length on friction factor full-length twisted-tape: tooth angle=10 deg; corrugation angle =60 deg, P/e=2.0437, AR=0.5

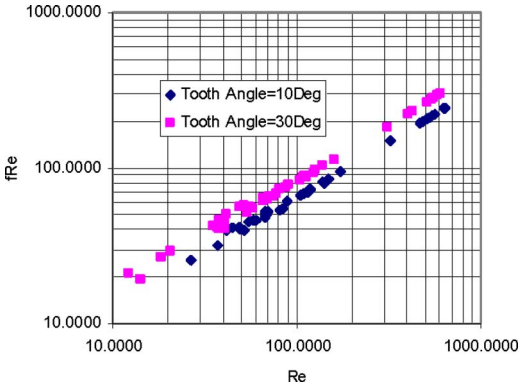

Fig. 14 Effect of tooth angle on friction factor full-length twisted-tape: t_{hl}=0.01538; corrugation angle=30 deg, P/e =5.6481, AR=0.5

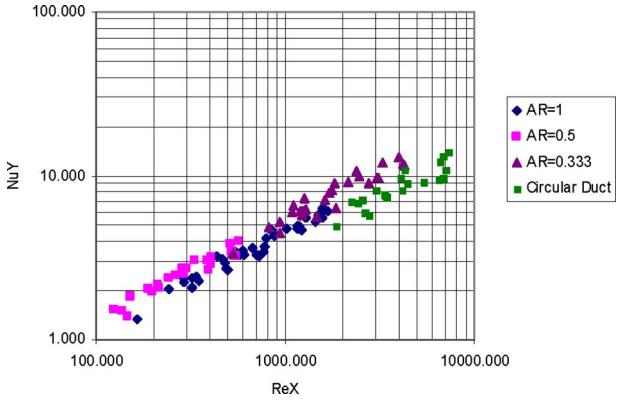

Fig. 17 Effect of duct aspect aspect ratio on nu short length twisted-tape: tooth angle=10 deg, t_{hl}=0.01538; corrugation angle=30 deg, P/e=2.0437

The results shown in Figs. 8–15 are explained by the fluid mixing with associated momentum and pressure losses, secondary flow, boundary layer separation, and flow reattachment with consequent different velocity profiles.

4.5 Heat Transfer Results. For the present experimental situation, the heat transfer coefficient is not uniform along the corrugation and the twisted-tape, and exact agreement of theoretical result and experimental data cannot be expected. Therefore, even if the simplified theoretical solutions are obtained, the simulation will not be the exact replica of the real-life situation. In the present section, heat transfer results of the present investigation are discussed. The effect of duct geometry and fin geometry on heat transfer characteristics is generally similar to that in the case of pressure drop results, Figs. 17–21. The results can be explained by the fluid mixing with associated momentum and pressure losses, thermal energy transport, secondary flow, boundary layer separation, and flow reattachment with consequent different velocity and temperature profiles.

In very few cases, anomalous behavior has been observed. This is perhaps because of intertwined effects of too many parameters on the complicated thermal and flow physics associated with thermofluid dynamics.

The present experimental data compared well within ±15% with the experimental Nusselt number data, Eq. (1) of Abdel-Kariem and Fletcher [4], Fig. 22.

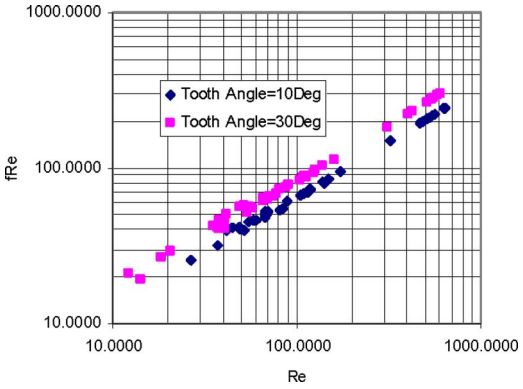

Fig. 15 Regularly spaced twisted-tape elements: effect of tooth angle on friction factor; corrugation angle=30 deg, P/e =2.0437, t_{hl}=0.01538

5 Correlations

Friction factor correlation and Nusselt number correlation have been developed by log-linear regression analysis. The correlations predict 97% experimental data within ±11%, Figs. 23 and 24. The correlations are as follows:

- *Short-length twisted-tape and full-length twisted-tape and axial corrugation.*

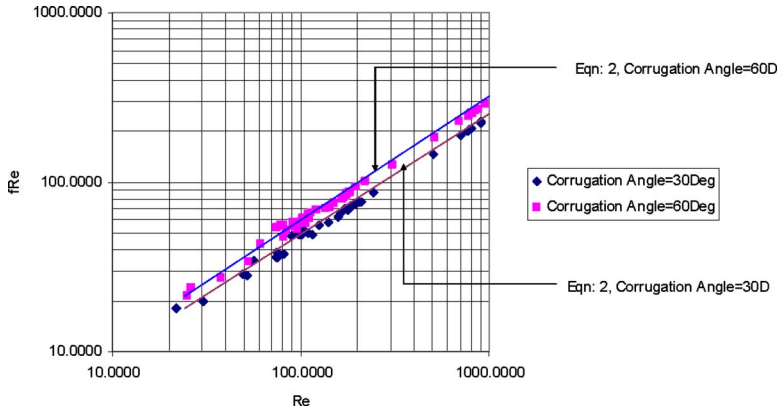

Fig. 16 Comparison of present experimental friction factor data with the experimental friction factor data, Eq. (2) of Abdel-Kariem and Fletcher [4]

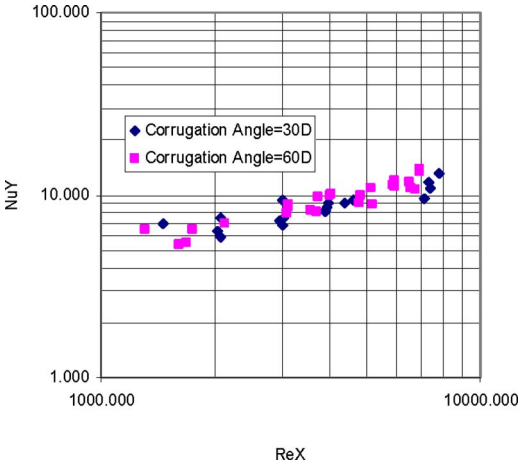

Fig. 18 Effect of corrugation angle on Nu full-length twisted-tape: tooth angle=10 deg, t_{hl}=0.01538, P/e=2.0437, AR=0.5

$$f\ \mathrm{Re} = 45.8129\left(1 + 10^{-6}\left(\frac{\mathrm{Re}}{\sqrt{y}}\right)^{2.67}\right)^{1/7}(\mathrm{AR})^{-1.39} \times \left(1 + \frac{\left(\frac{2\theta}{\pi}\right)^{0.1859} l^{0.226}}{\left(\frac{P}{e}\right)^{0.612}}\right) \times A \qquad (3)$$

l=1 for full-length twisted-tape.

$$A = \left(1 + 0.3624\left(\frac{\mathrm{Re}}{\sqrt{y}}\right)^{0.0521} t_{hl}^{0.183} e^{0.0291 \sin \alpha}\right) \quad \text{for full-length twisted-tape}$$

$$A = \left(1 + 0.8542\left(\frac{\mathrm{Re}}{\sqrt{y}}\right)^{0.1269} t_{hl}^{0.1743} e^{0.0357 \sin \alpha}\right) \quad \text{for short-length twisted-tape}$$

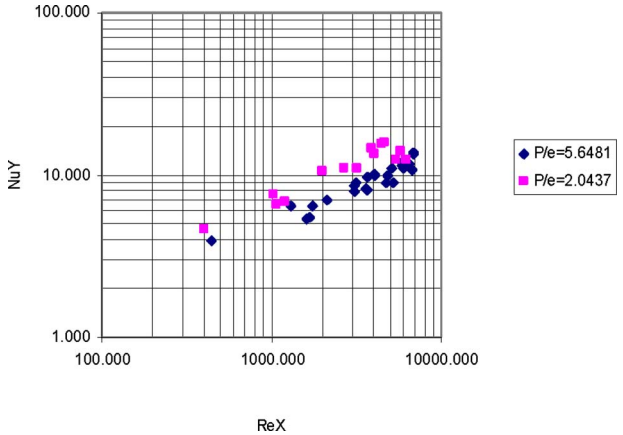

Fig. 19 Effect of corrugation pitch on Nu full-length twisted-tape: tooth angle=10 deg, t_{hl}=0.01538; corrugation angle =30 deg, AR=0.5

$$\mathrm{Nu}_m = 5.172\left[\left((1 + 0.08932\ \mathrm{Gz}^{0.9125})^{2.5} + 8.2273 \times 10^{-6}\left(\frac{\mathrm{Re}}{\sqrt{y}} \cdot \mathrm{Pr}^{0.565}\right)^{2.655}\right)^{2.0} + 1.5638 \times 10^{-15}(\mathrm{Re}\ \mathrm{Ra})^{2.18}\right]^{0.1} \times \left(\frac{\mu_b}{\mu_w}\right)^{0.14} \times \left(\frac{1}{\mathrm{AR}} + 0.1\right)^{0.15} \left(1 + \frac{\left(\frac{2\theta}{\pi}\right)^{0.1346} l^{0.183}}{\left(\frac{P}{e}\right)^{0.584}}\right) \times B \qquad (4)$$

l=1 for full-length twisted-tape.

$$B = \left(1 + 0.5436\left(\frac{\mathrm{Re}}{\sqrt{y}}\right)^{0.01752} t_{hl}^{0.186} e^{0.512 \sin \alpha}\right) \quad \text{for full-length twisted-tape}$$

$$B = \left(1 + 0.3289\left(\frac{\mathrm{Re}}{\sqrt{y}}\right)^{0.0895} t_{hl}^{0.2186} e^{0.06239 \sin \alpha}\right) \quad \text{for short-length twisted-tape}$$

- *Regularly spaced twisted-tape elements.*

$$f\ \mathrm{Re} = 45.8129\left(1 + 10^{-6}\left(\frac{\mathrm{Re}}{\sqrt{y}}\right)^{2.67}\right)^{1/7}(\mathrm{AR})^{-1.25} \times \left(1 + \frac{\left(\frac{2\theta}{\pi}\right)^{0.1742} \frac{d^{0.168}}{s^{1.183}}}{\left(\frac{P}{e}\right)^{0.559}}\right) \times A$$

$$A = \left(1 + 0.7329\left(\frac{\mathrm{Re}}{\sqrt{y}}\right)^{0.1561} t_{hl}^{0.1432} e^{0.0451 \sin \alpha}\right) \qquad (5)$$

$$\mathrm{Nu}_m = 5.172\left[\left((1 + 0.08932\ \mathrm{Gz}^{0.9125})^{2.5} + 8.2273 \times 10^{-6}\left(\frac{\mathrm{Re}}{\sqrt{y}} \cdot \mathrm{Pr}^{0.565}\right)^{2.655}\right)^{2.0} + 1.5638 \times 10^{-15}(\mathrm{Re}\ \mathrm{Ra})^{2.18}\right]^{0.1} \times \left(\frac{\mu_b}{\mu_w}\right)^{0.14} \times \left(\frac{1}{\mathrm{AR}} + 0.1\right)^{0.15} \left(1 + \frac{\left(\frac{2\theta}{\pi}\right)^{0.1648} \frac{d^{0.141}}{s^{1.325}}}{\left(\frac{P}{e}\right)^{0.216}}\right) \times B$$

$$B = \left(1 + 0.03187\left(\frac{\mathrm{Re}}{\sqrt{y}}\right)^{0.0639} t_{hl}^{0.1861} e^{0.04587 \sin \alpha}\right) \qquad (6)$$

6 Performance Evaluation

Performance of the present duct geometry has been evaluated based on the performance criteria defined by Bergles et al. [30]. Bergles et al. [30] suggested several criteria for the performance evaluation of enhancement devices. The performance of the present geometry has been evaluated on the basis of the following two important criteria:

- Criterion 1: Basic geometry fixed, pumping power fixed, increase heat transfer, performance ratio R_1

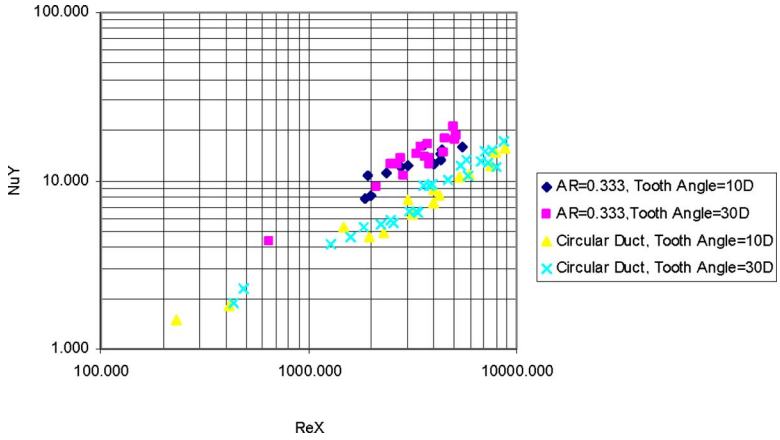

Fig. 20 Regularly spaced twisted-tape elements: effect of tooth angle on Nu; corrugation angle=30 deg, $P/e=2.0437$, $t_{hl}=0.01538$

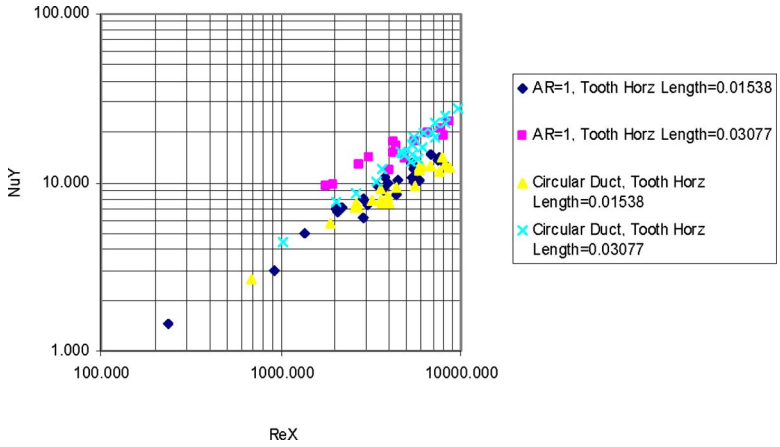

Fig. 21 Regularly spaced twisted-tape elements: effect of t_{hl} on Nu; corrugation angle=30 deg, $P/e=2.0437$, tooth angle=10 deg

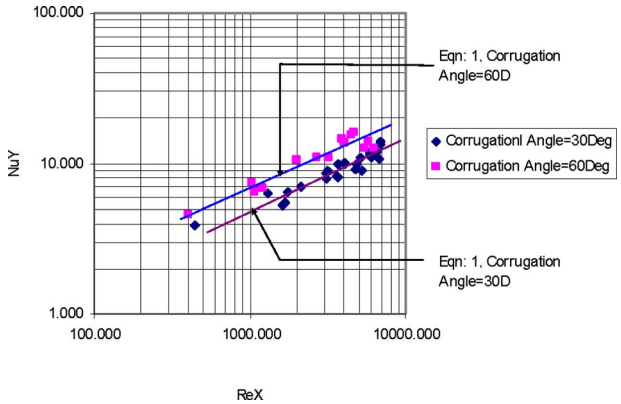

Fig. 22 Comparison present Nusselt number data with the experimental friction factor data, Eq. (1) of Abdel-Kariem and Fletcher [4]

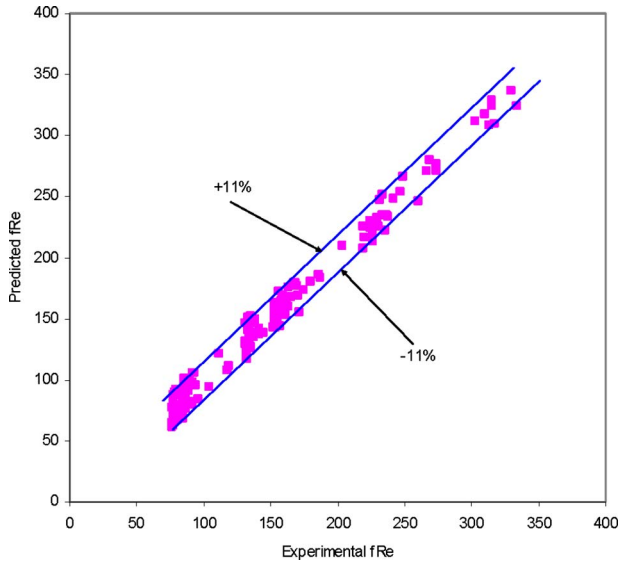

Fig. 23 Comparison of experimental friction factor data with that predicted from correlation

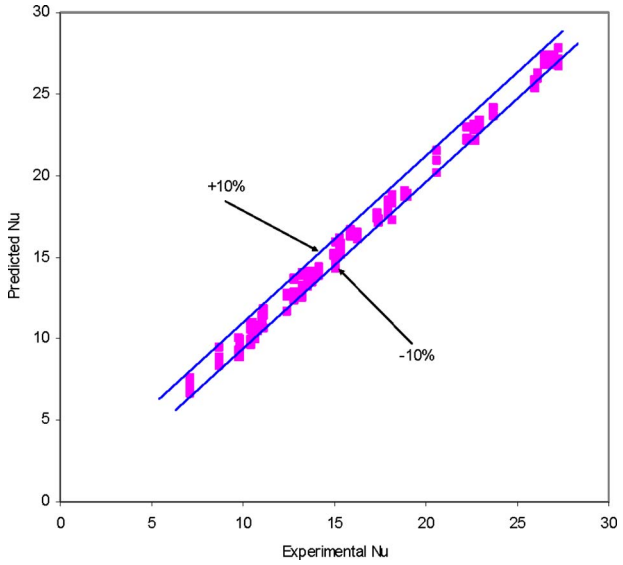

Fig. 24 Comparison of experimental Nusselt number data with that predicted from correlation

- Criterion 2: Basic geometry fixed, heat duty fixed, reduce pumping power, performance ratio R_2

$$R_1 = \frac{\mathrm{Nu}_{\mathrm{cttc}}}{\mathrm{Nu}_{\mathrm{ott,oc}}}$$

The subscript "cttc" refers to combined twisted-tape and corrugation. The subscripts "ott" and "oc" refer to only twisted tapes and only corrugation, respectively.

Also

$$R_2 = \frac{(f\ \mathrm{Re}^3\ A_c)_{\mathrm{cttc}}}{(f\ \mathrm{Re}^3\ A_c)_{\mathrm{ott,oc}}}$$

On constant heat duty basis, the pumping power has been reduced up to 30% for combined axial corrugations and twisted-tape inserts cases compared with individual axial corrugations and twisted-tape inserts cases. On constant pumping power basis, up to 45% heat duty increase has been observed, Table 1.

7 Conclusions

The heat transfer and the pressure drop characteristics of laminar flow of viscous oil through rectangular and square ducts with internal axial corrugations on all four surfaces of the ducts and with twisted-tape inserts have been studied experimentally. Circular duct has also been used. The axial corrugations in combination with twisted-tape inserts have been found to perform much better than either axial corrugations and twisted-tape inserts acting alone and the axial corrugation-twisted-tape inserts combination for laminar flow heat transfer is recommended.

Acknowledgment

The author gratefully acknowledges the generous financial support received from the Department of Science and Technology, Ministry of Science and Technology, Government of India through the Grant No. DST Project SR/S3/MERC-35/2004 dated March 22, 2006. The author is also grateful to ENEA, Casaccia Research Center, Institute of Thermal Fluid Dynamics, Italy for its financial support in the present research.

Nomenclature

A = heat transfer area, m^2
A_c = axial flow cross-sectional area, m^2
A_o = plain duct flow cross-sectional area, $=W \cdot D$, m^2
AR = aspect ratio $=W/D$, dimensionless.
C_p = constant pressure specific heat, J/kg K
D = depth of the duct cross section, m
D_h = hydraulic diameter of the test duct, $=4A_o/P$, m
d = nondimensional diameter of the rod connecting two successive tape elements
d^* = actual diameter of the rod $=d \cdot D_h$, m
f = fully developed Fanning friction factor $=(1/2) \times[\Delta P'/(\rho V_0^2)](D_h/z)$, dimensionless
g = gravitational acceleration, m/s^2
G = mass flux $=\dot{m}/A_c$, kg/m^2 s
Gr = Grashof number $=g\beta\rho^2 D_h^3 \Delta T_w/\mu^2$, dimensionless
Gz = Graetz number $=\dot{m}C_p/kL$, dimensionless
H = pitch for 180 deg rotation of twisted-tape, m
h_z = axially local heat transfer coefficient, $W/(m^2\ K)$
k = fluid thermal conductivity, $W/(m\ K)$
L_T = length of twisted-tape, m
l = nondimensional twisted-tape length $=L_T/L$, dimensionless
L = axial length, length of the duct, m
$\dot{m}$ = mass flow rate, kg/min
Nu_m = axially averaged Nusselt number $=1/L\int_0^L (h_z D_h dz/k)$, dimensionless
ΔP_z = pressure drop, mm
$\Delta P'$ = pressure drop, N/m^2
P = wetted perimeter in the particular cross section of the duct, rib spacing, m

Table 1 t_{hl}=0.01538, θ=30 deg, $(P/e)_1$=2.0437, $(P/e)_2$=5.6481, $\alpha(1)$=10 deg, $\alpha(2)$=30 deg y=2.5, s=2.5: performance ratios R_1 and R_2

		cttc/ott				cttc/oc			
AR		$\alpha(1)\ (P/e)_1$	$(P/e)_2$	$\alpha(2)\ (P/e)_1$	$(P/e)_2$	$\alpha(1)\ (P/e)_1$	$(P/e)_2$	$\alpha(2)\ (P/e)_1$	$(P/e)_2$
1	R_1	1.068	1.108	1.116	1.125	1.358	1.326	1.451	1.223
	R_2	0.915	0.931	0.955	0.816	0.828	0.819	0.701	0.811
0.5	R_1	1.118	1.243	1.327	1.322	1.334	1.279	1.144	1.323
	R_2	0.933	0.856	0.574	0.758	0.813	0.791	0.951	0.847
0.333	R_1	1.322	1.335	1.455	1.285	1.408	1.388	1.166	1.239
	R_2	0.766	0.812	0.718	0.816	0.711	0.755	0.921	0.867
Circular duct	R_1	1.216	1.151	1.288	1.188	1.169	1.146	1.347	1.258
	R_2	0.931	0.964	0.851	0.931	0.926	0.922	0.752	0.879

Pr = fluid Prandtl number $= \mu C_p / k$, dimensionless
q_1 = electrical energy input to the system, W
q_2 = fluid enthalpy gain, W
q'' = $0.5/\pi D_h L(q_1+q_2)$, W/m^2
Ra = Rayleigh number = Gr·Pr
Re = Reynolds number based on plain duct diameter $= (\rho V_0 D_h)/\mu$, dimensionless
S = space between two successive tape elements, m
s = space ratio $= S/D_h$, dimensionless
T = temperature, K
ΔT_w = wall to fluid bulk temperature difference, K
t_{hl} = nondimensional tooth horizontal length, $t_{hl} = t^*_{hl}/H$, dimensionless
t^*_{hl} = tooth horizontal length, m
V_a = mean axial velocity $= \dot{m}/\rho A_c$, m/s
V_o = mean velocity based on plain duct diameter $= \dot{m}/\rho A_0$, m/s
W = width of the duct cross section, m
W = width of the duct cross section, m
y = twist ratio $= H/D_h$, dimensionless
X = Pr^n, the value of n depends on the exponent of Pr in the correlation
Y = $(\mu_b/\mu_w)^{-0.14} \times 1/4.364$
z = axial length, the distance between the measuring pressure taps, m

Greek Symbols

α = twisted-tape tooth angle, deg
θ = corrugation angle, deg
μ = fluid dynamic viscosity, kg/ms
ρ = density of the fluid, kg/m^3

Subscripts

b = at bulk fluid temperature
h = hydraulic diameter
i = inlet
m = axially averaged
o = outlet
w = at duct wall temperature
z = local value

References

[1] Focke, W. W., Zachariades, J., and Oliver, I., 1985, "The Effect of the Corrugation Inclination Angle on the Thermohydraulic Performance of Plate Heat Exchanger," Int. J. Heat Mass Transfer, **28**, pp. 1469–1479.
[2] Stasiek, J., Collins, M. W., Ciofalo, M., and Chew, P. E., 1996, "Investigation of Flow and Heat Transfer in Corrugated Passages—I. Experimental Results," Int. J. Heat Mass Transfer, **39**, pp. 149–164.
[3] Focke, W. W., and Knibbe, P. G., 1986, "Flow Visualization in Parallel Plate Ducts With Corrugated Walls," J. Fluid Dyn., **165**, pp. 73–77.
[4] Abdel-Kariem, A. H., and Fletcher, L. S., 1999, "A Comparative Analysis of Heat Transfer and Pressure Drop in Plate Heat Exchangers," *Proceedings of the ASME-JSME Joint Thermal Engineering Conference*, San Diego, CA, March 14–19, Paper No. AJTE99-6291.
[5] Bergles, A. E., and Joshi, S. D., 1983, "Augmentation Techniques for Low Reynolds Number in-Tube Flow," *Low Reynolds Number Flow Heat Exchangers*, Hemisphere, Washington, DC, pp. 694–720.
[6] Marner, W. J., and Bergles, A. E., 1985, "Augmentation of Highly Viscous Laminar Tubeside Heat Transfer by Means of a Twisted Tape Insert and an Internally Finned Tube," *Advances in Enhanced Heat Transfer 1985*, ASME Symposium, S. M. Shenkman, J. E. O'Brien, I. S. Habib, and J. A. Kohler, eds., Vol. 43, pp. 19–28.
[7] Marner, W. J., and Bergles, A. E., 1978, "Augmentation of Tube-Side Laminar Flow Heat Transfer by Means of Twisted-Tape Inserts, Static Mixer Inserts and Internally Finned Tubes," *Heat Transfer 1978*, Proceedings of the Sixth Heat Transfer Conference, Hemisphere, Washington, DC, Vol. 2, pp. 583–588.
[8] Date, A. W., 1974, "Prediction of Fully-Developed Flow in a Tube Containing a Twisted-Tape," Int. J. Heat Mass Transfer, **17**, pp. 845–859.
[9] Hong, S. W., and Bergles, A. E., 1976, "Augmentation of Laminar Flow Heat Transfer in Tubes by Means of Twisted-Tape Inserts," ASME J. Heat Transfer, **98**, pp. 251–256.
[10] Date, A. W., and Singham, J. R., 1972, "Numerical Prediction of Friction and Heat Transfer Characteristics of Fully Developed Laminar Flow in Tubes Containing Twisted Tapes," ASME Paper No. 72-HT-17.
[11] Saha, S. K., and Dutta, A., 2001, "Thermohydraulic Study of Laminar Swirl Flow Through a Circular Tube Fitted With Twisted Tapes," ASME J. Heat Transfer, **123**, pp. 417–427.
[12] Patil, A. G., 2000, "Laminar Flow Heat Transfer and Pressure Drop Characteristics of Power-Law Fluids Inside Tubes With Varying Width Twisted Tape Inserts," ASME J. Heat Transfer, **122**, pp. 143–149.
[13] Saha, U. N., Gaitonde, U. N., and Date, A. W., 1989, "Heat Transfer and Pressure Drop Characteristics of Laminar Flow in a Circular Tube Fitted With Regularly Spaced Twisted-Tape Elements," Exp. Therm. Fluid Sci., **2**, pp. 310–322.
[14] Date, A. W., and Saha, S. K., 1990, "Numerical Prediction of Laminar Flow in a Tube Fitted With Regularly Spaced Twisted-Tape Elements," Int. J. Heat Fluid Flow, **11**(4), pp. 346–354.
[15] Li, F., Meindersma, W., de Haan, A. B., and Reith, T., 2005, "Novel Spacers for Mass Transfer Enhancement in Membrane Separations," J. Membr. Sci., **253**(1–2), pp. 1–12.
[16] Sivashanmugam, P., and Suresh, S., 2006, "Experimental Studies on Heat Transfer and Friction Factor Characteristics of Laminar Flow Through a Circular Tube Fitted With Helical Screw-Tape Inserts," Appl. Therm. Eng., **26**(16), pp. 1990–1997.
[17] Chang, S., Yu, K. W., and Lu, M., 2005, "Heat Transfer in Tubes Fitted With Single, Twin, and Triple Twisted Tapes," Exp. Therm. Fluid Sci., **18**(4), pp. 279–294.
[18] Dewan, A., Mahanta, P., Raju, K. S., and Kumar, P. S., 2004, "Review of Passive Heat Transfer Augmentation Techniques," Proc. Inst. Mech. Eng., Part A, **218**(7), pp.509–527.
[19] Hong, M., Deng, X., Huang, K., and Li, Z., 2007, "Compound Heat Transfer Enhancement of a Convergent-Divergent Tube With Evenly Spaced Twisted Tapes," Chin. J. Chem. Eng., **15**(6), pp. 814–820.
[20] Rahimi, M., Shabanian, S. R., and Alsairafi, A. A., 2009, "Experimental and CFD Studies on Heat Transfer and Friction Factor Characteristics of a Tube, Equipped With Modified Twisted-Tape Inserts," Chem. Eng. Process., **48**(3), pp. 762–770.
[21] Sarac, B. A., and Bali, T., 2007, "An Experimental Study on Heat Transfer and Pressure Drop Characteristics of Decaying Swirl Flow Through a Circular Pipe With a Vortex Generator," Exp. Therm. Fluid Sci., **32**(1), pp. 158–165.
[22] Jaisankar, S., Radhakrishnan, T. K., and Sheeba, K. N., 2009, "Experimental Studies on Heat Transfer and Friction Factor Characteristics of Thermosyphon Solar Water Heater System Fitted With Spacer at the Trailing Edge of Twisted Tapes," Appl. Therm. Eng., **29**(5–6), pp. 1224–1231.
[23] Chang, S. W., Su, L. M., Yang, T. L., and Chiou, S. F., 2007, "Enhanced Heat Transfer of Shaker-Bored Piston Cooling Channel With Twisted-Tape Insert," Heat Transfer Eng., **28**(4), pp. 321–334.
[24] Cazan, R., and Aidun, C. K., 2009, "Experimental Investigation of the Swirling Flow and the Helical Vortices Induced by a Twisted-Tape Inside a Circular Pipe," Phys. Fluids, **21**, pp. 037102.
[25] Ramakrishna, S., Pathipaka, G., and Sivashanmugam, P., 2009, "Heat Transfer and Pressure Drop Studies in a Circular Tube Fitted With Straight Full Twist," Exp. Therm. Fluid Sci., **33**(3), pp. 431–438.
[26] Hans, V. S., Saini, R. P., and Saini, J. S., 2009, "Performance of Artificially Roughened Solar Air Heaters—A Review," Renew. Sustain. Energy Rev., **13**(8), pp. 1854–1869.
[27] Saha, S. K., and Mallick, D. N., 2005, "Heat Transfer and Pressure Drop Characteristics of Laminar Flow in Rectangular and Square Plain Ducts and Ducts With Twisted Tapes," ASME J. Heat Transfer, **127**(9), pp. 966–977.
[28] Pramanik, D., and Saha, S. K., 2006, "Thermohydraulics of Laminar Flow Through Rectangular and Square Ducts With Transverse Ribs and Twisted Tapes," ASME J. Heat Transfer, **128**(10), pp. 1070–1080.
[29] Kline, S. J., and McClintock, F. A., 1953, "Describing Uncertainties in Single Sample Experiments," Mech. Eng. (Am. Soc. Mech. Eng.), **75**(1), pp. 3–8.
[30] Bergles, A. E., Blumenkrantz, A. R., and Taborek, J., 1974, *Proceedings of the Fifth International Heat Transfer Conference on Performance Evaluation Criteria for Enhanced Heat Transfer Surfaces*, Tokyo, Paper No. FC 6.3, Vol. II, pp. 239–243.

Multi-Objective Optimization of Heat Exchanger Design by Entropy Generation Minimization

Jiangfeng Guo

Lin Cheng

Mingtian Xu[1]
e-mail: mingtian@sdu.edu.cn

Institute of Thermal Science and Technology,
Shandong University,
Jinan 250061, P. R. China

In the present work, a multi-objective optimization of heat exchanger thermal design in the framework of the entropy generation minimization is presented. The objectives are to minimize the dimensionless entropy generation rates related to the heat conduction under finite temperature difference and fluid friction under finite pressure drop. Constraints are specified by the admissible pressure drop and design standards. The genetic algorithm is employed to search the Pareto optimal set of the multi-objective optimization problem. It is found that the solutions in the Pareto optimal set are trade-off between the pumping power and heat exchanger effectiveness. In some sense, the optimal solution in the Pareto optimal set achieves the largest exchanger effectiveness by consuming the least pumping power under the design requirements and standards. In comparison with the single-objective optimization design, the multi-objective optimization design leads to the significant decrease in the pumping power for achieving the same heat exchanger effectiveness and presents more flexibility in the design process. [DOI: 10.1115/1.4001317]

Keywords: heat exchanger, heat and mass transfer, heat conduction, genetic algorithm (GA)

1 Introduction

With the decline of storage capacity for fossil fuels, to use energy sources efficiently is one of most effective ways to reduce the energy demand. Heat exchangers are used to transfer thermal energy between two or more media and widely applied to power engineering, petroleum refineries, chemical industries, food industries, and so on. Hence, it is of great importance to improve the performance of heat exchange devices by decreasing the unnecessary energy dissipation.

The performance evaluation criteria for heat exchanger are generally classified into two groups: the first is based on the first law of thermodynamics; the second is based on the combination of the first and second laws of thermodynamics. In recent decades, the second group has attracted a lot of attention [1]. The heat transfer in heat exchangers usually involves the heat conduction under finite temperature difference, the fluid friction under finite pressure drop and fluid mixing. These processes are characterized as irreversible nonequilibrium thermodynamic processes. Inspired by the minimum entropy production principle advanced by Prigogine [2], Bejan [3,4] developed the entropy generation minimization (EGM) approach to the heat exchanger optimization design. In this approach, Bejan [3] took into account of two types of the irreversibilities in heat exchanger, namely, the transfer of heat across the stream-to-stream temperature difference and the frictional pressure drop that accompanies the circulation of fluid through the apparatus. Therefore, the total entropy production rate denoted by $\dot{S}_{\mathrm{gen}}$ is the sum of entropy productions associated with heat conduction and fluid friction. Bejan [4] demonstrated that EGM may be used by itself in the preliminary stages of design, in order to identify trends and the existence of optimization opportunities. Shah and Skiepko [5] discussed the relations between the heat exchanger effectiveness and the temperature difference irreversibility for complex flow arrangements. Vargas et al. [6] developed an approach to optimizing the global performance of the crossflow heat exchanger used in the environmental control system of a modern aircraft, with the aim of minimizing the total entropy generation rate of the installation. Based on the EGM, Oğulatu et al. [7] analytically carried out an optimization design of a crossflow plate heat exchanger, and examined the optimum result by the experimental data. An optimization has been developed for the designs of crossflow plate-fin heat exchangers with offset strip fins, which aims at minimizing the number of entropy generation units for a specified heat duty under given space restriction in Ref. [8]. In Ref. [9], the single-objective optimization design of the shell-and-tube heat exchanger based on the EGM was carried out by using the genetic algorithm (GA), in which the sum of entropy generations caused by heat conduction and fluid friction was taken as the objective function. Mohamed [10] analyzed the heat transfer and fluid flow thermodynamic irreversibilities in counterflow double pipe heat exchanger.

Note that the entropy generation rate usually changes with the mass flow rate, heat transfer rate, and so on in a heat exchanger; thus, for a fixed value of the entropy generation rate, it may correspond to different heat transfer rates. In such a circumstance, it is difficult to assess the performance of heat exchangers only in terms of entropy generation rate. Therefore, it is necessary to nondimensionalize entropy generation rates for the heat exchanger performance evaluation [1]. Various dimensionless entropy generation rates have been proposed. Among them, the most popular one is obtained by nondimensionalizing the entropy generation rate by the heat capacity flow rate [11]. The dimensionless entropy generation rate defined in such a way is called entropy generation number $N_{\mathrm{s}}=\dot{S}_{\mathrm{gen}}/\dot{m}c_p$. For a balanced counterflow heat exchanger, the following approximate expression for N_{s} was derived by Bejan [3]:

$$N_{\mathrm{s}}=\frac{\tau^2}{\frac{4L}{D}\mathrm{St}(\mathrm{Re}_D,\mathrm{Pr})}+\frac{R}{c_p}\frac{G^2}{\sqrt{2\rho P}}f(\mathrm{Re}_D)\frac{4L}{D} \tag{1}$$

where $\tau=|T_{\mathrm{c,i}}-T_{\mathrm{h,i}}|/\sqrt{T_{\mathrm{h,i}}T_{\mathrm{c,i}}}$ ($T_{\mathrm{h,i}}$ and $T_{\mathrm{c,i}}$ are the inlet temperatures of the hot and cold fluids, respectively), L is the path length, D is the duct hydraulic diameter, $\mathrm{Re}_D=4\dot{m}/(\pi\mu D)$, St is the Stan-

[1]Corresponding author.

Contributed by the Heat Transfer Division of ASME for publication in the JOURNAL OF HEAT TRANSFER. Manuscript received November 6, 2009; final manuscript received February 2, 2010; published online June 2, 2010. Assoc. Editor: Giulio Lorenzini.

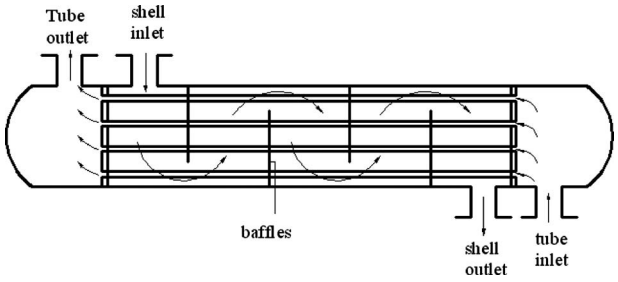

Fig. 1 Diagram of a typical shell-and-tube heat exchanger

ton number, which depends on Reynolds number and Prandtl number (Pr), f is the friction factor depending on the Reynolds number, c_p is the specific heat at constant pressure, P is the pressure, ρ is the density, G is the mass flow rate, and R is the ideal gas constant. The first term on the right side of Eq. (1) represents the heat conduction irreversibility and the second term accounts for fluid friction irreversibility. It is evident that the duct aspect ratio $(4D/L)$ has opposite influence on the heat conduction and fluid friction irreversibilities. Therefore, there exists a best balance point between the entropy generations caused by heat conduction and fluid friction, respectively. This is one of the key points of the EGM developed by Bejan [3]. However, the entropy generation associated with fluid friction is normally negligible for liquid-to-liquid heat exchangers in comparison with the entropy generation induced by heat conduction, which will be discussed in detail in Sec. 3.2. Thus, the single-objective optimization of heat exchanger design with the entropy generation number taken as the objective function would lead to significant increase in pressure drop. In order to eliminate this drawback of the single-objective optimization of heat exchanger design and more appropriately apply the EGM approach, we attempt to develop a multi-objective optimization of heat exchanger design, in which the dimensionless entropy generation rates related to heat conduction and fluid friction are set to two separate objective functions. And the multi-objective genetic algorithm is employed to search the Pareto optimal set, which theoretically represent the best trade-off between the entropy generation rates caused by heat conduction and fluid friction.

Finally, the method of nondimensionalizing entropy generation rate by the heat capacity flow rate $\dot{m}c_p$ causes some paradoxes [12–14]. In an effort to resolve these paradoxes, a number of ways for nondimensionalizing the entropy generation are proposed, such as Q/T_a [15,16] (Q is the heat transfer rate, T_a is the ambient temperature) and $Q/T_{c,i}$ ($T_{c,i}$ is the inlet temperature of cold fluid in heat exchanger) [13], the latter is employed to nondimensionalize the entropy generation in the following discussion.

2 Thermal Calculation of Shell-and-Tube Heat Exchanger

In the present section, the basic calculations of heat transfer and pressure drop in shell-and-tube heat exchanger are presented. Here, the shell-and-tube heat exchanger (as shown in Fig. 1) serves as an example to exemplify the application of the multi-objective optimization design since it is the most common type of heat exchanger applied in thermal engineering. The multi-objective optimization designs for other kinds of working fluids and heat exchangers are followed in the similar way.

2.1 Heat Transfer Calculation. Under the usual assumptions such as no longitudinal heat conduction, negligible potential and kinetic energy changes, negligible heat transfer between the exchanger and its surroundings and so on [17], the energy balance equation for heat exchanger is written as

$$Q = (\dot{m}c_p)_h(T_{h,i} - T_{h,o}) = (\dot{m}c_p)_c(T_{c,o} - T_{c,i}) \tag{2}$$

where Q is the heat transfer rate, $\dot{m}$ is the mass flow rate, c_p is the specific heat of fluid at constant pressure and assumed to be constant, T represents the temperature, the subscripts h and c refer to the hot and cold fluids, respectively, the subscripts i and o refer to the inlet and outlet of heat exchanger, respectively. The heat exchanger effectiveness is defined as the ratio of the actual heat transfer rate to the possible maximum heat transfer rate (Q_{max}) as follows [18]:

$$\varepsilon = \frac{Q}{Q_{max}} \tag{3}$$

The shell inner diameter is expressed as [19]

$$D_s = (1.1\sqrt{n} - 1)s + 3d_o \tag{4}$$

where D_s is the shell inner diameter, n is the number of heat exchange tubes, s is the tube pitch for the equilateral triangular arrangement of tubes, d_o is the outer diameter of heat exchange tube. According to the Bell–Delaware method, the shell-side heat transfer coefficient can be expressed as follows [18]:

$$\alpha_s = j_o c_{p,s}\left(\frac{\dot{m}_s}{A_s}\right)\left(\frac{\mu_s}{\mu_{s,w}}\right)^{0.14} \mathrm{Pr}_s^{-2/3} \tag{5}$$

where $\dot{m}_s$ is the shell-side mass flow rate, A_s is the crossflow area at the centerline of shell for one crossflow between two baffles, $c_{p,s}$ is the specific heat of the shell-side fluid, μ_s is the shell-side fluid dynamic viscosity at bulk temperature, $\mu_{s,w}$ is the fluid dynamic viscosity at wall temperature, Pr_s is the shell-side Prandtl number, and j_o is heat transfer factor. For details about the Bell–Delaware method, please refer to Refs. [18–20].

For the case that the hot fluid is in the tube-side, the Dittus–Boelter equation gives rise to the following expression of the tube-side heat transfer coefficient [18]:

$$\alpha_t = 0.023\frac{\lambda}{d_i}\left(\frac{\rho_t v_t d_i}{\mu_t}\right)^{0.8} \mathrm{Pr}_t^{0.3} \tag{6}$$

where the part in brackets represents the tube-side Reynolds number denoted as Re_t, d_i is the inner diameter of the heat exchange tube, ρ_t is the tube-side fluid density, μ_t is the tube-side fluid dynamic viscosity at bulk temperature, Pr_t is the tube-side Prandtl number, and v_t is the tube-side flow velocity and can be calculated by

$$v_t = \frac{4\dot{m}_t}{\rho_t n\pi(d_i)^2} \tag{7}$$

where n is the number of heat exchange tube. From Eqs. (5) and (6), the total heat transfer coefficient based on the external surface area of the heat exchange tube is written as

$$K_o = \left[\frac{1}{\alpha_t}\left(\frac{d_o}{d_i}\right) + r_t\left(\frac{d_o}{d_i}\right) + \frac{\delta_w}{\lambda_w}\left(\frac{d_o}{d_i}\right) + r_s + \frac{1}{\alpha_s}\right]^{-1} \tag{8}$$

where δ_w is the wall thickness of the heat exchange tube, λ_w is the wall thermal conductivity, r_t and r_s stand for the tube-side and shell-side fouling resistances, respectively.

2.2 Pressure Drop Calculation. The total tube-side pressure drop includes three parts: pressure loss along tube, pressure loss in bend, and inlet and outlet pressure losses. Ignoring the second part for the single tube pass, the total tube-side pressure drop is written as [18,19]

$$\Delta P_t = \left(4f_t\frac{L}{d_i}\left(\frac{\mu_t}{\mu_{t,w}}\right)^{-0.14} + 1.5\right)\frac{\rho_t v_t^2}{2} \tag{9}$$

where f_t is the tube-side friction factor and L is the total length of tube passes. For the heat exchanger with multiple passes, pressure loss in elbows should also be taken into account.

According to the Bell–Delaware method, three correction fac-

tors are applied for the shell-side pressure drop [18,19]: correction factor for bundle bypass effects R_b, correction factor for baffle leakage effects R_l, and correction factor for unequal baffle spacing at inlet and/or outlet R_s. In our calculation, the correction factors are curved-fitted as follows [18]:

$$R_l = \exp[-1.33(1+p_s)]p_{lm}{}^z \tag{10}$$

with

$$z = [-0.15(1+p_s)+0.8] \tag{11}$$

$$p_s = \frac{S_{sb}}{S_{sb}+S_{tb}} \tag{12}$$

$$p_{lm} = \frac{S_{sb}+S_{tb}}{S_m} \tag{13}$$

where S_{sb} is the shell-to-baffle leakage area, S_{tb} the tube-to-baffle leakage area, and S_m the crossflow area at bundle centerline. The expression for R_b is [18]

$$R_b = \exp[-C_{bp}F_{sbp}(1-p_{ss}{}^{1/3})] \tag{14}$$

where $C_{bp}=3.7$, F_{sbp} is the ratio of the bypass area to the overall crossflow area, p_{ss} is the ratio of the number of sealing strips (pairs) in one baffle to the number of tube rows in one crossflow section. The equal baffle spacing at inlet and outlet is adopted in the present work, so $R_s=1$ [19]. At last, the total shell-side pressure drop is obtained as follows [18,19]:

$$\Delta P_s = [(N_b-1)\Delta P_{bk}R_b + N_b\Delta p_{wk}]R_1 + 2\Delta P_{bk}R_b\left(1+\frac{N_{cw}}{N_c}\right)R_s \tag{15}$$

where N_b is the number of baffles, ΔP_{bk} is the pressure drop for an ideal crossflow section, ΔP_{wk} is the pressure drop for the ideal window section, N_{cw} is the effective number of tube rows crossed in the baffle window, and N_c is the number of tube rows in one crossflow section. More detained information about the shell-side pressure drop in the Bell–Delaware method can be found in Refs. [18–20]. From Eqs. (8) and (9) the total pumping power can be written as [21]

$$W = \frac{1}{\eta}\left(\frac{\dot{m}_t}{\rho_t}\Delta P_t + \frac{\dot{m}_s}{\rho_s}\Delta P_s\right) \tag{16}$$

3 Thermodynamic Optimization of the Heat Exchanger Design

3.1 Entropy Generation and Its Nondimensionalization. The irreversible losses in heat exchanger are detrimental to the performance of heat exchanger and can be quantified in terms of entropy generation. By thermodynamic optimization, it means to minimize the entropy generation. In heat exchanger the heat conduction under finite temperature difference and fluid friction are two main irreversible factors to induce the entropy generation. In the following, we first calculate the entropy generation rates related to these irreversible losses, and then the optimization design of heat exchanger by EGM is discussed.

First, the entropy generation rate $\dot{S}_{gen,\Delta T}$ caused by heat conduction in heat exchanger is expressed as follows [17]:

$$\dot{S}_{gen,\Delta T} = \int_i^o \left(\frac{\dot{m}c_p dT}{T}\right)_{h,c} = (\dot{m}c_p)_h \ln\frac{T_{h,o}}{T_{h,i}} + (\dot{m}c_p)_c \ln\frac{T_{c,o}}{T_{c,o}} \tag{17}$$

Nondimensionalizing the entropy generation rate by the heat capacity flow rate $\dot{m}c_p$ yields

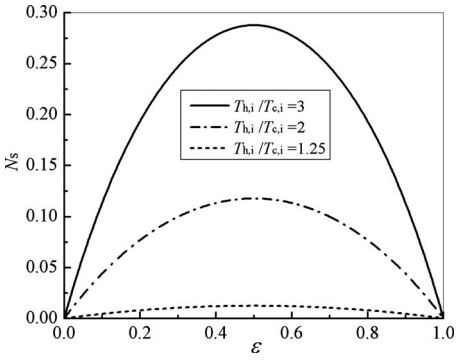

Fig. 2 Bejan's entropy generation number versus the effectiveness

$$N_{s,\Delta T} = \frac{\dot{S}_{gen,\Delta T}}{\dot{m}c_p} \tag{18}$$

Theoretically, when $N_{s,\Delta T}$ decreases, the irreversible losses in heat exchanger are reduced and the performance of heat exchanger should become better. While the reality is that with increasing the heat exchanger effectiveness, $N_{s,\Delta T}$ first increases and reaches its maximum value, then decreases, for a counterflow heat exchanger, as shown in Fig. 2. Therefore, we cannot say that the smaller the entropy generation, the better the heat exchanger performance is. Bejan called this phenomenon the "entropy generation paradox" [12]. In order to eliminate this paradox, Hesselgreaves proposed another kind of nondimensionalizing method for the entropy generation rate as follows [13]:

$$N_{s1,\Delta T} = \frac{T_{c,i}\dot{S}_{gen,\Delta T}}{Q} \tag{19}$$

which is called the modified entropy generation number related to the irreversible loss caused by the heat conduction in heat exchanger. $N_{s1,\Delta T}$ decreases monotonously with increasing the exchanger effectiveness as discussed by Hesselgreaves [13]. Therefore, $N_{s1,\Delta T}$ avoids the entropy generation paradox.

For the incompressible fluid and under the nonadiabatic condition, the entropy generation rate related to fluid friction is expressed as follows [17]:

$$\dot{S}_{gen,\Delta P} = \left(\dot{m}\frac{\Delta P}{\rho}\frac{\ln(T_o/T_i)}{T_o-T_i}\right)_{h,c} = \frac{\Delta P_t}{\rho_t}\dot{m}_t\frac{\ln(T_{h,o}/T_{h,i})}{T_{h,o}-T_{h,i}} + \frac{\Delta P_s}{\rho_s}\dot{m}_s\frac{\ln(T_{c,o}/T_{c,i})}{T_{c,o}-T_{c,i}} \tag{20}$$

For the case of ideal gas with constant specific heat, the entropy generation contributed by pressure drop can be written as [22]

$$\dot{S}_{gen,\Delta P} = -(\dot{m}R)_h \ln\frac{P_{h,o}}{P_{h,i}} - (\dot{m}R)_c \ln\frac{P_{c,o}}{P_{c,i}} \tag{21}$$

where R is the ideal gas constant. Thus, applying the same nondimensionalizing method as done to the entropy generation rate caused by heat conduction yields

$$N_{s1,\Delta P} = \frac{T_{c,i}\dot{S}_{gen,\Delta P}}{Q} \tag{22}$$

which is the modified entropy generation number associated with the irreversible loss induced by the fluid friction.

3.2 Single-Objective Optimization. In order to compare with the multi-objective optimization of heat exchanger design, we first discuss the single-objective optimization of heat exchanger design based on the combination of EGM and GA. The total modified entropy generation number N_{s1} is defined as follows:

Table 1 The known data for heat exchanger design with the fixed heat transfer area

	Hot fluid (tube-side)	Cold fluid (shell-side)
Inlet temperature T_i (K)	368.15	283.15
Mass flow rate $\dot{m}$ (kg/s)	50	20
Density ρ (kg/m^3)	970	991.15
Specific heat at constant pressure c_p (J/(kg K))	4200	4174
Dynamic viscosity μ (Pa s)	326×10^{-6}	690×10^{-6}
Entrance pressure P_i (MPa)	6.5	5
Fouling resistance r ((m^2 K)/W)	0.000086	0.00017
Prandtl number Pr	2.015	4.5878

$$N_{s1} = N_{s1,\Delta T} + N_{s1,\Delta P} \tag{23}$$

And it is taken as the objective function in the single-objective optimization design of shell-and-tube heat exchanger. The known data for the heat exchanger design are documented in Table 1. The working fluids on tube-side and shell-side are water in our consideration. Equation (1) indicates that the geometric parameters of the heat exchanger have significance influences on the entropy generations due to heat conduction and fluid friction, in comparison with the nearly ideal heat exchanger represented by Eq. (1) the practical heat exchanger discussed in this work is so complicated that it is impossible to be simplified to two parameters, i.e., diameter and length, therefore more design variables are selected and their ranges are as follows:

(1) The tube outer diameter d_o, its discrete values, and the corresponding tube pitches are listed in Table 2.
(2) The whole number of heat exchange tubes n ranging from 50 to 550.
(3) The ratio of the baffle spacing to the shell inner diameter Bs varies between 0.2 and 1.0.
(4) The central angle of baffle cut θ ranging from 1.8546 to 2.9413 in radians.

The constraint conditions for the heat exchanger design are as follows:

(1) length-diameter ratio is between 6 and 10
(2) baffle spacing is greater than 50 mm
(3) tube-side pressure drop is less than 5×10^4 Pa
(4) shell-side pressure drop is less than 5×10^4 Pa [23]

In our design, the heat transfer surface area is fixed at 60 m^2. This optimization problem formulated above will be solved by GA. The reason for us to utilize GA is explained in the following.

The traditional approaches, which require the information of the gradients of objective functions, suffer from getting trapped at the local optimum. Thus, they cannot ensure that the global optimal solution is achievable [24]. Although direct search method does not require any information about the gradient of the objective function, it depends heavily on the initial point, and frequently points to local optimum unless the objective function is unimodal [25,26]. The genetic algorithm starts the search from a population of points; the dependence of GA on the initial point is not as strong as direct search method. Furthermore, it provides a high level of robustness by simulating nature's adaptation in the evolution process [25,27]. More importantly, GA has very strong capability to find the global optimum [28,29]. Therefore, the genetic algorithm [30] is employed to search the solution of the optimization problem. The initial generation, which satisfies the constraint conditions, is randomly generated.

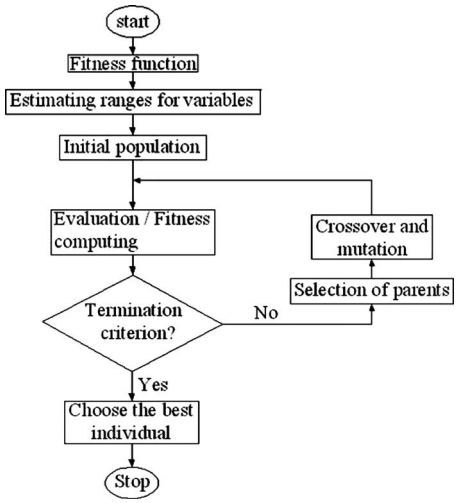

Fig. 3 Flow chart of a genetic algorithm

In the genetic algorithm method, a metric called *fitness function* is first defined that allows each potential solution (individual) to be quantitatively evaluated. The parameters are structured in the form of floating point, and the number of heat exchange tube is assigned to the nearest integer, which is no less than the value obtained by the genetic algorithm method. After a random initial population in the ranges of design variables is generated, the algorithm creates a sequence of new generations iteratively until the stopping criterion is met. In this process, offspring are generated by merging two individuals in current generation with a *crossover operator*, or by modifying a chromosome with a *mutation operator*. A new generation is formed by some parents and offspring based on fitness values, the population size is kept invariant by eliminating the inferior ones. The chromosomes with higher fitness values have higher probabilities to survive; this ensures the convergence to a best individual after certain number of generations, which probably represents the optimal solution of the given problem [31,32]. The flow chart of the genetic algorithm is shown in Fig. 3.

For each generation in the evolution process, according to the values of the fitness function of every individual, a best individual is selected, the corresponding values of $N_{s1,\Delta T}$, $N_{s1,\Delta P}$, and N_{s1} are thus obtained. Their variations with respect to the number of generations are depicted in Figs. 4 and 5. From Fig. 4, one can see that in comparison with the initial value, the modified entropy generation number decreases by 10.44% through the optimization process. It seems that the single-objective optimization of heat exchanger works well. However, the observation of Fig. 5 shows that although the modified entropy generation number related to heat conduction is reduced by 10.60% through the optimization process, the modified entropy generation number caused by fluid friction is enlarged by 324%. Why the fluid friction has such a significant increase? The reason is analyzed in the following.

Bejan [3] introduced the irreversibility distribution ratio ϕ to describe the relative importance of the two irreversibilities. Ac-

Table 2 Tube outer diameter and the corresponding tube pitch

d_o (mm)	10	12	14	16	19	20	22	25	30	32	35	38	45	50	55	57
s (mm)	13.4	16	19	22	25	26	28	32	38	40	44	48	57	64	70	72

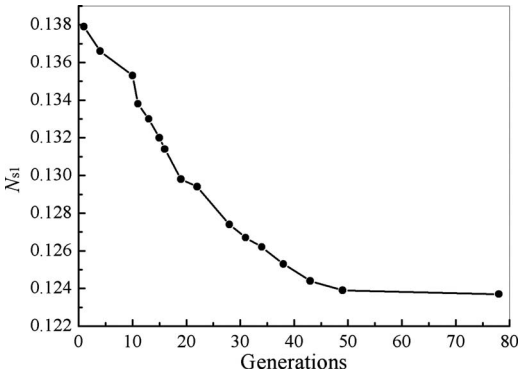

Fig. 4 Variation in N_{s1} with the number of generations

cording to Eqs. (19) and (22), the irreversibility distribution ratio for incompressible fluid in one passage of a heat exchanger is given as follows:

$$\phi = \frac{\dot{S}_{\mathrm{gen},\Delta T}}{\dot{S}_{\mathrm{gen},\Delta P}} = \frac{c_p \rho (T_o - T_i)}{\Delta P} \tag{24}$$

Particularly, for the above single-objective optimization design of the heat exchanger with the known data listed in Table 1, the irreversibility distribution ratio in the shell-side is

$$\phi = \frac{\dot{S}_{\mathrm{gen},\Delta T}}{\dot{S}_{\mathrm{gen},\Delta P}} = \frac{c_p \rho (T_o - T_i)}{\Delta P} = 4481.8 \tag{25}$$

It is evident that the entropy generation rate caused by heat conduction significantly overweight that caused by fluid friction. Generally, if the working fluid is water ϕ can be estimated in the following manner. According to Ref. [33], we have

$$c_p \sim 10^3, \quad \rho \sim 10^2 \tag{26}$$

The order of magnitude for the difference between outlet temperature and inlet temperature is about 10^1 K. The upper limit of pressure drop in shell-and-tube heat exchanger is about 5×10^4 Pa [23]. Therefore, the orders of magnitude for irreversibility distribution ratio ϕ are usually no less than 10^2 in most situations. For the other liquids, the order of magnitude of the irreversibility distribution ratio can also be obtained by using magnitude analysis according to their thermodynamic properties [33]. If the balance point between entropy generations caused by heat transfer and fluid friction is achieved, the order of magnitude of pressure drop is at least 10^6 according to Eqs. (25) and (26), which exceeds the upper limit of allowable pressure drop for liquid in most situations of heat exchanger design.

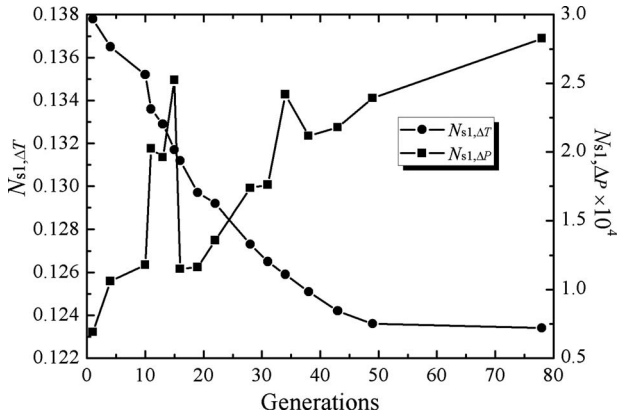

Fig. 5 Variations in $N_{s1,\Delta T}$ and $N_{s1,\Delta P}$ with the number of generations for single-objective optimization

In order to correctly reflect the influence of fluid friction in EGM, one may form a single-objective function by linearly combing separate objectives using some fixed weights prescribed by the user [34]. The objective function expressed in Eq. (23) can be regarded as the sum of $N_{s,\Delta T}$ and $N_{s,\Delta P}$, which are multiplied by weight coefficient 1. The weight coefficient might be 10, 100, or 1000, depending on the user's will. This method seems to be very straightforward, but different choices of the weight usually give rise to different solutions of a same optimization problem [34], and the weight coefficients have no definite physical meaning. Furthermore, setting an appropriate balance between the objectives to result in a full exploration of the desired range of tradeoffs within the objective space, can be difficult, especially where a nonconvex objective space is explored [35].

Another alternative to improve the single-objective optimization design of heat exchanger in the framework of EGM is to utilize the multi-objective optimization approach. Specifically, the entropy generation rates induced by the heat conduction and fluid friction can be set to two separate objective functions. Then the multi-objective genetic algorithm is employed to solve this multi-objective optimization problem. Theoretically, it leads to a set of solutions that represent the best trade-off between the two objective functions [36]. In addition, the genetic algorithm demonstrates obvious advantages in comparison with other methods for solving optimization problems. First, it does not necessitate the calculation of the objective function gradient with respect to the design variables, which is particularly helpful for multi-objective optimization. Second, the genetic algorithm usually explores a large portion of the design space and converges to the global optimum. Therefore, we attempt to establish the multi-objective optimization of heat exchanger design based on EGM in the following subsection.

3.3 Multi-Objective Optimization. Mathematically, multi-objective optimization minimizes several objectives simultaneously, with a number of inequality or equality constraints. It can be mathematically expressed as follows:

$$\min_{\mathbf{x} \in X} \mathbf{f}(x) = [f_1(x), f_2(x), \ldots, f_k(x)] \tag{27}$$

Subject to

$$g_j(x) = 0, \quad j = 1,2, \ldots, M$$

$$h_k(x) \le 0, \quad k = 1,2, \ldots, K$$

where x is a vector and is also called the decision vector and X is the parameter space.

If and only if, $f_i(x) \le f_i(y)$ for $i = 1,2,\ldots,k$ and $f_j(x) < f_j(y)$ for least one objective function j, a feasible solution x is said to dominate another feasible solution y. A solution, which is not dominated by any other solution in the feasible region, is called Pareto optimal solution. The set of all nondominated solutions in X is called as the Pareto optimal set (P^*), the values of objective functions corresponding to the Pareto optimal set are called Pareto front (PF^*) [36,37]

$$PF^* := \{\mathbf{f}(x) | x \in P^*\} \tag{28}$$

Specifically, the modified entropy numbers caused by heat conduction and fluid friction, respectively, are taken as two separate objective functions. The design parameters, their bounds and the constraints remain the same as specified in Sec. 3.2 for the single-objective optimization design. Here, for exemplifying the multi-objective optimization approach, only four design variables are selected. The optimization problems with more design variables can be solved by following the similar procedure.

In addition, the population type is *double vector*, and the size of initial population is set as 75. As for the creation function which creates the initial population, *Feasible population operator* is selected to generate a random initial population that satisfy all

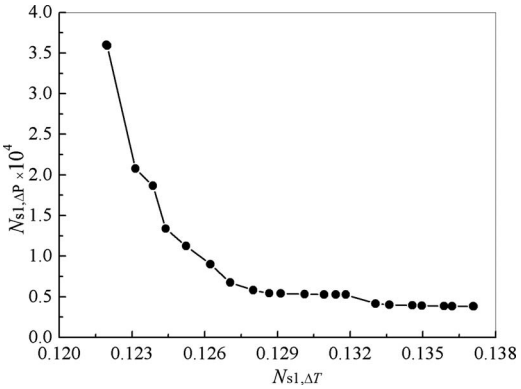

Fig. 6 The Pareto front obtained by multi-objective optimization for a fixed heat transfer area

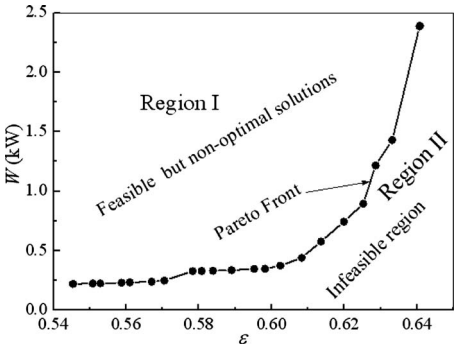

Fig. 7 The pumping power and effectiveness for a Pareto optimal set

bounds and constraints of design parameters, since it's biased to create individuals that are on the boundaries of the constraints, and to create well-dispersed populations [38]. The algorithm for choosing parents from individuals is *tournament*. Set the *crossover fraction* to be 0.8 so that 80% of the next generation is produced by crossover operator. *Scattered crossover* function is used to combine two individuals, or parents, to form a child for the next generation. *Gaussian mutation* function is used, the values of *scale* and *shrink* parameters are fixed as one, which means that the standard deviation shrinks linearly from 1 to 0 as the last generation is reached. The direction of *migration* is forward, i.e., the nth subpopulation migrates into the $(n+1)$th subpopulation, and migration takes place every 20 generations.

A controlled elitist genetic algorithm [39] (a variant of NSGA-II [36]) is adopted for searching the optimal solution, which can help increase the diversity of the population even if they have lower fitness values. The diversity of population is controlled by the elite members of the population in the process; the *distance crowding* function helps to maintain diversity by favoring individuals that are relatively far away on the front. The *Pareto fraction* is set to 0.35 so as to limit the number of individuals in the current population that are on the *Pareto front* to 35% of the population size. The total number of generations is set to 1000, which serves as the stopping criteria to terminate the iterative process.

3.3.1 Fixed Heat Transfer Area. In the present subsection, the multi-objective optimization is applied to design a shell-and-tube heat exchanger with fixed heat transfer area and the multi-objective genetic algorithm is employed to search the Pareto optimal set. The Pareto front obtained by the multi-objective optimization design is shown in Fig. 6. On the leftmost point of the curve represents the Pareto set, $N_{s1,\Delta T}$ reaches its minimum value, while $N_{s1,\Delta P}$ achieves its maximum value. Similarly, on the rightmost point $N_{s1,\Delta T}$ reaches its maximum value and $N_{s1,\Delta P}$ arrives at its minimum value. It indicates that the multi-objective optimization solutions are trade-off between the two irreversible losses caused by heat conduction and fluid friction, respectively. Therefore, for the multi-objective optimization the entropy generation caused by fluid friction is not neglected, but plays an important role in determining the optimal solutions.

In order to illustrate the meaning of the Pareto optimal set, the pumping power and heat exchanger effectiveness corresponding to the individual solution in the Pareto optimal set are depicted in Fig. 7. One can see that the total region is divided into two regions by the Pareto optimal set. The designs with the pumping power and exchanger effectiveness located in the region I are feasible, but not optimal. The ones in the region II are infeasible. Therefore, the solution in Pareto set is optimal in the sense that its exchanger effectiveness achieves the maximum value by consuming the least pumping power under the design requirements and constraints. Note that normally the optimal solution for the multi-objective optimization design is not unique. The designer can select one from the Pareto set according to the specific design requirements. Therefore, the multi-objective optimization design of heat exchanger is more flexible than the single-objective optimization design.

3.3.2 Fixed Heat Load. In this subsection, the multi-objective optimization design of heat exchanger is applied to the case that the heat load is given. The known data for the heat exchanger design is listed in Table 3. In comparison with the last example, the outlet temperature of cold fluid is selected as an additional design variable, and its values range from 313.15 K to 343.15 K.

The initial population can be specified by the users. However, since the size of the initial population is too large, the manner of stochastic generation is employed for the sake of simplicity in the present work. The Pareto front obtained by the multi-objective optimization is shown in Fig. 8. The randomly selected initial design solutions satisfying the design requirements and constraints and some representative optimal solutions in Pareto set are listed in Table 4. From Table 4, one can see that in compassion with the initial designs the exchanger effectiveness of the optimal solutions is significantly improved and the pumping power dramatically decline, but at the cost of the increase in the number of exchanger heat transfer units.

In comparison with the result of the single-objective optimization shown in Table 5, both approaches can yield almost the same heat exchanger effectiveness, which is about 0.71. However, the pumping power required for the single-objective optimization as shown in Table 5 is 552 W, while for the multi-objective optimization approach it is only about 260 W as seen from Table 4. Therefore, more than 50% decrease in the pumping power has been achieved for the multi-objective optimization in comparison with the single-objective optimization approach. Due to the reduc-

Table 3 The known data for heat exchanger design with the fixed heat load

	Fluid 1 (tube-side)	Fluid 2 (shell-side)
Inlet temperature T_i (K)	368.15	283.15
Outlet temperature T_o (K)	343.15	—
Mass flow rate $\dot{m}$ (kg/s)	50	—
Density ρ (kg/m^3)	970	991.15
Constant pressure specific heat c_p (J/kg K)	4200	4174
Kinematic viscosity v (m^2/s)	3.36×10^{-7}	6.96×10^{-7}
Entrance pressure P_i (MPa)	6.5	5
Fouling resistance r (m^2 K/W)	0.000086	0.00017
Prandtl number Pr	2.015	4.5878

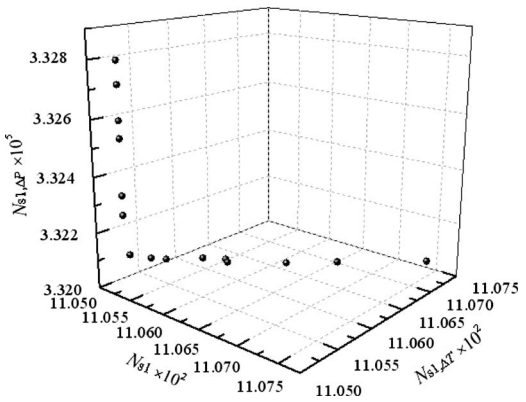

Fig. 8 The relations of N_{s1} with $N_{s1,\Delta T}$ and $N_{s1,\Delta P}$ in a Pareto optimal set for fixed heat duty

tion in entropy generation rate caused by fluid friction, the total entropy generation rates of the first two optimal solutions in Table 4 obtained by the multi-objective optimization design are slightly smaller than that obtained by the single-objective optimization approach in Table 5. As expected, the multi-objective optimization approach avoids the drawback of the single-objective optimization approach, which has not correctly reflected the role played by the fluid friction in EGM. Therefore, the multi-objective optimization design of heat exchanger, which can give rise to the best trade-off between the dimensionless entropy generation rates caused by heat conduction and fluid friction, respectively, is more suitable for applying EGM in heat exchanger design.

4 Concluding Remarks

The single-objective optimization of heat exchanger design based on EGM suffers the drawback that the role played by the entropy generation caused by the heat conduction under finite temperature difference is overwhelmingly enlarged for the liquid-to-liquid heat exchanger. In an attempt to resolve this problem, a multi-objective optimization design approach for heat exchanger is developed, in which the entropy generations induced by heat conduction and fluid friction are taken as two separate objective functions. Theoretically, the optimal solutions in the Pareto set obtained from the multi-objective genetic algorithm are the best trade-off between the two irreversible losses due to heat transfer and fluid friction. The results for two heat exchanger optimization design problems show that for achieving the same exchanger effectiveness the multi-objective optimization of heat exchanger design requires less pumping power in comparison with the single-objective optimization design. Therefore, the multi-objective optimization of the heat exchanger design really leads to the best trade-off between the two losses caused by heat conduction and fluid friction in heat exchanger which is the basic notion of EGM.

The multi-objective optimization yields the Pareto optimal set, which includes several optimal solutions. This gives the designer a great flexibility to choose a final solution from the Pareto optimal set by fully considering the specific requirements and constraints of the heat exchanger design. Furthermore, in the multi-objective optimization of heat exchanger design, all kinds of requirements, such as cost, weight and so on, may be treated as the optimization constraints and can be mathematically formulated in the multi-objective optimization of heat exchanger design. Therefore, the multi-objective optimization of heat exchanger design demonstrates obvious advantages and great flexibility.

Acknowledgment

The support of our research by the National Basic Research Program of China (Project No. 2007CB206900) is greatly appreciated.

Nomenclature

c_p = specific heat at constant pressure (J/kg K)
d_i = inner diameter of heat exchange tube (m)
d_o = outer diameter of heat exchange tube (m)
D_s = shell inner diameter (m)
f = friction factor
f_i = function i
$f(x)$ = objective value of solution x
G = mass velocity (kg/m^2 s)
j = heat transfer correct factor
K = heat transfer coefficient (W/m^2 K)
L = total length of tube pass (m)
$\dot{m}$ = mass flow rate (kg/s)
N_b = number of baffles
N_c = number of effective tube rows in one crossflow section
N_{cw} = number of effective tube rows crossed in baffle window
Ntu = number of heat transfer units
N_s = entropy generation number

Table 4 The initial designs and the optimal solutions for the heat exchanger with the fixed heat duty

	d_o (m)	n	Bs	θ (rad)	$T_{c,o}$ (K)	Ntu	W (W)	ε	$N_{s1,\Delta T}$	$N_{s1,\Delta P}$	N_{s1}
Initial design	0.016	361	0.72	2.81	314.54	0.55	1555	0.37	0.152	2.11×10^{-4}	0.152
	0.016	327	0.68	2.65	322.61	0.75	2094	0.46	0.140	2.77×10^{-4}	0.140
	0.016	327	0.68	2.35	326.47	0.89	1970	0.51	0.134	2.59×10^{-4}	0.134
Multi-objective	0.022	283	1.000	2.2675	343.13	1.5000	260.35	0.7100	0.1105	3.320×10^{-5}	0.1105
	0.022	283	0.995	2.2662	343.15	1.5000	260.84	0.7100	0.1105	3.332×10^{-5}	0.1105
	0.022	283	1.000	2.6666	343.15	1.5008	260.79	0.7059	0.1105	3.327×10^{-5}	0.1105
	0.022	283	1.000	2.2836	342.99	1.4928	260.29	0.7040	0.1107	3.321×10^{-5}	0.1107
	0.022	283	0.998	2.2656	343.08	1.5008	260.52	0.7059	0.1105	3.324×10^{-5}	0.1105

Table 5 The optimal solution of the single-objective optimization design for heat exchanger with the fixed heat duty

d_o (m)	n	Bs	θ (rad)	$T_{c,o}$ (K)	Ntu	W (W)	ε	$N_{s1,\Delta T}$	$N_{s1,\Delta P}$	N_{s1}
0.016	526	0.70	2.33	343.0	1.5	552	0.71	0.1105	6.98×10^{-5}	0.1106

N_{s1} = modified entropy generation number
Nu = Nusselt number
n = number of heat exchange tube
P = pressure (Pa)
P^* = Pareto optimal set
PF^* = Pareto front
Pr = Prandtl number
Q = heat transfer rate (W)
r = fouling resistance (m^2 K/W)
R = ideal gas constant (J/kg K)
Re = Reynolds number
$\dot{S}_{gen}$ = entropy generation rate (W/K)
s = tube pitch (m)
St = Stanton number
T = temperature (K)
v = velocity (m/s)
W = total pumping power (W)
X = solution set

Greek Symbols

α = heat transfer coefficient (W/m^2 K)
δ_t = thermal boundary layer thickness (m)
ε = the heat exchanger effectiveness
η = overall pumping efficiency
θ = central angle of baffle cut (rad)
λ = thermal conductivity (W/m K)
μ = fluid dynamic viscosity (Pa s)
ρ = density (kg/m^3)
τ = dimensionless temperature difference
ϕ = irreversibility distribution ratio
ΔP = pressure drop (Pa)
ΔT = temperature gradient (K)

Subscripts

c = cold fluid
h = hot fluid
i = inlet
o = outlet
s = shell-side
t = tube-side
w = wall

References

[1] Yilmaz, M., Sara, O. N., and Karsli, S., 2001, "Performance Evaluation Criteria for Heat Exchangers Based on Second Law Analysis," Int. J. Exergy, **1**(4), pp. 278–294.
[2] Prigogine, I., 1967, *Introduction to Thermodynamics of Irreversible Processes*, 3rd ed., Wiley, New York, pp. 76–77.
[3] Bejan, A., 1982, *Entropy Generation Through Heat and Fluid Flow*, Wiley, New York, pp. 118–134.
[4] Bejan, A., 1996, *Entropy Generation Minimization*, CRC, Boca Raton, FL, pp. 47–112.
[5] Shah, R. K., and Skiepko, T., 2004, "Entropy Generation Extrema and Their Relationship With Heat Exchanger Effectiveness—Number of Transfer Unit Behavior for Complex Flow Arrangements," ASME J. Heat Transfer, **126**(6), pp. 994–1003.
[6] Vargas, J., Bejan, A., and Siems, D. L., 2001, "Integrative Thermodynamic Optimization of the Crossflow Heat Exchanger for an Aircraft Environmental Control System," ASME J. Heat Transfer, **123**(4), pp. 760–770.
[7] Oğulatu, U., Doba, F., and Yilmaz, T., 2000, "Irreversibility Analysis of Cross Flow Heat Exchangers," Energy Convers. Manage., **411**, pp. 585–1599.
[8] Mishra, M., Das, P. K., and Sarangi, S., 2009, "Second Law Based Optimization of Crossflow Plate-Fin Heat Exchanger Design Using Genetic Algorithm," Appl. Therm. Eng., **29**(14–15), pp. 2983–2989.
[9] Guo, J. F., Cheng, L., and Xu, M. T., 2009, "Optimization Design of Shell-and-Tube Heat Exchanger by Entropy Generation Minimization and Genetic Algorithm," Appl. Therm. Eng., **29**(14–15), pp. 2954–2960.
[10] Mohamed, H. A., 2006, "Entropy Generation in Counter Flow Gas to Gas Heat Exchangers," ASME J. Heat Transfer, **128**(1), pp. 87–93.
[11] Bejan, A., 1977, "The Concept of Irreversibility in Heat Exchanger Design: Counterflow Heat Exchanger for Gas-to-Gas Applications," ASME J. Heat Transfer, **99**(3), pp. 374–380.
[12] Bejan, A., 1980, "Second Law Analysis in Heat Transfer," Energy, **5**, pp. 720–732.
[13] Hesselgreaves, J. E., 2000, "Rationalisation of Second Law Analysis of Heat Exchangers," Int. J. Heat Mass Transfer, **43**(22), pp. 4189–4204.
[14] Ogiso, K., 2003, "Duality of Heat Exchanger Performance in Balanced Counter-Flow Systems," ASME J. Heat Transfer, **125**(3), pp. 530–533.
[15] Witte, L. C., and Shamsundar, N., 1983, "A Thermodynamic Efficiency Concept for Heat Exchange Devices," ASME J. Eng. Power, **105**, pp. 199–203.
[16] London, A. L., and Shah, R. K., 1981, "Costs of Irreversibilities in Heat Exchanger Design," Heat Transfer Eng., **4**, pp. 59–73.
[17] Shah, R. K., and Sekulic, D. P., 2003, *Fundamentals of Heat Exchanger Design*, Wiley, New York.
[18] Kuppan, T., 2000, *Heat Exchanger Design Handbook*, Marcel Dekker, New York.
[19] Shi, M. Z., and Wang, Z. Z., 1996, *Principia and Design of Heat Transfer Device*, Southeast University Press, Nanjing, China, in Chinese.
[20] Palen, J. W., 1986, *Heat Exchanger Sourcebook*, Hemisphere, Washington, DC.
[21] Caputo, A. C., Pelagagge, P. M., and Salini, P., 2008, "Heat Exchanger Design Based on Economic Optimization," Appl. Therm. Eng., **28**(10), pp. 1151–1159.
[22] Bejan, A., 1988, *Advanced Engineering Thermodynamics*, Wiley, New York.
[23] State Bureau of Quality and Technical Supervision, 1999, *Tubular Heat Exchangers*, *GB151-1999*, Standards Press of China, Beijing, China, in Chinese.
[24] Babu, B. V., and Munawar, S. A., 2007, "Differential Evolution Strategies for Optimal Design of Shell-and-Tube Heat Exchangers," Chem. Eng. Sci., **62**, pp. 3720–3739.
[25] Oh, Y. H., Chung, T. K., Kim, M. K., and Jung, H. K., 1999, "Optimal Design of Electric Machine Using Genetic Algorithms Coupled With Direct Method," IEEE Trans. Magn., **35**(3), pp. 1742–1745.
[26] Mohammed, O. A., and Uler, G. F., 1997, "A Hybrid Technique for the Optimal Design of Electromagnetic Devices Using Direct Search and Genetic Algorithms," IEEE Trans. Magn., **33**(2), pp. 1931–1934.
[27] Wang, Q. W., Zhang, D. J., and Xie, G. N., 2009, "Experimental Study and Genetic-Algorithm-Based Correlation on Pressure Drop and Heat Transfer Performance of a Cross-Corrugated Primary Surface Heat Exchanger," ASME J. Heat Transfer, **131**(6), p. 061802.
[28] Fanni, A., Marchesi, M., Serri, A., and Usai, M., 1997, "A Greedy Genetic Algorithm for Continuous Variables Electromagnetic Optimization Problems," IEEE Trans. Magn., **33**(2), pp. 1900–1903.
[29] Wang, Q. W., Xie, G. N., Peng, B. T., and Zeng, M., 2007, "Experimental Study and Genetic-Algorithm-Based Correlation on Shell-Side Heat Transfer and Flow Performance of Three Different Types of Shell-and-Tube Heat Exchangers," ASME J. Heat Transfer, **129**(9), pp. 1277–1286.
[30] Houck, C. R., Joines, J. A., and Kay, M. G., 1995, "A Genetic Algorithm for Function Optimization: A MATLAB Implementation," North Carolina State University Technical Report No. NCSU-IE-TR-95-09.
[31] Selbaş, R., Kızılkan, Ö., and Reppich, M., 2006, "A New Design Approach for Shell-and-Tube Heat Exchangers Using Genetic Algorithms From Economic Point of View," Chem. Eng. Process., **45**(4), pp. 268–275.
[32] Xie, G. N., Sunden, B., and Wang, Q. W., 2008, "Optimization of Compact Heat Exchangers by a Genetic Algorithm," Appl. Therm. Eng., **28**, pp. 895–906.
[33] Raznjevic, K., 1995, *Handbook of Thermodynamic Tables*, 2nd ed., Begell House, New York.
[34] Hilbert, R., Janiga, G., Baron, R., and Thévenin, D., 2006, "Multi-Objective Shape Optimization of a Heat Exchanger Using Parallel Genetic Algorithms," Int. J. Heat Mass Transfer, **49**, pp. 2567–2577.
[35] Barakat, T. M., Fraga, E. S., and Sørensen, E., 2008, "Multi-Objective Optimisation of Batch Separation Process," Chem. Eng. Process., **47**(12), pp. 2303–2314.
[36] Deb, K., 2001, *Multi-Objective Optimization Using Evolutionary Algorithms*, Wiley, Chichester, UK.
[37] Copiello, D., and Fabbri, G., 2009, "Multi-Objective Genetic Optimization of the Heat Transfer From Longitudinal Wavy Fins," Int. J. Heat Mass Transfer, **52**(5–6), pp. 1167–1176.
[38] Matlab Company, 2009, "MATLAB User Guide: Version 7.9.0."
[39] Deb, K., and Goel, T., 2001, "Controlled Elitist Non-Dominated Sorting Genetic Algorithms for Better Convergence," Lect. Notes Comput. Sci., **1993**, pp. 67–81.

Modeling Carrier-Phonon Nonequilibrium Due to Pulsed Laser Interaction With Nanoscale Silicon Films

Arvind Pattamatta
e-mail: apattamatta@gmail.com

Cyrus K. Madnia[1]
e-mail: madnia@buffalo.edu

Department of Mechanical and Aerospace Engineering,
University at Buffalo,
Buffalo, NY 14260-4400

Ultrashort-pulsed laser irradiation on semiconductors creates a thermal nonequilibrium between carriers and phonons. Previous computational studies used the "two-temperature" model and its variants to model this nonequilibrium. However, when the laser pulse duration is smaller than the relaxation time of the carriers or phonons or when the carriers' or phonons' mean free path is larger than the material dimension, these macroscopic models fail to capture the physics accurately. In this article, the nonequilibrium between carriers and phonons in silicon films is modeled via numerical solution of the Boltzmann transport model (BTM), which is applicable over a wide range of length and time scales. The BTM is solved using the discontinuous Galerkin finite element method for spatial discretization and the three-stage Runge–Kutta temporal discretization. The BTM results are compared with previous computational studies on laser heating of macroscale silicon films. The model is then used to study laser heating of nanometer size silicon films, by varying parameters such as the laser fluence and pulse duration. From the laser pulse duration study, it is observed that the peak carrier number density, and maximum carrier and phonon temperatures are the highest for the shortest pulse duration of 0.05 ps and decreases with increasing pulse duration. From the laser fluence study, it is observed that for fluences equal to or higher than 1000 J/m^2, due to the Auger recombination, a second peak in carrier temperature is observed. The use of carrier-acoustic phonon coupling leads to equilibrium phonon temperatures, which are approximately 400 K higher than that of carrier-optical phonon-acoustic phonon coupling. Both the laser pulse duration and fluence are found to strongly affect the equilibrium time and temperature in Si films. [DOI: 10.1115/1.4001101]

Keywords: Si, Boltzmann transport model, carrier-phonon nonequilibrium, nanoscale energy transport, ultrashort-pulsed laser, RKDG

1 Introduction

Short-pulsed laser heating of semiconductors has extensive applications such as fabrication of sophisticated micro-/nanostructures, syntheses of advanced semiconductor materials, measurement of thin-film properties, laser annealing and damage, and electronic desorption process [1–5]. The use of ultrashort-pulsed duration laser has also found application in the field of laser recovery of stiction-failed microstructures [6]. Experiments with femtosecond laser pulses of high fluences have demonstrated ultrafast phase transformation on a subpicosecond time scale [7–9]. Under ultrashort-pulsed laser excitation of semiconductors, high-density and high-temperature electrons could be excited from the valence band into the conduction band. As a result, lattice instability occurs prior to the significant heating of the phonon subsystem, and this damage is referred to as nonthermal melting [10]. The physics of short-pulse laser heating of semiconductors is very complex, and hence, it is necessary to understand energy absorption, transport, and storage phenomena in detail. When a semiconductor is excited with a short laser pulse, some electrons absorb the photon energy and move from the valence band to the conduction band. This interband transition of the electrons creates holes in the valence band. The electron-hole pairs generated in this manner are responsible for heat transfer and are referred to as the "carriers" [11]. The excess energy of these electron-hole pairs, which is the difference between the incident laser energy $h\nu$ and the bandgap energy of silicon E_g, is the kinetic energy that leads to elevated carrier temperatures. As the excited carriers undergo spatial and temporal evolutions, a number of them recombine via the Auger process. In the meantime, new carriers are generated via impact ionization [11]. The carriers then thermalize into the Fermi–Dirac distribution via carrier-carrier collisions. Meanwhile, collisions between carriers and phonons occur, which eventually leads to a thermal equilibrium between carriers and phonons. The relaxation time for the carrier-phonon collisions is typically in the range of 0.1–0.5 ps for silicon [12]. Measurements of carrier-phonon nonequilibrium parameters such as carrier number density, and phonon and carrier temperatures prove to be difficult due to the very small length and time scales involved. Thus, computational modeling plays an important role in obtaining detailed information on the energy transport between carriers and phonons. Previous computational studies [6,11,13–16] used the two-temperature model to simulate the energy transport for laser heating of a semiconductor film. The thermal coupling between carriers and phonons are modeled by considering separate carrier and phonon temperatures in semiconductors. Fushinobu et al. [6] suggested a new way to recover stiction-failed microstructures using ultrashort-pulsed laser irradiation. Lee et al. [13] performed a parametric study for optimizing the laser parameters for laser irradiation on macroscale thick films. However, the two-temperature models used in the above computational studies do not take into account the energy current generated due to the large

[1]Corresponding author.

Contributed by the Heat Transfer Division of ASME for publication in the JOURNAL OF HEAT TRANSFER. Manuscript received April 8, 2009; final manuscript received December 19, 2009; published online June 4, 2010. Assoc. Editor: Pamela M. Norris.

temperature gradients in the semiconductor film. In order to account for the work done in generating carrier energy current, van Driel [11] used a parabolic rate equation for carrier energy to incorporate the additional work term. He applied this model to study the kinetics of high-density plasmas generated in silicon by picosecond laser pulses with two different wavelengths, and found that the carrier temperature exhibited two peaks as a function of time due to laser heating as well as Auger heating. Chen et al. [14] used similar equations as van Driel [11] and applied them to compute for the damage threshold of Si and Ge, and obtained reasonably good agreement with the experiment. However, for the cases when the laser pulse duration is smaller than the relaxation time of the energy carriers or when the carriers' mean free path (MFP) is larger than the material dimension, the two-temperature models fail to accurately capture the nonequilibrium between the energy carriers [12,17–19]. These phenomenological models cannot be used to describe heat transfer in highly nonequilibrium situations as seen in the case of nanometer thin semiconductor films irradiated with laser pulse durations comparable to the carrier-phonon relaxation time. In order to model this nonequilibrium accurately, the coupled Boltzmann transport equations (BTEs) for the carriers and phonons [12,18] are solved numerically. The BTE can be used to model heat transport over a wide range of length and time scales. The main objective of the present study is to model the energy transport in silicon (Si) films. Emphasis is placed on studying strong nonequilibrium created during the interaction of femtosecond pulse duration laser with nanometer size films. The temperature dependant phonon properties for Si obtained from the phonon dispersion model are used. A parametric study is conducted for Si films to study the effect of laser pulse duration and fluence on the carrier-phonon nonequilibrium characteristics.

2 Theory

In this section, the problem description, details of the Boltzmann transport model (BTM), calculation of carrier and phonon thermal properties, and computational methodology are discussed.

2.1 Problem Description. The carrier-phonon interactions are studied by applying a laser beam with a wide range of pulse duration and fluence to a silicon (Si) film with thicknesses in the range of nano- to micrometers. The laser beam diameter is much larger than the optical and carrier penetration depths, and hence, a one-dimensional model can describe the physical problem [17]. The laser intensity is given as [6]

$$I(x,t) = \frac{2\sqrt{\ln 2}\phi(1-R)}{\sqrt{\pi}t_p}\exp\left(-\int_0^x \alpha dz\right)\exp(-4\ln 2((t-2t_p)/t_p)^2) \tag{1}$$

where ϕ is the fluence carried by the laser pulse, R is the reflectivity, t_p is the laser pulse duration defined as full width at half maximum of the laser pulse shape, α is the absorptivity of Si, and x is the depth measured from the front surface. The laser beam is Gaussian in both time and space. From Eq. (1), the peak of the laser intensity occurs at time $t=2t_p$.

2.2 Boltzmann Transport Model. The carrier-phonon interaction in a semiconductor is modeled via the BTM consisting of two coupled BTEs describing the carrier and phonon energy transports. The BTEs are formulated in the relaxation time approximation to describe the energy densities of carriers and phonons, denoted by u_c and u_p, respectively. The carrier or phonon energy density is defined as the flux of energy per unit volume and per unit solid angle in the direction $\boldsymbol{s}$. The carrier energy density u_c is related to its distribution function f_c

Table 1 Physical properties of Si

Property	Value	Ref.
C_c (J/m^3 K)	$3N_c k_B$	[16]
C_p (J/m^3 K)	Table 2	[16]
C_{OP} (J/m^3 K)	7.15×10^5	[34]
K_c (W/m K)	$-0.556+7.13\times10^{-3}T_c$	[16]
K_p (W/m K)	Table 2	[34]
v_c (m/s)	$\sqrt{(3k_bT_c)/(2.3\times10^{-31})}$	-
v_p (m/s)	Table 2	[25,34]
$\tau_{c\text{-}c}$ (s)	$3K_c/(C_c v_c^2)$	-
$\tau_{c\text{-}p}$ (s)	$\tau_0[1+(N_c/N_{cr})^2]$ $\tau_0=0.5\times10^{-12}$ $N_{cr}=2\times10^{27}$	[11,16]
$\tau_{p\text{-}p}$ (s)	$3K_p/(C_p v_p^2)$	-
E_g (eV)	$1.167-0.0258(T_p/300)-0.0198(T_p/300)^2$	[15]
α (1/m)	$\alpha=\alpha_1+\sigma_{fc}N_c$ $E'=(h\nu)+1.1214-E_g$ $\alpha_1=250{,}000\exp(2.48(E'-1.79))$ $\sigma_{fc}=5.1\times10^{-22}[1.17/(h\nu)]^2[T_p/300]$	[15]
β (m/W)	2.0×10^{-11}	[11]
Θ (1/s)	$3.6\times10^{10}\exp(-1.5E_g/k_bT_c)$	[11]
γ (m^6/s)	3.8×10^{-43}	[16]
R	0.32	[11]

$$u_c(\boldsymbol{r},\boldsymbol{s},t) = \int (E-E_f) f_c(\boldsymbol{r},\boldsymbol{s},t) D_c(E) dE \tag{2}$$

where $\boldsymbol{r}$ denotes the position vector, $(E-E_f)$ is the electron band energy relative to the Fermi energy, and $D_c(E)$ is the carrier density of states per unit volume. The equilibrium distribution of carriers is represented by the Fermi–Dirac distribution [20]. Similarly, the phonon energy density u_p is related to its distribution function f_p [21]

$$u_p(\boldsymbol{r},\boldsymbol{s},t) = \sum \int \hbar\omega f_p(\boldsymbol{r},\boldsymbol{s},t) D_p(\omega) d\omega \tag{3}$$

where $\hbar$ is the Planck's constant divided by 2π, ω is the phonon frequency, and $D_p(\omega)$ is the phonon density of states per unit volume; the integration is over all the phonon frequencies up to the Debye frequency, and the summation is over the three phonon polarization modes. The equilibrium distribution of phonons is represented by the Bose–Einstein distribution [22].

If the incident photons have energies greater than the bandgap of the semiconductor, electron-hole pairs are formed, which act as the heat carriers. The carrier number density of electron-hole pairs N_c is determined from the following conservation equation [6]

$$\frac{\partial N_c}{\partial t} = \frac{\alpha_1 I}{h\nu} + \frac{\beta I^2}{2h\nu} - \gamma N_c^{\,3} + \Theta N_c \tag{4}$$

The terms on the right-hand side of Eq. (4) represent the carrier generation rates from the linear (one-photon) and nonlinear (two-photon) absorptions, the Auger recombination, and the impact ionization, respectively. The expressions for α_1, β, γ, and Θ are given in Table 1.

When the carriers are assumed to transfer their energy directly to the acoustic phonons, the interaction is referred to as the carrier-acoustic phonon (C-AP) interaction. The frequency independent BTM for coupled carrier and acoustic phonon energy densities can be expressed as [18,23]

$$\frac{\partial u_c}{\partial t} + v_c\left(\mu\frac{\partial u_c}{\partial x}\right) = \frac{u_{\mathrm{eq}(c)}-u_c}{\tau_{(c\text{-}c)}} - \frac{\partial (N_c E_g)}{\partial t} - \frac{C_c(T_c-T_p)}{4\pi\tau_{(c\text{-}p)}} + \frac{\alpha I(x,t)+\beta I^2(x,t)}{4\pi} \tag{5}$$

$$\frac{\partial u_{\mathrm{AP}}}{\partial t} + v_p\left(\mu\frac{\partial u_{\mathrm{AP}}}{\partial x}\right) = \frac{u_{\mathrm{eq(AP)}} - u_{\mathrm{AP}}}{\tau_{(p\text{-}p)}} + \frac{C_c(T_c - T_p)}{4\pi\tau_{(c\text{-}p)}} \tag{6}$$

where the subscripts c and AP denote the carrier and acoustic phonons, respectively, and T_p denotes the acoustic phonon temperature. The terms on the left-hand side of Eq. (5) represent the time rate of change in the carrier kinetic energy per unit volume and carrier convective transport, respectively. The terms on the right-hand side of Eq. (5) represent the carrier-carrier collisions approximated by the relaxation time, time rate of change in the bandgap energy per unit volume, energy loss due to carrier-phonon collisions, and the laser source, respectively. The terms on the left-hand side of Eq. (6) represent the time rate of change in the acoustic phonon kinetic energy per unit volume and acoustic phonon convective transport, respectively. The terms on the right-hand side of Eq. (6) represent the acoustic phonon-acoustic phonon collisions approximated by the relaxation time, and the energy gain due to carrier-phonon collisions, respectively. The acoustic phonon temperature T_p in Eqs. (5) and (6) are calculated from Eq. (14). The equilibrium energies are given by

$$u_{\mathrm{eq}(c)} = \frac{1}{2}\int_{-1}^{1} u_c d\mu \quad \text{and} \quad u_{\mathrm{eq(AP)}} = \frac{1}{2}\int_{-1}^{1} u_{\mathrm{AP}} d\mu \tag{7}$$

where μ is the x-direction cosine.

However, the carriers generally interact with the optical phonons directly, which then subsequently transfer their energy to the acoustic phonons. This involves a set of equations which consider the energy densities of the carriers, optical phonons, and acoustic phonons, and their interactions. The BTM for the case of carrier-optical phonon-acoustic phonon (C-OP-AP) interaction can be expressed as [24]

$$\frac{\partial u_c}{\partial t} + v_c\left(\mu\frac{\partial u_c}{\partial x}\right) = \frac{u_{\mathrm{eq}(c)} - u_c}{\tau_{(c\text{-}c)}} - \frac{\partial(N_c E_g)}{\partial t} - \frac{C_c(T_c - T_{\mathrm{OP}})}{4\pi\tau_{(c\text{-}p)}} + \frac{\alpha I(x,t) + \beta I^2(x,t)}{4\pi} \tag{8}$$

$$\frac{\partial u_{\mathrm{OP}}}{\partial t} = \frac{C_c(T_c - T_{\mathrm{OP}})}{4\pi\tau_{(c\text{-}p)}} - \frac{C_{\mathrm{OP}}(T_{\mathrm{OP}} - T_p)}{4\pi\tau_{(p\text{-}p)}} \tag{9}$$

$$\frac{\partial u_{\mathrm{AP}}}{\partial t} + v_p\left(\mu\frac{\partial u_{\mathrm{AP}}}{\partial x}\right) = \frac{u_{\mathrm{eq(AP)}} - u_{\mathrm{AP}}}{\tau_{(p\text{-}p)}} + \frac{C_{\mathrm{OP}}(T_{\mathrm{OP}} - T_p)}{4\pi\tau_{(p\text{-}p)}} \tag{10}$$

where the subscript OP and AP denote the optical and acoustic phonons, respectively. The term on the left-hand side of Eq. (9) represent the time rate of change in the optical phonon kinetic energy per unit volume. The terms on the right-hand side of Eq. (9) represent the energy gain due to carrier-optical phonon collisions, and the energy loss due to optical phonon-acoustic phonon collisions, respectively. In Eqs. (8)–(10), it is assumed that the relaxation time for carrier-optical phonon collisions is the same as that for carrier-acoustic phonon collisions in Eqs. (5) and (6). This assumption was tested by varying the value of the relaxation time for the carrier-optical phonon collisions by an order of magnitude compared with the relaxation time for the carrier-acoustic phonon collisions. The values obtained for the equilibrium time and equilibrium temperature corresponding to this variation do not change significantly. For the C-OP-AP coupling, the phonon temperature T_p is defined as

$$T_p = \frac{C_p T_{\mathrm{AP}} + C_{\mathrm{OP}} T_{\mathrm{OP}}}{C_p + C_{\mathrm{OP}}} \tag{11}$$

2.3 Carrier and Phonon Properties. The solution to the BTM requires knowledge of the carrier and phonon relaxation times, group velocities, thermal conductivities, and heat capacities. The physical properties of silicon used in the present simulations are listed in Table 1. The specific heat and group velocity for acoustic phonons are calculated as a function of temperature using the phonon sine function dispersion model [25,26] and listed in Table 2. The group velocity and specific heat of phonons are calculated using the contribution of acoustic phonons only, since the optical phonons have negligible group velocity, and hence, do not transport energy. The mean free path of acoustic phonons calculated using the sine function dispersion model is approximately 280 nm. Linear interpolation is used to calculate the properties between any two temperatures given in Table 2.

Table 2 Phonon properties

T (K)	K_p (W/m K)	C_p ($\times 10^6$) (J/m^3 K)	v_p (m/s)
300	154.80	0.96	1740
400	99.90	0.9950	1690
500	70.10	1.01	1670
600	60.30	1.02	1660
700	50	1.02	1650
800	41.70	1.02	1640
900	36	1.02	1630
1000	30	1.02	1620

2.4 Computational Methodology. The coupled BTEs for carriers and phonons are solved numerically using the Runge–Kutta discontinuous Galerkin (RKDG) method [27–29]. The RKDG method incorporates the local conservation property of the finite volume schemes and the higher order accuracy of finite element methods [27]. The discontinuous Galerkin (DG) methods have some attractive properties that make them good alternatives to existing methods for problems described using hyperbolic equations such as those encountered in fluid flows or thermal radiation. These properties include high-order local approximation using polynomials, ease of parallelization, elementwise conservation, and geometric flexibility of conventional finite elements. High resolution temporal discretization is achieved using a three-stage Runge–Kutta (RK) time stepping scheme that allows the RKDG method to be numerically stable [28].

The RKDG scheme using Legendre polynomials as basis functions has been developed by the authors for the BTEs for carriers and phonons [18]. Two Legendre bases involving the piecewise constant and piecewise linear functions are used for higher-order spatial discretization. The angular discretization of the BTEs is achieved using piecewise constant basis functions in the angular space [30]. This allows for exact analytical evaluation of the integrals in the BTEs without the use of quadratures.

Detailed spatial, angular, and temporal resolution studies have been performed to test the grid independence of the solution. It is found that a spatial grid with 120 elements and an angular decomposition with 50 elements provide the best resolution of the temperature profiles. A temporal resolution study has also been performed, and a value of Courant number equal to 0.2 is found to ensure accurate transient solution using the RK time stepping.

During the very short duration of laser heating, heat losses from the front and back surfaces of the semiconductor are found to be negligible, and hence, are treated as adiabatic. These surfaces are modeled as specularly reflecting boundaries, on which the following conditions on carrier and phonon thermal intensities are imposed

$$u_c(0,\mu,t) = u_c(0,-\mu,t); \quad u_c(L,-\mu,t) = u_c(L,\mu,t) \tag{12}$$

$$u_{\mathrm{AP}}(0,\mu,t) = u_{\mathrm{AP}}(0,-\mu,t); \quad u_{\mathrm{AP}}(L,-\mu,t) = u_{\mathrm{AP}}(L,\mu,t) \tag{13}$$

The initial energy densities for carriers and phonons are assumed to be constants and are calculated at $T=300$ K. In the case of a carrier coupled with acoustic phonons only, the energy densities

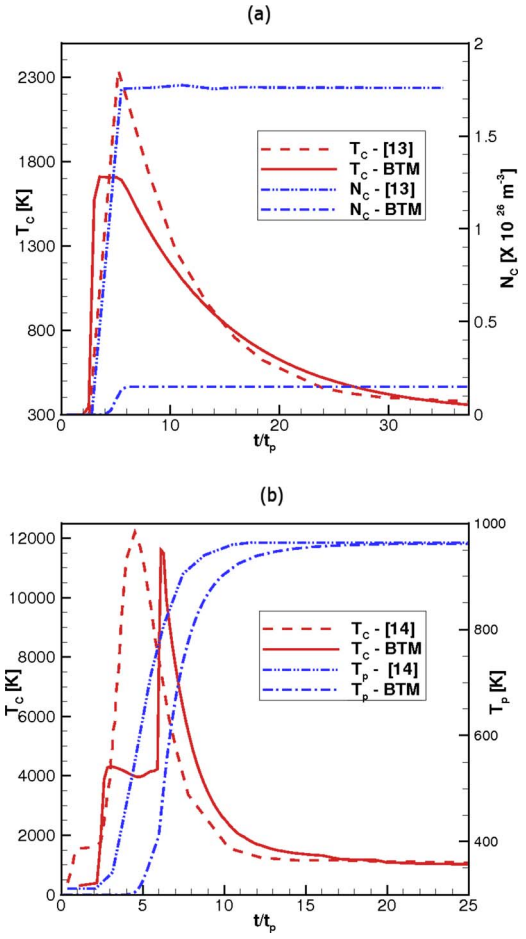

Fig. 1 (*a*) **Carrier temperature and number density profiles at the front surface of a Si film for $L=2$ μm, $t_p=75$ fs, and $\phi=38.2$ J/m^2; (*b*) carrier and phonon temperature profiles at the front surface of a Si film for $L=20$ μm, $t_p=500$ fs, and $\phi=1500$ J/m^2**

obtained from solving the BTEs are used to determine the carrier and acoustic phonon temperatures from

$$\int_0^{T_c} C_c dT = u_c(x,\theta)\Delta\Omega; \quad \int_0^{T_p} C_p dT = u_{\mathrm{AP}}(x,\theta)\Delta\Omega \tag{14}$$

where $\Delta\Omega=4\pi\sin\theta\sin(0.5\Delta\theta)$ is the volume of the "finite angle." In the case of a carrier coupled with optical and acoustic phonons, the acoustic and optical phonon temperatures are obtained from their respective energy densities as

$$\int_0^{T_{\mathrm{AP}}} C_p dT = u_{\mathrm{AP}}(x,\theta)\Delta\Omega; \quad \int_0^{T_{\mathrm{OP}}} C_{\mathrm{OP}} dT = u_{\mathrm{OP}}(x,\theta)\Delta\Omega \tag{15}$$

and the average phonon temperature is then calculated from Eq. (11). The integrals in Eqs. (14) and (15) are evaluated using the trapezoidal rule, and the temperatures are obtained iteratively using the bisection method. At nanoscales, the temperature, as such, has no physical meaning, except that it is an indicator of the local energy density of the system.

3 Results and Discussion

The results of the BTM with C-OP-AP coupling is compared with the results of the two-temperature models of Lee et al. [13] and Chen et al. [14], as shown in Figs. 1(*a*) and 1(*b*), respectively. Figure 1(*a*) shows the time evolution of the carrier number density and the carrier temperature at the front surface for a Si film thickness $L=2$ μm, laser pulse duration $t_p=75$ fs, laser fluence $\phi=38.2$ J/m^2, and laser wavelength $\lambda=790$ nm. The physics of carrier-phonon nonequilibrium for this case cannot be accurately captured using the classical two-temperature model since the laser pulse duration is much smaller than the carrier-phonon relaxation time of 500 fs. It is observed from Fig. 1(*a*) that the peak carrier number density obtained using the BTM is approximately an order of magnitude smaller than the peak number density obtained from the two-temperature model of Lee et al. [13]. The value of the peak carrier temperature obtained by Lee et al. [13] is approximately 35% higher than that of the BTM. This may be due to the excessive diffusion present in the two-temperature model, which leads to overprediction of the peak carrier temperature. This excessive diffusion is also observed with the two-temperature models when applied to the case of laser heating of metal films [18,23]. The BTM, due to its hyperbolic nature, can model the transport of carriers and phonons more realistically without excessive diffusion. Figure 1(*b*) shows the comparison of the carrier and phonon temperatures between the BTM and the computations of Chen et al. [14]. The parameters for this case correspond to a Si film thickness $L=20$ μm, laser pulse duration $t_p=500$ fs, laser fluence $\phi=1500$ J/m^2, and laser wavelength $\lambda=775$ nm. The two-temperature model used in the computations of Chen et al. [14] is similar to that used by van Driel [11]. From Fig. 1(*b*), it is observed that the carrier temperature has a double peak, which is predicted by both the BTM and the two-temperature model. The first peak in the carrier temperature is attained due to the laser excitation of carriers, while the second peak is attributed to the Auger recombination process. In the silicon film, band-to-band Auger recombination occurs simultaneously with the collision between two like carriers. The energy released by the recombination process is transferred during the collision to the surviving carrier. Subsequently, this highly energetic carrier "thermalizes" and loses energy in small steps through collisions with the phonons [31]. Consequently, this causes the phonon temperature to increase until an equilibrium is attained between the carrier and phonon temperatures. Figure 1(*b*) shows that for this case, the time evolution of T_c and T_p predicted by the BTM and Chen et al. [14] differ from each other. The first peak in T_c predicted by the BTM is higher than that of the model of Chen et al. [14]. The location of the peak carrier temperature predicted by the models are different from each other but the value of the second peak in the carrier temperature predicted by both models are close to each other. The equilibrium temperature predicted by the BTM is in good agreement with that of Chen et al. [14], as seen in Fig. 1(*b*).

Table 3 Summary of parameters

Category	L (nm)	t_p (ps)	ϕ (J/m^2)
1	28	0.05–10	500
2	28	0.075	10–3000

The BTM is applied to the problem of laser heating of Si film by varying different parameters and studying their impact on the thermal transport in nanometer size films. The categories considered for the parametric study are summarized in Table 3. It has been found that varying the film thickness of Si while keeping the laser fluence and pulse duration fixed does not have a significant effect on the peak carrier and phonon temperatures. Therefore, only two categories are considered. For each category, several simulations are performed. In category 1, the effect of laser pulse duration in the range of 0.05–10 ps is studied, keeping the thickness and fluence fixed at 28 nm and 500 J/m^2, respectively. The Si film thickness of 28 nm is approximately ten times smaller than the phonon mean free path of 280 nm. In category 2, the laser fluence is varied while maintaining the film thickness and pulse

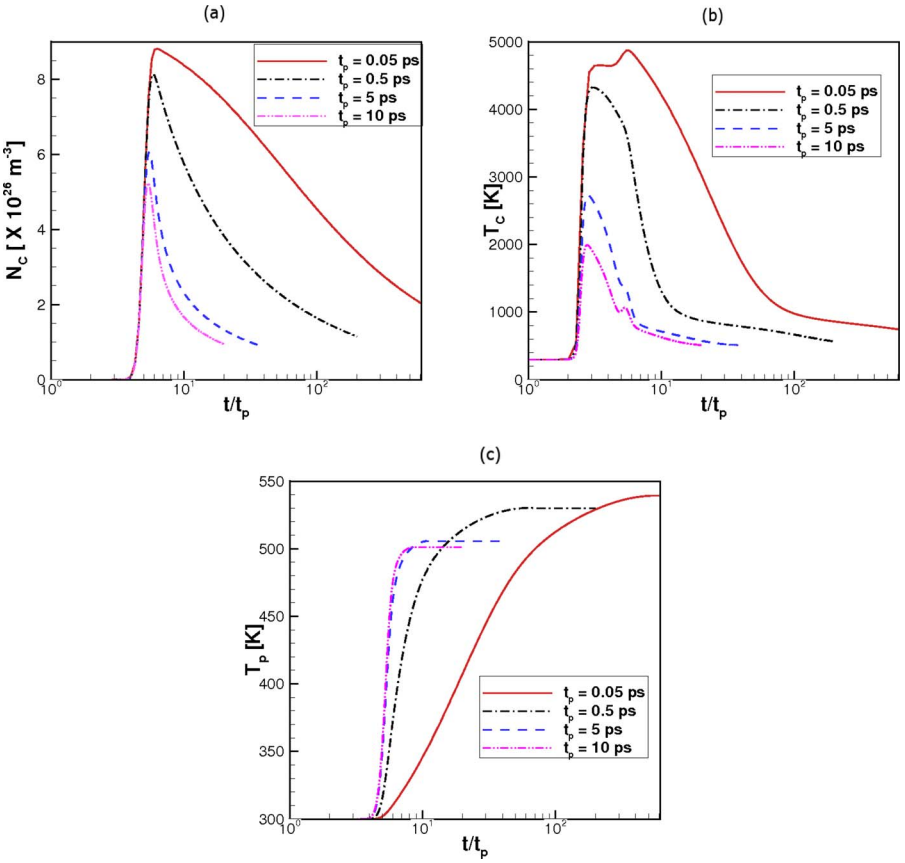

Fig. 2 Temporal variations in the (*a*) carrier number density, (*b*) carrier temperature, and (*c*) phonon temperature with pulse duration at the front surface for $L=28$ nm and $\phi=500$ J/m^2

duration at 28 nm and 75 fs, respectively. The pulse duration of 75 fs is smaller than the carrier-phonon collision time of 500 fs. The nanoscale film thickness, short pulse duration, and relatively high fluence used in this study are chosen to create a strong nonequilibrium between the energy carriers. A laser wavelength of 550 nm, which is in the visible wavelength regime, is used throughout this study. The effects of laser pulse duration and fluence are studied by considering the C-OP-AP coupling. The resulting equilibrium time and temperatures using this model are compared with the results of C-AP coupling.

3.1 Temporal Characteristics of Carrier-Phonon Nonequilibrium. Figure 2 shows the temporal evolution of the carrier number density, and carrier and phonon temperatures at the front surface of Si film for varying laser pulse durations (category 1 of Table 3). For all the cases considered in this study, it is found that the impact ionization term in Eq. (4) is negligible while the two-photon absorption term in this equation is significant only for values of laser fluence above 1000 J/m^2. From Fig. 2(*a*), it is observed that at very early times, the laser pulse is mainly supplying energy to the carriers, whereas it is not significantly increasing the number density of them. The number density of carriers exhibits a sharp increase at a time instant of four times the pulse duration. This figure shows that with increasing laser pulse duration, the peak value of the carrier number density decreases. The rate of decrease in the carrier number density is the steepest for the largest pulse duration, which can be attributed to the Auger recombination. With the increasing laser pulse duration, there is an increase in the carrier-carrier collisions, resulting in the enhanced recombination of electron-hole pairs. From Fig. 2(*b*), it is observed that the carrier temperature starts to increase at a time instant of approximately twice the pulse duration, earlier than the increase in the carrier number density. Due to the absorbed laser thermal energy, the carrier temperature increases rapidly to several thousands Kelvin as compared with the phonon temperature of few hundreds Kelvin. This is due to the heat capacity of the carriers being several orders of magnitude smaller than the phonon heat capacity. For example, at room temperature, the carrier heat capacity is approximately ten orders of magnitude smaller than the phonon heat capacity. During the initial time period extending to four times the pulse duration, the carriers are quite energetic. However, they do not transfer their energy to the phonons. Beyond this time, the carriers begin to transfer their energies to the phonons, resulting in an increase in the phonon temperatures. From Fig. 2(*b*), it is depicted that the peak carrier temperature is the highest for the smallest pulse duration of 0.05 ps and decreases with increasing pulse duration. This is attributed to the strong nonequilibrium present for small laser pulse duration cases. For a value of the laser pulse duration of 0.05 ps, which is an order of magnitude smaller than the relaxation time of carriers, ballistic effects are dominant due to the hyperbolic nature of the carrier energy transport. For this case, the temporal evolution of T_c is different from the other cases in the sense that the first peak in the carrier temperature is lower than the second peak. For a pulse duration of 0.5 ps, only a single peak in the carrier temperature is observed while a second peak due to Auger recombination appears for longer laser pulse durations, as seen in Fig. 2(*b*). The Auger recombination results in the transfer of the bandgap energy into the carrier energy, leading to an increase in the carrier temperature, which results in the second peak. In the BTM model with C-OP-AP coupling, the carriers first transfer their energy to the optical phonons, which then interact with acoustic phonons before reaching thermal equilibrium. From Fig. 2(*c*), it is observed

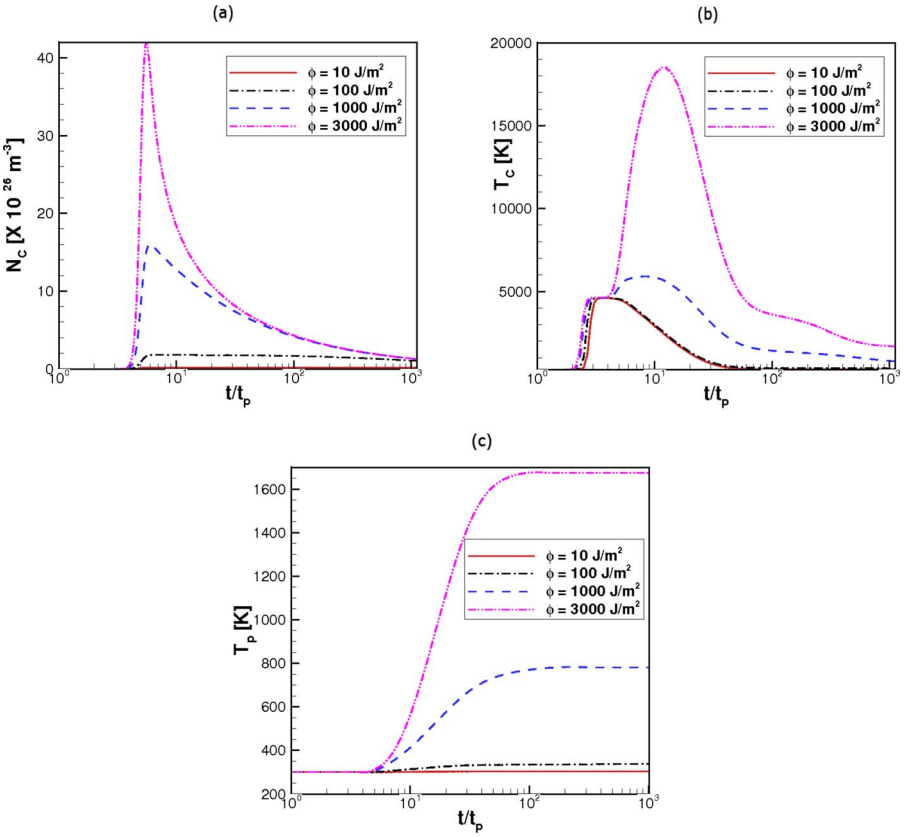

Fig. 3 Temporal variations in the (*a*) carrier number density, (*b*) carrier temperature, and (*c*) phonon temperature with laser fluence at the front surface for $L=28$ nm and $t_p=75$ fs

that the rate of increase in the phonon temperature is the highest for the case of larger pulse duration for which the Auger effects are dominant. From this figure, it is also observed that the peak phonon temperature decreases with increasing pulse duration.

Figure 3 shows the temporal evolution of the carrier number density, and carrier and phonon temperatures at the front surface of Si film for category 2 of Table 3. From Fig. 3(*a*), it is observed that for fluences of 10 J/m^2 and 100 J/m^2, the carrier number density increases and reaches constant values, since the Auger recombination is not dominant at small fluences. For higher laser fluences, the carrier number density increases rapidly and reaches a maximum after which it sharply decreases due to the Auger recombination, which is proportional to the cubic power of the carrier number density. Figure 3(*b*) shows the time evolution of the carrier temperature for several values of laser fluences. The carrier temperature starts to increase ahead of the increase in the carrier number density. For fluences less than or equal to 100 J/m^2, the carrier temperature decreases after reaching the peak. However, at higher fluences, due to the Auger recombination, a second peak higher than the first peak in the carrier temperature is observed. The carrier energy is transferred to the phonons, thus leading to an increase in the phonon temperature, as seen in Fig. 3(*c*). The carriers and phonons thermalize with each other and finally reach equilibrium. From Fig. 3 it is observed that the equilibrium temperature is a strong function of the laser fluence, with the maximum value of the equilibrium temperature observed for the largest fluence of 3000 J/m^2. The equilibrium temperature for the case of largest laser fluence reaches a value close to the melting temperature of 1680 K for Si, while it is close to 300 K for the smallest fluence.

In order to understand the effect of the carrier-phonon coupling, the phonon temperature for the laser fluence of 3000 J/m^2 is compared for the cases of C-AP and C-OP-AP couplings in Fig. 4. The carrier-phonon coupling is found to affect the time evolution of the phonon temperature without significantly affecting the time evolution of the carrier number density and carrier temperature. From Fig. 4, it is observed that the use of C-AP coupling leads to equilibrium phonon temperature, which is approximately 400 K higher than that of C-OP-AP coupling. Thus the use of C-AP coupling leads to equilibrium phonon temperatures that are well

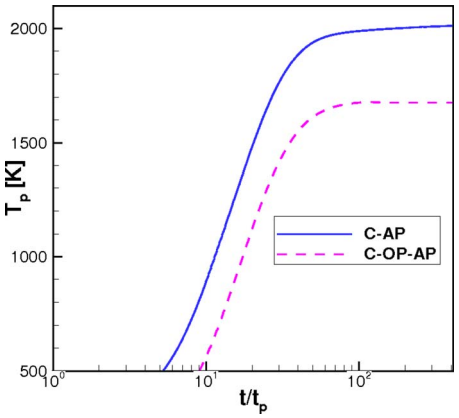

Fig. 4 Effect of carrier-phonon coupling on the temporal evolution of phonon temperature for $L=28$ nm and $\phi=3000$ J/m^2

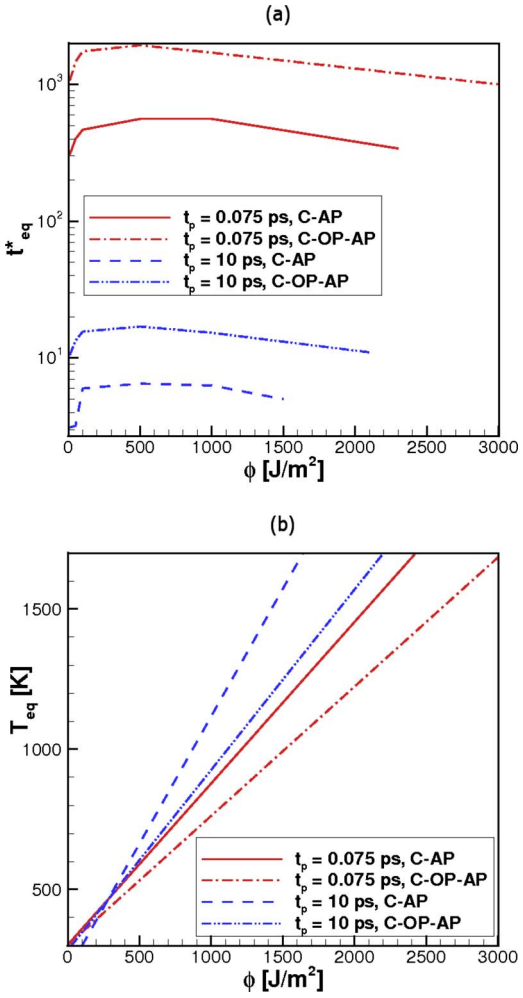

Fig. 5 Variations in the (*a*) equilibrium time and (*b*) equilibrium temperature with laser fluence for $L=28$ nm

above the melting temperature of 1680 K for Si. This is attributed to the carriers' energy being directly transferred to the acoustic phonons in the case of C-AP coupling, thereby leading to a higher phonon temperature. However, in the case of C-OP-AP coupling, the carriers' energy is transferred to the acoustic phonons through coupling with the optical phonons, and hence, smaller values of phonon temperature is obtained for this case.

3.2 Equilibrium Time, Equilibrium Temperature, and Melting Threshold Fluence. The equilibrium time t_{eq} is defined as the time when the relative difference between the carrier and phonon temperatures becomes less than 1% [18]. The equilibrium time is nondimensionalized with the laser pulse duration and is denoted as t^*_{eq}. The equilibrium temperature T_{eq} is defined as the temperature corresponding to the equilibrium time. Figure 5 shows the variation in t^*_{eq} and T_{eq} with laser fluence for laser pulse durations of 0.075 ps and 10 ps. The effect of the carrier-phonon coupling is also shown in this figure. From Fig. 5(*a*), it is observed that the equilibrium time decreases with increasing laser pulse duration, indicating that the nonequilibrium state remains longer when the pulse duration is shorter. The equilibrium time also shows an increase with the laser fluence and reaches a maximum value for a value of ϕ around 500 J/m^2. For larger laser fluences, however, the equilibrium time decreases with increasing fluence. This can be attributed to the steep increase in the phonon temperature with time for values of laser fluence above 500 J/m^2, as seen in Fig. 3(*c*), leading to smaller values of the equilibrium time. For the case of $t_p=0.075$ ps, the silicon film reaches the

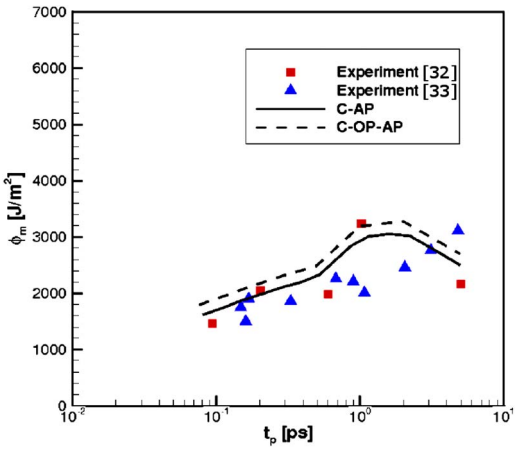

Fig. 6 Comparison of the BTM melting fluence threshold with the experiment

melting temperature with C-AP coupling, and hence, no equilibrium between the carriers and phonons is reached for values of fluence above 2400 J/m^2, as seen in Fig. 5(*a*). For the case of $t_p=10$ ps, no equilibrium between the carriers and phonons is reached with both C-AP and C-OP-AP couplings for relatively high fluences above 1500 J/m^2. It is observed that both the laser pulse duration as well as the laser fluence have strong influences on the equilibrium time. The use of C-OP-AP coupling leads to approximately an order of magnitude increase in the equilibrium time. This is primarily due to a considerably longer time for the carriers to reach thermal equilibrium through interaction with both optical and acoustic phonons. Figure 5(*b*) shows the variation in the equilibrium temperature T_{eq} with the laser fluence for laser pulse widths of 0.075 ps and 10 ps. This figure shows that the equilibrium temperature increases with increasing laser fluence. For fluences smaller than 500 J/m^2, T_{eq} for different pulse durations are close to each other. Beyond this value of laser fluence, the value of the equilibrium temperature is higher for the longer laser pulse duration. Also for small laser fluences, T_{eq} are close to each other for both C-AP and C-OP-AP couplings. Thus it can be inferred from Fig. 5(*b*), that for fluences less than 500 J/m^2, both C-AP and C-OP-AP couplings would lead to similar values of the equilibrium temperature. However, for larger laser fluences, the use of C-OP-AP coupling results in a decrease in the equilibrium temperature. For the case of $t_p=0.075$ ps, the equilibrium temperature is approximately 250 K smaller for the laser fluence of 2400 J/m^2. For the value of $\phi=3000$ J/m^2, T_{eq} obtained using the C-AP coupling is higher than the Si melting temperature, while the C-OP-AP coupling predicts values lower than the melting temperature. For the case of $t_p=10$ ps, the equilibrium temperature is approximately 300 K smaller for the laser fluence of 1500 J/m^2.

For laser microstructuring applications that require high precision, determination of the melting threshold fluence ϕ_m is of importance. For that reason, the dependence of the absorbed threshold fluence on the laser pulse duration for a film thickness of 28 μm and a laser wavelength of 775 nm are shown in Fig. 6. The melting threshold fluence is defined as the value of laser fluence at which the carrier number density reaches the critical value of 2×10^{27} m^{-3} for Si [16]. The melting threshold fluence calculated using the BTM is in agreement with the experimental data of Pronko et al. [32] and Allenspacher et al. [33]. The melting fluence for the C-AP coupling is observed to be slightly smaller than that of the C-OP-AP coupling. From Fig. 6, it is observed that the predicted value of laser fluence required to melt the Si film increases with the pulse duration until 2 ps, after which the

melting threshold decreases. This is in accordance with Fig. 2, which predicts a decrease in the maximum carrier number density with an increase in the pulse duration.

4 Conclusions

The carrier-phonon nonequilibrium due to laser heating of silicon films has been previously studied using the two-temperature model. However, when either the laser pulse duration is smaller than the relaxation time of the energy carriers or when the carriers' mean free path is larger than the material dimension, these macroscopic models fail to capture the physics of nonequilibrium accurately. In this study, the BTM has been introduced to study the carrier-phonon nonequilibrium due to short pulsed laser interaction with thin silicon films. The BTM results are compared with the previous computational results of two-temperature models. For the case of laser pulse duration smaller than the interaction time between carriers and phonons, the maximum carrier number density and temperature predicted by the two-temperature model of Lee et al. [13] is found to be higher than that of the BTM. Comparison of the BTM results with that of the modified two-temperature model of Chen et al. [14] shows that the time evolution of the carrier temperature profiles predicted by the models are different. However, the equilibrium temperature predicted by the BTM is in good agreement with that of the computation of Chen et al. [14].

The BTM is then applied to perform a parametric study of the effect of the laser pulse duration and fluence on the nonequilibrium between the energy carriers for a fixed silicon film thickness of 28 nm. The laser pulse duration and fluence are varied between 0.05 ps to 10 ps, and 10 J/m^2 to 3000 J/m^2, respectively. From the laser pulse duration study, it is observed that the maximum values of the carrier number density, and carrier and phonon temperatures are the highest for the smallest pulse duration of 0.05 ps and decreases with increasing pulse duration. For a value of laser pulse duration of 0.05 ps, the temporal evolution of the carrier temperature is qualitatively different from the other cases due to ballistic energy transport. For larger laser pulse durations, a double peak due to Auger recombination is observed in the carrier temperature profile. The rate of increase in the phonon temperature is the highest for the cases with larger pulse duration where Auger effects are dominant. From the laser pulse duration study, it is also observed that the peak phonon temperature decreases with increasing pulse duration. From the laser fluence study, it is observed that for fluences less than or equal to 100 J/m^2, the carrier temperatures decrease continuously after attaining the peak. However, for higher fluences, due to the Auger recombination, a second peak higher than the first peak in the carrier temperature is observed. The equilibrium temperature for the case of the largest laser fluence of 3000 J/m^2 reaches values close to the melting temperature of 1680 K for Si, while it is close to 300 K for the smallest fluence.

For the value of laser fluence of 3000 J/m^2, the use of C-AP coupling leads to equilibrium phonon temperature, which is approximately 400 K higher than that of the C-OP-AP coupling. Thus, the C-AP coupling leads to equilibrium phonon temperatures that are well above the melting temperature of 1680 K for Si. It is found that the equilibrium time decreases with increasing laser pulse duration. The use of C-OP-AP coupling leads to approximately an order of magnitude increase in the equilibrium time. The use of this coupling is also found to decrease the equilibrium temperature. For the case of $t_p = 0.075$ ps, the silicon film reaches the melting temperature with C-AP coupling, and hence, no equilibrium between carriers and phonons is reached for values of fluence above 2400 J/m^2. For this case, the equilibrium temperature with C-OP-AP coupling is approximately 250 K smaller for the laser fluence of 2400 J/m^2. Both the laser pulse duration and fluence are found to strongly affect the equilibrium time and equilibrium temperature in Si films. The melting threshold fluence calculated using the BTM are found to compare well with the experimental data [32,33].

Nomenclature

C_c = carrier volumetric heat capacity (J/m^3 K)
C_{OP} = optical phonon volumetric heat capacity (J/m^3 K)
C_p = phonon volumetric heat capacity (J/m^3 K)
D_c = carrier density of states per unit volume (m^{-3})
D_p = phonon density of states per unit volume (m^{-3})
E = electron band energy (J)
E_f = electron Fermi energy (J)
E_g = energy bandgap (eV)
f_c = Fermi–Dirac distribution function
f_p = Bose–Einstein distribution function
h = Planck's constant (J s)
I = laser energy source ($W m^{-3}$)
k_b = Boltzmann constant (J/K)
K_c = carrier thermal conductivity (W/m K)
K_p = phonon thermal conductivity (W/m K)
Kn = Knudsen number, Λ/L
L = film thickness
m = mass of free electron (kg)
N_c = carrier number density (m^{-3})
n = number density of free electron (m^{-3})
p = phonon polarization mode
R = reflectivity
$\boldsymbol{r}$ = position vector
$\boldsymbol{s}$ = direction vector
T_{AP} = acoustic phonon temperature (K)
T_c = carrier temperature (K)
$T_{c_{max}}$ = maximum carrier temperature (K)
T_{OP} = optical phonon temperature (K)
T_p = phonon temperature (K)
t = time
t_{eq} = equilibrium time
t^*_{eq} = nondimensional equilibrium time
t_m = melting time
t_p = laser pulse duration
u_{AP} = acoustic phonon kinetic energy density per unit solid angle ($J m^{-3} sr^{-1}$)
u_c = carrier energy kinetic density per unit solid angle ($J m^{-3} sr^{-1}$)
u_{OP} = optical phonon kinetic energy density per unit solid angle ($J m^{-3} sr^{-1}$)
u_p = phonon kinetic energy density per unit solid angle ($J m^{-3} sr^{-1}$)
$u_{eq(c)}$ = carrier equilibrium kinetic energy density ($J m^{-3}$)
$u_{eq(AP)}$ = phonon equilibrium kinetic energy density ($J m^{-3}$)
v_c = average carrier group velocity (m/s)
v_p = average phonon group velocity (m/s)
x = coordinate
$x*$ = nondimensional x-coordinate, x/L
α = one-photon absorptivity of Si
β = two-photon absorptivity of Si
γ = Auger recombination coefficient
θ = polar angle (rad)
Θ = impact ionization coefficient
Λ = phonon mean free path
λ = phonon wavelength
μ = x-directional cosine
$\tau_{(c\text{-}c)}$ = carrier relaxation time

$\tau_{(c\text{-}p)}$ = carrier-phonon relaxation time
$\tau_{(p\text{-}p)}$ = phonon relaxation time
ϕ = laser fluence (J m^{-2})
ϕ_m = melting fluence (J m^{-2})
ω = phonon frequency (Hz)
Ω = solid angle (Sr)

References

[1] Chlipala, J. D., Scarforne, L. M., and Lu, C. Y., 1989, "Computer-Simulated Explosion of Poly-Silicide Links in Laser-Programmable Redundancy for VLSI Memory Repair," IEEE Trans. Electron Devices, **36**, pp. 2433–2439.

[2] Simon, R., 1991, "High-T_c Thin Films and Electronic Devices," Phys. Today, **44**, pp. 64–70.

[3] Narayan, J., Godbole, V. P., and White, G. W., 1991, "Laser Method for Synthesis and Processing of Continuous Diamond Films on Nondiamond Substrates," Science, **252**, pp. 416–418.

[4] Kumar, A. V., Bansal, S. K., and Srivastava, G. P., 1996, "Laser Induced Damage in GaAs at 1.06 mm Wavelength: Surface Effects," Opt. Laser Technol., **28**, pp. 25–34.

[5] Phinney, L. M., and Tien, C. L., 1998, "Electronic Desorption of Surface Species Using Short-Pulse Lasers," ASME J. Heat Transfer, **120**, pp. 765–771.

[6] Fushinobu, K., Phinney, L. M., Kurosaki, Y., and Tien, C. L., 1999, "Optimization of Laser Parameters for Ultrashort-Pulse Laser Recovery of Stiction-Failed Microstructures," Numer. Heat Transfer, Part A, **36**, pp. 345–357.

[7] Shank, C., Yen, R., and Hirlimann, C., 1983, "Time-Resolved Reflectivity Measurements of Femtosecond-Optical Pulse-Induced Phase Transitions in Silicon," Phys. Rev. Lett., **50**, pp. 454–457.

[8] Govorkov, S., Schroeder, T., Shumay, I., and Heist, P., 1992, "Transient Gratings and Second-Harmonic Probing of the Phase Transformation of a GaAs Surface Under Femtosecond Laser Irradiation," Phys. Rev. B, **46**, pp. 6864–6868.

[9] Sokolowski-Tinten, K., and von der Linde, D., 2000, "Generation of Dense Electron-Hole Plasmas in Silicon," Phys. Rev. B, **61**, pp. 2643–2650.

[10] Van Vechten, J. A., Tsu, R., and Saris, F. W., 1979, "Nonthermal Pulsed Laser Annealing of Si: Plasma Annealing," Phys. Lett. A, **74**, pp. 422–426.

[11] van Driel, H. M., 1987, "Kinetics of High-Density Plasmas Generated in Si by 1.06- and 0.53-μm Picosecond Laser Pulses," Phys. Rev. B, **35**, pp. 8166–8176.

[12] Tien, C., Majumdar, A., and Gerner, F., 1997, *Microscale Energy Transport*, Taylor & Francis, New York.

[13] Lee, S.-H., Lee, J.-S., Park, S., and Choi, Y.-K., 2003, "Numerical Analysis on Heat Transfer Characteristics of a Silicon Film Irradiated by Pico- to Femtosecond Pulse Lasers," Numer. Heat Transfer, Part A, **44**, pp. 833–850.

[14] Chen, J. K., Tzou, D., and Beraun, J. E., 2005, "Numerical Investigation of Ultrashort Laser Damage in Semiconductors," Int. J. Heat Mass Transfer, **48**, pp. 501–509.

[15] Meyer, J. R., Kruer, M. R., and Bartoli, F. J., 1980, "Optical Heating in Semiconductors: Laser Damage in Ge, Si, InSb, and GaAs," J. Appl. Phys., **51**, pp. 5513–5522.

[16] Agassi, D., 1984, "Phenomenological Model for Picosecond Pulse Laser Annealing of Semiconductors," J. Appl. Phys., **55**, pp. 4376–4383.

[17] Qiu, T. Q., and Tien, C. L., 1993, "Heat Transfer Mechanisms During Short-Pulse Laser Heating of Metals," ASME J. Heat Transfer, **115**, pp. 835–841.

[18] Pattamatta, A., and Madnia, C. K., 2009, "A Comparative Study of Two-Temperature and Boltzmann Transport Models for Electron-Phonon Non-Equilibrium," Numer. Heat Transfer, Part A, **55**, pp. 611–633.

[19] Chen, G., Borca-Tasciuc, D., and Yang, R., 2004, "Nanoscale Heat Transfer," *Encyclopedia of Nanoscience and Nanotechnology*, Vol. 17, H. S. Nalwa, ed., American Scientific Publishers, pp. 429–459.

[20] Ashcroft, N. W., and Mermin, N. D., 1976, *Solid State Physics*, Holt, Rinehart and Winston, New York.

[21] Joshi, A., and Majumdar, A., 1993, "Transient Ballistic and Diffusive Phonon Heat Transport in Thin Films," J. Appl. Phys., **74**, pp. 31–39.

[22] Ziman, J. M., 1960, *Electrons and Phonons*, Oxford University Press, London, UK.

[23] Pattamatta, A., and Madnia, C. K., 2009, "Modeling Electron-Phonon Non-Equilibrium in Gold Films Using Boltzmann Transport Model," ASME J. Heat Transfer, **131**, p. 082401.

[24] Majumdar, A., Fushinobu, K., and Hijikata, K., 1995, "Effect of Gate Voltage on Hot-Electron and Hot-Phonon Interaction and Transport in a Submicrometer Transistor," J. Appl. Phys., **77**, pp. 6686–6694.

[25] Chen, G., 1997, "Size and Interface Effects on Thermal Conductivity of Superlattices and Periodic Thin-Film Structures," ASME J. Heat Transfer, **119**, pp. 220–229.

[26] Pattamatta, A., and Madnia, C. K., 2009, "Modeling Heat Transfer in Bi_2Te_3–Sb_2Te_3 Nanostructures," Int. J. Heat Mass Transfer, **52**, pp. 860–869.

[27] Cockburn, B., Karniadakis, G. E., and Shu, C.-W., 2000, *Discontinuous Galerkin Methods: Theory, Computation and Applications*, Springer-Verlag, Berlin.

[28] Cockburn, B., and Shu, C.-W., 2001, "Runge–Kutta Discontinuous Galerkin Methods for Convection-Dominated Problems," J. Sci. Comput., **16**(3), pp. 173–261.

[29] Cui, X., and Li, B. Q., 2004, "A Discontinuous Finite-Element Formulation for Internal Radiation Problems," Numer. Heat Transfer, Part B, **46**, pp. 223–242.

[30] Chai, J. C., Lee, H. S., and Patankar, S. V., 1994, "Finite Volume Method for Radiation Heat Transfer," J. Thermophys. Heat Transfer, **8**(3), pp. 419–425.

[31] Pierret, R. F., 2003, *Advanced Semiconductor Fundamentals: Modular Series on Solid State Devices*, Vol. VI, Prentice-Hall, Englewood Cliffs, NJ.

[32] Pronko, P., VanRompay, P., Horvath, C., Loesel, F., Juhasz, T., Liu, X., and Mourou, G., 1998, "Avalanche Ionization and Dielectric Breakdown in Silicon With Ultrafast Laser Pulse," Phys. Rev. B, **58**, pp. 2387–2390.

[33] Allenspacher, P., Huttner, B., and Riede, W., 2003, "Ultrashort Pulse Damage of Si and Ge Semiconductors," Proc. SPIE, **4932**, pp. 358–365.

[34] Madelung, O., 2004, *Semiconductors:Data Handbook*, 3rd ed., Springer, New York.

Particle Aspect-Ratio and Agglomeration-State Effects on the Effective Thermal Conductivity of Aqueous Suspensions of Multiwalled Carbon Nanotubes

Anna S. Cherkasova

Jerry W. Shan
e-mail: jshan@jove.rutgers.edu

Department of Mechanical and Aerospace Engineering,
Rutgers University,
Piscataway, NJ 08854-8054

*The effective thermal conductivities of aqueous nanofluids containing surfactant-stabilized multiwalled carbon nanotubes were measured and compared with the predictions of effective medium theory (Nan, C.-W., et al., 1997, "Effective Thermal Conductivity of Particulate Composites With Interfacial Thermal Resistance," J. Appl. Phys., **81**(10), pp. 6692–6699). Detailed characterization of nanotube morphology was carried out through electron microscopy, while the nanotube agglomeration state was monitored through optical microscopy and absorption measurements. An optimum surfactant-to-nanotube mass ratio was found for the particular surfactant, sodium dodecylbenzene sulfonate, which resulted in the greatest increase in thermal conductivity. Taking into consideration the volume-weighted aspect ratio of the nanotubes, the measured thermal conductivities of the suspensions were shown to be in good agreement with calculations for a reasonable choice of interfacial resistance on the particle/liquid interface. The effect of particle aspect ratio on the suspension's thermal conductivity was further demonstrated and compared with theory by reducing the nanotube length through intense ultrasonication. The effect of particle aggregation on the thermal conductivity was also investigated by destabilizing previously stable suspensions with ethanol addition, which causes surfactant desorption and bundling of nanotubes. The measured thermal conductivities were correlated with absorption measurements and microscopic visualizations to show that particle aggregation decreases the thermal conductivity of the nanofluid by reducing the effective particle aspect ratio.* [DOI: 10.1115/1.4001364]

Keywords: nanofluid, multiwalled nanotubes, thermal conductivity, aspect ratio, agglomeration, interfacial resistance, effective medium theory

1 Introduction

Recent experimental studies on conductive heat transfer in composite materials have shown a significant enhancement of thermal conductivity with the addition of nanoparticles [1–5]. In particular, a number of experiments have investigated the thermal properties of suspensions of carbon nanotubes (CNTs) in liquids [6–9]. The increase in thermal conductivity has been attributed to the unique thermal and physical properties of CNTs, for instance, their high thermal conductivity, which, for single-walled nanotubes (SWNT), is five to ten times greater than that of even very good thermal conductors such as aluminum or copper and is comparable with the thermal conductivity of diamond. With diameters ranging down to 1 nm and lengths on the order of microns, CNTs can have length-to-diameter ratios as high as 10^3. There has been disagreement in the literature as to whether existing macroscopic theories adequately describe the effective thermal conductivity of these nanofluids. Initial experiments reported enormous, "anomalous" thermal-conductivity enhancements in nanofluids containing both spherical particles and nanotubes [1–12]. This stimulated a number of theoretical analyses of possible heat-transfer amplification mechanisms at the nanoscale. Brownian motion [13–18], particle clustering [19–24], and ballistic phonon transport [25] have all been evaluated as possible mechanisms behind the remarkable thermal conductivity increase in nanofluids. However, later theoretical work by Nan et al. [26] pointed out that, when the unusually high aspect ratio of CNTs is taken into account, the experimental data for carbon-nanotube suspensions at least are within the bounds of effective medium theory (EMT). The predictions of EMT have been experimentally validated for suspensions of micron-sized SiC particles [27], but not for nanotubes, which have larger aspect ratios and can have significant thermal resistance at the particle/liquid interface due to their small size.

This work details an experimental study of the effective thermal conductivity of aqueous suspensions of multiwalled nanotubes (MWNTs). Careful characterization of the nanotube aspect ratio and dispersion states allows for quantitative comparison with EMT. The length of the dispersed nanotubes was varied to directly show the influence of aspect ratio on the effective conductivity of the nanofluid. The effect of particle dispersion state and aggregation on the thermal conductivity of the nanofluid was also investigated by varying the surfactant-to-nanotube mass ratio and the absolute concentration of surfactant, as well as destabilizing already dispersed samples by means of ethanol addition. The experimental data are analyzed in light of Nan's EMT theory.

Contributed by the Heat Transfer Division of ASME for publication in the JOURNAL OF HEAT TRANSFER. Manuscript received September 22, 2009; final manuscript received February 17, 2010; published online June 9, 2010. Assoc. Editor: Pamela M. Norris.

The theoretical basis of describing heat transfer in composite materials dates back to Maxwell [28], who derived an expression for the effective electrical conductivity of a medium containing dispersed macroscopic spheres, which can be successfully applied to thermal conductivity as well. Later, this approach was generalized for the case of spheroidal inclusions by Fricke [29]. Both models deal with macroscopic particles because they neglect thermal resistance at the particle/matrix interface, which can play an important role in heat transport as the characteristic scale decreases. Nan et al. [26] incorporated interfacial thermal resistance into an effective medium theory for the thermal conductivity, k, of a composite material containing spheroidal particles:

$$k = k_b\left[1 + \frac{\varphi(2\beta_{11} + \beta_{33})}{3 - \varphi(2\beta_{11}L_{11} + \beta_{33}L_{33})}\right] \tag{1}$$

where

$$\beta_{ii} = \frac{k_{ii} - k_b}{k_b + L_{ii}(k_{ii} - k_b)} \tag{2}$$

The so-called depolarization factors for a prolate spheroid are given as

$$L_{11} = \frac{a^2}{2(a^2 - 1)} - \frac{a}{2(a^2 - 1)^{3/2}}\cosh^{-1} a$$

$$L_{33} = 1 - 2L_{11} \tag{3}$$

The thermal conductivities of the dispersing (base fluid) and dispersed (particle) phases are k_b and k_p, respectively, and φ is the volumetric concentration of dispersed spheroids. The length-to-diameter aspect ratio of the spheroidal particles is a. To include interfacial resistance, R_K, on the liquid-solid boundary, equivalent thermal conductivities of inclusions along two spheroidal axes are introduced [30]:

$$k_{33} = \frac{k_p}{1 + 2k_pR_K/L}$$

$$k_{11} = \frac{k_p}{1 + 2k_pR_K/d} \tag{4}$$

In the above equations, d and L are the diameter and the length of a spheroid.

As seen from the theory, the effective thermal conductivity of suspensions depends not only on particle conductivity and volume fraction but also on the aspect ratio of the dispersed particles. Carbon nanotubes typically have very high length-to-diameter ratios, in addition to high thermal conductivity, and thus would appear to be ideal filler materials for an efficient heat-transfer fluid if added at even very low volume fractions. However, neat (nonfunctionalized) nanotubes tend to agglomerate or form bundles in many fluids, such as water. Moreover, because of the size of MWNTs, interfacial resistance can reduce the effective thermal conductivity of the suspension. In the following, we systematically investigate the impact of both nanotube aspect ratio and dispersion state on the effective thermal conductivity of aqueous suspensions of surfactant-stabilized MWNTs. In addition to thermal-conductivity measurements, the nanofluid samples were characterized through a combination of transmission-electron-microscopy (TEM) imaging, optical microscopy, and absorbance measurements, to enable quantitative comparison with theory. It is shown that EMT predictions are consistent with the measured conductivities for a reasonable choice of interfacial resistance. The particle aspect ratio and agglomeration state are found to have a profound effect on the effective thermal conductivity of the MWNT suspension, as can be expected from EMT.

2 Experiment and Methods

The nanotube suspensions were prepared in two steps. First, sodium dodecylbenzene sulfonate (NaDDBS) (Sigma-Aldrich, St. Louis, MO) was mixed with water at mass fractions ranging from 10 to 200 g/l. The mixtures were sonicated and stirred vigorously until the surfactant was dispersed completely. Then, MWNTs (Nanostructured and Amorphous Materials, Inc., Houston, TX) were added to the solution to obtain nanofluids with particle volume concentrations from 0.01% up to 1%. The surfactant-to-nanotube mass ratio ranged from 5 to 100. After mixing, all suspensions were sonicated again in a low-power bath sonicator for 30 min to ensure even dispersions.

The thermal conductivity of nanofluid suspensions was measured using a transient hot-wire apparatus (KD-2 Thermal Properties Analyzer, Decagon Devices, Pullman, WA). The hot-wire device, which utilizes the classical solution of the heat-transfer equation for sudden heating of a thin probe (wire) immersed in a testing material, conforms to ASTM D5334 and IEEE 442-1981 standards for determining thermal conductivity. The material's conductivity is determined from the rate of temperature rise at a constant heating rate. In the KD-2, the heating wire and temperature sensor are encapsulated in a metal sheath to avoid possible problems caused by electrically conductive fluids. The device's stated accuracy of 5% was confirmed by reproducing the literature values for thermal conductivities of ethanol, mineral oil, glycerin, and ethylene glycol.

Every experimental data point for thermal conductivity was obtained by averaging five consecutive measurements at $20.0 \pm 0.3\,^{\circ}\mathrm{C}$. Error bars on shown figures represent the 95% confidence interval for expected mean values of thermal conductivities. To keep temperature constant, the suspension and hot-wire apparatus were immersed in a recirculating thermal bath. Maintaining steady temperature is essential for the hot-wire method because convection can significantly distort the temperature field around the probe and corrupt the measurements. In the present study, the temperature variation did not exceed $0.1\,^{\circ}\mathrm{C}$ for repeated measurements of a single sample and differed by a maximum of $0.3\,^{\circ}\mathrm{C}$ from the one sample to another. Even though the enormous increase in thermal conductivity of nanofluids in some recent studies has been attributed to possible problems with hot-wire probes [31], recent data by Li et al. [32] show good agreement between hot-wire and steady-state cut-bar results for aqueous Al_2O_3 nanofluids at room temperature. Also, Louge and Chen [33] showed recently that particle migration due to the temperature gradient away from the hot wire toward cold regions, the so-called positive thermophoresis, cannot be responsible for the anomalous increase in thermal conductivity of nanofluids. Thus we conclude that the hot-wire technique used in present study is an accurate method for measuring thermal conductivity of nanotube suspensions.

In order to carry out a full comparison of experimental data with theory, we need to know the detailed morphology of the nanotubes. The multiwalled nanotubes used in this study are short, with nominal lengths of $0.5-2\ \mu$m and outer diameters of 30–50 nm, as reported by the manufacturer. Such nanotubes having relatively low-aspect ratio are better dispersible than those of higher aspect ratio and are also likely to be easier to characterize. Actual CNT diameter and length distributions were obtained from TEM images. In order to carry such TEM analysis, the nanofluid was diluted with 1:100 with ethanol to remove the surfactant from the nanotubes. The resulting suspension, which was blotted onto a TEM-thin substrate, contained around 10^{10} tubes per ml, which was sufficiently concentrated for TEM analysis, but still low enough to remain stable for handling. Figure 1 shows a representative TEM image of a sample prepared from a suspension originally containing 0.1% CNTs by volume. The diameters and lengths of a total of 216 CNTs were measured from five such TEM images of the nanotube suspension. For tubes that were curved, the arclength (contour length) along the tube was measured. The measured diameters of the individual nanotubes ranged from 11 nm to 38 nm, while the lengths were as high as $1.4\ \mu$m.

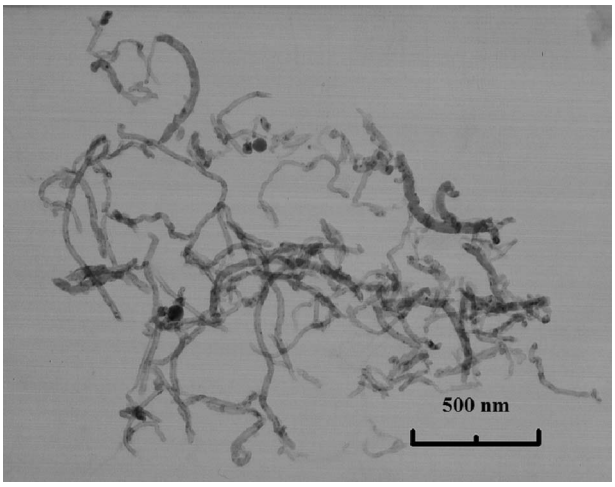

Fig. 1 TEM of dried sample originally containing 0.1% vol MWNTs. Such images were used to measure the length and diameter distribution of nanotubes in suspension.

Using the experimentally determined aspect-ratio distribution, we calculated the volume-weighted average aspect ratio as

$$\overline{a_V} = \frac{\sum_i a_i V_i}{\sum_i V_i} \tag{5}$$

where a_i and V_i are the aspect ratio and volume of ith nanotube. For the as-prepared samples (without aggressive tip-sonication to break the nanotubes, as discussed later), the overall volume-weighted aspect ratio was 32.9, while the aspect ratios of individual nanotubes ranged from 2 up to 80.

3 Results and Discussion I: Thermal Conductivity of Nanofluids

As the first step of this work, we evaluated the effect of nanotube dispersion characteristics on the thermal conductivity of surfactant-stabilized nanofluids for surfactant ratios from 1 up to 200 g per 1 l of water (Table 1). NaDDBS was chosen as the surfactant because of its efficiency in dispersing nanotubes. Islam et al. [34] reported that ~63% of SWNTs were individualized in aqueous NaDDBS suspensions for CNT concentrations as high as 20 g/l (~2% volume fraction for SWNTs) and that those suspensions remained stable much longer than those containing sodium dodecyl sulfate (SDS) or Triton X-100. Islam et al. also found an optimal surfactant-to-SWNT mass ratio of 10:1 that resulted in stable suspensions for over 3 months at concentrations up to 20 g/L. In our aqueous suspensions with nanotube volume fractions ranging from 0.01% up to 1%, we observed good stability in all samples with NaDDBS concentration below ~20 g/l. No aggregation or sedimentation was detected in these samples during a period of a few weeks (Fig. 2). However, above a critical NaDDBS concentration of ~20–50 g/l, sedimentation occurred regardless of the nanotube volume fraction. This is seen in Figs. 2(*a*) and 2(*b*), which shows suspensions containing 0.01% up to 1% of MWNTs and 5× and 100× mass ratios of surfactant. It is clearly seen that sedimentation occurred in samples with different nanotube volume fractions but at the same critical concentration of surfactant.

The critical concentration of NaDDBS at ~20 g/l is believed to be due to a surfactant phase transition. Although no detailed phase diagram is available for the CNT-NaDDBS-water system, the suspension may behave similarly to a SDS-water system, in

Table 1 NaDDBS and MWNT concentrations in nanofluids

NT volume fraction (%)	Surfactant concentration at 5× surfactant ratio (g/l)	10× (g/l)	20× (g/l)	100× (g/l)
0.01	1.0	2.0	4.0	20
0.02	2.0	4.0	8.0	40
0.03	3.0	6.0	12	60
0.05	5.0	10	20	100
0.08	8.0	16	32	160
0.1	10	20	40	200
0.2	20	40	80	-
0.5	50	100	200	-
1	100	200	-	-

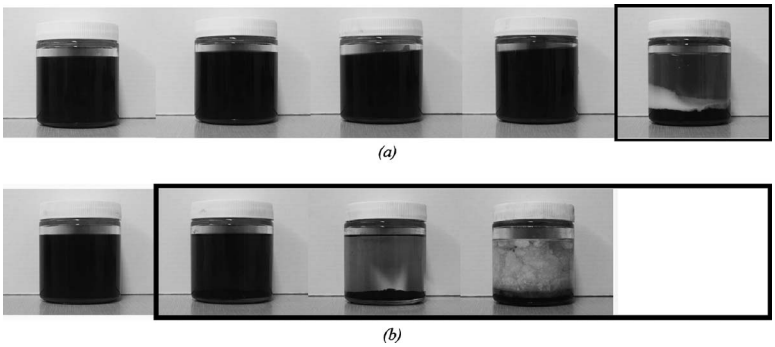

Fig. 2 Suspensions with NaDDBS to CNT mass ratios (*a*) 5× and (*b*) 100× 1 week after preparation. From right to left, the MWNT volume fractions are 0.01%, 0.03%, 0.05%, 0.1%, and 1% vol. The unstable suspensions, which had NaDDBS concentrations exceeding 20–50 g/l, are indicated with black borders.

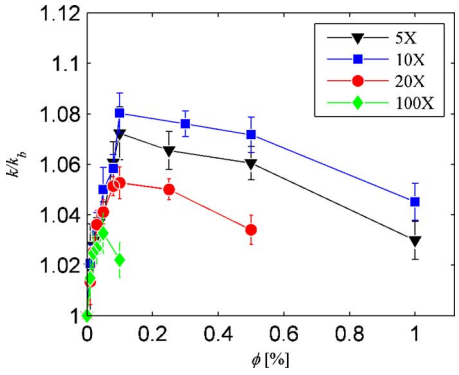

Fig. 3 Measured thermal conductivities of aqueous suspensions of MWNTs. Mass ratio of NaDDBS to MWNTs is indicated in legend.

which a micellar regime extends up to 40% surfactant concentration by weight, followed by a hexagonal phase with more complicated surfactant structure or mixed regimes [35]. Such a transition would explain the critical volume fraction of NaDDBS of approximately 20–50 g/l that we observe in the MWNT suspensions. It should be noted that the sample testing temperature of 20°C is below the reported Krafft temperature for NaDDBS water [36]; however, the presence of a third component such at CNTs can alter the Krafft point of the system.

The measured thermal conductivity increases for NaDDBS-stabilized suspensions containing from 0.01% up to 1% nanotubes by volume are presented in Fig. 3. The thermal conductivity increases are almost linear with CNT concentration for samples containing less than ~20 g/l of NaDDBS, which is the maximum surfactant concentration for which nanofluid stability was observed. For the MWNTs used, an optimum surfactant-to-CNT mass ratio of 10:1 yielded the largest increase in thermal conductivity for a given CNT volume fraction. The difference is most apparent for CNT concentrations approaching 0.1% by volume. The existence of such an optimum surfactant ratio suggests that the dispersion state of the nanotubes in suspension in some way affects the thermal conductivity of the CNT suspension. It should be noted that it appears to be a coincidence that the optimum surfactant concentration is the same as that reported by Islam et al. [34] for SWNTs, since it likely depends on type and diameter of nanotubes (e.g., MWNT versus SWNT).

Once the nanofluids become unstable against aggregation and settling, their thermal conductivity cannot be readily compared with EMT, which was developed under the assumption that the suspension contains a stable concentration of particles of fixed aspect-ratio distribution. Thus, it is not possible to compare all data presented in Fig. 3 with EMT predictions. We instead compare the measured thermal conductivities with the predictions of effective medium theory for only the well-dispersed suspensions in which the thermal-conductivity enhancement is almost linear with CNT volume fraction ($\varphi \leq 0.1\%$). This linear regime corresponds to NaDDBS surfactant concentrations less than 20–50 g/l. Beyond this surfactant concentration, the nanotubes aggregate and sediment out of suspension, as seen in the images of Fig. 2. Because of the critical surfactant concentration of ~20 g/l, the thermal conductivities obtained for different surfactant-to-MWNT-ratios reach their maxima at different nanotube concentrations, as can be seen by comparing the peaks of the 5×, 10×, 20×, and 100× lines in Fig. 3. In the following, we compare our experimental data with theoretical predictions only for the stable, well-dispersed suspensions of volume fraction $\varphi \leq 0.1\%$.

In order to make such quantitative comparison with theory, several additional parameters should be known: (1) the aspect ratio of the dispersed particles, (2) the interfacial resistance between the particles and fluid, and (3) the thermal conductivities of both solid and liquid phases. For the aspect ratio, it was previously shown that for a suspension containing particles of widely varying aspect-ratio, the volume-weighted average aspect ratio is the appropriate measure of aspect ratio to use in Eq. (3) [27]. In the present case, based on TEM measurements of the aspect-ratio distribution for our MWNTs in suspension, we use a volume-averaged aspect ratio of 32.9 in Eq. (3) for MWNTs.

The Kapitza, or interfacial resistance [37], R_K, becomes increasingly important as the size of dispersed particles decreases since the total surface area of particle/liquid interface is increasing. It can be expressed as a Kapitza length, L_K, as the thickness of a liquid or solid layer equivalent to the interface from the thermal point of view:

$$L_K = k_i R_K \tag{6}$$

where k_i is either k_b or k_p. When the thermal conductivity of the dispersed phase is extremely high (e.g., CNTs) and/or the particles are small such that L_K is comparable to the characteristic dimensions of the particle, measurable effects due to interface resistance to heat transport can be expected. For many solid/liquid interfaces, the Kapitza resistance is typically of the order 10^{-8} m^2 K/W. Molecular-dynamics simulations have reported an interfacial resistance in the range of $(4.5-14.7)\times 10^{-8}$ m^2 K/W for SWNTs in octane [38]. These results are believed to be representative of SWNTs in non- or slightly polar solvent molecules. Experiments by Huxtable et al. [39] find an interfacial resistance of 8.3×10^{-8} m^2 K/W for single-walled carbon nanotubes suspended in SDS micelles in water. Based on an estimated interfacial resistance of 8.3×10^{-8} m^2 K/W, a typical Kapitza length would be estimated to be 45 nm for a base fluid of thermal conductivity $k_b = 0.56$ W/m K, as in our case. However, there are currently no data on the interfacial resistance of NaDDBS-stabilized carbon nanotubes in aqueous suspension. As for the interfacial resistance in other nanoscale systems, R_K values above 10^{-8} m^2 K/W are usually referred only to weakly bonded (non-wetting) interfaces [40]. For strongly bonded interfaces (for example, AuPd nanoparticles in water), reported resistances are around 10^{-8} m^2 K/W and even lower [41,42]. Molecular-dynamics simulations for wetting systems have reported Kapitza lengths of order 1 nm, corresponding to an interfacial resistance of 10^{-9} m^2 K/W [43]. In our later analysis, we will take R_K to be an unknown parameter and use the measured suspension thermal conductivities in order to estimate R_K from an EMT curve fit.

In addition to the interfacial resistance, the thermal conductivities of both dispersed and dispersing media must be known in order to compare the experimental data with theoretical predictions. The thermal conductivity of the base fluid was measured directly for each surfactant concentration. The reported thermal conductivity of MWNTs varies widely in the literature but fortunately has minimal impact on the effective conductivity of the suspension once the ratio of conductivities of suspended and suspending media, $\delta = k_p/k_b$, is high enough [27]. For spherical particles, further increase in particle thermal conductivity after $\delta \approx 100$ has little impact on the resulting k, i.e., k saturates at

$$k = k_b\left(1 + \frac{3\varphi}{1-\varphi}\right) \tag{7}$$

for $\delta \geq 100$. For the aspect ratio of the particles used in this study ($a = 32.9$), k_p has only minimal effect on the effective suspension conductivity when the particle-to-fluid conductivity ratio exceeds 2000 and has essentially no effect for $\delta \geq 5000$. Measured MWNT thermal conductivities vary depending on the diameter of nanotubes and the measurement technique. Measurements using a microfabricated suspending device with the length of 2.5 μm by Kim et al. [44] and Small et al. [45] have shown a thermal conductivity exceeding 3000 W/m K for individual MWNTs with diameters of 14 nm. This result should be even higher if thermal contact resistance (TCR) at the nanotube-measuring device junc-

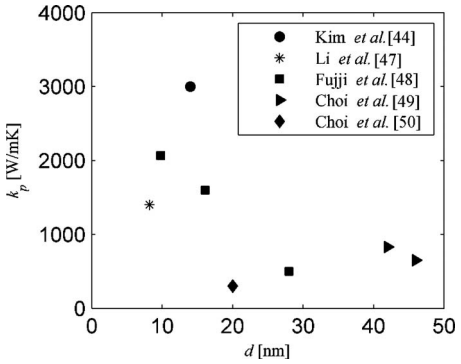

Fig. 4 Reported axial thermal conductivities of MWNTs as a function of tube diameter

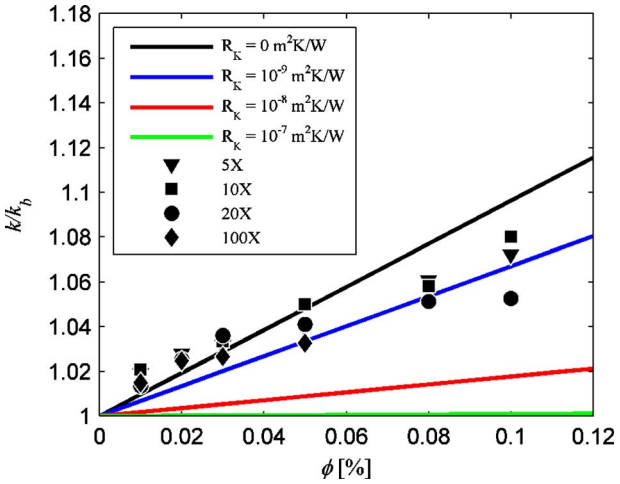

Fig. 5 Measured thermal conductivities of aqueous suspensions of MWNTs compared with EMT calculations for different Kapitza resistances. Different symbols indicate different surfactant-to-MWNT mass ratios.

tion is taken into account [46]. To avoid possible errors caused by TCR, Li et al. [47] recently introduced a noncontact, Raman-spectra-shift method. The thermal conductivity of extremely long MWNT with length $L=60$ μm and $d=8.2$ nm was found to be 1400 ± 250 W/m K. Fujii et al. [48] showed that the k_p of MWNTs dropped from 2069 W/m K to around 500 W/m K as the nanotube diameter changes from 9.8 nm to 28 nm. Choi et al. [49] measured the thermal conductivity of MWNTs to be 630–850 W/m K with a 3-ω method for $d=42-45$ nm nanotubes, and later found $k_p=300$ W/m K for $d=20$ nm MWNTs utilizing a four-point-probe variation in the 3-ω method to eliminate possible TCR effects [50]. Somewhat surprisingly, the thermal conductivity of the thinner nanotube turned out to be smaller even though the thermal resistance effect was minimized. A number of other experimental studies have reported MWNT thermal conductivities similar to those of Choi et al. [49]. Shioya et al. [51] found $k_p=950$ W/m K for 10 nm in diameter tubes by measuring the thermal conductivity of MWNTs pillars. Yang et al. [52] obtained a thermal conductivity of only 200 W/m K, but no information was provided about tube diameter. The results of Shioya et al. [51] and Yang et al. [52] are indirect methods in which the thermal conductivities of individual tubes are calculated from measured thermal properties of MWNTs pillars and films correspondingly. We summarize the above data on the thermal conductivity of MWNTs in Fig. 4. Although reported thermal conductivities differ, it is apparent in general that the conductivity of MWNTs depends on nanotube diameter (decreasing with increasing number of carbon layers) and length (saturating at some length). Based on the data, we conclude that $k_p=1000$ W/m K is a reasonable estimate of the thermal conductivity of our MWNTs, which have a volume-weighted average diameter of 21.6 nm. Higher thermal conductivities were only reported for single-walled nanotubes and multi-walled nanotubes with diameter less than $10-15$ μm, while lower thermal conductivities were typically only reported for thicker nanotubes (with the exception of one of the results of Choi et al. [50]). For the moderate aspect-ratio particles of the present study, variations in the value of k_p about the estimated value of 1000 W/m K would have a minimal effect on the thermal conductivity of the suspension, as $\delta\approx1700$. It should be noted that the data in Fig. 4 represent the axial thermal conductivity of the MWNT. The thermal conductivity in the radial direction is much less and comparable with that of graphite [52,53]. We use value of 5.6 W/m K in our calculations [53].

Using the estimated axial and radial thermal conductivities of MWNTs from the literature, the measured thermal conductivities of the suspensions are compared with EMT predictions in Fig. 5 for various Kapitza resistances. It can be seen that the measured thermal conductivities are approximately linear with particle volume fraction, as expected from EMT at these low concentrations. The thermal-conductivity increase goes up to 8% for the nanofluid containing 0.1% MWNTs by volume. It should be noted that, while such an enhancement is small in absolute terms, it is nonetheless significant in light of the very small volume fraction of particles. In other words, had the particles been of lower aspect ratio and thermal conductivity than the nanotubes, it is likely that no detectable increase in thermal conductivity would be found for a particle volume fraction of only 0.1%. However, the measured conductivities for the MWNT suspensions are higher than predicted by EMT if the Kapitza resistance is $10^{-8}-10^{-7}$ m^2 W/K. The data suggest an interfacial resistance of order 10^{-9} m^2 W/K, which is indicative of a strongly bound system, and is lower than reported for SDS-stabilized suspensions of MWNTs [39]. It is, however, of the same order as reported by molecular-dynamics simulations for a wetting liquid-solid interface [43]. We note that a higher interfacial resistance of $R_K\approx10^{-8}$ m^2/W K would be predicted to cause a significant decrease in the effective thermal conductivity for suspensions of sufficiently small spherical nanoparticles. However, no such results have been reported. All data for nanofluids containing spherical particles show an increase in thermal conductivity [1–5,54]. The strong adsorption of the NaDDBS onto the nanotube surface may reduce the thermal interfacial resistance as compared with the neat interface or to SDS-stabilized nanotubes. Additional data on R_K for CNTs in aqueous suspension with NaDDBS are desirable to confirm the interfacial resistance value of 10^{-9} m^2 W/K suggested by the EMT curve fits to our experimental data.

Of the parameters that could affect the EMT calculations, the volume fraction of the dispersed particles and the thermal conductivity of based fluid were measured directly and are unlikely to bias the results. It is also unlikely that percolation is significant since the suspensions used in present study are dilute enough for particles to rotate freely with no tube-tube interactions. The transition from this "dilute" regime to the "semidilute" regime where particles can interact occurs at a crossover volume fraction φ_0 defined as the following [55]:

$$\varphi_0 \approx 24\left(\frac{d}{L}\right)^2 \tag{8}$$

For nanotubes with an aspect ratio of 32.9, this critical volume fraction is about 2.2% vol, and we capped our experiments at 1% vol. Moreover, the enhancement in thermal conductivity due to percolation would be more pronounced at higher concentrations, which is not seen in the data here. The thermal conductivity of the MWNTs, as shown before, also has a minimal effect on EMT-predicted thermal conductivities for such large δ.

Table 2 Measured characteristics of MWNTs for varying durations of intense tip ultrasonication

Sonication time (min)	N of particles	$\overline{d}$ (nm)	$\overline{d}_V$ (nm)	$\overline{L}_C$ (nm)	$\overline{L}_C\|_V$ (nm)	a_V
0	216	21.6	24.3	587	772	32.9
5	169	21.3	25.0	313	513	20.3
10	145	22.4	24.0	250	350	15.0
15	253	22.1	26.3	198	390	14.5

One possible mechanism affecting heat transfer in the MWNT suspensions, which is not accounted for by EMT, is the bending of the nanotubes. The persistence length, L_P, of long objects deposited and equilibrated on a 2D surface is given by [56]

$$\langle L_{\mathrm{EE}}^2 \rangle = 4L_P L_C \left[1 - \frac{2L_P}{L_C}(1 - e^{(-1/2L_P)}) \right] \tag{9}$$

where L_C is the contour length and L_{EE} is the end-to-end length of the nanotubes. From images of our MWNTs dried onto the TEM grid, we calculated the persistence length for our MWNT samples to be $L_P = 397$ nm, which is considerably shorter than the volume-weighted average length of 771 nm. This relatively short persistence length is consistent with recent data by Lee and Yun [57] who measured persistence lengths to be only 271 nm for 21 nm in diameter MWNTs with a volume-weighted contour length of 1.3 μm. Theoretical calculations by Arroyo et al. [58] also estimate persistence lengths of about 500 nm for MWNTs. Since the majority of tubes in our suspensions are longer than L_P, the nanotubes can experience significant bending due to the thermal fluctuations. This thermally driven bending motion may enhance heat transfer in this suspension, although is it unlikely to be a first-order effect. It should be noted that this motion is not purely Brownian rotation or translation and is distinct from the Brownian-motion effect that has been previously considered as a possible contributor to the thermal-conductivity enhancement in nanofluids [13,15,18]. The possible effect of nanotube curvature on the thermal-conductivity enhancement of a nanotube suspension has also been considered by Deng et al. [59].

4 Results and Discussion II: Aspect-Ratio Effect on Thermal Conductivity

We next attempted to reduce the nanotube length by ultrasonication in order to directly investigate the effect of particle aspect ratio on the thermal conductivity of the suspensions. Sonication, depending on its intensity, is not only a powerful tool for dispersing particles in the suspensions by untangling the agglomerates but can also damage and break nanotubes, especially at defect sites. Milder bath sonication is reported to have little effect on nanotube structure and is used widely for dispersing nanotubes [34], while more powerful tip sonication is a typical method to shorten CNTs [3,60]. Experiments by Yang et al. [7] show a reduction in nanotube aspect ratio from 300 down to 49 after only 5 min of tip-sonication of an oil-based MWNT suspension. Further shortening to $a = 30$ was obtained after an additional 25 min of ultrasonication. In this study, we used tip-sonication to reduce the aspect ratio of the MWNTs in aqueous dispersion and further investigate the thermal conductivity of a MWNT suspension with fixed nanotube volume fraction, but varying particle shape.

We compared suspensions containing 0.1% MWNTs by volume and 10× fraction of surfactant by weight because this sample showed significant stability against aggregation and sedimentation. Measurements of the optical absorbance that will be shown later indicate that nanofluid in this case is well dispersed and contains mostly individualized nanotubes.

The sonication time varied from 5 to 15 min in a high-power tip-sonicator. Unlike the bath sonication we used for initially dispersing the nanotubes, the tip-sonication was very intense and accompanied by extensive cavitation and heating. All samples were allowed to cool every 5 min to minimize the effects due to elevated temperature. For every sample, the nanotube diameter, contour length L_C and end-to-end length L_{EE} of at least 145 nanotubes were measured from several TEM micrographs (Table 2). The volume-averaged aspect ratio was then calculated from the measured aspect-ratio distribution. As seen in Fig. 6, the initially broad aspect-ratio distribution narrowed and shifted toward shorter particles after sonication. The volume-weighted aspect ratio of MWNTs was reduced from 32.9 to 20.3 after 5 min of tip-sonication, and ultimately reduced to 14.5 (a factor of 2 from the original length) after a total of 15 min of sonication (Table 2).

The thermal-conductivity measurements were coupled to TEM characterization of the aspect ratio of MWNTs in aqueous suspension after varying tip-sonication times. As seen in Fig. 7, the thermal-conductivity enhancement of the suspension (0.1% MWNTs by volume) dropped in half, from 8% to 4%, after the first 5 min of sonication. The thermal conductivity was reduced even more, to 1%, after 10 min of processing, but was then insensitive to further sonication. The decrease in conductivity was correlated with the decrease in MWNT aspect ratio, which dropped rapidly initially, and then was essentially unchanged after 10 min of tip-sonication. However, comparison with EMT indicates that the decrease in thermal conductivity with decreasing aspect occurs somewhat faster than predicted by theory, assuming the measured aspect ratios given in Table 2. Such a greater than predicted drop in thermal conductivity is likely to be a consequence of a reduction in the thermal conductivity of the MWNTs themselves due to sonication-induced defects in their structure [60,61]. Such defects, which also limit the thermal conductivity of very long nanotubes, lead to enhanced phonon scattering and a reduction in the phonon mean free path and thermal conductivity of the CNTs. The difference in the rate of nanofluid thermal-conductivity change with aspect ratio between our experiment and EMT may thus be attributable to the fact that the calculations assume a constant k_p. Nonetheless, the results clearly show that the effective thermal conductivity of the MWNT suspension is a direct function of particle aspect ratio, as predicted by EMT.

It should be noted that, since the nanofluid was already well dispersed by the initial bath sonication, the additional tip-sonication acts mostly to shorten the nanotubes rather than to further individualize them. In fact, any possible breakup of existing nanotube agglomerates by the tip-sonication should only increase the conductivity with sonication time, which is opposite to the observed trend.

5 Results and Discussion III: Aggregation Effect on Thermal Conductivity

The effective aspect ratio of MWNTs in suspension can also be affected by particle agglomeration into low-aspect-ratio flocs. In order to investigate the effect of MWNT flocculation on the nanofluid's thermal conductivity, we destabilized the surfactant-stabilized aqueous suspensions with the addition of ethyl alcohol and carried out a further set of thermal-conductivity measure-

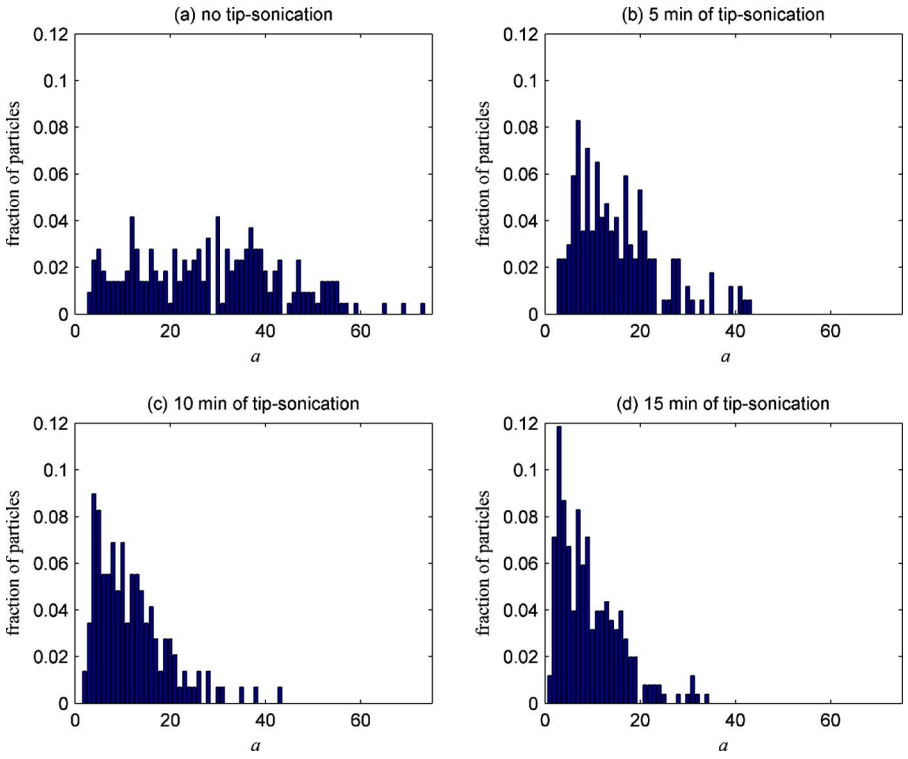

Fig. 6 Aspect-ratio distributions for MWNTs before and after varying durations of intense tip ultrasonication

ments. These measurements were coupled with microscopic observations and absorption measurements of destabilized suspensions.

Ethyl and methyl alcohol are widely used for removing surfactant adsorbed on nanotube surfaces. Experiments by Zhang et al. [62], aimed at investigating the effectiveness of different CNT-surface-cleaning procedures in order to improve the electrical contact between nanotube and the electrode in CNT field-effect transistors, showed complete removal of SDS from SWNT surfaces by means of ethanol immersion. Such desorption of surfactant from the nanotubes after addition of alcohol promotes the aggregation of nanotubes into larger agglomerates [63].

The optical signature of the particle aggregation process was studied with measurements of the absorption

$$A = -\log_{10}\left(\frac{I}{I_0}\right) \tag{10}$$

where I and I_0 are transmitted and incident light intensities [64]. I_0 was taken to be the transmitted light intensity of the base fluid in absence of the particles. Thus, the calculated absorbance corresponds to the absorbance due to dispersed nanotubes only, not including any absorbance due to the surfactant-water-ethanol base fluid. Absorption was determined by passing a helium-neon laser through samples housed in a glass cuvette and by measuring the transmitted intensity with a photodiode. A cuvette of short path length of 1 mm allowed the use of fairly concentrated suspensions of nanotubes. This was first done for the suspension containing 0.1% MWNTs by volume and 10× fraction of surfactant by weight without alcohol. As seen in Fig. 8, the measured absorbance for the sample approaches a plateau after an initial decay

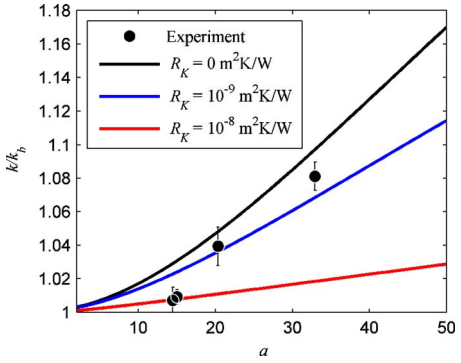

Fig. 7 Measured thermal conductivities of 0.1% vol MWNT suspensions as a function of volume-weighted particle aspect ratio

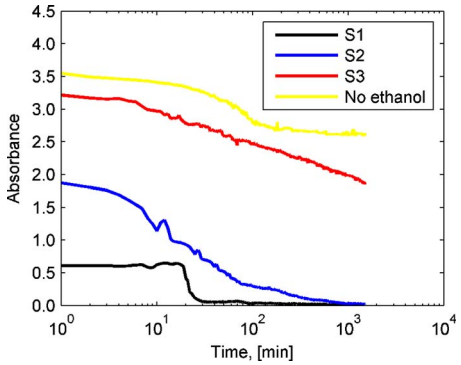

Fig. 8 Measured absorbance as function of time for nanofluids containing different fractions of ethanol

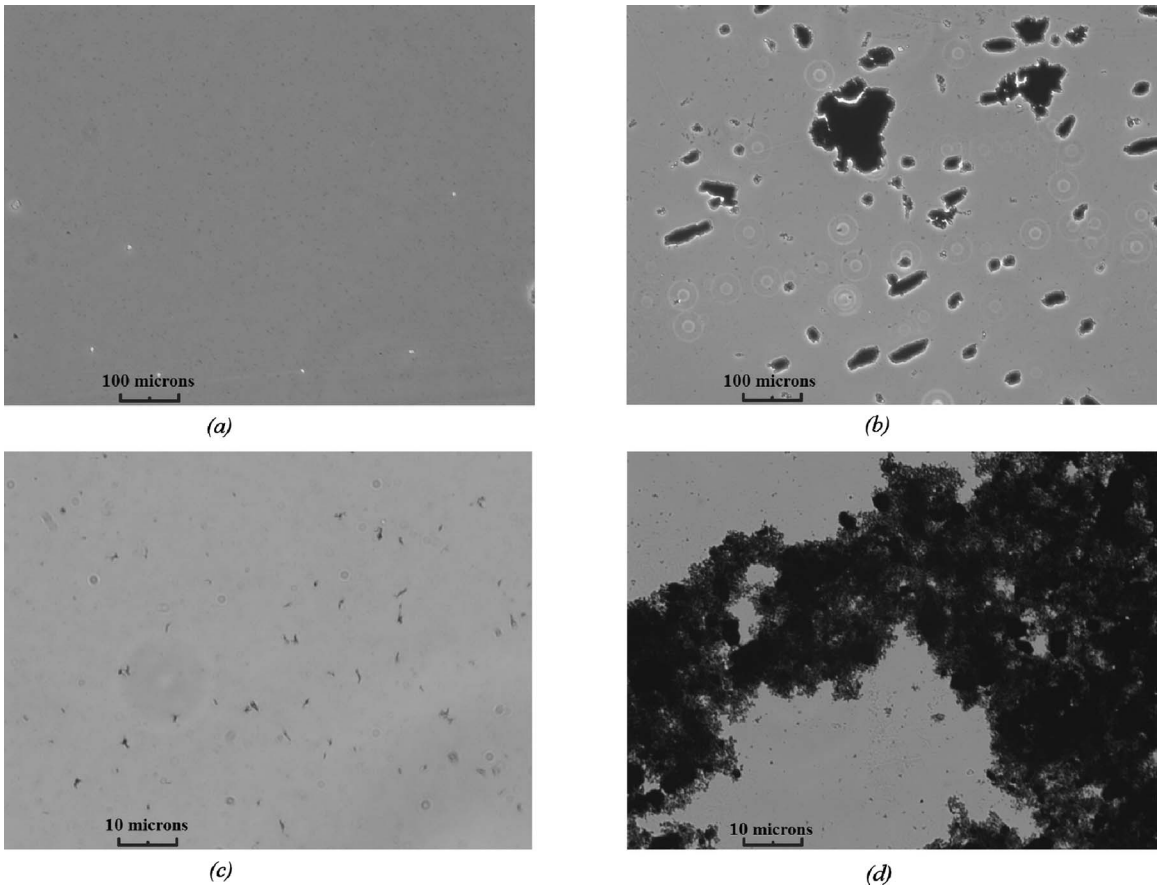

Fig. 9 Optical micrographs at different magnifications of suspensions containing 0.1% vol MWNTs. Aqueous suspensions without ethanol are shown in (*a*) and (*c*), while aqueous suspensions containing 50% ethanol by volume (S1) are shown in (*b*) and (*d*).

over ~100 min. The plateau in absorbance is about 80% of the initial absorbance, which corresponds to an ~20% drop in the nanotube concentration according to the Beer–Lambert law, which postulates that absorbance is linearly proportional to the molar concentration of dispersed particles, c:

$$A = \varepsilon \lambda c \tag{11}$$

Here, ε is a molar absorptivity of the absorber and λ is the path length. In practice, Eq. (11) holds for $A \approx 1$, and at higher absorbances the dependence between the absorbance and the concentration can become nonlinear due to interparticle interaction, e.g., shading effects. The initial decrease in absorbance indicates that mild agglomeration occurs in the suspension during the first 2 h. Overall, however, consistent with visual observation, we conclude that the bath-sonicated nanofluid containing 0.1% of MWNTs by volume and 10× fraction of surfactant is well dispersed and stable since the absorbance remains relatively constant for at least 22 h after the slight initial decay.

Nanotube agglomeration was then induced by diluting aqueous nanofluid of an initial 20g/l mass fraction of NaDDBS with ethanol. By varying the initial volume fraction of MWNTs, the volume fraction of nanotubes after the addition of varying amounts of ethanol was maintained constant at 0.1% for all suspensions. Before the addition of ethanol all suspensions showed good stability as evidenced by absorbance measurements. After mixing the base nanofluid with ethanol at 1:1 (S1), 2:1 (S2), and 3:1 (S3) ratios, absorption measurements showed immediate agglomeration of MWNTs, with initial ($t=0$) absorbances lower than the absorbance of the nanofluid in the absence of ethanol. Large MWNT flocs can be seen in optical micrographs (Fig. 9) of the ethanol-destabilized suspensions, with the largest agglomerates seen for the highest ethanol fraction. For comparison, optical micrographs of the original 0.1% vol suspension are also shown in the Fig. 9. Sedimentation of the large MWNT agglomerates in the destabilized suspensions then causes decay in absorbance as absorbing/scattering particles are removed from the light path. The almost exponential decay in absorption after an initial agglomeration/settling time is consistent with classical Mason–Weaver theory for the sedimentation of small particles under a gravitational force [65]. The initial desorption of surfactant from the nanotubes (and consequent change in light absorption due to particle aggregation) is nearly instantaneous, however, and correlated with the amount of added ethanol.

The microscopic observations and absorption measurements of destabilized suspensions were coupled with thermal-conductivity measurements of the 0.1% MWNT suspensions (Fig. 10). Suspension thermal conductivities were measured starting 10 min after the ethanol was added and then every 10 min for 3 h. An additional, final measurement was taken 24 h after the addition of ethanol. The least-diluted (S3) suspension, containing 0.1% MWNT and ethanol at 1:3 ratio to the base fluid, showed a thermal-conductivity increase of 6.8%, compared with a thermal-conductivity enhancement of 8.6% averaged over 24 h period for the aqueous-NaDDBS suspension without ethanol (Fig. 10). For the (S2) suspension containing a 1:2 ethanol/base fluid ratio, the mean thermal-conductivity increase was 4.6%, while the (S1) suspension diluted 1:1 with ethanol showed no enhancement in thermal conductivity for the same 0.1% by volume MWNT loading. As seen from Fig. 10, the thermal conductivity remains stable for all suspensions during the 24 h observation time. The sedimenta-

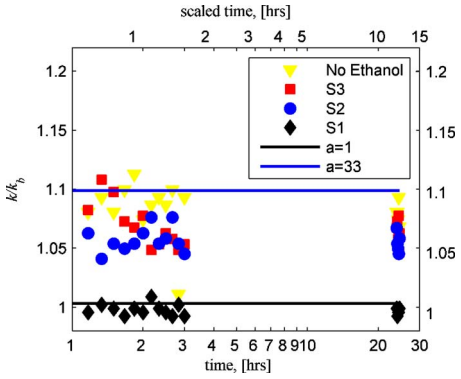

Fig. 10 Measured thermal conductivities of ethanol destabilized nanofluids. The lower axis is the real time for the thermal-conductivity measurement. The upper axis shows a time scaled to allow comparison with the optical absorption measurements of Fig. 8 (i.e., divided by 5 due to the smaller size of the absorption cuvette). For comparison, EMT and Maxwell (spherical-particle) predictions are shown assuming no interfacial resistance.

tion times for the destabilized suspensions are much less than 24 h, however. In the thermal-conductivity test cell (which has a different height than the absorption cuvette), complete sedimentation for the S1 sample occurs about 1.5 h after the addition of ethanol. The Stokes sedimentation law can be used for a simple estimate of sedimentation time:

$$t = \frac{4.5\mu H}{(\rho_p - \rho_b)gr^2} \tag{12}$$

where H is the characteristic height, g is the gravity, μ is the viscosity of a base fluid, and ρ_p and ρ_b are the densities of dispersed and dispersing phases, respectively. Since sedimentation time is proportional to the height, we expect complete sedimentation in the optical cuvette to occur around five times faster than in the smaller sample holder used for measuring thermal conductivity. For instance, full sedimentation in the optical cuvette occurs after 20 min and 16 h in S1 and S2, while it takes around 1.5 h and at several days in the thermal-conductivity sample holder. This means that the first six data points presented in Fig. 10 for S1 were taken when some agglomerates were still suspended in the liquid, followed by complete CNT sedimentation. However, the thermal conductivity remained essentially unchanged from its initial value, indicating a negligible fraction of individualized nanotubes (which contribute the most to thermal-conductivity increase) remained shortly after the addition of ethanol in a 1:1 ratio. The fact that thermal conductivity does not change significantly over 24 h for all samples means that agglomeration begins immediately after addition of ethanol, and thereafter the amount of individualized CNTs remains relatively constant. This is consistent with the absorption measurements, which showed an immediate change in absorbance with the introduction of ethanol. Thus, the thermal conductivity is primarily affected by the presence of individualized high-aspect ratio nanotubes in suspension. Once ethanol-induced surfactant desorption occurs and rapid particle aggregation begins, the thermal conductivity is essentially unchanged as low-aspect ratio aggregates contribute negligibly to the suspension thermal conductivity compared with long, individualized nanotubes.

6 Conclusions

In summary, we have experimentally validated the EMT prediction that the thermal conductivity of an aqueous suspension is enhanced by the presence of large aspect-ratio nanotubes. An increase of 8% was found for a MWNT volume fraction of 0.1%. While small, the enhancement was significant in light of the very small volume fraction of particles. Sodium dodecylbenzene sulfonate was found to be effective in dispersing MWNTs in water for NaDDBS concentrations up to 20 g/l; higher surfactant concentrations destabilized the suspension and reduced the conductivity enhancement. The optimal surfactant-to-nanotube mass ratio yielding the highest thermal-conductivity enhancement was found to be 10:1. The effective medium theory was found to be in a good agreement with measured conductivities using the TEM-measured volume-weight aspect ratio of particles, and for reasonable values for particle thermal conductivity and nanotube/liquid interfacial resistance. Bending of the MWNTs under thermal (Brownian) fluctuation and other mechanisms may also influence the effective thermal conductivity of the suspension. However, no anomalous increase in thermal conductivity beyond the limits of what can be predicted by EMT was observed.

Particle aspect-ratio and agglomeration effects on the effective thermal conductivity of MWNT suspensions were further investigated by directly varying nanotube length by intense tip-sonication and by destabilizing suspensions with the addition of ethanol. The effective thermal conductivity of the suspension was shown to be a direct function of particle aspect ratio, with the measured thermal conductivity decreasing as the MWNT aspect ratio was reduced. The experimental data were consistent with EMT predictions, with a slightly faster reduction in thermal conductivity with decreasing particle aspect ratio possibly due to the sonication-induced damage to the nanotubes. Particle aggregation, caused by ethanol-induced surfactant desorption from the MWNTs, was shown through absorption measurements and microscopy to occur immediately upon the introduction of ethanol; slow growth and sedimentation of MWNT aggregates followed. The thermal-conductivity enhancement due to MWNTs also changed immediately upon ethanol addition, indicating that the conductivity increase was due mostly to the presence of long individualized tubes rather than low-aspect-ratio aggregates. Suspensions showing negligible amounts of individually suspended tubes also showed zero thermal-conductivity enhancements. Thus, both the aspect ratio and dispersion state of MWNTs in suspension are shown to have a profound effect on the effective thermal conductivity of an aqueous MWNT suspension.

Nomenclature

k = nanofluid thermal conductivity
k_b = base fluid thermal conductivity
k_p = particle thermal conductivity
δ = ratio of particle-to-base-matrix thermal conductivities
φ = particle volume fraction
φ_0 = critical particle volume fraction for transition from dilute to semidilute regimes
R_K = Kapitza resistance
L_K = Kapitza length
d = nanotube diameter
L = nanotube length
L_C = contour length of nanotube
L_{EE} = end-to-end length of nanotube
L_P = persistence length of nanotube
a = length-to-diameter (aspect) ratio of nanotube
V = volume of nanotube
A = absorbance
I = transmitted light intensity
I_0 = incident light intensity
ε = molar absorptivity of fluid
λ = path length of transmitted light
c = molar concentration of dispersed particles
β_{ii} = coefficients in EMT equation (1)
L_{ii} = depolarization factors in Eq. (1)
H = fluid layer height
g = gravity

μ = viscosity of base fluid
ρ_p = density of dispersed particles
ρ_b = density of base fluid

Indices

11 = transverse axis of spheroid
33 = longitudinal axis of spheroid
p = particle
b = base fluid
V = volume averaged

References

[1] Eastman, J. A., Choi, S. U. S., Li, S., Yu, W., and Thompson, L. J., 2001, "Anomalously Increased Effective Thermal Conductivities of Ethylene Glycol-Based Nanofluids Containing Copper Nanoparticles," Appl. Phys. Lett., **78**, pp. 718–720.

[2] Patel, H., Das, S., Sundararajan, T., Sreekumaran, N. A., George, B., and Pradeep, T., 2003, "Thermal Conductivities of Naked and Monolayer Protected Metal Nanoparticle Based Nanofluids: Manifestation of Anomalous Enhancement and Chemical Effects," Appl. Phys. Lett., **83**(14), pp. 2931–2933.

[3] Yang, B., and Han, Z. H., 2006, "Temperature-Dependent Thermal Conductivity of Nanorod-Based Nanofluids," Appl. Phys. Lett., **89**, p. 083111.

[4] Xie, H., Wang, J., Xi, T., Liu, Y., and Ai, F., 2002, "Thermal Conductivity of Suspension Containing SiC Particles," J. Mater. Sci. Lett., **21**, pp. 193–95.

[5] Lee, S., Choi, S., Li, S., and Eastman, J. A., 1999, "Measuring Thermal Conductivity of Fluids Containing Oxide Nanoparticles," ASME J. Heat Transfer, **121**(2), pp. 280–289.

[6] Choi, S. U. S., Zhang, Z. G., Yu, W., and Grulke, E. A., 2001, "Anomalous Thermal Conductivity Enhancement in Nanotube Suspensions," Appl. Phys. Lett., **79**, pp. 2252–2254.

[7] Yang, Y., Grulke, E. A., Zhang, Z. G., and Wu, G., 2006, "Thermal and Rheological Properties of Carbon Nanotube-in-Oil Dispersions," J. Appl. Phys., **99**, p. 114307.

[8] Xie, H., Lee, H., Youn, W., and Choi, M., 2003, "Nanofluids Containing Multiwalled Carbon Nanotubes and Their Enhanced Thermal Conductivities," J. Appl. Phys., **94**(8), pp. 4967–4971.

[9] Chen, L., and Xie, H., 2009, "Silicon Oil Based Multiwalled Carbon Nanotubes Nanofluid With Optimized Thermal Conductivity Enhancement," Colloids Surf., A, **352**, pp. 136–140.

[10] Choi, T. E., Maneshian, M. H., Kang, B., Chang, W. S., Han, C. S., and Poulikakos, D., 2009, "Measurement of the Thermal Conductivity of a Water-Based Single-Wall Carbon Nanotube Colloidal Suspension With a Modified 3-ω Method," Nanotechnology, **20**, p. 315706.

[11] Glory, J., Bonetti, M., Helezen, M., Mayne-L'Hermite, M., and Reynaud, C., 2008, "Thermal and Electrical Conductivities of Water-Based Nanofluids Prepared With Long Multiwalled Carbon Nanotubes," J. Appl. Phys., **103**, p. 094309.

[12] Xie, H., and Chen, L., 2009, "Adjustable Thermal Conductivity in Carbon Nanotube Nanofluids," Phys. Lett. A, **373**, pp. 1861–1864.

[13] Prasher, R., Bhattacharya, P., and Phelan, P. E., 2005, "Thermal Conductivity of Nanoscale Colloidal Solutions (Nanofluids)," Phys. Rev. Lett., **94**, p. 025901.

[14] Krishnamurthy, S., Bhattacharya, P., Phelan, P. E., and Prasher, S. P., 2006, "Enhanced Mass Transport in Nanofluids," Nano Lett., **6**, pp. 419–423.

[15] Jang, S., and Choi, S., 2004, "Role of Brownian Motion in the Enhanced Thermal Conductivity," Appl. Phys. Lett., **84**, pp. 4316–4318.

[16] Koo, J., and Kleinstreuer, C., 2004, "A New Thermal Conductivity Model for Nanofluids," J. Nanopart. Res., **6**(6), pp. 577–588.

[17] Evans, W., Fish, J., and Keblinski, P., 2006, "Role of Brownian Motion Hydrodynamics on Nanofluid Thermal Conductivity," Appl. Phys. Lett., **88**, p. 093116.

[18] Vladkov, M., and Barrat, J. L., 2006, "Modeling Transient Absorption and Thermal Conductivity in a Simple Nanofluid," Nano Lett., **6**(6), pp. 1224–1228.

[19] Prasher, R., Phelan, P. E., and Bhattacharya, P., 2006, "Effect of Aggregation Kinetics on the Thermal Conductivity of Nanoscale Colloidal Solutions (Nanofluid)," Nano Lett., **6**, pp. 1529–1534.

[20] Prasher, R., Evans, W., Meakin, P., Fish, J., Phelan, P., and Keblinski, P., 2006, "Effect of Aggregation on Thermal Conduction in Colloidal Nanofluids," Appl. Phys. Lett., **89**, pp. 143119.

[21] Wang, B. X., Zhou, L. P., and Peng, X. F., 2003, "A Fractal Model for Predicting the Effective Thermal Conductivity of Liquid With Suspension of Nanoparticles," Int. J. Heat Mass Trans., **46**(14), pp. 2665–2672.

[22] Xuan, Y. M., Li, Q., and Hu, W. F., 2003, "Aggregation Structure and Thermal Conductivity of Nanofluids," AIChE J., **49**(4), pp. 1038–1043.

[23] Lee, D., Kim, J. W., and Kim, B. G., 2006, "A New Parameter to Control Heat Transport in Nanofluids: Surface Charge State of the Particle in Suspension," J. Phys. Chem. B, **110**(9), pp. 4323–4328.

[24] Hong, K. S., Hong, T. K., and Yang, H. S., 2006, "Thermal Conductivity of Fe Nanofluids Depending on the Cluster Size of Nanoparticles," Appl. Phys. Lett., **88**(3), pp. 031901.

[25] Keblinski, P., Phillpot, S. R., Choi, S. U. S., and Eastman, J. A., 2002, "Mechanism of Heat Flow in Suspensions of Nano-Sized Particles (Nanofluids)," Int. J. Heat Mass Transfer, **45**, pp. 855–863.

[26] Nan, C.-W., Birringer, R., Clarke, D. R., and Gleiter, H., 1997, "Effective Thermal Conductivity of Particulate Composites With Interfacial Thermal Resistance," J. Appl. Phys., **81**, pp. 6692–6699.

[27] Cherkasova, A. S., and Shan, J. W., 2008, "Particle Aspect-Ratio Effects on the Thermal Conductivity of Micro- and Nanoparticle Suspensions," ASME J. Heat Transfer, **130**, pp. 082406.

[28] Maxwell, J. C., 1954, *A Treatise on Electricity and Magnetism*, Dover, New York.

[29] Fricke, H., 1924, "A Mathematical Treatment of the Electric Conductivity and Capacity of Disperse Systems," Phys. Rev., **24**(5), pp. 575–587.

[30] Nan, C.-W., Shi, Z., and Lin, Y., 2003, "A Simple Model for Thermal Conductivity of Carbon Nanotube-Based Composites," Chem. Phys. Lett., **375**(5–6), pp. 666–669.

[31] Vadasz, J. J., Govender, S., and Vadasz, P., 2005, "Heat Transfer Enhancement in Nano-Fluids Suspensions: Possible Mechanisms and Explanations," Int. J. Heat Mass Transfer, **48**(13), pp. 2673–2683.

[32] Li, C.-C., and Chang, M.-H., 2004, "Colloidal Stability of CuO Nanoparticles in Alkanes via Oleate Modifications," Mater. Lett., **58**, pp. 3903–3907.

[33] Louge, M., and Chen, X., 2008, "Heat Transfer Enhancement in Suspensions of Agitated Solids. Part III: Thermophoretic Transport of Nanoparticles in the Diffusion Limit," Int. J. Heat Mass Transfer, **51**(21–22), pp. 5130–5143.

[34] Islam, M. F., Rojas, E., Bergey, D. M., Johnson, A. T., and Yodh, A. G., 2003, "High Weight Fraction Surfactant Solubilization of Single-Wall Carbon Nanotubes in Water," Nano Lett., **3**(2), pp. 269–273.

[35] Tadros, T. F., 2005, *Applied Surfactants: Principles and Application*, Wiley-VCH, New York.

[36] Segota, S., Heimer, S., and Tezak, D., 2006, "New Catanionic Mixtures of Dodecyldimethylammonium Bromide/Sodium Dodecylbenzenesulphonate/Water I. Surface Properties of Dispersed Particles," Colloids Surf., A, **274**, pp. 91–99.

[37] Kapitza, P. L., 1941, "Heat Transfer and Superfluidity of Helium II," Phys. Rev., **60**, pp. 354–355.

[38] Shenogin, S., Xue, L., Ozisik, R., Keblinski, P., and Cahill, D. G., 2004, "Role of Thermal Boundary Resistance on the Heat Flow in Carbon-Nanotube Composites," J. Appl. Phys., **95**, pp. 8136–8144.

[39] Huxtable, S., Cahill, D., Shenogin, S., Xue, L., Ozisik, R., Barone, P., Usrey, M., Strano, M., Siddons, G., Shim, M., and Keblinski, P., 2003, "Interfacial Heat Flow in Carbon Nanotube Suspensions," Nature Mater., **2**, pp. 731–734.

[40] Ge, Z., Cahill, D., and Braun, P., 2004, "AuPd Metal Nanoparticles as Probes of Nanoscale Thermal Transport in Aqueous Solution," J. Phys. Chem. B, **108**(49), pp. 18870–18875.

[41] Plech, A., Kotaidis, V., Gresillon, S., Dahmen, C., and Von Plessen, G., 2004, "Laser-Induced Heating and Melting of Gold Nanoparticles Studied by Time-Resolved X-Ray Scattering," Phys. Rev. B, **70**, pp. 195423.

[42] Wilson, M. W., Hu, X., Cahill, D. G., and Braun, P. V., 2002, "Colloidal Metal Particles as Probes of Nanoscale Thermal Transport in Fluids," Phys. Rev. B, **66**, p. 224301.

[43] Xue, L., Keblinski, P., Phillpot, S. R., Choi, S. U. S., and Eastman, J. A., 2003, "Two Regimes of Thermal Resistance at a Liquid-Solid Interface," J. Chem. Phys., **118**(1), pp. 337–339.

[44] Kim, P., Shi, L., Majumdar, A., and Mceuen, P. L., 2001, "Thermal Transport Measurements of Individual Multiwalled Nanotubes," Phys. Rev. Lett., **87**(21), p. 215502.

[45] Small, J. P., Shi, L., and Kim, P., 2003, "Mesoscopic Thermal and Thermoelectric Measurements of Individual Carbon Nanotubes," Solid State Commun., **127**, pp. 181–186.

[46] Prasher, R., 2008, "Thermal Boundary Resistance and Thermal Conductivity of Multiwalled Carbon Nanotubes," Phys. Rev. B, **77**, p. 075424.

[47] Li, Q., Liu, C., Wang, X., and Fan, S., 2009, "Measuring the Thermal Conductivity of Individual Carbon Nanotubes by the Raman Shift Method," Nanotechnology, **20**, p. 145702.

[48] Fujii, M., Zhang, X., and Takahashi, K., 2006, "Measurements of Thermal Conductivity of Individual Carbon Nanotubes," Phys. Status Solidi B, **243**(13), pp. 3385–3389.

[49] Choi, T.-Y., Poulikakos, D., Tharian, J., and Sennhauser, U., 2005, "Measurement of Thermal Conductivity of Individual Multiwalled Carbon Nanotubes by the 3-Method," Appl. Phys. Lett., **87**, p. 013108.

[50] Choi, T.-Y., Poulikakos, D., Tharian, J., and Sennhauser, U., 2006, "Measurement of the Thermal Conductivity of Individual Carbon Nanotubes by the Four-Point Three-ω Method," Nano Lett., **6**, pp. 1589–1593.

[51] Shioya, H., Iwai, T., Kondo, D., Nihei, M., and Awano, Y., 2007, "Evaluation of Thermal Conductivity of a Multi-Walled Carbon Nanotube Using the Delta V-Gs Method," Jpn. J. Appl. Phys., Part 1, **46**(5A), pp. 3139–3143.

[52] Yang, D. J., Wang, S. G., Zhang, Q., Sellin, P. J., and Chen, G., 2004, "Thermal and Electrical Transport in Multi-Walled Carbon Nanotubes," Phys. Lett. A, **329**(3), pp. 207–213.

[53] Che, J., Cagun, T., and Goddard, W. A. I., 2000, "Thermal Conductivity of Carbon Nanotubes," Nanotechnology, **11**, pp. 65–69.

[54] Kwak, K., and Kim, C., 2005, "Viscosity and Thermal Conductivity of Copper Oxide Nanofluid Dispersed in Ethylene Glycol," Korea-Aust. Rheol. J., **17**(2), pp. 35–40.

[55] Larson, R. G., 1999, *The Structure and Rheology of Complex Fluids*, Oxford University Press, New York.

[56] Abels, J. A., Moreno-Herrero, F., Van Der Heijden, T., Dekker, C., and Dekker, N. H., 2005, "Singlemolecule Measurements of the Persistence Length of Double-Stranded RNA," Biophys. J., **88**, pp. 2737–2744.

[57] Lee, H. S., and Yun, C. H., 2008, "Translational and Rotational Diffusions of Multiwalled Carbon Nanotubes With Static Bending," J. Phys. Chem. C, **112**, pp. 10653–10658.
[58] Arroyo, M., and Belytschko, T., 2003, "A Finite Deformation Membrane Based on Inter-Atomic Potentials for the Transverse Mechanics of Nanotubes," Mech. Mater., **35**(3–6), pp. 193–215.
[59] Deng, F., Zheng, Q. S., and Wang, L. F., 2007, "Effects of Anisotropy, Aspect Ratio, and Nonstraightness of Carbon Nanotubes on Thermal Conductivity of Carbon Nanotube Composites," Appl. Phys. Lett., **90**, p. 021914.
[60] Wang, S., Liang, R., Wan, B., and Zhang, C., 2009, "Dispersion and Thermal Conductivity of Carbon Nanotube Composites," Carbon, **47**, pp. 53–57.
[61] Zhang, M., Yudasaka, M., Koshio, A., Jabs, C., Ichihashi, T., and Iijima, S., 2002, "Structure of Single Wall Carbon Nanotubes Purified and Cut Using Polymer," Appl. Phys. A: Mater. Sci. Process., **74**, pp. 7–10.
[62] Zhang, Z.-B., Cardenas, J., Campbell, E. E. B., and Zhang, S.-L., 2005, "Reversible Surface Functionalization of Carbon Nanotubes for Fabrication of Field-Effect Transistors," Appl. Phys. Lett., **87**, p. 043110.
[63] Eda, G., Fanchini, G., Kanwal, A., and Chhowalla, M., 2008, "Bundling Dynamics of Single Walled Carbon Nanotubes in Aqueous Suspensions," J. Appl. Phys., **103**(9), p. 093118.
[64] Ingle, J. D. J. and Crouch, S. R., 1988, *Spectrochemical Analysis*, Prentice-Hall, Upper Saddle River, NJ.
[65] Mason, M., and Weaver, W., 1924, "The Settling of Small Particles in a Fluid," Phys. Rev., **23**, pp. 412–426.

Impact of Thermodiffusion on Carbon Nanotube Growth by Chemical Vapor Deposition

Andrew C. Lysaght

Wilson K. S. Chiu[1]
e-mail: wchiu@engr.uconn.edu

Department of Mechanical Engineering,
University of Connecticut,
191 Auditorium Road,
Storrs, CT 06269-3139

Thermal diffusion, the process by which a multicomponent mixture develops a concentration gradient when exposed to a temperature gradient, has been studied in order to understand if its inclusion is warranted in the modeling of single-wall carbon nanotubes (SWNTs) synthesis by thermal chemical vapor deposition (CVD). A fully coupled reactor-scale model employing conservation of mass, momentum, species, and energy equations with detailed gas phase and surface reaction mechanisms has been utilized to describe the evolution of hydrogen and hydrocarbon feed streams as they undergo transport, as well as homogeneous and heterogeneous chemical reaction within a CVD reactor. Steady state velocity, temperature, and concentration fields within the reactor volume are determined, as well as concentrations of adsorbed species and SWNT growth rates. The effect of thermodiffusion in differing reactor conditions has been investigated to understand the impact on SWNT growth. Thermal diffusion can have a significant impact on SWNT growth, and the first approximation of the thermal diffusion factor, based on the Chapman–Enskog molecular theory, is sufficient for modeling thermophoretic behavior within a CVD reactor. This effect can be facilitatory or inhibitory, based on the thermal and mass flux conditions. The results of this investigation are useful in order to optimize model and reactor designs to promote optimal SWNT deposition rates.
[DOI: 10.1115/1.4001099]

Keywords: carbon nanotube, chemical vapor deposition, thermodiffusion

1 Introduction

To better understand the subtleties of mass transport and chemical reaction during single-wall carbon nanotube (SWNT) synthesis within a chemical vapor deposition (CVD) reactor, this paper presents an investigation into the impact of thermodiffusion on reactor evolution and carbon nanotube growth. Thermodiffusion, also called the Soret effect, is the process by which a temperature gradient induces a concentration gradient in a multicomponent mixture [1]. In a gaseous mixture, this behavior is attributed to intermolecular forces and is heavily dependent on species diameter and molecular weight. Typically, larger and heavier molecules move toward cooler regions (positive thermal diffusion, Fig. 1), while smaller and lighter molecules typically move toward warmer regions [2]. This behavior was initially observed in liquids by Ludwig, and later, theoretically explained in the gas phase independently by Chapman and Enskog, as detailed in Ref. [1].

A primary goal of this investigation was to determine if thermal diffusion warranted incorporation while modeling a tubular carbon nanotube (CNT) reactor. Previous investigations of diverse CVD processes have resulted in controversy as to whether incorporating this complex behavior is necessary. Several researchers have shown that deposition rates can be significantly impacted due to high temperature gradients and large molecular weight discrepancies common within CVD reactors [3,4]. Conversely, while modeling a CVD process within a cold wall reactor, Hitchman [5] demonstrated, through an order of magnitude analysis, that thermodiffusion can often be neglected. In this study, we illustrate complex coupling between thermophretic-induced species transport and reaction mechanisms, warranting its inclusion in modeling efforts.

In an effort to investigate the importance and impact of thermophoretic motion on a carbon nanotube CVD synthesis process, a steady state reactor-scale deposition model of a horizontal tube flow reactor is being modeled. Thermal diffusion factors were calculated by the model using a complete first approximation of the Chapman–Enskog molecular theory. Validation of this method was conducted against experimental observations. Analysis of the impact on CNT deposition rates has been conducted with specific attention to how different deposition regimes are impacted by the transport phenomena.

The modeled temperature range was selected based on observed envelopes of single-wall nanotube growth. Methane can spontaneously decompose into graphite and hydrogen at temperatures above 923 K [6], and poisonous catalyst-substrate reactions (dependent on substrate and nanoparticle materials, as well as particle size [7–9]) begin occurring around 1273 K. In order to maintain a high degree of confidence in model results, the parameter space was maintained within these constraints, between 1023 K and 1198 K. In every deposition case presented in this work, acetylene concentrations remained well below 0.1 mol % to avoid the deposition of an amorphous carbon film [10], and within the nanotube growth regime. In order to ensure that soot and other undesirable byproducts do not occur in this study, SWNT deposition was modeled for feed stream varying between 1% and 20% methane [11,12] with the remainder of the flow being hydrogen. This work was performed as part of a series of investigations with the goal of better understanding reactor dynamics in the open-air laser induced CVD process presented by Kwok and Chiu [13].

2 Method of Approach

In order to describe the complex chemical, thermal, and hydrodynamic evolution of feed stream gases as they transport through a horizontal tube flow CVD reactor, a reactor-scale deposition model, previously presented and validated by the authors, was utilized. This model (built in COMSOL Multiphysics and described in detail in Ref. [14]) contains a 20 step chemical reaction mechanism, defining both volumetric and surface chemical reactions for hydrogen and hydrocarbon feed stream depositing on catalytic iron nanoparticles. This reaction system was compiled from CVD investigations conducted by Coltrin and Dandy [15], Grujicic et al. [16], and Klinke et al. [17]. The complete reaction mechanism is presented in Ref. [14].

These reactions are coupled with conservation of mass, momentum, energy, and species equations (Eqs. (1)–(4)) [18], incorporating thermophoretic flux via the D^T term

$$\nabla \cdot (\rho \boldsymbol{u}) = 0 \tag{1}$$

$$\rho \boldsymbol{u} \cdot \nabla \boldsymbol{u} = \nabla \cdot \left[-p\mathbf{I} + \eta(\nabla \boldsymbol{u} + (\nabla \boldsymbol{u})^T) - \left(\frac{2\eta}{3}\right)(\nabla \cdot \boldsymbol{u})\mathbf{I} \right] \tag{2}$$

$$\nabla\left(-k \nabla T + \sum_i h_i \boldsymbol{N}_{D,i} \right) = Q - \rho C_p \boldsymbol{u} \nabla T \tag{3}$$

[1]Corresponding author.

Contributed by the Heat Transfer Division of ASME for publication in the JOURNAL OF HEAT TRANSFER. Manuscript received April 18, 2008; final manuscript received December 28, 2009; published online June 4, 2010. Assoc. Editor: Pamela M. Norris.

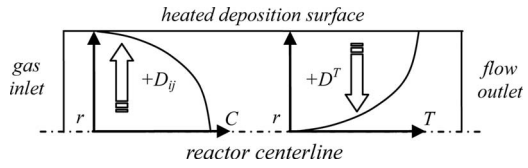

Fig. 1 Schematic of horizontal tube flow chemical vapor deposition reactor for carbon nanotube synthesis

$$\nabla \cdot (\boldsymbol{j}_i + \rho\omega_i \boldsymbol{u}) = R_i, \quad \boldsymbol{j}_i = -D_i^T \nabla \ln T - \rho_i \sum_{j=1}^{n} \tilde{D}_{ij} \boldsymbol{d}_j \tag{4}$$

The reactor geometry used for this investigation is based on the methane deposition work of Ruckenstein and Hu [19]. A schematic of the reactor ($L=0.3$ m, $D=0.02$ m) is presented in Fig. 1, with deposition occurring on iron nanoparticles located on the heated radial surface. Boundary conditions were applied, as specified in Ref. [14].

2.1 Thermal Diffusion Coefficient Calculation. Thermal diffusion coefficients were defined as $k_T=(D_i^T/\rho \text{Đ}_{ij})(x_i x_j/\omega_i \omega_j)$, where $k_T=\alpha_T x_i x_j$ [20]. Combining these two expressions allows D^T to be calculated via the determination of the thermal diffusion factor (α_T), as well as the flow properties already computed by the model. Using the work of Holstein [21], based on the Chapman–Enskog molecular theory of gases [22], α_T can be calculated knowing the species molecular weights and the Lennard-Jones parameters (σ_i, ε_i). Using the complete first approximation, *without* introducing the assumptions that $M_j/M_i \to 0$ and $x_i/x_j \to 0$, α_T can be defined as presented in Eq. (5). Derivations of the components of Eq. (5) are presented in Refs. [21,23]

$$\alpha_T = \frac{1}{6\lambda_{ij}} \left(\frac{S^{(i)} x_i - S^{(j)} x_j}{X_\lambda - Y_\lambda} \right) (6C_{ij}^* - 5) \tag{5}$$

These equations were programmed into COMSOL, which allowed for the direct evaluation of thermal diffusion coefficients, as well as flow dependant parameters, during each iteration. Boundary integration was conducted along the surfaces of the model to ensure that mass and energy were conserved; at most, 0.5% of mass and 1% of energy were unaccounted for within the computational domain. The model geometry was meshed with a prescribed cell size at the deposition surface and the cell size was allowed to expand slightly toward the tube center. The geometry had 626 elements and 14,546 degrees of freedom; further refinement of the mesh yielded no change in model predictions. The UMFPACK direct solver was utilized, and the solution time was 0.75–1.5 h on an Intel Core 2 2.13 GHz CPU with 2 GB of RAM.

3 Results and Discussion

3.1 Validation. Validation of the deposition model, not incorporating thermodiffusion, has been performed previously by the authors [14]. Therefore, validation in this work is confined to verification of the first-order approximation of the thermal diffusion coefficient within the conditions of the CVD reactor. For this the experimental work of Dunlop and Bignell [24] and Ibbs [25], investigating the thermally driven separation in a mixture of H_2 and N_2 was considered. This mixture was chosen because it most closely approximated the molecular size and weight of the two main components of the SWNT deposition model, H_2 and CH_4.

The model predicts the thermophoretic behavior accurately in binary systems with low solute mole fractions, i.e., $x_{\text{solute}} < 0.30$ (Fig. 2(*a*)). However, for cases with near equal mole fractions, the model predicted separation with up to 20% error from the experimental values. Figure 2(*b*) demonstrates that the model predicts accurate gas phase separation over a wide range of thermal conditions. Experimental and model agreement is very good at low temperature ratios, and error increases slightly with larger temperature gradients and solute fractions.

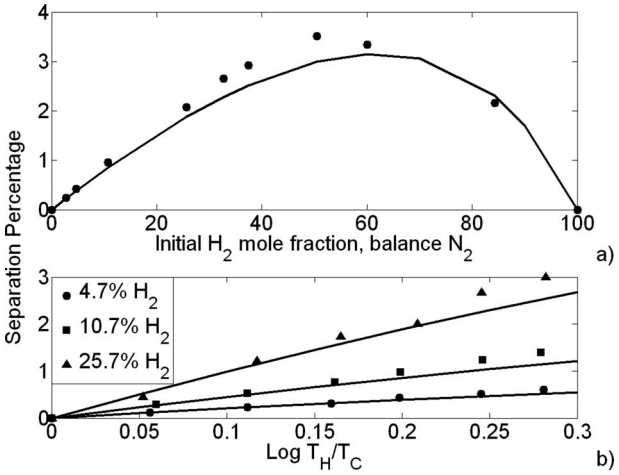

Fig. 2 Percent separation of a binary mixture of H_2 and N_2 (*a*) as a function of initial mole fraction when $T_C=284$ K and $\log_{10}(T_H/T_C)=0.2$; (*b*) presents separation percentage for three mixtures as a function of temperature ratio. In both plots, the data points represent experimental data reported by Ibbs [25] and the curves represent diffusion model predictions.

Due to the nature of the SWNT deposition process being modeled, with the H_2 carrier species making up 80–99% of the reactor feed stream and the low concentrations of the pyrolytic radicals being formed, it is reasonable to consider the system binary with regards to each species and H_2. In each of these trials, the low solute fraction criterion is met and the reactor temperature ratio T_H/T_C is within the validated range (between 1.75 and 2.1 in the cases presented below). Therefore, the complete first-order formulation of α_T will provide sufficient accuracy to analyze the impacts of thermodiffusion on SWNT growth [26].

3.2 Impacts on Nanotube Growth and Deposition Regime. The reactor Reynolds number remained below unity for every trial, and the Prandtl number of the flow varied (with composition and reactor wall temperature) from 0.689 to 0.776. These calculations indicate a small (<3%) thermal entry length. However, a temperature gradient exists for much of the reactor length, due to endothermic-volumetric reactions, driving thermal diffusion.

Using an order of magnitude analysis, an initial estimation of the relative importance of thermal diffusion was determined. Beginning with the species conservation equation, Eq. (4), Hitchman [5] stated that thermodiffusion could be neglected if Eq. (6) is true

$$-\ln\left(\frac{T_{\text{inlet}}}{T_{\text{wall}}}\right) \ll \frac{\text{Sc}}{\text{Pr} \cdot \alpha_T} \tag{6}$$

The ratio of the Schmidt (Sc) to Prandtl number (Pr) is equivalent to the ratio of (energetic) thermal diffusivity to mass diffusivity. By multiplying the denominator by the thermal diffusion factor, this term effectively becomes the ratio of the thermal diffusivity of energy to the thermal diffusivity of mass. In all cases presented in this study, $0.580 \leq -\ln(T_{\text{inlet}}/T_{\text{wall}}) \leq 0.738$ and $1.778 \leq \text{Sc}/(\text{Pr} \cdot \alpha_T) \leq 2.443$, thus, Eq. (6) is not satisfied, suggesting that thermodiffusion may impact SWNT deposition.

A comparison of predicted SWNT growth rates (averaged along the reactor length), with and without thermodiffusion, is presented in Fig. 3. In these trials, the reactor length was 0.3 m and the diameter was 0.02 m. Inlet gases enter at 1 atm and 573 K, having a parabolic laminar velocity profile averaged at 2.227 mm/s. Nanoparticle density was 1×10^{13} particles/m^2 with an active site density of 500 sites/particle [14]. Deposition, as a function of

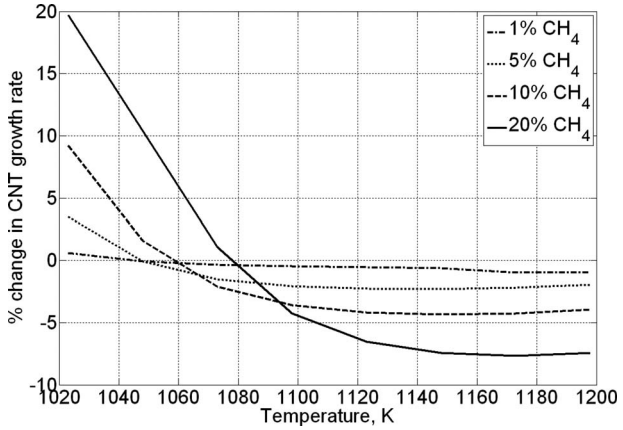

Fig. 3 Percent change in predicted carbon nanotube growth rate (averaged along the reactor length) when the thermophoretic effect is incorporated in the model

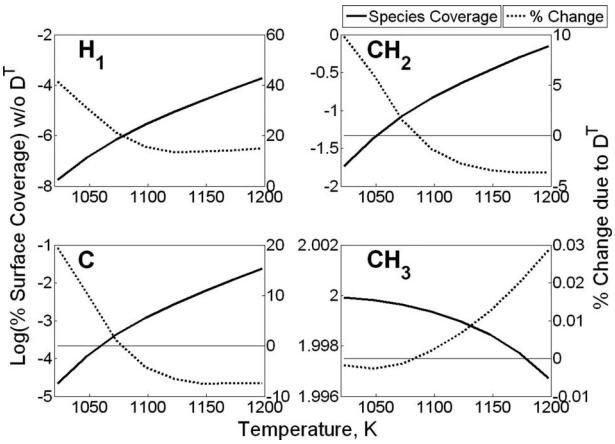

Fig. 4 Percent surface coverage (averaged along reactor length) for a surface bound species as a function of the reactor wall temperature (left-axis). The right *y*-axis presents the percent change in the surface coverage when thermal diffusion is considered. All data are for carbon nanotube deposition with 20% methane.

the reactor wall temperature and inlet concentrations, was studied to examine the change in growth predictions as a result of thermophoretic motion. At low temperatures, thermodiffusion increased the rate of SWNT growth by as much as 20% (dependent on reactor inlet conditions). However, as the reactor temperature increases, thermophoretic motion causes reductions in the predicted growth rate by over 7%.

Analysis of diffusive flux within the reactor volume demonstrates that hydrogen species exhibit negative thermal diffusion (diffusion against the temperature gradient), while hydrocarbon species display positive thermophoretic behavior. This causes the hydrogen species to aggregate near the heated deposition surface while simultaneously causing lower near surface concentrations of hydrocarbons.

For the parameter space studied, the reaction Damköhler number never exceeds 0.0512, indicating that the reaction remains kinetically limited and that the deposition regimes described in Ref. [14] apply. Within the *hydrogen abstraction regime* (low deposition temperatures and high inlet $[CH_4]$), volumetric H_1 (atomic hydrogen) is the limiting reactant; thermophoretic flux drives the reaction faster. However, transition to the hydrocarbon adsorption regime (temperature where there is zero change in Fig. 3 when the limiting reactant becomes volumetric CH_3) shifts to a lower temperature when thermophoretic flux is incorporated. This behavior results in lower deposition rates throughout this regime.

The surface chemistry demonstrates a complex behavior in response to thermal diffusion. Figure 4 presents the % surface coverage (averaged along the reactor length) for four surface bound species (CH_3, CH_2, C, and H_1), calculated without consideration of the thermal diffusion (solid lines, left *y*-axis). The dotted line (right *y*-axis) is the percent change in surface coverage observed when D^T is incorporated in the model.

Over the entire temperature range, concentrations of surface bound H_1 are significantly higher (15–40%) for cases considering thermodiffusion. This is expected as higher concentrations of gas phase H_1 are observed near the surface, and fewer hydrocarbons are available to bind active sites. Surface bound CH_2 and C also behave as predicted. Thermophoretic motion causes these species to have larger surface concentrations (as much as 10% and 20% respectively) at low temperatures, corresponding to increased hydrogen abstraction and growth rates. As the reactor temperature nears the transition point, the percent change declines and becomes negative.

Surface concentrations of CH_3, on the other hand, do not behave as expected. At low temperatures, thermal diffusion induces a small drop in CH_3-bound active sites. This results from reduced concentrations of gas phase CH_3 near the surface and increased rates of hydrogen abstraction, driving higher SWNT growth rates. While this change is very small, CH_3 is the primary surface species [27], so small changes significantly increase active sites available for other chemical species. However, at temperatures above the transition point, CH_3 shows a slight *increase* in surface coverage. This is contrary to the prediction that reduction in gas phase CH_3 concentrations would cause lower concentrations of the surface bound species.

Investigation of the heterogeneous reactions occurring within the reactor suggests that higher concentrations of H_2, coupled with less CH_3 near the surface, causes a relative increase in activation of the hydrocarbon desorption and addition pathways. Comparison of cases that were run with and without thermodiffusion shows that the ratio of hydrocarbon adsorption to desorption declines by 16% for deposition at 1198 K with 20% methane. The result of this new equilibrium condition is that the surface CH_3 coverage increases slightly, but the rate of abstraction decreases, reducing SWNT growth.

4 Conclusions

The Chapman–Enskog molecular theory was used in a reactor-scale model, employing coupled conservation equations with detailed gas phase and surface reaction mechanisms to predict thermophoretic flux during deposition of SWNTs. Diffusion model predictions adequately matched mixture separation experiments previously published in the literature over a wide range of temperatures and molecular weight ratios. Due to the approximately binary nature of this system, The Chapman–Enskog molecular theory (Eq. (5)) is sufficient to describe thermodiffusion in a CVD reactor with gas flow comprised predominantly of one carrier gas (i.e., $x_{solvent} > 0.7$), one precursor gas, and several dilute species.

Analysis of the effects of thermodiffusion within the CVD reactor demonstrated that the temperature gradient driven motion can have large impacts on predicted SWNT growth rates. The degree of impact is heavily dependent on the limiting reaction. Growth rates increased by as much as 20% when the deposition limiting process was dependent on surface reactions with volumetric H_1, and decreased by over 7% when the limiting reaction was CH_3 adsorption. Therefore, thermodiffusion should be considered when studying a SWNT deposition reactor.

Acknowledgment

Financial support from the National Science Foundation and the University of Connecticut Accelerated Masters Program is gratefully acknowledged.

Nomenclature

C = molar concentration (mol/m^3)
C_p = specific heat at constant pressure ($J/kg\,K$)
D = binary diffusion coefficient (m^2/s)
Đ = multicomponent diffusion coefficient (m^2/s)
D^T = thermal diffusion coefficient ($Pa\,s$)
h = enthalpy (J/kg)
j = mass flux ($kg/m^2\,s$)
k = thermal conductivity ($W/m\,K$)
k_T = thermal diffusion ratio
M = molar mass ($kg/kmol$)
p = pressure (Pa)
Q = volumetric heat generation (W/m^3)
R = rate of production ($mol/m^3\,s$ or $mol/m^2\,s$)
T = absolute temperature (K)
u = velocity (m/s)
x = mole fraction

Greek Letters

α_T = thermal diffusion factor
ε = Lennard-Jones potential well depth (J)
η = dynamic viscosity ($Pa\,s$)
ρ = density (kg/m^3)
σ = Lennard-Jones collision diameter (Å)
ω = mass fraction

Subscripts/Superscripts

i, j, k = species
T = thermal property coefficient
* = reduced (dimensionless) value

References

[1] Grew, K. E., and Ibbs, T. L., 1952, *Thermal Diffusion in Gases*, Cambridge University Press, Cambridge, England.
[2] Ferziger, J. H., and Kaper, H. G., 1972, *Mathematical Theory of Transport Processes in Gases*, North-Holland, Amsterdam.
[3] Juza, J., and Cermák, J., 1982, "Phenomenological of the CVD Epitaxial Reactor," J. Electrochem. Soc., **129**, pp. 1627–1634.
[4] Jenkinson, J., and Pollard, R., 1984, "Thermal Diffusion Effects in Chemical Vapor Deposition Reactors," J. Electrochem. Soc., **131**, pp. 2911–2917.
[5] Hitchman, M. L., 1980, "A Consideration of the Effect of the Thermal Boundary Layer on CVD Growth Rates," J. Cryst. Growth, **48**, pp. 394–402.
[6] Finnie, P., Li-Pook-Than, A., Lefebvre, J., and Austing, D. G., 2006, "Optimizing of Methane Cold Wall Chemical Vapor Deposition for the Production of Single Walled Carbon Nanotubes and Devices," Carbon, **44**, pp. 3199–3206.
[7] Jung, Y. J., Wei, B., Vajtai, R., Ajayan, P. M., Homma, Y., Prabhakaran, K., and Ogino, T., 2003, "Mechanism of Selective Growth of Carbon Nanotubes on SiO_2/Si Patterns," Nano Lett., **3**, pp. 561–564.
[8] Takagi, D., Homma, Y., and Kobayashi, Y., 2004, "Selective Growth of Individual Single-Walled Carbon Nanotubes Suspended Between Pillar Structures," Physica E (Amsterdam), **24**, pp. 1–5.
[9] Homma, Y., Kobayashi, Y., Ogino, T., Takagi, D., Ito, R., Jung, Y. J., and Ajayan, P. M., 2003, "Role of Transition Metal Catalysts in Single-Walled Carbon Nanotube Growth in Chemical Vapor Deposition," J. Phys. Chem. B, **107**, pp. 12161–12164.
[10] Murphy, D. B., Carroll, R. W., and Klonowski, J. E., 1997, "Analysis of Products of High-Temperature Pyrolysis of Various Hydrocarbons," Carbon, **35**, pp. 1819–1823.
[11] Dikonimos Makris, Th., Giorgi, R., Lisi, N., Pilloni, L., Salernitano, E., Sarto, F., and Alvisi, M., 2004, "Carbon Nanotube Growth by HFCVD: Effect of the Process Parameters and Catalyst Preparation," Diamond Relat. Mater., **13**, pp. 305–310.
[12] Reilly, P. T. A., and Whitten, W. B., 2006, "The Role of Free Radical Condensates in the Production of Carbon Nanotubes During the Hydrocarbon CVD Process," Carbon, **44**, pp. 1653–1660.
[13] Kwok, K., and Chiu, W. K. S., 2005, "Growth of Carbon Nanotubes by Open-Air Laser-Induced Chemical Vapor Deposition," Carbon, **43**, pp. 437–446.
[14] Lysaght, A. C., and Chiu, W. K. S., 2008, "Modeling of the Carbon Nanotube Chemical Vapor Deposition Process Using Methane and Acetylene Precursor Gases," Nanotechnology, **19**, p. 165607.
[15] Coltrin, M., and Dandy, D. S., 1993, "Analysis of Diamond Growth in Subatmospheric DC Plasma-Gun Reactors," J. Appl. Phys., **74**, p. 5803.
[16] Grujicic, M., Cao, G., and Gersten, B., 2002, "Optimization of the Chemical Vapor Deposition Process for Carbon Nanotubes Fabrication," Appl. Surf. Sci., **199**, pp. 90–106.
[17] Klinke, C., Bonard, J. M., and Kern, K., 2005, "Thermodynamic Calculations on the Catalytic Growth of Multiwall Carbon Nanotubes," Phys. Rev. B, **71**, p. 035403.
[18] Kee, R. J., Coltrin, M. E., and Glarborg, M., 2003, *Chemically Reacting Flow: Theory and Practice*, Wiley, New York.
[19] Ruckenstein, E., and Hu, Y. H., 1998, "Catalytic Preparation of Narrow Pore Size Distribution Mesopourous Carbon," Carbon, **36**, pp. 269–275.
[20] Bird, R. B., Stewart, W. E., and Lightfoot, E. N., 2002, *Transport Phenomena*, 2nd ed., Wiley, New York.
[21] Holstein, W., 1988, "Thermal Diffusion in Metal-Organic Chemical Vapor Deposition," J. Electrochem. Soc., **135**, pp. 1788–1793.
[22] Hirschfelder, J. O., Curtiss, C. F., and Bird, R. B., 1954, *Molecular Theory of Gases and Liquids*, Wiley, New York.
[23] Neufeld, P., Janzen, A., and Aziz, R., 1972, "Empirical Equations to Calculate 16 of the Transport Collision Integrals $\Omega^{(l,s)^*}$ for the Lennard-Jones (12-6) Potential," J. Chem. Phys., **57**, p. 1100.
[24] Dunlop, P., and Bignell, C., 1987, "Diffusion and Thermal Diffusion in Binary Mixtures of Methane with Noble Gases and of Argon with Krypton," Physica A, **145**, pp. 584–598.
[25] Ibbs, T., 1925, "Thermal Diffusion Measurements," Proc. R. Soc. London, Ser. A, **107**, pp. 470–486.
[26] Grujicic, M., Cao, G., and Gersten, B., 2003, "Reactor Length-scale Modeling of Chemical Vapor Deposition of Carbon Nanotubes," J. Mater. Sci., **38**, pp. 1819–1830.
[27] Lysaght, A. C., and Chiu, W. K. S., 2009, "The Role of Surface Species in Chemical Vapor Deposited Carbon Nanotubes," Nanotechnology, **20**, p. 115605.

Analytical Solution for Forced Convection in a Sector Duct Filled With a Porous Medium

C. Y. Wang
Departments of Mathematics and Mechanical Engineering,
Michigan State University,
East Lansing, MI 48824
e-mail: cywang@mth.msu.edu

The fully developed viscous flow through a sector duct filled with a porous medium is studied. The Darcy–Brinkman and energy equations are solved analytically by series expansions in Bessel functions of the first kind. The problem is governed by a porous medium parameter s, which is proportional to the inverse square root of the permeability. For large s there exists a boundary layer on the walls, and the resistance increases greatly. The Nusselt number for the H1 heat transfer problem also increases. If the apex angle is acute, the local velocity and heat transfer are very low. If the apex angle is obtuse, the local shear and heat transfer are large. Tables for the friction factor-Reynolds number products and Nusselt numbers are determined for various s and apex angles. [DOI: 10.1115/1.4001102]

Keywords: Darcy–Brinkman, porous, sector duct, fully developed flow, heat transfer

1 Introduction

The study of convection in porous media is important in many practical situations including ground water movement, packed bed reactors, thermal insulation, oil and gas recovery, etc. [1,2]. Analytical solution for fully developed flow and heat transfer in a parallel plate channel was first solved by Kaviany [3] and Nakayama et al. [4]. Circular and annular ducts were first solved by Poulikakos and Kazmierczak [5], and Parang and Keyhani [6]. More difficult two dimensional problems are governed by partial differential equations. Haji-Sheikh [7], and Hooman and Merrikh [8] used infinite series to study the flow in a rectangular duct. Recently Wang [9] used a mixture of coordinates to analyze the flow through a semicircular duct.

The aim of the present paper is to present a rare analytic solution, i.e., forced flow through a circular sector duct. Sector ducts model ducts covering the corner edges or circular ducts with internal longitudinal fins. The study will also shed light on the flow and heat transfer characteristics near narrow crevices and sharp fins. The results will be compared with the semicircular duct as a special case.

2 Formulation

Figure 1 shows the cross section of a sector duct, where the radius is L and the opening apex angle is 2β. The cylindrical coordinates (r', θ) are placed at the vertex, with $\theta=0$ being the symmetry line. For parallel flow, the Darcy–Brinkman equation is reduced to

$$\mu_e \nabla^2 w' - \frac{\mu}{K} w' = -G \tag{1}$$

where μ_e is the effective viscosity of the matrix, $w'(r', \theta)$ is the locally averaged velocity in the longitudinal z'-direction, μ is the viscosity of the fluid, K is the permeability, and $G=-p_x$ is the constant applied pressure gradient. Normalizing the lengths by L and velocities by $W=GL^2/\mu_e$ and dropping the primes, Eq. (1) becomes

$$\nabla^2 w - s^2 w = -1 \tag{2}$$

where $s=L\sqrt{\mu/\mu_e K}$ is the porous medium parameter. The boundary condition is that $w=0$ on the walls of the duct. If $s=0$ Eq. (2) reduces to the pure viscous flow limit. If $s\to\infty$ and $w\sim s^{-2}$, then Eq. (2) becomes the Darcy equation. Let $A=\beta$ be the cross sectional area (normalized by L^2) and $P=2(1+\beta)$ be its normalized perimeter. The average velocity is then

$$V = \frac{2}{\beta}\int_0^\beta \int_0^1 w r dr d\theta \tag{3}$$

Define a hydraulic diameter $D_h=4AL/P=2\beta L/(1+\beta)$. The friction factor-Reynolds number product is

$$f\,\mathrm{Re} = \frac{GD_h^2}{2\mu_e VW} = \frac{2\beta^2}{(1+\beta)^2 V} \tag{4}$$

For constant heat flux q on the boundary, or the H1 problem, a heat balance on an elemental segment of the duct gives

$$VW\frac{\partial T^*}{\partial z} = \frac{qP}{\rho c_p A} \tag{5}$$

where T^* is the temperature, ρ is the density, and c_p is the specific heat of the fluid. The energy equation is

$$\frac{k}{\rho c_p L^2}\nabla^2 T^* = \frac{wW}{L}\frac{\partial T^*}{\partial z} \tag{6}$$

For the H1 problem, the walls are highly conductive along the perimeter [10]. The temperature can be expressed as a combination of surface temperature $T_s^*(z)$ and its deviation in the interior

$$T^*(r,\theta,z) = T_s^*(z) + \frac{qLP}{kVA}\tau(r,\theta) \tag{7}$$

where k is the thermal conductivity and τ is a nondimensional temperature function, which is zero on the walls. Since

$$\frac{\partial T^*}{\partial z} = \frac{dT_s^*}{dz} \tag{8}$$

Equations (5)–(7) yield

$$\nabla^2 \tau = w \tag{9}$$

After τ is obtained, the mean temperature is

$$T_m^*(z) = \frac{2}{VA}\int_0^\beta \int_0^1 w T^* r dr d\theta = T_s^*(z) + \frac{2qLP}{kA^2V^2}S \tag{10}$$

where

$$S = \int_0^\beta \int_0^1 w\tau r dr d\theta \tag{11}$$

Using Eq. (11) the Nusselt number is

$$\mathrm{Nu} = \frac{qD_h}{(T_s^* - T_m^*)k} = \frac{\beta^3 V^2}{2(1+\beta)^2|S|} \tag{12}$$

3 The Solution

First we solve for the flow field. Let

Contributed by the Heat Transfer Division of ASME for publication in the JOURNAL OF HEAT TRANSFER. Manuscript received August 25, 2009; final manuscript received January 6, 2010; published online June 4, 2010. Assoc. Editor: Sung Jin Kim.

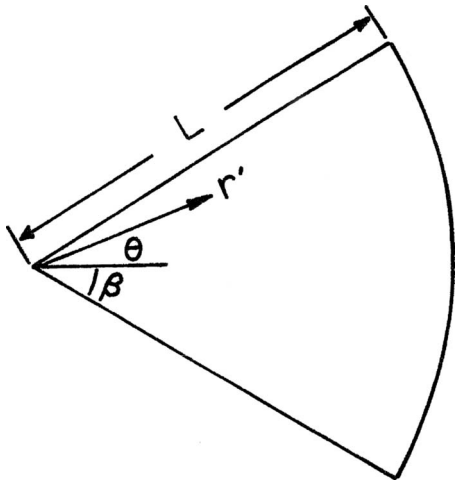

Fig. 1 Cross section of the sector duct

$$w = \sum_{n=1}^{\infty} a_n \cos(\alpha_n \theta) f_n(r) \tag{13}$$

where $\alpha_n = (n-1/2)\pi/\beta$ and w satisfies the no-slip on the flat sides. The coefficient a_n is from the expansion of unity in a Fourier series

$$1 = \sum_{n=1}^{\infty} a_n \cos(\alpha_n \theta), \quad a_n = \frac{4(-1)^{n+1}}{(2n-1)\pi} \tag{14}$$

Equation (2) reduces to the ordinary differential equation

$$f_n''(r) + \frac{1}{r} f_n' - \frac{\alpha_n^2}{r^2} f_n - s^2 f_n = -1 \tag{15}$$

The homogeneous solution to Eq. (15) is in terms of modified Bessel functions $I_\alpha(sr)$ and $K_\alpha(sr)$, which have neither zeros nor orthogonality properties for real arguments.

Let us instead expand f_n in terms of Bessel functions of the first kind

$$f_n = \sum_{i=1}^{\infty} A_{ni} J_{\alpha_n}(l_{ni} r) \tag{16}$$

where l_i are the zeros of $J_{\alpha_n}(l_i) = 0$. Now w satisfies the no-slip conditions on all walls. Using Bessel's equation, Eq. (15) becomes

$$\sum_{i=1}^{\infty} A_{ni}(s^2 + l_{ni}^2) J_{\alpha_n}(l_{ni} r) = -1 \tag{17}$$

Multiplying Eq. (17) by $rJ_\alpha(l_{ni}r)$ and integrating from 0 to 1, the orthogonality conditions then yield

$$A_{ni} = \frac{-2F_{ni}}{(s^2 + l_{ni}^2) J_{\alpha_n - 1}(l_{ni}) J_{\alpha_n + 1}(l_{ni})} \tag{18}$$

where

$$F_{ni} = \int_0^1 r J_{\alpha_n}(l_{ni} r) dr \tag{19}$$

is an important integral discussed in the Appendix. The solution for the velocity is thus

$$w = \sum_n \sum_i a_n A_{ni} \cos(\alpha_n \theta) J_{\alpha_n}(l_{ni} r) \tag{20}$$

The total flow rate is simply

$$Q = \beta V = 2 \int_0^{\beta} \int_0^1 w r dr d\theta = \sum_n \sum_i \frac{2(-1)^{n+1}}{\alpha_n} a_n A_{ni} F_{ni} \tag{21}$$

For the heat transfer problem, Eqs. (2) and (9) give

$$\nabla^2 \tau = \frac{1}{s^2}(\nabla^2 w + 1) \tag{22}$$

Using Eqs. (14) and (22) gives

$$\nabla^2(\tau - w/s^2) = \sum_n a_n \cos(\alpha_n \theta)/s^2 \tag{23}$$

Let

$$\tau - w/s^2 = \sum_n a_n \cos(\alpha_n \theta) g_n(r)/s^2 \tag{24}$$

Since both τ and w are zero on $r=1$, we find

$$g_n(r) = \frac{1}{(4 - \alpha_n^2)}(r^2 - r^{\alpha_n}) \tag{25}$$

provided that $\alpha_n \neq 2$ or $\beta \neq \pi/4, 3\pi/4$. If $\alpha_n = 2$, then the solution is $g_n = r^2 \ln r/4$. Thus, the temperature field is

$$\tau = \frac{1}{s^2}\left(w + \sum_n a_n \cos(\alpha_n \theta) g_n(r)\right) = \frac{1}{s^2} \sum_n a_n \cos(\alpha_n \theta)[f_n(r) + g_n(r)] \tag{26}$$

Equation (11) gives

$$S = \int_0^1 \int_0^{\beta} w \tau d\theta r dr = \frac{\beta}{2s^2} \sum_n a_n^2 \int_0^1 f_n(f_n + g_n) r dr \tag{27}$$

But g_n can be expanded as

$$g_n = \sum_i B_{ni} J_{\alpha_n}(l_{ni} r), \quad B_{ni} = \frac{-2C_{ni}}{J_{\alpha_n - 1}(l_{ni}) J_{\alpha_n + 1}(l_{ni})} \tag{28}$$

where

$$C_{ni} = \int_0^1 g_n(r) J_{\alpha_n}(l_{ni} r) r dr \tag{29}$$

is tabulated in the Appendix. Using orthogonality and Eqs. (16) and (28), Eq. (27) becomes

$$S = \frac{\beta}{2s^2} \sum_n \sum_i a_n^2 A_{ni}[C_{ni} - J_{\alpha_n - 1}(l_{ni}) J_{\alpha_n + 1}(l_{ni}) A_{ni}/2] \tag{30}$$

Then Eqs. (4) and (21) give f Re, and Eqs. (12) and (A1) give the Nusselt number. Usually, taking 30 terms in the series is adequate for four figure accuracy.

4 Results and Discussions

Table 1 shows the computed results using our formulas.

These results compare well with those of the semicircular duct obtained by a completely different method [9] (for $\beta = \pi/2$), where the results are 16.78 (4.115), 39.95 (4.592), and 106 (5.280) for $s = 1$, 5, and 10, respectively. On the other hand, our formulas are singular in the pure viscous flow limit, where $s = 0$. Without going through the necessary asymptotic expansions for small s, we note in Ref. [9] that the error of f Re and Nu for small s is of order s^2, and we can compare our $s = 0.1$ results with the $s = 0$ results with about 1% error. From Refs. [11,12,10] we find that the pure viscous flow ($s = 0$) through a sector duct is 14.171 (3.479), 15.200 (3.906), and 15.767 (4.089) for $\beta = \pi/6$, $\pi/3$, and $\pi/2$, respectively. (For a semicircular duct, a *closed form* solution for pure viscous flow is given in Ref. [9].) These confirm our values. From Table 1 we conclude that as the porous media factor

Table 1 *f* Re and Nu (in parenthesis) for various porous media parameters *s* and half vertex angles β

	s					
β	0.1	1	2.5	5	7.5	10
$\pi/6$	14.173(3.477)	14.499(3.485)	16.215(3.529)	22.216(3.668)	31.883(3.859)	44.939(4.069)
$\pi/4$	14.773(3.743)	15.300(3.756)	18.065(3.821)	27.673(4.021)	43.037(4.276)	63.710(4.536)
$\pi/3$	15.207(3.904)	15.914(3.923)	19.620(4.011)	32.419(4.267)	52.794(4.569)	80.208(4.858)
$\pi/2$	15.777(4.088)	16.779(4.115)	22.014(4.245)	39.942(4.590)	68.349(4.954)	106.59(5.276)
$3\pi/4$	16.242(4.218)	17.561(4.256)	24.418(4.436)	47.730(4.865)	84.570(5.277)	134.24(5.619)
π	16.486(4.285)	18.022(4.333)	25.990(4.544)	52.968(5.022)	95.570(5.457)	153.00(5.814)

increases, Nu increases slightly but *f* Re increases greatly. As the apex angle increases, both *f* Re and Nu increase slightly.

Typical velocity and temperature distributions for low *s* are almost parabolic, contained by the sector boundary, as those of pure viscous flow. The results are different for large *s*. The velocity rises sharply in a boundary layer near the wall, and is almost flat in the interior (Fig. 2(*a*)). The temperature profile, however, does not show such boundary layer character (Fig. 2(*b*)). This is probably the reason for the sharp rise in *f* Re but not Nu as *s* is increased.

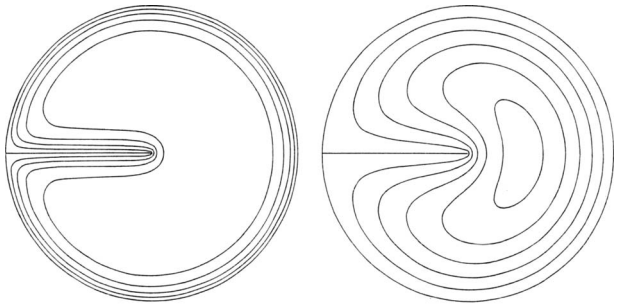

Fig. 2 The case when $s=10$ and $\beta=\pi$: (*a*) constant velocity lines $\Delta w=0.002$; (*b*) constant temperature lines $\Delta\tau=-0.00025$

Let us consider the singularity near the apex (origin). For *r* much smaller than $1/s$, Eq. (2) reduces to the Laplace equation. The solution for *w*, which is bounded at the origin, is proportional to $r^{\lambda}\cos(\lambda\theta)$ $(\lambda\geq 0)$. In order to satisfy no-slip on the straight walls, $\lambda=(n-1/2)\pi/\beta$. The lowest (dominant) term is $n=1$ or $w\sim r^{\pi/(2\beta)}\cos[\pi\theta/(2\beta)]$. This shows *w* is zero at the apex. Form the velocity the shear stress is found to be proportional to $r^{\pi/(2\beta)-1}$, which is zero at the apex if $\beta<\pi/2$, and is singular if $\beta>\pi/2$. Thus for an acute angle the velocity is very low near the apex (both velocity and shear are near zero there). For an obtuse angle (as in Fig. 2(*a*)) infinite shear occur near the origin. Similar analysis shows that the temperature has the same characteristics. Thus the addition of fins has definite advantages in terms of heat and mass transfer.

Table 2 The integral F_{ni}

	α_n							
i	0	1	2	3	5	10	20	50
1	0.2159	0.1795	0.1520	0.1319	0.1048	0.0702	0.0431	0.0205
2	−0.0616	−0.0233	−0.0058	0.0034	0.0119	0.0165	0.0148	0.0093
3	0.0314	0.0344	0.0354	0.0354	0.0342	0.0297	0.0228	0.0135
4	−0.0197	−0.0108	−0.0051	−0.0011	0.0037	0.0084	0.0096	0.0075
5	0.0138	0.0157	0.0168	0.0175	0.0180	0.0176	0.0153	0.0104
6	−0.0104	−0.0066	−0.0038	−0.0017	0.0013	0.0049	0.0068	0.0061
7	0.0082	0.0093	0.0101	0.0107	0.0114	0.0119	0.0112	0.0084
8	−0.0066	−0.0046	−0.0029	−0.0016	0.0004	0.0032	0.0050	0.0051
9	0.0055	0.0063	0.0069	0.0073	0.0080	0.0087	0.0087	0.0071
10	−0.0047	−0.0034	−0.0023	−0.0014	0.0000	0.0022	0.0039	0.0044

Table 3 The integral C_{ni}

	α_n					
i	0	1	2	5	10	20
1	−0.03733	−0.01223	−0.00576	−0.00136	−0.00033	−0.00007
2	0.00202	0.00047	0.00008	−0.00008	−0.00005	−0.00002
3	−0.00042	−0.00033	−0.00026	−0.00014	−0.00006	−0.00002
4	0.00042	0.00006	0.00002	−0.00001	−0.00001	−0.00001
5	−0.00006	−0.00006	−0.00005	−0.00004	−0.00002	−0.00001
6	0.00003	0.00002	0.00001	−0.00000	−0.00000	−0.00000
7	−0.00002	−0.00002	−0.00002	−0.00001	−0.00001	−0.00000
8	0.00001	0.00001	0.00000	−0.00000	−0.00000	−0.00000
9	−0.00001	−0.00001	−0.00001	−0.00001	−0.00000	−0.00000
10	0.00001	0.00000	0.00000	−0.00000	−0.00000	−0.00000

In conclusion, a rare analytic solution for the porous media flow in a sector duct is presented. The solution not only describes the fundamental transport processes but also serves as a benchmark for numerical solutions for more complicated situations.

Appendix

The integrals F_{ni} and C_{ni} can be expressed in terms of a sum. These integrals are of the form [13]

$$\int_0^1 r^{\delta} J_{\alpha}(lr)dr = \frac{\Gamma\left(\frac{\alpha+\delta+1}{2}\right)}{l\Gamma\left(\frac{\alpha-\delta+1}{2}\right)} \sum_{k=0}^{\infty} \frac{(\alpha+2k+1)\Gamma\left(\frac{\alpha-\delta+1}{2}+k\right)}{\Gamma\left(\frac{\alpha+\delta+3}{2}+k\right)} J_{\alpha+2k+1}(l) \tag{A1}$$

and can be evaluated using the sum. However, it is much easier to integrate F_{ni} and C_{ni} numerically by quadratures. They are tabulated as follows (see Tables 2 and 3). For given β and n, the value of α_n is found, and F_{ni} and C_{ni} are interpolated.

We see that both F_{ni} and C_{ni} decrease to zero as α_n or i becomes large.

References

[1] Kaviany, M., 1991, *Principles of Heat Transfer in Porous Media*, Springer, New York.

[2] Nield, D. A., and Bejan, A., 1999, *Convection in Porous Media*, 2nd ed., Springer, New York.

[3] Kaviany, M., 1985, "Laminar Flow Through a Porous Channel Bounded by Isothermal Parallel Plates," Int. J. Heat Mass Transfer, **28**, pp. 851–858.

[4] Nakayama, A., Koyama, H., and Kuwahara, F., 1988, "An Analysis on Forced Convection in a Channel Filled With a Brinkman-Darcy Porous Medium: Exact and Approximate Solutions," Waerme- Stoffuebertrag., **23**, pp. 291–295.

[5] Poulikakos, D., and Kazmierczak, M., 1987, "Forced Convection in a Duct Partially Filled With a Porous Material," ASME J. Heat Transfer, **109**, pp. 653–662.

[6] Parang, M., and Keyhani, M., 1987, "Boundary Effects in Laminar Mixed Convection Flow Through an Annular Porous Medium," ASME J. Heat Transfer, **109**, pp. 1039–1041.

[7] Haji-Sheikh, A., 2006, "Fully Developed Heat Transfer to Fluid Flow in Rectangular Passages Filled With Porous Materials," ASME J. Heat Transfer, **128**, pp. 550–556.

[8] Hooman, K., and Merrikh, A. A., 2006, "Analytical Solution of Forced Convection in a Duct of Rectangular Cross Section Saturated by a Porous Medium," ASME J. Heat Transfer, **128**, pp. 596–600.

[9] Wang, C. Y., 2008, "Analytical Solution for Forced Convection in a Semi-Circular Channel Filled With a Porous Medium," Transp. Porous Media, **73**, pp. 369–378.

[10] Shah, R. K., and London, A. L., 1978, *Laminar Flow Forced Convection in Ducts*, Academic, New York.

[11] Eckert, E. R. G., Irvine, T. F., and Yen, J. T., 1958, "Local Laminar Heat Transfer in Wedge Shaped Passages," Trans. ASME, **80**, pp. 1433–1438.

[12] Sparrow, E. M., and Haji-Sheikh, A., 1965, "Laminar Heat Transfer and Pressure Drop in Isosceles, Triangular, Right Triangular and Circular Sector Ducts," ASME J. Heat Transfer, **87**, pp. 426–427.

[13] Abramowitz, M., and Stegun, I. A., 1965, *Handbook of Mathematical Functions*, Dover, New York.

Transient Temperature Data Analysis for a Supersonic Flight Test

Niranjan Sahoo
Associate Professor
e-mail: shock@iitg.ernet.in

Ravi Kumar Peetala
Research Scholar
e-mail: ravi_peetala@yahoo.co.in

Department of Mechanical Engineering,
Indian Institute of Technology Guwahati,
Guwahati 781 039, India

Determination of transient surface heat flux from the temperature data is one of the traditional techniques applied in many engineering applications. With respect to high speed flight experiments, the time scale of measured temperature data is usually very small (~ms). So, one-dimensional heat conduction analysis is expensively used to infer surface heating rates on the body. For an analytical modeling, it is necessary to obtain a closed form solution from experimentally measured temperature data. In this paper, a temperature data obtained from a nickel film sensor during a supersonic flight test is considered for analysis. Three different curve fitting techniques are used to recover the temperature history of real time flight, namely, piecewise linear fit, polynomial fitting, and cubic-spline method. A one-dimensional transient heat transfer modeling is used to infer surface heating rates from the closed form temperature solutions. Results obtained from these analysis are compared and it is seen that peak surface heat flux values match very closely for polynomial and cubic-spline fitting of temperature data. But, the piecewise linear fit of temperature data underpredicts the peak surface heat flux value by four times from its counterparts. [DOI: 10.1115/1.4001128]

Keywords: surface heat flux, semi-infinite analysis, thin film approximation, inverse analysis

1 Introduction

Transient heat transfer phenomena plays an important role in many industrial and environmental problems. As a matter of fact, there is no direct method by which the heating rates can be measured during a process. Rather, transient temperatures are obtained by various types of temperature sensors, and then, heating rates are predicted from temperature data. In the open literatures, various temperature measurement techniques, such as thermocouples, liquid crystal gauges, infrared thermography, etc., have been discussed. Most of these measurements are performed on turbine blades/rotors in wind tunnels/blow down facilities to study wake interactions, growth of boundary layers, and turbulent intensities [1–5].

With respect to the high speed flow environment, convective surface heat transfer measurements play a vital role to infer various controlling parameters. The major applications include the design of a thermal protection system for aerodynamic surfaces [6–9] and the study of boundary layer transition [10,11]. For high speed flights, the most popular method of surface temperature measurements is the film type metal resistances (called as sensing element) mounted on the insulating surfaces (i.e., substrate). The sensing element is usually platinum/nickel, and the substrate material is MACOR/quartz [12]. In order to infer the surface heating rates from the temperature data, a one-dimensional heat conduction model is widely used mainly because of the fact that the time scale of the measurement of the experimental signal is very small (~few milliseconds).

The time-dependent analysis of temperature is based on the fact that the sensor made out of conducting material (medium 1) is mounted on an insulating surface (medium 2), as shown in Fig. 1. The basic one-dimensional equations solved for the case of step function input of heat transfer are given by [12]

$$\frac{\partial^2 T_1}{\partial x^2} = \left(\frac{\rho_1 c_1}{k_1}\right)\frac{\partial T_1}{\partial t} \tag{1}$$

$$\frac{\partial^2 T_2}{\partial x^2} = \left(\frac{\rho_2 c_2}{k_2}\right)\frac{\partial T_2}{\partial t} \tag{2}$$

where the temperature (T) is measured along the depth (x) of the substrate. Surfaces 1 and 2 refer to the thermal sensor and backing material (substrate), respectively, as shown in Fig. 1. If the surface heat transfer is $\dot{q}_S(t)$, then

$$-k_1\frac{\partial T_1}{\partial x} = \dot{q}_S \quad \text{at} \quad x = 0 \tag{3}$$

The reduction in surface heating rates from the temperature data is based on a semi-infinite/thin film concept and thick film approximation/inverse heat conduction analysis [13]. In most of the previous works [7–9], the surface heating rates were inferred from the transient temperature data measured during a short time scale (~few milliseconds). The analysis was mainly based on a one-dimensional heat conduction model with semi-infinite principle because the effect of lateral conduction and heat penetration into the surface becomes insignificant during a short time period. When the time scale of the temperature measurement becomes higher, the thickness of the sensing element needs to be considered. The present work is aimed in analyzing the transient temperature data to infer surface heating rates for a supersonic flight data [14,15]. The temperature data were recorded for 10 s from a nickel film sensor (1 μm thick) mounted on a cylindrical quartz substrate (2 mm in diameter and 4 mm in length). The temperature and Mach number history for the flight experiment is shown in Figs. 2(*a*) and 2(*b*). As seen from this figure, the flight reaches supersonic speeds at 0.566 s after initial firing, and remains at supersonic speeds till 10 s. With the gauge-substrate (nickel-quartz) system, surface heating rates are predicted with semi-infinite/thin film analysis and thick film approximation for a one-dimensional model. Then, the inferred surface heating rates obtained from various methods are compared with respect to baseline heat transfer modelling (i.e., semi-infinite principle). For all the methods, the experimental temperature data are discretized for developing analytical schemes for heat transfer analysis.

2 Semi-Infinite and Thin-Film Gauges Analysis

Heat transfer data can be inferred from the temperature measurements by modeling the substrate as a semi-infinite one-dimensional medium (Fig. 3(*a*)). However, the assumption holds good only for short time scales, low thermal conductivity of the substrate, high thermal diffusivity, and deep substrates [16,17]. Again, the medium can be considered semi-infinite, as the thermal penetration distance during experimental run-times is small compared with the linear dimension of the gauge. The system shown in Fig. 3(*a*), can be modeled in the form of a strip, in which the surfaces are well-insulated from surroundings, and the heat flow is possible only in one direction (i.e., along the depth of substrate). There is no lateral heat conduction through the substrate, and that heat is conducted only in the direction normal to the surface. Thus, the temperature rise of the substrate at the infinity is zero.

Contributed by the Heat Transfer Division of ASME for publication in the JOURNAL OF HEAT TRANSFER. Manuscript received October 26, 2009; final manuscript received January 7, 2010; published online June 9, 2010. Assoc. Editor: He-Ping Tan.

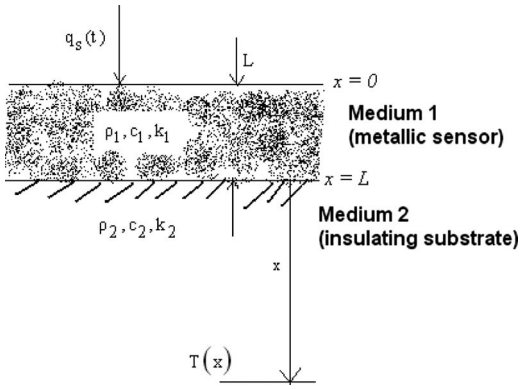

Fig. 1 Schematic representation of one-dimensional heat conduction model

In the thin film gauge analysis, it is assumed that the thickness of the film is very small and the rise in rear surface temperature of the film is equal to the rate of rise in mean temperatures (Fig. 3(*b*)). Also, the substrate material is a perfect insulator, i.e., no heat losses at the back surface of the film.

The physical model applied to both methods assumes the fact that the sensor is mounted on a semi-infinite substrate composed of different materials. The instantaneous temperature $T_2(t)$ is measured at $x=L$, and it is desired to calculate the surface temperature and heat flux at $x=0$. For the semi-infinite body extending from $x=L$ to $x\to\infty$, the conditions at both the boundaries are known, i.e., $x=L$, $T_2=T_2(L)$, $(\partial T_2/\partial x)=0$, and $x\to\infty$; $T_2=T_0$. When the thermal properties of the substrate are constant and the time-dependent solution of surface heating rates is given by the convolution integral [12]

$$q_L(t)=\sqrt{\frac{\rho_2 c_2 k_2}{\pi}}\left[\frac{T(t)}{\sqrt{t}}+\frac{1}{2}\int_0^t\frac{T(t)-T(\tau)}{(t-\tau)}d\tau\right] \tag{4}$$

For the quartz substrate, the density, specific heat, and thermal conductivity are taken as $\rho_2=2200$ kg/m^3; $c_2=670$ J/kg K; $k_2=1.4$ W/m K. Since, the thickness of the film is very small and the same heat flux must leave the substrate, the surface heat flux at $x=0$ can be taken as $q_L(t)=q_S(t)$. Equation (4) is the most convenient form of temperature data analysis when the heat transfer rate is not constant. However, there is a singularity in the integral term at $t=\tau$ that introduces errors in heat flux estimation. The errors are larger when the experimental time scale is small. In many practical cases, the function $T(\tau)$ cannot be described by a simple expression. So, it is necessary to perform numerical integration by discretizing temperature data.

If the interface temperature between successive times is assumed to vary linearly with time, then the piecewise linear function can be assumed for temperature data [12,16]

$$\{T_2(\tau)\}_{\text{linear}}=T_2(t_{i-1})+\frac{T_2(t_i)-T_2(t_{i-1})}{\Delta t}(\tau-t_{i-1})$$

$$\text{where}\quad \tau=t_i=i(t/n)=i\Delta t;\quad i=0,1,2,\ldots,n \tag{5}$$

The simplified expression for Eq. (4) is given by

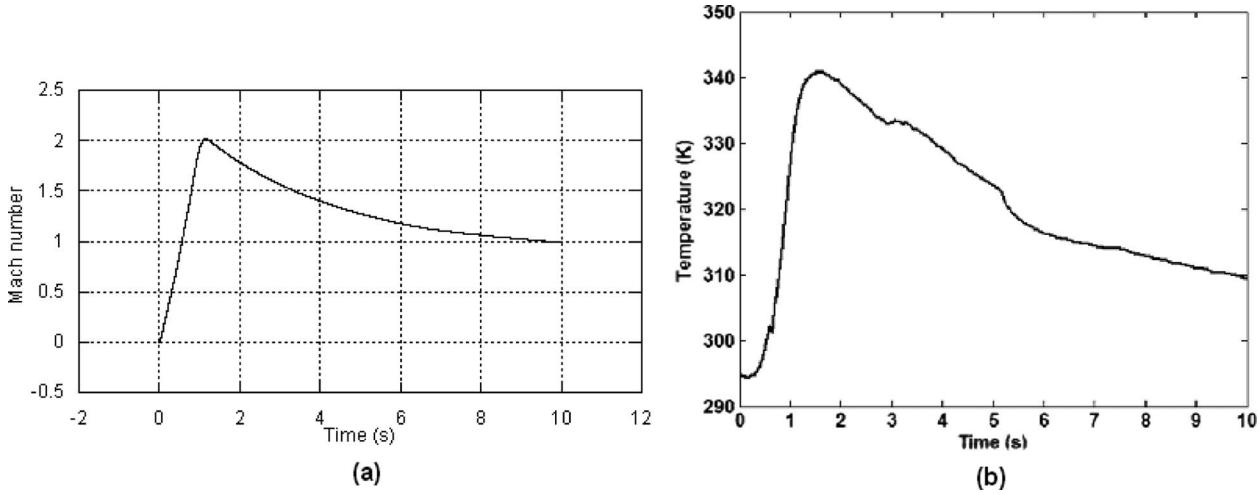

Fig. 2 Supersonic flight data: (*a*) Mach number history; (*b*) temperature history

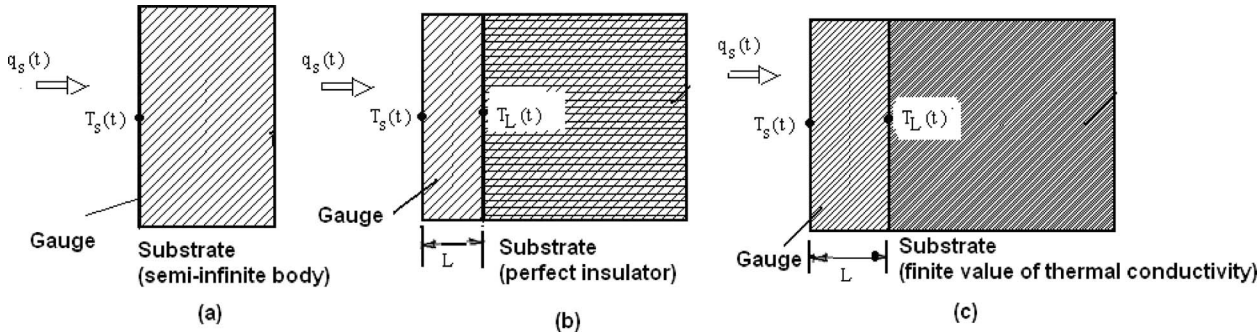

Fig. 3 One-dimensional heat conduction analysis: (*a*) semi-infinite body, (*b*) thin film approximation, and (*c*) inverse analysis

$$\{q_L(t)\}_{\text{linear}} = 2\sqrt{\frac{\rho_2 c_2 k_2}{\pi}}\sum_{i=1}^{n}\frac{T_2(t_i)-T_2(t_{i-1})}{(t_n-t_i)^{1/2}-(t_n-t_{i-1})^{1/2}} \quad (6)$$

Polynomial regression data fitting techniques can also be applied for transient surface temperature response given by the expression

$$\{T_2(t)\}_{\text{poly}} = A_0 + A_1 t + A_2 t^2 + A_3 t^3 + A_4 t^4 + \ldots + A_m t^m = \sum_{i=0}^{m} A_i t^i \quad (7)$$

The corresponding surface heat flux obtained from Eq. (4) is given by the following expression [13]:

$$\{q_L(t)\}_{\text{poly}} = 2\sqrt{\frac{\rho_2 c_2 k_2}{\pi}}\left(\left[A_1\sqrt{t}+\sum_{i=2}^{m} iA_i t^{(2i-1)/2}\right]\left[1+(i-1)!\sum_{n=1}^{i-1}\frac{(-1)^n}{(2n+1)n!(i-1-n)!}\right]\right) \quad (8)$$

With regression analysis and matrix inversion technique, the coefficients $A_0, A_1, A_2, \ldots, A_m$ for Eq. (8) can be obtained [18]. The present analysis deals with a 5-deg polynomial fitting for surface temperature and heat flux.

The polynomial fitting of temperature data allows the calculation of high-order derivatives, but may not reproduce real data points, especially when the time spread of the fitted data is large [13]. Another technique to fit the experimental temperature data is given by the cubic-spline method, and the mathematical expression is given by

$$\{T_2(\tau)\}_{\text{spline}} = a_{1,i} + a_{2,i}(\tau-\tau_i) + \frac{1}{2}a_{3,i}(\tau-\tau_i)^2 + \frac{1}{6}a_{4,i}(\tau-\tau_i)^3$$

$$(\text{for } \tau_i \le \tau \le \tau_{i+1}, i = 1,2,\ldots,M) \quad (9)$$

The constants appearing in this can be determined by the following expressions:

$$a_{1,i} = T_2(\tau_i); \quad a_{2,i} = T_2'(\tau_i); \quad a_{3,i} = T_2''(\tau_i); a_{4,i} = T_2'''(\tau_i) \quad (10)$$

The surface heat flux is then estimated for $M=1,2,\ldots(J-1)$ as

$$\{q_L(t)\}_{\text{spline}} = \left[2\sqrt{\frac{\rho_2 c_2 k_2}{\pi}}\sum_{i=1}^{M-1}\left\{V_i(P_i^{1/2}-R_i^{1/2}) - \frac{W_i}{3}(P_i^{3/2}-R_i^{3/2}) + \frac{a_{4,i}}{10}(P_i^{5/2}-R_i^{5/2})\right\} + 2\sqrt{\frac{\rho_2 c_2 k_2}{\pi}}\left(V_M P_M^{1/2} - \frac{W_M}{3}P_M^{3/2} + \frac{a_{4,M}}{10}P_M^{5/2}\right)\right] \quad (11)$$

where

$$P_i = \tau_{M+1} - \tau_i; \quad R_i = \tau_{M+1} - \tau_{i+1};$$

$$F_i = a_{1,i} + a_{2,i}P_i + \frac{a_{3,i}}{2}P_i^2 + \frac{a_{4,i}}{6}P_i^3$$

$$V_i = \frac{dF_i}{d\tau_{M+1}}; \quad W_i = \frac{d^2F_i}{d\tau_{M+1}^2} \quad (12)$$

3 Inverse Heat Conduction Analysis

The estimation of the surface heat flux becomes more complex when the heat is transferred to the substrate during the experimental time scale of measurement. If the heat received by the sensor from the mainstream flows is largely stored within the gauge while a small portion is transferred to the substrate (as shown in Fig. 3(*c*)), then such problems can be addressed by inverse analysis by considering the thickness of the sensor into consideration. Thus, the interface temperature of the gauge-substrate system can be different from that of the temperature history measured at the surface of the sensor. This approach is similar to that of the semi-infinite/thin film analysis discussed in Sec. 2. First, the transient heating rates corresponding to the interface temperature history is determined, followed by the unknown surface heating flux that causes temperature change on the gauge surface. Thus, after measuring the interface heat flux ($\dot{q}_L$) from the interface temperature at $x=L$, the surface temperature and heat flux are then determined as

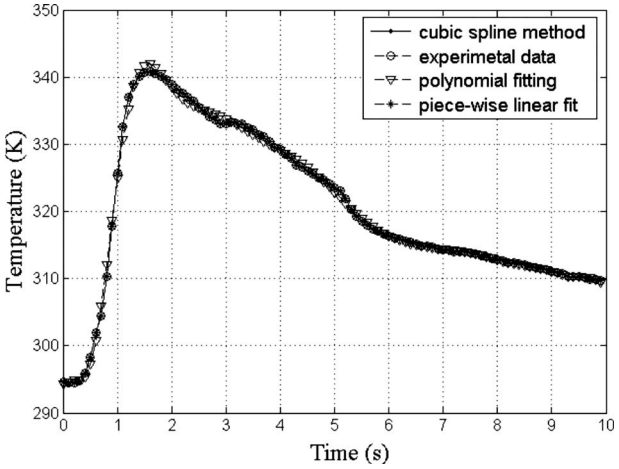

Fig. 4 Comparison of temperature history

$$T_s = T_1(0,t); \quad q_S(0,t) = -k_1\left.\frac{\partial T_1(0,t)}{\partial x}\right|_{x=0} \quad (13)$$

Taler [13] proposed the inverse solution of surface temperature and heat flux, that is

$$T_1(x,t) = T_2(t) + \left[\sum_{n=1}^{\infty}\frac{1}{(2n)!}\frac{(L-x)}{\alpha_1^n}\frac{d^nT_2}{dt^n}\right] + \left(\frac{L-x}{k_1}\right)\left[q_L(t) + \sum_{n=1}^{\infty}\frac{1}{(2n+1)!}\frac{(L-x)^{2n}}{\alpha_1^n}\frac{d^nq_L}{dt^n}\right] \quad (14)$$

and

$$q_s(t) = -k_1\,\partial T_1/\partial x|_{x=0} = q_L(t) + \left[k_1\sum_{n=1}^{\infty}\frac{L^{2n-1}}{(2n-1)!}\frac{1}{\alpha_1^n}\frac{d^nT_2}{dt^n}\right] + \left[\sum_{n=1}^{\infty}\frac{L^{2n}}{(2n)!}\frac{d^nq_L}{dt^n}\frac{1}{\alpha_1^n}\right] \quad (15)$$

where $T_L(t)$ is approximated by a third order spline given by Eq. (9) and $\alpha_1 = k_1/\rho_1 c_1$. For the nickel film senor, the properties are $\rho_1 = 8900$ kg/m^3; $c_1 = 444$ J/kg K; $k_1 = 90.7$ W/m K. The solutions are obtained by truncating Eqs. (14) and (15) to second order derivatives.

4 Results and Discussion

The temperature data (Fig. 2(*b*)) obtained from the flight test are analyzed to infer one-dimensional surface heating rates by the analytical heat transfer modeling techniques discussed in Secs. 2 and 3. First, the temperature data are discretized by various curve fitting techniques: piecewise linear fit (Eq. (5)), polynomial fitting (Eq. (7)), and cubic-spline method (Eq. (9)). The transient temperature distributions obtained from various techniques are compared with the experimental temperature history (Fig. 4). The re-

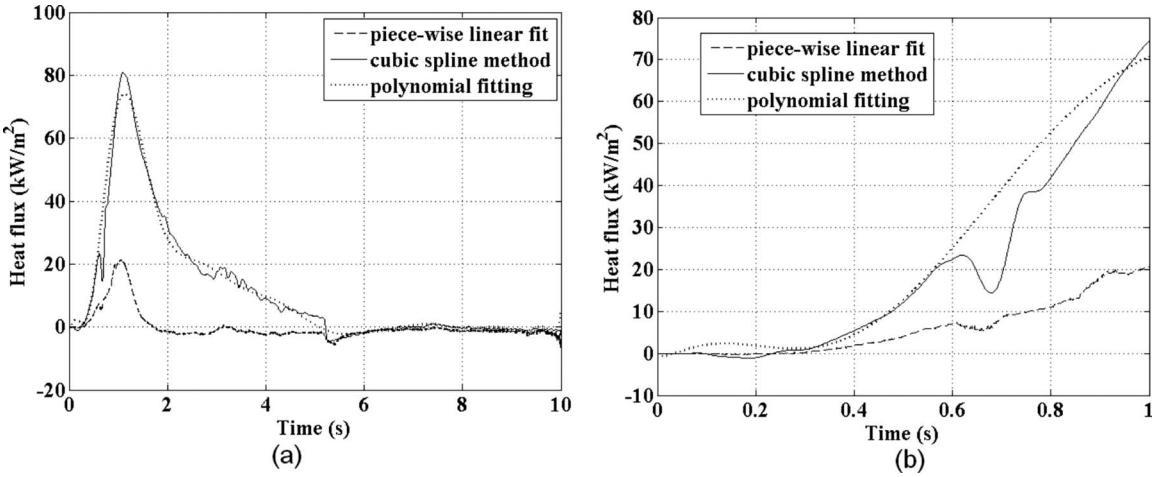

Fig. 5 Comparison of transient surface heat flux: (*a*) time scale=10 s; (*b*) time scale=1 s

sults show a very good recovery of analytical distribution of transient temperature data. The one-dimensional surface heating rates predicted by various methods are shown in Fig. 5. It is seen that the surface heating rates predicted by the polynomial and cubic-spline fitting of temperature data shows a good match, whereas the piecewise linear fitting of temperature data underpredicts the surface heat transfer values. The peak surface heat flux is almost four times lower in the case of the piecewise linear fit of temperature data. However, when the results are plotted for 1 s (Fig. 5(*b*)), it is observed that there is a very good match during the first 0.3 s of the surface heat flux values, for all the analytical temperature distributions discussed above. Thus, it is evident that when the experimental time scale is very small, the piecewise linear fitting of temperature data is a very good approximation because it reduces the computational time with the same accuracy in the analysis. In most of the reported literatures [7–9], this method is widely used to determine the surface heat flux on aerodynamic surface experiencing hypersonic flows. Such types of flows are experienced by the aerodynamic model for a very short duration (~few milliseconds).

When the surface heat flux values are plotted beyond 0.3 s (Fig. 5(*b*)), there is an increasing trend for the temperature data of the cubic-spline and polynomial fitting of temperature data. Since the polynomial fitting of temperature data does not reproduce the real data points exactly, the trend of the surface heat flux is slightly different. The trend of the surface heat flux distribution predicted by the cubic-spline fit of temperature data matches closely with the experimental temperature distribution. So, the third order cubic-spline temperature distribution is a very good approximation for estimating a one-dimensional surface heat flux for longer duration experimental data.

The effect of the sensor thickness is studied by considering the thin film approximation and inverse approach to infer the surface heating rates from the transient temperature data. In both methods, the cubic-spline method is used to discretize the temperature data. With thin film approximation, the surface heat flux is measured by using Eq. (11). In case of inverse analysis, the thickness of the sensor was considered in the analysis (Eq. (15)). The results are plotted in Fig. 6 and it is seen that both the results match very closely. In the present analysis, the thickness of the sensing element (nickel) was 1 μm, which is very small, compared with that of the substrate (quartz of 4 mm thick). Thus, the effect of the sensor thickness on surface heating rates was not felt even at 1 s time scale.

5 Conclusions

A one-dimensional heat conduction model is used to infer transient surface heat flux from the temperature history. The experimental temperature data is obtained from the nickel film sensor

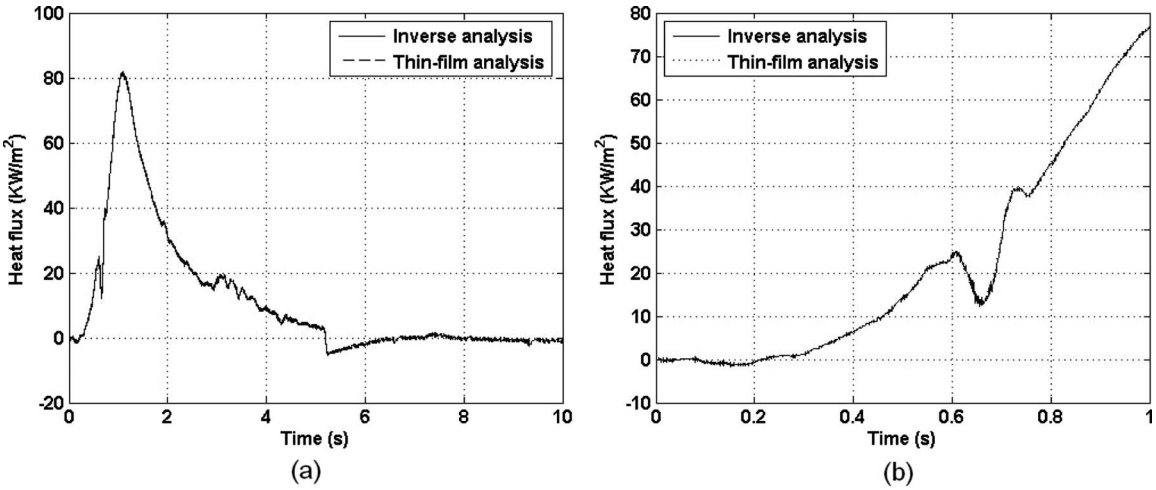

Fig. 6 Inverse analysis and thin film approach for transient surface heat flux: (*a*) time scale=10 s; (*b*) time scale=1 s

for a supersonic flight test. Curve fitting techniques are used to recover the actual experimental signal, and the comparison shows a very good agreement. The temperature data obtained from various techniques are used in one-dimensional heat conduction modeling, and transient surface heat fluxes are predicted. It is seen that during a small experimental time scale (0.3 s), piecewise linear fitting of temperature data predicts surface heat flux values with reasonable accuracy and it also reduces the computational time. However, for a longer duration, the third order cubic-spline method can be a better approximation since it reproduces the experimental data points more closely compared with polynomial fitting of temperature data. Since the thickness of the nickel film (sensor) is very small compared with that of quartz (substrate), its effect was insignificant, and both the thin film approximation and inverse heat conduction results matched more closely.

Acknowledgment

The surface temperature data and Mach number history presented in this paper was obtained during a supersonic flight test conducted at Australia. It was a performed by Sahoo during his academic visit to University of Queensland (UQ), Australia. It was supported by the Department of Science and Technology (DST), Government of India, under the BOYSCAST fellowship program. Also, the authors are very much thankful to Prof. D.J. Mee, Head of Mechanical Engineering, UQ, and the engineers of the Australian Space Research Institute (ASRI) for providing the necessary facilities while conducting the flight test.

Nomenclature

c = specific heat (J/kg K)
k = thermal conductivity (W/m K)
q = heat flux (kW/m^2)
t = time (s)
L = length of sensor (μm)
T = temperature (°C)
x = distance along the depth of substrate (mm)

Symbols

ρ = density (kg/m^3)
τ = dummy time variable

Subscripts

S = surface
0 = ambient conditions

References

[1] Camci, C., and Arts, T., 1991, "Effect of Incidence on Wall Heating Rates and Aerodynamics on a Film-Cooled Transonic Turbine Blade," ASME J. Turbomach., **113**(3), pp. 493–501.
[2] Haldeman, C. W., Dunn, M. G., Barter, J. W., Green, B. R., and Bergholz, R. F., 2005, "Aerodynamic and Heat Flux Measurements With Predictions on a Modern One and One-Half State High Pressure Transonic Turbine," ASME J. Turbomach., **127**(3), pp. 522–531.
[3] Korakianitis, T., Papagiannidis, P., and Vlachopoulos, N. E., 2002, "Unsteady Flow/Quasi-Steady Heat Transfer Computations on a Turbine Rotor and Comparison With Experiments," ASME J. Turbomach., **124**(1), pp. 152–159.
[4] Guo, S. M., Lai, C. C., Jones, T. V., Oldfield, M. L. G., Lock, G. D., and Rawlinson, A. J., 2000, "Influence of Surface Roughness on Heat Transfer and Effectiveness for a Fully Film Cooled Nozzle Guide Vane Measured by Wide Band Liquid Crystals and Direct Heat Flux Gages," ASME J. Turbomach., **122**(4), pp. 709–716.
[5] Wright, L., and Schobeiri, M. T., 1999, "The Effect of Periodic Unsteady Flow on Aerodynamics and Heat Transfer on a Curved Surface," ASME J. Heat Transfer, **121**(1), pp. 22–33.
[6] Wilbur, L. H., 1988, *Re-Entry Aerodynamics (AIAA Education Series)*, AIAA, Washington, DC.
[7] Stewart, D. A., and Chen, Y. K., 1994, "Hypersonic Convective Heat Transfer Over 140-deg Blunt Cones in Different Gases," J. Spacecr. Rockets, **31**(5), pp. 735–743.
[8] Jagadeesh, G., Reddy, N. M., Nagashetty, K., and Reddy, K. P. J., 2000, "Fore Body Convective Hypersonic Heat Transfer Measurements Over Large Angle Blunt Cones," J. Spacecr. Rockets, **37**(1), pp. 137–139.
[9] Sahoo, N., 2003, "Simultaneous Measurement of Aerodynamic Forces and Convective Surface Heat Transfer Rates for Large Angle Blunt Cones in Hypersonic Shock Tunnel," Ph.D. thesis, Department of Aerospace Engineering, Indian Institute of Science, Bangalore, India.
[10] Gurentsov, E. V., Sokolskii, A. A., Shikov, V. K., 1995, "An Experimental Investigation of Heat Transfer in a Highly Cooled Turbulent Boundary Layer of Supersonic Flow of Air—Measurement Procedure and Results," High Temp., **33**(5), pp. 743–752.
[11] Schneider, S. P., 1999, "Flight Data for Boundary-Layer Transition at Hypersonic and Supersonic Speeds," J. Spacecr. Rockets, **36**(1), pp. 8–20.
[12] Schultz, D. L., and Jones, T. V., 1973, "Heat Transfer Measurements in Short-Duration Hypersonic Facilities," Report No. AGARDograph-AG-165.
[13] Taler, J., 1996, "Theory of Transient Experimental Techniques for Surface Heat Transfer," Int. J. Heat Mass Transfer, **39**(17), pp. 3733–3748.
[14] Sahoo, N., 2008, "Boundary-Layer Transient Experiment in a Supersonic Flight," Department of Science and Technology, India, Research Report No. 1.
[15] Kawale, B., Peetala, R., Kulkarni, V., and Sahoo, N., 2009, "Numerical Methods for Determining Convective Heating Rates on Aerodynamic Surfaces," *Proceedings of the Centenary International Conference and Exhibition on Aerospace Engineering*, Indian Institute of Science, Bangalore, India, pp. 99–104.
[16] Cook, W. J., and Felderman, E. J., 1966, "Reduction of Data from Thin-Film Heat-Transfer Gauge: A Concise Numerical Technique," AIAA J., **4**, pp. 561–562.
[17] Renganathan, K., and Turton, R., 1989, "Data Reduction From Thin-Film Heat Gauges in Fluidized Beds," Powder Technol., **59**, pp. 249–254.
[18] Jain, M. K., Iyengar, S. R. K., and Jain, R. K., 2003, *Numerical Methods for Scientific and Engineering Computation*, 4th ed., New Age International, New Delhi, India.